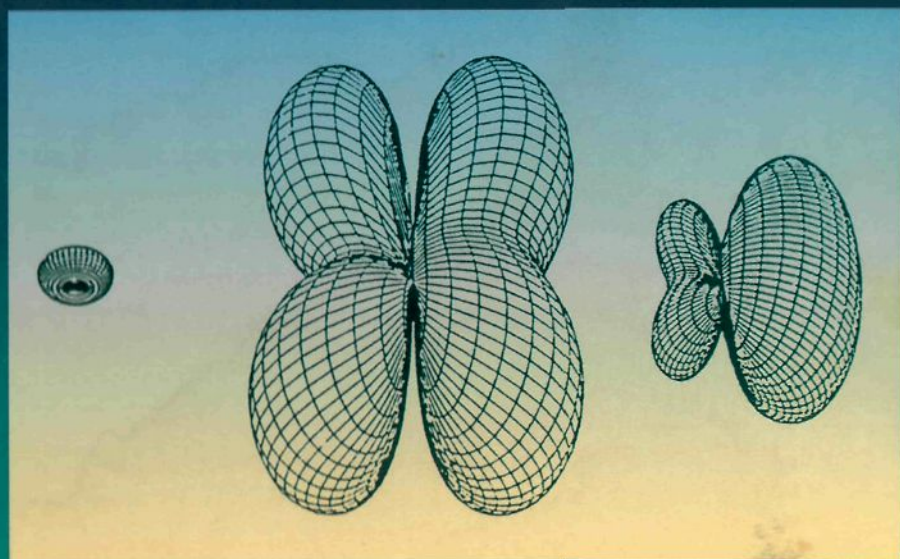# Acoustic Interactions with Submerged Elastic Structures

With a foreword by Hans A. Bethe

Part III: Acoustic Propagation and Scattering, Wavelets and Time Frequency Analysis

Editors

Ardéshir Guran, Adrianus De Hoop, Dieter Guicking & Francesco Mainardi

World Scientific

Acoustic Interactions with Submerged Elastic Structures

SERIES ON STABILITY, VIBRATION AND CONTROL OF SYSTEMS

Series Editors: Ardéshir Guran & Daniel J. Inman

About the Series

Rapid developments in system dynamics and control, areas related to many other topics in applied mathematics, call for comprehensive presentations of current topics. This series contains textbooks, monographs, treatises, conference proceedings and a collection of thematically organized research or pedagogical articles addressing dynamical systems and control.

The material is ideal for a general scientific and engineering readership, and is also mathematically precise enough to be a useful reference for research specialists in mechanics and control, nonlinear dynamics, and in applied mathematics and physics.

Selected Volumes in Series B

Proceedings of the First International Congress on Dynamics and Control of Systems, Chateau Laurier, Ottawa, Canada, 5–7 August 1999
Editors: A. Guran, S. Biswas, L. Cacetta, C. Robach, K. Teo, and T. Vincent

Selected Topics in Structronics and Mechatronic Systems
Editors: A. Belyayev and A. Guran

Selected Volumes in Series A

Vol. 1   Stability Theory of Elastic Rods
Author: T. Atanackovic

Vol. 2   Stability of Gyroscopic Systems
Authors: A. Guran, A. Bajaj, Y. Ishida, G. D'Eleuterio, N. Perkins, and C. Pierre

Vol. 3   Vibration Analysis of Plates by the Superposition Method
Author: Daniel J. Gorman

Vol. 4   Asymptotic Methods in Buckling Theory of Elastic Shells
Authors: P. E. Tovstik and A. L. Smirinov

Vol. 5   Generalized Point Models in Structural Mechanics
Author: I. V. Andronov

Vol. 6   Mathematical Problems of the Control Theory
Author: G. A. Leonov

Vol. 7   Vibrational Mechanics: Theory and Applications to the Problems of Nonlinear Dynamics
Author: Ilya I. Blekhmam

Acoustic Interactions with Submerged Elastic Structures

With a foreword by Hans A. Bethe

Part III: Acoustic Propagation and Scattering, Wavelets and Time Frequency Analysis

A Herbert Überall Festschrift Volume

Editors

Ardéshir Guran
Institute for Structronics, Canada

Adrianus De Hoop
Technical University of Delft, The Netherlands

Dieter Guicking
University of Göttingen, Germany

Francesco Mainardi
University of Bologna, Italy

STABILITY, VIBRATION AND CONTROL OF SYSTEMS

Editor-in-chief: Ardéshir Guran
Co-editor: Daniel J. Inman

Advisory Board

Left to right: Prof. A. Guran, Dr. and Mrs. R. Carbo-Fité, Prof. H. Überall.

Foreword

Interference phenomena led to the discovery of the wave nature of acoustic signals, of light and finally of material particles. Herbert Überall has gone the other way: he has studied the manifold phenomena, caused by interference, in the scattering of acoustic and electromagnetic waves by bodies of different shapes and material properties.

He came to this field from fundamental physics: The bremsstrahlung emitted by electrons of GeV energy when going through a single crystal nearly parallel to a crystal axis is concentrated at relatively low frequency. He calculated its spectrum and intensity and showed that it is highly polarized. This work led to a general understanding of channeling radiation in crystals, a field in which he is very active.

Überall's work in acoustic and electromagnetic scattering has evoked much interest, in the U.S. as well as abroad, because of its possible practical applications, as well as the theoretical understanding. Many collaborators have been inspired by it, and have now contributed to this volume.

This volume appears at the retirement of Überall from the university. But he is right in the midst of his productive work, and will undoubtedly make many further contributions to his chosen field.

The book is an excellent contribution to the literature of Acoustics and Wave Propagation. Professor Guran is to be congratulated for organizing and editing this volume.

<div style="text-align: right">

Hans A. Bethe
Cornell University

</div>

This page is intentionally left blank

Preface

The present Part III of the set of volumes *Acoustic Interactions with Submerged Elastic Structures* commences with a set of three chapters dealing with sound propagation in oceanic or layered environments. This set continues a corresponding group of chapters in Part II of this series that deal with ocean sound propagation models (Alexandra Tolstoy, Paul C. Etter) or reflections from the ocean floor (Rafael Carbó-Fité). The first chapter of Part III, authored by Stewart A. L. Glegg and Joseph M. Riley, presents a comprehensive overview of underwater sound propagation in three dimensions over a sloping ocean bottom. The present status of this field is reviewed here, and is followed by describing the model experiments done by the authors at Florida Atlantic University in a tank with sound-penetrable bottom, also presenting their own analytic work on this topic as well as other important theories (notably that of M. J. Buckingham). Field experiments are discussed or mentioned in addition, in particular the famous horizontal-refraction experiment by Doolittle, Tolstoy and Buckingham. The chapter represents an exhaustive review of all important propagation information in an oceanic wedge that has been accumulated to-date.

The following Chapter 2, by Juan I. Arvelo, Yianren Yuan, Herbert Überall and Khalid Chouffani, deals with the model description of some of the preceding author Glegg's tank propagation experiments involving an elastic bottom, both horizontal and downslope. Three propagation models are used for interpreting Glegg's data that differ in their mathematical algorithms: a fast-field model (SAFARI), a normal-mode model (KRAKENC), and a parabolic-equation model (FEPES). The degree to which their predictions agree with the data allows conclusions on the models' applicability to the various cases.

The third sound propagation study, i.e. Chapter 3 by Pier Paolo Delsanto, E. Ruffino and D. Iordache, deals with the propagation of sound pulses in layered media, including oblique incidence on these. This problem is treated here in a novel way, namely by the use of a massive parallel computer (the "connection machine" located at the Naval Research Laboratory) which permits large computational economy for these otherwise too cumbersome transient problems. An illuminating visualization of the propagation of sound pulses is made possible by this method.

The subsequent Chapter 4, by Paul J. T. Filippi and Daniel Mazzoni of the well-known Laboratory of Mechanics and Acoustics (CNRS/LMA) at Marseille, France, treats the problem of fluid flow past a plate or a cavity that leads to the generation of an acoustic response. A turbulent boundary layer is described by models of Corcos or Chase and the sound generation is obtained by modal or boundary element methods. Power spectra and directivities of the generated radiation are obtained, indicating resonant modes.

Chapter 5 is authored by a large group of researchers at the famous acoustics laboratory LAUE, of the University of Le Havre, France: led by Francine Luppé, these are Jean-Marc Conoir, M. Ech Cherif el Kettani, Olivier Lenoir, Jean-Louis Izbicki and Jean Duclos; and in addition Bernard Poirée of the Direction des Recherches, Etudes, et Techniques (DRET), well-known as the editor of the standard French work on acoustic scattering "La Diffusion Acoustique" (CEDOCAR Paris, 1987), who is also one of the pioneers of the subject of this chapter: evanescent and inhomogeneous waves. This chapter represents a sequel to the three related chapters in Part I, by Oswald Leroy, Marc Deschamps, Martine Rousseau and Philippe Gatignol dealing with inhomogeneous waves, but the current chapter also includes the topic of interface waves. Very general and detailed descriptions of evanescent and interface waves are presented here.

Proceeding now to the subject of acoustic scattering, of which various aspects have been treated in the previous parts of this book series, two novel approaches are described in the following two chapters, namely the wavelet approach, and time-frequency analysis. In Chapter 6, William Tobocman of the Case Western Reserve University in Cleveland, Ohio, uses wavelet analysis for solving acoustic inverse scattering problems. Integral equations characterizing the target can be shown to be solved in a very economic fashion by "wavelet compression". Examples of noisy square pulses are analyzed, and are reproduced by Fourier and wavelet analysis. In Chapter 7, acoustic scattering of pulses is analyzed with a time-frequency approach by Manell Zakharia and François Magand of CPE, Lyon, France, and Jean-Pierre Sessarego and Jean Sageloli of the CNRS/LMA Marseille. This powerful mathematical approach furnishes the so-called Wigner–Ville diagrams that can be used for an analysis of various types of surface waves on elastic target objects that are generated in the scattering process.

The following Chapter 8, by Harald Peine and Dieter Guicking of the Third Physics Institute at the University of Göttingen, Germany (an institute with an outstanding history of acoustics research), continues the subject of acoustic scattering by submerged elastic targets, in particular using the acoustic resonance scattering theory (RST) of Professor Überall and collaborators that has been amply elaborated on in the earlier parts of this book series. The present study applies their theory to the case of targets that exhibit overlapping resonances, and it utilizes the Wigner–Eisenbud R-matrix theory (which was also dealt with earlier by Prof. Überall) in order to describe the overlapping-resonance situation in a suitable fashion.

The scattering resonances also form the topic of the following Chapter 9, by Pier Paolo Delsanto, Ardéshir Guran, Anton Nagl and Herbert Überall. Here, they are employed for a possible solution of the inverse scattering problem, the determination of target properties from the acoustic echoes. Various examples are considered to illustrate this approach to target recognition: determination of acoustic absorptivity of layers, of the content of cavities, of the layers of a seafloor, and notably the concept of "acoustic resonance spectroscopy" as illustrated by the dependence of the resonance pattern on target shape.

The scattering theory forms the topic of the following Chapter 10, by Michael Werby of the NRL Stennis Space Center in Mississippi (presently Catholic University of America, Washington, DC), and Natalia Sidorovskaia of the University of New Orleans. The chapter presents an overview of present-day acoustic scattering theory and applications and includes many numerical implementation with applications, such as elastic shells and their resonances.

A different subject is approached in the Chapter 11, by Alain Gérard, of the Laboratory of Physical Mechanics at the University Bordeaux I, France: the application of ultrasonic analysis to a study and assessment of damage (cracks) in ceramic composites. This important technical problem is shown here to be well soluble by appropriate ultrasonic evaluation.

In the last Chapter 12 on Some Aspects of Nonlinear Wave Propagation Professor Jeffrey provides a tutorial style introduction to many of the key ideas and techniques for nonlinear wave propagation problems that have proven useful over the past 30 years. Starting with a discussion of linear wave propagation, Jeffrey introduces important concepts such as dispersion, phase velocity and group velocity. Then, the effect of the nonlinearity is described by focusing on characteristics for scalar hyperbolic equations. This leads to a more general discussion of conservation laws, quasilinear systems and their associated Riemann invariants. Relaxing the requirement that the wave profiles be differentiable, shock wave solutions to hyperbolic equations are discussed along with the generalized Rankine–Hugoniot jump

condition and the entropy conditions. To finish the discussion of hyperbolic waves, Glimm's random choice method is described.

The second half of the chapter moves to a discussion of nonlinear diffusive and dispersive wave techniques, starting with a section on the canonical Burgers equation and its exact solution via the Hopf–Cole transformation. Some special traveling wave solutions such as the Burgers shock are described. Dispersive waves are introduced with a discussion of the KdV equation and its associated soliton solutions. The reductive perturbation approach to analysing the asymptotic nature of a general dispersive wavetrain is then described, focusing on how several of the standard evolution equations arise. A description of Backlund transformation techniques which have proven useful for deriving special solutions to a wide range of nonlinear models is included. The chapter finishes with a derivation of a special class of traveling wave solutions to the mKdV equation.

In conclusion, it can be said that the presentation and discussion of the variety of acoustic subjects that are contained in Part III of the present book series, all of current interest and including such advanced methods as wavelets and time-frequency analysis, will prove highly useful to researchers in the field both for bringing them up to date on the present status of various aspects of acoustic scattering and propagation, as well as stimulating and guiding them in their own research work.

Ardéshir Guran   Dieter Guicking   Adrianus De Hoop   Francesco Mainardi
Ottawa, Canada   Göttingen, Germany   Delft, The Netherlands   Bologna, Italy

This page is intentionally left blank

Contributors

J. I. Arvelo
Johns Hopkins Applied Physics Laboratory
Johns Hopkins Rd., Laurel
MD 20723, USA

K. Chouffani
Department of Physics
Catholic University of America
Washington, DC 20064, USA

J. M. Conoir
LAUE, URA, CNRS 1373
Université du Havre
Place Robert Schuman
76610, Le Havre, France

P. P. Delsanto
INFM - Dip. di Fisica, Politecnico di Torino
C.so Duca degli Abruzzi 24 - Torino, Italy

P. P. Delsanto
Dipartimento di Fisica
Politecnico Torino, I-10129, Italy

J. Duclos
LAUE, URA, CNRS 1373
Université du Havre
Place Robert Schuman
76610, Le Havre, France

M. Ech-Cherif El Kettani
LAUE, URA, CNRS 1373
Université du Havre
Place Robert Schuman
76610, Le Havre, France

P. J. T. Filippi
Laboratoire de Mécanique et d'Acoustique
31 Chemin Joseph Aiguier
13402 Marseille Cedex 20, France

A. Gérard
Laboratoire de Mécanique Physique
University Bordeaux I
351 cours de la Libération
33405 Talence Cedex, France

S. A. L. Glegg
Center for Acoustics and Vibration
Florida Atlantic University
Boca Raton, FL 33431, USA

D. Guicking
Drittes Physikalisches Institut
Universität Göttingen, Bürgerstraße 42–44
D-37073 Göttingen, Germany

A. Guran
Institute for Structronics
275 Slater Street
Ottawa, Canada KIP 5H9

D. Iordache
Physics Department of Bucuresti Politehnica
Splaiul Independentei 313 - Bucharest
Romania

J. L. Izbicki
LAUE, URA, CNRS 1373
Université du Havre
Place Robert Schuman
76610, Le Havre, France

A. Jeffrey
Department of Mathematics
City University of Hong Kong (and)
Department of Engineering Mathematics
University of Newcastle upon Tyne, UK

O. Lenoir
LAUE, URA, CNRS 1373
Université du Havre
Place Robert Schuman
76610, Le Havre, France

F. Luppé
LAUE, URA, CNRS 1373
Université du Havre
Place Robert Schuman
76610, Le Havre, France

F. Magand
CPE Lyon, LISA (EPJoo92, CNRS)/
    LASSSO
Laboratoire d'Acoustique Systèmes
Signaux et Sonar
25 rue du Plat, 69288 Lyon Cedex 02
France

D. Mazzoni
Laboratoire de Mécanique et d'Acoustique
31 Chemin Joseph Aiguier
13402 Marseille Cedex 20, France

A. Nagl
Physics Department
Catholic University of America
Washington, DC 20064, USA

H. Peine
Drittes Physikalisches Institut
Universität Göttingen, Bürgerstraße 42–44
D-37073 Göttingen, Germany

B. Poireé
DRET, STRDT, G6
26 Boulevard Victor
00460 Armées, France

J. M. Riley
Center for Acoustics and Vibration
Florida Atlantic University
Boca Raton, FL 33431, USA

E. Ruffino
P. P. Delsanto
INFM - Dip. di Fisica, Politecnico di Torino
C.so Duca degli Abruzzi 24 - Torino, Italy

J. Sageloli
CNRS, LMA (UPR7051, CNRS)
Equipe ASM2, 31 Chemin J. Aiguier
13402 Marseille Cedex 20, France

J.-P. Sessarego
CNRS, LMA (UPR7051, CNRS)
Equipe ASM2, 31 Chemin J. Aiguier
13402 Marseille Cedex 20, France

N. A. Sidorovskaia
Physics Department
University of New Orleans
New Orleans, LA 70148, USA

W. Tobocman
Physics Department
Case Western Reserve University
Cleveland, OH 44106, USA

M. F. Werby
Naval Research Laboratory
Code 7181, Stennis Space Center
MS 39529, USA

H. Überall
Physics Department
Catholic University of America
Washington, DC 20064, USA

J. Yuan
Department of Physics
Catholic University of America
Washington, DC 20064, USA

M. E. Zakharia
CPE Lyon, LISA (EPJ0092, CNRS)/
    LASSSO
Laboratoire d'Acoustique Systèmes
Signaux et Sonar
25 rue du Plat, 69288 Lyon Cedex 02
France

Contents

THREE DIMENSIONAL UNDERWATER SOUND PROPAGATION OVER SLOPING BOTTOMS

STEWART A.L.GLEGG AND J.M.RILEY
Center for Acoustics and Vibration
Florida Atlantic University
Boca Raton, FL 33431,USA

ABSTRACT

This article reviews the work which has been carried out over the past few years on three dimensional underwater sound propagation over sloping bottoms. When sound propagates across a slope three dimensional effects can cause shadow zones and mode cut off effects to occur, which could not be predicted by a two dimensional model. For many years the theory for this type of propagation over realistic ocean floors, which can support both compressional and shear waves, eluded workers in this field. Recently the complete solution for the acoustic field in a "wedge domain with penetrable boundaries" has been developed, and this has allowed for complete understanding of three dimensional bottom interacting sound propagation. These theories have been verified by a series of laboratory scale experiments and excellent agreement has been obtained. However only one full scale ocean experiment has been carried out on three dimensional, bottom interacting, acoustic propagation. This showed significant horizontal refraction of sound propagating across a continental slope and further verifies the importance of bottom slopes on underwater sound propagation.

1. Introduction

Sound propagation in shallow water is strongly affected by it's interaction with the sea floor. The surface and the bottom form a sound channel in which the sound waves are trapped, and will propagate almost without loss unless they are absorbed by their interaction with the bottom. Typically the sea floor is characterized as a solid which can support shear waves and it is the conversion of acoustic energy in the water column into the shear and compressional waves in the sea floor which is the dominant mechanism of propagation loss for long range sound propagation. Shallow water regions on the continental shelf are usually associated with large areas of almost constant depth. Consequently shallow water sound propagation studies have assumed a uniformly flat and range independent environments, or, more recently, two dimensional range dependent environments in which the acoustic waves are assumed to propagate along straight paths without refraction in the horizontal plane. However in regions close to beaches and on the edges of the continental shelves the bottom can have slopes which are typically 2° but can be as large as 20° in some areas. These slopes and other range dependent features can cause the sound rays to bend in the horizontal direction as they propagate away from the source and this effect is called horizontal refraction. In this chapter we will consider this problem and review the progress which has been made over the last few years to improve the understanding of three dimensional bottom interacting underwater sound propagation, especially when the sea floor has many different layers and can support shear waves.

The effect which causes horizontal refraction over sloping bottoms is illustrated in
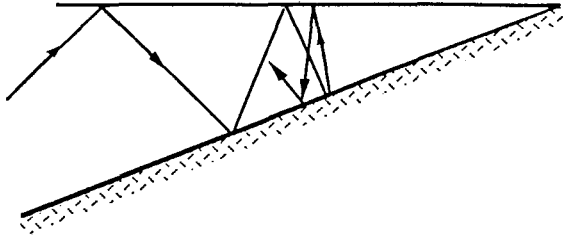
Figure 1: Rays propagating upslope in a perfect wedge showing ray turn around.

figure 1, which shows a sound ray which initially propagates upslope (figure 1) over a perfectly reflecting sloping bottom. On each bottom reflection the angle of the ray to the horizontal is increased until eventually its angle to the bottom causes it to be reflected in the downslope direction. After turn around the ray becomes increasingly horizontal on each bottom bounce as it propagates back towards deep water. This illustration only considers propagation which is directly upslope, but the same effect will also occur if the ray is traveling in the across slope direction. To illustrate this figure 2 shows the bending of the ray paths in the horizontal as they propagate away from the source. Notice how the rays which have a initial launch direction towards the shore line are bent so they eventually propagate away from the shore line.

Shore Line
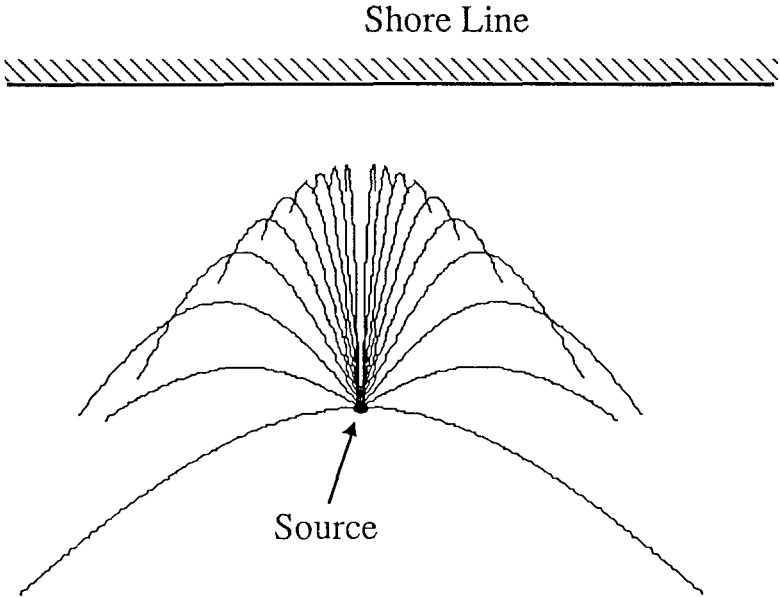
Figure 2: Ray paths showing horizontal refraction in an ideal wedge.

This has two effects: first no sound reaches the shallow water close to the shore and secondly a shadow region is created across slope from the source. This is dramatically different from the situation where the bottom is flat, and the rays propagate away from the source with little or no variation from straight line paths in the horizontal.

When the bottom is not perfectly reflecting then ray turn around does not always occur. The propagating ray in the upslope direction will be transmitted into the bottom if the grazing angle exceeds the critical angle for total internal reflection, as illustrated in figure 3. When the grazing angle is less than the critical angle (as shown for the first bottom reflection in figure 3) the ray is bounced back towards the surface. However because the direction of propagation has been increased relative to the horizontal, the grazing angle for the next bottom bounce exceeds the critical angle so the ray penetrates the bottom and is partially absorbed. There will be some reflected sound but this is absorbed on the next bounce, and the net result is that little energy propagates back down slope. This effect only occurs when the sea floor can support compressional waves which propagate at a speed which exceeds the speed of sound in the water.
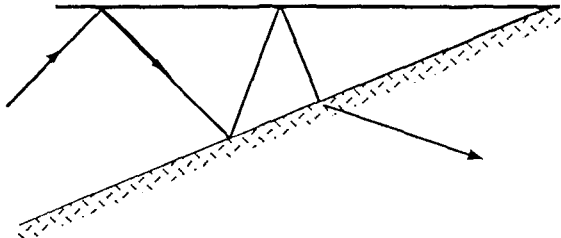
Figure 3: Rays propagating upslope in a penetrable wedge.When the critical grazing angle is exceeded the ray penetrates the bottom.

When rays are propagating slightly across slope the steepening of the ray only applies to the component of the propagation vector which points upslope. Consequently the grazing angle of the ray to the sloping bottom will include a component associated with the horizontal propagation and a component associated with the upslope propagation. The geometry becomes quite complex, but as we will show later, ray turn around can occur without the critical angle being exceeded. This leads to the specification of three regions as shown in figure 4: an inner region where the rays propagating upslope eventually exceed the critical angle to the bottom and are not turned around, an outer region where ray turn around occurs, and a shadow region where there is no sound propagation.

Underwater sound transmission over sloping bottoms has traditionally been described by idealized wedge structures as illustrated in figures 1 and 3. The upper surface of the wedge is a pressure release surface representing the sea surface, and the lower surface represents the sea floor. The understanding of acoustic propagation in this environment was lead by a number of theoretical and experimental studies on "ideal" wedges which have perfectly reflecting bottoms, and we will review these results in the next section. The more complex problem of sound propagation over a sloping penetrable bottom has only been solved relatively recently and this will be discussed in section 3. In section 4 experimental verification of these theories will be described. Finally, in section 5, experimental measurements of across slope and downslope propagation in the ocean will be reviewed.

Shore Line
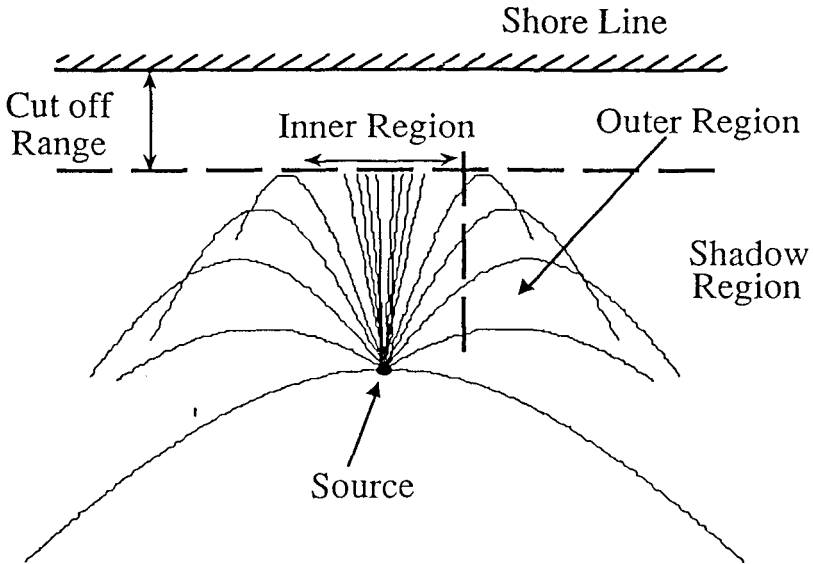
Figure 4: Ray paths showing horizontal refraction in a penetrable wedge.The cut off range is determined by the point where the rays penetrate thebottom.

The focus of this paper is on the three dimensional effects which occur for across slope propagation. A great deal of work has been done on downslope propagation, assuming a two dimensional model. However relatively little work has been done on three dimensional effects, and so this will be the focus of this review.

2. The Ideal Wedge

The first theoretical description of the three dimensional field in a wedge with rigid boundaries can be found in an article by Biot and Tolstoy[1] where they discuss both a modal solution and a solution based on the method of images. When the wedge subtends an angle which is an exact sub multiple of 180°, the field can be described by an number of image sources as shown in figure 5. This approach will be discussed in detail below, but we note here that the complete three dimensional field in the wedge and all the boundary conditions can be satisfied by summing together the contribution from each image source. The physical interpretation of this is that each image source represents one of the rays which reaches the source after multiple bottom bounces (or equivalently an eigenray). The number of surface or bottom reflections which each ray undergoes is determined by the number of image surfaces crossed by the path from the image source to the observer.

The work of Biot and Tolstoy[1] however did not show the important shadow zone regions in the three dimensional field in the wedge. This was discussed by Weston[2] and Harrison[3] who used the method of ray invariants to show that bathymetric refraction could cause shadow zones in the horizontal plane. A complete understanding of these effects was given by Buckingham[4] who developed a modal solution of the field in a wedge with pressure release boundaries and specified the edges of the shadow zones.
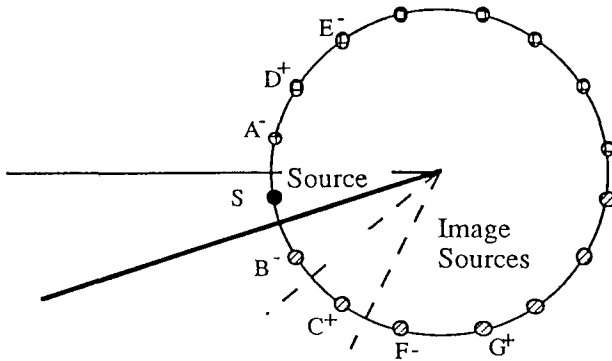
Figure 5: The location of the image sources for an ideal wedge with pressure release boundary conditions.

To obtain the solution for the field in a wedge a cylindrical coordinate system (r,θ,z) is used as shown in figure 6. The z axis is parallel to the apex of the wedge, and the angle of the wedge is θ_O which for the purpose of this illustration must be an exact submultiple of π such that $\theta_O = \pi/J$. The angular coordinate θ is measured from the surface and is positive in the downwards direction. The acoustic field generated by a point source located at the point $(r',\theta',0)$ must satisfy the pressure release boundary conditions on the upper and lower surfaces of the wedge. To ensure that this boundary condition is satisfied on the upper surface for the wave field propagating directly from the source, an image source can be introduced as shown in figure 5 at the location A⁻ with an amplitude which is equal and opposite to the source at S. To satisfy the boundary condition on the lower surface an image source is introduced at B⁻ to cancel the waves incident on the surface from the source. Note how all the sources lie at the same distance from the wedge apex. However the image sources A⁻ and B⁻ do not satisfy the boundary condition on the lower surface for the field generated by the source at A⁻ and so another image source must be introduced at C⁺ whose amplitude is equal and opposite to that of A⁻ or equivalently equal to the amplitude of S. This procedure must be repeated for the upper surface introducing the sources at E⁻ and D⁺ and so on until a complete circle of image sources is created as shown in figure 5, with the superscript ± indicating whether the image sources are in or out of phase with the actual source. The locations of each of the image sources are given by

$$S = (r',\theta',0) \qquad A^- = (r',-\theta',0) \qquad B^- = (r',2\theta_o - \theta',0)$$

$$C^+ = (r',2\theta_o + \theta',0) \qquad D^+ = (r',-2\theta_o + \theta',0) \qquad E^- = (r',-2\theta_o - \theta',0)$$

The angle of each source can be represented by the two sequences

$$\theta_j^+ = 2j\theta_o + \theta' \qquad \theta_j^- = 2j\theta_o - \theta' \qquad J^- < j < J^+$$

(1)
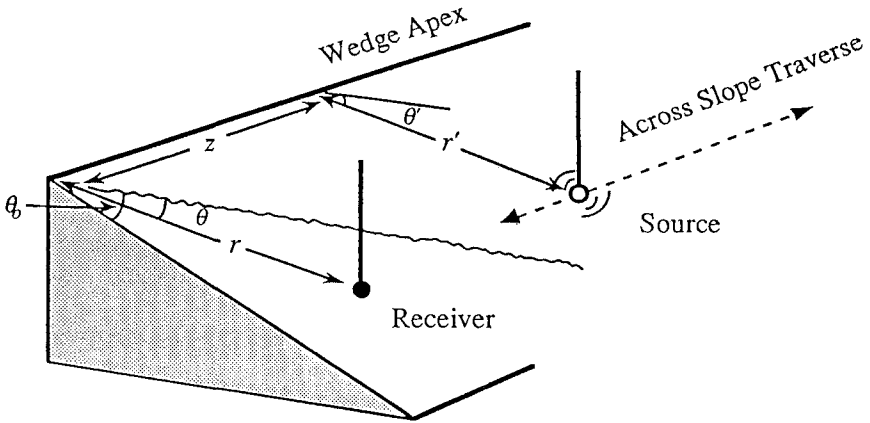
Figure 6: The arragement for the source and receiver in a wedge domain

where for odd values of J the limits are set by $J^{\pm} = \pm(J-1)/2$ and for even values of J the limits are $J^- = J/2$ and $J^+ = J/2-1$. The angles $\theta^{\pm}$ give the locations of the positive or negative sources respectively. The acoustic field is then given by the superposition of all the image sources and the velocity potential of the acoustic field for a source with volume velocity $Qe^{-i\omega\tau}$ can be represented by the summation

$$\phi = Qe^{-i\omega\tau} \sum_{j=J^-}^{J^+} \left\{ \frac{e^{ikR_j^+}}{4\pi R_j^+} - \frac{e^{ikR_j^-}}{4\pi R_j^-} \right\} \tag{2}$$

$$R_j^{\pm} = \left[r^2 + r'^2 - 2rr' \cos(\theta_j^{\pm} - \theta) + z^2 \right]^{1/2}$$

This is a finite sum and is a relatively simple expression to evaluate, giving the complete three dimensional field in a wedge shaped domain with pressure release boundaries. A particular case of interest is when the volume velocity of the source is not harmonic as given above but rather a broadband pulse with a time history given by $q(t)$. Then the acoustic field is given by

$$\phi = \sum_{j=J^-}^{J^+} \left\{ \frac{q(t - R_j^+ / c)}{4\pi R_j^+} - \frac{q(t - R_j^- / c)}{4\pi R_j^-} \right\} \tag{3}$$

where c is the speed of sound. This shows that the time history for a point source in a wedge will consist of a finite number of pulses which correspond to the number of image sources required to match all the boundary conditions. The acoustic signature will extend

over a time interval which is determined by the propagation distance from the nearest and most distant source. In the downslope direction this is given by *2r'/c* , which may a significant period. In the across slope direction the path length differences are much smaller and so the acoustic signature will be much more compressed.

The method of images result given above does not show the modal nature of the sound field, but this follows from some simple transformations. The Greens function which is the solution to the Helmholtz equation can be written in cylindrical co-ordinates using the expansion (Morse & Ingard[5])

(4)

$$\frac{e^{ikR}}{4\pi R} = \sum_{m=0}^{\infty} \frac{i\varepsilon_m}{4\pi} \cos(m(\theta - \theta')) \int_0^{\infty} J_m(\mu r) J_m(\mu r') e^{i\sigma |z|} \frac{\mu d\mu}{\sigma}$$

where $\sigma = \sqrt{(k^2 - \mu^2)}$ and $Im(\sigma) > 0$. Substituting this into Eq. (1) we see that the summation over j is of the form

(5)

$$\sum_{j=J^-}^{J^+} \cos(m(2j\theta_o \pm \theta' - \theta)) = \sum_{j=0}^{J-1} \cos(m(2\pi j/J + \theta_J \pm \theta' - \theta)) \qquad \theta_J = 2\pi J^- / J$$

This summation is only non-zero when m is an integer multiple of J, and the resulting sum is simply $J\cos(mJ(\pm\theta' - \theta))$. Then by using the trigonometric identity

$$\cos(mJ(\theta' - \theta)) - \cos(mJ(\theta' + \theta)) = 2\sin(mJ\theta)\sin(mJ\theta')$$

Eq. (1) may be re-written as

(6)

$$\phi = Qe^{-i\omega t} \sum_{m=0}^{\infty} \frac{J}{\pi} \sin(mJ\theta)\sin(mJ\theta') I_{mJ}(r,r',z)$$

where

(7)

$$I_{mJ}(r,r',z) = i\int_0^{\infty} J_{mJ}(\mu r) J_{mJ}(\mu r') e^{i\sigma |z|} \frac{\mu d\mu}{\sigma}$$

The amplitude of each mode is given by the function I_{mJ}, which is a function of position (r,r',z) and frequency. Eq.(6) shows that the image source solution is identical to a modal type solution with the "wedge modes" given by $\sin(mJ\theta) = \sin(m\pi\theta/\theta_o)$. These modes form an infinite set which satisfy the boundary conditions on the upper and lower surfaces of the wedge given by $\theta = 0$ and $\theta = \theta_O$. The modal amplitudes are given by the integral in Eq. (7), and Buckingham[4] shows how this integral may be reduced to a form which is easier to evaluate using approximate methods. In this approach the product of the Bessel functions is expanded as
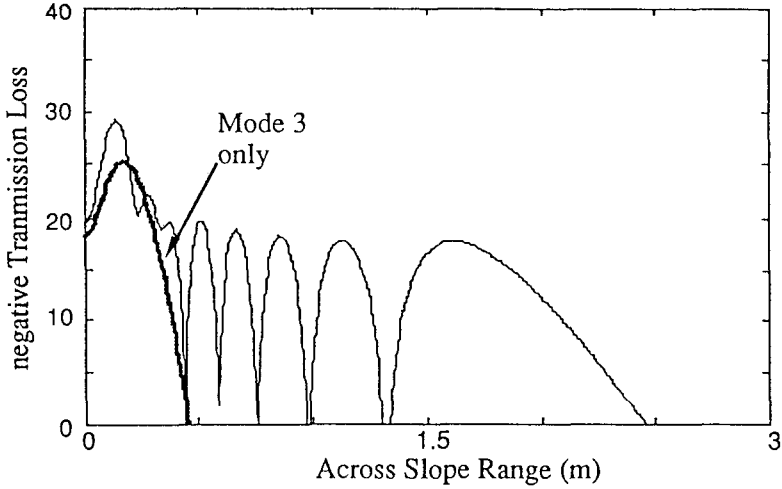
Figure 7: Transmission loss in the across slope direction. Source range is 40 cm and located at 1/2 of the depth of the water column. Receiver range is 60 cm and receiver depth is 1/2 of the depth of the water column. Wedge angle is 15°.

$$J_{mJ}(\mu r)J_{mJ}(\mu r') = \frac{1}{\pi}\int_0^{\pi} J_o\left(\mu\sqrt{r^2 + r'^2 - 2rr'\cos(\alpha)}\right)\cos(mJ\alpha)d\alpha$$

The integral in Eq. (7) is then of the form

$$I_{mJ}(r,r,z') = \frac{1}{\pi}\int_0^{\pi}\cos(mJ\alpha)\int_0^{\infty} J_o\left(\mu\sqrt{r^2 + r'^2 - 2rr'\cos(\alpha)}\right)e^{i\sigma|z|}\frac{i\mu d\mu}{\sigma}d\alpha$$

The inner integral may be evaluated exactly (Watson [6]) giving the mode amplitude as

(8)

$$I_{mJ}(r,r',z) = \frac{1}{2\pi R_o}\int_0^{\pi}(e^{imJ\alpha - ikR_o\beta} + e^{-imJ\alpha - ikR_o\beta})\frac{d\alpha}{\beta}$$

$$R_o = (r^2 + r'^2 + z^2)^{1/2}$$

$$\beta = (1 - 2a\cos\alpha)^{1/2} \qquad a = rr'/R_o$$

As with any other waveguide, there will be regions where modes propagate energy and regions where the amplitude decays rapidly. For each mode, an interference pattern exists which is described by the function $I_{mJ}(r,r',z)$. This gives standing-wave patterns in

both the up/down-slope directions and the across-slope directions. For example, figure 7 illustrates the interference pattern in the across slope direction. The vertical axis is negative Transmission Loss (in dB) which is obtained from the modulus of Eq.(8) computed using the method of stationary phase (Doolittle et al.[7], Wang and Pace[8]). In this example the source and receiver are placed at mid water depth and so even order modes are not excited. The amplitude of mode *3J* is shown and this is seen to cut off at a relatively short across slope range. The outer part of the curve is therefore dominated by the lowest order mode.

The function I_{mJ} defined in Eq. (8) is given by a harmonic integral. In general, *mJ* is large and so the integrand will oscillate rapidly as a function of the variable of integration. The integral will then be zero unless $\exp(-ikR_o\beta\pm imJ\alpha)$ has a stationary phase point when α lies in the interval $0<\alpha<\pi$. The stationary phase point is given by the value of α for which

$$(9)$$

$$\frac{\partial}{\partial\alpha}\left(\pm mJ\alpha - kR_o\beta\right) = 0$$

The derivative of $kR_o\beta$ is given by

$$kR_o\frac{\partial\beta}{\partial\alpha} = kR_o\frac{a\sin\alpha}{\beta}$$
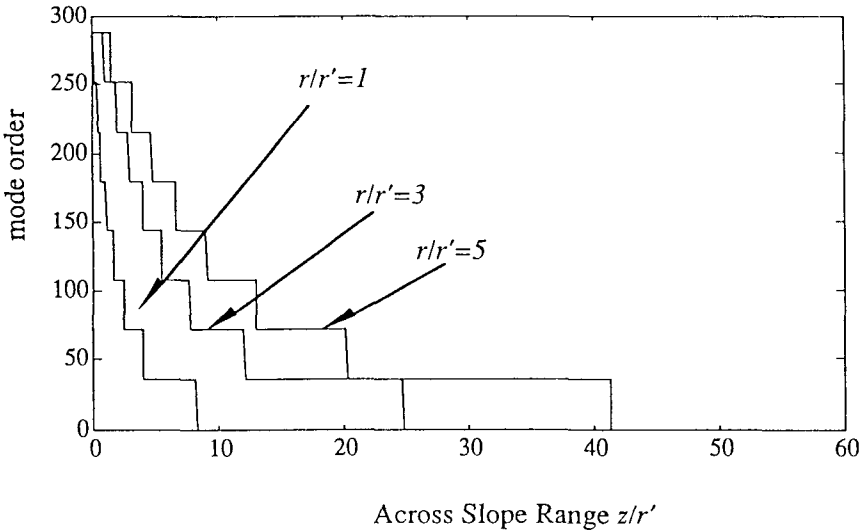
Figure 8 : Propagating mode orders as a function of across slope range for a frequency $kr'=300$ and a wedge angle of 5°.

and has a maximum value of

$$kR_o\left[\frac{\partial\beta}{\partial\alpha}\right]_{max} = kR_o\sqrt{\frac{1-(1-4a^2)^{1/2}}{2}} \qquad (10)$$

and a minimum value of zero in the range of integration. So, for Eq. (9) to have a solution the frequency given by Eq. (10) must be greater than mJ. Therefore for a mode to have a significant amplitude we require $mJ<M$ where

$$M = int\left[kR_o\sqrt{\frac{1-(1-4a^2)^{1/2}}{2}}\right] \qquad (11)$$

Here, int[ ] is the integer part of the value in parentheses. Eq. (11) can be used to define a three dimensional region of the wedge where modes can propagate. For example, figure 8 shows the propagating mode order as function of across slope range for different source and receiver locations at a non-dimensional frequency of $kr'=300$ for a wedge with an angle of 5°. In this case $J=36$ and figure 8 shows how the mode order jumps in multiples of J. As the across slope range is increased the higher order modes are cut off until the shadow region is reached where even the lowest order mode does not propagate. Notice how the lowest order mode is always the last to be cut off and the outer region of the acoustic field only has one mode which can propagate.
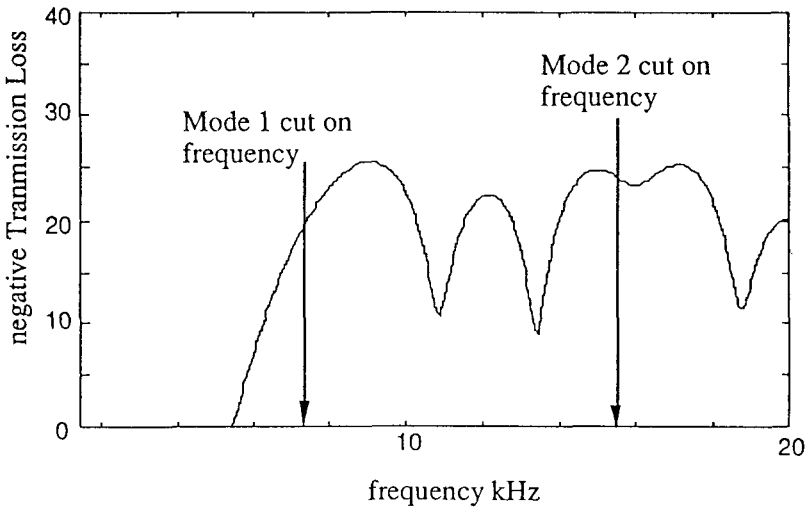
Figure 9: Spectrum of transmission loss at a point showing mode interference effects. Source range is 40 cm and located at 1/3rd of the depth of the water column. Receiver range is 60 cm and across slope range is 20 cm. Wedge angle is 15° and receiver depth is 1/3rd of the depth of the water column.
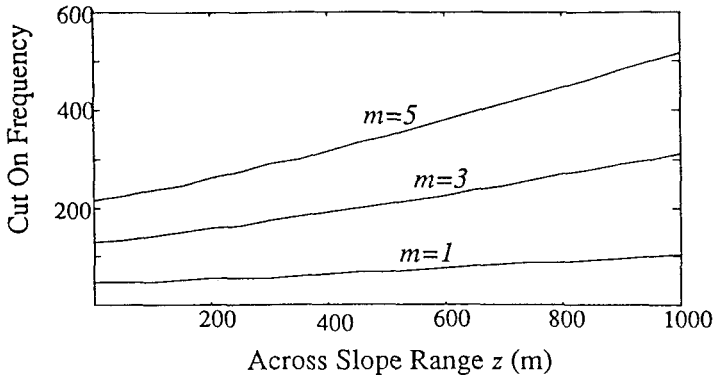
Figure 10 : Cut on frequencies for each mode for a source and receiver 500 m from the shore line over a 2° slope as a function of across slope range.

It should be realized that the acoustic field is frequency dependent and that as the frequency is lowered the cutoff range is reduced. This is illustrated in figure 9, which shows a typical spectrum at a point in the wedge. At frequencies below the cut-on frequency for mode 1, the spectrum level decreases abruptly, and above this frequency interference dips occur. Also note the change in shape which occurs due to the cut-on of the second-order mode. The cut-on frequencies are clearly important and can be obtained by rewriting Eq.(11) to give the m_J^{th} mode cut-on frequency as

$$f_m = \frac{mc_0}{R_0 \theta_0 \sqrt{2[1 - (1 - 4a^2)^{1/2}]}}$$

Figure 10 shows how the cut-on frequencies change with respect to the horizontal range z parallel to the apex. This result is significant because it demonstrates how the cut-on frequency increases with across slope range. This means that the insonified region of any frequency is always smaller than that of a higher frequency. It also shows how the effect is largest for the higher order modes. Consequently even well away from the shadow region boundary, which is determined by the lowest order mode, three dimensional effects are important because the higher order modes are cut off.

3. The Penetrable Wedge

For many years the solution for sound propagation in a wedge with arbitrary boundary conditions eluded workers in this field. However a series of papers by Deane[9,10,11]and Westwood[12,13,14] have provided complete solution to this problem. When the lower surface of the wedge can absorb sound the modal solution is not appropriate because the modes become range dependent, and this causes a number of theoretical difficulties(Buckingham[15]). The method used by Deane and Westwood is based on the method of images, and does not rely on a modal expansion of the sound field for its solution. Consequently it does not suffer from the same problems as the "wedge modes" when bottom absorption is introduced.

To properly account for the bottom reflection in the method of images we must consider a source next to an infinite reflecting plane. The reflection of sound from the plane can be described by the Rayleigh reflection coefficient which correctly matches the boundary conditions for a plane wave incident on the surface. To obtain the total field from a point source which lies a distance d away from a plane surface (figure 11), the spherical wave from the source is expanded into a set of plane waves using the integral relationship

$$\frac{e^{ikR}}{4\pi R} = \frac{i}{8\pi^2} \int_{-\infty}^{\infty} \int_{-\infty}^{\infty} \frac{e^{ik.(x-x_0)}}{k_y} dk_x dk_z \qquad k_y = \sqrt{k^2 - k_x^2 - k_z^2} \quad \text{Im}(k_y) > 0$$

where $k=(k_x,k_y,k_z)$ is the wavenumber vector of each plane wave component in the expansion and the source is located at x_0. This shows that the field emitted by the source can be represented by plane waves traveling in the direction of the wave vector k. The plane waves can then be considered as reflected from the surface with the angle of incidence equal to the angle of reflection as illustrated in figure 11. The reflected field is then equivalent to the field from an image source which lies at $x_I=x_0-2d n$ where n is the normal to the surface and the angle of incidence to the surface is given by

$$\varphi = \cos^{-1}(k.n/k)$$

(12)

The reflected field from the source is constructed by multiplying the field from the image source by the reflection coefficient of the surface giving

(13)

$$\phi = \frac{iQ}{8\pi^2} \int_{-\infty}^{\infty} \int_{-\infty}^{\infty} \frac{V(\varphi)e^{ik.(x-x_I)}}{k_y} dk_x dk_z$$

where $V(\varphi)$ is the plane wave reflection coefficient. Summing the direct field and the reflected field gives
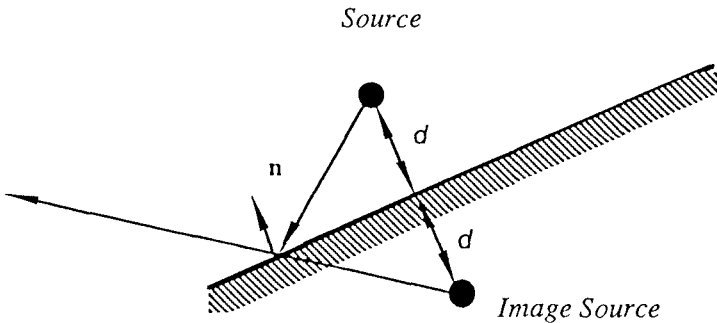
Figure 11 : The reflection of sound from a plane and the location of the image source

(14)

$$\phi = \frac{iQ}{8\pi^2} \int\limits_{-\infty}^{\infty} \int\limits_{-\infty}^{\infty} \frac{e^{i\mathbf{k}\cdot(\mathbf{x}-\mathbf{x}_o)} + V(\varphi)e^{i\mathbf{k}\cdot(\mathbf{x}-\mathbf{x}_I)}}{k_y} dk_x dk_z$$

It is a trivial matter to show that this equation satisfies the boundary conditions at the interface and also gives a solution to the Helmholtz equation in the region above the interface.

If we consider a fluid/fluid interface then the reflection coefficient will be given by

(15)

$$V(\varphi) = \frac{\rho_1 c_1 \cos(\varphi) - \rho c \cos(\varphi_1)}{\rho_1 c_1 \cos(\varphi) + \rho c \cos(\varphi_1)} \qquad\qquad \cos(\varphi_1) = \sqrt{1 - \left(\frac{c_1}{c}\right)^2 \sin^2(\varphi)}$$

where ρ and ρ_1 are the densities and c and c_1 are the speeds of sound above and below the interface respectively. However the reflection coefficient given by (15) is a relatively simple form which does not allow for shear waves in the bottom or multiple layers below the surface. To extend the analysis to the more general case we introduce an interface impedance defined as $Z=i\omega\rho\phi/\rho c(\partial\phi/\partial n)$ where the top line represents the pressure on the interface and the bottom line the particle velocity normal to the surface multiplied by a normalizing factor ρc so that Z is non-dimensional. The reflection coefficient then takes the form

(16)

$$V(\varphi) = \frac{k_n Z - k}{k_n Z + k}$$

where k_n=k.n. For the case of the fluid/solid interface Z is given by

(17)

$$Z = \frac{\rho_1}{\rho}\left[\frac{C}{\sqrt{\left(\frac{c}{c_1}\right)^2 - 1 + \left(\frac{k_n}{k}\right)^2}} + D\sqrt{\left(\frac{c}{b_1}\right)^2 - 1 + \left(\frac{k_n}{k}\right)^2} \right]$$

where

$$C = \left[1 - 2\left(\frac{b_1}{c}\right)^2 \left\{ 1 - \left(\frac{k_n}{k}\right)^2 \right\} \right]^2 \qquad\qquad D = 4\left\{ 1 - \left(\frac{k_n}{k}\right)^2 \right\}\left(\frac{b_1}{c}\right)^4$$

The total field can therefore be determined by the evaluation of the integral in Eq.(14) for any type of bottom, and providing the correct form of the impedance is introduced, the effect of shear waves in the region below the boundary will automatically be included. However we must be careful when evaluating this integral because Z may be a complicated function, and even for the simplest cases of interest will include multiple valued functions as shown by Eq. (15).
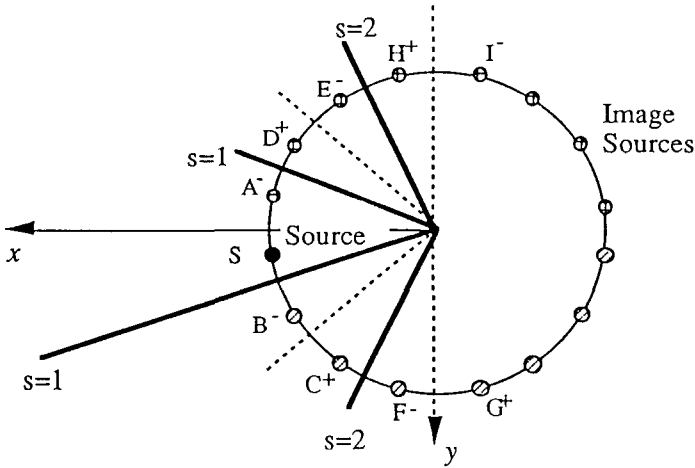
Figure 12: The location of the image sources for an penetrable wedge.

To allow for absorbing planes in the image source theory we must re-consider the definition of the field from the image source distribution shown in figure 5. To account for the reflection we re-draw the images as shown in figure 12 where the surfaces $s=1,2,3$ represent the interfaces which image the bottom boundary. In this new arrangement the source at A⁻ remains the same since it gives the field from the first surface reflection. The sources B⁻ and D⁺ represent the first bottom reflection and it's image from the ocean surface (i.e. the path which propagates from the source to the bottom, is reflected and then bounces off the surface before reaching the observer). Consequently the field from these sources need to be corrected for the bottom reflection. The sources C⁺ (which represents the path via the surface and then the bottom) and E⁻ (surface/bottom/surface) both have additional surface reflections while the sources F⁻ (bottom/surface/bottom) and H⁺ (bottom/surface/bottom/surface) both have two bottom reflections. The sum of the contributions from each source given by Eq. (2) must then be modified to include the bottom reflection using Eq. (12) and this gives

$$(18)$$

$$\phi = \frac{iQ}{8\pi^2} \sum_{j=J_-}^{J_+} \int_{-\infty}^{\infty} \int_{-\infty}^{\infty} \left[\left\{ \prod_{s=1}^{|j|} (-1)V(\varphi_{sj}^+) \right\} e^{-i\mathbf{k}.\mathbf{x}_j^+} - \left\{ \prod_{s=1}^{|j|} (-1)V(\varphi_{sj}^-) \right\} e^{-i\mathbf{k}.\mathbf{x}_j^-} \right] \frac{e^{i\mathbf{k}.\mathbf{x}}}{k_y} dk_x dk_z$$

where $\varphi_{sj}^{\pm}$ is the angle of incidence of the plane waves from the source at $\theta_j^{\pm}$ onto the

surface defined by the integer *s*. To obtain $\varphi^{\pm}_{sj}$ we write

$$\mathbf{n}_s = (\sin((2s-1)\theta_o), -\text{sgn}(j)\cos((2s-1)\theta_o), 0)$$

and use Eq. (12) to show that

$$\varphi^{\pm}_{sj} = \cos^{-1}(\mathbf{k}.\mathbf{n}_s / k) = \varphi_s$$

which depends on the source lying in the upper or lower part of figure 12 and is otherwise independent of source position. Hence Eq. (18) may be simplified as

(19)

$$\phi = \frac{iQ}{8\pi^2} \sum_{j=J_-}^{J_+} \int_{-\infty}^{\infty} \int_{-\infty}^{\infty} \left[\left\{ \prod_{s=1}^{|j|} (-1)V(\varphi_s) \right\} (e^{-i\mathbf{k}.\mathbf{x}_j^+} - e^{-i\mathbf{k}.\mathbf{x}_j^-}) \right] \frac{e^{i\mathbf{k}.\mathbf{x}}}{k_y} dk_x dk_z$$

This is an exact expression for the field in the wedge domain which satisfies the Helmholtz equation and the boundary conditions on the upper and lower surfaces. However the difficulty with using this expression to calculate the acoustic field is evaluating the two integrals. The integrands are harmonic which makes them unsuitable for direct numerical calculation and the reflection coefficient is a multivalued function with several branch lines in the complex plane so contour integration is difficult. To overcome these problems Westwood[14] and Deane[11] have used different approaches. Westwood[14] uses the method of steepest descent to identify the part of the integrand which makes the main contribution to the result, while Deane[11] expands the terms in { } as a series in which each term is integrable, and so gives an exact solution. Here we will consider an approximate solution obtained by writing the integral as

(20)

$$\phi = \frac{iQ}{8\pi^2} \sum_{j=J_-}^{J_+} \int_{-\infty}^{\infty} \int_{-\infty}^{\infty} \left[e^{-i\mathbf{k}.\mathbf{x}_j^+} - e^{-i\mathbf{k}.\mathbf{x}_j^-} \right] \frac{e^{i\mathbf{k}.\mathbf{x} + \sum_{s=1}^{|j|} \ln(-V(\varphi_s))}}{k_y} dk_x dk_z$$

The integrand is now in the form of a harmonic function which oscillates rapidly in the (k_x, k_z) plane. We note from Eq. (16) that

(21)

$$\ln(-V(\varphi)) = \ln(k - k_n Z) - \ln(k + k_n Z) = \Phi(\varphi) + i\Gamma(\varphi)$$

For fluid bottoms (*D=0* in Eq. (17)) this function will be either entirely real or entirely imaginary, but for the general case of shear supporting bottoms then the value of Eq.(21) will be complex when the shear wave speed b_l is less then the speed of sound in the water. The largest contribution to the integral comes from the part of the integrand where the phase is changing least rapidly. This is determined by the solutions to

$$\frac{\partial}{\partial k_x} \left(\mathbf{k}.(\mathbf{x} - \mathbf{x}_j^{\pm}) + \sum_{s=1}^{|j|} \Gamma(\varphi_s) \right) + \frac{\partial}{\partial k_z} \cdot \left(\mathbf{k}.(\mathbf{x} - \mathbf{x}_j^{\pm}) + \sum_{s=1}^{|j|} \Gamma(\varphi_s) \right) = 0$$

Evaluating this expression gives

(22)

$$
(x - x_j^{\pm}) + z - (y - y_j^{\pm})\frac{(k_x + k_z)}{k_y} +
$$

$$
+ \sum_{s=1}^{|j|}\left[\sin((2s-1)\theta_o) + \operatorname{sgn}(j)\cos((2s-1)\theta_o)\frac{(k_x + k_z)}{k_y}\right]\frac{\partial \Gamma(\varphi_s)}{\partial k_n} = 0
$$

In the simplest case when the reflection coefficient is real valued the last term can be dropped and the solution is found from the first three terms. It is easy to show that the solution occurs when the wave vector k is in the same direction as the vector from the image source to the observer, so that $kR_j^{\pm} = k(x-x_j^{\pm})$. This corresponds to a particular value of φ_s which we will define as $\beta_{sj}^{(\pm)}$. Since the integrand oscillates rapidly we approximate the integral by assuming that the amplitude of the integrand is constant and given by its value at $\beta_{sj}^{(\pm)}$. Hence

$$
\phi = \frac{iQ}{8\pi^2}\sum_{j=J_-}^{J_+}\left\{\prod_{s=1}^{|j|}(-1)V(\beta_{sj}^{(+)})\right\}\int_{-\infty}^{\infty}\int_{-\infty}^{\infty}\frac{e^{i\mathbf{k}.(\mathbf{x}-\mathbf{x}_j^+)}}{k_y}dk_x dk_z
$$

$$
-\left\{\prod_{s=1}^{|j|}(-1)V(\beta_{sj}^{(-)})\right\}\int_{-\infty}^{\infty}\int_{-\infty}^{\infty}\frac{e^{i\mathbf{k}.(\mathbf{x}-\mathbf{x}_j^-)}}{k_y}dk_x dk_z
$$

The integrals in this expression can be evaluated exactly to give

(23)

$$
\phi = \frac{iQ}{4\pi}\sum_{j=J_-}^{J_+}\left\{\prod_{s=1}^{|j|}(-1)V(\beta_{sj}^{(+)})\right\}\frac{e^{ikR_j^+}}{R_j^+} - \left\{\prod_{s=1}^{|j|}(-1)V(\beta_{sj}^{(-)})\right\}\frac{e^{ikR_j^-}}{R_j^-}
$$

This result shows that a reflection coefficient must be applied to each image source with the amplitude of the reflection coefficient determined by the angle of incidence on each surface between each source and the observer. This corresponds to using a ray tracing approach in which each ray is specularly reflected from the bottom with an amplitude reduction corresponding to the reflection coefficient for the angle of incidence of the ray. However in arriving at this result we have not considered the case when the reflection coefficient is complex valued and this can have an important effect because the last term in Eq. (22) will affect the solution to the equation. For example figure 13 shows a plot of $k(\partial\Gamma/\partial k_n)$ for a typical sediment in the ocean with a shear wave speed of 300 m/s. We see that for low values of k_n/k this function varies only slowly with wavenumber, but at angles close to the critical angle the variation of the function is large. However in many applications the reflection from a plane is only important at low grazing angles, and this leads to the effective depth approximation. This assumes that $k_n/k \ll 1$ and that Z may be approximated by it's value at $k_n = 0$. This approximation is shown on figure (13) and is seen to work well apart from close to the critical angle.
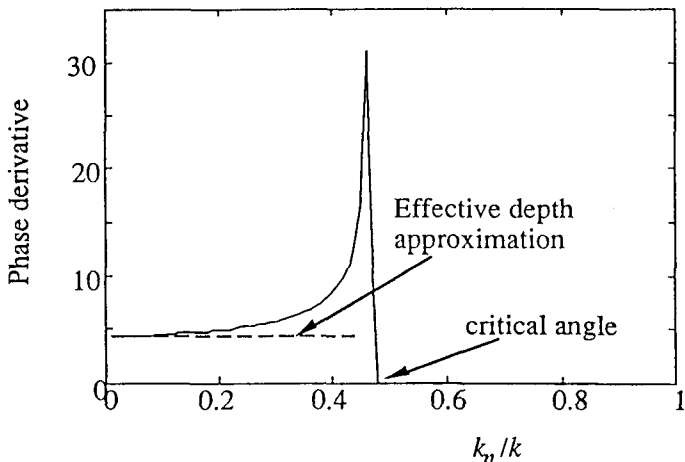
Figure 13: The derivative of the phase function $k\partial\Pi\partial kn$ for a typical shear supporting bottom.

To apply this approximation we reconsider the reflection coefficient and apply the effective depth approximations to give

$$\ln(-V(\varphi)) = \ln(1 - Zk_n / k) - \ln(1 + Zk_n / k) \approx -2Zk_n / k \qquad (24)$$

Here we see a linear dependence on the wavenumber component normal to the surface and we can define

$$\Phi = \ln(|V(\varphi)|) \approx -2real(Z)k_n / k \qquad \Gamma \approx -2imag(Z)k_n / k$$

To calculate the acoustic field in the wedge we apply this approximation to the imaginary part of the reflection coefficient and write

$$\sum_{s=1}^{|j|} \ln(-V(\varphi_s)) \approx \sum_{s=1}^{|j|} \ln(|V(\varphi_s)|) - 2imag(Z)\sum_{s=1}^{|j|} \frac{i\mathbf{k}.\mathbf{n}_s}{k} = \sum_{s=1}^{|j|} \ln(|V(\varphi_s)|) + i\mathbf{k}.\mathbf{x}_c^{(j)}$$

where

$$(28)$$

$$\mathbf{x}_c^{(j)} = 2\Delta\sum_{s=1}^{|j|} \mathbf{n}_s \qquad \Delta = -imag(Z)/k$$

The acoustic field is then obtained as before by writing the field in the form

(29)

$$\phi = \frac{iQ}{8\pi^2} \sum_{j=J_-}^{J_+} \left\{ \prod_{s=1}^{|j|} | V(\beta_{sj}^{(+)}) | \right\} \int_{-\infty}^{\infty} \int_{-\infty}^{\infty} \frac{e^{ik.(x-x_j^+ +x_c^{(j)})}}{k_y} dk_x dk_z$$

$$- \left\{ \prod_{s=1}^{|j|} | V(\beta_{sj}^{(-)}) | \right\} \int_{-\infty}^{\infty} \int_{-\infty}^{\infty} \frac{e^{ik.(x-x_j^- +x_c^{(j)})}}{k_y} dk_x dk_z$$

where the angle of incidence onto each surface is now taken as the angle from the source displaced by $x_c^{(j)}$ rather than the actual source position. This leads to an expression for the acoustic field which is identical to (21) but with $-V$ replaced by the magnitude of the reflection coefficient and the source images shifted by $x_c^{(j)} = (x_c^{(j)}, y_c^{(j)}, 0)$. It is noteworthy that the image sources are only shifted in the (x,y) plane.

The concept of using a beam displacement or a shifted image source location is described by Brekhovskikh and Lysanov [16] and it was shown by Glegg [17] that the sound propagation in a uniform depth channel with an arbitrary bottom could be modeled as a channel with a pressure release lower surface displaced by Δ. For the case of the wedge we have now shown that the bottom displacement must be applied to each reflecting surface where perfect reflection does not occur. The sum of all the bottom displacements can be shown as equivalent to moving the apex of the wedge horizontally away from the source by a distance $\Delta/\sin(\theta_o)$. This will give a new set of locations for all the image sources using a simple geometrical correction. This correction is precisely the same as was proposed by Buckingham [15] for the penetrable wedge problem. In that theory only a fluid bottom was considered and so the reflection coefficient was taken as having unit amplitude for small grazing angles. Buckingham was then able to derive equivalent wedge modes for the penetrable wedge. This theory was based on intuitive arguments and here we have shown that by using the method of images the same correction for the penetrable bottom can be achieved. However this theory has allowed for a shear supporting layered bottom with an arbitrary bottom impedance.

The correction for the image source locations given by the effective depth displacement is shown by Eq. (28) to be inversely proportional to frequency and so this correction tends to zero when the acoustic wavelength is small compared with the depth of the water column. Therefore the approximate solution is expected to work better at high frequencies. The approximation however does not apply when the impedance changes rapidly with angle of incidence which is the case when stationary phase point is close to the critical angle. In this case the image source displacements will be much larger and which is equivalent to applying large beam displacements to the reflected waves. This is most significant for propagation in the downslope direction. In the across slope direction, at large distances from the source, the angle of incidence from any of the image sources to any of the bottom interfaces is always small. To show this we note that the dominant wave vector is in the direction $k/k=(x-x_j^{\pm}+x_c^{(j)})/R_j^{\pm}$ and the angle of incidence to the bottom is given by $k.n_j/k=n_j.(x-x_j^{\pm}+x_c^{(j)})/R_j$. Since the normal to the surface only has components in
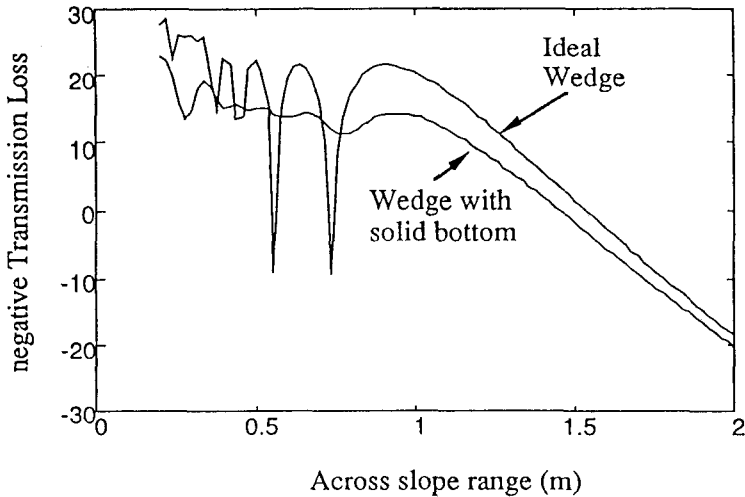
Figure 14: Transmission loss in the across slope direction for an ideal wedge and a penetrable wedge. Source range is 15 cm and located at 1/2 of the depth of the water column. Receiver range is 15 cm and receiver depth is 1/2 of the depth of the water column. Wedge angle is 20° and frequency is 110 kHz.

the (x,y) directions and at large distances across slope $R_j^{\pm} \approx z$ the grazing angle to each surface tends to zero in the across slope direction when z is large. Consequently the effective depth approximation given above will be adequate. However in the downslope direction there will always be an image source field which will be incident on a reflecting plane at a large grazing angle and so the approximation given here does not apply.

It is interesting to compare the across slope propagation for a penetrable bottom with that for an ideal bottom as is shown in figure 14. This calculation shows that the effect of the absorbing bottom is to reduce the amplitude of the acoustic field. The nulls which occur in the ideal wedge solution are not as dramatic in the penetrable wedge and displaced across slope further from the source. The shift however is small and most easily identified by the more rapid decay of the field in ideal wedge as the observer moves into the shadow zone region. This is not unexpected because the shift of the wedge apex caused by beam displacement causes the observer to be effectively further downslope than in the ideal wedge case, and in this region the shadow zone boundary decays less rapidly with across slope distance.

In this section we have shown how an exact expression for the acoustic field in a wedge with any type of lower boundary condition may be specified in terms of a double wavenumber integral. The evaluation of that integral has been carried out using an effective depth approximation which applies when the grazing angle of the waves incident on any reflecting surface is small. This method is only useful for across slope calculations and to obtain the solution for downslope propagation more accurate methods[11,14] need to be used. The advantage of the approach given here is that it allows the apparent shift of the image sources to be specified for the situation where the bottom boundary causes beam displacement.

4. Laboratory Scale Experiments

The first experimental demonstration of the three dimensional propagation effects described above was given by A.B. Wood[18] who presented the results of an experiment showing a visual picture of horizontal refraction. The experiment was conducted in a rectangular tank made of concrete, with dimensions of 1.05mx0.83mx0.1m. A wedge domain was constructed by resting one edge of a glass plate on the bottom of the concrete tank, while the opposite edge rested on the side of the tank. To obtain the sound field characteristics, the glass plate was painted with a water soluble paint. When the region was insonified using a frequency of 1 MHz, the variation of the sound level on the sloping bottom appeared on the painted surface, showing the interference pattern illustrated in figure 2.

To evaluate the acoustic field in the water column Tindle et al[19] measured the propagation of modes directly downslope of the source. They generated individual modes by using an array of transducers which preferentially excited only one mode in the water column. They were able to show that the mode propagated as a "wedge" mode into the deeper water and was not converted into modes of different order. However their results primarily addressed downslope propagation and so will not be reviewed in detail here.

The three dimensional field in an ideal was investigated by Glegg and Yoon[20]. They carried out an experimental study to verify the theoretical solution given by Buckingham[4] for a wedge with perfectly reflecting pressure-release boundaries and to demonstrate pulse distortions as a function of propagation distance. The experiments were carried out at model scale in a large water tank as illustrated in figure 15, with a wedge domain constructed using a triangular, air-filled Plexiglas tank.
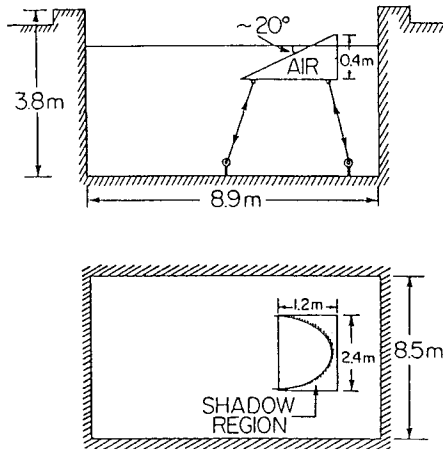
Figure 15: Glegg and Yoon's experiment using an air filled tank to form a wedge with pressure release boundaries.

The size of the Plexiglas tank was chosen so that the shadow region of the acoustic field from a point source at the center eliminated edge reflections; also the attenuation of sound in the down-slope direction minimized the effect of the boundaries in this direction. This arrangement was, therefore, found to correspond well with free-field conditions.

The lower surface of the wedge was formed using a 12.7-mm Plexiglas sheet with a calculated reflection coefficient of -0.997. This surface was, therefore, almost identical to an ideal pressure-release boundary as considered in the exact normal-mode theory. Also, by adjusting the lengths of the wires which hold the tank below the surface, the angle of the wedge could be altered. The wedge angles considered were between $\pi/10$ (18°) and $\pi/8$ (22.5°), and the source frequency was varied between 7.5 and 8.5 kHz. The source was placed up slope of the receiver at a range of 37.5 cm from the wedge apex, and the receiver was traversed through the acoustic field. Both transducers were placed at middepth to maximize the acoustic field and signal-to-noise ratio. A typical result is illustrated in figure 16, which shows a comparison between the measurement and the theoretical calculations discussed in the previous section. This result shows how the level changes as the observer moves in the across-slope z direction at two different fixed down-slope ranges. Note how the highest levels do not occur at $z=0$, which is closest to the source, but rather at $z=20$ and 45 cm for receiver ranges of $r=44.16$ and 69.66 cm, respectively. This indicates an effective beaming of the sound due to the interference pattern in the wedge. However, of most interest is the edge of the shadow region where the level drops at a rate which is nearly 20 dB per doubling of distance from the source.
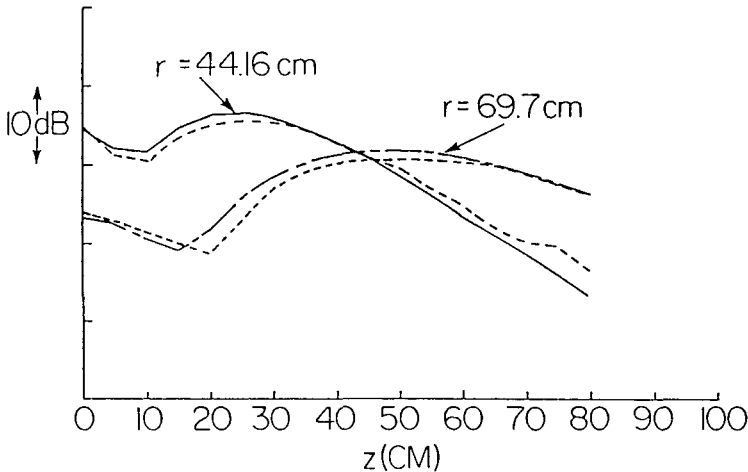
Figure 16: Variation in level in the across slope direction. Comparison of theory and experiment at receiver ranges of $r=44.2$ cm and 69.7 cm. Source frequency is 8 kHz, wedge angle 22.5°, and source range 37.5 cm. Source and receiver are at mid depth.
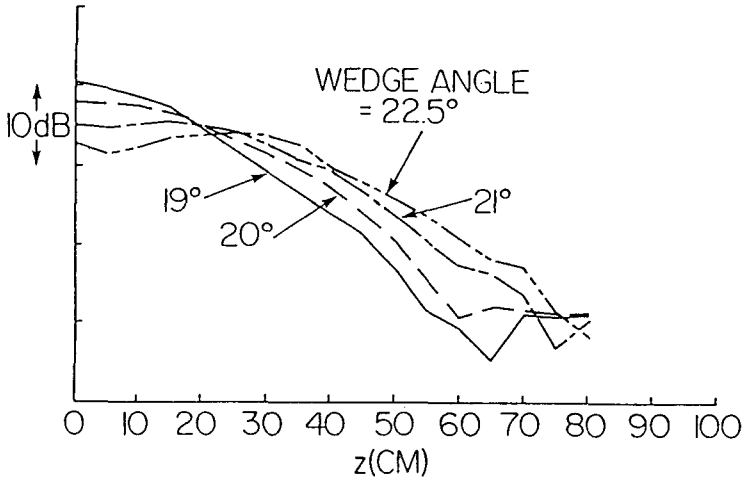
Figure 17: The effect of small changes in wedge angle: The curves show the variation in level in the across slope direction for a receiver range of $r=44.2$ cm, source range 37.5 cm, and source frequency 7.5 kHz, for different wedge angles.

One of the necessary assumptions of the theoretical derivation of Eq. (2) is the requirement for the wedge angle to be an exact submultiple of π. If this is not the case then the field diffracted by the wedge apex must be added to the modal field given by Eq. (6). This was investigated experimentally by making small adjustments to the wedge angle between $\pi/10$ (18°) and $\pi/8$ (22.5°) (figure 17). Large variations in level (10 dB) were found at fixed source and receiver positions, but on analysis these were consistent with a linear variation between the predicted levels at the two angles $\pi/10$ and $\pi/8$ for which the modal theory is exact.

The frequency dependence of the field is illustrated in figure 18, which shows the frequency spectrum of a broadband pulse, and the predicted spectrum obtained using the theoretical result, Eq.(2), corrected for the transmitting response of the source. Note how the lower frequency parts of the pulse are cut off as the range increases, and how the dips and peaks in the spectrum are well predicted by the theory.

Glegg, Deane and House[21] carried out an experiment to investigate the sound field in a wedge with a layered shear supporting bottom.   In this experiment the sea floor was modeled by a concrete block covered by an epoxy layer, mounted in a test pool as illustrated in figure 19. The model was considered representative of a sediment layer over a hard rock substrate since the acoustic properties of the epoxy and the concrete are similar to those found in many near shore environments, where terriginous sediments, such as sands and silts, overlie a rock substrate, such as basalt or limestone. The block dimensions were chosen to be 1.2m x 2.88m x 0.3m. For the sediment layer a two part laminating epoxy was used with a thickness of 5.8 cm.

Eleven different parameters are required to describe the geo-acoustic properties of this model. These are the compressional and shear wave speeds in both the epoxy and the concrete, and the associated attenuation coefficients. The material densities and the layer
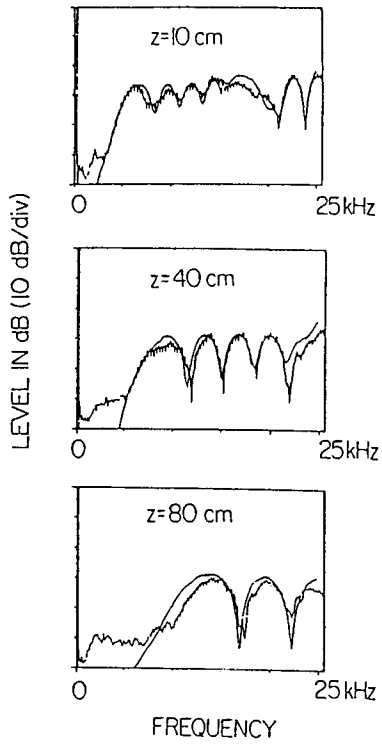
Figure 18: Spectrum of pulses at different across slope locations. The two curves show the comparison between measurements (jagged line) and theory (continuous line).

9.2 m
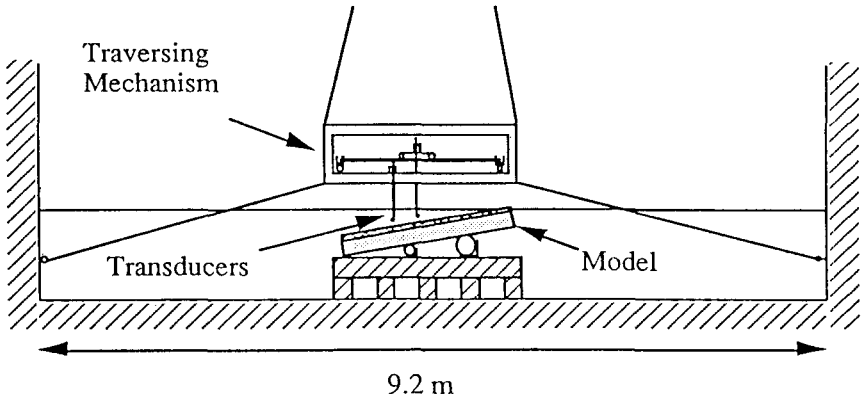
Figure 19: The experiment by Glegg, Deane and House. The model of a solid bottom was mounted in a test pool forming a wedge region as shown.

thickness must also be known. In a previous study[22] this model was used to investigate the acoustic field over a flat bottom and it was found that excellent agreement between measurements and numerical predictions could be achieved over the whole data set if the geo-acoustic parameters were optimized (see [22] for details) to obtain the best fit at a high and a low frequency (30 kHz and 15 kHz). The results given in[22] therefore provide a geo-acoustic calibration of the model.

The measured propagation loss curves as a function of across slope range have been compared with the theory given in the previous section and showed good agreement. However there were some significant differences which occurred at low frequencies. The best agreement was obtained at high frequencies and a typical result is shown in figure 20 for a source frequency of 110kHz . The plot shows the propagation loss as function of across slope range. There is excellent agreement between the measurements and the predictions at this frequency, and the only discrepancy occurs where the experimental levels reach the noise floor at a propagation loss of 12dB. Note that the shadow zone is clearly identified and that the details of the interference pattern in the acoustic field is well predicted by the source image theory. In general the levels are reduced with increasing source/receiver separation, and the shadow zone is preceded by a broad intensity maximum.

At lower frequencies the results showed a different trend, and a typical example is shown in figure 21 for a source frequency of 70 kHz. It is seen that the theory predicts a shadow zone at a smaller source/receiver separation than was measured. The major features of the propagation loss curve are predicted, but it would appear that the measured and theoretical curves are misplaced in range. The discrepancy is worst at low frequencies and at the smaller downslope ranges of the traverse. It is noteworthy that these effects are largest where the horizontal refraction of the modes is most pronounced .

Apart from the discrepancy shown in figure 21 this series of experiments has served as excellent verification of the theories described in sections 2 and 3. Figure 20 shows almost exact agreement with the image source theory for three dimensional sound propagation over a layered shear supporting sea floor and no other numerical or analytical method has been able to reproduce results with this accuracy in such a complex environment.
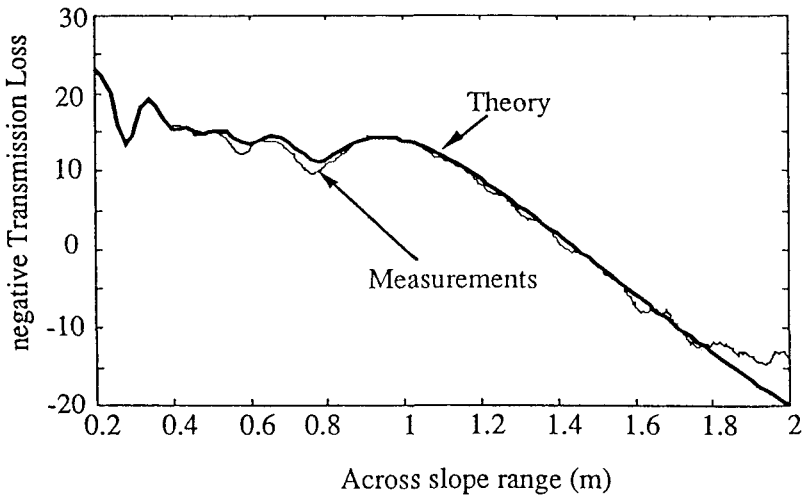
Figure 20: Comparison of the image source theory and measurements at 110kHz for a source and receiver 15cm downslope of the wedge apex.
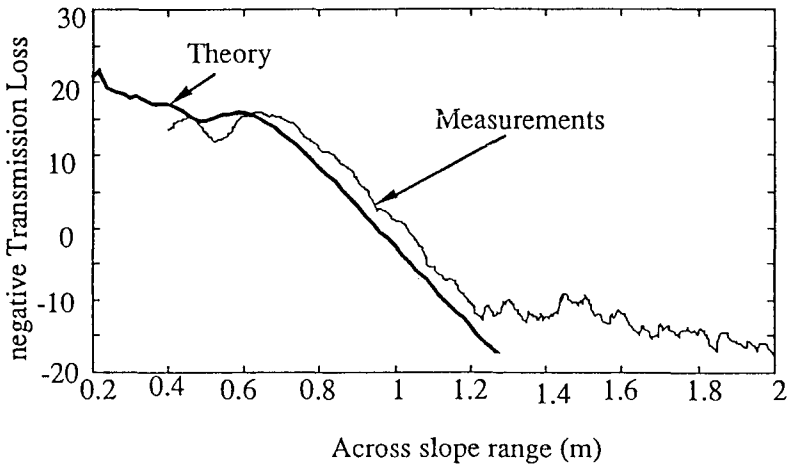
Figure 21: Comparison of the image source theory and measurements at 70kHz for a source and receiver 15cm downslope of the wedge apex.

5. Ocean Acoustic Experiments

As described above, a number of studies have used laboratory scale measurements to identify the effects of sloping bottoms on underwater sound propagation. However, there have been only a few ocean acoustic experiments designed to measure these effects. Horizontal refraction was investigated by Doolittle et al. [7] on the east Australian continental slope. Additional work on downslope enhancement was investigated by Carey et al. [23] in the Gulf of Mexico, and also by Dosso and Chapman [24] off the west coast of Canada.

The experiment by Doolittle et al. [7] investigated horizontal refraction of underwater sound propagation over a sloping bottom. The experiment took place over the continental slope on the east coast of Australia. The slope of the shelf ranged from 0.43° nearshore, to 17° 50 kilometers from shore. Over most of the region, the bottom consisted of a smooth-sandy sediment at least 200 meters deep. The experiment consisted of two ships initially 34 km apart and 30 km from the shoreline. One ship towed a 152 Hz CW source at 80 meters water depth, and the other towed an array of receivers at a depth of 60 meters. The two ships started in approximately 500 meters water depth and proceeded out to deeper water keeping the heading of the source at an angle of 38 degrees from the receiving array. The signals from the array were beamformed using conventional and minimum variance (MV) algorithms. MV processing was used to suppress interfering noise, and spatially whiten the noise field. In the absence of horizontal refraction, the acoustic energy should arrive at angles close to 38 degrees. (Some deviation of the source heading occurred during the experiment but this was less than 8 degrees). The azimuthal arrival angles of acoustic energy significantly varied from 38 degrees, with some arrivals coming in at angles as large as 88 degrees, thus implying the presence of horizontal refraction. Simulated beamforming results using ideal wedge theory [4] helped confirm the results of the experiment.

In addition to the investigation of horizontal refraction, downslope enhancement has also been studied with ocean experiments. Downslope enhancement is an ocean acoustic feature of propagation over sloping bottoms. The effect has been described as a megaphone effect. As sound propagates downslope, each bottom reflection reduces the bottom angle by twice the slope angle. Therefore, the propagation angles of shallow water sound energy are reduced significantly enough to be trapped in the deep sound channel when they reach deep water away from the continental shelf. This energy propagates without bottom interactions, and the acoustic energy propagates long distances with very little attenuation. This phenomenon is described as downslope enhancement.

This feature of propagation over sloping bottoms was investigated by Carey et al. [23] in the Gulf of Mexico. The experiment was conducted over the Florida Plain for a range of 200 km at a depth of 3400 meters until the West Florida Escarpment was encountered. The source was then traversed over the 8.6 degree slope of the escarpment. The sound speed profiles taken along the track of the experiment had a strong negative gradient, therefore making the acoustic propagation bottom interacting. The experiment used a towed source driven at 67 and 173 Hz, operating at a depth of 100 meters. The receiver was a seismic streamer composed of 64 groups of hydrophones spaced at 4.75 meter intervals. The array was towed at 400 meters depth, and individual hydrophone and range averaged pressures were recorded. Estimates of downslope enhancement were made by comparing the measured transmission loss to the flat-bottom transmission loss model FACT. Downslope enhancement for propagation over the slope was estimated to be 2-4 dB on the average, and as high as 6 dB at 67 Hz. At 173 Hz, the maximum downslope enhancement was also estimated at 6 dB. Frequency dependent propagation effects were observed as the source traversed upslope. At the higher frequency, transmission loss increased rapidly after the source crossed the range of maximum downslope enhancement. However, at the lower

frequency, the transmission loss remained almost constant as the source traversed upslope. The variation in transmission loss over the slope as a function of frequency was believed to be caused by frequency dependent propagation characteristics of the seafloor.

Downslope enhancement was also investigated by Dosso and Chapman[24] off the west coast of Canada. This experiment took place over the deep ocean basin, at a depth of 2500 meters, the continental slope, which was elevated nominally at 5 degrees, and the continental shelf, at an average depth of 150 meters. On the continental slope, a pinnacle from an ocean bottom ridge is present. Two ships were used in the experiment, the first ship dropped SUS charges which were detonated at a depth of 22 meters. The second ship maintained position and monitored an array of hydrophones suspended at a depth of about 300 - 400 meters below a surface buoy. The placement of the array was at the axis of the sound channel, thus maximizing the effects of downslope enhancement. To estimate the magnitude of downslope enhancement, a flat-bottom transmission loss model was compared to the experimental measurements. As the source traversed over the pinnacle on the continental slope, the measured transmission loss was 7 dB less than the prediction of the flat-bottom model at a source frequency of 400 Hz. (Before the onset of the slope, the measured and modeled transmission loss were nearly identical.) As the source crossed the top of the continental shelf, the measured transmission loss was 15 dB less than the prediction of the flat-bottom model at 400 Hz. At a location farther over the shelf, bottom interaction with the shelf increased the transmission loss rapidly. In addition to the downslope enhancement, frequency dependent propagation effects were also observed. For propagation over the deep ocean basin and the shelf, transmission loss increased with increasing source frequency, due to attenuation in the bottom. However, at the range of maximum downslope enhancement, there was very little frequency dependence. This is due to the rays only encountering one or two bottom bounces before being trapped in the sound channel.

6. Conclusion

This article has reviewed the current theory and experimental results which have addressed the problem of fully three dimensional underwater sound propagation over a sloping bottom. Particular attention has been paid to across slope propagation because this includes significant three dimensional effects. The results have shown that the theory for acoustic propagation over a bottom of any type with a constant slope is now complete and has been verified by laboratory scale experiments. However there has only been one full scale ocean experiment on horizontal refraction. This showed a significant three dimensional effect, and it seems surprising that further work has not been done in this area.

One of the limitations of the wedge models described in the article is that they all have assumed a uniform sound velocity profile in the water column. In the ocean the sound speed will vary significantly with depth and also with range and further work needs to be done in extending these theories to the case where the sound speed profile either reduces or enhances the horizontal refraction of the sound waves. Furthermore the models have assumed bottoms with constant slope and uniform bottom properties. These never occur in the real ocean and extensions need to be made in this area. One approach which incorporates all these features is the Gaussian beam method developed by Bucker[25], which has been successfully verified using the ideal penetrable wedge theory[11].

7. Acknowledgments

8. References

1. M.A. Biot and I. Tolstoy, "Formulation of wave propagation in infinite media by normal coordinates with an application to diffraction," *J. Acoust. Soc. Am.* **29**, pp 381-391 (1957).
2. D.E. Weston, "Horizontal refraction in a three dimensional medium of variable stratification", *Proc. Roy. Soc London*78 pp 46-52, 1961.
3. C.H. Harrison, "Acoustic shadow zones in the horizontal plane," *J. Acoust. Soc. Am.* **65**, pp 56-61 (1979).
4. M.J. Buckingham, "Acoustic propagation in a wedge-shaped ocean with perfectly reflecting boundaries," *NRL Report 8793*, March 1984.
5. P.M. Morse and K. U. Ingard in *Theoretical Acoustics,* McGraw Hill, 1968
6. G.N. Watson in *A treatise on the Theory of Bessel Functions,* second edition, Cambridge University Press,1958. p416
7. R. Doolittle, A. Tolstoy, M.J. Buckingham, "Experimental confirmation of horizontal refraction of cw acoustic radiation from a point source in a wedge-shaped environment", *J. Acoust. Soc. Am.* **83**, pp 2117-2125 (1988).
8. L.S. Wang and N.G. Pace, "Evaluations of the analytic solution for the acoustic field in an ideal wedge and the approximate solution in a penetrable wedge," *J. Acoust. Soc. Am.* **89**, pp 115-124 (1991).
9. C.T. Tindle and G.B. Deane, "Sound propagation over a sloping bottom using rays with beam displacement," *J. Acoust. Soc. Am.* **78**, pp 1366-1374 (1985).
10. G.B. Deane and C.H. Tindle,"A three-dimensional analysis of acoustic propagation in a penetrable wedge slice," *J. Acoust. Soc. Am.* **92**, pp 1583-1592 (1992).
11. G.B. Deane and M.J. Buckingham, "An analysis of the three-dimensional sound field in a penetrable wedge with a stratified fluid or elastic basement," *J. Acoust. Soc. Am.* **93**, pp 1319-1327 (1993).
12. E.K. Westwood, "Complex ray methods for acoustic interaction at a fluid-fluid interface," *J. Acoust. Soc. Am.* **85**, pp 1872-1884 (1989).
13. E.K. Westwood, "Ray methods for flat and sloping shallow water wave guides," *J. Acoust. Soc. Am.* **85**, pp 1885-1894 (1989).
14. E.K. Westwood, "Broadband modeling of the three-dimensional penetrable wedge," *J. Acoust. Soc. Am.* **92**, 2212-2222 (1992).
15. M.J. Buckingham, "Theory of three-dimensional acoustic propagation in a wedgelike ocean with a penetrable bottom," *J. Acoust. Soc. Am.* **82**, pp 198-210 (1987).
16. L.M. Brekhovskikh and Y.P. Lysanov, *Fundamentals of Ocean Acoustics* (Springer Series on Wave Phenomena, New York 1991)
17. S.A.L. Glegg, "The effective depth approximation for sound propagation in shallow water over a sediment layer and a hard rock basement," *J. Acoust. Soc. Am.* **94**, pp 3302-3311 (1993).
18. A.B. Wood, "Model experiments on sound propagation in shallow seas," *J. Acoust. Soc. Am.* **31**, 1213-1235 (1959).
19. C.T. Tindle, H. Hobaek, and T.G. Muir, "Downslope propagation of normal modes in a shallow water wedge," *J. Acoust. Soc. Am.* **81**, 275-286 (1987).
20. S.A.L. Glegg and J.R. Yoon, "Experimental measurements of three-dimensional propagation in a wedge-shaped ocean with pressure-release boundary conditions," *J. Acoust. Soc. Am.* **87**, 101-105 (1990).

21. S.A.L. Glegg, G.B. Deane, and I.G. House, "Comparison between theory and model scale measurements of three-dimensional sound propagation in a shear supporting penetrable wedge," *J. Acoust. Soc. Am.* **94**, 2334-2342 (1993).
22. S.A.L. Glegg, A.J. Hundley, J.M. Riley, J. Yuan, H. Uberall, "Laboratory scale measurements and numerical predictions of underwater sound propagation over a sediment layer," *J. Acoust. Soc. Am.* **92**, 1624-1630 (1993).
23. W.M. Carey, I.B. Gereben, B.A. Bronson, "Measurement of sound propagation downslope to a bottom-limited sound channel", *J. Acoust. Soc. Am*, **81**, pp 244-257, 1987
24. S.E. Dosso, N.R. Chapman, "Measurement and modeling of downslope acoustic propagation loss over a continental slope"; *J. Acoust. Soc. Am.*, **81**, pp 258-268, 1987
25. H.Bucker, "A simple 3-D Gaussian beam sound propagation model for shallow water"; *J. Acoust. Soc. Am.*, **95**, pp 2437-2440, 1994

MODELING OF SOUND PROPAGATION OVER A SHEAR-SUPPORTING SEDIMENT LAYER AND SUBSTRATE

JUAN I. ARVELO
Alliant Techsystems Inc.,
Advanced Technology Center
Arlington, VA 22209

JIANREN YUAN, HERBERT ÜBERALL and KHALID CHOUFFANI
Department of Physics
Catholic University of America
Washington, DC 20064

A series of model tank measurements carried out by Glegg et al. at Florida Atlantic University (FAU) has furnished data for range-independent and for downslope sound propagation over consolidated bottom sediments simulating the ocean floor. The modeled ocean floor consisted of an epoxy layer over a semi-infinite concrete basement. The measured range-independent transmission loss is compared here against predicted results from a fast-field propagation model, a normal-mode propagation model, and a parabolic-equation propagation model at frequencies of 15, 20, 25, and 30kHz. The measured downslope transmission loss is compared against predicted results from the normal-mode and the parabolic-equation models at frequencies of 15, 20, and 30kHz. The three models were selected for their treatment of bottom elasticity which cannot be neglected in such a hard-bottom case. Mode coupling did not seem to be a significant contributor to sound propagation in the 5-degree downslope case. These comparisons show some unexpected agreement between models and against the measured data in a controlled environment.

1. Introduction

Since 1986 some benchmark test cases were created to compare results of acoustic propagation models in range-dependent and range-independent simple waveguides[1,2]. Each test case was supposed to have an exact analytical solution in order to compare each model's results against the benchmark. A large number of papers were published with results from individual models in several of the benchmark test cases[3].

The accuracy of models should also be tested in "real world" situations by comparing their results against accurate experimental measurements. Comparison against experimental measurements is not as easy for the lack of a controlled environment where the measurements are made with minimum temporal and spatial fluctuations. It is also very difficult to measure the bottom composition to the desired accuracy.

In an attempt to provide a set óf reliable measurements, Glegg[4,5], at Florida Atlantic University, developed a model waveguide consisting of a 7.6m wide test pool which contained a 2.88m long, 30cm thick water-immersed concrete slab (modeling a limestone basement) covered with a 5.88cm

thick epoxy layer (modeling an ocean bottom sediment). A sound source was placed at a constant depth of 5cm and a receiver was placed at various depths and ranges. A continuous-wave signal at the desired frequency was emitted by the source. The coatings at the side walls of the tank absorbed most of the incident energy.

The sound speed in the water column is 1510m/s, its density is 1gm/cc and its attenuation is zero. The epoxy sediment had a compressional speed of 2100m/s, compressional attenuation of 1.14dB/λ, a shear speed of 970m/s, a shear attenuation of 4.0dB/λ, and a density of 1.03gm/cc. This epoxy layer overlays a concrete basement with estimated compressional speed of 3300m/s, compressional attenuation of 0.1dB/λ, shear speed of 1937m/s, shear attenuation of 0.147dB/λ, and density of 2.6gm/cc.

Two types of measurements were carried out:

(1) Range-independent[4]:
Transmission loss measurements in the range-independent model were made at ranges of 1.0m to 2.2m in increments of 0.2m, and at depths of 0.1cm to 14.0cm in increments of 0.05cm. The depth of the water column is 15cm. Measurements were made at the frequencies of 15, 20, 25, and 30kHz.

(2) Downslope propagation[5]:
The same concrete slab from the range-independent case has tilted to a 5-degree downslope angle relative to the test pool. The water depth is 15cm at the source position. Transmission loss versus depth measurements were made at ranges of 0.4m to 2.0m in increments of 0.4m. These measurements were made at frequencies of 15, 20, and 30kHz.

Previous publications compared a small sample of the measurements against a modeled prediction[6,7]. Our attempt here is to compare every piece of available experimental data against predicted results from multiple propagation models, and to show some unexpected agreements and disagreements between the models and against the data.

Three models were selected to estimate sound propagation in this tank waveguide. The models are representations of three low-frequency approaches which can account for sediment elasticity. It is very important to understand the features and limitations of each model for a successful interpretation of their results.

The objective of the three models is to find the solution to the linear homogeneous equation of motion in an elastic medium, where λ and μ are the Lame constants, ρ is the density, and $\xi=\{u,v,w\}$ is the displacement vector in the medium

$$\rho \frac{\partial^2 \xi}{\partial t^2} = \mathbf{f} + (\lambda + \mu)\nabla\Theta + \Theta\nabla\lambda + \mu\nabla^2\xi + 2\nabla\mu\cdot\mathbf{S},$$

f being an external force, $\Theta = \nabla\cdot\xi$, and the strain tensor is († = transpose)

$$\mathbf{S} = \tfrac{1}{2}[\nabla\xi + (\nabla\xi)^\dagger].$$

This equation must be solved for a waveguide with a pressure-release surface and an elastic layered bottom. At low frequencies, bottom penetration is expected and wave-theory based models are suitable.

The SAFARI model[8] is a fast-field approach developed by Henrik Schmidt. This range-independent model uses a direct, global matrix approach to determine the depth-dependent Green function. It directly evaluates the contour integral numerically to obtain the acoustic pressure field. Given the correct integration parameters, its results correctly account for the continuous spectrum

of the wavenumber. However, the number of Green function evaluations increases proportionally with increasing range. Also the asymptotic form of the Hankel function limits its accuracy to ranges greater than the order of the wavelength.

The KRAKENC model[9] is a normal-mode approach developed by Michael Porter. The contour integral is evaluated by adding the complex poles of the Green function. This model makes use of Richardson extrapolation to aid its eigenvalue search in the complex wavenumber plane. Since only the trapped modes are used in the computation of the complex pressure field, this model is limited to far-field propagation. This model can also search for interface modes given all the time it needs for proper convergence. The adiabatic approximation is the only available method for treating the range-dependent waveguide with elastic bottom sediments. This approach is valid only for slow horizontal variations. Therefore, energy conservation is an issue in range-dependent cases.

The FEPES model[10] is a parabolic-equation approach developed by Michael Collins. This range-dependent model uses finite-difference to solve, in closed form, a modified wave equation. The elliptic Helmholtz equation is approximated by a parabolic equation which is valid for a vertical angle near the horizontal. This particular parabolic equation model has an energy-conservation correction and accounts for forward mode coupling.

Algorithms based on finite-difference[11] and finite-elements[12] are excluded from this comparison because their computational requirements are extensive. Coupled-mode models[13] are excluded from this study because they do not handle bottom elasticity. A ray-theory based model was developed and used for some of the low-frequency test case benchmarks[14] proving that excellent agreement can be achieved with a ray-theory model in a low-frequency problem, but this model has not been generalized for more complicated waveguide problems.

2. Results

2.1. Range-independent

In these comparisons, all dimensions and frequencies have been scaled by a factor of 1000 in order to feed the models with values in the typical ocean range and avoid possible numerical errors. The water depth is scaled to 150m, the source is 50m deep, and the frequencies are 15, 20, 25, and 30Hz. The experimental measurements where scaled accordingly by adding 60dB to the given transmission loss. The attenuations are scaled assuming a linear dependence with frequency.

The self-starter[15] in FEPES was used to generate the field at the source; the depth of the false bottom was set to 1000m. A convergence test was made with each propagation model. Convergence in FEPES was achieved with four Padé coefficients using range and depth increments of two meters for all frequencies. This same increment was used as the depth spacing in KRAKENC. The results from the convergence test are not shown here in an attempt to minimize the number of figures in this paper.

The minimum and maximum phase speeds in KRAKENC were set from zero to 3300.0m/s. The maximum phase speed in SAFARI was set constant at 1×10^8m/s; the minimum phase speed was 150m/s in the 15Hz case, 200m/s in the 20Hz case, 250m/s in the 25Hz case, and 300m/s in the 30Hz case to keep the range increment constant in all cases. A sampling of 4096 or 8192 was enough for SAFARI to converge at all frequencies.

The highest frequency of 30Hz can excite a total of four trapped modes as shown in Figure 1. For this same case SAFARI displayed the possible existence of at least one additional mode as shown by the peaks of the integrand in Figure 2. This mode is part of the radiating spectrum and it is not possible to detect it by KRAKENC. This additional contribution is of much concern when using KRAKENC in this case because the ranges are relatively short. The minimum range of one kilometer is about seven times the water depth. The maximum range of 2.2 kilometers is about 14
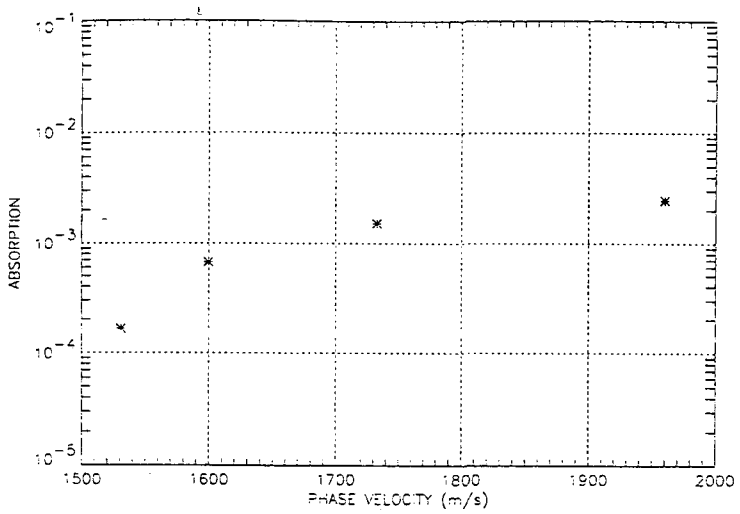
Figure 1. The four complex eigenvalues found by KRAKENC in the 30Hz range-independent case.
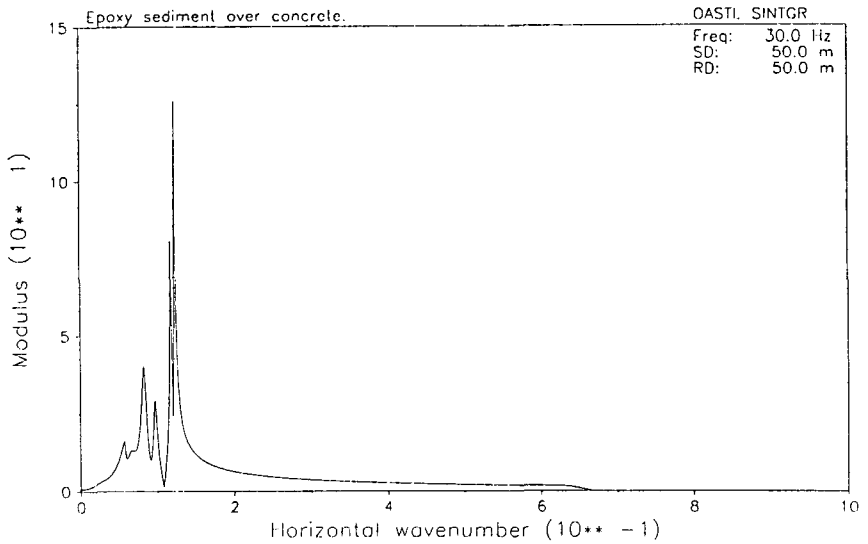
Figure 2. Integrand computed by SAFARI in the 30Hz range-independent case.

times the water depth. At this larger range, the radiating spectrum is expected to be attenuated and KRAKENC should compare more favorably.
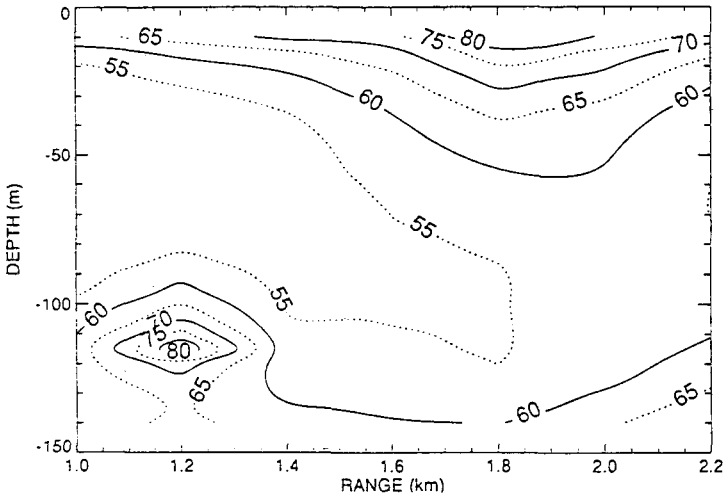
Figure 3a. Measured propagation field scaled for 30Hz signal.
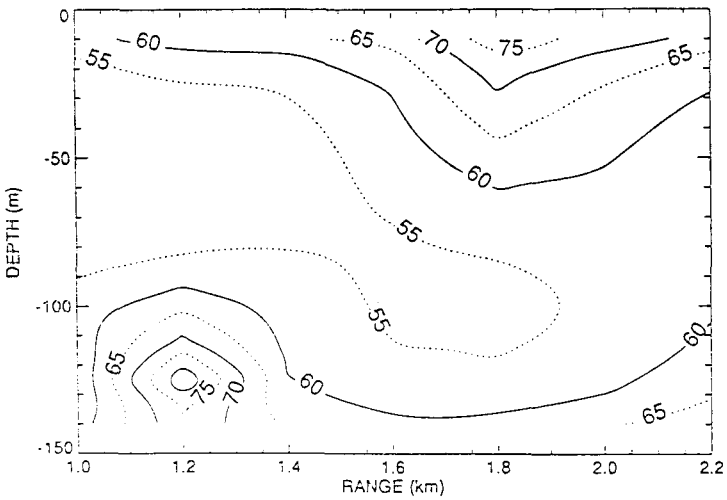
Figure 3b. Predicted propagation field by SAFARI for 30Hz signal.
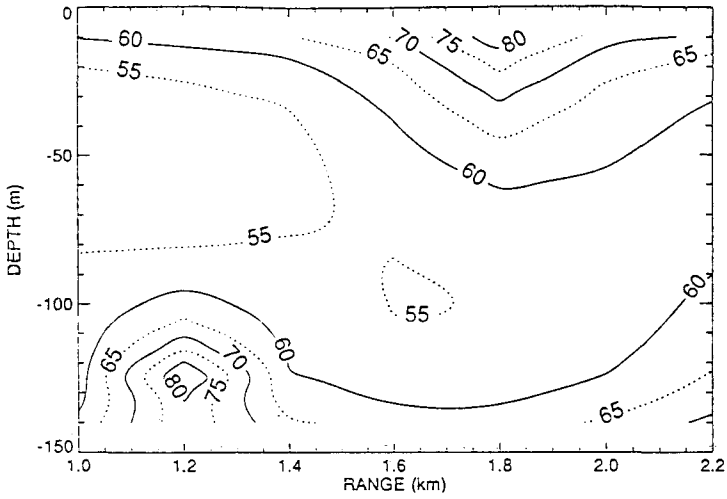
Figure 3c. Predicted propagation field by KRAKENC for 30Hz signal.
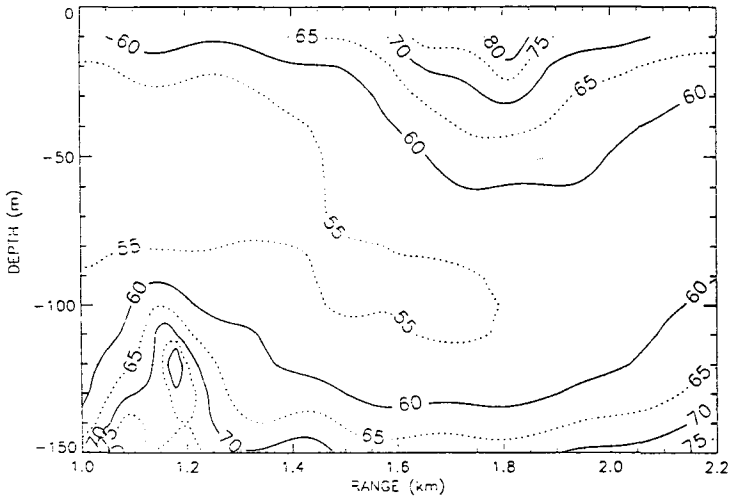
Figure 3d. Predicted propagation field by FEPES for 30Hz signal.

Figure 3a is a contour plot using the 30Hz measured transmission loss data as a function of range and depth. Figures 3b, 3c, and 3d are the estimated propagation according to SAFARI, KRAKENC, and FEPES, respectively. Excellent agreement can be seen with the exception of FEPES' prediction near the bottom and at close distance from the source. This may be attributed

to the limitation in the vertical angle of propagation in such a hard bottom case. Otherwise, FEPES performs as well as the other models. In using FEPES, the user is advised to avoid placing the source or receiver near any interface. Also note that KRAKENC slightly overestimates the loss by
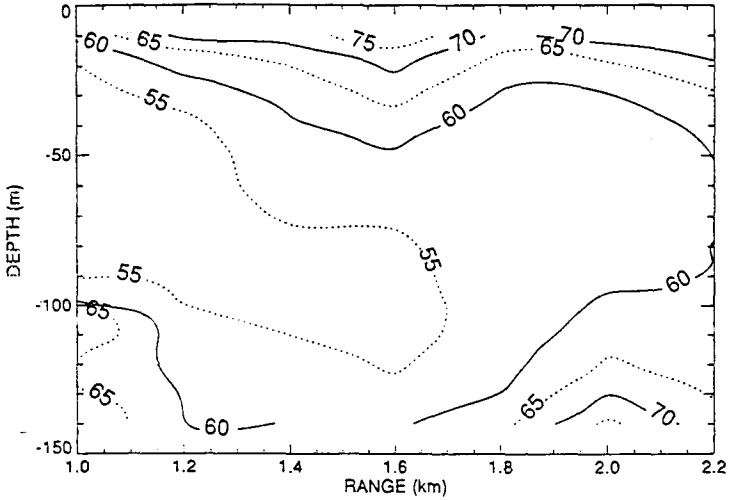
Figure 4a. Measured propagation field scaled for 25Hz signal.
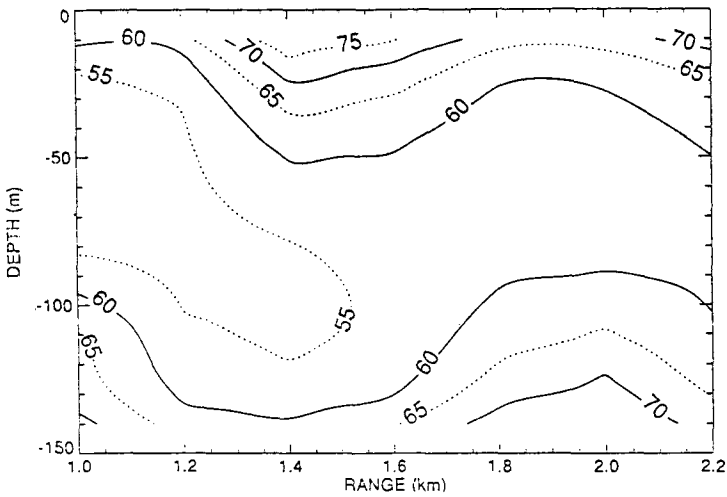
Figure 4b. Predicted propagation field by SAFARI for 25Hz signal.
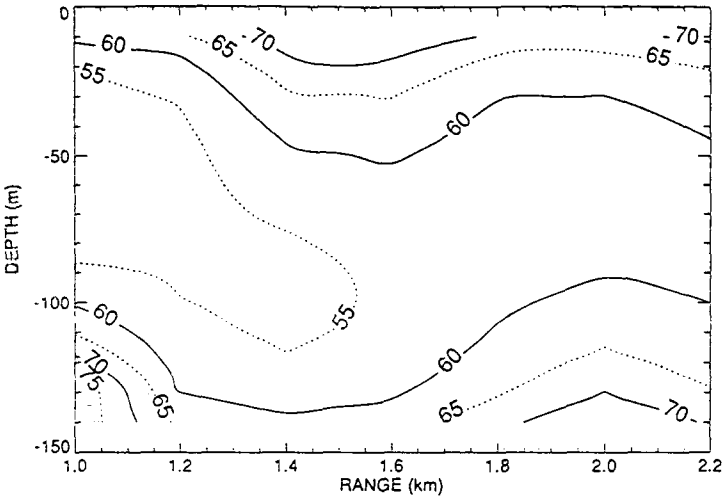
Figure 4c. Predicted propagation field by KRAKENC for 25Hz signal.
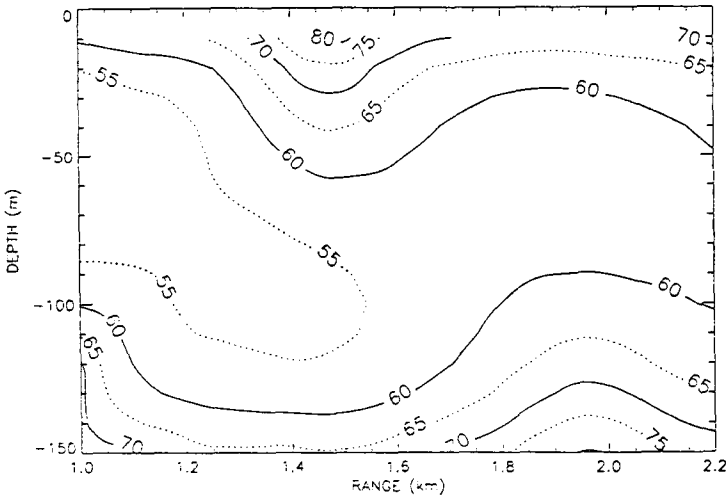
Figure 4d. Predicted propagation field by FEPES for 25Hz signal.

a decibel or two. In this case, SAFARI was closest to the measured data with KRAKENC and FEPES off by a small amount.

Figures 4 compare the propagation at 25Hz. In this case, the models compare slightly better against each other than against the measured data. The best agreement can be found between

SAFARI and KRAKENC. Note that FEPES disagrees somewhat near the surface and the bottom interfaces in areas with relatively high transmission loss. This might be attributed to numerical errors associated with the approach. Remember that KRAKENC was not expected to agree with
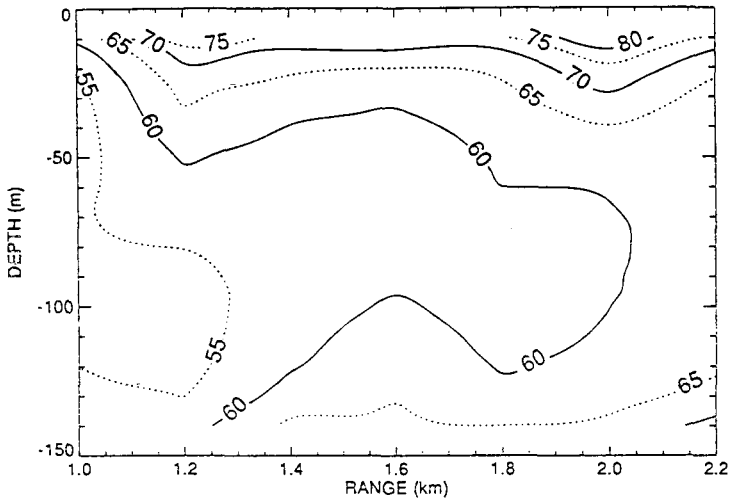
Figure 5a. Measured propagation field scaled for 20Hz signal.
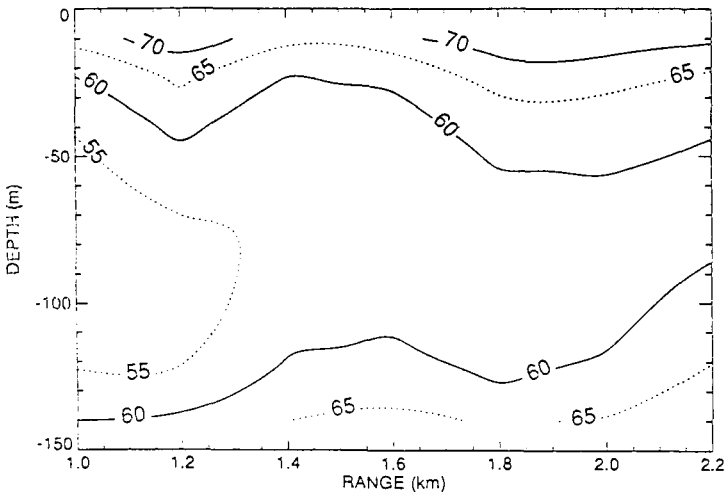
Figure 5b. Predicted propagation field by SAFARI for 20Hz signal.
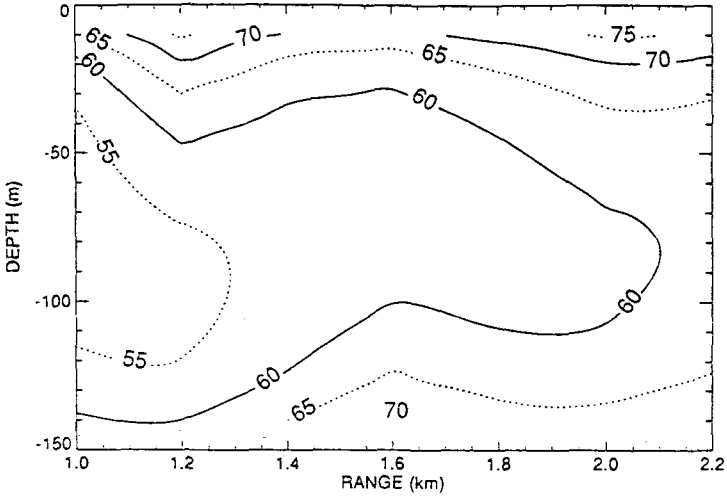
Figure 5c. Predicted propagation field by **KRAKENC** for 20Hz signal.
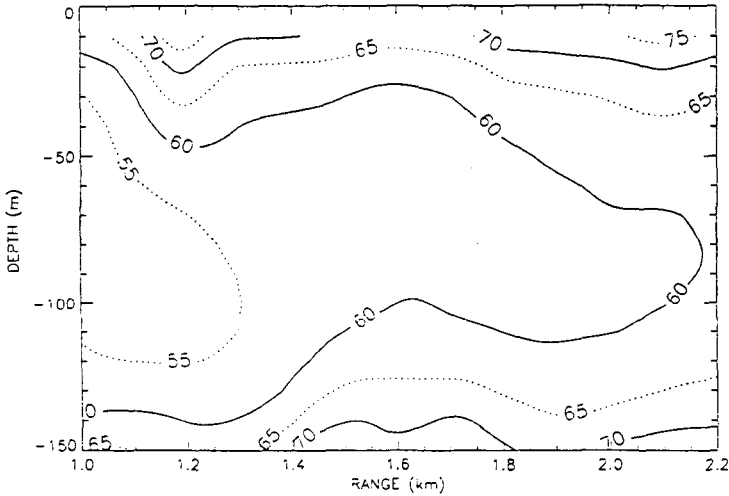
Figure 5d. Predicted propagation field by FEPES for 20Hz signal.

SAFARI at ranges shorter than about ten times the water depth for the expected contribution of the radiating wavenumber spectra. The agreement in these figures indicates that the waveguide's hard layered bottom is damping this energy faster than expected.

Figures 5 display the results at 20Hz. Note that SAFARI predicts that sound propagates farther

in range than the other models and the measured data. In this case KRAKENC compared slightly better against the data. Inter-model comparison at this frequency shows the best agreement between KRAKENC and FEPES. At this frequency we are reaching cutoff. It seems that the models are
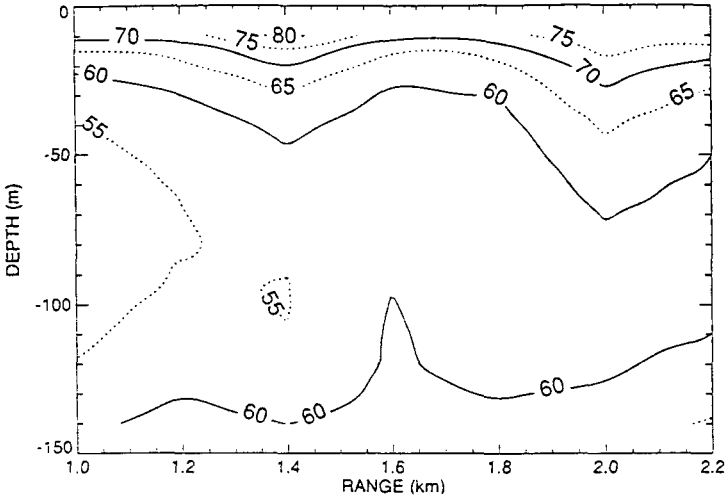
Figure 6a. Measured propagation field scaled for 15Hz signal.
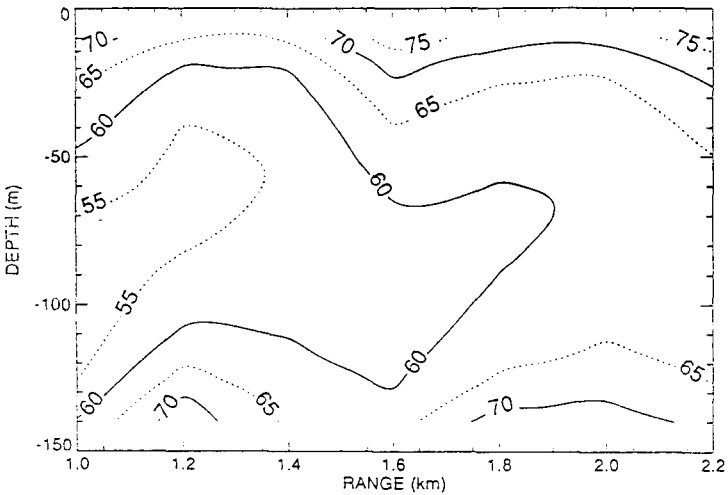
Figure 6b. Predicted propagation field by SAFARI for 15Hz signal.
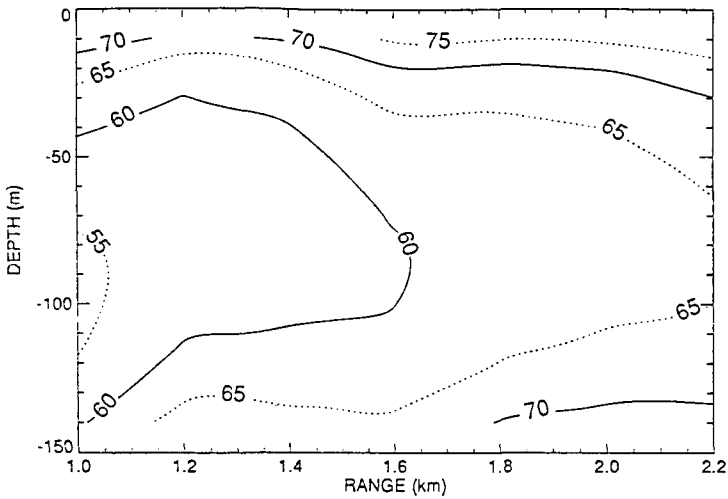
Figure 6c. Predicted propagation field by KRAKENC for 15Hz signal.
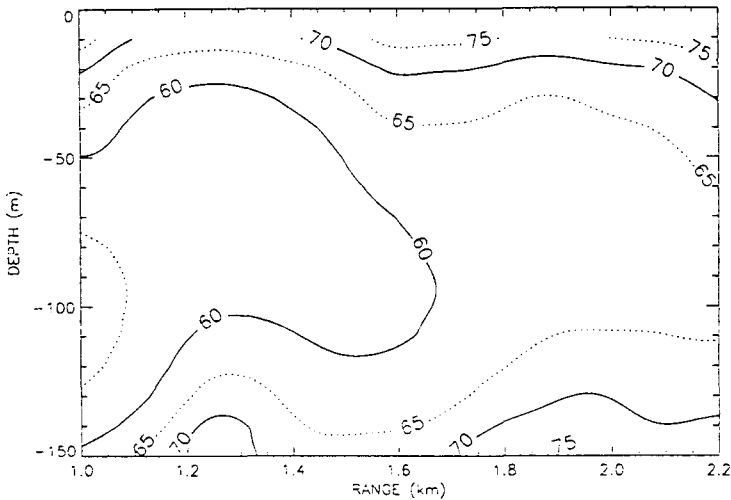
Figure 6d. Predicted propagation field by FEPES for 15Hz signal.

increasingly erroneous as we reach the waveguide's cutoff frequency.

Figures 6 show the final results at 15Hz. The modeled results no longer resemble the measured propagation conditions. The models themselves disagree more against each other. Inter-model comparison shows the most agreement between KRAKENC and FEPES, but their agreement is

poor. The SAFARI model is still predicting less transmission loss than the other models. At this frequency, the ranges vary from 10 to 20 times the acoustic wavelength. All the models have some kind of approximation at such short ranges. The Hankel functions in KRAKENC and SAFARI, for example, are substituted by their asymptotic solution. This solution is valid at ranges much greater than a wavelength. The approximations in FEPES also include a far-field assumption to reduce the cylindrical wave equation.

However, it is also possible for the acoustic properties of the concrete basement to be inaccurate. This possibility surfaces when we compare the sediment thickness of 58.8 meters to the acoustic wavelength. The comparison at 30Hz was favorable because the wavelength is shorter than the layer thickness. At 25Hz, the wavelength is nearly equal to the sediment thickness. At the lower frequencies, basement interaction is no longer negligible and the erroneous inputs show their effects.

A series of SAFARI runs were made to determine the degree of influence of the semi-infinite concrete basement at the four frequencies of interest. These additional runs were made without the concrete basement. Instead, the bottom was modeled as a semi-infinite epoxy basement. The resulting transmission loss contour showed a negligible variation of the field at 25 and 30Hz, a somewhat poorer propagation at 20Hz, and a totally different field at 15Hz. This simple experiment shows the obvious influence of the concrete basement on the propagated field at the lower frequencies. Since the disagreements between measured and modeled fields occur at these lower frequencies, it is very possible that the acoustic properties of the concrete basement are inaccurately known. The results from these additional runs are not shown in an attempt to reduce the number of figures.

Measurements were also made at a frequency of 8kHz[4]. These measurements are below the 10kHz cut-off frequency of the waveguide and the modeled results did not agree well with the data. It was suggested by Glegg that the disagreement could be caused by the finite thickness of the concrete slab. The concrete has been modeled as a semi-infinite basement. However, we were not able to obtain a fair agreement with the finite slab. For this reason the comparisons at 8kHz are not shown in this paper.

2.2 Downslope propagation

The number of transmission loss measurements versus depth varied from range to range. Also, these measurements were made at ranges of 0.4, 0.8, 1.2, 1.6, and 2.0m. These two facts made it inconvenient to display contour plots as was done in the range-independent case. Therefore, the comparisons are made by overlaying measured and modeled data for each frequency/range combination.

Many of the input parameters given to the FEPES propagation model in the downslope cases were unchanged from those in the range-independent cases. The range-dependent waveguide was modeled by eleven segments representing the 5-degree tilt of the bottom. Each segment was 20cm in range and each step was 1.75cm deeper with increasing segment. This same segmentation of the waveguide was applied to the KRAKENC model where a set of normal modes had to be computed for each segment before computing the field using the adiabatic approximation. The self-starter was used and a total of four Padé coefficients was found to be sufficient in the field computation by FEPES.

The downslope comparisons are shown in Figures 7, 8, and 9 for the transmission loss at 30, 20, and 15kHz, respectively. Figures 7 present the comparisons to the 30kHz data at the receiver ranges of (a) 0.4m, (b) 0.8m, (c) 1.2m, (d) 1.6m, and (e) 2.0m. The FAU transmission loss measurements are here represented by stars, the KRAKENC results by a solid curve, and FEPES
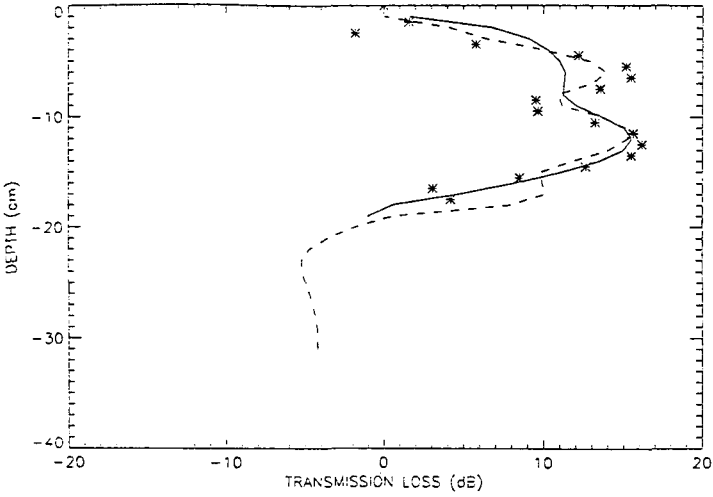
Figure 7a. Overplot of measured (stars), KRAKENC (solid), and FEPES (dash) fields for 30kHz signal and 0.4m range.
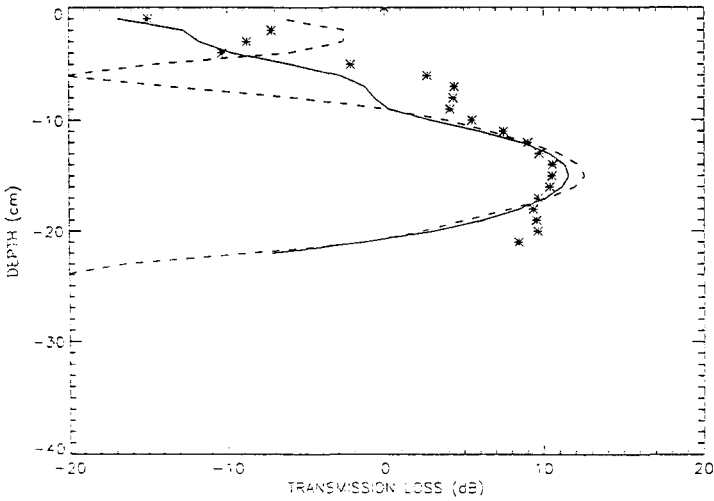
Figure 7b. Overplot of measured (stars), KRAKENC (solid), and FEPES (dash) fields for 30kHz signal and 0.8m range.
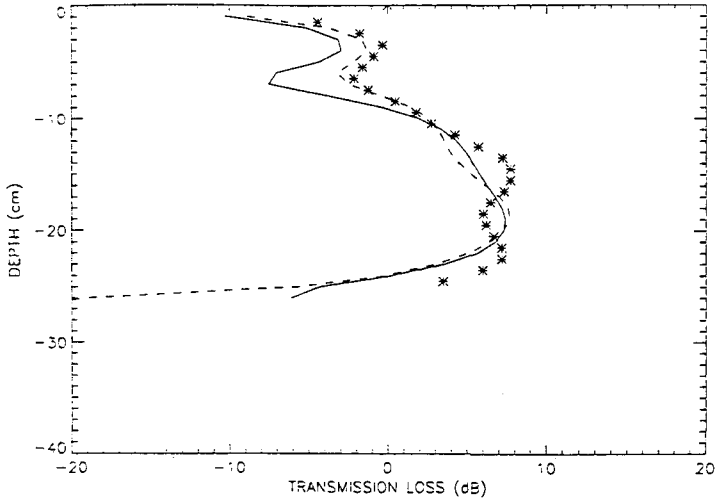
Figure 7c. Overplot of measured (stars), KRAKENC (solid), and FEPES (dash) fields for 30kHz signal and 1.2m range.
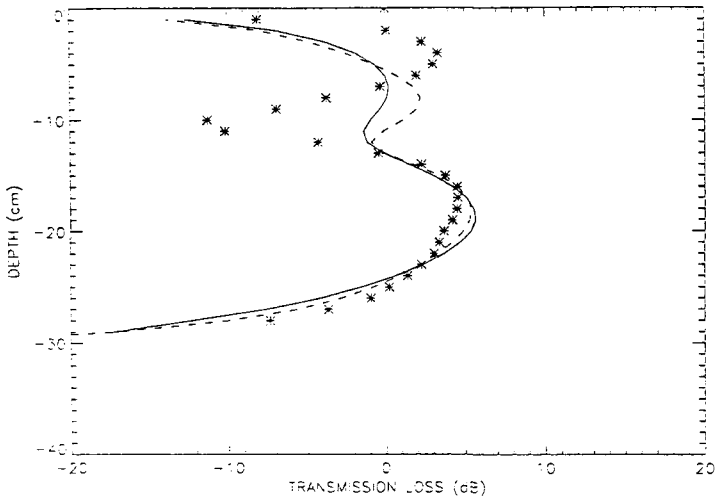
Figure 7d. Overplot of measured (stars), KRAKENC (solid), and FEPES (dash) fields for 30kHz signal and 1.6m range.
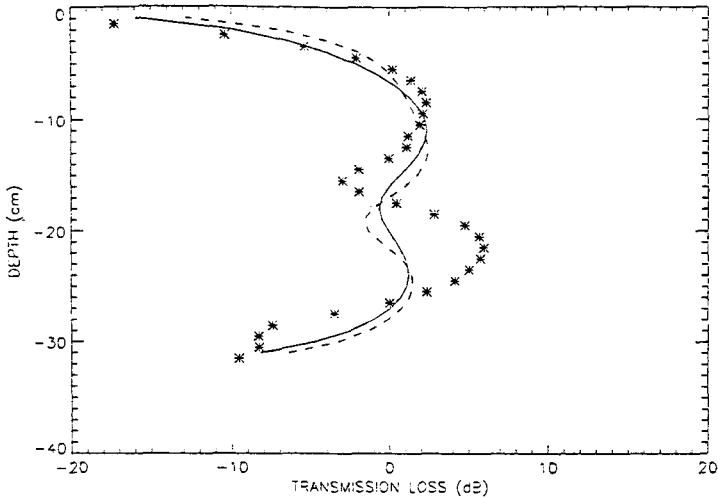
Figure 7e. Overplot of measured (stars), KRAKENC (solid), and FEPES (dash) fields for 30kHz signal and 2.0m range.

by a dashed curve. Note the drastic difference in the modeled curves at the shorter ranges compared to those at ranges larger than about a meter. The shorter ranges are three to six times the water depth. None of the models are expected to perform well at such short ranges. The normal mode model does not account for the radiating spectra and the parabolic equation model was shown to give poor results at short ranges and near the surface or bottom interfaces. Slightly better agreement between the models is found at larger ranges. While the magnitudes are not always in numerical agreement at the maxima or minima of the data, the location in depth of these extreme, and the extreme themselves, are always reproduced at least qualitatively.

The comparisons at 20kHz are displayed in Figures 8. Note that the modeled results are in better agreement when compared against each other and against the data. The favorable inter-model comparison show the satisfactory accuracy of the adiabatic approximation in a downslope case with a 5-degree bottom slope. Since FEPES accounts for the mode coupling that is neglected under the adiabatic approximation, these inter-model comparisons show little need for mode coupling in this case.

The results of the 15kHz downslope case are shown in Figures 9. In this case, the agreement between the two models increases with increasing range. This same tendency is also observed in the 30kHz downslope case in Figures 7. However, this observation is not obvious in the 20kHz downslope case in Figures 8. Note in Figures 9(a) and 9(b) that the results from FEPES were significantly closer to the measured data than those of KRAKENC. However, the models predicted more loss at the larger ranges than what was observed. This could be attributed in part to the inaccurately known properties of the concrete basement.
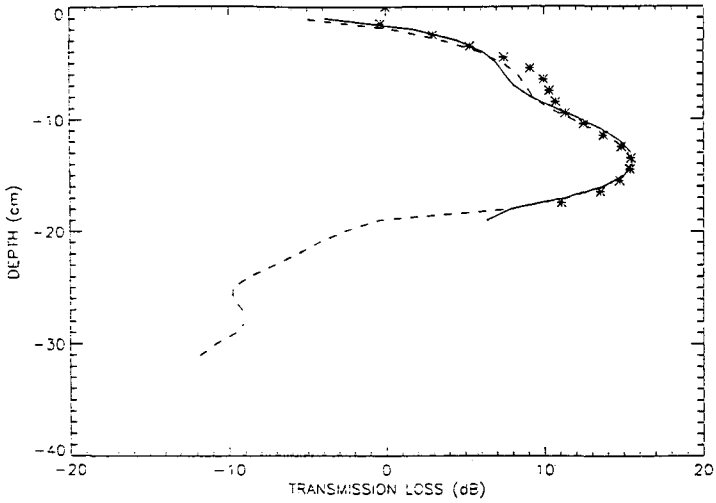
Figure 8a. Overplot of measured (stars), KRAKENC (solid), and FEPES (dash) fields for 20kHz signal and 0.4m range.
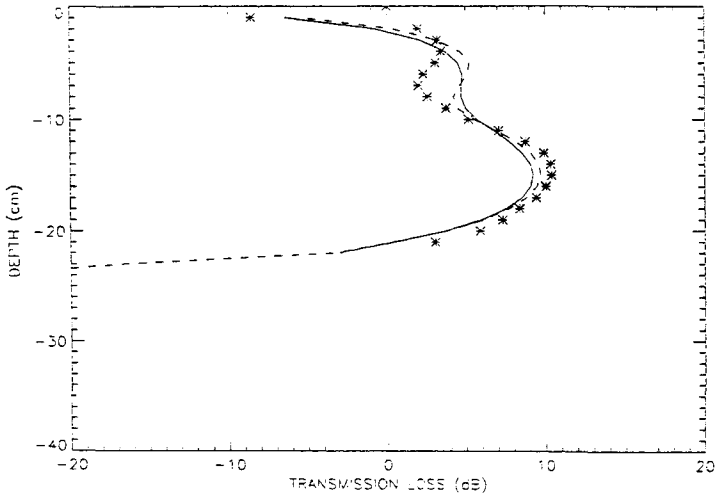
Figure 8b. Overplot of measured (stars), KRAKENC (solid), and FEPES (dash) fields for 20kHz signal and 0.8m range.
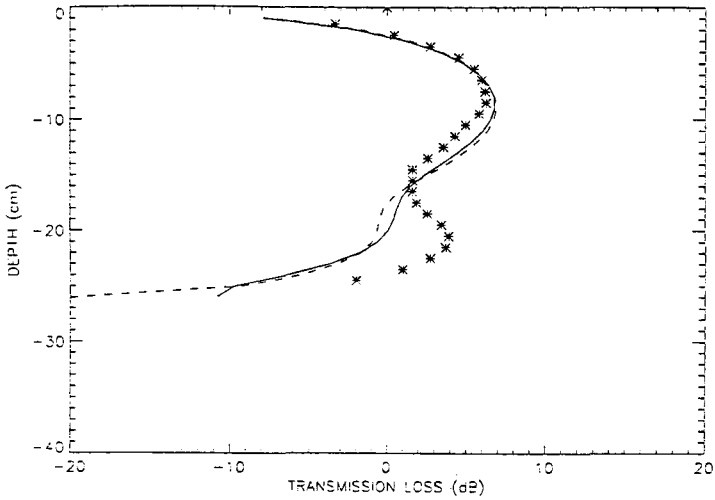
Figure 8c. Overplot of measured (stars), KRAKENC (solid), and FEPES (dash) fields for 20kHz signal and 1.2m range.
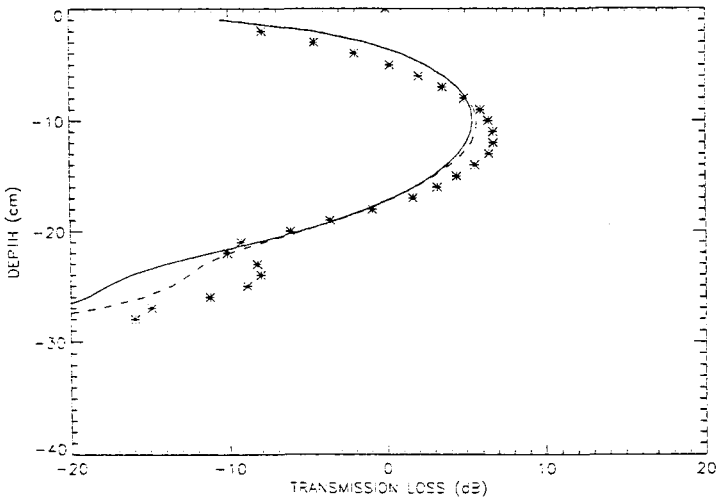
Figure 8d. Overplot of measured (stars), KRAKENC (solid), and FEPES (dash) fields for 20kHz signal and 1.6m range.
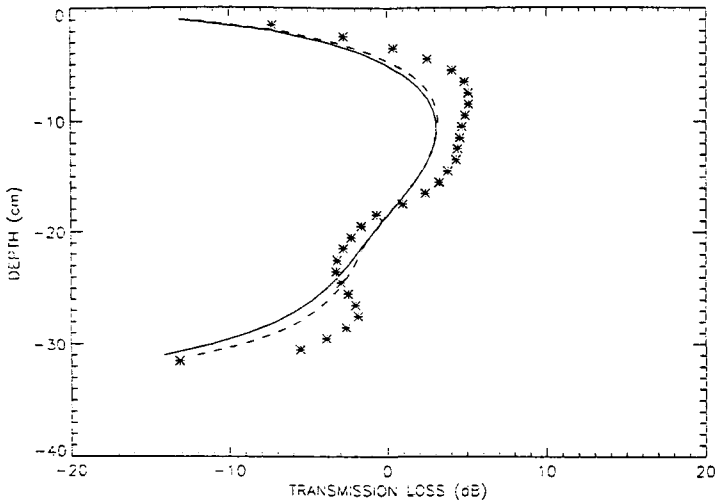
Figure 8e. Overplot of measured (stars), KRAKENC (solid), and FEPES (dash) fields for 20kHz
    signal and 2.0m range.

3. Summary

A series of experimental data have been taken by Glegg et al. at the FAU model tank facility,
which models an ocean environment consisting of a single sediment layer (represented by epoxy
resin) overlaying a chalk-bottom substrate (represented by a concrete slab). In the first part of this
study, we have compared the results from three propagation models to the range-independent
measured data. The models are based on the normal-mode, the parabolic-equation, and the fast-
field solutions to the wave equation. In the second part, we compared the results from two of the
models to the downslope data.

In general, the models compare very well against each other as long as the frequency is much
greater than the cutoff frequency. The greatest inter-model disagreements can be found near the
surface, near the bottom, and near the source. The SAFARI fast-field model displayed a tendency
of under-predicting the transmission loss at the lower frequencies when compared against the other
models. All the models displayed a tendency of over-predicting the transmission loss near the cut-
off frequency (about 10kHz) in the range-independent case and the downslope case. This was
attributed to the inaccurately known concrete basement.

The FEPES parabolic-equation model displayed problems predicting the field near the surface
and bottom interfaces. The adiabatic approximation used with the KRAKENC normal-modes
model was shown to give satisfactory results in a 5-degree downslope waveguide.

Tables 1 show a qualitative summary of the level of agreement between each model and the
measured data in each case. In the range-independent cases, the results from KRAKENC tended
to agree with those of SAFARI at the higher frequencies but they agreed better with those of
FEPES at the lower frequencies. The results from the three models agreed poorly with the
measured data near the cutoff frequency. In the downslope cases, the performance of both models
against the data was equivalent. It is also observed that the level of disagreement between
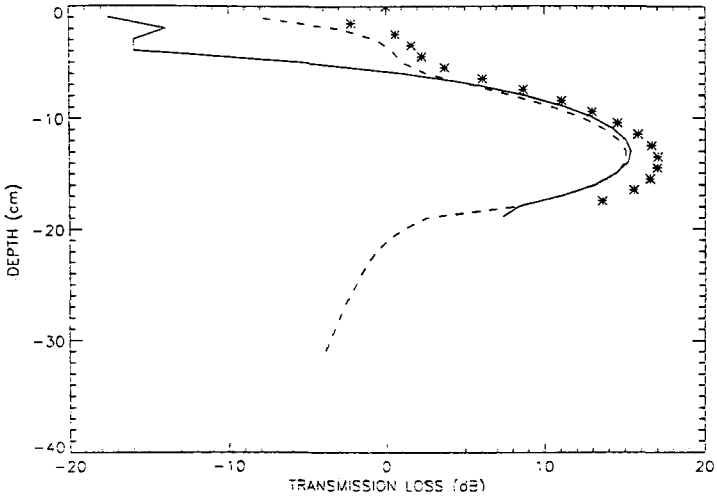
Figure 9a. Overplot of measured (stars), KRAKENC (solid), and FEPES (dash) fields for 15kHz signal and 0.4m range.
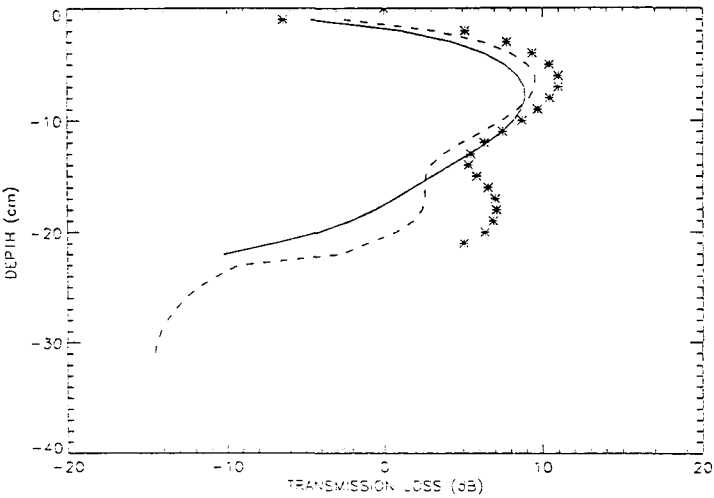
Figure 9b. Overplot of measured (stars), KRAKENC (solid), and FEPES (dash) fields for 15kHz signal and 0.8m range.
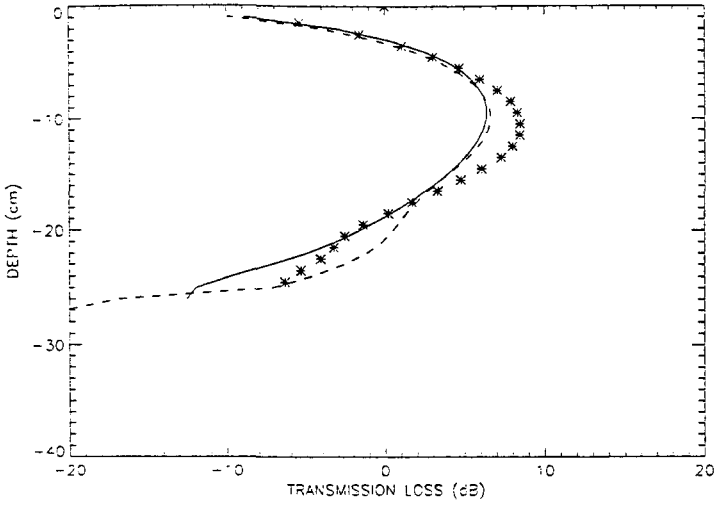
Figure 9c. Overplot of measured (stars), KRAKENC (solid), and FEPES (dash) fields for 15kHz signal and 1.2m range.
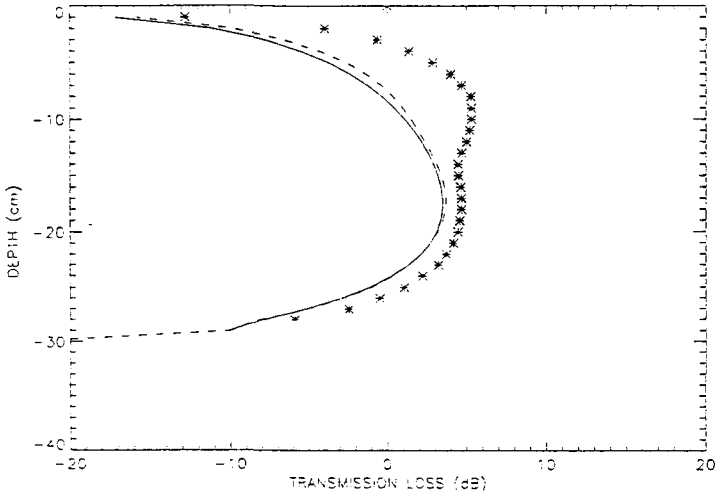
Figure 9d. Overplot of measured (stars), KRAKENC (solid), and FEPES (dash) fields for 15kHz signal and 1.6m range.
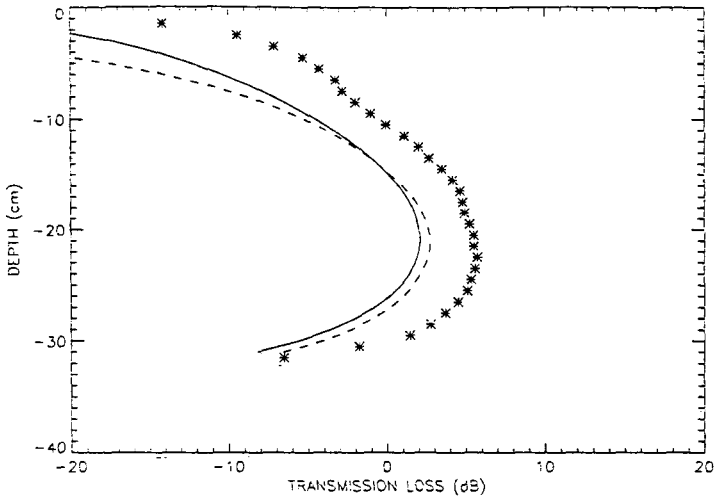
Figure 9e. Overplot of measured (stars), KRAKENC (solid), and FEPES (dash) fields for 15kHz-
    signal and 2.0m range.

KRAKENC and FEPES increased with increasing frequency as also observed in the range-
independent cases. Very good agreement was observed, between the modeled and measured data,
at the higher frequencies (>20kHz) in the range-independent case. However, this degree of
agreement was not observed in the downslope case. An explanation for this observation has not
been found.

4. Acknowledgements

5. References

1. First IMACS Symposium on Computational Acoustics, Yale University, 6-8 August 1986.
2. Panel Discussions: What Benchmarks are Relevant?, *J. Acoust. Soc. Am.* Suppl. 1, **80**
   (1986) p. S38.
3. Solutions to range-dependent underwater acoustics benchmark problems, *J. Acoust. Soc. Am.*
   87 (1990) 1497-1545.
4. S. A. L. Glegg and A. J. Hundley, "Experimental results of sound propagation in a uniform
   depth water column with a bottom which can support shear," Center for Acoustics and
   Vibration report, Florida Atlantic University, 1990.
5. S. A. L. Glegg and I. G. House, "Experimental results of downslope sound propagation over
   a bottom which can support shear," Center for Acoustics and Vibration report, Florida Atlantic

Table 1.
Qualitative agreement between the models and against the measurements.

RANGE-INDEPENDENT CASE			
Frequency	SAFARI	KRAKEN	FEPES
30Hz	Good	Good ←→ Good	Average
25Hz	Good	Good ←→ Good	Average
20Hz	Average	Fair	Fair ←→ Excellent
15Hz	Poor	Poor ←→ Poor	Poor

DOWNSLOPE CASE		
Frequency	KRAKEN	FEPES
30Hz	Average	Average
20Hz	Good ←→ Good	Good
15Hz	Poor ←→ Poor	Poor

LEGEND	
⊕	Excellent
⊖	Good
○	Average
⊜	Fair
●	Poor
←→	Significant agreement between the models

University, 1991.

6. J. Yuan, H. Überall, L. Hargenrader, J. I. Arvelo, and S. A. L. Glegg, "Normal mode studies of underwater sound horizontal or downslope propagation over a sediment-covered ocean floor," in Computational Acoustics - Proceedings of the 3rd IMACS International Symposium on Computational Acoustics, Harvard University, Cambridge, MA, USA, 26-28 June 1991 (D. Lee, R. Vichnevetsky, and A. R. Robinson, eds.), Elsevier Science Publishers, Amsterdam, The Netherlands, Vol. 2, pp. 269-281.

7. S. A. L. Glegg, A. J. Hundley, J. M. Riley, J. Yuan, and H. Überall, "Laboratory scale measurements and numerical predictions of underwater sound propagation over a sediment layer," *J. Acoust. Soc. Am.* **92** (1992) 1624-1630.

8. H. Schmidt, "SAFARI User's Guide", SACLANTCEN SR-113, SACLANT Undersea Research Centre, La Spezia, Italy, 1988.

9. M. Porter, "The KRAKEN Normal Mode Program," SACLANTCEN SM-245, SACLANT Undersea Research Centre, La Spezia, Italy, 1991.

10. M. D. Collins, "A higher-order parabolic equation for wave propagation in an ocean overlying an elastic bottom," *J. Acoust. Soc. Am.* **86** (1989) 1459-1464.

11. R. A. Stephens, "User's Guide for FINDIF at SACLANTCEN," Woods Hole Technical Memorandum, WHOI-07-92, 1992.

12. J. E. Murphy and S. A. Chin-Bing, "A finite-element model for ocean acoustic propagation and scattering," *J. Acoust. Soc. Am.* **86** (1990) 1478-1481.

13. R. B. Evans, "A coupled mode solution for acoustic propagation in a waveguide with stepwise depth variations of a penetrable bottom," *J. Acoust. Soc. Am.* **74** (1983) 188-195.

14. E. K. Westwood, "Ray model solutions to the benchmark wedge problems," *J. Acoust. Soc. Am.* Vol. **87** (1990) pp. 1539-1545.

15. M. D. Collins, "A self-starter for the parabolic equation method," *J. Acoust. Soc. Am.* **92** (1992) 2069-2074.

PROPAGATION OF ACOUSTIC PULSES
IN LAYERED MEDIA

P.P. DELSANTO, E. RUFFINO
INFM - Dip. di Fisica, Politecnico di Torino
C.so Duca degli Abruzzi 24 - Torino - Italy

and
D.IORDACHE
Physics Dept. of Bucuresti Politehnica
Splaiul Independentei 313 - Bucharest - Romania

Abstract

In order to solve the general problem of acoustic or ultrasonic wave prop-
agation in layered media, it is necessary to solve the wave equation both in
the homogeneous region inside each layer and at the interfaces between layers.
Under special assumptions these problems may be solved analytically. Explicit
formulas are given for the wave amplitudes in the case of oblique incidence of
harmonic plane waves on interfaces between two solid materials. Since ana-
lytical methods become extremely laborious in non elementary cases and do
not allow for a realistic treatment, e.g. in the case of pulses induced by finite
aperture transducers, a short review of numerical techniques is included. In
particular, the application of a local interaction simulation approach (LISA),
which is particularly suitable for parallel processing, is reviewed.

1. Introduction

For the purpose of the present work, we define a multilayer as an infinite medium,
enclosed in the space region $0 \leq x \leq H$ and consisting of $N \geq 1$ layers, separated by
N-1 interfaces located at $x = h_n$ with n=1, N-1. Consequently, in order to study the
propagation of acoustic or ultrasonic waves or pulses in layered media, it is sufficient
to be able to solve the two basic problems
   i) solution of the wave equation within a single layer, i.e. in a homogeneous region
   ii) treatment of the interface between two layers. This problem must include also
the treatment of the external surfaces $x = 0$ and $x = H$ with specified boundary
conditions.
Solutions to the first of these two problems are given in Sec.2 for plane waves
and/or isotropic media, after a brief derivation of the equation of motion in Sec.2.1.
The second problem is treated in Sec.3. First the elementary case of normal incidence
is treated in great detail, in order to provide the basic physical concepts with a
minimum of mathematical formalism. Next the case of oblique incidence is examined

and the partial mode conversion effect is explained. Here the calculations become very cumbersome and explicit formulas for the displacement amplitudes of the longitudinal and shear reflected and transmitted waves are given, both in the case of longitudinal and shear incident waves. These formulas may be useful to experimentalists[1] or to verify numerical solutions. Similar formulas, but for the potential amplitudes, are reported in Ref.2. In Sec.2 only the case of disturbances, which are uniform in planes of constant phase, and, more specifically, of harmonic waves is considered.

Although, in principle, any multilayer problem may be solved, under the stated assumptions, by repeatedly applying the formulas and methods discussed in Sections 2 and 3, the calculation may quickly become extremely laborious, even if few interfaces are involved. Matrix methods, such as commonly used in other fields, such as Optics[3], may be of help. Two such methods are introduced in Sec.3. First an S matrix is defined, which yields the amplitudes of the "final" (reflected and transmitted) waves as a linear combination of the amplitudes of the incident waves. Then a reflection and a transmission matrix are defined for both longitudinal and shear waves in the case of oblique incidence. A comprehensive review of matrix methods is given by Rokhlin[4], who classifies transfer matrices according to the size: 8×8 for piezoelectric layers, 6×6 for anisotropic layers[5], 4×4 for isotropic layers[6-10] and 2×2 for special cases, such as normal incidence, SH-waves, fluids, etc[11-14]. By repeatedly applying matrix methods (to propagate waves from an interface or boundary to the next one and across) one can reduce a wave propagation problem in a multilayer into the calculation of products and/or powers of matrices and thus obtain compact solutions. Simple examples of important applications are the calculation of total reflection from a single layer embedded in a fluid[15] and periodically stratified fluid media[16].

In complex cases analytical methods are, however, of very difficult application. Also, they are restricted to special assumptions, as mentioned. In a realistic situation in which, e.g., a piezoelectric transducer is used to input a pulse into a specimen, the above mentioned assumptions are not valid and analytical solutions can offer, at best, a rough estimate of the results. It becomes necessary to apply numerical techniques, especially finite element (FE) and finite difference (FD) equations.

There exists a vast body of literature devoted to FE techniques. For a very comprehensive bibliography on the subject see Ref.17. An overview of FE analysis and its applications to the modelling of ultrasonic NDE phenomena has been presented by Lord and collaborators[18]. FE methods are also used as tools for computer simulation[19].

FD equations have also been widely used to study the propagation of ultrasonic waves. In fact, it is quite natural to transform, for a numerical analysis, a partial differential equation into a FD equation. Many of the applications are due to geophysicists, who have developed FD methods as a tool for the quantitative interpretation of seismograms[20-25]. General treatises on FD equations can be found in Ref.26-30. They are also treated in monographies on the numerical solution of partial differential equations[31,32], some of which are specifically devoted to applications in acoustics and ultrasonics[33,34].

Although FD techniques are very efficient and useful, some caution must be exercised upon applying them, since problems of convergence and stability may arise[32]. This issue, particularly in the context of the treatment of interfaces, is discussed in Sec.4.1.

FD techniques are particulary suitable for computer simulations, since they are apt to reduce a problem from a global to a local level. The advent of highly parallel computation and the anticipation of its wide diffusion and projected progress[35] give a special urgency to the need of developing efficient simulation techniques, which exploit this novel computing architecture. In fact, parallel computers, which control millions of independent processor, are natural tools for simulating the behaviour of a material at a local level, since a correspondence can be created between the processors and spatial "cells" in the material. A local simulation interaction approach (LISA), which is particularly suitable for parallel processing is described in Sec.4.2.

In the framework of LISA it is possible to find a solution to the above mentioned problem of treating interfaces with FD techniques. A sharp interface model (SIM), which provides an exact treatment of the interface by matching displacements and stresses on both sides of it, is discussed in Sec.4.3. Recursive equations for the interface gridpoints are explicitly derived in the elementary 1-D case and reported for the general 3-D case (they may be obtained from the general "crosspoint" formulas derived elsewhere[36,37]).

Due to space limitations, many topics, which are relevant to the general theme of acoustic wave propagation in layered media, have been omitted. Among them are the treatment of attenuative, viscoelastic, dispersive, nonlinear media, Epstein layers, etc. For a discussion of these topics we refer to some of the articles and books quoted previously and to the classical work of Brekhovskikh[38].

2. One layer

2.1. The equation of motion

Acoustic or ultrasonic pulses and waves usually entail extremely small particle displacements, compared to the travelled distance. Therefore the linearized theory of elasticity[39] may be applied. In the absence of body forces one immediately obtains, from basic Mechanics, the so called Cauchy's first law of motion

$$\tau_{ij,i} = \rho(\bar{x})\ddot{u}_j \qquad (1)$$

where τ is the stress tensor, ρ is the density and u is the displacement vector. Here and in the following we denote with a comma the differentiation with respect to the space coordinates and with a dot the differentiation with respect to time, i.e.

$$f_{,i} = \frac{\partial f}{\partial x_i} \qquad\qquad \dot{f} = \frac{\partial f}{\partial t}$$

Also, the summation convention is implied, as usual, for twice repeated indices.

Constitutive relationships bind the stress to the strain. In the linearized theory of elasticity they are given by Hooke's law

$$\tau_{ij} = C_{ijkl}(\bar{x})\epsilon_{kl} \tag{2}$$

where C_{ijkl} represents the second order elastic constants tensor and ϵ_{kl} the small-strain tensor

$$\epsilon_{kl} = \frac{1}{2}(u_{k,l} + u_{l,k}) \tag{3}$$

Due to the symmetries of the elastic constants tensor

$$C_{ijkl} = C_{jikl} = C_{ijlk} = C_{klij} \tag{4}$$

from Eqs.(1) to (3) we obtain the equation of motion

$$(C_{ijkl}\ u_{k,l})_{,i} = \rho(\bar{x})\ddot{u}_j \tag{5}$$

2.2 Solution within a layer

Within a layer, i.e. in a homogeneous region, Eq.(5) becomes

$$C_{ijkl}u_{k,il} = \rho\ddot{u}_j \tag{6}$$

with C_{ijkl} and ρ being constant.

A plane wave solution of Eq.(6) may be easily found. Assuming harmonic plane waves travelling in the direction $\hat{p} = p_n\hat{x}_n$, we write

$$u_i = Ad_i exp(i\eta) \tag{7}$$

where

$$\eta = kp_nx_n - \omega t \tag{8}$$

and d_i are the components of the displacement direction unit vector $\hat{d}$. Substituting into Eq.(6) it follows

$$(C_{ijkl}k^2 p_ip_l - \rho\omega^2\delta_{jk})u_k = 0 \tag{9}$$

which may be conveniently rewritten as

$$(\lambda_{jk} - \rho v^2\delta_{jk})u_k = 0 \tag{10}$$

where

$$\lambda_{jk} = C_{ijkl}p_ip_l \tag{11}$$

and

$$v = \frac{\omega}{k} \tag{12}$$

Eq.(10) is usually referred to as Christoffel's equation[40]. Since it implies that

$$det(\lambda_{jk} - \rho v^2 \delta_{jk}) = 0 \tag{13}$$

one finds that, for each propagation direction $\hat{p}$, there are, in general, three different phase velocities, which may be easily computed by solving Eq.(13).

It may be useful to remark that, by measuring in a homogeneous specimen the phase velocities for the appropriate waves in a sufficient number of propagation directions $\hat{p}$, it is possible, at least in principle, to determine all the second order elastic constants of the material by means of Eqs.(11) and (13). A difficulty with this approach is that, experimentally, one usually measures group velocities, while the above equations refer to phase velocities and, for anisotropic or dispersive media , the phase and group velocities do not generally coincide.[41]

2.3 Helmholtz decomposition

For isotropic materials the elastic constant tensor may be written as

$$C_{ijkl} = \lambda \delta_{ij}\delta_{kl} + \mu(\delta_{ik}\delta_{jl} + \delta_{il}\delta_{jk}) \tag{14}$$

where λ and μ are the so-called Lame' elastic constants.

Then the equation of motion in homogeneous media, Eq.(6) becomes

$$\mu u_{i,jj} + (\lambda + \mu)u_{j,ij} = \rho \ddot{u}_i \qquad (i = 1,3) \tag{15}$$

The three Eqs.(15) may be decoupled by means of a decomposition of the form

$$\bar{u} = \nabla \varphi + \nabla \wedge \bar{\psi} \tag{16}$$

where φ and $\bar{\psi}$ are the scalar and vector potentials, resp.
In the tensorial notation

$$u_m = \varphi_{,m} + e_{mnp}\psi_{p,n} \tag{17}$$

where e_{mnp} is the so-called "alternating" or Levi-Civita tensor, whose components are defined as follows:

$$e_{mnp} = \begin{cases} +1 & \text{if mnp represents an even permutation of 123} \\ 0 & \text{if any two of the mnp indices are equal} \\ -1 & \text{if mnp represents an odd permutation of 123} \end{cases}$$

By substituting Eq.(17) into Eq.(15) and using the identity

$$e_{jnp}\psi_{p,nj} = 0 \tag{18}$$

we obtain

$$\varphi_{,jj} = \frac{1}{v^2}\ddot{\varphi} \tag{19}$$

$$\psi_{p,jj} = \frac{1}{\tilde{v}^2}\ddot{\psi}_p \quad (p = 1, 3) \tag{20}$$

where

$$v = \sqrt{\frac{(\lambda + 2\mu)}{\rho}} \tag{21}$$

$$\tilde{v} = \sqrt{\frac{\mu}{\rho}} \tag{22}$$

The uncoupled wave equations (19) and (20) refer to longitudinal and transversal (or shear) waves, resp. It is easy to prove that, as expected, v and $\tilde{v}$ (twice repeated) are the three solutions of Eq.(13) for the isotropic case. Since $\bar{u}$ has three scalar components while φ and $\bar{\psi}$ have four, an additional constraint may be imposed, e.g. $\psi_{p,p}=0$.

In the case of slightly anisotropic homogeneous specimens, a perturbation treatment may be usefully adopted to obtain explicit solutions of the equation of motion[42].

3. Treatment of interfaces

3.1. Normal incidence

Having discussed, albeit very cursorily, the solution of the single layer problem, we now turn our attention to the treatment of interfaces. We restrict our analysis to the propagation of harmonic plane waves, such as given by Eq.(7), in isotropic media.

In this Subsection we consider the elementary case of normal incidence of a longitudinal acoustic wave on an interface between two different materials. For simplicity we assume that the interface is located in the plane x=0 and put

$$\hat{d} = \hat{p} = \hat{x} \tag{23}$$

The problem then becomes in every respect one-dimensional. We call ρ, v, λ, μ the density, phase velocity and Lame' constants of the material to the left of the interface $(x < 0)$ and ρ', v', λ', μ' the corresponding quantities to its right $(x > 0)$. We consider the possibility of an incident wave u_0 from the left or u'_0 from the right and call u and u' the corresponding reflected or transmitted waves (see Fig.1)

$$u_0 = A_0 exp(i\eta_0); \quad u'_0 = -A'_0 exp(i\eta'_0); \quad u = -A exp(i\eta); \quad u' = A' exp(i\eta') \tag{24}$$

where

$$\eta_0 = k(x - vt); \quad \eta'_0 = k'(-x - v't); \quad \eta = k(-x - vt); \quad \eta' = k'(x - v't) \tag{25}$$

From Eqs.(2), (3) and (14) it follows

$$\tau = \tau_{11} = \sigma \frac{du}{dx} \tag{26}$$
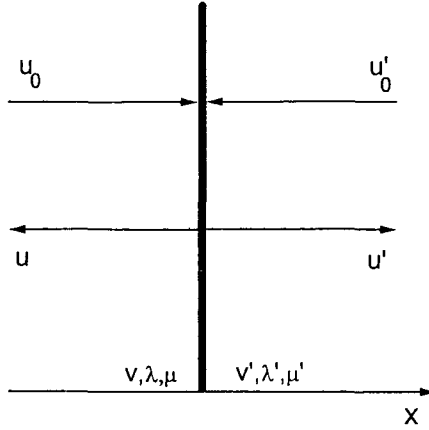
Figure 1: Normal incidence: reflected and transmitted waves

where

$$\sigma = \lambda + 2\mu \tag{27}$$

Likewise for the corresponding primed quantities to the right of the interface. Therefore, in analogy with the displacements, we have for the stress

$$\tau_0 = ik\sigma A_0 exp(i\eta_0) \qquad \tau_0' = ik'\sigma' A_0' exp(i\eta_0')$$
$$\tau = ik\sigma A exp(i\eta) \qquad \tau' = ik'\sigma' A' exp(i\eta') \tag{28}$$

At this point it is necessary to make a model of the matching of the two media at the interface. We consider only the most relevant case of a perfect conctact, in which both displacements and stresses are continuous at the interface. It follows, for x=0

$$u_0 + u = u_0' + u'$$
$$\tau_0 + \tau = \tau_0' + \tau' \tag{29}$$

Since this system must be satisfied for all values of t, the exponentials in it must appear only as common factors. It follows

$$kv = k'v' \tag{30}$$

The system then becomes

$$A_0 - A = -A_0' + A'$$
$$ZA_0 + ZA = Z'A_0' + Z'A' \tag{31}$$

where the impedance Z is defined as:

$$Z = \rho v = \frac{\sigma}{v} \tag{32}$$

The system (31) can be easily solved for the amplitudes of the reflected and trans-mitted waves:

$$\begin{pmatrix} A' \\ A \end{pmatrix} = S \begin{pmatrix} A_0 \\ A'_0 \end{pmatrix}$$ (33)

where

$$S = \begin{pmatrix} t & r' \\ r & t' \end{pmatrix} \qquad (det S = +1)$$ (34)

and r, r' and t, t' are the reflection and transmission coefficients from left to right and viceversa, resp.

$$r = \frac{\zeta - 1}{\zeta + 1} \qquad r' = -r \qquad t = \frac{2}{\zeta + 1} = 1 - r \qquad t' = \frac{2\zeta}{\zeta + 1} = 1 + r \qquad (35)$$

where ζ is the impedance ratio $\zeta = \frac{Z'}{Z}$.

Similar results may be easily obtained for the case of an incident shear wave and for stress waves.

It may be useful to show that the amplitudes, given by Eqs.(33)-(35), satisfy the requirements of energy conservation. In fact, the instantaneous rate of work of the traction acting on a unit area element, is given by[39]

$$P(x,t) = \rho v \dot{u}^2$$ (36)

For the incident wave u_0, it follows

$$P_i = Z A_0^2 \omega^2 [Re(i \; exp \; i\eta_0)]^2$$ (37)

Likewise the reflected and transmitted powers per unit area are given by

$$\frac{P_r}{P_i} = r^2 = \frac{(\zeta - 1)^2}{(\zeta + 1)^2} \qquad \frac{P_t}{P_i} = \frac{Z'}{Z} t^2 = \frac{4\zeta}{(\zeta + 1)^2}$$ (38)

from which it immediately follows

$$P_r + P_t = P_i$$ (39)

3.2. Oblique Incidence

In the case of oblique incidence it is necessary to specify the nature of the incident wave, which may be longitudinal (P), vertically polarized shear (SV) or horizontally polarized shear (SH). In the first case the directions of propagation and displacement vectors coincide, while in the second and third case they are orthogonal. Assuming, as before, that the interface is located in the plane $x_1 = 0$, the displacement vector is in the plane of the propagation vector and of $\hat{x}_1$ in the second case (SV-waves) and normal to it in the third case (SH-waves).
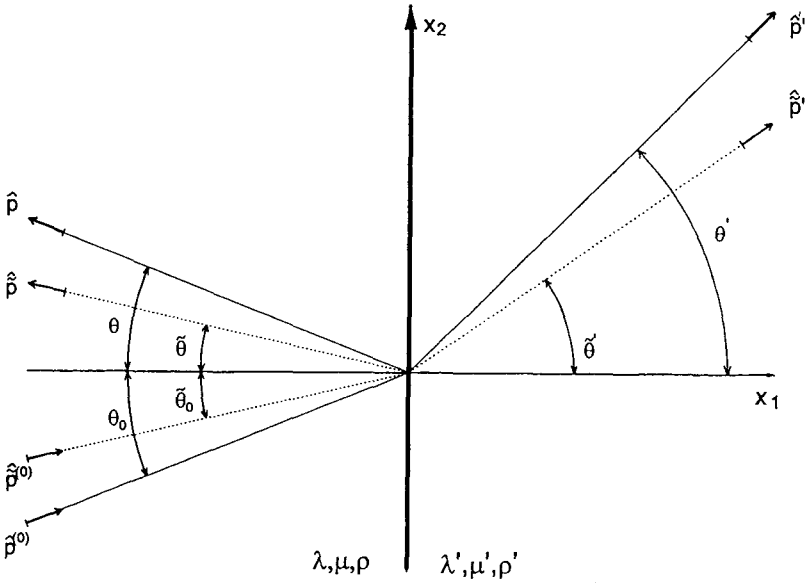
Figure 2: Oblique incidence of P- and/or SV-waves. Reflected and transmitted P- and SV-waves

The case of incident SH-waves is elementary and can be treated similarly to the normal incidence case examined previously. A detailed treatment may be found in ref.39. The case of incident P-waves or SV-waves is more complex, because it gives rise in general to a partial mode conversion (from P to SV or viceversa) and will be studied in the remainder of this Section.

Again we use unprimed symbols for the quantities in the material to the left of the interface ($x_1 < 0$) and primed symbols to its right ($x_1 > 0$). Furthermore we use a tilde to distinguish symbols which refer to SV-waves from the corresponding ones for P-waves: see Fig.2. The incident wave may be a P-wave: $u^{(0)}$, or a SV-wave: $\tilde{u}^{(0)}$. In both cases we impose, as before, the continuity of both the displacements and stresses at the interface $x_1=0$ at all times. Since both the displacements and stresses are in the plane of $\hat{x}_1$ and of the incident propagation vector $\hat{p}^{(0)}$ or $\hat{\tilde{p}}^{(0)}$, four scalar equations are required. For incident P-waves they are

$$u_1^{(0)} + u_1 + \tilde{u}_1 = u_1' + \tilde{u}_1'$$
$$u_2^{(0)} + u_2 + \tilde{u}_2 = u_2' + \tilde{u}_2'$$
$$\tau_{11}^{(0)} + \tau_{11} + \tilde{\tau}_{11} = \tau_{11}' + \tilde{\tau}_{11}'$$
$$\tau_{12}^{(0)} + \tau_{12} + \tilde{\tau}_{12} = \tau_{12}' + \tilde{\tau}_{12}' \tag{40}$$

Similar equations with $u^{(0)}$ and $\tau^{(0)}$ replaced by $\tilde{u}^{(0)}$ and $\tilde{\tau}^{(0)}$ hold for incident SV-waves. In either case, since there are four scalar matching conditions, it is not possible

in general to satisfy them with only two unknowns, i.e. the amplitudes of the reflected and transmitted P-waves (or SV-waves). Therefore a partial mode conversion is in general necessary, as mentioned before.

· Proceeding as in Sec. 3.1 we observe that, since Eqs.(40) must be satisfied at all times and for all values of x_2 at $x_1 = 0$, the exponentials included in the expressions of the displacements and stresses must all be equal. It follows

$$k_0 \sin \theta_0 = \tilde{k}_0 \sin \tilde{\theta}_0 = k \sin \theta = \tilde{k} \sin \tilde{\theta} = k' \sin \theta' = \tilde{k}' \sin \tilde{\theta}'$$
$$k_0 v = \tilde{k}_0 \tilde{v} = kv = \tilde{k}\tilde{v} = k'v' = \tilde{k}'\tilde{v}' \tag{41}$$

Once the incident wave number, k_0 or $\tilde{k}_0$, and angle, θ_0 or $\tilde{\theta}_0$, are specified, the reflected and transmitted wave numbers k, $\tilde{k}$, k' and $\tilde{k}'$, and angles θ, $\tilde{\theta}$, θ' and $\tilde{\theta}'$, may be easily obtained from Eqs.(41). It is then possible, although rather laborious, to solve the system (40). Its solution may be given in terms of a 4×4 S matrix, such as in Eq.(33). It is more convenient, however, to represent the solution, i.e. the amplitudes of the reflected waves, A and $\tilde{A}$, and of the transmitted waves, A' and $\tilde{A}'$, in terms of a reflection matrix R and a transmission matrix T.

$$\begin{pmatrix} A \\ \tilde{A} \end{pmatrix} = R \begin{pmatrix} A_0 \\ \tilde{A}_0 \end{pmatrix} \tag{42}$$

$$\begin{pmatrix} A' \\ \tilde{A}' \end{pmatrix} = T \begin{pmatrix} A_0 \\ \tilde{A}_0 \end{pmatrix} \tag{43}$$

R and T are the generalizations of the reflection and transmission coefficients defined in Eq.(35). Their explicit expression are

$$R = \frac{1}{D} \begin{pmatrix} (B - B')(\tilde{B} - \tilde{B}') - (L - N)(L' - N) & 2\frac{\tilde{v}}{v}(L'\tilde{B}' + N\tilde{B}) \\ 2\frac{v}{\tilde{v}}(LB' - NB) & (B + B')(\tilde{B} - \tilde{B}') - (L + N)(L' + N) \end{pmatrix} \tag{44}$$

$$T = \frac{2\rho G}{D} \begin{pmatrix} \frac{v}{v'} a(\tilde{B} + \tilde{B}') & \frac{\tilde{v}}{v'}\tilde{a}(L + N) \\ \frac{v}{\tilde{v}'} a(L' - N) & \frac{\tilde{v}}{\tilde{v}'}\tilde{a}(B + B') \end{pmatrix} \tag{45}$$

where

$a = \cot \theta;\ a' = \cot \theta';\ \tilde{a} = \cot \tilde{\theta};\ \tilde{a}' = \cot \tilde{\theta}'$
$G = (\frac{v}{\sin \theta_0})^2 = (\frac{\tilde{v}}{\sin \tilde{\theta}_0})^2$
$M = 2(\mu' - \mu),\ Q = \rho' - \rho,\ N = QG - M$
$p = N + \rho G,\ p' = -N + \rho' G,\ L = -a\tilde{a}'M,\ L' = a'\tilde{a}M$
$B = ap,\ B' = a'p',\ \tilde{B} = \tilde{a}p,\ \tilde{B}' = \tilde{a}'p'$
$D = (B + B')(\tilde{B} + \tilde{B}') - (L + N)(L' - N)$

By following the same procedure or as special cases of the above equations, it is possible to obtain the corresponding formulas for interfaces between a fluid and solid or between two fluids.

4. Numerical Techniques

4.1. Finite difference methods

Finite difference (FD) methods are a most natural way to solve partial differential equations (PDE) numerically. By replacing the derivatives with finite differences, it is easy to obtain schemes for the reconstruction of the solution, starting from given initial or boundary conditions. The basic idea is to define a sufficiently fine grid, in which the independent coordinates are discretized. E.g. in the 1-D case we replace the continuous variables x and time with $i\epsilon$ and $t\delta$, resp., where i and t are integers and ϵ and δ represent very small space and time "units". Then, if the PDE contains a single first order time derivative $\dot{y}$, one may adopt a "one step" scheme, such as

$$\dot{y}(x,t) \rightarrow \frac{y(i,t+1) - y(i,t)}{\delta} \tag{46}$$

or a "two steps" scheme

$$\dot{y}(x,t) \rightarrow \frac{y(i,t+1) - y(i,t-1)}{2\delta} \tag{47}$$

By discretizing also the space derivatives and solving for $y(i,t+1)$, one obtains "evolution" equations, that yield $y(i,t+1)$ as a function of initially assigned or previously computed values of y in i and adjacent gridpoints only at the time t in the first case (one step scheme) and at the times t and $t-1$ in the second case. If the PDE contains second order time derivatives, only ≥ 2 steps schemes are, of course, possible. In either case, if the scheme adopted insures a good convergence and stability, and if ϵ and δ are sufficiently small, the set of values $y(i,t)$ represents a satisfactory or even excellent approximation to the PDE solution for a large number of time steps.

Since several FD schemes, such as Eqs.(46) and (47) are possible both for the time and space derivatives, FD methods are very versatile and varied. Problems of convergence and stability may, however, seriously impair the reliability and usefulness of FD techniques[32,43] and should be carefully investigated before employing them. In the present context we are concerned, in particular, with their use in the proximity of an interface between different layers.

To be explicit, let us refer to the wave equation (Eq.5). In the 1-D case, i.e. when a plane wave travels in the direction normal to the interface, Eq.(5) becomes

$$\frac{d}{dx}[\sigma(x)\frac{du}{dx}] = \rho(x)\ddot{u} \tag{48}$$
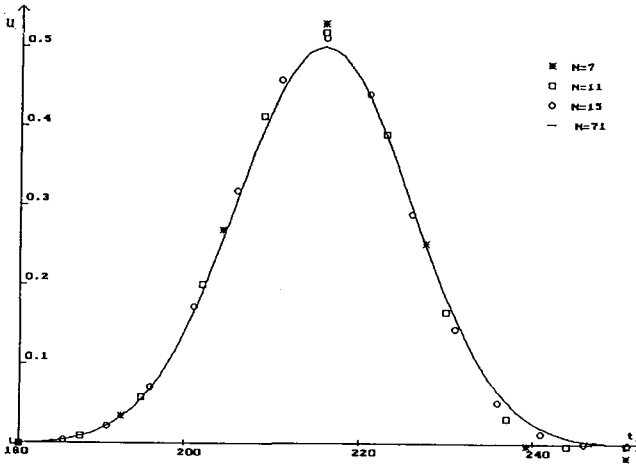
Figure 3: Transmitted pulse, as computed with the model 2a for the elastic constants ratio $\frac{\sigma'}{\sigma} = 3$ and various values of N (number of nodepoints used to represent the pulse)

Across the interface, in general, both $\sigma(x)$ and $\rho(x)$ vary in a discontinuous way since, in a multilayer, interfaces are assumed to be sharp. A rigorous FD treatment requires, however, that the coefficients of the PDE be continuous. Therefore $\sigma(x)$ and $\rho(x)$ must be "smoothed out" over a certain range Δx, which is, of course, arbitrary. This arbitrariness may affect the results and lead to large errors and/or instabilities[44].

To investigate the problem, several "smoothing" models have been considered and simulations of the propagation of a gaussian pulse across an interface have been correspondingly performed. In the models called 1, 2, 3, resp., the smoothing has been performed between $I - \frac{1}{2}$ and $I + \frac{1}{2}$, I and $I + 1$, $I - 1$ and $I + 1$, the interface being located at x=$I\epsilon$. While for models 2b and 3a the mean values of the variables are deduced starting from the values of the parameters corresponding to the adiacent media, for models 2a and 3b they are averaged only over the adjacent intervals. (For more details, see Ref.44). The question of the convergence with respect to the number of the nodepoints N, used to describe a pulse of arbitrary shape, has also been addressed.

By comparing the computed values of the transmitted pulse (i.e. after crossing the interface) with the results of an exact calculation, it has been found that
a)   model 1 has always perfect convergence and stability
b)   model 2a is stable, but its convergence is good only if N is sufficiently large (see Fig.3)
c)   model 2b and 3a do not converge to the correct result for large values of the ratio $\frac{\sigma'}{\sigma}$ (in fact the discrepancy may be very large; see Fig.4), even for smaller values of $\frac{\sigma'}{\sigma}$ the difference is still small, especially for model 3a (Fig.5).
d)   model 3b has a good convergence up to a point, but then it becomes unstable.
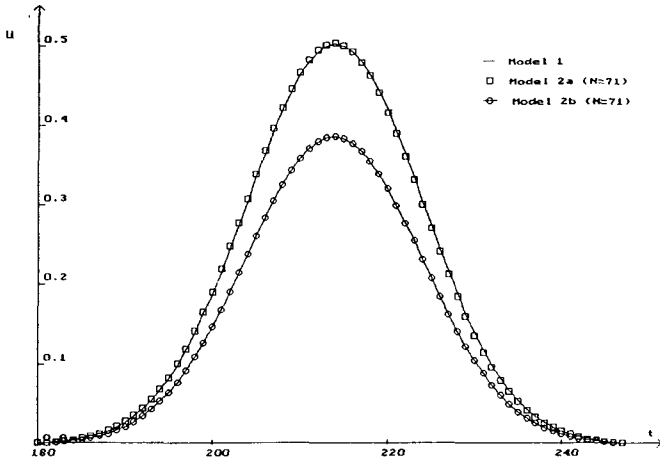
Figure 4: Transmitted pulse, as computed with models 1, 2a and 2b for $\frac{\sigma'}{\sigma} = 3$ and N=71
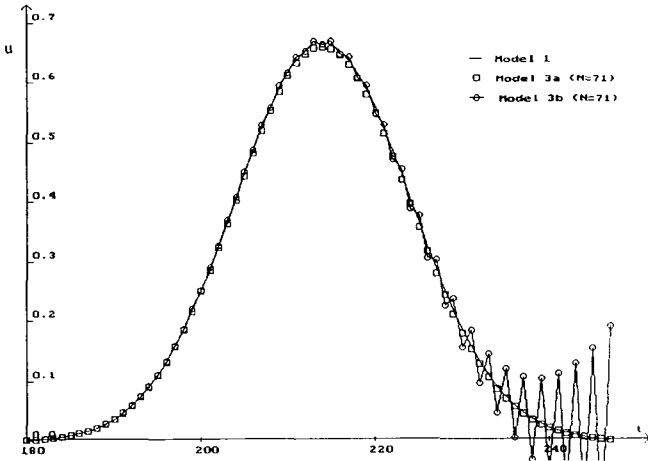
Figure 5: Transmitted pulse, as computed with models 1, 3a and 3b for $\frac{\sigma'}{\sigma}=2$ and N=71

The above analysis illustrates some of the problems, which may be faced when dealing with interfaces or boundaries by means of conventional FD techniques. In 2-D and 3-D the situation becomes even worse, since in general it is not possible to find FD schemes, which provide a complete convergence and stability. Also, it is very difficult to determine, a priori, the reliability of a particular model.

These difficulties occur only if the ratio $\frac{\sigma'}{\sigma}$ is sufficiently large, as shown in the previous examples. Also, the propagation directions of both reflected and transmitted waves are not affected. Only the amplitudes may be wrong (to the extent of even disappearing). In many practical applications one is mostly interested in times-of-flight measurements, so that the amplitudes are far less critical. However, since real pulses may be missing or fictitious ones obtained[36], an unreliable simulation procedure may be very misleading.

In order to thwart these difficulties, while retaining the favorable features of FD techniques, a sharp interface model (SIM) has been proposed in the framework of the local interaction simulation approach (LISA)[45,36]. In the two next Subsections, the basic concepts of LISA and its application to SIM are reviewed.

4.2. The local interaction simulation approach

The time and space discretization, introduced in the previous Subsection, and the concept of evolution equations suggest the use of massively parallel computers[35,46]. In fact one can establish a biunivocal correspondence between the spatial gridpoints (or cells) and the processors of the parallel computer, e.g. a Connection Machine (CM)[47]. At this point the "rules of the game" governing the propagation of the disturbance from cell to cell are "taught" to each processor, by means of an iteration equation (the evolution equation), which allows to evaluate independently the displacements of each node at the time $t + 1$, as a function of the displacements of that node and neighboring ones at times t and $t - 1$.

In fact, since all the CM processors are independent of each other, also the material "cells" can be independent, i.e. they can have different physical properties. Therefore, if we want to study an arbitrarily complex material specimen, we divide it into a sufficiently large number of cells. The physical properties are kept constant within each cell, but may vary from cell to cell, in order to match as precisely as possible with the physical properties of the real specimen. Thus a multilayered specimen can be represented by one or more cells (all of equal physical properties) for each layer.

Within each layer the iteration equations may be obtained heuristically, by an inspection of the local interaction among cells. Or, if a PDE, such as Eq.(6) or (15), is available to describe the propagation in the specimen under investigation, the iteration equation may be obtained directly from the PDE by means of FD formulas, such as Eqs. (46) and (47). E.g., in the 1-D case, Eq. (15) becomes

$$\sigma \frac{d^2 u}{dx^2} = \rho \ddot{u} \tag{49}$$

Upon transformation to a FD equation, it follows

$$u_{i,t+1} = c(u_{i+1,t} + u_{i-1,t}) + 2(1-c)u_{i,t} - u_{i,t-1} \tag{50}$$

where

$$c = \left(\frac{v}{\epsilon/\delta}\right)^2 \tag{51}$$

In Eq.(50) the ratio c , which is the square of the so called Courant number: $C = v\delta/\epsilon$, can be considered as a free parameter, since both ϵ and δ may be chosen at will. From the theory of FD equations[26] we know that the best choice in terms of convergence and stability, is given by $c = 1$, which yields

$$u_{i,t+1} = u_{i+1,t} + u_{i-1,t} - u_{i,t-1} \tag{52}$$

The treatment may be easily extended to 2-D[36] or 3-D[37] and to attenuative media[45]. It is important to remark that all these equations (and also the ones obtained for the interface nodes: see next Subsection) require the same amount of work for each processor and a minimal amount of processor memory. The first consideration is important in order to obtain a perfect "speed-up", i.e. to reduce the computer time of a factor equal to the number of processors. A minimal requirement of memory is also important, because if "ceteris paribus" the number of processors becomes very large, the amount of memory for each of them decreases accordingly.

4.3. The sharp interface model

An exact treatment of the interface in the perfect contact case (see Sec. 3.1.) may be obtained in the framework of LISA by matching at the interfaces both displacements and stresses. Considering, for simplicity, the 1-D case, it is necessary first to set a nodepoint right at the interface, so that the continuity of the displacements at the interface is automatically insured at the initial times $t = 0$ and $t = 1$. We then consider two points P and Q on the two sides of the interface and infinitely close to it. Since

$$\ddot{u} \approx \frac{u_{t+1} + u_{t-1} - 2u_t}{\delta^2} \tag{53}$$

the continuity of u at all later times $(t \geq 2)$ is ensured by imposing

$$\ddot{u}_P = \ddot{u}_Q \tag{54}$$

Likewise the continuity of the stresses is obtained by imposing at all times

$$\tau_P = \tau_Q \tag{55}$$

i.e.

$$\sigma\left(\frac{du}{dx}\right)_P = \sigma'\left(\frac{du}{dx}\right)_Q$$

From Eqs. (53) and (54) it follows

$$\sigma(\frac{d^2u}{dx^2})_P \approx \frac{2\sigma}{\epsilon}[(\frac{du}{dx})_P - \frac{u_i - u_{i-1}}{\epsilon}] = \rho\Omega$$
$$\sigma'(\frac{d^2u}{dx^2})_Q \approx \frac{2\sigma'}{\epsilon'}[\frac{u_{i+1} - u_i}{\epsilon'} - (\frac{du}{dx})_Q] = \rho'\Omega$$

$$(57)$$

where σ', ρ' and ϵ' are the elastic constant, density and grid step, resp., in the region past the interface. Ω is the common value of $\ddot{u}_P$ and $\ddot{u}_Q$. The grid step ϵ' must be chosen according to the phase velocity v', so that the condition $c = 1$ is satisfied for all the layers.

In Eqs. (56)-(57) the three unknowns are $(\frac{du}{dx})_P$, $(\frac{du}{dx})_Q$ and Ω. By eliminating the first two and solving for the third one, one obtains the iteration formula for the interface nodepoints

$$u_{i,t+1} = t'_i u_{i+1,t} + t_i u_{i-1,t} - u_{i,t-1} \tag{58}$$

where t_i and t'_i are the transmission coefficients given by Eq. (35).

The procedure may be generalized to 2-D and 3-D. Then the interface points between two materials become "crosspoints" at the intersection of 4, resp. 8 possibly different materials. The calculation becomes very cumbersome, since the number of equations in the system is 16 and 72 in the two cases (2-D and 3-D), resp. By elimination of the unknowns it is possible, however, to obtain the recursive equations for the crosspoints: see Refs. 36 and 37. In the case of multilayers, these recursive equations yield in 3-D:

$$
\begin{aligned}
u_{t+1} = {} & 2u - u_{t-1} + \frac{2\delta^2}{\epsilon^2(\rho + \rho')}\Big(\sigma u(i-1) + \sigma' u(i+1) - u(\sigma + \sigma' + 2\mu + 2\mu') \\
& + \frac{\mu + \mu'}{2}[u(j+1) + u(j-1) + u(k+1) + u(k-1)] \\
& + \frac{\lambda + \mu}{4}[v(i-1, j-1) - v(i-1, j+1) + w(i-1, k-1) - w(i-1, k+1)] \\
& + \frac{\lambda' + \mu'}{4}[v(i+1, j+1) - v(i+1, j-1) + w(i+1, k+1) - w(i+1, k-1)] \\
& + \frac{\lambda' - \mu' - \lambda + \mu}{4}[v(j+1) - v(j-1) + w(k+1) - w(k-1)]\Big)
\end{aligned}
$$

$$(59)$$

where the three components of the displacement vector have been called $u_t(i,j,k)$, $v_t(i,j,k)$ and $w_t(i,j,k)$. For brevity, the subscripts and arguments have been omitted, whenever equal to t,i,j,k, resp. Similar recursive equations hold for the other two components of the displacement v_{t+1} and w_{t+1}. As a first example of application of the LISA/SIM procedure, we show in Fig.6, the propagation of a sine pulse in a three-layered plate made of fictitious non attenuative materials, of impedance $Z = 14.5$, 42
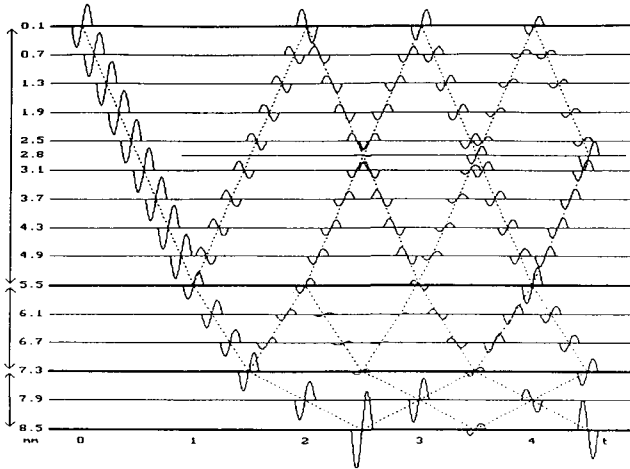
Figure 6: Pulse propagation in a three-layered plate made of fictitious non attenuative materials

and 25×10^6 kg/m²s, resp. The propagation is normal to the plate but, for a clarer representation, is plotted vs. the time (in μs). As a visual aid, a dashed line is drawn to show the propagation directions. All the reflections and refractions are obtained automatically, as a consequence of the formalism.

To show also a 2-D example, we report from Ref.36, the plot of a longitudinal plane wave, which is spatially infinite but gaussian in time, incident at an angle $\theta_0 = 20°$ into an Al plate (see Fig.7). We first see (at $t = 260$ a.u.) the wave propagating into the plate, then doubling at the bottom free surface ($t = 280$ and 320 a.u.), due to the constructive interference between arriving and reflected waves. Finally we observe ($t = 360$ and 380 a.u.) both the reflected longitudinal and mode converted shear waves, travelling at a different angle and velocity, as discussed in Sec. 3.2. The propagation angles and amplitudes of the transmitted and reflected waves are in perfect agreement with the predictions of Eqs.(42)-(45) . Again it is remarkable that also mode conversion effects are automatically provided by the formalism. The computer time to obtain a videofilm of the pulse propagation, or a few snapshots as shown in Fig.7, on a Connection Machine is of the order of a few minutes or less[48].

5. Acknowledgments
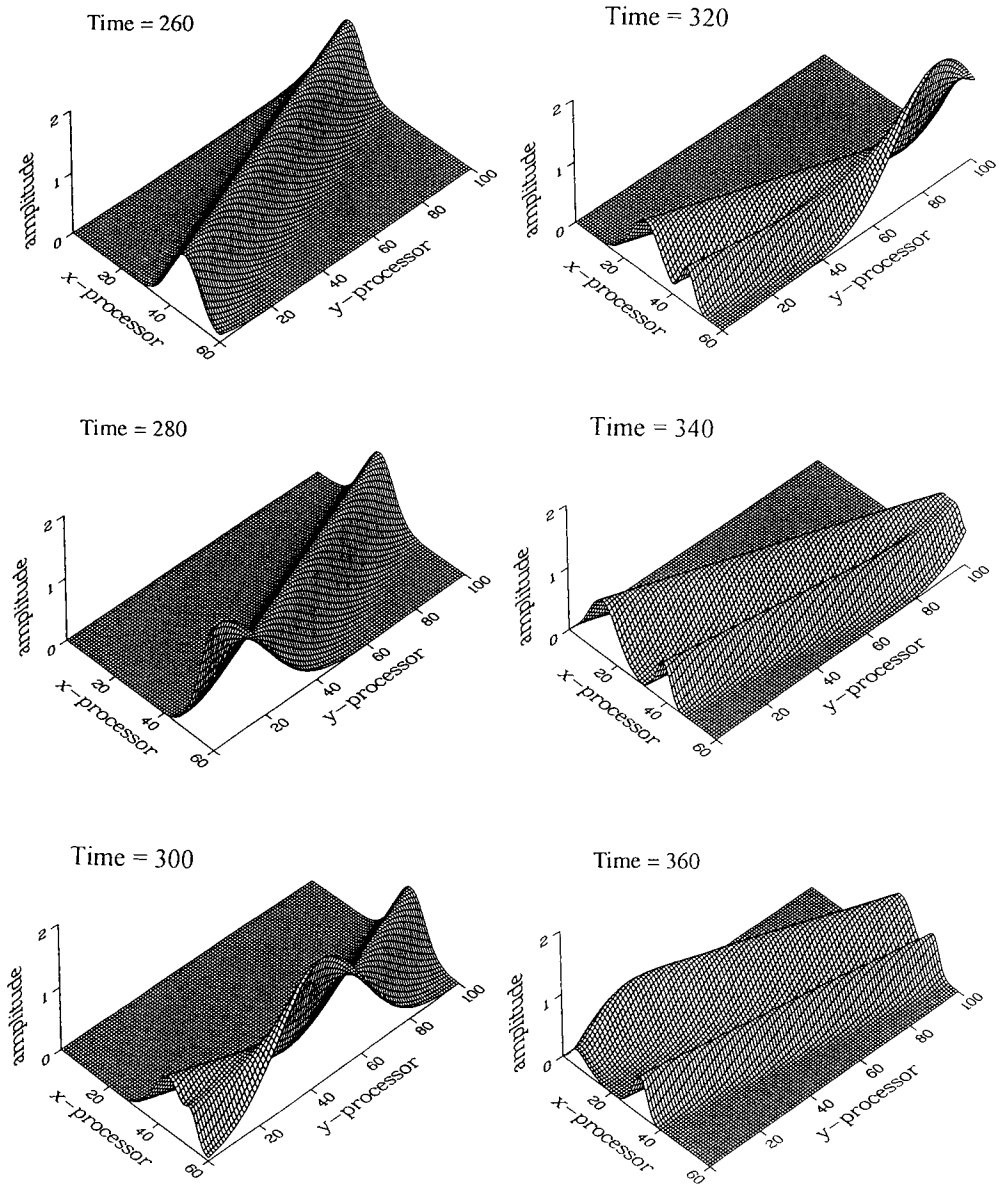
Figure 7: Propagation of a longitudinal plane wave entering an Al plate with an incidence angle $\theta_0 = 20°$

6. References

1. N.K.Batra, T. Berruti, P.P. Delsanto and S. Sassone, *Ultrasonic Interferometric Characterization of Highly Attenuative Materials Plates*, to appear in the Proc. IEEE Int. Ultrasonic Symp., Cannes, Nov. 1994

2. W.M. Ewing, W.S. Jardetzky and F. Press, *Elastic Waves in Layered Media*, Mc Graw-Hill, NY 1957

3. a) A. Gerrard and J.M. Burch, *Introduction to Matrix Methods in Optics*, J.Wiley, NY 1975; b) J. Lekner, *Theory of Reflection of Electromagnetic and Particle Waves*, MrNijhoff Publ., Dordrecht-Boston-Lancaster 1987

4. S.I. Rokhlin, *Advances in Waves in Layered Media*, Jour. de Physique IV **2** (1992) 819-26

5. C.P.A. Wapenaar, A.J. Borkhout, J.Acoust.Soc.Am. **93** (1993) 2024-34

6. W.T. Thomson, Journ.Appl.Phys **21** (1950) 89-93

7. R.P. Shaw, P. Bugl, J.Acoust.Soc.Am. **46** (1968) 649-54

8. D.L. Folds, C.D. Loggins, J.Acoust.Soc.Am. **62** (1977) 1102-09

9. A.H. Nayfeh, T.W. Taylor, Trans. ASME **112** (1990) 260-65

10. S.I. Rokhlin, Y.J. Wang, J.Acoust.Soc.Am. **89** (1991) 503-15

11. P.C. Wuenschel, Geophysics **25** (1960) 106-29

12. A.H. Nayfeh, J.Acoust.Soc.Am. **86** (1989) 2007-12

13. J. Lekner, J.Acoust.Soc.Am. **87** (1990) 2319-24

14. D.M. Pei, J.Acoust.Soc.Am. **88** (1990) 2415-17

15. O. Lenoir, These de doctorat de l'Universite de Havre, 1990

16. K.E. Gilbert, J.Acoust.Soc.Am. **73** (1983) 137-42

17. A.K. Noor, Appl.Mech. Rev. **44** (1991) 307

18. W. Lord, R. Ludwig and Z. You, Journ. of Nondestr.Ev. **9** (1990) 129

19. K. Harumi and M. Uchida, Journ. of Nondestr.Ev. **9** (1990) 81

20. A. Ungar and A. Ilan, Journ. Geophys.**43** (1970) 33

21. D.M. Boore, in: *Methods in Computational Physics*, Academic Press (1972) Vol.11, 1

22. R.M Alford, K.R. Kelly and D.M. Boore, Geophysics **39** (1974) 834

23. J.Virieux, Journ.Geophys.**49** (1984) 1033

24. O. Terki-Hassaine and E.L. Leiss, Int.Journ.Supercomp.Appl.**2** (1988) 49

25. J.S. Sochachi et al.,Geophysics **56** (1991) 168-81

26. F.B. Hildebrand, *Methods of Applied Mathematics*, Prentice-Hall, Englewood Cliffs, NJ (1958)

27. B. Carnahan, H.A. Luther, J.O. Wilkes, *Applied Numerical Methods*, J.Wiley (1969)

28. W.F. Ames, *Numerical Methods for Partial Differential Equations*, Academic Press (1977)

29. W.H. Press, B.P. Flannery, S.A. Teukolsky and W.T. Vetterling, *Numerical Recipes*, Cambridge Univ.Press (1986)

30. F.B. Hildebrand, *Finite-Difference Equations and Simulation*, Prentice Hall (1968)

31. J. Noye, *Numerical Solutions of Partial Differential Equations*, North-Holland (1982)

32. J.C. Strikwerda, *Finite Difference Schemes and Partial Differential Equations*, Wadsworth Brooks, Pacific Grove, Ca., 1989

33. W.L. Siegmann, D. Lee and G. Botseas, in: *Computational Acoustics*, Elsevier Sci. (1988) 91-109

34. R.E. Mikens, ibid., 387-93

35. P.J. Denning and W.F. Tichy, *Highly parallel computation*, Science **250** (1990) 1222

36. P.P. Delsanto, *CM Simulation of Ultrasonic Wave Propagation in Materials II: the 2-D case*, Wave Motion **20** (1994) 295-314

37. P.P. Delsanto, G. Muzio and M. Scalerandi, *Simulation Techniques for the Propagation of Ultrasonic Pulses in Anisotropic Inhomogeneous Media*, Proc. Conf. ICA'95 - Trondheim, Vol.1 (1995) 329-32

38. L.M.Brekhovskikh, *Waves in Layered Media*, Academic Press (1980)

39. D.J. Achenbach, *Wave Propagation in Elastic Solids*,North-Holland Publ. 1973

40. H.F. Pollard, *Sound Waves in Solids*, Methuen, Inc., N.Y. 1977

41. S.K. Sahai, R.A. Kline and R. Mignogna, *Ultrasonics* **30** (1992) 373-82

42. P.P. Delsanto and A.V. Clark, *Rayleigh Wave Propagation in Deformed Anisotropic Materials*, J.Acoust.Soc.Am. **81** (1987) 952-60

43. N. Bellomo and L. Preziosi, *Modelling Mathematical Methods and Scientific Computation*, CRC Press (1995)

44. P.P. Delsanto, G. Kaniadakis and D. Iordache, *Comparison of Different Methods for the Computer Simulation of the Ultrasonic Wave Propagation in Multilayers*,Proc. 6-th European Conf. on Composite Mat., Woodhead Publ. (1993) 557-62

45. P.P. Delsanto, *CM Simulation of Ultrasonic Wave Propagation in Materials I: the 1-D case*, Wave Motion **16** (1992) 65-80

46. H.L. Li and Q.F. Stant, eds. *Reconfigurable Massively Parallel Computers*, Prentice-Hall, Englewood Cliffs, NJ (1991)

47. W. Daniel Hills, *The Connection Machine*, MIT Press, Cambridge, Ma. (1985)

48. R.S. Schechter, H.H. Chaskelis, R.B. Mignogna and P.P. Delsanto, *Real-Time Parallel Computation and Visualization of Ultrasonic Pulses in Solids Using the Connection Machine*, Science **265** (1994) 1188-92

RESPONSE OF A VIBRATING STRUCTURE TO A TURBULENT FLOW WALL PRESSURE: FLUID-LOADED STRUCTURE MODES SERIES AND BOUNDARY ELEMENT METHOD

Paul J.T. FILIPPI and Daniel MAZZONI
Laboratoire de Mécanique et d'Acoustique
31 Chemin Joseph Aiguier
13402 Marseille cedex 20 (France)

Abstract

This paper deals with the vibro-acoustic response of a simple structure (a baffled plate in free space, or a baffled plate closing a cavity) excited by the wall pressure exerted by a turbulent boundary layer.

It is well-known that the response of a mechanical system to a random excitation can be deduced from its response to a harmonic excitation. Thus, in a first step, the harmonic case is examined and two representations of the solution are proposed : a boundary integral representation which leads to a system of Boundary Integral Equations equivalent to the initial boundary value problem ; a series representation in terms of the fluid-loaded structure resonance modes (free oscillations).

Then the vibration field of the structure and the radiated sound pressure due to a random wall pressure are obtained through these two representations of the harmonic response of the system. The important role played by the resonance modes is pointed out.

A few numerical examples are proposed on two-dimension systems. A comparison between numerical predictions and experimental data shows a good agreement.

1   Introduction

Flow induced vibrations and noise appear in a very wide variety of real life situations. In transportation vehicles – cars, fast trains, planes, boats – the external flow induces on the structure a fluctuant wall pressure due to vortices or turbulence ; vibrations and sound fields are thus generated. The performances of inboard or pulled sonar devices are reduced because of the noise generated inside the shell containing

the transducers by the surrounding flow. In buildings, pipes carryinig fluids (water pipes, central heating systems, air conditioning, etc...) are noisy due to the wall pressure induced by the internal flow. Many other examples could be listed.

In this paper we are interested in vibrations and noise fields induced by turbulent flows only. The aim of this study is to help for a better understanding of the physical phenomena by looking at very simple examples and proposing an efficient numerical approach.

1.1   The physical systems here studied and the hypothesis made on the turbulence models

Two simple structures are looked at :

1. The first one is a thin plate extended up to infinity by a perfectly rigid baffle. Each of the two half-spaces limited by the baffled plate is occupied by a perfect fluid.

2. The second system is also composed of a thin baffled plate. One of the two half-spaces is occupied by a perfect fluid. In the second half-space there is a cavity partly bounded by the plate and containing a second perfect fluid.

The plate is excited by the wall pressure that a turbulent boundary layer exerts on it. Two assumptions are made :

◇ the plate vibrations do not modify the flow, and thus the turbulence character-istics are the same as in presence of a perfectly rigid plane surface ;

◇ the effect of the flow on the sound propagation equations can be neglected.

Among all the turbulence models which can be found in the literature, we have adopted to look at the most classical ones, that is the Corcos model and the Chase model. The theory here developed can easily be used to compute the response of the system to any other model of a turbulent boundary layer.

1.2   Short analysis of the existing literature

The number of papers dealing with this problem is very important, but it seems useless to give a rather exhaustive list of them. This study was mainly concerned with the resolution of the fluid-loaded structure problem under a random excitation, rather than with the fluid mechanics aspects. Thus, we limit the bibliography analysis to the papers which we found to be among the most significant ones.

One of the oldest and most interesting articles is due to H. DAVIES[1]. The author looks at the radiation of a baffled plate embedded in a homogeneous fluid extending up to infinity. He expands the solution into a series of the *in vacuo* plate resonance modes, and gives an approximation of the coefficients.

N.C. MARTIN and P. LEEHEY[2] are interested in recovering the turbulence charac-
teristics of a flow from the response of a baffled membrane in air. They start with an
analysis of the membrane response similar to that proposed in Ref.1. Under relatively
severe hypotheses, they can give an analytical approximation of it which depends on
the parameters of a turbulence model. By inversion of this analytical approximation,
they obtain the desired characteristics.

Similar approaches have been adopted more recently by different authors[3][4][5]. The
most interesting of these three papers is due to G. ROBERT[3]. The author presents a
comparison between numerical predictions and experimental data for a plate in air :
due to an experimental assembly of very high quality – the measurement data are
almost noiseless – the agreement between theory and experiment is quite good and
shows that the *light fluid* approximation which is used is reasonable for this case.

Finally, we will mention two recent papers by M.S. HOWE[6][7]. These papers deal
with simple structures. Starting from the Green's function of the fluid-loaded struc-
ture, the author obtains the response of the system to a turbulent wall pressure.
Then, he gives analytical approximations of the result. This approach is similar to
ours ; nevertheless, the results given are not as explicit as ours.

1.3 Summary of the different sections

Only linear mechanical systems are considered here. Thus, it is *a priori* obvious
that the response of such a system to a random excitation – more precisely, the
statistical charateristics of this response – can be deduced from its response to a point
harmonic force. Nevertheless, some non elementary (though classical) mathematics
is required to establish the relationships between the cross power spectral densities
of the various quantities of interest (structure displacement, sound pressure fields,
etc. . .) and the power spectral density of the excitation field. Here, we just present
the results which are established in Ref.8 and detailed inRef.9.

1.3.1 Response of a baffled fluid-loaded plate to a harmonic point force or to a random process excitation

Sections 2 and 3 are devoted to the example of a thin plate, extended by a perfectly
rigid plane surface (*baffled plate*) and immersed into two different fluids which extend
up to infinity. This is probably the simplest example which can be found. Its main
advantage is that the basic ideas of the present analysis can be developed through
rather simple calculations.

More precisely, in section 2, we consider the system *baffled plate – fluid* excited
by a point harmonic (deterministic) force. It is first shown that the boundary value
problem which governs this mechanical system can be transformed into a system of
Boundary Integral Equations. Then the modal aspect of the phenomenon is looked
at : the main difference with the most classical approaches encountered in Vibro-

Acoustics is that use is made of the *baffled plate – fluid* system resonance modes (free oscillations modes). The displacement of the plate due to a point harmonic force will be called the Green's function of the fluid-loaded plate.

In section 3, an excitation of the plate by a random process is considered. The process is assumed to depend randomly on both the time and the space variables. The second hypothesis, which seems to be necessary, is that the process has a zero time mean value and is stationary up to order 2 with respect to this variable. No hypothesis is made on the space dependence. It is shown that the Green's function of the fluid-loaded plate permits to express the statistical characteristics of the useful physical quantities in terms of the excitation characteristics. By introducing the resonance modes series of the Green's function, one gets a representation which shows that the plate acts on the random excitation wall pressure as filter.

1.3.2   Response of a baffled plate closing a cavity to a deterministic harmonic force or a random process excitation

This is the topic of section 4 in which the structure under consideration is somewhat more complex. Let us consider a baffled plate and the two half-spaces which it bounds. One of these two half-spaces is occupied by a perfect fluid. In the second half-space there is a closed domain having the plate as a part of its boundary ; this cavity is occupied by a second fluid.

As in the preceeding example, we are first interested in the Green's function of the fluid-loaded plate coupled to the cavity. Here again, two aspects are developed : first, a system of Boundary Integral Equations equivalent to the governing partial differential equations is established ; then, the solution of the problem is expanded into a series of the resonance modes (free oscillations modes) of the system *baffled plate – external fluid – cavity.*

Finally, the excitation of the plate by a turbulent wall pressure field is considered. Following the same steps as in section 3, the different power density spectra which describe the system response are related to the power spectral density of the excitation process through the Green's function. In that example too, the filtering effect due to each of the two components of the system – the plate and the cavity – is very clearly pointed out by the modal representation of the solution.

1.3.3   Numerical method and results

A fifth section is devoted to the numerical method that has been used and to a few examples which illustrate the theoretical analysis.

The first problem which must be solved numerically is that of the calculation of the Green's functions corresponding to the two examples which have been studied theoretically. We only paid attention to the resolution of the systems of Boundary Integral Equations. The modal aspect has not been considered in the numerical applications. The reason is that, to our opinion, one of the most powerful techniques

to compute the resonance modes is to define them by their boundary integral representation and to use a Boundary Element Method. Thus, the computation of the resonance modes is a by-product of the B.E.M. programme.

A first set of results shows the influence of the turbulence model : the ratio between the spectra corresponding to the two classical models (Corcos and Chase) is roughly a constant. Then a comparison between experimental data and a two-dimensional calculation is proposed and shows that, under the experimental conditions adopted, the Corcos model seems to describe correctly the phenomenon.

A final set of examples shows the respective filtering influences of the plate and of the cavity. Though it is not possible to make a mathematical difference between the resonance modes, it appears that some of them can be qualified as *plate modes* while the other must be considered as *cavity modes*.

2   Vibro-Acoustic   response of a baffled plate to a deterministic excitation

In this section, we are interested in the harmonic Green's function of the fluid-loaded baffled plate, that is its response to a point force excitation which will be used in the next section to describe the vibrations and acoustic fields resulting from a random excitation of the plate.

First, the geometrical and mechanical data of the problem are given together with the governing equations. Following the method developed by P.-O. MATTEI[10], the boundary value problem is reduced to a system of Boundary Integral Equations. Then the eigenmodes and resonance modes of the physical system *baffled plate – fluid* are defined, and the Green's function of the fluid-loaded baffled plate is expanded into a series of these modes.

It must be remarked that this problem is not self-adjoint, due to the energy loss at inifinity in the fluid. Thus, the classical theorems which prove the existence of a sequence of eigenmodes or resonance modes do not apply. Nevertheless, it is known from experiment that such resonance modes are likely to exist. In the following we make a first reasonable assumption that, for any frequency, there exists a sequence of eigenmodes on which the plate displacement can be expanded into a convergent series ; the second assumption is that there exists a sequence of resonance modes (free oscillations of the fluid-loaded baffled plate) on which the plate displacement can be expanded into a convergent series.

2.1   Statement of the problem

Let us consider two perfect fluids occupying the two half-spaces $\Omega^e (z > 0)$ and $\Omega^i (z < 0)$ and characterized by a density μ_e (resp. μ_i) and a sound velocity c_e (resp. c_i).

In the plane $z = 0$, a thin plate occupies a domain Σ with boundary $\partial\Sigma$. The plane complementary Σ' of $\overline{\Sigma}$ is a perfectly rigid surface. The unit vector normal to $\partial\Sigma$ and pointing out to Σ' is denoted $\vec{n}$. The mechanical characteristics of the plate are :

◇ h = thickness ;

◇ E = Young's modulus ;

◇ ν = Poisson's ratio ;

◇ $D = Eh^3/12(1 - \nu^2)$ = rigidity ;

◇ μ = surface density.

The plate is excited by a harmonic $(e^{-\iota\omega t})$ force with density F. Because we are interested in the plate Green's function, it is assumed that there is no acoustic source in the fluids.

Let us define the following notations :

◇ $u(M)$: plate displacement, positive in the $z > 0$ direction ;

◇ $p^e(Q)$: sound pressure in the domain Ω^e ;

◇ $p^i(Q)$: sound pressure in the domain Ω^i ;

◇ $P(x, y)$: pressure step across the plate surface

$$P(x, y) = \lim_{\varepsilon > 0 \to 0} \left[p^e(x, y, \varepsilon) - p^i(x, y, -\varepsilon) \right]$$

The functions $u(M)$, $p^e(Q)$ and $p^i(Q)$ satisfy the following system of partial differential equations :

$$\left(\Delta + k_e^2 \right) p^e(Q) \ = \ 0 \,, \ Q \in \Omega^e \tag{1}$$

$$\left(\Delta + k_i^2 \right) p^i(Q) \ = \ 0 \,, \ Q \in \Omega^i \tag{2}$$

$$\left(D\Delta^2 - \mu\omega^2 \right) u(M) + P(M) \ = \ F(M) \,, \ M \in \Sigma \tag{3}$$

$$\mathrm{Tr}\partial_z p^e(M) \ = \ \omega^2 \mu_e u(M) \,, \ M \in \Sigma$$
$$= \ 0 \,, \ M \in \Sigma' \tag{4}$$

$$\mathrm{Tr}\partial_z p^i(M) \ = \ \omega^2 \mu_i u(M) \,, \ M \in \Sigma$$
$$= \ 0 \,, \ M \in \Sigma' \tag{5}$$

$$\ell u(M) \ = \ \ell' u(M) \ = \ 0 \,, \ M \in \partial\Sigma \tag{6}$$

In these expressions we have :

⋄ $k_e^2 = \omega^2/c_e^2$; $k_i^2 = \omega^2/c_i^2$;

⋄ ℓ and ℓ' = boundary operators which define the boundary conditions that the plate satisfies.

The uniqueness of the solution is ensured by assuming that p^e and p^i satisfy a Sommerfeld condition, or any equivalent condition.

   In the numerical examples, the plate is assumed to be clamped along its boundary. Thus the boundary conditions (6) read :

$$\mathrm{Tr}u(M) = 0$$
$$\mathrm{Tr}\partial_n u(M) = 0$$

2.2 Green's representations of the sound pressure fields and of the plate displacement ; Boundary Integral Equations

2.2.1 Green's representation of the pressures p^e and p^i ; integro-differential equation for the plate displacement

   The system of equations (1–6) can be simplified by introducing the Green's representation of the pressures $p^e(Q)$ and $p^i(Q)$ in terms of the plate displacement $u(M)$, using the Green's kernel for the Neumann problem in the half-spaces Ω^e and Ω^i.

   Let $\mathcal{G}_\omega^e(Q, Q')$ be the Green's kernel of the Helmholtz equation (1) in Ω^e which satisfies the Neumann condition on $z = 0$ and the Sommerfeld condition at infinity ; and let $\mathcal{G}_\omega^i(Q, Q')$ be the Green's kernel of the Helmholtz equation (2) in Ω^i which satisfies the Neumann condition on $z = 0$ and the Sommerfeld condition at infinity. One has :

$$\mathcal{G}_\omega^{e,i}(Q, Q') = -\frac{e^{\imath k_{e,i} r(Q,Q')}}{4\pi r(Q, Q')} - \frac{e^{\imath k_{e,i} r(Q,Q'')}}{4\pi r(Q, Q'')} \text{ in } \mathbf{R}^3$$

$$\mathcal{G}_\omega^{e,i}(Q, Q') = -\frac{\imath}{4} H_0\left[k_{e,i} r(Q, Q')\right] - \frac{\imath}{4} H_0\left[k_{e,i} r(Q, Q'')\right] \text{ in } \mathbf{R}^2$$

where Q'' stands for the point symmetrical to Q' with respect to the plane (the line) $z = 0$ and $r(Q, Q')$ is the distance between the two points Q and Q'. The functions p^e and p^i can be expressed as functions of u by :

$$p^e(Q) = \omega^2 \mu_e \int_\Sigma u(M') \mathcal{G}_\omega^e(Q, M') d\Sigma(M') , \ Q \in \Omega^e$$
$$p^i(Q) = -\omega^2 \mu_i \int_\Sigma u(M') \mathcal{G}_\omega^i(Q, M') d\Sigma(M') , \ Q \in \Omega^i \tag{7}$$

Thus, p^e and p^i are no more unknown functions, and the pressure step $P(M)$ is immediately given by :

$$P(M) = \omega^2 \int_\Sigma u(M') \left[\mu_e \mathcal{G}_\omega^e(M, M') + \mu_i \mathcal{G}_\omega^i(M, M')\right] d\Sigma(M') , \ M \in \Sigma \tag{8}$$

Introducing (8) into (3), one gets an integro-differential equation for u which thus satisfies the following boundary value problem :

$$\left(D\Delta^2 - \mu\omega^2\right)u(M)$$

$$+\omega^2 \int_\Sigma u(M') \left[\mu_e \mathcal{G}^e_\omega(Q, M') + \mu_i \mathcal{G}^i_\omega(Q, M')\right] d\Sigma(M') \;=\; F(M)\,, \; M \in \Sigma$$

$$\ell u(M) \;=\; \ell'u(M) \;=\; 0\,, \; M \in \partial\Sigma \qquad (9)$$

2.2.2   Boundary Integral Equations equivalent to the initial boundary value problem

Let us introduce γ, the *in vacuo* infinite plate Green's kernel, that is the solution of

$$\left(D\Delta^2_M - \mu\omega^2\right)\gamma(M, M') \;=\; \delta_{M'}$$

which satisfies a suitable Sommerfeld condition at infinity. It is given by the well known expressions :

$$\gamma(M, M') \;=\; -\frac{\imath}{8\lambda^2 D}\left\{H^{(1)}_0\left[\lambda r(M, M')\right] - H^{(1)}_0\left[\imath\lambda r(M, M')\right]\right\} \text{ in } \mathbf{R}^2$$

$$=\; \frac{1}{4\lambda^3 D}\left[\imath e^{\imath\lambda|MM'|} - e^{-\lambda|MM'|}\right] \text{ in } \mathbf{R}$$

$$\text{with} \qquad \lambda^4 \;=\; \frac{\mu\omega^2}{D}$$

The plate displacement can be expressed as :

$$u(M) \;=\; \gamma * F(M) + \gamma * P(M) + \gamma * [s_1 + s_2](M)\,, \; M \in \Sigma \qquad (10)$$

This expression contains three kinds of terms :

⋄ the displacement due to the excitation force

$$u_0(M) \;=\; \gamma * F(M) \;=\; \int_\Sigma F(M')\gamma(M, M')d\Sigma(M')$$

⋄ the displacement due to the pressure step

$$u_P(M) \;=\; \gamma * P(M) \;=\; \int_\Sigma P(M')\gamma(M, M')d\Sigma(M')$$

⋄ the displacement due to fictitious sources s_1 and s_2 , supported by $\partial\Sigma$ and which account for the influence of the boundary conditions

$$u_{\partial\Sigma}(M) \;=\; \gamma * [s_1 + s_2](M)$$

(these sources are layers of different orders)

The Green's representation of the plate displacement will be adopted and, thus, the layers densities have the following physical interpretation :

◇ For clamped boundary conditions :

$$s_1 = S_1 \otimes \delta_{\partial\Sigma} \text{ simple layer defined by}$$
$$\gamma * S_1 \otimes \delta_{\partial\Sigma}(M) = \int_{\partial\Sigma} \gamma(M, M') S_1(M') \, d\varsigma(M') ;$$
$$s_2 = S_2 \otimes \delta'_{\partial\Sigma} \text{ double layer defined by}$$
$$\gamma * S_2 \otimes \delta'_{\partial\Sigma}(M) = -\int_{\partial\Sigma} \partial_{n(M')} \gamma(M, M') S_2(M') d\varsigma(M').$$

The source density S_1 reads : $-D[\text{Tr}\,\partial_n \Delta u + (1-\nu)\,\partial_s \text{Tr}\,\partial_n \partial_s u]$; the first term is the product of D by the normal gradient of the shear stress and the second one is the product of $(1-\nu)D$ by the tangential component of the twisting stress.
The density $S_2 = -D[\text{Tr}\,\Delta u - (1-\nu)\,\text{Tr}\,\partial_{s^2}u]$ is D–times the normal component of the bending moment.

◇ For free boundary conditions :

$$s_1 = S_1 \otimes \delta''_{\partial\Sigma} \text{ layer of order 2 defined by}$$
$$\gamma * S_1 \otimes \delta''_{\partial\Sigma}(M) = \int_{\partial\Sigma} \partial_{n^2(M')} \gamma(M, M') S_1(M') \, d\varsigma(M') ;$$

$$s_2 = S_2 \otimes \delta'''_{\partial\Sigma} \text{ layer of order 3 defined by}$$
$$\gamma * S_2 \otimes \delta'''_{\partial\Sigma}(M) = -\int_{\partial\Sigma} \partial_{n^3(M')} \gamma(M, M') S_2(M') \, d\varsigma(M')$$

The source density $S_1 = -D\,\text{Tr}\,\partial_n u$ is proportional to the plate slope.
The source density $S_2 = -D\,\text{Tr}\,u$ is proportinal to the plate displacement.

◇ For simply supported boundary conditions :

$$s_1 = S_1 \otimes \delta_{\partial\Sigma}$$
$$s_2 = S_2 \otimes \delta''_{\partial\Sigma}$$

The source density S_1 reads : $-D[\text{Tr}\,\partial_n \Delta u + (1-\nu)\,\partial_s \text{Tr}\,\partial_n \partial_s u]$, and the source density S_2 is equal to $-D\,\text{Tr}\,\partial_n u$.

Expression (8) of $P(M)$ and the representation (10) of $u(M)$ provide two integral equations relating these two functions and the boundary sources densities S_1 and S_2. Two additionnal equations are obtained by taking the values on $\partial\Sigma$ of u and $\partial_n u$ expressed in the form (10). Depending on the derivation orders which occur, it can be necessary to account for discontinuity steps (see, for example, Ref.11).

Remark

This is not the only possible choice. Other boundary integral equations can be obtained by taking the value on $\partial\Sigma$ of higher order derivatives of u. Though this leads to more singular kernels the equations so obtained can easily be used for numerical computation : the most singular equations have proved to be generally more sensitive to resonance frequencies.

2.3   Eigenmodes and resonance modes of the physical system baffled plate – external fluid ; modal series representations of the solution

It is first necessary to write the equations of motion in the energetic (weak) form. This formulation of the problem seems more suitable for defining the eigenmodes and the resonance modes of the system. Finally, the representations of the solution as series of eigenmodes and of resonance modes are established.

2.3.1   Weak form of the governing equations

Let ε_e anf ε_i stand for the ratios μ_e/μ and μ_i/μ respectively, and let us define the following forms :

$$
\begin{aligned}
\beta_\omega(u,v) &= \int_\Sigma \int_\Sigma u(M)\left[\varepsilon_e \mathcal{G}_\omega^e(M,M') + \varepsilon_i \mathcal{G}_\omega^i(M,M')\right] v^*(M')d\Sigma(M)d\Sigma(M') \\
\langle u,v\rangle &= \int_\Sigma u(M)v^*(M)d\Sigma(M) \\
a(u,v) &= D\int_\Sigma \left\{ \Delta u(M)\Delta v^*(M) + (1-\nu)\left[2\frac{\partial^2 u(M)}{\partial x \partial y}\frac{\partial^2 v^*(M)}{\partial x \partial y}\right.\right. \\
&\qquad \left.\left. -\frac{\partial^2 u(M)}{\partial x^2}\frac{\partial^2 v^*(M)}{\partial y^2} - \frac{\partial^2 u(M)}{\partial y^2}\frac{\partial^2 v^*(M)}{\partial x^2}\right]\right\} d\Sigma(M)
\end{aligned}
\tag{11}
$$

(in these expressions, v^* stands for the complex conjugate of v). The integro-differential system (9) is equivalent to the variational problem : find u such that

$$
a(u,v) - \mu\omega^2\left[\langle u,v\rangle - \beta_\omega(u,v)\right] = \langle F,v\rangle
\tag{12}
$$

for any v in a suitably chosen functional space.

2.3.2   Eigenvalues and eigenmodes of the system baffled plate – external fluid

The eigenmodes U_n and the eigenvalues Λ_n of the system are the non-trivial solutions of the homogeneous variational equation :

$$
a(U_n,v) = \Lambda_n\left[\langle U_n,v\rangle - \beta_\omega(U_n,v)\right]
\tag{13}
$$

It must be noticed that eigenmodes and eigenvalues are frequency dependent (this is a classical property wich appears in many problems of mathematical physics, as, for example, in room acoustics when the boundary properties depend on the excitation frequency).

We assume that there exist a countable sequence of such modes and that it defines a basis for the functional space which the plate displacement belongs to. As a consequence, the solution of (12) can be expanded into a series of the U_n. To each mode correspond two pressure fields given by :

$$P_n^e(Q) = \mu_e \omega^2 \int_\Sigma U_n(M') \mathcal{G}_\omega^e(Q, M') d\Sigma(M')$$

$$P_n^i(Q) = -\mu_i \omega^2 \int_\Sigma U_n(M') \mathcal{G}_\omega^i(Q, M') d\Sigma(M') \tag{14}$$

The eigenmodes satisfy an orthogonality relationship. Indeed, let us introduce $v = U_m^*$ in equation (13) ; one gets :

$$a(U_n, U_m^*) = \Lambda_n [\langle U_n, U_m^* \rangle - \beta_\omega(U_n, U_m^*)]$$

Taking into account that the forms involved in this equality satisfy symmetry relationships, it is easy to see that the following equality is true :

$$a(U_n, U_m^*) = \Lambda_m [\langle U_n, U_m^* \rangle - \beta_\omega(U_n, U_m^*)]$$

Assuming that all the Λ_n have an order of multiplicity equal to 1, the orthogonality relationship is obtained :

$$\langle U_n, U_m^* \rangle - \beta_\omega(U_n, U_m^*) = a(U_n, U_m^*) = 0 \text{ si } m \neq n \tag{15}$$

It can easily be proved that all the eigenvalues have a non zero imaginary part (the physical system loses energy by acoustic radiation).

2.3.3 Resonance modes and resonance angular frequencies of the system *baffled plate – external fluid*

A resonance mode w_n of the baffled fluid-loaded plate corresponds to a free oscillation of the system. The corresponding angular frequency ω_n has a non zero imaginary part because the system is a non-conservative one. The resonance modes are the non-trivial solutions of the folowing variational problem :

$$a(w_n, v) = \mu \omega_n^2 [\langle w_n, v \rangle - \beta_{\omega_n}(w_n, v)] \tag{16}$$

Here again, we assume the existence of a countable sequence of resonance modes and that this sequence is a basis for the functional space which the solution of the non-homogeneous equation belongs to : that is the forced displacement of the plate can be expanded into a convergent series of the resonance modes.

It must be remarked that the resonance modes and the resonance frequencies are related to the eigenmodes and eigenvalues by

$$\begin{aligned} w_n &= U_n(\omega_n) \\ \mu\omega_n^2 &= \Lambda_n(\omega_n) \end{aligned}$$

It is easily shown that if (w_n, ω_n) is a solution, then $(w_{-n} = w_n^*, \omega_{-n} = -\omega_n^*)$ is a solution too. Two pressure fields can be associated to every resonance mode by :

$$\begin{aligned} \Psi_n^e(Q) &= \mu_e\omega_n^2 \int_\Sigma U_n(M')\mathcal{G}_{\omega_n}^e(Q, M')d\Sigma(M') \\ \Psi_n^i(Q) &= -\mu_i\omega_n^2 \int_\Sigma U_n(M')\mathcal{G}_{\omega_n}^i(Q, M')d\Sigma(M') \end{aligned} \tag{17}$$

Finaly, we will admit that the angular eigenfrequecies ω_n, $(n = -\infty, \cdots, -2, -1, +1, +2, \cdots, +\infty)$ have a negative imaginary part (this property is not difficult to establish).

2.3.4   *Representation of the solution as a series of eigenmodes*

The solution of equation (12) is sought as a series of the U_n of the form :

$$u(M) = \sum_{n=1}^{\infty} \alpha_n U_n(M)$$

This leads to the following equation :

$$\sum_{n=1}^{\infty} \alpha_n \left\{ a(U_n, v) - \mu\omega^2 \left[\langle U_n, v \rangle - \beta_\omega(U_n, v) \right] \right\} = \langle F, v \rangle$$

The orthogonality relationship (15) leads to the result :

$$u(M) = \sum_{n=1}^{\infty} \frac{\Lambda_n}{\Lambda_n - \mu\omega^2} \frac{\langle F, U_n^* \rangle}{a(U_n, U_n^*)} U_n(M) \tag{18}$$

This series is defined for any real $\mu\omega^2$, because the Λ_n have a non zero imaginary part.

Series representations of the sound pressure fields $p^e(Q)$ and $p^i(Q)$ can be associated to this representation of the plate displacement :

$$\begin{aligned} p^e(Q) &= \sum_{n=1}^{\infty} \frac{\Lambda_n}{\Lambda_n - \mu\omega^2} \frac{\langle F, U_n^* \rangle}{a(U_n, U_n^*)} P_n^e(Q) \\ p^i(Q) &= \sum_{n=1}^{\infty} \frac{\Lambda_n}{\Lambda_n - \mu\omega^2} \frac{\langle F, U_n^* \rangle}{a(U_n, U_n^*)} P_n^i(Q) \end{aligned} \tag{19}$$

Starting from these three series we now deduce the representation of the solution in terms of the resonance modes.

2.3.5 Representation of the solution as a series of resonance modes

The resonance modes are naturally involved in the expression of the response of the system to a time dependent excitation : it can be obtained by taking the inverse Fourier Transform of the expressions of the harmonic regime.

Let us assume that the excitation of the plate is real (from the physical point of view, this is a realistic assumption ; from a mathematical point of view, there is no loss of generality). The response of the plate to an impulse force $F(M)\delta(t)$ is given by :

$$\tilde{u}(M,t) = \frac{1}{2\pi} \sum_{n=1}^{\infty} \int_{-\infty}^{+\infty} \frac{\Lambda_n}{\Lambda_n - \mu\omega^2} \frac{\langle F, U_n^* \rangle}{a(U_n, U_n^*)} U_n(M) e^{-\imath\omega t} d\omega$$

Each Fourier integral is calculated by the residue method which points out the poles of the denominators, i.e. :

$$\omega_n = \tilde{\omega}_n - \imath\tau_n \quad \text{et} \quad \omega_{-n} = -\tilde{\omega}_n - \imath\tau_n$$

It is easily shown that

$$\Lambda_n(-\omega^*) = \Lambda_n^*(\omega) \quad \text{and thus} \quad \Lambda_n'(-\omega^*) = -\Lambda_n'^*(\omega)$$

This implies that $\tilde{u}(M,t)$ is zero for $t < 0$ (this corresponds to the physics) ; for positive values of the time variable, one has :

$$\tilde{u}(M,t) = -\imath \sum_{n=1}^{\infty} \left\{ \frac{\mu\omega_n^2}{\Lambda_n'(\omega_n) - 2\mu\omega_n} \frac{\langle F, w_n^* \rangle}{a(w_n, w_n^*)} w_n(M) e^{-\imath\tilde{\omega}_n t - \tau_n t} \right.$$
$$\left. - \frac{\mu\omega_n^{*2}}{\Lambda_n'^*(\omega_n) - 2\mu\omega_n^*} \frac{\langle F, w_n^* \rangle^*}{a(w_n, w_n^*)^*} w_n^*(M) e^{\imath\tilde{\omega}_n t - \tau_n t} \right\} , \text{ for } t > 0$$

A direct Fourier Transform of this last expression provides the representation of the plate displacement as a series of the resonance modes :

$$u(M) = \imath \sum_{n=1}^{\infty} \left\{ \frac{\mu\omega_n^2}{\Lambda_n'(\omega_n) - 2\mu\omega_n} \frac{\langle F, w_n^* \rangle}{a(w_n, w_n^*)} \frac{w_n(M)}{\imath(\omega - \tilde{\omega}_n) - \tau_n} \right.$$
$$\left. - \frac{\mu\omega_n^{*2}}{\Lambda_n'^*(\omega_n) - 2\mu\omega_n^*} \frac{\langle F, w_n^* \rangle^*}{a(w_n, w_n^*)^*} \frac{w_n^*(M)}{\imath(\omega + \tilde{\omega}_n) - \tau_n} \right\} \tag{20}$$

The role of the resonance modes of the *fluid-loaded plate* appears clearly : when the excitation frequency is equal to the real part of a resonance frequency, the corresponding mode contribution is a leading term which, in many cases, contains the major part of the energy. This is, of course, a well known result. The less classical result (at least in the acoustic literature) is the mathematical form here presented. More classical is the representation of the fluid-loaded plate displacement by a series of the *in vacuo* modes.

Similar expressions for the pressure fields are easily obtained :

$$
\begin{aligned}
p^e(Q) &= \imath \sum_{n=1}^{\infty} \left\{ \frac{\mu\omega_n^2}{\Lambda_n'(\omega_n) - 2\mu\omega_n} \frac{\langle F, w_n^* \rangle}{a(w_n, w_n^*)} \frac{\Psi_n^e(M)}{\imath(\omega - \tilde{\omega}_n) - \tau_n} \right. \\
&\quad \left. - \frac{\mu\omega_n^{*2}}{\Lambda_n'^*(\omega_n) - 2\mu\omega_n^*} \frac{\langle F, w_n^* \rangle^*}{a(w_n, w_n^*)^*} \frac{\Psi_n^{e*}(Q)}{\imath(\omega + \tilde{\omega}_n) - \tau_n} \right\} \\
\Psi_n^e(Q) &= \mu_e\omega_n^2 \int_{\Sigma} w_n(M')\mathcal{G}_{\omega_n}^e(Q, M')d\Sigma(M') \\
p^i(Q) &= \imath \sum_{n=1}^{\infty} \left\{ \frac{\mu\omega_n^2}{\Lambda_n'(\omega_n) - 2\mu\omega_n} \frac{\langle F, w_n^* \rangle}{a(w_n, w_n^*)} \frac{\Psi_n^i(Q)}{\imath(\omega - \tilde{\omega}_n) - \tau_n} \right. \\
&\quad \left. - \frac{\mu\omega_n^{*2}}{\Lambda_n'^*(\omega_n) - 2\mu\omega_n^*} \frac{\langle F, w_n^* \rangle^*}{a(w_n, w_n^*)^*} \frac{\Psi_n^{i*}(Q)}{\imath(\omega + \tilde{\omega}_n) - \tau_n} \right\} \\
\Psi_n^i(Q) &= -\mu_i\omega_n^2 \int_{\Sigma} w_n(M')\mathcal{G}_{\omega_n}^i(Q, M')d\Sigma(M')
\end{aligned}
\tag{21}
$$

As a final remark, it must be noticed that other expressions of the pressure fields can be obtained by introducing expression (20) into (7) ; but the sound fields associated with the free oscillations of the plate will not appear any more.

3   Vibro-Acoustic   response of the system *baffled plate – fluid* to a random excitation

Let us now consider that the plate is excited by a random process. In order to avoid useless complications in the proofs and formulas, it will be assumed that the same fluid occupies both half-spaces Ω^e and Ω^i (for two different fluids, the changes to be made are obvious).

The excitation is described by a process which depends randomly on both the time vaviable and the space variables. As a function of time, the process is assumed to have a zero mean value and to be stationary up to order 2 ; no restrictive assumption is made on its space dependence.

In a first subsection, the relationships between the cross power spectral density of the exciting wall pressure and the cross power spectral densities of the plate displacement field and the radiated pressure fields are established. In the next subsection, the response of the system to the random process is expanded into a series of the resonance modes.Simplifications are possible if either the Corcos model of turbulence or the Chase model (or any similar model) is used.

3.1 Relationship between the cross power spectral density of the excitation and the cross power spectral densities of the system response

Let $f(M,t)$ be a random wall pressure field defined on the plane $z = 0$: as a function of time, it is assumed to have a zero mean value and to be stationary up to order 2. Let $\vec{M}$ be the vector with components the co-ordinates (x, y) of a point M in the $z = 0$ plane. Using a space Fourier transform, the variables (ξ, η), co-ordinates of a point Ξ, are associated to (x, y) ; and the vector $\vec{\Xi}$ is associated to $\vec{M}$. It can be shown (see Ref.12) that the cross power spectral density of the process f can be writen as :

$$S_f(M, M'; \omega) = \int_{\mathbf{R}^2} F(M, \Xi; \omega) e^{2i\pi \vec{M} \cdot \vec{\Xi}} S(\Xi; \omega) e^{-2i\pi \vec{M}' \cdot \vec{\Xi}} F^*(M', \Xi; \omega) d\xi d\eta \quad (22)$$

In general the functions $F(M, \Xi; \omega)$ and $S(\Xi; \omega)$ cannot be measured. But, if the process is stationary with respect to the space variables, one can choose $F(M, \Xi; \omega) = 1$; then, $S(\Xi; \omega)$, which is the space Frourier transform of $S_f(M, M'; \omega)$, becomes accessible to measurements. In the models of a turbulent wall pressure that they proposed, Corcos and Chase give analytical forms of this function.

In Ref.8, the author shows that the cross power spectral densities of the pate displacement and of the sound pressure fields have an expression quite similar to expression (22) :

$$S_u(M, M'; \omega) = \int_{\mathbf{R}^2} U(M, \Xi; \omega) S(\Xi; \omega) U^*(M', \Xi; \omega) d\xi d\eta$$

$$S_{p^e}(M, M'; \omega) = \int_{\mathbf{R}^2} P^e(M, \Xi; \omega) S(\Xi; \omega) P^{e*}(M', \Xi; \omega) d\xi d\eta$$

$$S_{p^i}(M, M'; \omega) = \int_{\mathbf{R}^2} P^i(M, \Xi; \omega) S(\Xi; \omega) P^{i*}(M', \Xi; \omega) d\xi d\eta \quad (23)$$

In these equalities, the set $[U(M, \Xi; \omega), P^e(M, \Xi; \omega), P^i(M, \Xi; \omega)]$ is the response of the system to the harmonic deterministic excitation $F(M, \Xi; \omega) e^{2i\vec{M}\vec{\Xi}}$. Let $[u_Q(M), p_Q^e(M), p_Q^i(M)]$ be the response of the system to a harmonic unit point force acting at point Q. Then the functions U, P^e and P^i write :

$$U(M, \Xi; \omega) = \int_\Sigma u_Q(M) F(Q, \Xi; \omega) e^{2i\vec{Q}\vec{\Xi}} d\Sigma(Q)$$

$$P^e(M, \Xi; \omega) = \int_\Sigma p_Q^e(M) F(Q, \Xi; \omega) e^{2i\vec{Q}\vec{\Xi}} d\Sigma(Q)$$

$$P^i(M, \Xi; \omega) = \int_\Sigma p_Q^i(M) F(Q, \Xi; \omega) e^{2i\vec{Q}\vec{\Xi}} d\Sigma(Q)$$

This implies the following result :

$$S_u(M, M'; \omega) = \int_\Sigma \int_\Sigma u_Q(M) S_f(Q, Q'; \omega) u_{Q'}^*(M') d\Sigma(Q) d\Sigma(Q')$$

$$S_{p^e}(M, M'; \omega) = \int_\Sigma \int_\Sigma p_Q^e(M) S_f(Q, Q'; \omega) p_{Q'}^{e\ *}(M') d\Sigma(Q) d\Sigma(Q')$$

$$S_{p^i}(M, M'; \omega) = \int_\Sigma \int_\Sigma p_Q^i(M) S_f(Q, Q'; \omega) p_{Q'}^{i\ *}(M') d\Sigma(Q) d\Sigma(Q') \qquad (24)$$

An intuitive proof can be given. The cross power spectral density $S_f(M, M'; \omega)$ of the exciting wall pressure can be estimated by taking the mean value, over a large number of events, of cross spectra of the form $\hat{f}(M; \omega)\hat{f}^*(M'; \omega)$, where $(\hat{f}(M; \omega)$ is the Fourier transform of $f(M, t))$. The corresponding plate displacement is given by :

$$u(M; \omega) = \int_\Sigma u_Q(M) \hat{f}(Q; \omega) d\Sigma(Q)$$

Its cross power spectral density $S_u(M, M'; \omega)$ is thus approximated by taking the mean value of expressions of the form :

$$u(M; \omega) u^*(M'; \omega) = \int_\Sigma \int_\Sigma u_Q(M) \hat{f}(Q; \omega) \hat{f}^*(Q'; \omega) u_{Q'}^*(M') d\Sigma(Q) d\Sigma(Q')$$

In this equality, the only random term is the product $\hat{f}(Q; \omega)\hat{f}^*(Q'; \omega)$. By taking the mean value $\overline{(u, u^*)}$ of $u(M; \omega)u^*(M'; \omega)$, the mean value $\overline{(f, f^*)}$ of $\hat{f}(Q; \omega)\hat{f}^*(Q'; \omega)$ appears :

$$\overline{(u, u^*)} = \overline{\left(\int_\Sigma \int_\Sigma u_Q(M) \hat{f}(Q; \omega) \hat{f}^*(Q'; \omega) u_{Q'}^*(M') d\Sigma(Q) d\Sigma(Q') \right)}$$

$$= \int_\Sigma \int_\Sigma u_Q(M) \overline{\left(\hat{f}(Q; \omega) \hat{f}^*(Q'; \omega) \right)} u_{Q'}^*(M') d\Sigma(Q) d\Sigma(Q')$$

By replacing $\overline{(f, f^*)}$ by $S_f(Q, Q'; \omega)$, the first equality (24) is established. Using (22), one gets (23).

3.2   Representation of the response of the system to a radom wall pressure by a resonance modes series

In terms of the resonance modes, the Green's kernel $u_Q(M)$ takes the form :

$$u_Q(M) = i \sum_{n=1}^\infty \left\{ \frac{\mu \tilde{\omega}_n^2}{\Lambda_n'(\tilde{\omega}_n) - 2\mu\tilde{\omega}_n} \frac{w_n(Q)}{a(w_n, w_n^*)} \frac{w_n(M)}{i(\omega - \tilde{\omega}_n) - \tau_n} \right.$$

$$\left. - \frac{\mu \tilde{\omega}_n^{*\,2}}{\Lambda_n'^*(\tilde{\omega}_n) - 2\mu\tilde{\omega}_n^*} \frac{w_n^*(Q)}{a(w_n, w_n^*)^*} \frac{w_n^*(M)}{i(\omega + \tilde{\omega}_n) - \tau_n} \right\} \qquad (25)$$

Let us define the following coefficients :

$$A_n = \frac{\mu \tilde{\omega}_n^2}{[\Lambda_n'(\tilde{\omega}_n) - 2\mu\tilde{\omega}_n] a(w_n, w_n^*)}$$

$$\chi_{nm}^1(\omega) = \int_\Sigma \int_\Sigma w_n(Q) S_f(Q,Q';\omega) w_m^*(Q') d\Sigma(Q) d\Sigma(Q')$$

$$\chi_{nm}^2(\omega) = \int_\Sigma \int_\Sigma w_n(Q) S_f(Q,Q';\omega) w_m(Q') d\Sigma(Q) d\Sigma(Q')$$

$$\chi_{nm}^3(\omega) = \int_\Sigma \int_\Sigma w_n^*(Q) S_f(Q,Q';\omega) w_m^*(Q') d\Sigma(Q) d\Sigma(Q') \qquad (26)$$

Then the cross power spectral density of the plate displacement writes :

$$\begin{aligned}
S_u(M,M';\omega) =& \sum_{n=1}^\infty \sum_{m=1}^\infty \frac{A_n w_n(M)}{\imath(\omega-\tilde\omega_n)-\tau_n} \chi_{nm}^1 \frac{A_m^* w_m^*(M')}{-\imath(\omega-\tilde\omega_m)-\tau_m} \\
&- \sum_{n=1}^\infty \sum_{m=1}^\infty \frac{A_n w_n(M)}{\imath(\omega-\tilde\omega_n)-\tau_n} \chi_{nm}^2 \frac{A_m w_m(M')}{-\imath(\omega+\tilde\omega_m)-\tau_m} \\
&- \sum_{n=1}^\infty \sum_{m=1}^\infty \frac{A_n^* w_n^*(M)}{\imath(\omega+\tilde\omega_n)-\tau_n} \chi_{nm}^3 \frac{A_m^* w_m^*(M')}{-\imath(\omega-\tilde\omega_m)-\tau_m} \\
&+ \sum_{n=1}^\infty \sum_{m=1}^\infty \frac{A_n^* w_n^*(M)}{\imath(\omega+\tilde\omega_n)-\tau_n} \chi_{mn}^1 \frac{A_m w_m(M')}{-\imath(\omega+\tilde\omega_m)-\tau_m} \qquad (27)
\end{aligned}$$

The importance of the resonance modes of the fluid-loaded plate appears clearly on this expression. Indeed, two kinds of terms are dependent of the angular frequency ω : the coefficients $\chi_{nm}^{1,2,3}(\omega)$ and the denominators $\pm\imath(\omega\pm\tilde\omega_n)-\tau_n$. The first kind of terms contains the frequency dependence of the random excitation, while the second kind describes the frequency response of the fluid-loaded plate. Within a frequency band centered at the real part $\tilde\omega_N$ of a resonance angular frequency, the corresponding component is, in general, the leading term of the series and, thus, can be sufficient to describe rather accurately the behaviour of the plate. Between two successive resonance frequencies, the response of the plate has a much lower amplitude.

In a similar way, the cross power spectral densities of the sound pressure fields can be expanded into the following series :

$$\begin{aligned}
S_{p^e}(M,M';\omega) =& \sum_{n=1}^\infty \sum_{m=1}^\infty \frac{A_n \Psi_n^e(M)}{\imath(\omega-\tilde\omega_n)-\tau_n} \chi_{nm}^1 \frac{A_m^* \Psi_m^{e\,*}(M')}{-\imath(\omega-\tilde\omega_m)-\tau_m} \\
&- \sum_{n=1}^\infty \sum_{m=1}^\infty \frac{A_n \Psi_n^e(M)}{\imath(\omega-\tilde\omega_n)-\tau_n} \chi_{nm}^2 \frac{A_m \Psi_m^e(M')}{-\imath(\omega+\tilde\omega_m)-\tau_m} \\
&- \sum_{n=1}^\infty \sum_{m=1}^\infty \frac{A_n^* \Psi_n^{e\,*}(M)}{\imath(\omega+\tilde\omega_n)-\tau_n} \chi_{nm}^3 \frac{A_m^* \Psi_m^{e\,*}(M')}{-\imath(\omega-\tilde\omega_m)-\tau_m} \\
&+ \sum_{n=1}^\infty \sum_{m=1}^\infty \frac{A_n^* \Psi_n^{e\,*}(M)}{\imath(\omega+\tilde\omega_n)-\tau_n} \chi_{mn}^1 \frac{A_m \Psi_m^e(M')}{-\imath(\omega+\tilde\omega_m)-\tau_m} \qquad (28)
\end{aligned}$$

$$S_{p^i}(M,M';\omega) = \sum_{n=1}^\infty \sum_{m=1}^\infty \frac{A_n \Psi_n^i(M)}{\imath(\omega-\tilde\omega_n)-\tau_n} \chi_{nm}^1 \frac{A_m^* \Psi_m^{i\,*}(M')}{-\imath(\omega-\tilde\omega_m)-\tau_m}$$

$$
\begin{aligned}
&- \sum_{n=1}^{\infty} \sum_{m=1}^{\infty} \frac{A_n \Psi_n^i(M)}{\imath\,(\omega - \tilde{\omega}_n) - \tau_n} \chi_{nm}^2 \frac{A_m \Psi_m^i(M')}{-\imath\,(\omega + \tilde{\omega}_m) - \tau_m} \\
&- \sum_{n=1}^{\infty} \sum_{m=1}^{\infty} \frac{A_n^* \Psi_n^{i\,*}(M)}{\imath\,(\omega + \tilde{\omega}_n) - \tau_n} \chi_{nm}^3 \frac{A_m^* \Psi_m^{i\,*}(M')}{-\imath\,(\omega - \tilde{\omega}_m) - \tau_m} \\
&+ \sum_{n=1}^{\infty} \sum_{m=1}^{\infty} \frac{A_n^* \Psi_n^{i\,*}(M)}{\imath\,(\omega + \tilde{\omega}_n) - \tau_n} \chi_{mn}^1 \frac{A_m \Psi_m^i(M')}{-\imath\,(\omega + \tilde{\omega}_m) - \tau_m} \qquad (29)
\end{aligned}
$$

These last expressions show the filtering exerted by the plate on the excitation wall pressure : indeed, the acoustic power radiated by the plate will present sharp peaks around the real part of each resonance frequency of the fluid-loaded plate.

4   Vibro-acoustic response of a baffled plate closing a cavity and excited by a deterministic harmonic force or a random wall pressure

In this section, a more complex structure is considered : a baffled plate in contact on one side with a fluid extending up to infinity, and on the other side with a mass of fluid contained in a bounded domain. We concentrate on the response of this system to a point harmonic force acting on the plate. Indeed, the response to a random process is obtained in exactly the same way as for the former example (for details, see D. Mazzoni[13]).

Here again, one of our objectives is to develop a Boundary Element Method approach, similar to that proposed by P.-O. Mattei in his thesis[10] for much simpler cases (baffled plates or cylindircal shells). The second objective is to develop the modal aspect, that is to expand the solution into a series of the resonance modes of the system *baffled plate – external fluid – cavity*.

The statement of the problem is given in the first subsection. Then the boundary value problem, which has a unique solution, is reduced to a system of Boundary Integral Equations : by a convenient choice of the boundary integral representations of the various unknown functions, this new system of equations has a unique solution too (subsection 2).

In subsection 3, eigenmodes and resonance modes are defined and the response of the system to a point harmonic force is expanded into a series of these modes. A fourth subsection the case of a radom wall pressure excitation is considered. Here again, it is pointed that the system composed of the plate and of the cavity acts as a filter on the excitation process.

4.1 Statement of the problem

Let us consider a perfect fluid which occupies the half-space $\Omega^e(z > 0)$, and which is characterized by a density μ_e and a sound speed c_e.

A thin elastic plate occupies the domain Σ of the $z = 0$ plane, with boundary $\partial\Sigma$. The plane complementary Σ' of $\overline{\Sigma}$ is a perfectly rigid surface. The unit vector normal to $\partial\Sigma$ and pointing out to Σ' is denoted by $\vec{n}$. The physical characteristics of the plate are :

⬥ h = thickness ;

⬥ E = Young's modulus;

⬥ ν = Poisson's ratio ;

⬥ $D = Eh^3/12\left(1 - \nu^2\right)$ = rigidity ;

⬥ μ = surface density.

Let Ω^i be a bounded domain in the half-space $z < 0$, with a boundary composed of Σ and a surface σ. The unit vector normal to σ and pointing out to the exterior of Ω^i is denoted by $\vec{\zeta}$. This domain is filled up with a perfect fluid characterized by a density μ_i and a sound speed c_i.

The plate is excited by a harmonic $(e^{-\iota\omega t})$ source with density F. Finally, it is assumed that there is no acoustic source in the fluid domains.

Let us adopt the following notations :

⬥ $u(M)$ is the plate displacement, positive in the $z > 0$ direction ;

⬥ $p^e(Q)$ is the acoustic pressure in the domain Ω^e ;

⬥ $p^i(Q)$ is the acoustic pressure in the domain Ω^i ;

⬥ $P(x, y)$ is the pressure discontinuity across the plate defined by

$$P(x, y) = \lim_{\varepsilon > 0 \to 0} \left[p^e(x, y, \varepsilon) - p^i(x, y, -\varepsilon)\right]$$

The functions $u(M)$, $p^e(Q)$ and $p^i(Q)$ are solution of the following boundary value problem :

$$\left(\Delta + k_e^2\right) p^e(Q) = 0 \, , \, Q \in \Omega^e \tag{30}$$

$$\left(\Delta + k_i^2\right) p^i(Q) = 0 \, , \, Q \in \Omega^i \tag{31}$$

$$\left(D\Delta^2 - \mu\omega^2\right) u(M) + P(M) = F(M) \, , \, M \in \Sigma \tag{32}$$

$$\mathrm{Tr}\partial_z p^e(M) = \omega^2 \mu_e u(M) \, , \, M \in \Sigma$$

$$= 0 \, , \, M \in \Sigma' \qquad (33)$$

$$\mathrm{Tr}\partial_z p^i(M) = \omega^2 \mu_i u(M) \, , \, M \in \Sigma \qquad (34)$$

$$\ell u(M) = \ell' u(M) = 0 \, , \, M \in \partial\Sigma \qquad (35)$$

$$\ell_i p^i(Q) = 0 \, , \, Q \in \sigma \qquad (36)$$

In these expressions we have :

⋄ $k_e^2 = \omega^2/c_e^2$; $k_i^2 = \omega^2/c_i^2$

⋄ ℓ and ℓ' = boundary operators which define the boundary conditions satisfied by the plate along $\partial\Sigma$;

⋄ ℓ_i = boundary operator which defines the boundary condition satisfied by p^i on σ.

The uniqueness of the solution is ensured by a Sommerfel condition on p^e.

For the numerical applications, the plate is assumed to be clamped ; thus, conditions (35) read :

$$\mathrm{Tr}u(M) = 0$$

$$\mathrm{Tr}\partial_n u(M) = 0$$

The acoustic pressure inside the cavity is assumed to satisfy a Dirichlet condition :

$$\mathrm{Tr}p^i(Q) = 0 \, , \, Q \in \sigma$$

4.2 System of boundary integral equations equivalent to the boundary value problem

The system of equations (30–36) can be simplified by introducing the Green's representation of the external pressure $p^e(Q)$ in terms of the plate displacement $u(M)$, using the Green's kernel for the Neumann problem in the half-space Ω^e :

$$p^e(Q) = \omega^2 \mu_e \int_\Sigma u(M')\mathcal{G}_\omega^e(Q,M')d\Sigma(M') \, , \, Q \in \Omega^e \qquad (37)$$

A further simplification could be obtained by introducing the Green's representation of the inner sound pressure in terms of the plate displacement, using the Green's function of the domain Ω^i. Due to possible real eigenfrequencies for the cavity, this expression does not exist for any real frequency. So we prefer to avoid to use this simplification.

To get a system of boundary integral equations equivalent to the boundary value problem (by "equivalent" we intend that the conditions for existence and uniqueness

of the solution are the same) use will be made of the following Green's representations :
a/ for the inner pressure :

$$
\begin{aligned}
p^i(Q) &= -\omega^2 \mu_i \int_\Sigma u(M') \mathcal{G}_\omega^i(Q, M') d\Sigma(M') + \int_\sigma \left\{ \mathrm{Tr} p^i(Q') \partial_{\zeta'} \mathcal{G}_\omega^i(Q, Q') \right. \\
&\quad \left. - \mathrm{Tr} \partial_{\zeta'} p^i(Q') \mathcal{G}_\omega^i(Q, Q') \right\} d\sigma(Q') \ , \ Q \in \Omega^i \ M \in \Sigma
\end{aligned}
\tag{38}
$$

(where $\mathcal{G}_\omega^i(Q, M')$ is the Green's function for the half-space $z < 0$ abd satisfying a Neumann condition on $z = 0$)
b/ for the plate displacement :

$$
u(M) = \gamma * F(M) - \gamma * P(M) + \gamma * [s_1 + s_2](M)
\tag{39}
$$

(expression identical to 10).

Expression (39) is the first boundary integral equation of the system that we are looking for. A set of two other boundary integral equations is deduced from the boundary conditions satisfied by the plate displacement :

$$
\begin{aligned}
\ell\gamma * P(M) - \ell\gamma * [s_1 + s_2](M) &= \ell\gamma * F(M) \ , \ M \in \partial\Sigma \\
\ell'\gamma * P(M) - \ell'\gamma * [s_1 + s_2](M) &= \ell'\gamma * F(M) \ , \ M \in \partial\Sigma
\end{aligned}
\tag{40}
$$

The expression of $P(M)$ gives an additional equation :

$$
\begin{aligned}
P(M) &= \omega^2 \int_\Sigma u(M') \left[\mu_e \mathcal{G}_\omega^e(M, M') + \mu_i \mathcal{G}_\omega^i(M, M') \right] d\Sigma(M') \\
&\quad - \int_\sigma \left\{ \mathrm{Tr} p^i(Q') \partial_{\zeta'} \mathcal{G}_\omega^i(M, Q') \right. \\
&\quad \left. - \mathrm{Tr} \partial_{\zeta'} p^i(Q') \mathcal{G}_\omega^i(M, Q') \right\} d\sigma(Q') \ , \ M \in \Sigma
\end{aligned}
\tag{41}
$$

The last boundary integral equation is obtained from the expression, on σ, of the integral representation of $p^i(Q)$:

$$
\begin{aligned}
-\frac{\mathrm{Tr} p^i(Q)}{2} &+ \int_\sigma \left\{ \mathrm{Tr} p^i(Q') \partial_{\zeta'} \mathcal{G}_\omega^i(Q, Q') - \mathrm{Tr} \partial_{\zeta'} p^i(Q') \mathcal{G}_\omega^i(Q, Q') \right\} d\sigma(Q') \\
&- \omega^2 \mu_i \int_\Sigma u(M') \mathcal{G}_\omega^i(Q, M') d\Sigma(M') = 0 \ , \ Q \in \sigma
\end{aligned}
\tag{42}
$$

It must be remarked that the two functions $\mathrm{Tr} p^i(Q)$ and $\mathrm{Tr} \partial_{\zeta'} p^i(Q')$ are related by the boundary condition satisfied by $p^i(Q)$ on σ. Thus the system of boundary integral equations is composed of equations (39), (40), (41) and (42).

4.3 Eigenmodes and resonance modes of the physical system baffled plate – external fluid – cavity ; modal series representations of the response to a harmonic deterministic force

To define these modes, it is useful, here again, to first introduce the energetic (weak) form of the governing equations. Let us introduce the classical scalar products

on Σ and in Ω^i :

$$\langle u, v \rangle = \int_{\Sigma} uv^* d\Sigma$$

$$\langle\langle p, \psi \rangle\rangle = \int_{\Omega^i} p\psi^* d\Omega^i$$

We also define two integral forms (derived from the expressions of the potential energy of the plate and of the radiated acoustic energy) :

$$a(u, v) = D \int_{\Sigma} \Big\{ \Delta u \Delta v^*$$
$$+ (1 - \nu) \left[2 \frac{\partial^2 u}{\partial x \partial y} \frac{\partial^2 v^*}{\partial x \partial y} - \frac{\partial^2 u}{\partial x^2} \frac{\partial^2 v^*}{\partial x^2} - \frac{\partial^2 u}{\partial y^2} \frac{\partial^2 v^*}{\partial y^2} \right] \Big\} d\Sigma$$

$$\beta_\omega^e(u, v) = \int_{\Sigma} \int_{\Sigma} \mathcal{G}_\omega^e(M, M') u(M) v^*(M') d\Sigma(M) d\Sigma(M')$$

4.3.1   Eigenvalues and eigenmodes

The eigenvalues Λ_n and eigenmodes U_n, P_n of the system are the non-zero solutions of the following variational problem :

$$a(U_n, v) - \langle \mathrm{Tr} P_n, v \rangle = \mu \Lambda_n \left[\langle U_n, v \rangle - \varepsilon_e \beta_\omega^e(U_n, v) \right]$$
$$-\langle\langle \nabla P_n, \nabla \psi \rangle\rangle + \omega^2 \mu_i \langle U_n, \mathrm{Tr} \psi \rangle$$
$$+ \int_\sigma \mathrm{Tr} \partial_{\zeta'} P_n \mathrm{Tr} \psi^* = -\frac{\Lambda_n}{c_i^2} \langle\langle P_n, \psi \rangle\rangle \tag{43}$$

In these expressions, v is any function of the functional space which the plate displacement belongs to : in particular, it satisfies the same boundary conditions. Similarly, ψ is any function of the functional space which the acoustic pressure p^i belongs to : it satisfies the same boundary condition on σ and a homogeneous Neumann condition on Σ. It will be assumed that a countable sequence of such modes exists and that this set is a basis of the space of solutions (u, p^i).

An orthogonality relationship between the eigenmodes can be established. To this end, (v, ψ) is replaced by (U_q^*, P_q^*) in (43). This gives :

$$a(U_n, U_q^*) - \langle \mathrm{Tr} P_n, U_q^* \rangle = \mu \Lambda_n \left[\langle U_n, U_q^* \rangle - \varepsilon_e \beta_\omega^e(U_n, U_q^*) \right]$$
$$-\langle\langle \nabla P_n, \nabla P_q^* \rangle\rangle + \omega^2 \mu_i \langle U_n, \mathrm{Tr} P_q^* \rangle$$
$$+ \int_\sigma \mathrm{Tr} \partial_{\zeta'} P_n \mathrm{Tr} P_q = -\frac{\Lambda_n}{c_i^2} \langle\langle P_n, P_q^* \rangle\rangle$$

By inverting n and q, a second set of equalities is obtained :

$$a(U_q, U_n^*) - \langle \mathrm{Tr} P_q, U_n^* \rangle = \mu \Lambda_q \left[\langle U_q, U_n^* \rangle - \varepsilon_e \beta_\omega^e(U_q, U_n^*) \right]$$
$$-\langle\langle \nabla P_q, \nabla P_n^* \rangle\rangle + \omega^2 \mu_i \langle U_q, \mathrm{Tr} P_n^* \rangle$$
$$+ \int_\sigma \mathrm{Tr} \partial_{\zeta'} P_q \mathrm{Tr} P_n = -\frac{\Lambda_q}{c_i^2} \langle\langle P_q, P_n^* \rangle\rangle$$

Accounting for symetrical terms and for the fact that P_n and P_q satisfy the same boundary condition on σ, the following equalities are deduced :

$$-\langle \mathrm{Tr}P_n, U_q^* \rangle + \langle \mathrm{Tr}P_q, U_n^* \rangle = \mu \left(\Lambda_n - \Lambda_q \right) \left[\langle U_n, U_q^* \rangle - \varepsilon_e \beta_\omega^e (U_n, U_q^*) \right]$$

$$\omega^2 \mu_i \left[\langle U_n, \mathrm{Tr}P_q^* \rangle - \langle U_q, \mathrm{Tr}P_n^* \rangle \right] = -\frac{\Lambda_n - \Lambda_q}{c_i^2} \langle\langle P_n, P_q^* \rangle\rangle$$

Assuming, for simplicity, that $\Lambda_n \neq \Lambda_q$ for $p \neq q$, an obvious linear combination of the former two equalities provide the orthogonality relationship :

$$\frac{\langle\langle P_n, P_q^* \rangle\rangle}{\omega^2 \mu_i c_i^2} + \mu \left[\langle U_q, U_n^* \rangle - \varepsilon_e \beta_\omega^e (U_q, U_n^*) \right] = 0 \ , \ \forall \ n \neq q \tag{44}$$

For $n = q$ we set :

$$N_q = \frac{\langle\langle P_q, P_q^* \rangle\rangle}{\omega^2 \mu_i c_i^2} + \mu \left[\langle U_q, U_q^* \rangle - \varepsilon_e \beta_\omega^e (U_q, U_q^*) \right] \tag{45}$$

It must recalled that U_n, P_n and Λ_n are frequency dependent.

4.3.2 Eigenmode series representation of the solution

The variational form of the governing equations (30–36) reads :

$$a(u,v) - \mu\omega^2 \left[\langle u, v \rangle - \varepsilon_e \beta_\omega^e (u,v) \right] - \langle \mathrm{Tr}p^i, v \rangle = \langle F, v \rangle$$

$$-\langle\langle \nabla p^i, \nabla \psi \rangle\rangle + \frac{\omega^2}{c_i^2} \langle\langle p^i, \psi \rangle\rangle + \omega^2 \mu_i \langle u, \mathrm{Tr}\psi \rangle + \int_\sigma \mathrm{Tr}\partial_{\zeta'} p^i \psi^* = 0 \tag{46}$$

Let us look for a series representation of the solution (u, p^i) of the form :

$$(u, p^i) = \left(\sum_n A_n U_n, \sum_n A_n P_n \right)$$

By introducing this series in (46), with (v, ψ) replaced by (U_q^*, P_q^*), one gets :

$$\sum_n A_n \left\{ a(U_n, U_q^*) - \mu\omega^2 \left[\langle U_n, U_q^* \rangle - \varepsilon_e \beta_\omega^e (U_n, U_q^*) \right] - \langle \mathrm{Tr}P_n, U_q^* \rangle \right\} = \langle F, U_q^* \rangle$$

$$\sum_n A_n \left\{ -\langle\langle \nabla P_n, \nabla P_q^* \rangle\rangle + \frac{\omega^2}{c_i^2} \langle\langle P_n, P_q^* \rangle\rangle + \mu\omega^2 \varepsilon \langle U_n, \mathrm{Tr}P_q^* \rangle \right.$$

$$\left. + \int_\sigma \mathrm{Tr}\partial_{\zeta'} P_n \mathrm{Tr}P_q d\sigma \right\} = 0$$

Then $a(U_n, U_q^*)$ and $\langle\langle \nabla P_n, \nabla P_q^* \rangle\rangle$ are replaced by their values :

$$\sum_n A_n \left\{ \mu \left(\Lambda_q - \omega^2 \right) \left[\langle U_n, U_q^* \rangle - \varepsilon_e \beta_\omega^e (U_n, U_q^*) \right] \right.$$

$$+\langle \text{Tr} P_q, U_n^*\rangle - \langle \text{Tr} P_n, U_q^*\rangle \Big\} \;\; = \;\; \langle F, U_q^*\rangle$$

$$\sum_n A_n \left\{ - \left(\Lambda_q - \omega^2\right) \frac{\langle\langle P_n, P_q^*\rangle\rangle}{c_i^2} + \mu\omega^2 \varepsilon_i \left[\langle U_n, \text{Tr} P_q^*\rangle \right. \right.$$

$$\left. -\langle U_q, \text{Tr} P_n^*\rangle \right] + \int_\sigma \text{Tr}\partial_{\zeta'} P_n \text{Tr} P_q d\sigma - \int_\sigma \text{Tr}\partial_{\zeta'} P_q \text{Tr} P_n d\sigma \left. \right\} \;\; = \;\; 0$$

Accounting for the orthogonality relationship (44) and recalling that P_n and P_q satisfy the same boundary condition, one gets :

$$A_q \;\; = \;\; \frac{\langle F, U_q^*\rangle}{N_q \left(\Lambda_q - \omega^2\right)} \tag{47}$$

The coefficients A_q are uniquely determined for any real angular frequency because all the eigenvalues Λ_q have a non-zero imaginary part.

4.3.3 Resonance frequencies and resonance modes of the physical system baffled plate – external fluid – cavity

The resonance angular frequencies ω_n and the resonance modes w_n are the non trivial sotutions of the following variational equations :

$$a(w_n, v) - \langle \text{Tr}\Psi_n, v\rangle \;\; = \;\; \mu\omega_n^2 \left[\langle w_n, v\rangle - \varepsilon_e \beta_{\omega_n}^e(w_n, v)\right]$$

$$-\langle\langle \nabla\Psi_n, \nabla\psi\rangle\rangle + \omega_n^2 \mu_i \langle w_n, \text{Tr}\psi\rangle$$

$$+ \int_\sigma \text{Tr}\partial_{\zeta'}\Psi_n \text{Tr}\psi^* \;\; = \;\; -\frac{\omega_n^2}{c_i^2}\langle\langle \Psi_n, \psi\rangle\rangle \tag{48}$$

It is obvious that they are related to the eigenvalues and eigenmodes by :

$$\omega_n^2 \;\; = \;\; \Lambda_n(\omega_n)$$
$$w_n \;\; = \;\; u_n(\omega_n)$$
$$\Psi_n \;\; = \;\; p_n(\omega_n) \tag{49}$$

As for the baffled plate case, it can be shown that the first equation (49) has two solutions with negative imaginary parts, and symmetrical with respect to the real axis :

$$\omega_n = \tilde{\omega}_n - i\tau_n \qquad \omega_{-n} = -\tilde{\omega}_n - i\tau_n$$

4.3.4 Resonance modes series representation of the solution

To get the resonance modes series which represent the response of the system to an external harmonic point force applied at a point M', the same method is used : in a first step an inverse Fourier transform is performed which gives the response of

the system to a point impulse force ; then a direct Fourier transform leads to the following result :

$$
u_{M'}(M;\omega) = \sum_{n=1}^{\infty} \left[\frac{w_n(M')w_n(M)}{N_n(\omega_n)\left[\Lambda_n'(\omega_n) - 2\omega_n\right](\omega - \omega_n)} - \frac{w_n^*(M')w_n^*(M)}{N_n^*(\omega_n)\left[\Lambda_n'^*(\omega_n) - 2\omega_n^*\right](\omega + \omega_n^*)} \right]
\tag{50}
$$

$$
p_{M'}^i(Q;\omega) = \sum_{n=1}^{\infty} \left[\frac{w_n(M')\Psi_n(Q)}{N_n(\omega_n)\left[\Lambda_n'(\omega_n) - 2\omega_n\right](\omega - \omega_n)} - \frac{w_n^*(M')\Psi_n^*(Q)}{N_n^*(\omega_n)\left[\Lambda_n'^*(\omega_n) - 2\omega_n^*\right](\omega + \omega_n^*)} \right]
\tag{51}
$$

$$
p_{M'}^e(Q;\omega) = \sum_{n=1}^{\infty} \left[\frac{w_n(M')\mu_0\omega_n^2}{N_n(\omega_n)\left[\Lambda_n'(\omega_n) - 2\omega_n\right](\omega - \omega_n)} \right.
$$
$$
\int_{\Sigma} w_n(M)\mathcal{G}_{\omega_n}(M,Q)d\Sigma(M)
$$
$$
- \frac{w_n^*(M')\mu_0\omega_n^{*2}}{N_n^*(\omega_n)\left[\Lambda_n'^*(\omega_n) - 2\omega_n^*\right](\omega + \omega_n^*)}
$$
$$
\left. \int_{\Sigma} w_n^*(M)\mathcal{G}_{\omega_n}^*(M,Q)d\Sigma(M) \right]
\tag{52}
$$

These expressions will be useful to represent the various cross power spectral densities which characterize the behaviour of the system when it is excited by a random process.

4.4 Response of the system baffled plate – external fluid – cavity to a random wall pressure

It is very easy to show that the cross power spectral densities of the plate displacement and of the acoustic pressure fields read :

$$
S_u(M,M';\omega) = \int_{\Sigma}\int_{\Sigma} u_N(M;\omega)S_f(N,N';\omega)u_{N'}^*(M';\omega)d\Sigma(N)d\Sigma(N')
$$
$$
S_{p^e}(Q,Q';\omega) = \int_{\Sigma}\int_{\Sigma} p_N^e(Q;\omega)S_f(N,N';\omega)p_{N'}^{e*}(Q';\omega)d\Sigma(N)d\Sigma(N')
$$
$$
S_{p^i}(Q,Q';\omega) = \int_{\Sigma}\int_{\Sigma} p_N^i(Q;\omega)S_f(N,N';\omega)p_{N'}^{i*}(Q';\omega)d\Sigma(N)d\Sigma(N')
\tag{53}
$$

Introducing the expansions (50), (51) and (52) in these expressions, the expansions of the former cross power spectral densities are obtained. Let us define the following coefficients :

$$
A_n = \frac{1}{N_n\left[\Lambda_n' - \omega_n\right]}
$$

$$\chi^1_{nm} = \int_\Sigma \int_\Sigma w_n(N) S_f(N, N'; \omega) w_m^*(N') d\Sigma(N) d\Sigma(N')$$

$$\chi^2_{nm} = \int_\Sigma \int_\Sigma w_n(N) S_f(N, N'; \omega) w_m(N') d\Sigma(N) d\Sigma(N')$$

$$\chi^3_{nm} = \int_\Sigma \int_\Sigma w_n^*(N) S_f(N, N'; \omega) w_m^*(N') d\Sigma(N) d\Sigma(N') \qquad (54)$$

Thus, the cross power spectral density of the plate displacement is given by :

$$
\begin{aligned}
S_u(M, M'; \omega) &= \sum_{n=1}^{\infty} \sum_{m=1}^{\infty} \frac{A_n w_n(M)}{\omega - \omega_n} \chi^1_{nm} \frac{A_m^* w_m^*(M')}{\omega - \omega_m^*} \\
&+ \sum_{n=1}^{\infty} \sum_{m=1}^{\infty} \frac{A_n^* w_n^*(M)}{\omega + \omega_n^*} \chi^1_{nm} \frac{A_m w_m(M')}{\omega + \omega_m} \\
&- \sum_{n=1}^{\infty} \sum_{m=1}^{\infty} \frac{A_n w_n(M)}{\omega - \omega_n} \chi^2_{nm} \frac{A_m w_m(M')}{\omega + \omega_m} \\
&- \sum_{n=1}^{\infty} \sum_{m=1}^{\infty} \frac{A_n^* w_n^*(M)}{\omega + \omega_n^*} \chi^3_{nm} \frac{A_m^* w_m^*(M')}{\omega - \omega_m^*} \qquad (55)
\end{aligned}
$$

Similar expressions for the two sound pressure fields are readily established.

On these various expressions, the importance of the resonance modes is obvious. Assume that ω is equal to the real part $\tilde{\omega}_q$ of the q-th angular resonance frequency ω_q. Then the q-th term has, in general, the largest value ; in many circumstances, its only contribution is rather sufficient to describe correctly the system within a relatively large frequency bandwidth.

5 Numerical solution of the Boundary Integral Equations for the fluid loaded structure problems and examples

As we have seen, the cross power spectral densities which characterize the behaviour of a fluid-loaded structure under a random excitation are deduced from its response to a point harmonic force. This section is devoted to a short description of the Boundary Element Method that we have used to compute such a response for each of the two systems which have been considered, that is the functions $u_Q(M)$, $p_Q^e(M)$ and $p_Q^i(M)$. Then a few results are presented : the responses of a system to different models of turbulence are discussed ; numerical predictions on a two-dimension system are compared to experimental data ; the respective influences of the two components of the system – the plate and the cavity – are pointed out.

5.1 Boundary Element Method for the system baffled plate – external fluid

To get a clearer presentation, it seems useful to introduce a first simplification by assuming that the two fluids are identical ; this leads to :

$$
\begin{aligned}
p^e_Q(M) &= \omega^2 \mu_0 \int_\Sigma u_Q(M') \mathcal{G}_\omega(M, M') d\Sigma(M') \ , \ M \in \Omega^e \\
p^i_Q(M) &= -\omega^2 \mu_0 \int_\Sigma u_Q(M') \mathcal{G}_\omega(M, M') d\Sigma(M') \ , \ M \in \Omega^i \qquad (56) \\
P_Q(M) &= p^e_Q(M) - p^i_Q(M) \\
&= 2\omega^2 \mu_0 \int_\Sigma u_Q(M') \mathcal{G}_\omega(M, M') d\Sigma(M') \ , \ M \in \Sigma \qquad (57)
\end{aligned}
$$

where $\mathcal{G}_\omega$ is the common Green's function for the Neumann problem in the half-spaces Ω^e and Ω^i.

Then, the boundary condititons are chosen. As an example, the plate is assumed to be clamped along its boundaries. This implies that its displacement takes the form :

$$
\begin{aligned}
u_Q(M) &= u^0_Q(M) + \int_\Sigma \gamma(M, M') P_Q(M') d\Sigma(M') \\
&\quad + \int_{\partial\Sigma} \left[\gamma(M, M') S_1(M') - \partial_{n'}\gamma(M, M') S_2(M') \right] d\varsigma(M') \\
u^0_Q(M) &= \gamma(M, Q) \qquad (58)
\end{aligned}
$$

The layer densities S_1 and S_2 are related to the displacement by :

$$
\begin{aligned}
S_1 &= -D \left[\mathrm{Tr}\, \partial_n \Delta u_Q + (1 - \nu)\, \partial_s \, \mathrm{Tr}\, \partial_n \partial_s u_Q \right] \\
S_2 &= -D \left[\mathrm{Tr}\, \Delta u_Q - (1 - \nu)\, \mathrm{Tr}\, \partial_{s_2} u_Q \right] \qquad (59)
\end{aligned}
$$

The modifications to account for other boundary conditions and different fluids will be obvious.

The four unknown functions $u_Q(M)$, $P_Q(M)$, $S_1(M')$ and $S_2(M')$ are solution of a system of Boundary Integral Equations :

$$
u_Q(M) - \int_\Sigma \gamma(M, M') P_Q(M') d\Sigma(M')
$$

$$
- \int_{\partial\Sigma} \left[\gamma(M, M') S_1(M') - \partial_{n'}\gamma(M, M') S_2(M') \right] d\varsigma(M') = u^0_Q(M), \ M \in \Sigma \quad (60)
$$

$$
P(M) - 2\omega^2 \mu_0 \int_\Sigma u_Q(M') \mathcal{G}_\omega(M, M') d\Sigma(M') = 0, \ M \in \Sigma \qquad (61)
$$

$$
-\mathrm{Tr} \left\{ \int_\Sigma \gamma(M, M') P_Q(M') d\Sigma(M') \right.
$$

$$
\left. - \int_{\partial\Sigma} \left[\gamma(M, M') S_1(M') - \partial_{n'}\gamma(M, M') S_2(M') \right] d\varsigma(M') \right\} = \mathrm{Tr}\, u^0_Q(M),
$$

$$M \in \partial\Sigma \qquad (62)$$

$$-\text{Tr}\partial_n \left\{ \int\!\!\int_\Sigma \gamma(M, M')P(M')d\Sigma(M') \right.$$

$$\left. -\int_{\partial\Sigma} [\gamma(M, M')S_1(M') - \partial_{n'}\gamma(M, M')S_2(M')]\, d\varsigma(M') \right\} = \text{Tr}\partial_n u_Q^0(M),$$

$$M \in \partial\Sigma \qquad (63)$$

The last two equations are obtained by taking the value on $\partial\Sigma$ of the expression (58) of $u_Q(M)$, and that of its normal derivative. Other integral equations can be obtained by taking the value on $\partial\Sigma$ of higher order derivatives of the same expression.

The following classical numerical method is adopted. The unknown functions are approximated by stepwise constant functions and a collocation system of linear algebraic equations is built up. More precisely, the surface Σ is devided into two sets of subelements :

◇ for equality (61), Σ is divided into N^u elements Σ_q^q with one interior collocation point M_q^u ; on such a surface element, $u_Q(M)$ is approximated by a constant u_q ;

◇ for the other three equalities, Σ is devided into N^p elements Σ_r^p with interior collocation points M_r^p ; on this surface element, $P_Q(M)$ is approximated by a constant P_r.

The plate boundary $\partial\Sigma$ is divided into N elements ς_s with interior collocation point M_s ; on this element, the functions $S_1(M')$ and $S_2(M')$ are approximated by constants $S_{1,s}$ and $S_{2,s}$ respectively.

Let us now define the following matrices :

$$\Gamma_{qr}^p = \int_{\Sigma_r^p} \gamma(M_q^u, M')d\Sigma(M') \quad , \quad q = 1, 2 \cdots, N^u \ , \ r = 1, 2, \cdots, N^p$$

$$\Gamma_{qs}^1 = \int_{\varsigma_s} \gamma(M_q^u, M')d\varsigma(M') \quad , \quad q = 1, 2 \cdots, N^u \ , \ s = 1, 2, \cdots, N$$

$$\Gamma_{qs}^2 = \int_{\varsigma_s} \partial_{n'}\gamma(M_q^u, M')d\varsigma(M') \quad , \quad q = 1, 2 \cdots, N^u \ , \ s = 1, 2, \cdots, N$$

$$G_{rq}^{\Sigma,\Sigma} = \int_{\Sigma_q^u} \mathcal{G}_\omega(M_r^p, M')d\Sigma(M') \quad , \quad q = 1, 2 \cdots, N^u \ , \ r = 1, 2, \cdots, N^p$$

$$\gamma_{tr}^p = \int_{\Sigma_r^p} \gamma(M_t, M')d\Sigma(M') \quad , \quad t = 1, 2, \cdots, N \ , \ r = 1, 2, \cdots, N^p$$

$$\gamma_{ts}^1 = \int_{\varsigma_s} \gamma(M_t, M')d\varsigma(M') \quad , \quad t = 1, 2, \cdots, N \ , \ s = 1, 2, \cdots, N$$

$$\gamma_{ts}^2 = \int_{\varsigma_s} \partial_{n'}\gamma(M_t, M')d\varsigma(M') \quad , \quad t = 1, 2, \cdots, N \ , \ s = 1, 2, \cdots, N$$

$$\gamma_{tr}^{p\,\prime} = \int_{\Sigma_r^p} \partial_n\gamma(M_t, M')d\Sigma(M') \quad , \quad t = 1, 2, \cdots, N \ , \ r = 1, 2, \cdots, N^p$$

$$\gamma_{ts}^{1\,\prime} = \int_{\varsigma_s} \partial_n \gamma(M_t, M')d\varsigma(M') \quad , \quad t = 1, 2, \cdots, N \ , \ s = 1, 2, \cdots, N$$

$$\gamma_{ts}^{2\,\prime} = \int_{\varsigma_s} \partial_n \partial_{n'} \gamma(M_t, M')d\varsigma(M') \quad , \quad t = 1, 2, \cdots, N \ , \ s = 1, 2, \cdots, N$$

An approximation of the system of Boundary Integral Equations is given by :

$$u_q - \sum_{r=1}^{N^p} \Gamma_{qr}^p P_r - \sum_{s=1}^{N} \Gamma_{qs}^1 S_{1,s} + \sum_{s=1}^{N} \Gamma_{qs}^2 S_{2,s} = u_0(M_q^u), \ q = 1, 2, \cdots, N^u \qquad (64)$$

$$-2\omega^2 \mu_0 \sum_{q=1}^{N^u} G_{rq}^{\Sigma, \Sigma} u_q + P_r = 0, \ r = 1, 2, \cdots, N^p \qquad (65)$$

$$-\sum_{r=1}^{N^p} \gamma_{tr}^p P_r - \sum_{s=1}^{N} \gamma_{ts}^1 S_{1,s} + \sum_{s=1}^{N} \gamma_{ts}^2 S_{2,s} = \text{Tr}\, u_0(M_t), \ t = 1, 2, \cdots, N \qquad (66)$$

$$-\sum_{r=1}^{N^p} \gamma_{tr}^{p\,\prime} P_r - \sum_{s=1}^{N} \gamma_{ts}^{1\,\prime} S_{1,s} + \sum_{s=1}^{N} \gamma_{ts}^{2\,\prime} S_{2,s} = \text{Tr}\, \partial_n u_0(M_t), \ t = 1, 2, \cdots, N \qquad (67)$$

This is the kind of linear system of $N^p + N^u + 2N$ algebraic equations which the classical collocation method leads to.

5.2   *Boundary Element Method for the system baffled plate – external fluid – cavity*

Here again, some simplifications are introduced : the two fluids are identical ; and the cavity boundary is perfectly rigid so that $p_Q^i(M)$ satisfies a Neumann condition on σ. Thus, the pressure fields are given by :

$$p_Q^e(M) = \omega^2 \mu_0 \int_{\Sigma} u_Q(M')\mathcal{G}_\omega(M, M')d\Sigma(M') \ , \ Q \in \Omega_e$$

$$p_Q^i(M) = -\omega^2 \mu_0 \int_{\Sigma} u_Q(M')\mathcal{G}_\omega(M, M')d\Sigma(M')$$

$$- \int_{\sigma} \text{Tr}\, \partial_{\vec{\zeta}'} p_Q^i(M')\mathcal{G}_\omega(Q, M')d\sigma(M') \ , \ Q \in \Omega_i \qquad (68)$$

where $\vec{\zeta}'$ stands for the exterior unit normal vector at M'. The pressure step across the plate is :

$$P_Q(M) = p_Q^e(M) - p_Q^i(M)$$

$$= 2\omega^2 \mu_0 \int_{\Sigma} u_Q(M')\mathcal{G}_\omega(M, M')d\Sigma(M')$$

$$+ \int_{\sigma} \text{Tr}\, \partial_{\vec{\zeta}'} p_Q^i(M')\mathcal{G}_\omega(M, M')d\sigma(M') \ , \ M \in \Sigma \qquad (69)$$

By taking the value on σ of expression (68), one gets an additional equation :

$$-\omega^2 \mu_0 \int_{\Sigma} u_Q(M')\mathcal{G}_\omega(Q, M')d\Sigma(M')$$

$$-\int_\sigma \text{Tr}\, \partial_{\vec{\zeta}'} p_Q^i(M') \mathcal{G}_\omega(Q, M') d\sigma(M') \;=\; 0 \;,\; Q \in \sigma \tag{70}$$

Equations (60), (62) and (63) are approximated like in the former example ; thus the algebraic equations (64), (66) and (67) are kept.

The surface σ is divided into N^σ elements σ_ι, with interior collocation point M_ι^σ. On each element the function $\partial_{\vec{\zeta}'} p_Q^i$ is approximated by a constant ϖ_ι. Let us define the following matrices :

$$G_{\iota\kappa}^{\sigma,\sigma} \;=\; \int_{\sigma_\iota} \mathcal{G}\omega(M_\kappa^\sigma, M') d\sigma(M') \;,\; \iota = 1, 2, \cdots, N^\sigma \;,\; \kappa = 1, 2, \cdots, N^\sigma$$

$$G_{\iota r}^{\sigma,\Sigma} \;=\; \int_{\sigma_\iota} \mathcal{G}\omega(M_r, M') d\sigma(M') \;,\; \iota = 1, 2, \cdots, N^\sigma \;,\; r = 1, 2, \cdots, N^p$$

$$G_{q\iota}^{\Sigma,\sigma} \;=\; \int_{\Sigma_q^u} \mathcal{G}\omega(M_\iota^\sigma, M') d\Sigma(M') \;,\; q = 1, \cdots, N^u \;,\; \iota = 1, 2, \cdots, N^\sigma$$

The approximation of equations (69) and (70) is given by :

$$-2\omega^2 \mu_0 \sum_{q=1}^{N^u} G_{rq}^{\Sigma,\Sigma} u_q - \sum_{\iota=1}^{N^\sigma} G_{\iota r}^{\sigma,\Sigma} \varpi_\iota + P_r \;=\; 0$$
$$r \;=\; 1, \cdots, N^p \tag{71}$$
$$\omega^2 \mu_0 \sum_{q=1}^{N^u} G_{r\kappa}^{\Sigma,\sigma} u_q + \sum_{\iota=1}^{N^\sigma} G_{\iota\kappa}^{\sigma,\sigma} \varpi_\iota \;=\; 0$$
$$\kappa \;=\; 1, \cdots, N^\sigma \tag{72}$$

We are thus left with a system of $N^p + N^u + 2N + N^\sigma$ linear algebraic equations which lead to an approximation of the solution.

5.3   *Response of the systems to a random wall pressure excitation*

In both cases, the cross power spectral densities which characterize the response of the system to a random wall pressure excitation are estimated by introducing the approximations of $u_Q(M)$, $p_Q^e(M)$ and $p_Q^i(M)$ into equations (24) or (53). This implies that the computations are carried out for a rather important set of values of the variables which are involved : the angular frequency ω, the point Q varying on Σ and the point M varying on Σ, in Ω_e or in Ω_i.

As it has been shown, the representation of the solution as a series of the resonance modes is probably the best form for analysing the physical phenomenon. The Boundary Element Method here presented apply for the computation of the resonance modes. The coefficients of the series which represents $u_Q(M)$ can be calculated analytically (the $\Lambda'_n(\omega_n)$ being estimated by any numerical method) or numerically by solving a truncated form of the inifinite linear system that they satisfy.

5.4 Numerical examples

Three examples are presented. In the first one, which concerns a two-dimension baffled plate, the emphasis is put on the influence of the turbulence model. The second example shows that experimental data can be resonably predicted by numerical calculations conducted on a two-dimension problem. The third example deals with the problem of a baffled plate coupled to a cavity (in dimension two) and shows the respective influences of each component of the system.

5.4.1 Influence of the model of turbulence

The modelisation of the wall pressure generated by a turbulent boundary layer is still a rather open problem in Fluid Mechanics. Nevertheless, various modelisations of the wall pressure exerted by a turbulent flow on a structure are available in the literature, which are satisfactory at least under more or less restrictive conditions. It is not our purpose here to discuss the validity of these models, but, instead, to introduce them in our calculations as rather realistic representations of a flow excitation. For this first approach, the turbulence models here considered are the most classical ones, that is the Corcos model[14] and the Chase model[15].
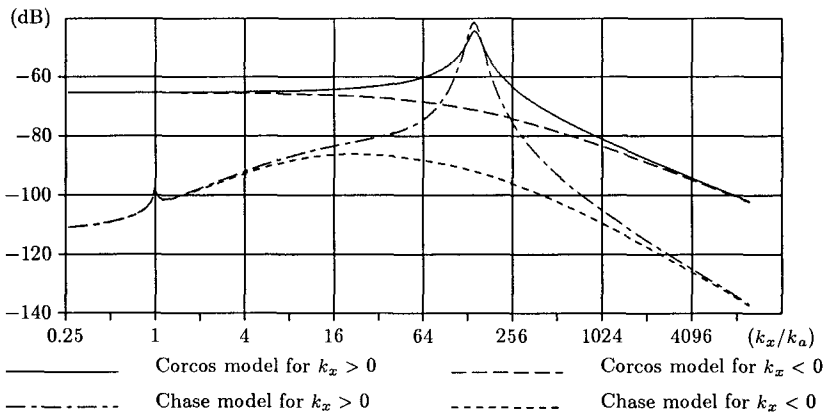
Figure 1: Space Fourier transform of the power spectral density of the wall pressure generated by a water flow with flow velocity at infinity 10 m/s : Corcos and Chase models (frequency = 1 kHz)

These authors give an analytical expression for the space Fourier transfrom of the wall pressure field power spectral density. These functions depend on different parameters : the thermo-mechanical properties of the fluid ; the flow velocity at

infinity ; the acoustical wavenumber $k_a = \omega/c$; the turbulent wavenumbers $k_x = 2\pi\xi$ and $k_y = 2\pi\eta$. In the example shown on figure (1) , the fluid is water, the flow velocity at infinity is 10 m/s and the frequency is 1 kHz. The models differ from each other on a wide range of variation of the parameter k_x/k_a. As the physical intuition and the calculations show, the plate is mainly sensitive to the lowest part of the spectrum and will thus reflect the differences which exist between the two models in that domain of turbulent wave numbers.

Calculations have been made on a two-dimensional geometry, with a water flow on one side of the plate only. The data are as follows :

1. for the plate :

   ◇ length (in the direction of the flow) = 0.60 m

   ◇ thickness = 0.005 m

   ◇ boundary conditions : clamped

   ◇ mass per unit area = 39.25 kg/m^2

   ◇ Young's modulus = 2 10^{11} kg/m^2

   ◇ Poisson's ratio = 0.3.

2. for the fluid :

   ◇ density = 1 000 kg/m^3

   ◇ sound velocity = 1 480 m/s.

Figure (2) represents the power spectral density of the plate displacement at its center as a function of the frequency. The two curves are much similar : the wall pressure given by the Corcos model is about 10 dB higher than that given by the Chase model. This result shows clearly that the plate is mainly sensitive to the components corresponding to low turbulent wavenumbers, that is to the components which have a slow space variation. The curves present a set of peaks which correspond to the resonance modes of the system *baffled plate – external fluid* : this proves that the response of the system is governed by these modes ; it also shows that the Boundary Element Method is a good tool to calculate such modes.

Figure (3) presents the power spectral density of the sound pressure at infinity in the direction normal to the plate, normalised by the the square of the pressure radiated by an isotropic unit point source. Here again the two models give curves which differ by 10 dB from each other.

The directivity patterm of the sound pressure radiated by the plate has also been calculated for different frequencies ; the Chase model has been used. The results are represented on figures (4) and (5), in which the same normalisation is adopted.
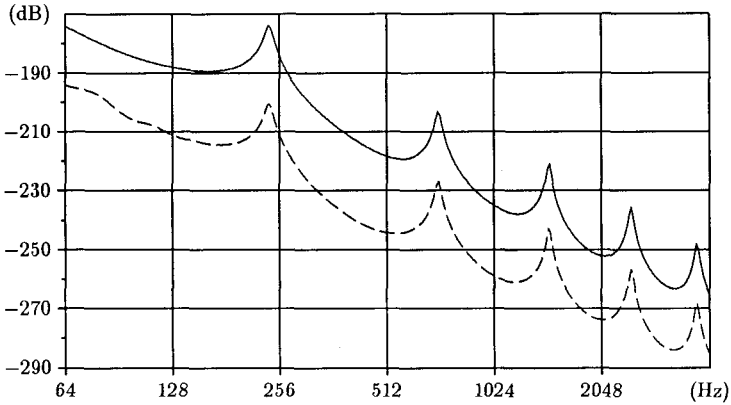
Figure 2: Power spectral densities of the plate displacement at the center point for the two models of turbulence : Corcos (continuous line) and Chase (discontinuous line)
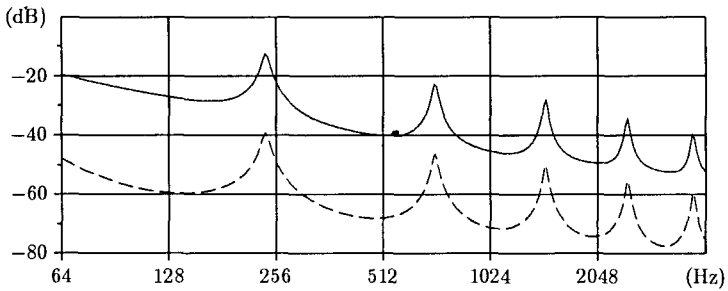
Figure 3: Power spectral densities of the sound pressure at infinity in the direction normal to the plate for the two models of turbulence : Corcos (continuous line) and Chase (discontinuous line)
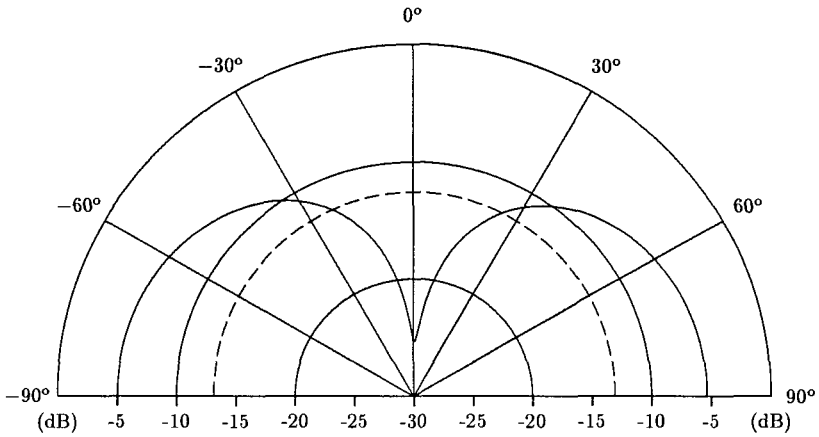
Figure 4: Directivity pattern of the radiated acoustic pressure : power spectral density obtained from Chase model, as a function of the direction at 160 Hz (continuous curve) and 240 Hz (discontinuous curve)
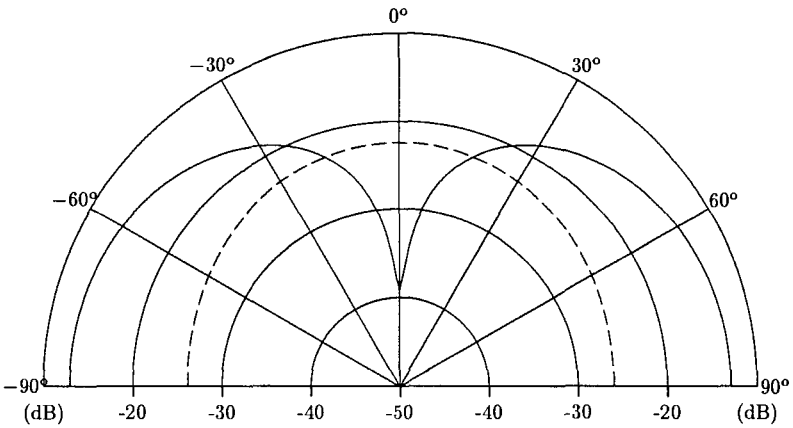
Figure 5: Directivity pattern of the radiated acoustic pressure : power spectral density obtained from Chase model, as a function of the direction at 160 Hz (continuous curve) and 240 Hz (discontinuous curve)

5.4.2 Comparison between numerical predictions and experimental data

Calculations have been made for a two-dimension system and compared to experimental data. To get a meaningful comparison, normalisation factors have been introduced : the power spectral density of the plate acceleration in the 2-D (resp. 3-D) case is divided by the squared acceleration at origin of a 2-D (resp. 3-D) infinite plate excited by a point harmonic unit isotropic force located at the co-ordinate origin. Thus, comparison is made between quantities of the same nature.

The geometrical and mechanical data are as follows :

1. for the experimental plate :

    ◇ length (in the direction of the flow) = 0.46 m

    ◇ width = 0.10 m

    ◇ thickness = 0.002 m

    ◇ boundary conditions : clamped

    ◇ mass per unit area = 15.7 kg/m^2

    ◇ Young's modulus = 2.1 10^{11} Pa

    ◇ Poisson's ratio = 0.33

2. for the numerical calculations :

    ◇ length (in the direction of the flow) = 0.46 m

    ◇ thickness = 0.002 m

    ◇ boundary conditions : clamped

    ◇ mass per unit area = 15.7 kg/m^2

    ◇ Young's modulus = 2.1 10^{11} Pa

    ◇ Poisson's ratio = 0.33

3. for the fluid :

    ◇ density = 1 000 kg/m^3

    ◇ sound velocity = 1 480 m/s

    ◇ flow velocity at infinity = 7 m/s and 10 m/s.

It is *a priori* obvious that the resonance frequencies of the experimental plate and those of the theoretical one cannot coincide. Thus, the comparison here proposed has two objectives :

◇ to check if one of the two classical models of turbulence can describe correctly the mean level of the acceleration power spectral density ;
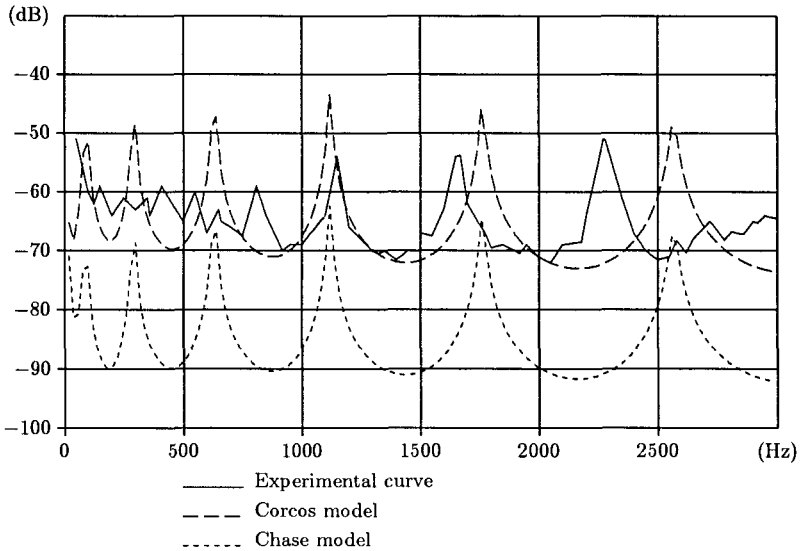
Figure 6: Comparison between the calculated and the experimental power spectral densities of the plate acceleration (flow velocitiy at infinity = 7 m/s)

⋄ if yes, to check if the relative amplitudes of the peaks given by the numerical programme are in agreement with the observed ones.

The results are presented on figures (6) and (7). The experimental data are due to R. NGUYEN VAN LAN et al.[16] : the plate is located along the boundary of a hydro-dynamic tunnel ; on one side it is in contact with the flow inside the tunnel ; on the other side there is a volume of fluid at rest limited by an anechoïc boundary.

    The first conclusion is that, for this series of experiments, the turbulent wall pressure exerted by the flow on the plate is better described by the Corcos model than by the Chase model. The shape of the numerical resonance peaks is in good agreement with that of the experimental ones, though a level difference can be observed. This difference is probably due to the anaylsis used : the frequency step is much smaller for the numerical results than for the experimental data. The global conclusion which can be stated is that the numerical method which has been developed in this paper is quite efficient for predicting vibro-acoustic phenomena due to a turbulent flow excitation ; the only requirement is that the wall pressure exerted by the flow on the structure boundary can be modelled either analytically or numerically. Furthermore, two-dimensional models appear to be efficient for studying the respective influences of the various mechanical and geometrical parameters of a system : indeed, they provide
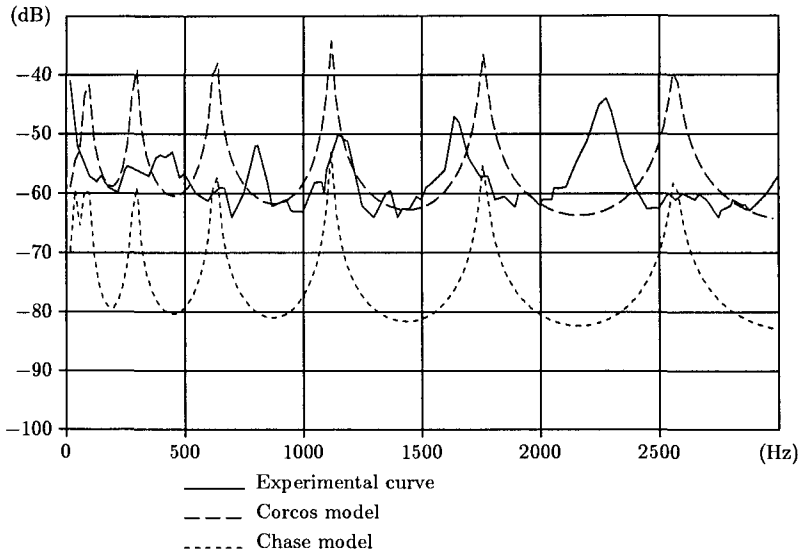
Figure 7: Comparison between the calculated and the experimental power spectral densities of the plate acceleration (flow velocitiy at infinity = 10 m/s)

results which are quantitatively comparable to those provided by a three-dimensional model, but the calculations require much less memory space, are less time consuming and can be implemented on rather small work stations.

5.4.3 Response of a fluid-loaded plate closing a cavity

This last example deals with a more complex two-dimensional structure : a baffled plate closing a cavity. The geometrical and mechanical data are the following :

1. Geometrical and mechanical data for the plate (slightly damped steel) :

   ⋄ length (in the direction of the flow) = 0.46 m

   ⋄ thickness = 0.001 5 m

   ⋄ boundary conditions : clamped

   ⋄ mass per unit area = 11.7 kg/m^2

   ⋄ Young's modulus (complex) = $2\ 10^{11}(1 + 10^{-3}i)$ Pa

   ⋄ Poisson's ratio = 0.33

2. Mechanical data for the fluid (water) :
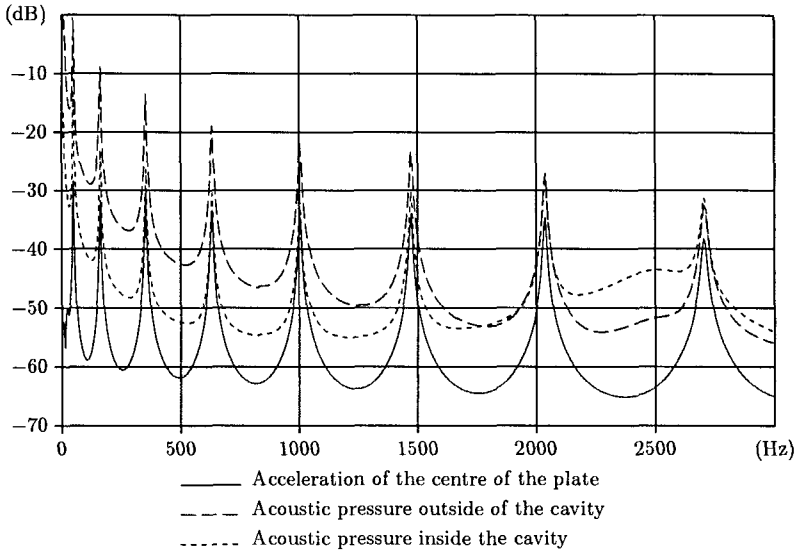
Figure 8: Power spectral densities of the plate acceleration and of the radiated acoustic pressures (turbulence model : Corcos ; flow velocity at infinity : 8m/s).

- ◇ density = 1 000 kg/m^3
- ◇ sound speed = 1 480 m/s

3. Geometrical data for the cavity :

- ◇ length (in the flow direction) = 0.46 m
- ◇ depth = 0.25 m
- ◇ boundary condition : Dirichlet condition

The turbulence is described by the Corcos model, for a flow speed at infinity equal to 8m/s. The results are shown on figures (8), (9), (10), (11) et (12).

The first figure presents the power spectral density of the acceleration of the center of the pate as a function of the frequency (continuous line) ; and the power spectral densities of the acoustic pressures at two points of the normal to the plate passing through its center : an exterior point at 0.125m off the plate (dashed line) ; an interior point at 0.175m off the plate (dotted line). Two remarks can be made. First, these three curves have sharp peaks which occur for identical values of the frequency. These are resonance frequencies of the system which can be qualified as *fluid-loaded plate resonance frequencies* : indeed, they are very close to the resonance frequencies of a
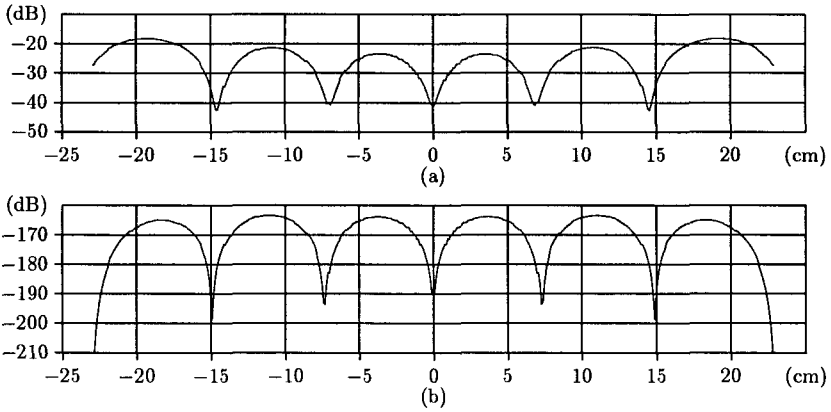
Figure 9: Value, at 330 Hz, of the power spectral densities of the interior acoustic pressure (a) and of the plate acceleration (b) as functions of the position (flow velocity at infinity : 8m/s)

baffled plate coupled to two semi-inifinite fluid domains. Secondly, the pressure curves cross each other around 1 800 Hz and present a weak maximum around 2 500 Hz. This is a resonance frequency of the system which can be qualified as *cavity resonance frequency* : indeed, in the vicinity of such a frequency, the level of the interior pressure power spectral density increases by about 10 dB. Finally, it must be noticed that this *cavity resonance* has a non significant influence on the plate response.

On the next four graphs, the power spectral densities of the plate acceleration (lower curves) and of the interior acoustic pressure (upper curves) are presented as functions of the point position for different frequencies. For the sound pressure, the point position varies along a line parallel to the plate, 0.05m apart of it. At low frequencies, the space dependence of the pressure is governed by the plate shape : the two curves are much similar. Then, as the frequency approaches the first *cavity resonance frequency*, the respective behaviours of each of the two components of the system – the plate and the cavity – start to differ from each other and finally look quite independent as if each sub-system was oscillating on its own. Finally, it can be remarked that for a constant acceleration level, the sound pressure level increases as the first cavity resonance frequency is approached : this is an intuitive result which is confirmed by the numerical study.
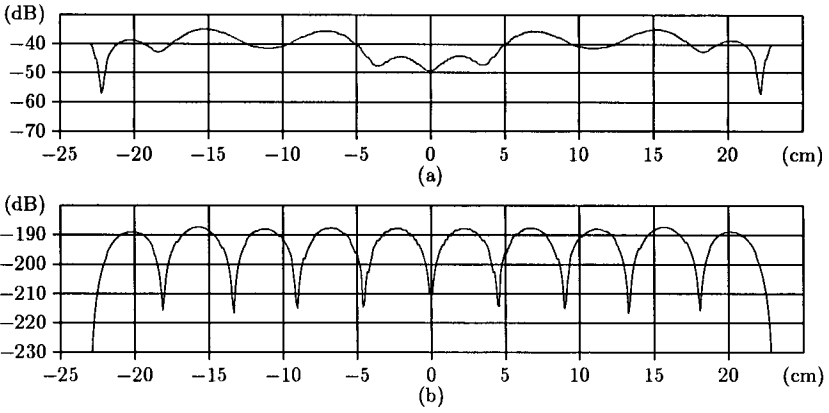
Figure 10: Value, at 1 050 Hz, of the power spectral densities of the interior acoustic pressure (a) and of the plate acceleration (b) as functions of the position (flow velocity at infinity : 8m/s)
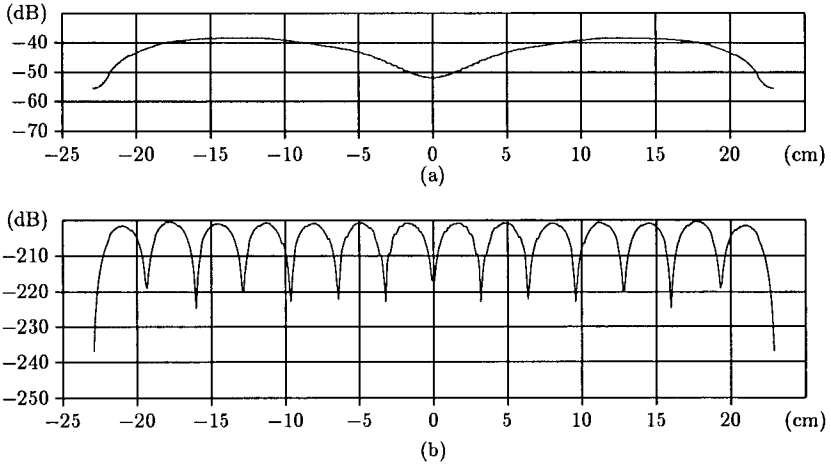
Figure 11: Value, at 2 070 Hz, of the power spectral densities of the interior acoustic pressure (a) and of the plate acceleration (b) as functions of the position (flow velocity at infinity : 8m/s)
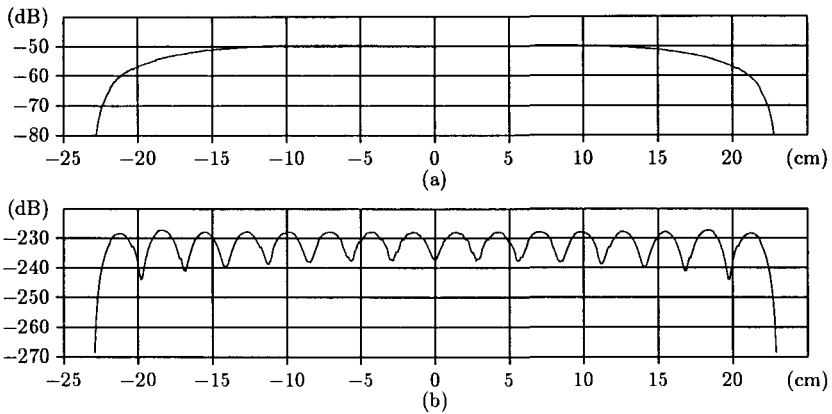
Figure 12: Value, at 3 000 Hz, of the power spectral densities of the interior acoustic pressure (a) and of the plate acceleration (b) as functions of the position (flowvelocity at infinity : 8m/s)

6 Concluding remarks

It is a well-kown result in structural dynamics that the response of a system can be described by a series of its free oscillation modes, also called resonance modes. The interest of such a representation is emphasized when the system excitation has a wide frequency range (this is the case with a turbulent wall pressure).

In Vibro-Acoustics, a classical method to compute the response of a fluid-loaded structure is to expand it as a series of the *in vacuo* modes. The disadvantage of such an expansion is that it does not point out explicitly the resonance properties of the system composed of the structure and of the surrounding fluid. One of the aim of this paper is to define the resonance modes and to express the response of the system to a random excitation as a series of these modes. Thus, it appears clearly that the system acts as a filter on the excitation process : the various cross power spectral densities have maxima for each value of the frequency which is equal to the real part of a resonance frequency.

The second aim of this paper is to show that Boundary Element Methods are quite efficient to compute the response of a fluid-loaded structure to a random excitation. The results here presented show that the resonances are easily described. Thus, this proves that the computation of the resonance modes can also be performed by a Boundary Element Method.

The last objective that we had in mind was to compare experimental data to the

numerical results obtained with a very simple model of the experimental assembly : it has been shown that the numerical study of the behaviour of a two-dimensional system can provide reasonable predictions of experimental data which, of course, concern a three-dimensional system.

Finally, let us mention that perturbation methods for the calculation of the system response when the fluid density is small compared to that of the structure can be used. The most classical way encountered, at least in Vibro-Acoustics, is to expand the response of the fluid-loaded structure as a series of its *in vacuo* modes : to avoid the failure of the series at each *in vacuo* resonance frequency, a matched asymptotic expansion is often proposed. A somewhat different method can be proposed. The perturbation method, as developed in Ref.17 and 18, provides an approximation of the resonance modes of the system composed of the elastic structure and the fluid. Then the exact resonance modes series representation of the solution is used. Of course, both methods lead to the same final result.

7   Acknowledgements

8   References

1. H.G. DAVIES, *Journal of the Acoustical Society of America*, **49**(3) (1969) 878–889.

2. N.C. MARTIN and P. LEEHEY, *Journal of Sound and Vibration*, **52**(1) 1977 95–120.

3. G. ROBERT, Thèse, Ecole Centrale de Lyon (réf. E.C.L. 84-02), 36 avenue Guy de Collongue, B.P. 163, 69131 Ecully, France (1984)

4. M.L. RUMERMAN, *Journal of the Acoustical Society of America*, **91**(2) (1992) 907–910.

5. L. JOURDAN et J.-P. GUIBERGIA S. BANO, R. MARMEY, *Journal d'Acoustique*, **5** (1992) 99–124.

6. M.S. HOWE, *Journal of Sound and Vibration*, **121**(1) (1988) 47–65.

7. M.S. HOWE, *Journal of Sound and Vibration*, **144**(2) (1988) 229–245.

8. D. MAZZONI, Thèse, Université d'Aix-Marseille II, Institut de Mécanique de Marseille, UNIMECA, Institut Méditerrannéen de Technologie (réf. 209448), Chemin de la Grave, 13451 Marseille cedex 20, France.

9. P.J.T. FILIPPI and D. MAZZONI, *Convention DCN – Ingénierie Sud, C 91 48 603 022 405 83 48* (1995).

10. P.-O. MATTEI, Thèse, Université d'Aix-Marseille II, Institut de Mécanique de Marseille, UNIMECA, Institut Méditerrannéen de Technologie (réf. 2079190), Chemin de la Grave, 13451 Marseille cedex 20, France.

11. J. VIVOLI and P. FILIPPI, *Journal of the Acoustical Society of America*, **55**(3) (1974) 562–567.

12. P. KRÉE et C. SOIZE, *Mécanique aléatoire* (Dunod – Bordas, Paris, 1983).

13. D. MAZZONI, *Boundary Elements, Abstracts and Newsletter*, **4**(4) (1993) 153–156.

14. G.M. CORCOS, *Journal of the Acoustical Society of America*, **35**(2) (1963)192–199.

15. D.M. CHASE, *Journal of the Acoustical Society of America*, **90**(2) (1990) 1032–1034.

16. R. NGUYEN VAN LAN, P. OLIVERO-BALLY, B.E. FORESTIER and C. GIANGRECO, in *Flow Noise Modelling Measurement and Control* (ASME, 1993), 57–62.

17. P.J.T. FILIPPI, O. LAGARRIGUE et P.-O. MATTEI, *Journal of Sound and Vibration*, **177**(2) (1994) 259–275.

18. P.J.T. FILIPPI and D. MAZZONI, in *ICA95 – International Congress on Acoustics,Trondheim, Norway, june 26-30 1995*.

PLANE EVANESCENT WAVES AND INTERFACE WAVES

F.LUPPÉ
J.M.CONOIR
M. ECH-CHERIF EL KETTANI
O.LENOIR
J.L.IZBICKI
J.DUCLOS

L.A.U.E., U.R.A. C.N.R.S. 1373, Université du Havre
place R. Schuman, 76610 Le Havre, France

and

B.POIRÉE
D.R.E.T., S.T.R.D.T., G6,
26 boulevard Victor, 00460 Armées, France

ABSTRACT

The evanescent plane wave formalism is used to obtain the characteristic equation
of the normal vibration modes of a plane elastic solid embedded in a perfect fluid.
Simple drawings of the real and imaginary parts of complex wave vectors make
quite clear the choice of the Riemann sheets on which the roots of the
characteristic equation are to be looked for. The generalized Rayleigh wave and
the Scholte - Stoneley wave are then described. The same formalism is used to
describe Lamb waves on an elastic plane plate immersed in water. The damping,
due to energy leaking in the fluid, is shown to be directly given by the projection
of evanescence vectors on the interface. Measured values of the damping
coefficient are in good agreement with those derived from calculations. The width
of the angular resonances associated to Lamb waves or Rayleigh waves is also
directly related to this same evanescence vectors projection, as well as the
excitation coefficient of a given Lamb wave excited by a plane incident wave.
This study shows clearly the strong correlation between the resonance point of
view and the wave one in plane interface problems.

1. Introduction

This chapter is intended to show the interest of using the evanescent plane wave formalism in the description of normal modes of vibration in the case of plane liquid-solid interfaces. Such a formalism helps in the determination of square roots occurring in dispersion relations, and, most of all, we show that the different characteristics of the evanescent waves which compose a given interface wave are strongly related to resonance characteristics and excitation coefficients of the Geometrical Theory of Diffraction.

The evanescent plane wave formalism is briefly recalled in section 2. It is used in section 3 and section 4 to describe the normal modes of vibration of the liquid-solid interface and of the immersed plate. Section 5 is devoted to the connection between the Resonance Scattering Theory (more precisely, the concept of angular resonances) and the normal mode description derived in the preceeding sections.

In the whole text, a harmonic time dependence in $\exp(-j\omega t)$ is assumed, and complex quantities are underlined for a better readibility.

2. The Evanescent Plane Wave Formalism

In this section, we recall the properties of both lamellar and torsional evanescent plane waves we shall need. Further information and demonstrations can be found in refs 1,2.

An evanescent plane wave is characterized by a complex wave vector $\underline{\vec{K}}$, the real and imaginary parts of which being orthogonal. The associated particle displacement $\underline{\vec{u}}$ can be then written as :

$$\underline{\vec{u}} = \underline{\vec{A}} \exp(j\underline{\vec{K}} \cdot \vec{r}) \tag{1}$$

where $\vec{r}$ stands for the position vector, $\underline{\vec{A}}$ for the complex amplitude vector, which does not depend on $\vec{r}$,

$$\underline{\vec{K}} = \vec{K}' + j\vec{K}'' \tag{2}$$

and

$$\vec{K}' \perp \vec{K}'' \tag{3}$$

The real part $\vec{K}'$ of the wave vector indicates the propagation direction of the phase, and its modulus K' is equal to the ratio of the angular frequency ω to the phase velocity c; it is called the propagation vector. The imaginary part $\vec{K}''$ indicates the direction in which the wave amplitude exponentially decays; it is called the evanescence vector.

In the following sections, we shall represent the evanescent plane wave by the drawing of both its propagation vector and its evanescence vector, as illustrated in Fig. 1.
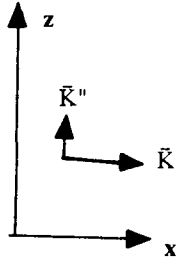
Fig.1 : Schematic representation of a plane evanescent
wave propagating in the x - direction whose
amplitude decays in the z - direction

The most general plane wave solution of the Helmholtz equation in an infinite perfect fluid, when no viscosity is taken into account, is the lamellar evanescent plane wave, whose associated particles displacement $\underline{\vec{u}}$ satisfies :

$$\vec{\nabla} \times \underline{\vec{u}} = \bar{0} \tag{4}$$

while the complex wave vector is related to the wave number k of the homogeneous longitudinal plane wave with the same angular frequency ω :

$$\underline{\vec{K}} . \underline{\vec{K}} = K'^2 - K''^2 = k^2 \tag{5}$$

In an infinite non viscous elastic solid, the most general plane wave solution for the displacement is the summation of lamellar evanescent plane waves and torsional ones. The torsional evanescent plane wave is associated with a particle displacement which satisfies :

$$\vec{\nabla} . \underline{\vec{u}} = 0 \tag{6}$$

The complex wave vectors $\underline{\vec{K}_L}$ and $\vec{K}_T$ of the lamellar and torsional waves are respectively related to the wave numbers k_l and k_t of the homogeneous longitudinal and shear plane waves by the same kind of relations as Eq. (5).

3. The Plane Elastic Solid / Perfect Fluid Interface

We describe the normal vibration modes of the solid / fluid plane interface as combinations of a lamellar evanescent plane wave in the fluid with a lamellar evanescent plane wave and a torsional one in the solid. The resolution of the characteristic equation involves the choice of different square root determinations. This can be done with the help of the three evanescent plane wave representation.

3.1. The Characteristic Equation

3.1.1. The Three Evanescent Plane Waves and the Interface Wave

Let the x - axis be on the plane fluid - solid interface; the fluid medium will occupy the z < 0 region, and the solid the z > 0 one. Translation invariance along the y - axis is assumed. The most general solution for the displacement in the fluid is a lamellar wave; in the solid it is a combination of a lamellar and a torsional wave. These three waves are linked by boundary conditions. The whole problem configuration is illustrated in Fig. 2.
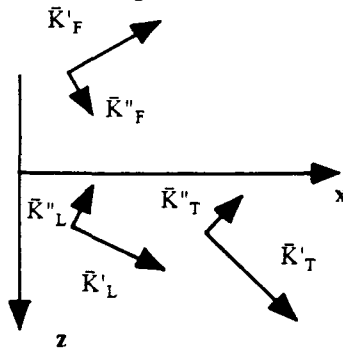
Fig.2. : The fluid / solid interface
and one possible configuration for the three evanescent plane waves

In Fig.2 and in the following, the F subscripts are related to the evanescent wave in the fluid, the L and T ones to the lamellar (L) and torsional (T) waves in the solid, while we shall use the f, l, t subscripts for the homogeneous waves in the fluid (f), the longitudinal (l) and the shear (t) waves in the solid.

We are looking for interface waves propagating in the positive x - direction : hence the common projection K'_x, due to the Snell-Descartes' laws, of all the propagation vectors on the interface is positive. Moreover, it seems natural for an interface wave propagating in the x - direction not to be amplified in that same positive x - direction, so that the common projection K''_x of all the evanescence vectors is also positive (or null).

The three evanescent plane waves verify the classical conditions at the z=0 interface :
- continuity of normal displacements,
- continuity of normal stresses.

These conditions, combined with those derived from the lamellar or torsional character of each wave, lead to a homogeneous set of equations, in which the unknown variables are, for example, the complex amplitudes of the normal displacements. For the solutions not to be all equal to zero, the following equation has to be satisfied :

$$\underline{K}_{Fz}\left[4\underline{K}_x^{\,2}\underline{K}_{Lz}\underline{K}_{Tz} + (2\underline{K}_x^{\,2} - k_t^{\,2})^2\right] + \frac{\rho_f}{\rho_s}k_t^{\,4}\underline{K}_{Lz} = 0 \qquad (7)$$

where ρ_f and ρ_s are the respective densities of the fluid (f) and the solid (s).

The unknown variable in Eq. (7) is the complex quantity $\underline{K}_x$, and the other complex quantities are defined as :

$$\underline{K}_x^{\,2} + \underline{K}_{Fz}^{\,2} = k_f^{\,2}$$

$$\underline{K}_x^{\,2} + \underline{K}_{Lz}^{\,2} = k_l^{\,2} \qquad (8)$$

$$\underline{K}_x^{\,2} + \underline{K}_{Tz}^{\,2} = k_t^{\,2}$$

We shall call Eq.(7) "the Stoneley equation", as in refs.3,4; it can be written [5] in terms of the interface wave celerity c, given by :

$$c = \frac{\omega}{K'_x} \qquad (9)$$

3.1.2. The complex wave vectors and the Riemann Sheets

It can be seen from Eq.(8) that the solutions of Eq.(7) depend on three square root determinations $(\underline{K}_{Fz}, \underline{K}_{Lz}, \underline{K}_{Tz})$; the combination of all roots in Eq.(7) gives rise to eight different determinations. These determinations depend on the sign of the real part of each square root; they are summarized in Table 1, the last column of which will be explained in the following.

Table 1 : The different determinations of the Stoneley equation, their notation in the text, and the corresponding interface wave

determination n°. (notation)	K'_{Fz}	K'_{Lz}	K'_{Tz}	Interface wave (name of)
1 (+++)	≥ 0	≥ 0	≥ 0	none
2 (++-)	≥ 0	≥ 0	≤ 0	none
3 (+-+)	≥ 0	≤ 0	≥ 0	none
4 (+--)	≥ 0	≤ 0	≤ 0	Scholte-Stoneley
5 (-++)	≤ 0	≥ 0	≥ 0	Scholte-Stoneley
6 (-+-)	≤ 0	≥ 0	≤ 0	none
7 (--+)	≤ 0	≤ 0	≥ 0	none
8 (---)	≤ 0	≤ 0	≤ 0	Rayleigh

Ansell[4] has performed an extensive study of the solutions of Eq.(7), showing that there are sixteen of them, with only three located in the first quadrant of the complex $\underline{K}_x$ plane (K'_x and K''_x positive), and four more corresponding to positive real values of $\underline{K}_x$. Each solution is a root of two "opposed" determinations of Eq.(7), as illustrated in Fig.3.
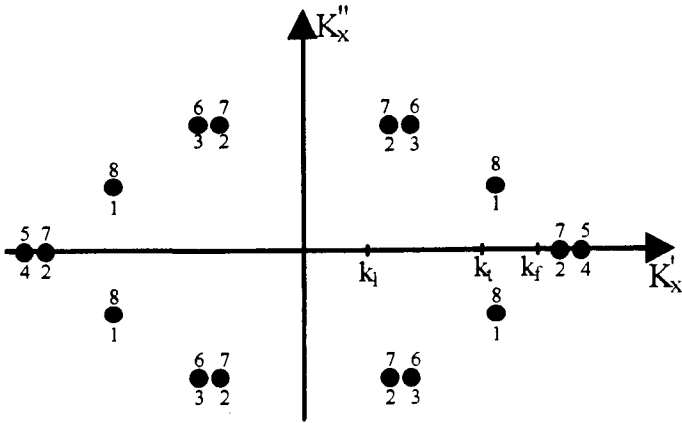
Fig.3. : *Schematic representation of the sixteen solutions*
of the Stoneley equation. Each solution corresponds
to two different determinations of the Stoneley equation.
Case of a water - aluminum interface.

Among the sixteen solutions of Fig.3, only two correspond to interface waves which have been either theoretically studied or experimentally observed. The other ones have yet received no name, as indicated in the last column of Table 1. In the following, we are going to show the link between the determinations associated to a given solution and its amplitude variation, in both parts of the interface, in the normal direction.

We restrict our discussion to solutions corresponding to interface waves whose fluid part could reach an observer located either in the liquid or on the interface. Such solutions correspond to an evanescent wave in the fluid which propagates either upwards or horizontally.

We consider at first the case of an observer located in the liquid. Determinations numbered from 1 to 4 of Eq.(7) are then excluded. The three complex solutions in the first quadrant (Fig.3) remain; they correspond to the last four different determinations of Table 1. The corresponding sets of evanescent waves are shown in Fig.4.
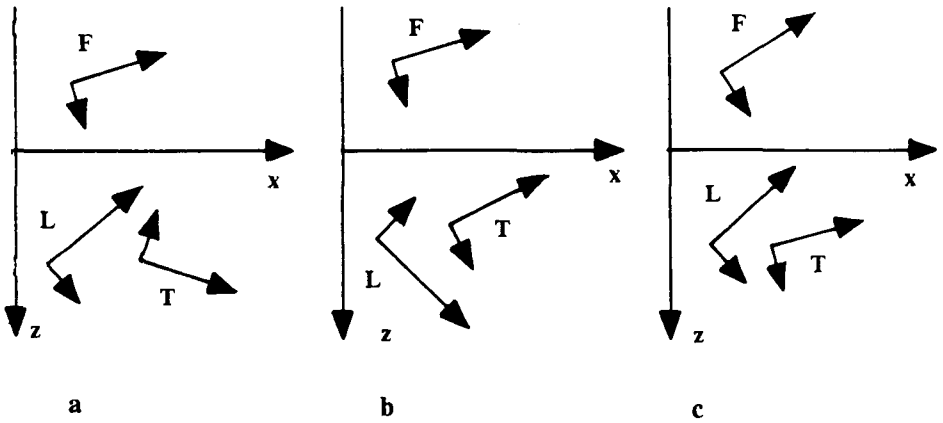
Fig.4 : The three evanescent waves associated to the three
non - real roots of the Stoneley equation located in the first
quadrant of the $\underline{K}_x$ plane
a : determination --+
b : determination -+-
c : determination ---

It can be seen in Fig.4 that in the case of the determinations --+ and -+-, the amplitude of the resulting interface wave exponentially grows as the normal distance to the interface increases, in both parts of the interface. Such interface waves have not been studied, and thus have no name. Different is the situation --- , as it corresponds to an interface wave which is actually localized in the near field of the interface, in the solid, but whose amplitude tends to infinity as the distance from the interface increases, in the fluid. The situation depicted in Fig.4c corresponds to the generalized Rayleigh wave[5-7].

We now look at the two real roots of Fig.3. Due to the orthogonality of the propagation vectors with their associated evanescence vectors, a real $\underline{K}_x$ implies that $K'_{Fz} = K'_{Lz} = K'_{Tz} = 0$, so that the corresponding interface wave propagates undamped along the interface, i.e. the observer is located on the interface.

The first real root of Fig.3 corresponds to the determinations ++- and --+. It may come onto the real axis of Fig.3 either from the first quadrant, or from the second one. In other words, it may be a limiting case $(K''_x = 0)$ of two different configurations per determination. These configurations are illustrated in Fig.5, for the determination ++- , and in Fig.6 for the determination --+.
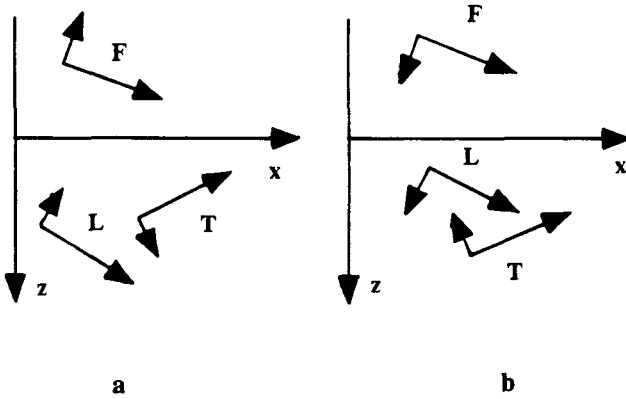
Fig. 5 : The two different sets of evanescent waves which can have the real solution ++-
of the Stoneley equation as a limiting case ($K''_x=0$)
a : $K''_x > 0$ b : $K''_x < 0$
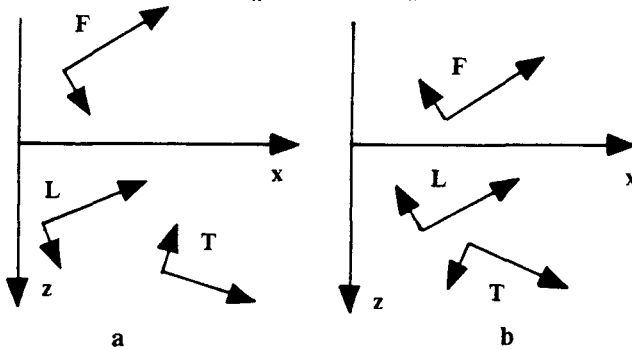
Fig. 6 : The two different sets of evanescent waves which can have the real solution --+
of the Stoneley equation as a limiting case ($K''_x=0$)
a : $K''_x > 0$ b : $K''_x < 0$

The Fig.5a and Fig.6b configurations, at the limit $K''_x = 0$, are identical; this is also the case for the Fig.5b and Fig.6a configurations.

The limiting case of Fig.5b and Fig.6a configurations represents an interface wave whose amplitude goes to infinity, in both the liquid and the solid, as the distance from the interface increases. It has not been studied and there is no name for it.

The limiting case of Fig.5a and Fig.6b configurations represents an interface wave, whose amplitude goes to infinity, as the distance from the interface increases. in the solid, while it decreases in the liquid. There is also no name for it.

The second root of Fig.3 corresponds to the determinations +-- and -++ . The configurations it may be a limiting case of are illustrated in Fig.7 for the determination +-- , and in Fig.8 for the determination -++ .
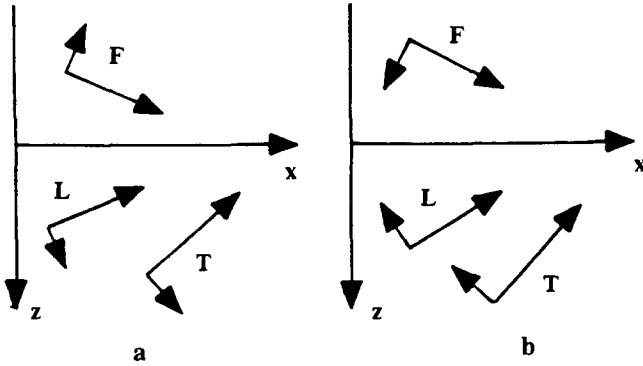
Fig. 7 : The two different sets of evanescent waves which can have the real solution +-- of the Stoneley equation as a limiting case ($K"_x=0$)
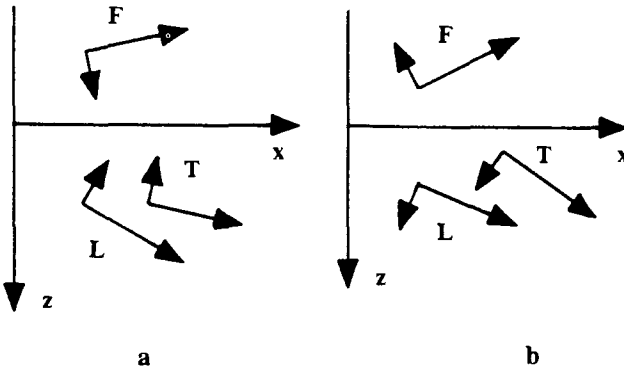
a : $K"_x >0$ b : $K"_x <0$

Fig. 8 : The two different sets of evanescent waves which can have the real solution -++ of the Stoneley equation as a limiting case ($K"_x=0$)

a : $K"_x >0$ b : $K"_x <0$

The Fig.7a and Fig.8b configurations, at the limit $K"_x = 0$, are identical; this is also the case for the Fig.7b and Fig.8a configurations.

The limiting case of Fig.7b and Fig.8a represents a wave whose amplitude goes to infinity in both directions perpendicular to the interface, while the one of Fig.7a and Fig.8b represents an interface wave whose amplitude decreases in both parts of the interface as the normal distance from it increases. This is the Scholte-Stoneley wave [5-7].

3.2. The Rayleigh Wave and the Scholte - Stoneley wave

We shall now focus our attention on the generalized Rayleigh wave, we shall call shortly "Rayleigh wave", and on the Scholte - Stoneley wave.

3.2.1. The Rayleigh Wave

It is once again depicted in Fig. 9. The θ_R angle is the angle under which the energy is leaking from the interface; it is given by :

$$\sin \theta_R = \frac{K'_x}{K'_F} \tag{10}$$
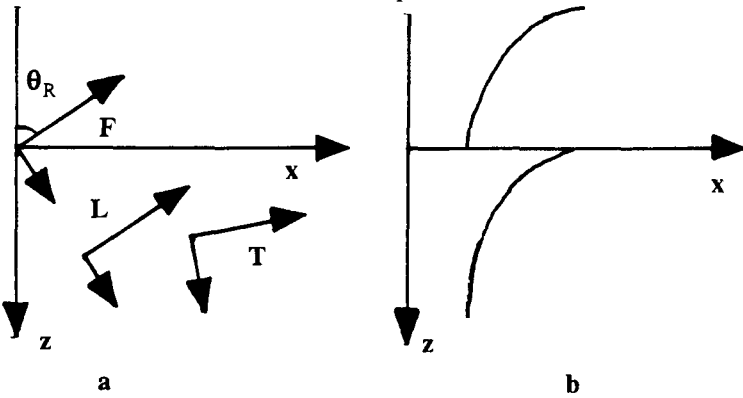
Fig.9 : The Rayleigh wave
a - The three evanescent waves and the reemission angle θ_R in the fluid
b - Energy repartition

K'_F and K''_F satisfy the same kind of relation as Eq.(5), so that :

$$\sin \theta_R = \frac{\sin \theta}{\sqrt{1 + \frac{K''_F{}^2}{k_f{}^2}}} \tag{11}$$

with

$$\sin \theta = \frac{K'_x}{k_f} \tag{12}$$

The ratio of the evanescence vector modulus K''_F to the propagation vector modulus k_f is very small for most usual cases[9] (around 0.01 for the water-aluminum interface), so that :

$$\sin \theta_R \approx \sin \theta \left(1 - \frac{1}{2} \frac{K''_F{}^2}{k_f{}^2} \right) \tag{13}$$

and θ_R is very close to θ.

The generation of a Rayleigh wave at a fluid-solid interface may be achieved in a variety of well-known ways. We shall partly discuss here the way of generating it by means of an incident wave in the liquid.

Strictly speaking, and because of the non zero imaginary part of $\underline{K}_x$, a single incident homogeneous plane wave can in no way give rise to a Rayleigh wave at the interface, as the Snell-Descartes laws can not be satisfied.

The decomposition of the field radiated by a spherical source[5] or a cylindrical one[10] in terms of plane waves (homogeneous and evanescent ones) of different directions shows that a Rayleigh wave is excited from the incidence of a narrow beam of plane waves at an incidence angle given by the resonance condition[5,11] of Eq.(12). The incidence of a Gaussian beam is studied in ref.12. In all these integral representations[5,10,12], the Rayleigh wave arises as a pole of the reflection coefficient of an incident homogeneous plane wave.

In the evanescent plane wave decomposition of Leroy[13], the Rayleigh wave is excited from the incidence of a single evanescent plane wave, at the incidence angle θ_R of Eq.(11), so that the generalized Snell-Descartes laws[14] are satisfied : the reflected wave is exactly the evanescent plane wave in the fluid of the Rayleigh wave representation of Fig.9a.

A schematic plot of the Rayleigh wave amplitude is shown in Fig.9b. The exponential growth of the amplitude in the fluid part of the interface is discussed in ref.[9], and it has been shown that in the realistic case of a finite amplitude incident beam, the radiated one, associated to the leaking of a Rayleigh wave, is also of finite amplitude. The study of the evanescence vector moduli of the three evanescent waves of Fig.9a shows also that the two waves inside the solid are decreasing much more quickly than the wave inside the fluid is increasing with distance from the interface. The most rapidly decaying wave is the lamellar wave in the solid[9].

3.2.2. The Scholte - Stoneley Wave

The limiting case of Fig.7a and Fig.8b, when $K''_x = 0$, is shown in Fig.10 : it represents the Scholte - Stoneley wave.
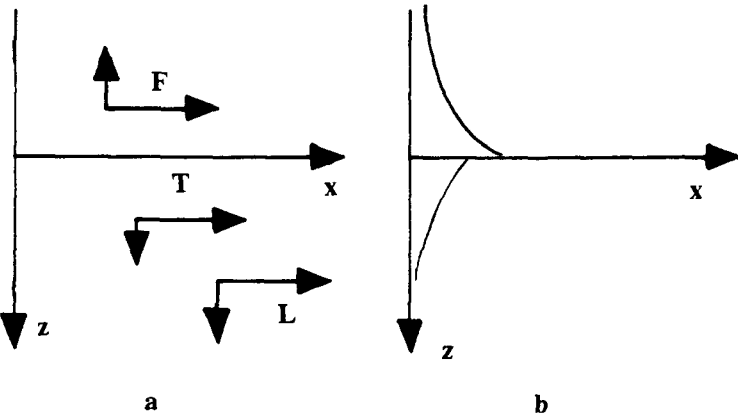
Fig.10. The Scholte - Stoneley wave
a - The three evanescent plane waves
b - Energy repartition

The Scholte-Stoneley wave is sometimes called Stoneley wave, and sometimes Scholte wave. Its existence has long been discussed by Cagniard[15] and Scholte[16], until Scholte[17] concluded that both a Rayleigh wave and what he called a Stoneley wave did exist at the fluid-solid interface. Because of this discussion, we have chosen[18,19] to call it "Scholte-Stoneley" wave.

The Scholte-Stoneley wave propagates undamped $(K''_x = 0)$ along the interface. Its velocity, given by Eq.(9), is the common phase velocity of all the three evanescent waves of Fig.10. Hence, and because of Eq.(5), it is smaller than the smallest velocity of all homogeneous waves :

$$c \leq \inf(c_f, c_l, c_t) \qquad (14)$$

The amplitude repartition on both parts of the interface is illustrated in Fig.8b. It can be seen easily, from Eq.(8), that the amplitude decrease of the lamellar wave in the solid is once more the largest one, while it is the smallest one in the fluid. The energy is then mostly concentrated in the fluid part of the interface.

As for the Rayleigh wave, the Scholte-Stoneley wave corresponds to a pole of the reflection coefficient of a homogeneous plane wave at the interface, and this pole does also lie on the physical Riemann sheet $(K''_{Lz} \geq 0$ and $K''_{Tz} \geq 0)$ over which the integration must be performed in the study of the scattering due to an incident spherical wave in the fluid[5]. Application of the resonance condition of Eq.(12) gives a value greater than unity for the sine. After Brekhovskikh[7], the Scholte-Stoneley wave may be excited from a sound wave in the liquid, at grazing incidence. The problem of its excitation has been studied these last years, and various methods can be cited.

The liquid wedge method[18,20,21] is illustrated in Fig.11.
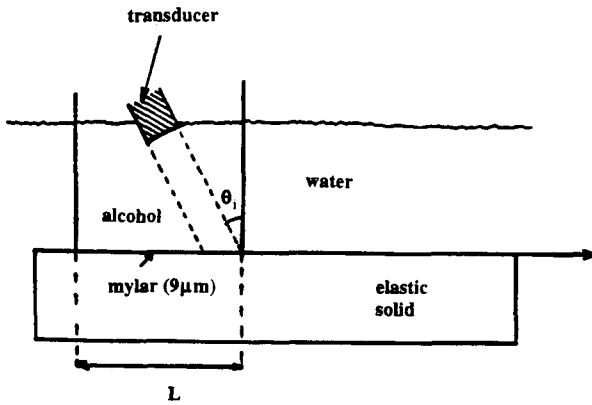
Fig.11. Excitation of a Scholte-Stoneley wave : the liquid-wedge method.

The alcohol in the little tank is ethanol; the velocity c_a of the homogeneous waves in it is about 1200 m/s. At an aluminum-water interface, the velocity c_s of the Scholte-Stoneley wave, as given by Eq.(9), is about 1478 m/s. The incidence angle in alcohol, given by :

$$\sin\theta_i = \frac{c_a}{c_s} \qquad (15)$$

is then real and approximately equal to $55°$. The main problems of this method are due to the dimensions of the whole set-up. The alcohol tank must be high enough to ensure hydrostatic equilibrium and a better alcohol-solid coupling; the length L of the alcohol tank must satisfy :

$$L > d\sin\theta_i \qquad (16)$$

for the distance between the emitting transducer and the wedge to be larger than the Fresnel distance d of the transducer in ethanol. When this last condition is not fulfilled (which is often the case), the experiment is rather uneasy. It should also be noticed that Eq.(15) gives a real value of the incidence angle only for the case of metallic samples, excluding plastic ones.

The comb-like transducer method[22-26] can be used at any type of interface. In Guzhev's experiments[22,23], the Scholte-Stoneley wave propagates at the surface of a piezoelectric crystal ($Bi_{12}GeO_{20}$) embedded in water. In Nasr's experiments[24-26], it is excited on a silica plate, which can be stuck to the sample on which propagation is to be achieved. Fig 12 is a schematic representation of Nasr's experimental set-up.

PVDF   **water**
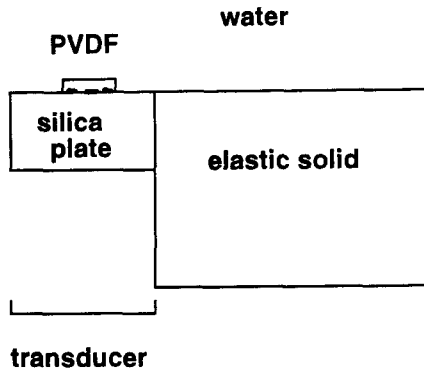
transducer

Fig.12. Generation of a Scholte-Stoneley wave by a PVDF
interdigital transducer

The actual transducer is made of a silica plate on which is etched a set of interdigital linear chromium electrodes, pasted on a piezoelectric polyvinylidene fluoride (PVDF) film.

The last method[27] is the simplest one. It may be used on any type of sample (metallic or plastic one), and requires no specific technologic abilities. It is illustrated in Fig.13.
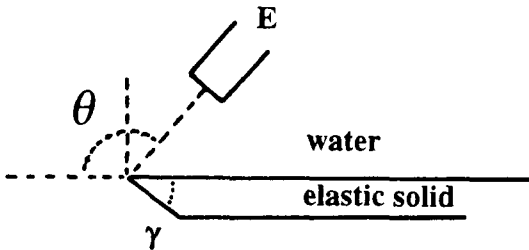
Fig.13. Scholte-Stoneley wave generation by the diffracting wedge
method. The propagation direction is x.

The transducer labeled E is a classical immersion one; it insonifies the sample wedge, of internal angle γ, under the incidence angle θ. $\theta = \pi$ corresponds to the propagation direction (x) of the Scholte-Stoneley wave. Optimal conversion is achieved at $\theta = 0$, i.e. at grazing incidence. In that case, however, it is rather uneasy to separate the Scholte-Stoneley wave from the longitudinal bulk wave

propagating in the liquid. Conversion takes place also at $\theta = \theta_R + \dfrac{\pi}{2}$ and at

$\theta = \gamma - \theta_R - \dfrac{\pi}{2}$, where θ_R stands for the critical excitation angle of the Rayleigh wave at the liquid-solid interface. The efficiency of the conversion process is the same for the two incidence directions, but it has been shown[28-29] to depend on the internal angle γ of the wedge : best efficiency is obtained at $\gamma \approx 45°$.

4. The Plane Elastic Plate in a Perfect Fluid

We describe the Lamb waves in an immersed plane plate as combinations of one evanescent plane wave on each side of the plate with two lamellar and two torsional evanescent plane waves in the solid. All these waves are linked by the boundary conditions on both faces of the plate and share a common projection of their complex wave vectors on the interface. This projection gives the damping coefficient of the Lamb wave and its phase velocity.

Sections 4.1 to 4.3 present this description of the Lamb waves, which are normal modes of vibration of the immersed plate.

4.1. The Characteristic Equations

We consider an elastic plane plate embedded in a perfect fluid. The plate occupies the $-e \leq z \leq +e$ region, and translation invariance is assumed along the y - axis. We look for waves propagating in the positive x - direction. The geometry is illustrated in Fig. 14. The most general plane wave solution in the fluid, on both sides of the plate, is a lamellar evanescent plane wave. In order for the wave to be able to reach an observer located either in the upper fluid or on the interface, the propagation vector of the evanescent wave in the upper fluid must have a positive (or null) projection on the z - axis. The propagation and evanescence vectors of the evanescent wave in the lower fluid are deduced from the ones in the upper fluid by symmetry considerations. In the solid plate, the number of evanescent plane waves to be taken into account is multiplied by two, with respect to the case of the semi-infinite solid, because of the second interface, at z = - e.
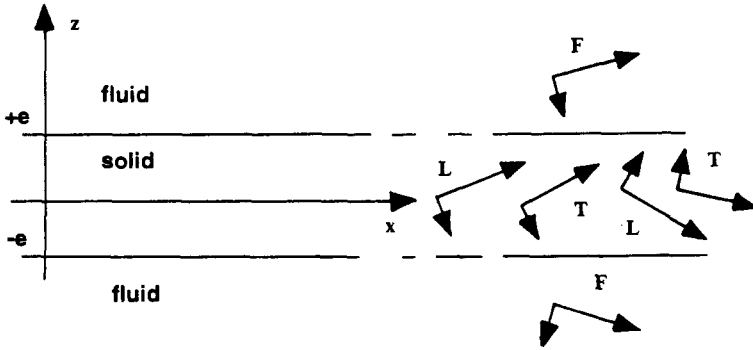
Fig.14. Geometry of the problem. The six evanescent plane waves.

The six evanescent plane waves may be described by the expressions of their corresponding displacements :

for the evanescent plane wave in the upper fluid :

$$\bar{\underline{u}}_1 = \bar{\underline{A}}_1 e^{j\underline{K}_{1z}z} e^{j\underline{K}_x x}, \mathrm{Re}\left[\underline{K}_{1z}\right] \geq 0 \qquad (17)$$

for the lamellar wave in the solid that propagates upwards :

$$\bar{\underline{u}}_{L1} = \bar{\underline{B}}_L e^{j\underline{K}_{Lz}z} e^{j\underline{K}_x x}, \mathrm{Re}\left[\underline{K}_{Lz}\right] \geq 0 \qquad (17)$$

for the lamellar wave in the solid that propagates downwards :

$$\bar{\underline{u}}_{L2} = \bar{\underline{A}}_L e^{-j\underline{K}_{Lz}z} e^{j\underline{K}_x x}, \mathrm{Re}\left[\underline{K}_{Lz}\right] \geq 0 \qquad (17)$$

for the torsional wave in the solid that propagates upwards :

$$\bar{\underline{u}}_{T1} = \bar{\underline{B}}_T e^{j\underline{K}_{Tz}z} e^{j\underline{K}_x x}, \mathrm{Re}\left[\underline{K}_{Tz}\right] \geq 0 \qquad (17)$$

for the torsional wave in the solid that propagates downwards :

$$\bar{\underline{u}}_{T2} = \bar{\underline{A}}_T e^{-j\underline{K}_{Tz}z} e^{j\underline{K}_x x}, \mathrm{Re}\left[\underline{K}_{Tz}\right] \geq 0 \qquad (17)$$

for the evanescent plane wave in the lower fluid :

$$\bar{\underline{u}}_2 = \bar{\underline{A}}_2 e^{-j\underline{K}_{1z}z} e^{j\underline{K}_x x}, \mathrm{Re}\left[\underline{K}_{1z}\right] \geq 0 \qquad (17)$$

The boundary conditions at the $z = e$ and $z = -e$ interfaces, combined with the relations derived from the lamellar or torsional character of each wave, lead to a homogeneous set of six equations which can be written as :

$$[S](D) = (0) \qquad (18)$$

where [S] is a rather complicated 6x6 matrix and (D) the following unknown vector :

$$(D) = \begin{pmatrix} \underline{A}_{Lx} \\ \underline{B}_{Lx} \\ \underline{A}_{Tx} \\ \underline{B}_{Tx} \\ \underline{A}_{1x} \\ \underline{A}_{2x} \end{pmatrix} \qquad (19)$$

The characteristic equation of all the Lamb modes is obtained by setting the determinant of the [S] matrix equal to zero. In order to achieve the distinction between symmetric and antisymmetric modes, combinations have to be done on the [S] matrix, so that the two following sub-systems are obtained :

$$[H_S](E_S) = (0),$$

$$[H_A](E_A) = (0)$$

$$(E_S) = \begin{pmatrix} \dfrac{\underline{A}_{Lx} + \underline{B}_{Lx}}{2} \\ \dfrac{\underline{A}_{Tx} + \underline{B}_{Tx}}{2} \\ \dfrac{\underline{A}_{1x} + \underline{A}_{2x}}{2} \end{pmatrix}, (E_A) = \begin{pmatrix} \dfrac{\underline{A}_{Lx} - \underline{B}_{Lx}}{2} \\ \dfrac{\underline{A}_{Tx} - \underline{B}_{Tx}}{2} \\ \dfrac{\underline{A}_{1x} - \underline{A}_{2x}}{2} \end{pmatrix} \qquad (20)$$

with [H_S] and [H_A] 3x3 matrices.

The symmetric Lamb waves correspond to the case :

$$\det[H_S] = 0$$
$$\det[H_A] \neq 0 \qquad (21)$$

with the first relation of Eq.(21) leading to the following dispersion relation :

$$4\underline{K}_{Lz}\underline{K}_{Tz}\underline{K}_x{}^2 \cot(\underline{K}_{Tz}e) + (k_t{}^2 - 2\underline{K}_x{}^2)^2 \cot(\underline{K}_{Lz}e) = j\frac{\rho_f}{\rho_s}\frac{\underline{K}_{Lz}}{\underline{K}_{1z}}k_t{}^4$$

or, after division by $k_t{}^4$:   (22)

$$c_s - j\tau = 0$$

The antisymmetric Lamb waves correspond to the case :

$$\det[H_A] = 0$$
$$\det[H_S] \neq 0 \qquad (23)$$

with the first relation of Eq.(23) leading to the following dispersion relation :

$$4\underline{K}_{Lz}\underline{K}_{Tz}\underline{K}_x{}^2 \tan(\underline{K}_{Tz}e) + (k_t{}^2 - 2\underline{K}_x{}^2)^2 \tan(\underline{K}_{Lz}e) = -j\frac{\rho_f}{\rho_s}\frac{\underline{K}_{Lz}}{\underline{K}_{1z}}k_t{}^4$$

or, after division by $k_t{}^4$:   (24)

$$c_a + j\tau = 0$$

The left hand terms of Eq.(22) and Eq.(24) are the same as the ones of the corresponding dispersion relations of the free plate. The right hand terms represent the effect of the fluid loading of the plate. The $\underline{K}_x$ solutions are complex; their real parts give the phase velocity c of the Lamb wave by use of Eq.(9), while their imaginary parts represent the damping coefficient of the Lamb wave. In most cases, K''_x is rather small, so that the phase velocity of a given Lamb mode in the fluid

loaded plate can be well approximated by its value in the case of the free plate. The dispersion curves of the fluid loaded plate are then usually similar to the ones of the free plate [6,30,31]. There are however a few exceptions, for example the modes S1 and S2 at low frequencies, whose dispersion curves differ from the ones of the free plate. as shown in reference 32. Two real roots appear also, which have no counterpart in the case of the free plate; they correspond to an antisymmetric and a symmetric Scholte-Stoneley wave [6,30,33,34].

We are not interested here in these particular cases, and we shall focus our attention on ordinary Lamb waves, with positive values of the K''_x damping coefficient. In the next section, we describe the displacements associated to symmetric and antisymmetric Lamb waves.

4.2. The Symmetric and Antisymmetric Lamb Waves

We consider first the case of the symmetric Lamb waves. From the second relation of Eq.(21), and using the relations describing the lamellar or torsional character of the evanescent waves, one can deduce that the two lamellar waves inside the plate have the same amplitude [36]; this is also the case of the torsional waves inside the plate. and of the two lamellar waves in the surrounding liquid. The displacements components of all evanescent waves are then [35] :
for the evanescent plane wave in the upper fluid :

$$\underline{u}_{1x} = -j\underline{A}_{Tx} \frac{k_t^2}{2\underline{K}_{Tz}\underline{K}_{1z}} \frac{\sin(\underline{K}_{Tz}e)}{\exp(j\underline{K}_{1z}e)} \exp(j\underline{K}_{1z}z)\exp(j\underline{K}_x x)$$

$$\underline{u}_{1z} = -j\underline{A}_{Tx} \frac{k_t^2}{2\underline{K}_{Tz}\underline{K}_x} \frac{\sin(\underline{K}_{Tz}e)}{\exp(j\underline{K}_{1z}e)} \exp(j\underline{K}_{1z}z)\exp(j\underline{K}_x x)$$

(25)

for the evanescent plane wave in the lower fluid :

$$\underline{u}_{2x} = -j\underline{A}_{Tx} \frac{k_t^2}{2\underline{K}_{Tz}\underline{K}_{1z}} \frac{\sin(\underline{K}_{Tz}e)}{\exp(j\underline{K}_{1z}e)} \exp(-j\underline{K}_{1z}z)\exp(j\underline{K}_x x)$$

$$\underline{u}_{2z} = j\underline{A}_{Tx} \frac{k_t^2}{2\underline{K}_{Tz}\underline{K}_x} \frac{\sin(\underline{K}_{Tz}e)}{\exp(j\underline{K}_{1z}e)} \exp(-j\underline{K}_{1z}z)\exp(j\underline{K}_x x)$$

(26)

for the total lamellar wave in the solid : (summation of the ones that propagate upwards and downwards)

$$\underline{u}_{Lx} = -\underline{A}_{Tx} \frac{k_t^2 - 2\underline{K}_x^2}{\underline{K}_{Lz}\underline{K}_{Tz}} \frac{\sin(\underline{K}_{Tz}e)}{\sin(\underline{K}_{Lz}e)} \cos(\underline{K}_{Lz}z)\exp(j\underline{K}_x x)$$

$$\underline{u}_{Lz} = -j\underline{A}_{Tx} \frac{k_t^2 - 2\underline{K}_x^2}{\underline{K}_{Tz}\underline{K}_x} \frac{\sin(\underline{K}_{Tz}e)}{\sin(\underline{K}_{Lz}e)} \sin(\underline{K}_{Lz}z)\exp(j\underline{K}_x x)$$

(27)

for the total torsional wave in the solid :

$$\underline{u}_{Tx} = 2\underline{A}_{Tx} \cos(\underline{K}_{Tz}z) \exp(j\underline{K}_x x)$$

$$\underline{u}_{Lx} = -2j\underline{A}_{Tx} \frac{\underline{K}_x}{\underline{K}_{Tz}} \sin(\underline{K}_{Tz}z) \exp(j\underline{K}_x x) \tag{28}$$

In the case of the antisymmetric Lamb waves, the displacements related to the evanescent plane waves in the upper and lower fluids are the same as the ones corresponding to the symmetric Lamb waves (Eq.(25) and Eq.(26)), and :

for the total lamellar wave in the solid : (summation of the ones that propagate upwards and downwards)

$$\underline{u}_{Lx} = j\underline{A}_{Tx} \frac{k_t^2 - 2\underline{K}_x^2}{\underline{K}_{Lz}\underline{K}_{Tz}} \frac{\cos(\underline{K}_{Tz}e)}{\cos(\underline{K}_{Lz}e)} \sin(\underline{K}_{Lz}z) \exp(j\underline{K}_x x)$$

$$\underline{u}_{Lz} = \underline{A}_{Tx} \frac{k_t^2 - 2\underline{K}_x^2}{\underline{K}_{Tz}\underline{K}_x} \frac{\cos(\underline{K}_{Tz}e)}{\cos(\underline{K}_{Lz}e)} \cos(\underline{K}_{Lz}z) \exp(j\underline{K}_x x) \tag{29}$$

for the total torsional wave in the solid :

$$\underline{u}_{Tx} = -2j\underline{A}_{Tx} \sin(\underline{K}_{Tz}z) \exp(j\underline{K}_x x)$$

$$\underline{u}_{Tx} = 2\underline{A}_{Tx} \frac{\underline{K}_x}{\underline{K}_{Tz}} \cos(\underline{K}_{Tz}z) \exp(j\underline{K}_x x) \tag{30}$$

As in the case of the symmetric Lamb wave, the two evanescent lamellar waves in the solid have the same amplitude, as do the two evanescent torsional waves [36].

4.3. The six Evanescent Plane Waves and the Damping Coefficient of the Lamb Wave

We are interested now in the study of the damping coefficient of the Lamb waves. This damping is due to continuous energy leaking in the fluid, as propagation goes on. Theoretically, it is given by the value of K''_x, obtained from the resolution of one of the two dispersion equations, Eq.(22) or Eq.(24). In this section, we shall compare it to experimental values obtained for a few modes, and we shall then discuss its relation to the surface displacements.

Given a Lamb mode at frequency f, the angle θ under which it can be excited from the incidence of an ultrasonic beam on the plate is about the same as the angle under which energy is leaking from the plate; it is given from a resonance condition similar to that of the Rayleigh wave :

$$\sin\theta = \frac{K'_x}{k_f} \tag{31}$$

The experimental set-up is shown in Fig. 15.
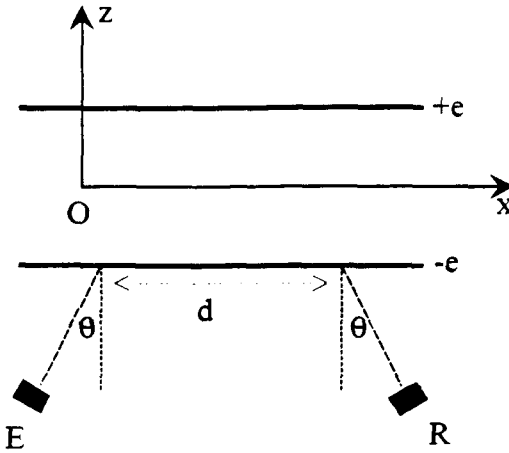
Fig.15. : The experimental configuration for the evaluation of
the damping coefficient of a given Lamb wave.

The receiving transducer R can be translated along the x - direction, and the received amplitude is plotted versus the propagation distance d. In dB units, this amplitude is linearly dependent on d, and the determination of the straight line slope gives the damping coefficient value [35,37]. The experiment has been carried out for different modes, at different frequencies and different angles, and the relative difference between the experimental value and the theoretical one never exceeds 20 %, such high errors occurring for the lowest values of the damping coefficient (around 0.01 cm^{-1}).

The damping coefficient value, then, describes quantitatively the rate of energy leaking. It is defined from the common projection, on the propagation direction of the Lamb wave, of all evanescence vectors. But the physical process involved in this energy leaking is not obvious.   Worlton [31] proposes a physical interpretation, based upon the study of the surface displacements of the Lamb wave. He considers that a wave, whose normal surface displacement is greater than the tangential one, can reasonably be supposed to radiate more than a wave for which the contrary is true. The damping coefficient value should then be related to the $r = \left| \underline{u}_z / \underline{u}_x \right|$ ratio at the $z = e$ interface, with $\underline{\underline{u}} = \underline{\underline{u}}_L + \underline{\underline{u}}_T$.

The next table shows results obtained for a few modes of an aluminum plate, at different frequency-thickness products. The modes are ordered by increasing values of their damping coefficient. Theoretical and experimental values of this damping coefficient are indicated, as well as the r ratio.

Table 2 : Theoretical and experimental values of the damping coefficient of a few Lamb waves of an aluminum plate. Comparison with the r ratio at the interface.

mode	frequency-thickness product (kHz m)	K''_x (cm^{-1}) theory	K''_x (cm^{-1}) experiment	$r = \left\| \dfrac{u_z}{u_x} \right\|$
S_4	9.7	0.06	0.07	0.17
A_6	14.5	0.12	0.13	0.26
A_4	8.0	0.16	0.17	0.31
A_4	8.5	0.28	0.27	0.76
A_5	10.5	0.72	0.71	0.21

One can notice that the r ratio actually increases with the damping coefficient, except for the mode A_5. It follows from this, and from other modes studied [37], that Worlton's assumption, which seems physically rather acceptable, is not valid in all cases.

We shall establish, in the next section, the relation of the damping coefficient with the angular resonance width associated to a Lamb wave (and also to a Rayleigh wave), and with the excitation coefficient of the Lamb wave.

5. Angular Resonances and Guided Waves

This section deals with the relation between the guided waves propagating along interfaces (the Rayleigh wave for the fluid-solid interface and the Lamb waves for the elastic plate) and the angular resonances. The concept of angular resonances has been introduced by Fiorito et al. [38] in the field of the Resonant Scattering Theory (R.S.T.). However, the angular resonances have not been studied in great detail in the usual literature and their physical meaning was unexplained. The study of the angular resonances is performed here with the use of the Phase Gradient Method (P.G.M.).

In a general way, the introduction of the Phase Gradient Method allows, on one hand, the complete characterization of an elastic plate in terms of resonances and, on the other hand, in terms of Lamb wave propagation [39]. It is based upon the study of the derivatives of the reflection coefficient phase, considered either as a function of a frequency variable or as a function of an angular variable. When the Breit-Wigner approximation is valid, the comparison with the Resonant Scattering Theory (R.S.T.) leads to the characterization of frequency or angular resonances in terms of positions and widths, by means of the location and of the magnitude of the phase derivative peaks [39]. This section is focused on the derivative with regard to the angular variable which allows to establish the link between the resonant theory derived from the R.S.T. and the previous normal mode theory.

5.1 Lamb Waves

We recall here the R.S.T. applied to the angular resonances and the main properties of the P.G.M. Then, we show the relation between the guided wave characteristics, K_x' and K_x'', and the angular resonances.

5.1.1 The Resonant Scattering Theory

The R.S.T. has been applied to the elastic plate angular resonances since a long time [40]. It is based upon the Breit-Wigner approximation of the reflection or transmission coefficients close to an angular resonance. More accurately, if we consider the reflection coefficient as a function of the angular variable $y = \sin\theta$, θ being the angle related to the incident homogeneous plane wave, the R.S.T. shows that at the vinicity of an angle of resonance $y^{(*)}$, the reflection coefficient can be written as :

$$\underline{R}(y) \approx \left(y - y^{(*)} - \bar{y}\right)\Big/\left(y - y^{(*)} - jy^{(*)}/2\right) \tag{32}$$

where $\gamma^{(*)}/2$ is the half-width of the angular resonance and $\bar{y}$ a shift that can be generally neglected when compared with $y^{(*)}$. As a consequence, the reflection coefficient contains the whole information on the resonant behavior of an elastic plate; it is the same for the transmission coefficient $\underline{T}(y)$. In fact, it is well known that the excitation of Lamb waves corresponds to more or less sharp minima in the curve representing the modulus of $\underline{R}(y)$ versus the angle and to maxima for the modulus of $\underline{T}(y)$. It is thus possible to quite precisely determine the angular resonances, but the width of the angular resonances cannot be easily evaluated with such an approach. This is the reason why the P.G.M. is used in this section.

5.1.2 The Angular Phase Gradient Method

The Phase Gradient Method is based on the derivative of the reflection coefficient phase ϕ_R. We can note that the phase ϕ_T of the transmission coefficient is equal to $\phi_R \pm \pi/2$. So, the derivative of the two phases are the same. The exact expression of the reflection coefficient can be written [40] as follows :

$$R = \frac{C_a C_s - \tau^2}{(C_a + j\tau)(C_s - j\tau)} \tag{33}$$

where the zeros of C_a and C_s are respectively the antisymmetric and symmetric vibration modes of the free plate and τ is a ratio of acoustic impedances, the derivative of the phase ϕ_R is the following one:

$$\partial\phi_R = \frac{C_s\partial\tau - \tau\partial C_s}{C_s^2 + \tau^2} - \frac{C_a\partial\tau - \tau\partial C_a}{C_a^2 + \tau^2} \tag{34}$$

One of the interests of the phase derivative is that we can always separate the contributions related to symmetric modes from those related to antisymmetric modes. The interest of this separation clearly appears when we study very close modes in a small angle range.

Practically, we calculate the derivative with respect to θ and then we deduce from this expression the derivative with respect to $y = \sin\theta$ in order to compare with the R.S.T. formalism. We have plotted the derivative $\partial\phi_R/\partial\theta$ for an aluminum plate when the frequency-thickness product is 3 MHz mm. As shown in Fig. 16, we can observe negative peaks clearly related to the Lamb waves S_1, A_1, S_0 and A_0. In addition, we can verify that the curve $\partial\phi_R/\partial\theta$ has the characteristics of a Breit-Wigner function because the angular resonance width $\gamma^{(*)}$ corresponds to the width of $|\partial\phi_R/\partial y| = |\partial\phi_R/\partial\theta|/\cos\theta$ at half heigth.
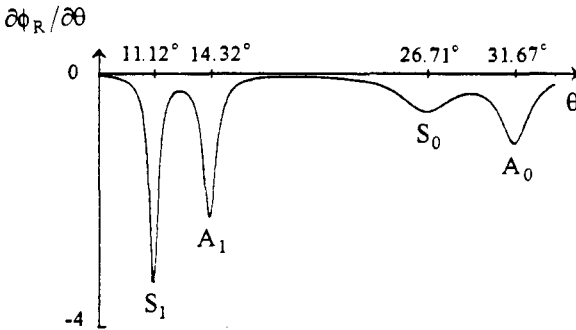
Fig.16 : Angular phase derivative of the reflection coefficient of the elastic plate at fd=3 MHz mm.

Another way to calculate the angular resonance width $\gamma^{(*)}$ is based on the Breit-Wigner approximation given by Eq. (32). As a matter of fact, there results from Eq. (32) the following relation :

$$\frac{\partial\phi_R}{\partial y} \approx \frac{-\gamma^{(*)}/2}{\left(y - y^{(*)}\right)^2 + \left(\gamma^{(*)}/2\right)^2} \tag{35}$$

which is valid close to the angle of resonance $y^{(*)}$. Consequently, the angular resonance width $\gamma^{(*)}$ is merely obtained by taking the minimum of the angular derivative at the angle of resonance $\gamma^{(*)}$ because:

$$\frac{\partial \phi_R}{\partial y}\left(y^{(*)}\right) \approx \frac{-2}{\gamma^{(*)}} \tag{36}$$

This study demonstrates that obtaining the coordinates ($y^{(*)}$, $\frac{\partial \phi_R}{\partial y}\left(y^{(*)}\right)$)

of the peaks of the angular derivative allows us to completely characterize the angular resonances of a plate, their width being deduced from Eq. (36). Moreover, the study of the angular derivative is more convenient for the characterization of resonances than the one of the transmission coefficient which can be considered as a sum of Breit-Wigner terms. Indeed, all the peaks of the transmission coefficient have the same unit amplitude, so it is really necessary to measure the widths, whereas the measurement of the amplitude of the peaks of the angular derivative is sufficient to obtain them. It is particularly convenient in the case of two close resonances.

5.1.3 Relation Between Lamb Waves and Angular Resonances

It is well known that the characteristic equation of the plate can be obtained by setting equal to zero the denominator of the reflection or transmission coefficient. So, the characteristic equation can be written (cf. Eq.(33)):

$$\left(C_a + j\tau\right)\left(C_s - j\tau\right) = 0 \tag{37}$$

For a given frequency-thickness product, it is equivalent to both Eq.(22) and Eq(24); it gives the different wave vectors projections $K_x' + jK_x''$ which mainly interest us. This result being recalled, it is obvious that Eq. (37) also gives the angular poles of the reflection coefficient, which can be written according to Eq. (32):

$$\underline{y}_p = \sin\theta_p + j\left(\gamma_p/2\right) \tag{38}$$

For a given frequency-thickness product, it is also well known that a Lamb wave propagating with velocity $c = c_f\left(k_f/K_x'\right)$ is excited by a plane wave with the angle θ_p defined by $\sin\theta_p = c_f/c$. As a consequence, we have the following resonance condition between K_x' and $\sin\theta_p$:

$$\frac{K_x'}{k_f} = \sin\theta_p \tag{39}$$

So, the Lamb wave velocities and the angles of resonance can be linked. However, the connection between the two points of view, namely, the wave propagation and the angular resonances, will be entirely established if we show that K_x'' is also in relation with $\gamma_p/2$. As for Eq. (39), we normalize the damping coefficient by k_f. The numerical verification of the equality :

$$\frac{K_x^{''}}{k_f} = \frac{\gamma_p}{2} \tag{40}$$

has been made for different modes. In the case of Lamb mode A_1, for different values of the frequency-thickness product, results are reported in Table 3.

Table 3 : Mode A_1 : comparison between the values of $K_x^{'}/k_f + j\, K_x^{''}/k_f$ and the angular resonances.

fd	$\sin \theta_p$	$\gamma_p/2$	$K_x^{'}/k_f$	$K_x^{''}/k_f$
2	0.167	4.66×10^{-3}	0.167	4.68×10^{-3}
3	0.247	7.46×10^{-3}	0.247	7.59×10^{-3}
4	0.306	1.27×10^{-2}	0.306	1.29×10^{-2}
5	0.378	1.08×10^{-2}	0.378	1.11×10^{-2}
6	0.419	6.79×10^{-3}	0.419	7.02×10^{-2}

We can note the good agreement between the two complex quantities $\underline{y}_p$ and $\underline{K}_x / k_f$, especially between their real parts. Differences appear between their imaginary parts, typically when the imaginary part $K_x^{''}/k_f$ becomes too large (> 0.1). In this case, the phase derivative no longer has a pronounced resonant character, so it becomes difficult to measure its maximum of amplitude. Nevertheless, we have shown, with the verification of Eq.(39) and Eq.(40), the equivalence of two different theoretical approaches: the resonant theory which allows to write the reflection coefficient as a sum of resonant contributions, but does not explicitly take into account the associated Lamb waves, and the normal mode theory which describes the vibrations of a plate by means of the propagation of evanescent plane waves. Thus, the angular derivative makes possible the establishment of the relationship between the angular resonances and the associated wave vectors of the Lamb waves.

5.2 Rayleigh Waves

We study now the problem of the Rayleigh wave at the fluid-solid interface : is it possible to consider this problem as a resonant one?

The reflection coefficient only depends on the incident angle θ. The Rayleigh wave propagating with a velocity smaller than the velocity of the shear waves in the solid, we consider the expression of the reflection coefficient for angles θ larger than the critical angle $\theta_c^{(T)}$ related to the vanishing of the shear waves. So, the reflection coefficient can be writen $(y = \sin \theta)$:

$$\underline{R}(y) = \frac{A(y) - jB(y)}{A(y) + jB(y)} \tag{41}$$

with

$$A(y) = \rho_s \sqrt{1 - y^2} \left[\left[n_t^2 - 2y^2 \right]^2 - 4y^2 \sqrt{y^2 - n_l^2} \sqrt{y^2 - n_t^2} \right] \tag{42}$$

$$B(y) = \rho_f n_t^4 \sqrt{y^2 - n_l^2} \tag{43}$$

where $n_t = c_f/c_t$ and $n_l = c_f/c_l$ are the indexes of refraction. We can note from Eq. (41) that the modulus of the reflection coefficient is always equal to 1; but its phase varies strongly. This is the reason why the Phase Gradient Method is interesting to analyse the reflection by the fluid-solid interface.

According to the Resonant Scattering Theory, the expansion of the functions $A(y)$ and $B(y)$ at the first order in the neighborhood of the Rayleigh angle θ_R yields :

$$A(y) \approx A(y_R) + (y - y_R) \frac{\partial A}{\partial y}(y_R) \tag{44}$$

$$B(y) \approx B(y_R) + (y - y_R) \frac{\partial B}{\partial y}(y_R) \tag{45}$$

where $y_R = \sin \theta_R$. The Rayleigh equation at the vacuum-solid interface being $A(y) = 0$, the first expression can be simplified because $A(y_R)$ is almost equal to zero. Retaining the main term in Eq.(45), the reflection coefficient takes the form of a Breit-Wigner function:

$$\underline{R}(y) \approx \frac{y - y_R + j\gamma_R/2}{y - y_R - j\gamma_R/2} \tag{46}$$

with

$$\gamma_R = -2 \frac{B(y_R)}{\dfrac{\partial A}{\partial y}(y_R)} \tag{47}$$

As a consequence, the angular derivative of the reflection coefficient phase Φ_R can be approximated by:

$$\frac{\partial \phi_R}{\partial y} \approx \frac{-\gamma_R}{(y - y_R)^2 + \gamma_R^2/4} \tag{48}$$

This function is always negative if $\gamma_R > 0$ and has the type of a Breit-Wigner function. It has an extremum for $y = y_R$, the value of which is $-4/\gamma_R$, and the full-width at half maximum is γ_R.

In order to verify the validity of the Breit-Wigner approximation, we can compare the curve corresponding to the exact angular derivative of ϕ_R:

$$\frac{\partial \phi_R}{\partial y} = -j \left[\frac{\partial A/\partial y - j \partial B/\partial y}{A - jB} - \frac{\partial A/\partial y + j \partial B/\partial y}{A + jB} \right] \tag{49}$$

with the curve corresponding to the Breit-Wigner approximation (cf. Eq. (48). The result is shown in Fig. 17, and we can see that the correspondence is very good.
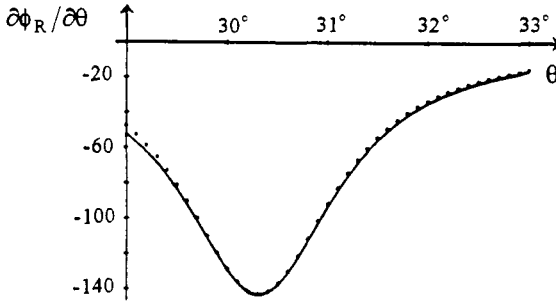
Fig.17 : Angular phase derivative of the reflection coefficient of the fluid-solid interface. Full line: exact calculation. Dot line: Breit-Wigner approximation.

So, it becomes possible to consider that the Rayleigh mode is an angular resonance of the fluid-solid interface. Moreover, it is possible to establish the link between the resonant formalism and the Rayleigh wave propagating at the interface [41]. As a matter of fact, according to the Breit-Wigner approximation, the angular pole of the reflection coefficient can be written as follows :

$$\underline{y}_p = y_R + j\frac{\gamma_R}{2} \tag{50}$$

so that the term of propagation along the x-axis takes the two following forms $\exp j\left(k_f \underline{y}_p x\right)$ or $\exp j(\underline{K}_x x)$. Consequently, we obtain :

$$\frac{\underline{K}_x}{k_f} = \frac{K_x'}{k_f} + j\frac{K_x''}{k_f} = \underline{y}_p = y_R + j\frac{\gamma_R}{2} \tag{51}$$

as for the previous case corresponding to the Lamb waves.

We have computed the numerical values of $\underline{K}_x$ by searching the zeroes of Eq. (7), and the numerical values of the angular resonances by using the P.G.M.. The results obtained by the two methods are in good agreement whatever the water-solid interface is, as shown in Table 4.

Table 4 : Rayleigh mode: comparison between the values of $\underline{K}_x/k_f$ and the angular resonances.

Solid	$\underline{K}_x/k_f$	$\underline{y}_p$
Aluminum	$0.505 + j\,1.414 \times 10^{-2}$	$0.505 + j\,1.441 \times 10^{-2}$
Glass	$0.464 + j\,1.581 \times 10^{-2}$	$0.464 + j\,1.608 \times 10^{-2}$
Brass	$0.747 + j\,1.356 \times 10^{-2}$	$0.747 + j\,1.361 \times 10^{-2}$
Copper	$0.649 + j\,8.490 \times 10^{-3}$	$0.649 + j\,8.509 \times 10^{-3}$
Nickel	$0.510 + j\,4.896 \times 10^{-3}$	$0.510 + j\,4.902 \times 10^{-3}$

We have shown that the Rayleigh wave propagating along the fluid-solid interface, as the Lamb waves propagating in the plate, has an angular resonant behavior. Thus, in a general way, it is possible to consider the scattering by plane interfaces in terms of angular resonances. Moreover, the description of guided waves propagating along plane interfaces by a set of evanescent waves seems adequate because it is possible to relate the angular resonance characteristics with the characteristics of the evanescent waves.

In the last section, we use Eq.(40) in order to establish the relation of the excitation coefficient of a given Lamb wave with its damping coefficient.

5.3. The Excitation / Reemission Coefficient of a Lamb Wave and the Damping Coefficient

The resonance condition Eq.(31) or Eq.(39) for Lamb waves is obtained in a similar way [5] than Eq.(12) for the Rayleigh wave, i.e. from the decomposition of a spherical source in the liquid in terms of plane waves of different directions, which are reflected from the plate with the reflection coefficient defined in Eq.(33). In addition to the resonance condition, this decomposition shows that the amplitude of the excited Lamb wave corresponds to the residue at the $\underline{y}_p$ pole of the reflection coefficient. This amplitude can be expressed as :

$$\underline{P}_{Lamb} = P_0\,\underline{\beta}\,\exp\left[jk_f\left(x\sin\underline{\theta}_{Lamb} + (z+z_0)\cos\underline{\theta}_{Lamb}\right)\right] \quad (52)$$

$$\sin\underline{\theta}_{Lamb} = \underline{y}_p \quad (53)$$

where P_0 is the source amplitude, $\underline{\beta}$ is defined as :

$$\underline{\beta} = 2j\pi \frac{c_a c_s - \tau^2}{\left[\dfrac{\partial}{\partial y}\left[(c_a + j\tau)(c_s - j\tau)\right]\right]_{\underline{\theta}_{Lamb}}} \quad (54)$$

and x, z, z_0 stand for the respective positions of the source S and the observation point P, as shown in Fig.18.
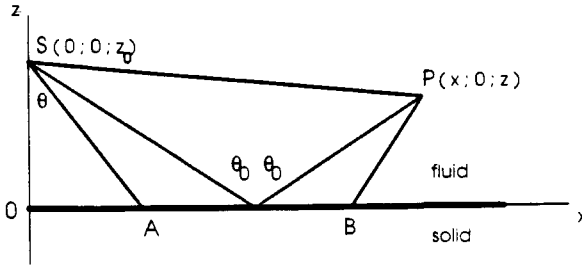
Fig.18.: The source S, the observer P, and the immersed plate

From geometrical considerations, and using Eq.(38), Eq.(39) and Eq.(53), it is easily shown that the exponential term of Eq.(52) represents propagation along the SA and BP paths in water and along AB as a Lamb wave on the plate,   so that $\underline{\beta}$ represents the product of the excitation and reemission coefficients of the Lamb wave propagating from A to B. Using the Breit-Wigner approximation (Eq.(32)) for the reflection coefficient instead of the exact expression (Eq.(33)), the product $\underline{\beta}$ is found [42] to be approximated as :

$$\underline{\beta} \cong j\frac{\gamma_p}{2} = j\frac{K''_x}{k_f} \tag{55}$$

This relation shows that the better the Lamb wave is excited, the better it radiates off.

Using the same experimental set-up as in Fig.15, one can obtain the amplitude of the excited Lamb wave. The amplitude (in dB) received by the transducer R is plotted versus the distance d. The amplitude that would be measured for a propagation d equal to zero, if there were no interference between the specularly reflected wave and the radiating Lamb wave, corresponds to the origin of the mean experimental straight line obtained. This amplitude A, converted in Volt, is then proportional to the modulus of the product $\underline{\beta}$. Fig.19 shows the results obtained for the modes S_3 and A_3 of an aluminum plate, for frequency-thickness products ranging from 5 kHz m to 17 kHz m. The dots indicate experimental values, which can be seen to be roughly linearly dependent on the normalized damping coefficient K''_x / k_f , so that Eq.(55) seems to be experimentally verified.
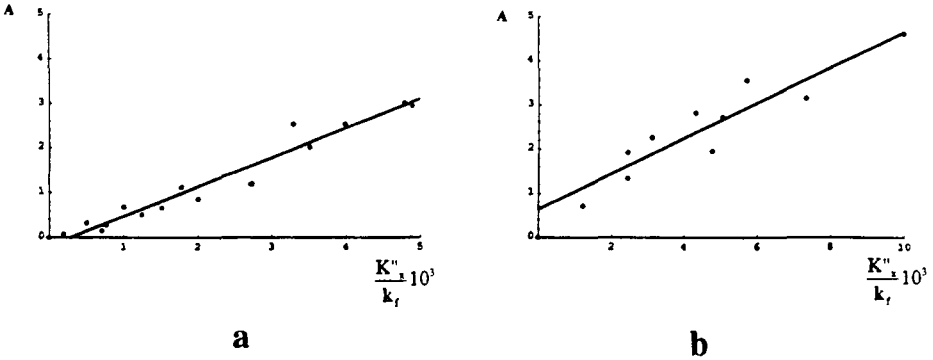
Fig.19 : The amplitude A of a given excited Lamb wave is roughly proportional to the normalized damping coefficient K''_x / k_f.

The frequency-thickness product varies from 5 kHz m to 17 kHz m.

a : mode S_3 of an aluminum plate

b : mode A_3 of an aluminum plate

6. Conclusion

Plane interface waves are localized waves, which hence may be easily described as combinations of plane evanescent waves. In such a description, the velocity of a given interface wave is given by the common projection of all propagation vectors, while its damping coefficient is given by the common projection of all evanescence vectors in the propagation direction.

The resonant character of an interface wave can be obtained from its evanescent plane waves description : the width of an angular resonance is given by the normalized damping coefficient. This last remark proves the usefulness of the evanescent plane waves description.

7. References

1 . B. Poirée, *Rev. du CETHEDEC 79*, (1984) 103.

2 . B. Poirée, *J. Acoust.* 2, (1989) 205.

3 . J.G. Scholte, *Proc. of the Section of Sciences, Proc. Kroninklijke nederlandse akademie van Wetenschappen Amsterdam* 45 (1942), **Part I**, 20, **Part II**. 159.

4 . J.H. Ansell. *Pure and Appl. Geophys.* 94 II, (1972) 172.

5 . H. Überall, *Physical Acoustics* X, (W. P. Mason, R. L. Thurston, Academic Press, New York, 1973), p 1.

6 . I. A. Viktorov, *Rayleigh and Lamb waves*, (Plenum Press, New York, 1967).

7 . L. M. Brekhovskikh, *Waves in layered media*, (Academic Press, New York, 1980).

8 . L. Sebbag, *thesis*, (Université Paris 7, France, 1987).

9 . G. Quentin, A. Derem, B. Poirée, *J. Acoust.* **3 (4)**, (1990) 321.

10 . A. Derem, private communications

11 . W. G. Neubauer, *Physical Acoustics* **X**, (W. P. Mason, R. L. Thurston, Academic Press, New York, 1973), p 61.

12 . M. Rousseau, Ph. Gatignol, *J. Acoust. Soc. Am.* **78** (1985) 1859.

13 . J. M. Claeys, O. Leroy, *J. Acoust. Soc. Am.* **72** (1982) 585.

14 . B. Poirée, L. Sebbag, *J. Acoust.* **4** (1991) 21.

15 . L. Cagniard, *thesis*, (Université des Sciences de Paris, Ed. Gauthier Villars, Librairie du Bureau des Longitudes de l'Ecole Polytechnique, France, 1939).

16 . J.G. Scholte, *Proc. Kroninklijke nederlandse akademie van Wetenschappen Amsterdam 51* (1948),**Part I,** 533, **Part III,** 828, **Part IV**, 969.

17 . J.G. Scholte, *Proc. Kon. Ned. Akad. v. Wetensch. Amsterdam* **52**, (1949) 652.

18 . F. Luppé, *thesis,* (Université Paris 7, France, 1987).

19 . B. Poirée, F. Luppé, *J. Acoust.* **4**, (1991) 575.

20 . F. Luppé, J. Doucet, *Acustica* **64** (1987) 46.

21 . F. Luppé, J. Doucet, *J. Acoust. Soc. Am.* **83** (1988) 1276.

22 . S. N. Guzhev, V. M. Levin, R. G. Maev, I. M. Kotelyanskii, *Sov. Phys. Tech. Phys.* **29** (1984) 817.

23 . S. N. Guzhev, V. M. Levin, *Sov. Phys. Acoust.* **33** (1987) 355.

24 . S. Nasr, J. Duclos, M. Leduc, *Electronics Letters* **24** (1988) 309.

25 . S. Nasr, J. Duclos, M. Leduc, *J. Acoust. Soc. Am.* **87** (1990) 507.

26 . S. Nasr, *thesis,* (Université du Havre, France, 1990).

27 . A. Tinel, J. Duclos, *Acoust. Lett.* **15** (1991) 30.

28 . A. Tinel, *thesis,* (Université du Havre, France, 1991).

29 . A. Tinel, J. Duclos, *J. Acoust. Soc. Am.* **95** (1994) 13.

30 . M.F.M. Osborne, S.D. Hart, *J. Acoust. Soc. Am.* **17** (1945) 1.

31 . D.C. Worlton, *J. Appl. Phys.* **32** (1961) 967.

32 . J. Duclos, O. Lenoir, J.M. Conoir, J.L. Izbicki, *J. Phys. IV C1* (1992) 691.

33 . J.L. Izbicki, G. Maze, J. Ripoche, *Acustica* **61** (1986) 137.

34 . A. Tinel, H. Duflo, J. Duclos, *J. Phys. IV C5* (1994) 1209.

35 . M. Ech-Cherif El Kettani, *thesis,* (Université du Havre, France, 1993).

36 . B.A. Auld, *Acoustic Fields and Waves in Solids II,* (Wiley-Interscience Publication, John Wiley & Sons, 1973).

37 . M. Ech-Cherif El Kettani, P. Pareige, F. Luppé, *Acoust.Lett.* **17** (1993) 41.

38 . R. Fiorito, H. Überall, *J. Acoust. Soc. Am.* **65** (1979) 914.

39 . O. Lenoir, J. Duclos, J.M. Conoir, J.L. Izbicki, *J. Acoust. Soc. Am* **94** (1993) 330.

40 . R. Fiorito, W. Madigosky, H. Überall, *J. Acoust. Soc. Am.* **66** (1979) 1857.

41 . J. Duclos, J.L. Izbicki, O. Lenoir, J.M. Conoir, *Acta Acustica* **2** (1994) 375.

42 . M. Ech-Cherif El Kettani, F. Luppé, J.M. Conoir, J. Ripoche, *J. Acoust. Soc. Am.* **97** (1995) 3394.

APPLICATION OF WAVELET ANALYSIS TO INVERSE SCATTERING

W. TOBOCMAN
Physics Department, Case Western Reserve University
Cleveland, OH 44106

ABSTRACT

We demonstrate the capability of wavelet analysis for compressing the information content of a signal pulse. We point out that this property of wavelet analysis can be useful for reducing the scale of a three-dimensional inverse scattering calculation to a manageable size. Some other applications of wavelet analysis to inverse scattering are described.

1. Introduction

In the conventional approach to inverse scattering the incident and scattered signal pulses are Fourier analyzed. The inverse scattering analysis employs the Fourier transforms because the analysis of the scattering problem is most simply done at fixed frequency. This approach is practical for one-dimensional problems. However, for two and three-dimensional inverse scattering problems the conventional approach leads to very large scale computations because of the many degrees of freedom, i.e. wavenumber vectors, that must be included. Examples of this are provided by Tobocman[1] and by Gutman and Klibanov[2].

In wavelet analysis one uses a set of pulselike orthogonal functions in place of the Fourier plane waves to analyze the signal pulses. By virtue of the fact that a fewer number of wavelet transform amplitudes than Fourier transform amplitudes are required to adequately encode the information carried by the signal pulses, an inverse scattering analysis in terms of wavelet transforms will result in a computation of smaller scale.

In Section II we introduce the harmonic wavelets that we will use in our calculations. Section III is devoted to comparing wavelet and Fourier analyses of a couple of sample pulses. Our results will illustrate the information compression capability of wavelet analysis vis-a-vis Fourier analysis. In Section IV we show how wavelet analysis can be substituted for Fourier analysis in an inverse scattering formalism. Finally, in Sec. V we describe some earlier applications of wavelet analysis to inverse scattering.

2. Wavelet analysis

We will employ the harmonic wavelets introduced by Newland[3]. These are particularly well suited to making comparisons with Fourier analysis. We will follow the conventions suggested by Newland, for the most part. The harmonic wavelets are defined to be

$$w_{jk}(x) = w(2^j x - k\Delta) \qquad\qquad \begin{aligned} j &= 0,1,2,... \\ k &= 0,\pm 1,\pm 2... \end{aligned} \qquad\qquad \text{(1a)}$$

where

$$w(x) = e^{i3\pi x/\Delta} \sin(\pi x/\Delta)/\pi x \qquad\qquad\qquad\qquad \text{(1b)}$$

Additionally, there is

$$w_{-1k}(x) = \phi(x - k\Delta) \qquad\qquad k = 0,\pm 1,\pm 2... \qquad\qquad \text{(2a)}$$

where

$$\phi(x) = e^{i\pi x/\Delta} \sin(\pi x/\Delta)/\pi x \qquad\qquad\qquad\qquad \text{(2b)}$$

The mother wavelets w and ϕ are seen to be sinc functions multiplied by phase factors. The wavelet orthogonality relations are

$$\langle w_{jk} | w_{j'k'} \rangle = (\Delta 2^j)^{-1}\delta_{jj'}\delta_{kk'} \qquad\qquad jj' = 0,1,2,... \qquad\qquad \text{(3a)}$$

and

$$\langle w_{jk} | w_{-1k'} \rangle = \Delta^{-1}\delta_{-1j} \, \delta_{kk'} \qquad\qquad j = -1,0,1,2,... \qquad\qquad \text{(3b)}$$

where

$$\langle \varphi | \chi \rangle = \int_{-\infty}^{\infty} dx \, \varphi(x)^*\chi(x) \qquad\qquad\qquad\qquad \text{(4)}$$

The wavelet Fourier transforms are

$$w_{jk}(\xi) = e^{-i\xi k\Delta 2^{-j}} w(\zeta 2^{-j})2^{-j} \qquad\qquad\qquad\qquad \text{(5a)}$$

where

$$w(\xi) = \begin{cases} 1/2\pi & 2\pi \le \xi\Delta < 4\pi \\ 0 & \text{elsewhere} \end{cases} \qquad\qquad\qquad\qquad \text{(5b)}$$

and

$$w_{-1k}(\xi) = e^{-i\xi k\Delta} \phi(\xi) \qquad\qquad\qquad\qquad \text{(6a)}$$

where

$$\phi(\xi) = \begin{cases} 1/2\pi & 0 \le \xi\Delta < 2\pi \\ 0 & \text{elsewhere} \end{cases} \qquad\qquad\qquad\qquad \text{(6b)}$$

with the Fourier transform defined to be

$$\hat{w}(\xi) = (2\pi)^{-1} \int_{-\infty}^{\infty} dx \; e^{-i\xi x} \; w(x) \tag{7}$$

The wavelet Fourier transforms are seen to be boxcar functions multiplied by phase factors.

Let $f(x)$ be a real pulse which decays to zero as $x \rightarrow \pm \infty$ so that

$$\int_{-\infty}^{\infty} dx \, |f(x)|^2 < \infty \tag{8}$$

By virtue of the completeness of the harmonic wavelets, as demonstrated by Newland[3], we can have a wavelet expansion of our pulse.

$$f(x) = \sum_{j=-1}^{\infty} \sum_{k=-\infty}^{\infty} \{a_{jk} \; w_{jk}(x) + c.c.\} \tag{9}$$

where

$$a_{jk} = 2^j \Delta < w_{jk} | f > \qquad j = 0,1,2,... \tag{10a}$$

and

$$a_{-1k} = \Delta < w_{-1k} | f > \tag{10b}$$

With the help of Parseval's theorem

$$<f|g> = \int_{-\infty}^{\infty} dx \; f^*(x) \; g(x)$$
$$= 2\pi \int_{-\infty}^{\infty} d\xi \; \hat{f}(\xi)^* \; \hat{g}(\xi) \; = 2\pi <\hat{f}|\hat{g}> \tag{11}$$

the wavelet amplitudes can be recast into

$$a_{jk} = 2\pi 2^j \Delta <\hat{w}_{jk} | \hat{f} > \tag{12a}$$

and

$$a_{-1k} = 2\pi \Delta <\hat{w}_{-1k} | \hat{f} > \tag{12b}$$

For computational purposes it is necessary to approximate our integrals by finite, discrete sums. We will use the following conventions.

$$\hat{f}(n\delta) = \hat{f}(\xi_n) = \hat{f}_n \quad f(m\varepsilon) = f(x_m) = \delta \; f_m \quad m,n = \text{integers} \tag{13a}$$

where

$$\delta = 2\pi/L \qquad\qquad \varepsilon = L/N \tag{13b}$$

Here L is the field of view, and N is the number of meshpoints. Then the integrals for the Fourier and inverse Fourier transforms are approximated by

$$\hat{f}_m = N^{-1} \sum_{n=0}^{N-1} e^{-i2\pi mn/N} f_n \tag{14a}$$

$$f_n = \sum_{m=0}^{N-1} e^{i2\pi nm/N} \hat{f}_m \tag{14b}$$

Discretization of Eq. (10) in accordance with this scheme gives

$$a_{j,k} = \frac{2\pi}{M(0)} \sum_{s=0}^{M(j)-1} e^{i2\pi ks/M(j)} \hat{f}_{M(j)+s} \tag{15a}$$

and

$$a_{-1,k} = \frac{2\pi}{M(0)} \sum_{s=0}^{M(0)-1} e^{i2\pi ks/M(0)} \hat{f}_s \tag{15b}$$

where

$$M(j) = 2^j L/\Delta = 2^j M(0) \qquad j \geq 0 \tag{15c}$$

$$M(-1) = L/\Delta = M(0) \qquad j = -1 \tag{15d}$$

We see that $a_{j,k}$ is a linear combination of M(j) Fourier amplitudes for $j \geq 0$, and $a_{-1,k}$ is a linear combination of M(0) Fourier amplitudes. Thus we will restrict the range of k accordingly. Eq. (9) is replaced by

$$f(x) \approx \sum_{j=-1}^{J} \sum_{k=-M(j)/2}^{M(j)/2-1} \{a_{j,k} \, w_{j,k}(x) + c.c.\} \tag{16}$$

The total number of terms in this sum is $M(0) \, 2^{J+2}$. We adjust J so that the total number of terms in the sum is equal to the number of meshpoints N.

$$N = M(0) \, 2^{J+2} \tag{17}$$

In order to be able to use fast Fourier transform computational routines, we need N and M(0) to be powers of two, so we choose

$$M(0) = 2^K \qquad N = 2^{K+J+2} \quad . \tag{18}$$

An attractive feature of the harmonic wavelet expansion is that the wavelet transforms $a_{j,k}$ can be calculated by doing inverse Fourier transforms on the Fourier transforms of f(x). Thus fast Fourier transform routines can be used to expedite the calculation. In addition, the ordering of the wavelet transforms can be arranged so that the first N(j) = 2^{K+j+2} wavelet transforms are calculated exclusively from the first N(j) Fourier transforms. This facilitates comparisons between Fourier and wavelet analysis.

Our formulation of the harmonic wavelet analysis scheme differs from Newland's[3] in that we have introduced an adjustable $\Delta = L/M(0)$. Our formulation reduces to that

of Newland upon choosing $M(0) = 2^K = 1$.

3. Comparison of Fourier and wavelet signal pulse reconstruction

Here we will compare the efficiencies of the discretized Fourier and wavelet signal pulse analyses on a couple of example pulses. The efficiency we are concerned with is the efficiency of information compression. We want to know which scheme is better able to concentrate an adequate description of the pulse into a small number of transformation amplitudes.

Both the Fourier analysis and the wavelet analysis are characterized by the field of view L and the number of meshpoints N. The wavelet analysis has one additional parameter, the wavelet spacing $\Delta = L/M(0)$, which can be adjusted to optimize the results.

The first example is a square pulse of width 0.4 and height 1.0 to which has been added noise in the form of random numbers having a Gaussian distribution with an rms deviation equal to 0.01. The pulse is centered in a field of view of length $L = 4.0$ and the number of meshpoints is $N = 512$ for both the Fourier and wavelet analyses. For the wavelet analysis we found that the choice $K = 1$ gave the best results. This then gives $J = 6$ for the maximum value of j and $\Delta = 2.0$ for the wavelet spacing.

We want to determine which type of analysis can most efficiently capture the square pulse that is partially obscured by the noise. Our procedure is to first calculate the Fourier and wavelet transforms. These transforms are then processed by stripping or filtering or both. In the stripping process we set equal to zero all transform amplitudes which are smaller in absolute magnitude than a given stripping factor SF times the absolute magnitude of the largest transform amplitude. In the filtering process we set equal to zero all Fourier transform amplitudes for wavenumbers greater than a given cutoff wavenumber $\xi(MAX)$. Filtering applied to wavelet analysis sets equal to zero all wavelet transform amplitudes having j greater than a given j(MAX). For the Fourier transform analysis the cutoff in frequency is smoothed by means of a Hamming filter.

After processing the transform amplitudes an inverse transform is done to reconstruct an image of the square pulse. The success of the reconstruction is measured by the image error with respect to f_o,

$$ERR = [\sum_{i=1}^{N} \{f(x_i) - f_0(x_i)\}^2 / \sum_{j=1}^{N} f_0(x_j)^2]^{1/2} \qquad (19)$$

where f is the reconstructed image and f_o is chosen as appropriate.

First of all, let us compare the Fourier and wavelet transforms of the noisy square pulse. The absolute magnitudes of these transforms are plotted against wavenumber in Fig. 1. To include the wavelet amplitude magnitudes on the plot we correlate the index values j and k with the wavenumbers $n\delta = \xi_n$ according to the scheme displayed in Table I. In this scheme wavelet transforms having negative k- values are mapped into transforms having k-values greater than $M(j)/2 - 1$ by means of the relationship

$$a_{j,-k} = a_{j,M(j)-k} \qquad (20)$$

that follows from Eq. (15).

The plots in Fig. 1 reveal the striking difference between the Fourier and wavelet analyses of the noisy square pulse. The Fourier transform has a lot of strength concentrated at small wavenumber values and the rest of the strength is distributed over a relatively wide range of wavenumbers. In contrast, the wavelet transform has its strength concentrated at a relatively few discrete j,k index values.

If pulse reconstruction is done without stripping or filtering, then Fourier reconstruction captures the noisy square pulse almost perfectly with an image error with respect to the noisy square pulse of 2.3×10^{-7}; the wavelet reconstruction only captures it with an image error of 0.053.

In Fig. 2 we display a filtered Fourier analysis pulse reconstruction of the noisy square pulse. We have chosen $\xi(MAX) = 201 = N\delta/2$ so that only 256 of the 512 Fourier amplitudes are retained. The image error is 0.089 where f_o in Eq. (19) is the noise-free square pulse. Some damping of the noise is seen but a Gibbs phenomenon oscillation obscures the sharp edge of the pulse.

A filtered wavelet analysis pulse reconstruction of the noisy square pulse is presented in Fig. 3. We choose $j(MAX) = 5$ which retained 256 of the 512 wavelet amplitudes. The image error with respect to the noise-free square pulse is 0.097. The damping of the noise is not as effective as was found in the filtered Fourier reconstruction. The Gibbs phenomenon obscuring of the sharp edge is similar.

An example of a stripped Fourier analysis pulse reconstruction of the noisy square pulse appears in Fig. 4. A stripping factor of 0.04 was used resulting in the retention of 106 of the 512 Fourier amplitudes. The result is similar to that found for our filtered Fourier analysis example. The image error with respect to the noise-free square pulse is 0.12.

Finally, in Fig. 5 is displayed the result of a stripped wavelet pulse reconstruction of the noisy square pulse. With a stripping factor of 0.06 we have retained 106 of the 512 wavelet amplitudes. We see very little smoothing but the sharp edge of the pulse is very successfully captured. The image error with respect to the noise-free square pulse is 0.072.

Thus the stripped wavelet analysis reconstruction is the most successful of the four filtered/stripped reconstructions examined. We see that the wavelet analysis is able to compress an adequate description of the pulse into just 106 out of the 512 pulses. It gives a much better picture of the small scale structure of the pulse than a filtered Fourier analysis that uses 256 out of 512 amplitudes.

One might be concerned that the ability of the stripped wavelet analysis to capture small scale structure will be of little practical significance because of the band-limited nature of experimental data. To investigate this possibility we take as our second example an ultrasound pulse reflected from a slice of human prostate tissue. In our analyses we used $N = 1024$ meshpoints and a field of view of $L = 15.36$. In our wavelet analysis we used a wavelet spacing of $\Delta = 0.24$ corresponding to $K = 6$.

The Fourier and wavelet transform amplitude absolute magnitudes for the reflected ultrasound pulse are compared in Fig. 6. The band limited nature of the pulse is apparent. Although Fourier amplitudes at wavenumbers up to $N\delta = 209.4$ are calculated, those at wavenumbers greater than 40 are negligible. In addition, there is very little strength at wavenumbers less than 4.

As was seen in the previous example, the wavelet amplitude strength is concentrated
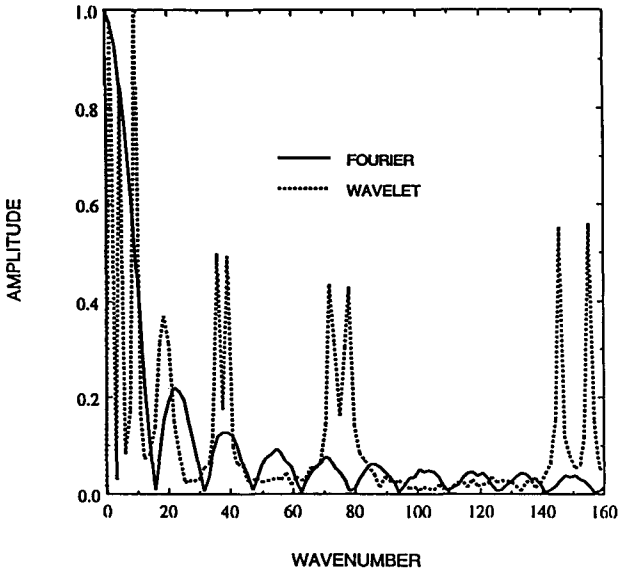
Figure 1.   Fourier transform amplitude versus wavenumber and wavelet transform amplitude versus wavenumber for the noisy square pulse shown in Fig. 2.   See Table I for the correlation between wavelet index and wavenumber.
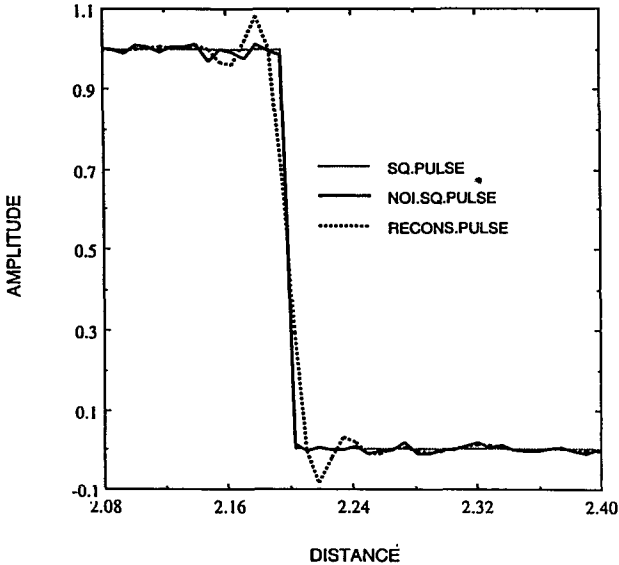
Figure 2.   Filtered Fourier transform reconstruction of the noisy square pulse. $\xi(MAX) = 201$.   256 out of 512 amplitudes retained.   Image error with respect to the noise-free square pulse is 0.089.
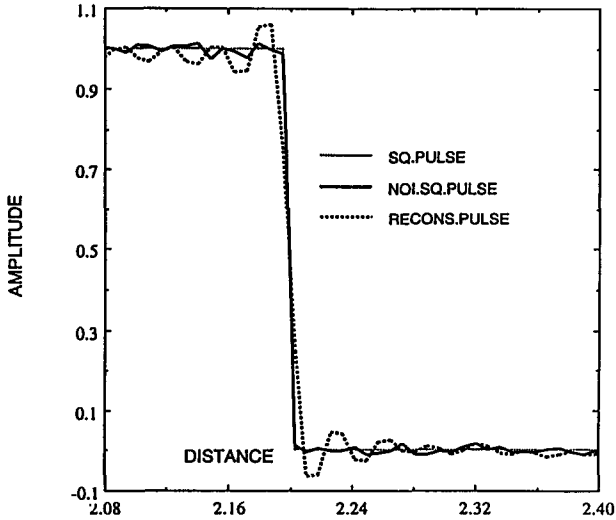
Figure 3.   Filtered wavelet transform reconstruction of the noisy square pulse. j(MAX) = 5.   256 out of 512 amplitudes retained.   Image error with respect to the noise-free square pulse is 0.097.
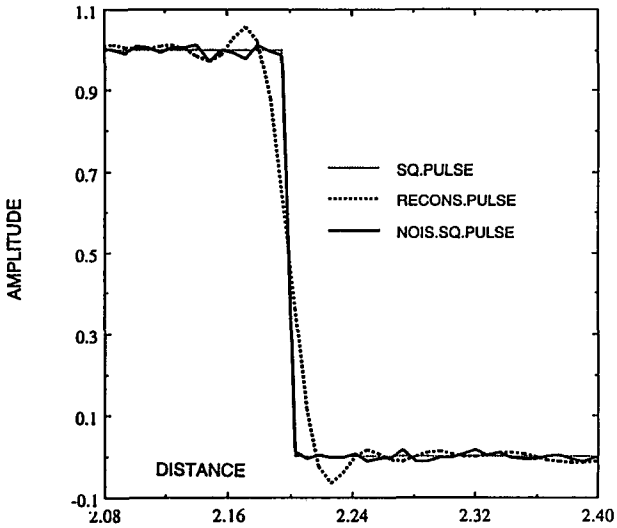
Figure 4.   Stripped Fourier transform reconstruction of the noisy square pulse. Stripping factor = 0.04.   106 out of 512 amplitudes retained.   Image error with respect to the noise-free square pulse is 0.123.

in fewer amplitudes than the Fourier amplitude strength. In Fig. 7 we show a filtered Fourier analysis reconstruction of the ultrasound pulse, and in Fig. 8 we show a stripped wavelet analysis reconstruction. The filtering cutoff wavenumber ξ(MAX) = 20.0 was used which caused 100 Fourier amplitudes to be retained. The wavelet stripping factor SF = 0.05 was used which resulted in 98 wavelet amplitudes being retained. The image error with respect to the observed pulse was 0.42 for the filtered Fourier analysis and 0.13 for the stripped wavelet analysis.

Examination of the pulse reconstructions displayed in Figs. 7 and 8 over the full 15.36 field of view reveals that the filtered Fourier analysis does a good job of capturing the small amplitude structure of the pulse but adds some distortion to the large amplitude structure. Just the reverse is true for the stripped wavelet analysis of the ultrasound pulse; the large amplitude structure is captured very well while much of the small amplitude structure is lost. Since the small amplitude structure is more vulnerable to corruption by noise, the performance of the stripped wavelet analysis reconstruction is to be preferred. In conclusion, this example provides an instance of successful information compression in that a very good representation of the ultrasound pulse has been provided by selecting 98 out of 1024 wavelet amplitudes.

4. Wave Analysis Compression Applied to an Inverse Scattering Formalism

We next present an example of how wavelet analysis compression might be applied to an inverse scattering problem. We consider the scattering of a scalar wave field in three dimensions by a localized target

$$(\Delta^2 + \xi^2)\psi = v\psi \tag{21a}$$

$$\psi(x) = e^{i\xi(\upsilon,x)} + \phi(x) \tag{21b}$$

$$\phi(x) = 0(1/|x|); \quad (\partial/\partial|x| - i\xi)|x|\phi = 0 \qquad |x| \rightarrow \infty \tag{21c}$$

where ξ is a positive constant and υ is a unit vector. Let v be a real function which is nonvanishing in a finite domain enclosing the origin $|x| = 0$. In the asymptotic region

$$\phi(\xi,\upsilon,x) = -f(\xi,\upsilon,\mu) \, e^{i\xi|x|}/4\pi|x| \qquad x = |x|\mu, \quad |x| \rightarrow \infty \tag{22a}$$

where

$$f(\xi,\upsilon,\mu) = <e^{i\xi(\mu,x)}|v(x)|\psi(\xi,\upsilon,x)> \tag{22b}$$

is the scattering amplitude.[4]

According to the two-potential formula[4] an alternative relationship connecting the scattering amplitude and the wave field is

$$f(\xi,\upsilon,\mu) - \widetilde{f}(\xi,\upsilon,\mu) = <\widetilde{\psi}^{(-)}(\xi,\mu,x)|v(x) - \widetilde{v}(x)|\psi(\xi,\upsilon,x)> \tag{23}$$

where
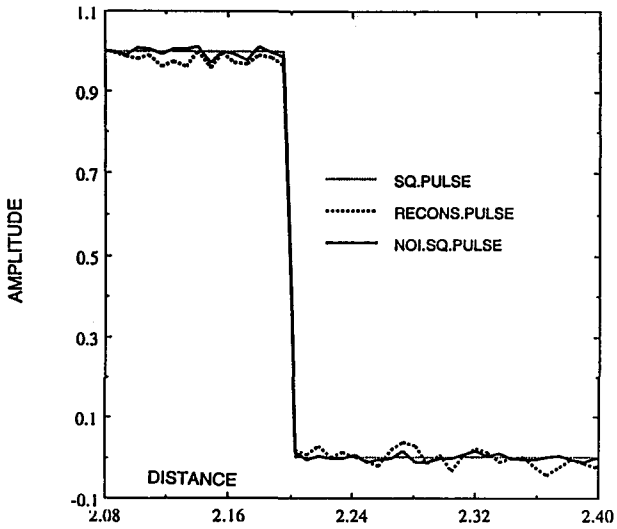
Figure 5.   Stripped wavelet transform reconstruction of the noisy square pulse.
Stripping factor = 0.06.   106 out of 512 amplitudes retained.   Image
error with respect to the noise-free square pulse is 0.072.
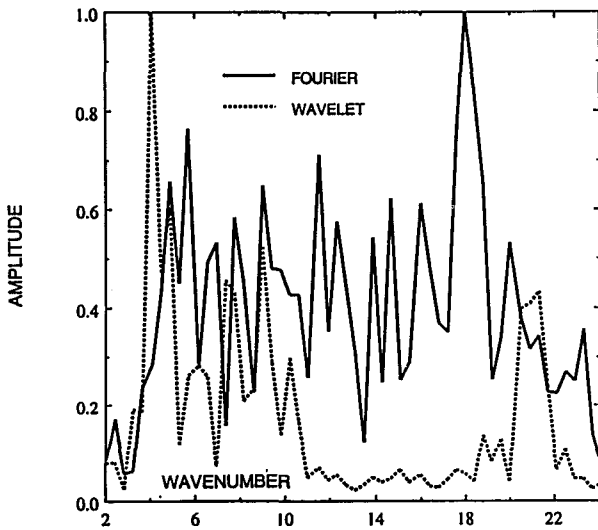
Figure 6.   Fourier transform amplitude versus wavenumber and wavelet transform
amplitude versus wavenumber for the reflected ultrasound pulse shown
in Fig. 7.   See Table I for the correlation between wavelet index and
wavenumber.
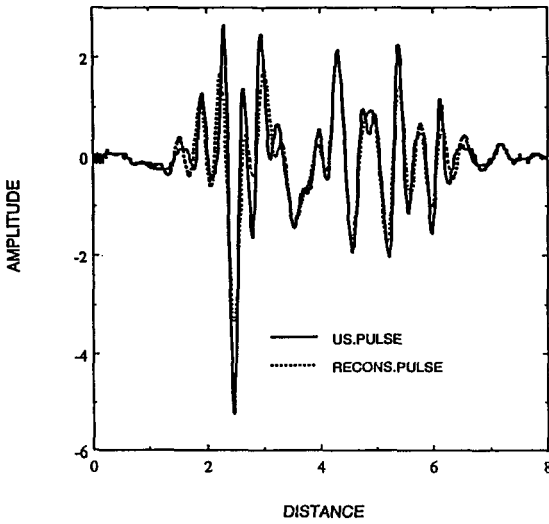
Figure 7.   Filtered Fourier transform reconstruction of the reflected ultrasound pulse. $\xi(MAX) = 20$.   100 out of 1024 amplitudes retained.   Image error with respect to the observed ultrasound pulse is 0.423.
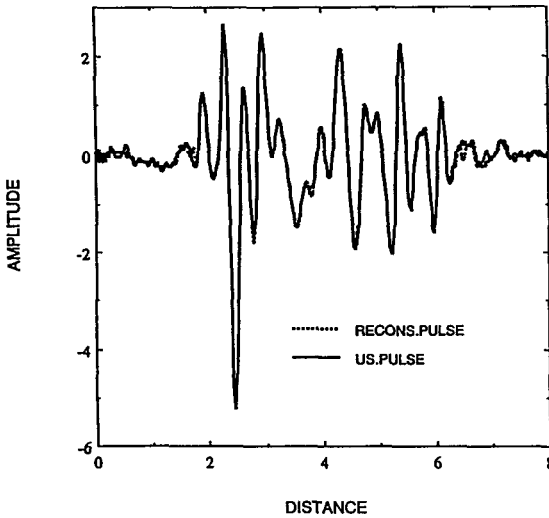
Figure 8.   Stripped wavelet transform reconstruction of the reflected ultrasound pulse.   Stripping factor = 0.05.   98 out of 1024 amplitudes retained. Image error with respect to the observed ultrasound pulse is 0.125.

$$(\nabla^2 + \xi^2)\widetilde{\psi}^{(\cdot)} = v\widetilde{\psi}^{(\cdot)} \tag{24a}$$

$$\widetilde{\psi}^{(\cdot)}(\xi,\mu,x) = e^{i\xi(\mu,x)} + \widetilde{\phi}^{(\cdot)}(\xi,\mu,x) \tag{24b}$$

$$\widetilde{\phi}^{(\cdot)}(\xi,\mu,x) = 0(1/x|); \quad (\partial/\partial|x| + i\xi)|x| \, \widetilde{\phi}^{(\cdot)} = 0 \qquad |x| \to \infty \tag{24c}$$

Approximating ψ by $\widetilde{\psi}$ in Eq. (23) gives the distorted wave Born approximation (DWBA)[5]

$$\Delta f(\xi,\upsilon,\mu) = \langle\widetilde{\psi}^{(\cdot)}(\xi,\mu,x)|\Delta v(x)|\widetilde{\psi}(\xi,\upsilon,x)\rangle \tag{25}$$

where $\Delta f = f - \widetilde{f}$ and $\Delta v = v - \widetilde{v}$.

The inverse scattering problem seeks to determine the scattering potential v from knowledge of the scattering amplitude f. Equation (25) provides a linear Fredholm equation of the first kind for v. Equation (25) provides a good approximation to Eq. (23) provided Δv is small. So we can use an iterative procedure. We first make a guess for v. Then we solve the direct scattering problems for $\widetilde{\psi}^{(\cdot)}$ and $\widetilde{\psi}$

$$\widetilde{\psi}(\xi,\upsilon,x) = e^{i\xi(\upsilon,x)} + \int d^3x'\Gamma(\xi,x,x') \, \widetilde{v}(x')\widetilde{\psi}(\xi,\upsilon,x) \tag{26}$$

$$\widetilde{\psi}^{(\cdot)}(\xi,\mu,x) = e^{i\xi(\mu,x)} + \int d^3x'\Gamma(\xi,x,x')^* \, \widetilde{v}(x') \, \widetilde{\psi}^{(\cdot)}(\xi,\mu,x) \tag{27}$$

where

$$\Gamma(\xi,x,x') = -\frac{e^{i\xi|x-x'|}}{4\pi |x-x'|} \tag{28}$$

and the asterisk denotes complex conjugation. Then $\widetilde{\psi}^{(\cdot)*}\widetilde{\psi}$ provides the kernel for Eq. 25 which may then be solved for v. The potential v is then substituted for $\widetilde{v}$ and the process is repeated. Iteration continues until convergence, i.e. $\Delta v = 0$, is attained.

Let us rewrite Eq. 25 to read

$$\Delta f(\xi,\upsilon,\mu) = \int d^3x \, K(k,\upsilon,\mu;x) \, \Delta v(x) \tag{29a}$$

where

$$K(\xi,\upsilon,\mu;x) = \widetilde{\psi}^{(\cdot)}(\xi,\mu,x)^* \, \widetilde{\psi}(\xi,\upsilon,x) \tag{29b}$$

The input data that drives this integral equation for the scattering potential $v(x)$ are the scattering amplitudes $f(\xi,\upsilon,\mu)$. Amplitude $f(\xi,\upsilon,\mu)$ is found by measuring the phase and magnitude of the wave field scattered in the direction μ when the target is illuminated by a plane wave of wave number ξ travelling in the direction υ. A large number of such measurements will be required if $v(x)$ is not simple. To simplify the matter with respect to the multiplicity of wavenumber values, one can illuminate the target with

broad band pulses and thus probe the target with a continuum of wavenumbers simultaneously.

Let us then suppose the target to be illuminated with a real pulse

$$F(\upsilon,x) = \int_{o}^{\infty} d\xi \ [e^{i\xi(\upsilon,x)}\hat{F}(\upsilon,\xi) + \text{c.c.}] \tag{30}$$

Then the wave field will be

$$\Psi(\upsilon,x) = \int_{o}^{\infty} d\xi \ [\psi(\xi,\upsilon,x) \ \hat{F}(\upsilon,\xi) + \text{c.c.}] \tag{31}$$

In the direction μ the scattered field will be

$$G(\upsilon,\mu,x) \approx -(1/4\pi|x|) \int_{o}^{\infty} d\xi \ [e^{i\xi(\mu,x)} \ f(\xi,\upsilon,\mu) \ \hat{F}(\upsilon,\xi) + \text{c.c.}] \tag{32}$$

Now the recorded data will be the incident pulses $F(\upsilon,x)$ and the reflected pulses $G(\upsilon,\mu,x)$. The Fourier transforms of these pulses are

$$\hat{F}(\upsilon,\xi) = (1/2\pi) \int_{-\infty}^{\infty} d(\mu,x) \ e^{-i\xi(\mu,x)} \ F(\upsilon,x) \tag{33}$$

and

$$\hat{G}(\upsilon,\mu,\xi) = \frac{1}{2\pi} \int_{-\infty}^{\infty} d(\mu,x) \ e^{-i\xi(\mu,x)} \ 4\pi|x| \ G(\upsilon,\mu,x)$$
$$= - f(\xi,\upsilon,\mu) \ \hat{F}(\upsilon,\xi) \tag{34}$$

It follows that the scattering amplitudes are just the ratios of the Fourier transforms of the incident and reflected pulses.

$$f(\xi,\upsilon,\mu) = - \hat{G}(\upsilon,\mu,\xi)/\hat{F}(\upsilon,\xi) \tag{35}$$

Substituting this into Eq. 29 gives

$$\Delta G(\upsilon,\mu,\xi) = \int d^3x \ M(\upsilon,\mu,\xi;x) \ \Delta v(x) \tag{36a}$$

where

$$M(\upsilon,\mu,\xi;x) = -\hat{F}(\upsilon,\xi) \ \tilde{\psi}^{(-)}(\xi,\mu,x)^* \ \tilde{\psi}(\xi,\upsilon,x) \tag{36b}$$

and

$$\Delta G(\upsilon,\mu,\xi) = \hat{G}(\upsilon,\mu,\xi) - \hat{\tilde{G}}(\upsilon,\mu,\xi) \tag{36c}$$

So now we have a set of integral equations for $v(x)$ where the driving terms are the Fourier transforms of the reflected pulses. Discretization approximates Eq. (36a) by a matrix equation

$$\Delta G_\alpha = \sum_{a=1}^{n} M_{\alpha a} \Delta v_a \tag{37}$$

Even through the dimension N of the index α is large, most of the contributions turn out to be redundant. So the set of equations displayed in Eq. (37) must be regarded as undetermined. Thus the optimal approximation to Δv of minimum norm[6] is

$$\Delta v_a = \sum_{\alpha=1}^{N} \sum_{\beta=1}^{N} M^\dagger_{a\alpha} ([MM^\dagger]^{-1})_{\alpha\beta} \Delta G_\beta \tag{38}$$

where the dagger denotes Hermitian conjugation. The ill-posed nature of this problem is reflected in the ill-conditioned nature of the Gram matrix $MM^\dagger$. This requires the diagonalization of $MM^\dagger$ as the first step.

For two- and three-dimensional inverse scattering problems the required dimension N of the index $\alpha(= \upsilon,\mu,\xi)$ is very large. This requires a large expenditure of computation time for calculating the matrices M and $MM^\dagger$ and for diagonalizing $MM^\dagger$. We suggest that this problem would benefit from wavelet compression. To implement this suggestion we use harmonic wavelets described in Sec. II. So let us take the wavelet transform of both sides of Eq. (36).

$$\Delta g(\upsilon,\mu,j,k) = \int d^3x \, m(\upsilon,\mu,j,k;x) \, \Delta v(x) \tag{39a}$$

where

$$\Delta g(\upsilon,\mu,j,k) = \int_{-\infty}^{\infty} d\xi \, \hat{w}_{jk}(\xi)^* \Delta G(\upsilon,\mu,\xi) \tag{39b}$$

and

$$m(\upsilon,\mu,j,k;x) = \int_{-\infty}^{\infty} d\xi \cdot \hat{w}_{jk}(\xi)^* M(\upsilon,\mu,\xi;x) \tag{39c}$$

Then Eqs. (36) and (37) can be replaced by

$$\Delta g_\alpha = \sum_{a=1}^{n} m_{\alpha a} \Delta v_a \tag{40}$$

and

$$\Delta v_a = \sum_{\alpha=1}^{N'} \sum_{\beta=1}^{N'} m^\dagger_{a\alpha} ([mm^\dagger]^{-1})_{\alpha\beta} \Delta g_\beta \tag{41}$$

What we should now find is that the strength of Δg_α, $\alpha = \upsilon,\mu,j,k$ as a function of the wavelet indices j and k is more concentrated than the strength of ΔG_α, $\alpha = \upsilon,\mu,\xi$ as a function of ξ. Then a stripping procedure can be implemented in which the smallest amplitudes Δg_α are deleted, thereby reducing the dimension N of the indices α and β. Then the calculation of Eq. (41) is expedited.

5. Earlier applications of wavelet analysis to inverse scattering

We will describe applications of wavelet analysis to inverse scattering by Patterson et al.[7] and by Donoho[8]. The analysis of Patterson et al. is appropriate to the one-dimensional scattering by a layered medium. For such a system Eq. 21 is replaced by

$$(d^2/dx^2 + \xi^2)\psi = v\psi \qquad\qquad v(x) = 0 \text{ for } x<0 \qquad\qquad (42a)$$

$$\psi(\xi,x) = e^{i\xi x} - f(\xi)e^{-i\xi x} \qquad\qquad x<0 \qquad\qquad (42b)$$

and Eq. (22) by

$$f(\xi) = <e^{-i\xi x} \mid v(x) \mid \psi(\xi,x)> \qquad\qquad (43)$$

Supposing the target to be illuminated with a real pulse

$$F(x) = \int_0^\infty d\xi \ [e^{i\xi x} \ \hat{F}(\xi) + \text{c.c.}] \qquad\qquad (44)$$

the reflected pulse is

$$G(x) = - \int_0^\infty d\xi \ [e^{-i\xi x} f(\xi) \ \hat{F}(\xi) + \text{c.c.}]. \qquad\qquad (45)$$

Thus the reflection amplitude is determined from the Fourier transforms of the incident and reflected pulses by

$$f(\xi) = -\hat{G}(\xi)/\hat{F}(\xi) \qquad\qquad (46)$$

To compensate for the bandlimited nature of the incident pulse and the corruption of the incident pulse by noise, Eq. (46) is replaced by a Wiener filter

$$f(\xi) \approx - \ \frac{\hat{F}(\xi)^* \ \hat{G}(\xi)}{\mid \hat{F}(\xi)\mid^2 + Q^2} \qquad\qquad (47)$$

where Q^2 is the stabilizing parameter.

Rather than seeking to recover the scattering potential v by an inverse scattering analysis, Patterson et al.[7] sought to recover the impulse response $G_o(x)$ via a deconvolution analysis. The impulse response is what the reflected pulse would have been if the incident pulse had been a δ-function, $F_o(x) = \delta(x)$, so that

$$\hat{F}_o(\xi) = 1/2\pi . \qquad\qquad (48)$$

It follows from Eq. (45) that the impulse response is

$$G_o(x) = -(1/2\pi)\int_0^\infty d\xi \ [e^{-i\xi x}f(\xi) + \text{c.c.}] \qquad\qquad (49)$$

where the scattering amplitude is determined from the data by Eq. (47).

Patterson et al.[7] applied wavelet analysis to this formalism by doing a stripped and

filtered wavelet analysis of the reflected pulse

$$\hat{G}(\xi) = \sum_j \sum_k \hat{w}_{jk}(\xi) \, \Delta(2^j + 1/2 \, \delta_{\text{-1j}}) \langle \hat{w}_{jk} \mid \hat{G} \rangle \tag{50}$$

where we use the conventions introduced in Sec. II for harmonic wavelets, although Patterson et al. used the D4 wavelets of Daubechies.[9] The stripping is achieved by setting equal to zero all coefficients $\langle \hat{w}_{jk} \mid \hat{G} \rangle$ smaller than some criterion. The filtering is achieved by imposing an upper limit j(MAX) on the sum on index j. The stripping and filtering serve to mitigate against corruption of the reflected signal pulse by noise. Thus the sums in Eq. (50) are appropriately truncated and the result substituted in Eq. (47).

In more recent work Patterson and DeFacio[10] have found improved results using other types of Daubechies[9] wavelets in conjunction with a more sophisticated nonlinear wavelet amplitude stripping procedure.

The application of wavelet analysis suggested by Donoho[8] is appropriate to the three-dimensional inverse scattering problem discussed in Sec. IV. Donoho's approach starts by considering the singular value decomposition (SVD) of $MM^\dagger$ in Eq. (38). SVD of $MM^\dagger$ starts by diagonalizing that Hermitian matrix. This provides the eigenfrequencies (singular functions) $\{\hat{u}_s\}$ and eigenvalues (singular values) λ_s^2 of $MM^\dagger$

$$MM^\dagger u_s = \lambda_s^2 u_s \tag{51}$$

Given these quantities, the inverse of $MM^\dagger$ is just

$$(MM^\dagger)^{-1} = \sum \mid \hat{u}_s \rangle \, \lambda_s^{-2} \, \langle \hat{u}_s \mid \tag{52}$$

assuming the $\{\hat{u}_s\}$ to be normalized. The ill-conditioning of $MM^\dagger$ is manifested by the presence of small eigenvalues λ_s^2. This problem can be mitigated by dropping those terms from the sum or by replacing Eq. (52) by a regularized expression

$$(MM^\dagger)^{-1} = \sum_s \mid \hat{u}_s \rangle \, \frac{\lambda_s^2}{\lambda_s^4 + \alpha^4} \, \langle \hat{u}_s \mid \tag{53}$$

where α^4 is the Tikhonov regularization parameter.

Substitution of Eq. (53) into Eq. (38) gives

$$\Delta v = \sum_s M^\dagger \hat{u}_s \, \frac{\lambda_s^2}{\lambda_s^4 + \alpha^4} \, \langle \hat{u}_s \mid \Delta G \rangle \tag{54}$$

Let us define v_s by

$$M^\dagger \hat{u}_s = \lambda_s \, v_s \tag{55a}$$

so that

$$M \ v_s = \lambda_s \hat{u}_s \tag{55b}$$

and the v_s's are eigenfunctions of $M^\dagger M$ with eigenvalues λ_s^2. Thus the v_s's are an orthogonal set just like the $\hat{u}_s$'s. Now Eq. (54) can be written

$$\Delta v = \sum_s v_s \ \frac{\lambda_s^3}{\lambda_s^4 + \alpha^4} \ <\hat{u}_s| \ \Delta G> \tag{56}$$

In this context the application of wavelet analysis compression suggested in Sec. IV consists in the replacement of the operator M by the reduced operator m = PM, where P is the projection operator

$$P = \sum \sum \ | \ \hat{w}_{jk}>2\pi\Delta(2^j + 1/2 \ \delta_{-1j}) \ <\hat{w}_{jk} \ | \tag{57}$$

with the sum restricted to those wavelets $\hat{w}_{jk}$ having the greatest overlap with the reflected pulse Fourier transform $\hat{G}$.

Donoho observed[8] that the success of the inverse scattering analysis provided by Eq. (56) depends on the effectiveness of the orthogonal functions $\{\hat{u}_s\}$ in representing $\hat{G}$ and the effectiveness of the orthogonal functions $\{v_s\}$ in representing the potential v with a relatively small number of terms. He reasoned that if these functions could be replaced by wavelets or wavelet-like functions, the inverse scattering analysis would be more likely to be successful.

Donoho showed that for certain inverse scattering problems the SVD can be replaced by a wavelet-vaguelette decomposition (WVD) which involves three sets of functions: one set $\{\psi_s\}$ is an orthogonal wavelet basis and two sets, $\{\hat{u}_s\}$ and $\{\hat{v}_s\}$, which are wavelet-like and biorthogonal. These satisfy the quasi-singular value relations

$$M \ \psi_s = \lambda_j \ \hat{v}_s \tag{58a}$$

$$M^\dagger \ \hat{u}_s = \lambda_j \ \psi_s \tag{58b}$$

Here s represents wavelet index pair j,k. The quasi-singular values λ_j depend only on the resolution index j and not on the spatial index k. The vaguelet bases satisfy the biorthogonality relationship

$$<\hat{u}_s \ | \ \hat{v}_t> = \delta_{st} \tag{58c}$$

The decomposition, when it exists, gives in place of Eq. (54)

$$\Delta v \approx \sum_s \psi_s \ \frac{\lambda_j^3}{\lambda_j^4 + \alpha^4} \ <\hat{u}_s|\Delta G> \tag{59}$$

Taking $\hat{v}_s = \hat{u}_s$ requires ψ_s to be the eigenfunction of $M^\dagger M$ for eigenvalue λ_j^2 and we recover the SVD. In the WVD the $\{\hat{v}_s\}$ and the $\{\hat{u}_s\}$ follow from the $\{\psi_s\}$ by

$$\hat{v}_s = \lambda_j^{-1} M \psi_s \tag{60a}$$

and

$$\hat{u}_s = (MM^\dagger)^{-1} \lambda_j M \psi_s \tag{60b}$$

For the WVD to succeed it is necessary for the $\{\hat{u}_s\}$ and $\{\hat{v}_s\}$ to satisfy Eq. (58c) and for the $\{\hat{u}_s\}$ and the $\{\hat{v}_s\}$ to inherit in some measure the pulse-like nature of the $\{\psi_s\}$. Donoho shows[8] that for three dilation-homogeneous operators M - integration, fractional integration, and Radon transformation - all sufficiently well-behaved wavelet bases lead to a WVD of M.

6. Acknowledgements

7. References

1.   W. Tobocman, *Inverse Problems* **D5** (1989) 1131-1144.
2.   S. Gutman and M. Klibanov, *Inverse Problems* **10** (1994) 573-599.
3.   David E. Newland, *Proc. Roy. Soc. Lond.* **A443** (1993) 203-225.
4.   John R. Taylor, *Scattering Theory* (John Wiley and Sons, 1972).
5.   William Tobocman, *Theory of Direct Nuclear Reactions* (Oxford University Press, 1961).
6.   William Menke, *Geophysical Data Analysis: Discrete Inverse Theory* (Academic Press, 1983).
7.   D. M. Patterson, B. DeFacio, S. P. Neal and C. R. Thompson, *Rev. Progr. in Quant. NDE* **12** (1993) 719-726.
8.   D. L. Donoho, *Nonlinear Solution of Linear Inverse Problems by Wavelet-Vaguelette Decomposition* (Dept. of Statistics, Stanford University, 1992, Technical Report No. 403).
9.   I. Daubechies, *Ten Lectures on Wavelets*, vol. 61 of CBMS-NSF Regional Conference Series in Applied Mathematics (SIAM Press, 1992).
10. D. M. Patterson and B. DeFacio, *Wavelet inversions of elastic wave data for nondestructive evaluation.* SPIE Inverse Optics III Proc. **2241** (1994) 172-184.

Table I. Correlation between wavenumber $k_n = n\delta$ and wavelet index pair j,k.

n	j	k
0	-1	0
1	-1	1
2	-1	2
...	...	...
M(0)-1	-1	M(0)-1
M(0)	0	0
M(0)+1	0	1
M(0)+2	0	2
...	...	...
2M(0)-1	0	M(0)-1
M(1)	1	0
M(1)+1	1	1
M(1)+2	1	2
...	...	...
2M(1)-1	1	M(1)-1
M(2)	2	0
M(2)+1	2	1
M92)+2	2	2
...	...	...
2M(2)-1	2	M(2)-1
M(3)	3	0
M(3)+1	3	1
M(3)+2	3	2
...	...	...

APPLICATION OF TIME-FREQUENCY ANALYSIS
TO THE CHARACTERIZATION OF ACOUSTICAL SCATTERING

MANELL E. ZAKHARIA and FRANÇOIS MAGAND
CPE Lyon, LISA (EPJ0092, CNRS)/LASSSO
Laboratoire d'Acoustique Systèmes, Signaux et Sonar
25 rue du Plat, 69288 Lyon Cedex 02, FRANCE

and

JEAN-PIERRE SESSAREGO and JEAN SAGELOLI
CNRS, LMA (UPR7051, CNRS), Equipe ASM2,
31 Chemin J. Aiguier, 13402 Marseille Cedex 20, FRANCE

ABSTRACT

The physical phenomena involved in the echo formation mechanisms and in the acoustical scattering implicitly assume the existence of joint time and frequency phenomena, especially when dealing with dispersive waves. This implicit time-frequency approach can be explicited by using a joint time-frequency analysis of wide band echoes (target impulse response). For several reasons, studied in details in this paper, the so-called Smoothed Pseudo Wigner-Ville Distribution (SPWVD) will be used. One of its advantages is that the characteristics of the propagation phenomena can be displayed and measured in the time-frequency plane. This is mainly relevant in the case of velocity dispersion for which a Wigner-Ville based analysis can be used for a quantitative estimation of group velocity, even in the case of important dispersion, multiple modes or multi-component signals. The relevance of the proposed approach is first supported by simulation results. Analysis is then applied to the study of Lamb waves in thin plates before being used to describe a more complex case: impulse response of a spherical shell and surface acoustic waves characterization.

1. Introduction

Scattering of an acoustical plane wave by simple shape targets has been a problem of particular interest for these last years.[5,18,20,24,31,32] Many theoretical derivations and experiments have led to a better understanding of echo formation mechanisms.

Although these mechanisms are complex ones, they can be modelled by a combination of several components that may overlap in the time domain: specular echo, waves transmitted in the target and surface acoustic waves (whispering gallery, Franz, Rayleigh ...).

In the case of simple shape targets (spheres, cylinders, ellipsoids,...), several authors have pointed out the importance of surface acoustic waves in the scattering phenomena and have expressed the relations between these waves and the "acoustical resonance" of a target.[6,11,29,33] In the case of a spherical shell, for instance, a resonance appears each time constructive interferences take place between surface acoustic waves that have circumnavigated an odd number of half-wavelengths along the shell circumference.

Some of these surface acoustic waves are very dispersive one. The velocity dispersion of these waves establishes an unavoidable relationship between their temporal and their spectral properties. Various methods have tried to characterize these surface acoustic waves, either in the time domain,[28] or in the frequency domain.[21] The temporal methods are based on the propagation of impulsive signals (under the assumption that no significant dispersion exists) and the spectral methods are based on the propagation of steady waves (free modes or quasi- stationary regime with *a priori* information on the characteristics of such a regime); they both lead to a major limitation: the spectral resolution is directly related to the duration of observation (the time resolution is directly related to the spectral resolution). On one hand, spectral methods start failing when dealing with very close resonance frequencies (even if they are due to different types of surface acoustic waves that could be separated in the time domain). On the other hand, temporal methods start failing when dealing with overlapping components (even if they can be separated in the frequency domain).

One can overcome these limitations by using an explicit joint *time and frequency* representation of the echoes (inspired from the joint time and frequency relation implicitly expressed in the velocity dispersion relations). Such a representation can even be used in order to separate, in the time-frequency plane, features that can hardly be separated, either in the time domain (by gating), or in the frequency domain (by filtering).

For various reasons, that we will develop in this paper, the representation we will use is the so-called Wigner-Ville.[10,13,36,37] Some papers have shown the interest of using such a distribution either for a qualitative,[7,38,39] or for a quantitative[16,17,30,40,41] echo description.

In this paper, the processing of simulated signals (with simple structure) will first be shown. Processing will then be applied to a simple acoustical case: wide band estimation of group velocity dispersion for Lamb surface acoustic waves on thin plates. Finally the analysis of the impulse response of a spherical shell will be presented. It is important to point out that, in all the cases that will be described, the whole information will be extracted from a single wide band echo corresponding to an estimation of the system impulse response.

2. Motivation of a Time-Frequency approach: the example of a spherical shell

2.1. Introduction

The problem of the scattering of a plane wave by a spherical shell has been widely studied during these last years.[6,18,24] Various works have led to an accurate knowledge of the surface acoustic waves characteristics (velocity dispersion, attenuation, re-emission) and of the corresponding resonance (location and damping). Echo formation mechanisms are summarized in figure 1: a plane acoustical wave is propagating in a fluid (considered as an ideal one) and impinging a spherical elastic shell filled with a fluid (air).

For a given incident plane wave, the direct problem consists in deriving the pressure field scattered by the shell and received at a given point M. The expression of the scattered pressure is given by the classical modal theory. The solution can be expressed as a series development known as Rayleigh series.[6,18]

incident
plane wave

elastic shell

① ←

③
② ←
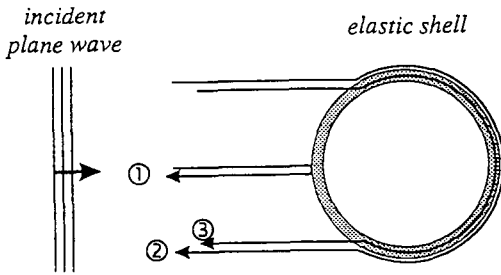
Figure 1: Echo formation mechanisms. 1: specular reflection, 2 and 3: surface acoustic waves propagating either in the external fluid or in the shell.

The coefficients of this development have then to be found. This leads to compute a determinant (of 6th order, for a hollow target) issued from the boundary conditions (stress and displacements) on both interfaces: $r = a$ (outer radius) and $r = b$ (inner radius).

The total pressure $p_M(t)$ is expressed as the sum of the incident field and the scattered field: $p_M(t) = p_i(t) + p_{sc}(t)$. It is given by the following relation:

$$p_M(t) = P_0 \exp(-i\omega t) \sum_{n=0}^{\infty} i^n \frac{1}{\sqrt{r}} (n + \frac{1}{2}) \left\{ H_{n+\frac{1}{2}}^{(2)}(kr) + \frac{D_n^{(1)}}{D_n} H_{n+\frac{1}{2}}^{(1)}(kr) \right\} P_n(\cos\theta). \quad (1)$$

where P_0 is the amplitude of the incident wave, k is the wave-number in the water ($k = \frac{\omega}{c}$) and r is the distance between the target centre and the observation point. P_n are the Legendre Polynomials, $H_{n+\frac{1}{2}}^{(1)}$ and $H_{n+\frac{1}{2}}^{(2)}$ are the Hankel functions of the first and of the second kind. The expressions of the determinants $D_n^{(1)}$ and D_n are related to the boundary conditions.[18,19,34]

Commonly, one would rather deal with the far field form function (and, in particular, its magnitude), $F_\infty(ka)$. This function can be related to the back scattered pressure P_{sc} by

$$P_{sc} = P_0 \frac{a}{2r} \exp i(kr - \omega t) F_\infty(ka). \quad (2)$$

Figures 2 show plots of the form function for spherical shells of various thickness. The shell metal is Hastelloy (Nickel-Molybden alloy) with the following characteristics: density $\rho = 9\ 217\ g.cm^{-3}$, Young Modulus $E = 217\ 000\ MPa$ and Poisson coefficient $\nu = 0.29$. These figures display a very complex structure, constituted by rapid amplitude variations of the spectrum directly related to the acoustical resonances of the shell. The resonance frequencies are given by the zeros of a determinant D_ν obtained from the determinant D_n by an extension of the integer index n to the complex associated values ν.[18] It is important to note that very small variations of the shell thickness induce large variations of the corresponding form function.
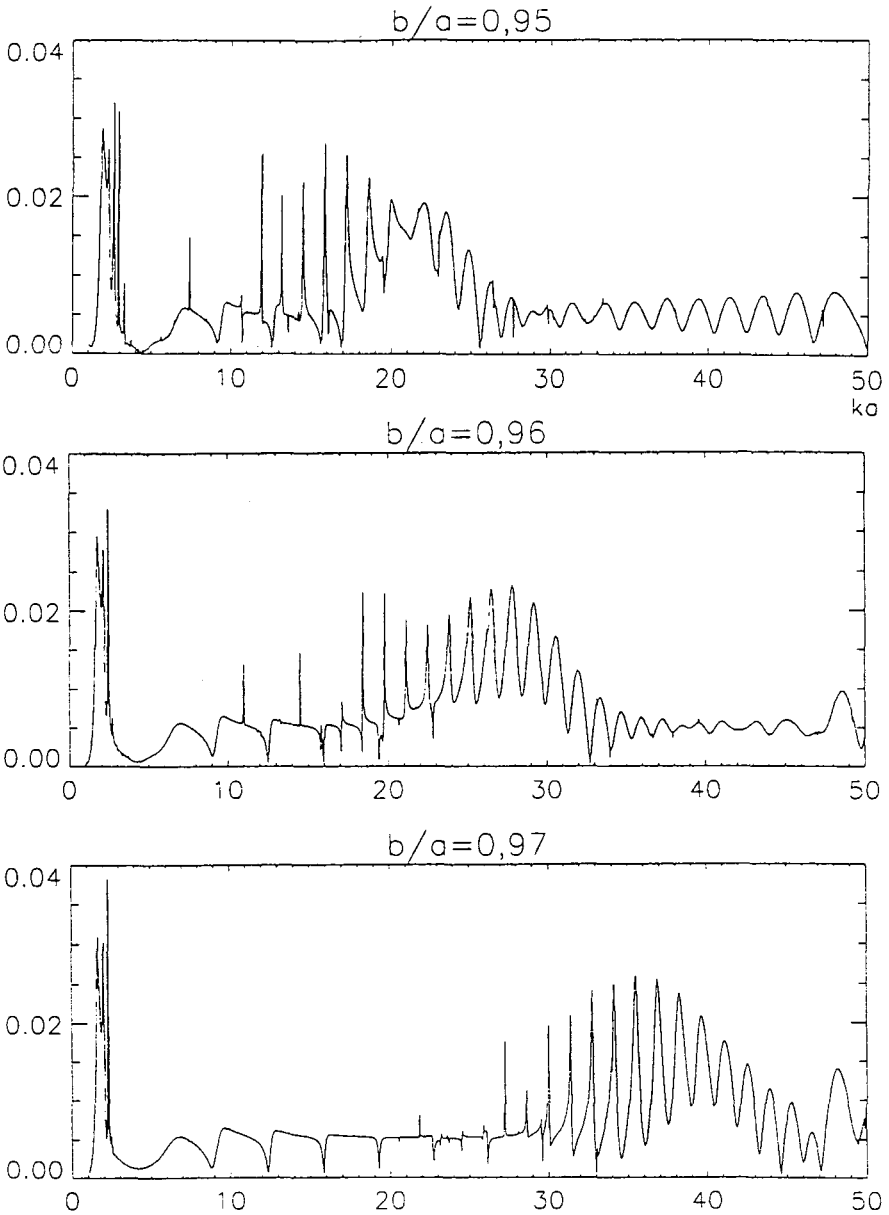
Figure 2: Form function of air filled spherical shells of Hastelloy, a =external radius (15 mm), b = internal radius (variable).

2.2. Resonance and surface acoustic waves

The conditions of existence of surface acoustic waves are given by the characteristic equation:

$$D_\nu(ka) = 0. \tag{3}$$

The solutions can be gathered in groups of integer index l. They are usually represented by Regge trajectories[18,33] which is a well known representation in quantum mechanics. The resonance frequencies are the solutions of the equation:

$$\mathcal{R}e\,[\nu_l(ka^*)] - \frac{1}{2} = n, \tag{4}$$

where ka^* is the value of the normalized frequency ka at the resonance.

The resonance damping factor is given by the relation:

$$\Gamma_{nl} = 2\frac{\mathcal{I}m\,[\nu_l(ka^*)]}{\nu'_l(ka^*)} \qquad \text{with } \nu'_l(ka^*) = \left.\frac{\partial\nu_l(x)}{\partial x}\right|_{x=ka^*}. \tag{5}$$

Some authors[6,11,18,32,33] showed that resonance and surface waves are very closely connected phenomena. A resonance takes place each time a surface wave circumnavigates the sphere with a travel length corresponding to $n + \frac{1}{2}$ wavelengths.

This statement clearly points out the time and frequency duality: acoustical resonance (spectral domain) are closely related to propagation of surface acoustic waves (temporal domain) via velocity dispersion (joint temporal and spectral domain).

2.3. Resonance classification: Regge trajectories

The Regge trajectories cited above, are used to classify the various resonance encountered. For a resonance corresponding to a given order n, we can define its order l. Each resonance will be defined by a pair of parameters (n, l). We can then plot a family of curves (fig. 3) where ka corresponds to the horizontal axis, the mode n to the vertical axis and l to the resonance order. Such plots correspond to the Regge trajectories associated to the target. Each trajectory can be associated to a specific surface acoustic wave.

For such a simple shape, we can set up a correspondence between the values of the parameter l and the surface wave type:

- $l = 0$ corresponds to the Franz wave,
- $l = 1$ corresponds to the Rayleigh wave,
- $l = 2$ corresponds to the first whispering gallery wave,
- $l = 3$ corresponds to the second whispering gallery wave.
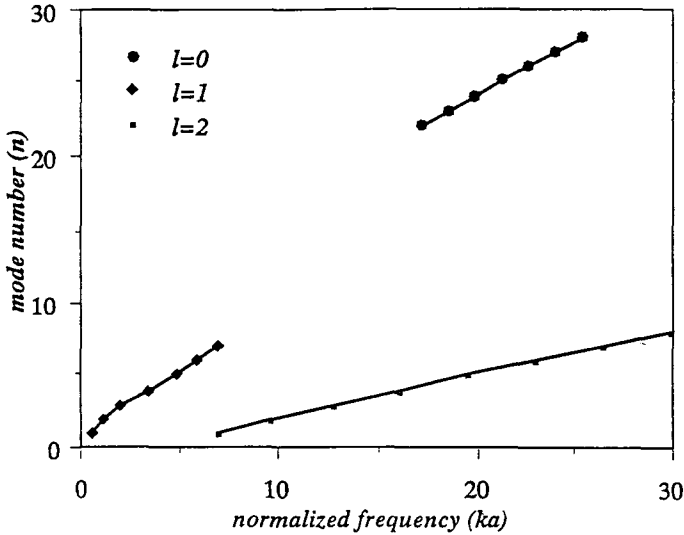
Figure 3: Regge trajectories for a spherical shell (Hastelloy $b/a = 0.956, a = 15$ mm).

2.4. Derivation of phase and group velocities from Regge trajectories

Some authors[18,33] have shown that group and phase velocities can be obtained, for each frequency, from the Regge trajectories.

The phase velocity c_ϕ can be obtained by the following relation :

$$\frac{ka^*}{n + \frac{1}{2}} = \frac{c_\phi}{c_0}, \tag{6}$$

where c_0 is the sound velocity in the water.

This link between the parameter n and the phase velocity clearly shows that the Regge trajectories can be interpreted, for each wave type, as a dispersion law. It is, in fact, the most primitive time-frequency representation of the shell echo (as no energy distribution is considered) that could be used to construct the skeleton of more sophisticated representations.

The group velocity c_g can be obtained from the phase velocity c_ϕ by the following relation:

$$c_g = c_\phi + k\frac{\partial c_\phi}{\partial k}. \tag{7}$$

n	ka^*	Γ	$\omega^*/2\pi$(kHz)	c_ϕ (ms^{-1})	c_g (ms^{-1})
order $l = 0$					
22	17.12^+	0.008	389^+	1130	1939^+
23	18.45^+	0.017	419^+	1166	1968^+
24	19.80	0.035	450	1200	1999
25	21.16^+	0.067	481^+	1233	2009^+
26	22.54^+	0.126	512^+	1263	2008^+
27	23.91	0.227	543	1291	2094
28	25.34	0.405	576	1320	2134
order $l = 1$					
1	0.54	2.59	12	535	811
2	1.21	3.70	28	719	988
3	1.95^+	4.34	44^+	827	1871^+
4	3.41^+	4.93	78^+	1125	2017^+
5	4.90	5.51	111	1323	1538
6	5.96	4.95	135	1362	1479
7	6.97^+	4.84	158^+	138	1485^+
order $l = 2$					
1	6.89^+	1.81	157^+	6821	5088^+
2	9.54	0.80	217	5664	4981
3	12.71	0.36	289	5391	5061
4	16.05^+	0.18	365^+	5297	5103^+
5	19.46^+	0.10	442^+	5254	5137^+
6	22.90^+	0.06	520^+	5233	5139^+
7	26.36	0.03	599	5218	5151
8	29.82	0.02	678	5209	5131

Table 1: Resonances of a spherical shell (Hastelloy, $b/a = 0.960, a = 15$ mm).

These relations were used in order to set up table 1 where resonance frequencies are listed together with their order, their mode, their damping and their group velocity.

This table gives an idea on the way the resonance will be excited and on the importance of their contribution in the echo reflected by the spherical shell.

2.5. Motivation for a joint time-frequency analysis

The velocity dispersion of surface acoustic waves clearly appears in table 1. Among the resonance frequencies some have been marked by a plus sign $(+)$.

These frequencies have been selected and displayed, by pairs, in table 2.

$ka^\star$	c_g (ms^{-1})	order l	$\omega^\star/2\pi$ (kHz)
close frequencies			
6.89	5088	2	157
6.97	1485	1	158
16.05	5103	2	365
17.12	1939	0	389
18.45	1968	0	419
19.46	5137	2	442
22.54$^+$	2008	0	512
22.90$^+$	5139	2	520
close velocities			
1.95	1871	1	44
17.12	1939	0	389
21.16	2009	0	481
3.41	2017	1	78

Table 2: Motivation of a time-frequency approach; examples of surface acoustic waves with close resonance frequencies or close group velocities.

This table shows two types of waves that would be very hard to separate by classical mean:

- waves corresponding to close resonance frequencies that cannot be separated by spectral discrimination: ($f^+ = 157$ kHz and $f^+ = 158$ kHz), ($f^+ = 365$ kHz and $f^+ = 389$ kHz), ($f^+ = 419$ kHz and $f^+ = 442$ kHz), ($f^+ = 512$ kHz and $f^+ = 520$ kHz).

- waves with close group velocities that cannot be separated by time gating: ($c_g = 1939$ ms^{-1} and $c_g = 1871$ ms^{-1}), ($c_g = 2009$ ms^{-1} and $c_g = 2017$ ms^{-1}).

A close look at these waves shows that, in fact, they correspond to different physical phenomena involved in echo formation mechanisms (different order l and mode n): frequency resonance, very close in the spectral domain, correspond to waves with different velocities; in the same way, waves with very close velocities correspond to resonance clearly separated in the frequency domain.

This statement, illustrated in table 2, clearly shows the relevance and the necessity of a time-frequency approach of the problem in order to separate, in the time-frequency plane, waves that cannot be separated either in the time domain, or in the frequency domain.

It is important to point out that the need of a joint time-frequency approach of the problem is essentially due to the dispersive nature of the surface acoustic waves. Velocity dispersion clearly states that any time delay measurement has to be associated to an operating frequency and that no temporal measurement can be made without its spectral correspondence.

3. Time-Frequency analysis methods

3.1. *General formulation*

Let us first have a look at the time-frequency approaches and the correspondence between existing methods in the acoustics and the signal processing areas. In a stationary situation (steady state monochromatic wave), spectral analysis and its physical interpretation can be easily achieved via Fourier transform.[4] For non stationary signals (transients such as sonar target impulse response), the purpose of a time-frequency analysis is to perform a time dependant spectral analysis. Unfortunately, it can be shown[13] that there is no unique solution for solving this problem.

Nevertheless, if a bilinear energy distribution is considered and shift invariance properties are imposed, it is possible to give a general time-frequency formulation ρ_z for finite energy signals (Cohen's class):[10,13,14,36,37]

$$\rho_z(t, f, \Pi) = \int_{-\infty}^{+\infty} W_z(u, n)\Pi(u - t, n - f)dudn, \qquad (8)$$

where W_z is the so-called Wigner-Ville distribution:[36,37]

$$W_z(t, f) = \int_{-\infty}^{+\infty} z(t + \tau/2)z(t - \tau/2)\exp(-2i\pi f\tau)d\tau, \qquad (9)$$

and where $z(t)$ is the analytic signal associated to the (real valued) received echo, f is the frequency and Π is a weighting function. It turns out that specifying this weighting function leads to various analysis methods.

3.2. *Spectrogram, Sonagram and acoustical correspondence*

A first very intuitive approach, commonly used, consists in considering a non stationary signal as the concatenation of "quasi- stationary" signals, for which the classical spectral approach is relevant.

The signal can then be gated and analyzed via a short-time window $h(t)$. This leads to the spectrogram:

$$SP_z(t, f) = \left| \int_{-\infty}^{+\infty} z(u)h(t - u)\exp(-2i\pi fu)du \right|^2. \qquad (10)$$

This short-time Fourier transform approach is equivalent to the so- called "ultrasonic spectroscopy". Its interest can be easily illustrated either in the case of slowly modulated chirp signal (large time-bandwidth product) or in the case of events that could be separated by time gating. From equation (10), one can see that the signal is first split into "time slices" and Fourier transform is then applied to each "slice" . Each time interval is considered "small enough" so that the assumption of "quasi-stationarity" is valid (or that only a single event is included in the window); if not, the frequency sweep will be so important that the signal "slice" cannot be considered any more as a monochromatic one (or time events will be mixed).

In such an approach, one will be faced to two antagonist constraints:

- on one hand, reducing the time window duration will lead to reducing the frequency resolution;

- on the other hand, increasing this duration will improve the frequency resolution but will weaken the stationarity assumption (i.e. reduction of the effective time resolution).

It is important, for such an analysis, to find a trade off between the time and the frequency resolution.

This trade off is closely related to modulation properties of the analyzed signal. It is implicitly achieved in ultrasonic spectroscopy, as time gating is defined using *a priori* information on the echo to analyze.

Sonagram is equivalent to the spectrogram but it operates in the frequency domain:

$$SO_z(t, f) = \left| \int_{-\infty}^{+\infty} Z(u) H^*(f - n) \exp(+2i\pi nt) dn \right|^2 . \qquad (11)$$

It consists in filtering the signal to analyze through a bank of filters (with constant bandwidth) and displaying the output energy, for each filter, as a function of time. The trade off can be expressed, in this case, in terms of relation between the filters bandwidth (frequency resolution) and the duration of their impulse response (time resolution).

This approach is very often used in acoustic measurements although it is seldom explicitly expressed in such a way. Measuring a transfer function of a linear acoustic system by varying the frequency of a pure tone burst with a *constant duration* can be assimilated to analyzing its impulse response through a set of filters (centered around the bursts frequency) with constant bandwidth (corresponding to the inverse of the duration). Filtering is, in fact, achieved, by the excitation signal, at the system input instead of using a bank of filters at the output.

When pure tone bursts with a *constant number of periods* are used (*i.e.* burst duration varies with frequency), this will be equivalent to analyzing the system impulse response through a set of filters with constant Q (bandwidth varies with central frequency). This analysis is closely related to wavelet transforms that have been widely studied these last years[23]. Time window optimization is implicitly included in the experiments using pure tone bursts[22] where "burst waves" are considered as a "quasi-stationary", "quasi-monochromatic"ones (whose frequency corresponds to the burst frequency).

This assumption is questionable (and even non valid) when dealing with highly dispersive waves or/and highly resonant systems.

In the first case (highly dispersive waves), the time resolution constraint will lead to the transmission of a short signal (wide band); velocity dispersion can modify considerably the signal "shape" and smear the received echo making energy localization very hard to achieve. This problem is often overcome by splitting the processing frequency range in several narrow sub-bands, in order to consider the medium as a "quasi non dispersive" one, for each sub-band. The narrower the bandwidth (i.e. the longest the burst duration), the better this assumption. For experiments conducted in a limited space, duration increase is, of course, limited by spurious reflections.

In the second case (highly resonant systems), the resonance localization is based on the important assumption that the received energy and the transmitted one can be

attributed to the same frequency. This assumption is only valid for a monochromatic wave. As mentioned in the first case, the use of a finite duration burst will spread the transmitted spectrum (and thus the received spectrum). Increasing the burst duration will reduce its spectrum and improve the spectral resolution but it will deteriorate the temporal localization and resolution.

The problems that may arise while using pure tone burst for resonance localization will be illustrated lately, by the use of time-frequency analysis (section 4.4).

In a general case, the limitations and the errors due to the implicit assumptions are hard to evaluate as a lot of *a priori* information is needed on the physical phenomena involved in the echo formation.

3.3. *Wigner-Ville Distribution*

As the assumptions cited above (quasi-stationarity, no significant dispersion) can be too restrictive, we need a more general approach that gets rid of explicit (or implicit) hypotheses on the signal evolution.

This can be achieved via the Wigner-Ville Distribution expressed in equation (9). In such an analysis, no *a priori* assumption is made on the stationarity or the dispersion properties of the signal to analyze.

In some way, it can be considered as a "blind" time-frequency analysis of the signal. Although this particular distribution is not the unique way of avoiding the cited assumptions on the processed signal. its key role is supported by the many properties listed in the following sub-section.

3.4. *Some properties of the Wigner-Ville Distribution*

The Wigner-Ville distribution possesses a lot of interesting properties with respect to both signal processing and acoustical aspects of the propagation problem:[8,9,10,12,14]

3.4.1. Energy conservation

Integrating the distribution over the whole time-frequency plane leads to the signal energy E_z:

$$E_z = \int_{-\infty}^{+\infty} \int_{-\infty}^{+\infty} W_z(t, f) dt df. \tag{12}$$

3.4.2. Marginal values

Integrating the distribution along the time axis leads to the energy spectrum ES:

$$ES(f) = |Z(f)|^2 = \int_{-\infty}^{+\infty} W_z(t, f) dt. \tag{13}$$

Integrating the distribution along the frequency axis leads to the instantaneous power IP:

$$IP(t) = |z(t)|^2 = \int_{-\infty}^{+\infty} W_z(t, f) df. \tag{14}$$

3.4.3. Bandwidth and duration preservation

The distribution of a time limited (respectively frequency limited) signal is limited on the same time (respectively frequency) interval T (respectively B):

$$z(t) \equiv 0 \ \text{for} \ t \notin T \Rightarrow W_z(t, f) = 0 \ \text{for} \ t \notin T, \tag{15}$$

$$Z(f) \equiv 0 \ \text{for} \ f \notin B \Rightarrow W_z(t, f) = 0 \ \text{for} \ f \notin B. \tag{16}$$

This property is interesting for localizing waves and echo components.

3.4.4. Shift invariance

The distribution of a time (or frequency) shifted signal is shifted by the same amount:

$$\text{let} \ y = z(t - t_0), \ \text{then} \ W_y(t, f) = W_z(t - t_0, f), \tag{17}$$

$$\text{let} \ Y = Z(f - f_0), \ \text{then} \ W_y(t, f) = W_z(t, f - f_0). \tag{18}$$

The first part of this property makes the interpretation of propagation phenomena very easy to achieve.

3.4.5. Input-output relationship for linear filters

The distribution associated to $F(z(t))$ resulting of passing a signal $z(t)$ through a linear filter with an impulse response $r(t)$ can be obtained by the convolution of the signal distribution and the filter response distribution over the time variable:

$$W_{F(z)}(t, f) = \int_{-\infty}^{+\infty} W_z(t - u, f) W_r(u, f) du. \tag{19}$$

This property is very interesting for the interpretation of the diffraction and the absorption phenomena as they both can be viewed as a linear filtering of the transmitted signal.

3.4.6. Instantaneous frequency

The instantaneous frequency f_i is commonly defined as the derivative of the phase of the analytic signal[2,3] and can be obtained by computing, at a given date, the first order moment of the distribution along the frequency axis:

$$f_i(t) = \frac{1}{2\pi} \frac{d}{dt} \arg\left[z(t)\right] = \frac{\int_0^{+\infty} W_z(t, f) f df}{\int_0^{+\infty} W_z(t, f) df}. \tag{20}$$

This property can be very useful in a sonar situation in order to describe accurately the modulation laws of the received echoes.

3.4.7. Group delay

The group delay τ_g, as defined for linear filters,[2,3,27] can be obtained, for a given frequency, by the first order moment along the time axis:

$$\tau_g(f) = \frac{1}{2\pi}\frac{d}{dt}\arg[Z(f)] = \frac{\int_0^{+\infty} W_z(t,f)t\,dt}{\int_0^{+\infty} W_z(t,f)dt}. \tag{21}$$

3.5. Acoustical correspondence

Let us consider a plane monochromatic wave travelling from a point A to a point B in an isotropic non dispersive fluid medium. Let P_A be the pressure in A, P_B the pressure in M, r the distance AB (AB perpendicular to the wave front) f_0 the wave frequency, c_0 the velocity of the compressional waves and $k_0 = \frac{2\pi f_0}{c_0}$ the wavenumber.

The pressure in A can be expressed as:

$$p_A(t) = \exp(i2\pi f_0 t) \rightarrow P_A(f) = 2\pi\delta(f - f_0) \tag{22}$$

and the pressure in B as:

$$p_B(t) = \exp(i2\pi f_0 t - ik_0 r) \rightarrow P_B(f) = 2\pi\delta(f - f_0)\exp\left(\frac{-i2\pi f r}{c_0}\right). \tag{23}$$

where $\rightarrow$ expresses the Fourier transform and δ the Dirac distribution.

A plane impulsive wave can be considered as the sum of a great number of monochromatic plane waves in phase at $t = 0$.

$$\delta(t) = \int_{-\infty}^{+\infty} \exp(i2\pi ft)df. \tag{24}$$

If such a plane impulsive wave $\delta(t)$ is transmitted at point A, then the pressure at point B is $\delta(t - \frac{r}{c})$, in the case of a ideal medium.

In the case of a dispersive medium, the phase velocity is a function of frequency: $c_\varphi = c_\varphi(f)$.

The pressure signal in B is no more a Dirac pulse but a distorted waveform:

$$p_B(t) = \int_{-\infty}^{+\infty} \exp\left(\frac{-i2\pi f r}{c_\varphi(f)}\right)\exp(i2\pi ft)df. \tag{25}$$

We know from previous work,[12] that the first moment of the Wigner- Ville distribution is equal to the so-called group delay $\tau_g(f)$ (equation (21)). Let us try to connect this group delay to the group velocity defined for dispersive waves:[35]

$$c_g(f) = \frac{1}{2\pi}\frac{df}{dk}. \tag{26}$$

From equation (7), the group velocity c_g can be expressed as a function of the phase velocity c_φ :

$$c_g(f) = \frac{c_\varphi(f)}{1 - \frac{f}{c_\varphi(f)} \frac{\partial c_\varphi(f)}{\partial f}}. \tag{27}$$

From equation (23), we can extract $P_b(f)$:

$$P_b(f) = exp\left(\frac{i2\pi fr}{c_\varphi(f)}\right). \tag{28}$$

Then we can write:

$$arg[P_B(f)] = \frac{2\pi fr}{c_\varphi(f)}. \tag{29}$$

As expressed in equation (21) , the group delay $\tau_g(f)$, given as the first moment of the Wigner-Ville distribution is equal to:

$$\tau_g(f) = -\frac{1}{2\pi}\frac{\partial}{\partial f}[Arg(P_B(f))] = \frac{-2\pi r}{c_\varphi(f)}\left[1 - \frac{f}{c_\varphi(f)}\frac{\partial c_\varphi(f)}{\partial f}\right]. \tag{30}$$

From the comparison of equations (29) and (30) , it is clear that, for each frequency f, the group delay estimated by the Wigner-Ville distribution is equal to the one defined in acoustics:

$$\tau_g(f) = \frac{1}{2\pi}\frac{\partial}{\partial f}[Arg(P_B(f))] = \frac{r}{c_g(f)}. \tag{31}$$

This property is one of the most important, in the case of acoustical propagation and scattering. It means that, aside qualitative information,[17,38,39] the Wigner-Ville distribution can lead to quantitative physical information (such as group velocity)[16,40,41] on the acoustical phenomena involved in echo formation mechanisms. The price to pay for all these interesting properties is the bilinearity of this distribution that can lead to interpretation difficulties, especially in the case of complex targets and multi-component echoes where spurious interference features may appear.[13]

As we will see, interference structures can be reduced via time or (and) frequency smoothing while using "Smoothed Pseudo Wigner-Ville Distribution":[13]

$$SPWz(t,f) = \int_{-\infty}^{+\infty} q(\tau)\left[\int_{-\infty}^{+\infty} g(u-t)P_B(u+\frac{\tau}{2})P_B^*(u-\frac{\tau}{2})du\right]e^{-2i\pi f\tau}d\tau. \tag{32}$$

where $q(\tau) = \left|h(\frac{\tau}{2})\right|^2$ and $h(\tau) = h(-\tau)$.

3.6. Digital implementation of the Smoothed Pseudo Wigner-Ville Distribution

When dealing with digitized signal. the Digital Smoothed Pseudo Wigner-Ville Distribution (DSPWVD) can be expressed as:[15]

$$DSPWVDz(t,f) = 2 \sum_{n=N+1}^{N-1} |h(n)|^2 \, K_M(t,n)e^{-i4\pi fn}, \tag{33}$$

where:

$$K_M(t,n) = \sum_{n=M+1}^{M-1} g(m)z(t+m+n)z*(t+m-n), \tag{34}$$

h is a short-time window defined on $(2N-1)$ samples, g is a smoothing window defined on $(2M-1)$ samples and f is the reduced frequency $(0 < f < 1/2)$.

Equations (33) and (34) show that a separate control of time and frequency resolutions is possible.

Computing this distribution can be easily implemented via Fast Fourier Transform algorithm. Although the periodicity of equation (33) is twice that of the conventional Digital Fourier Transform, no aliasing problem occurs due to the use of analytic signal.[14,15] As we will see, on simulation examples, a judicious choice of the smoothing functions f and g can help in reducing the importance of the interference terms.

3.7. Graphical interpretation of propagation phenomena in the time-frequency plane

The properties of the Wigner-Ville distribution will make the propagation phenomena very simple to describe and to interpret in the time-frequency plane. Acousticians often deal with plane monochromatic waves. Such waves can be represented, in the time-frequency plane by a single horizontal line (Figure 4) corresponding to the frequency f_0 (infinite duration, infinitely narrow bandwidth). The summing of an infinite number of monochromatic waves at various frequencies will lead to a "plane impulsive wave" (figure 4) occurring at the date t_0. In this case, the equiphase surface is a plane one, for every frequency component of the impulsive wave. This wave description is very convenient for the interpretation of propagation phenomena, but theoretical derivations often go through its Fourier decomposition. The time signal is then obtained by summing all the monochromatic contributions. Such a wave corresponds to a vertical line in the time-frequency plane (infinite bandwidth, infinitely narrow duration.

In all real cases, we will deal with signals possessing a finite effective duration and a finite effective bandwidth. The wave propagation of an impulsive plane wave is illustrated in figures 5 and 6 for various propagation conditions: non dispersive medium (figure 5), dispersive and absorbing medium (figure 6).

This intuitive description was made possible thanks to the various properties of the Wigner-Ville distribution cited above (mainly 3.4.3, 3.4.4 and 3.4.5). The simplest case is the propagation through an ideal medium (non dispersive and non absorbing): propagation from a to b (figure 5), is only a translation. Translation delay is the same for all frequency components and thus for the whole (impulsive) signal without loss of energy. The propagation delay τ is simply expressed as the ratio of the travelled distance and the velocity c $(\tau = d/c)$.

When dealing with a dispersive and absorbing medium (propagation from a to c, figure 6), velocity and absorption are frequency dependent: frequency components transmitted at the same time with the same level (plane impulsive wave) will reach
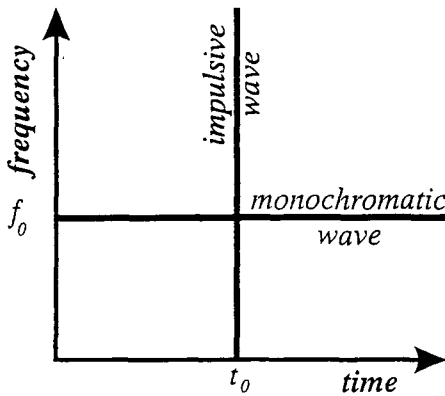
Figure 4: Waves description in the time-frequency plane.

the observation point at various arrival times $\delta(t-\tau)$ (dispersion: $\tau = \tau(f)$) and with various levels (attenuation $\alpha = \alpha(f,\tau)$).

The relevance of the Wigner-Ville distribution for describing dispersive phenomena is emphasized by the derivations developed in acoustical correspondence paragraph: in addition to the qualitative description of wave propagation, the distribution will provide with a quantitative measurement of the group velocity.

4. Simulations results

Before analyzing real data, it is interesting to evaluate processing performance on some simulation examples illustrating both the choice of the Wigner-Ville distribution as a time-frequency analyzing tool and the use of the smoothing windows (SPWVD) for reducing interference terms.

4.1. Test signal

The computed signal is a sketchy version of the first components of a shell echo; it consists in the sum of a impulsive signal (specular echo) and a chirp (dispersive surface acoustic wave). The time-frequency structure of the test signal is shown in figure 7.

4.2. Spectrogram and Wigner-Ville distribution

Figures 8, 9 and 10 show three examples of the test signal analysis via spectrograms with various time windows: short (figure 8), medium (figure 9) and long duration (figure 10). These figures show an important dependence of the spectrogram analysis on the analyzing window and clearly display the duality between time and frequency resolutions.
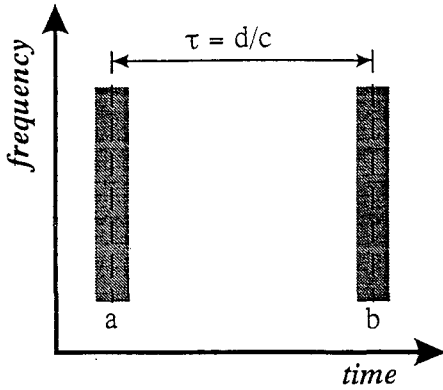
Figure 5: Description of the propagation in an ideal medium.
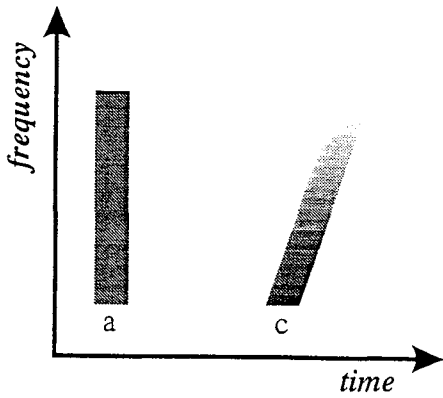
Figure 6: Description of the propagation in a dispersive and absorbing medium.
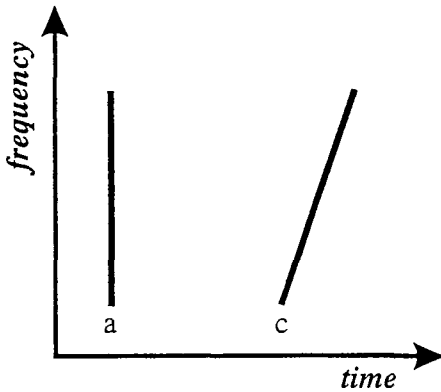
Figure 7: Time-frequency structure of the test signal.

On another hand, the Wigner-Ville distribution (figure 11) gives a nice description of the signal structure by concentrating the energy around the modulation laws but it suffers from interference terms between components and a higher noise level.

For all these figures (as well as for figures 11 and 12) the same analysis parameters have been used:

- vertical axis: frequency(40 kHz/division)

- horizontal scale: time (20 μs/division)

- grey scale: logarithmic, 3 dB by grey scale total dynamic range: 24 dB

- figure also show the processed signal (horizontal) and it power spectrum (vertical)

- h and g windows (h: Kaiser-Bessel, g: rectangular) are also given.

4.3. Smoothed Digital Pseudo Wigner-Ville Distribution

For the Smoothed Pseudo Wigner-Ville distribution, temporal and spectral smoothing are independent:[14] and have been optimized separately in order to reduce interference terms. Figure 12 illustrates, for the test signal, the improvement provided by this approach over spectrograms (figures 8, 9 and 10). Smoothed Pseudo Wigner-Ville Distribution flexibility provides a convenient trade off between the joint time and frequency resolution and the importance of the interference terms. As an intermediate step between Wigner-Ville distribution and the spectrogram, it allows to clarify the display of the former without imposing the too restrictive conditions associated to the latter.
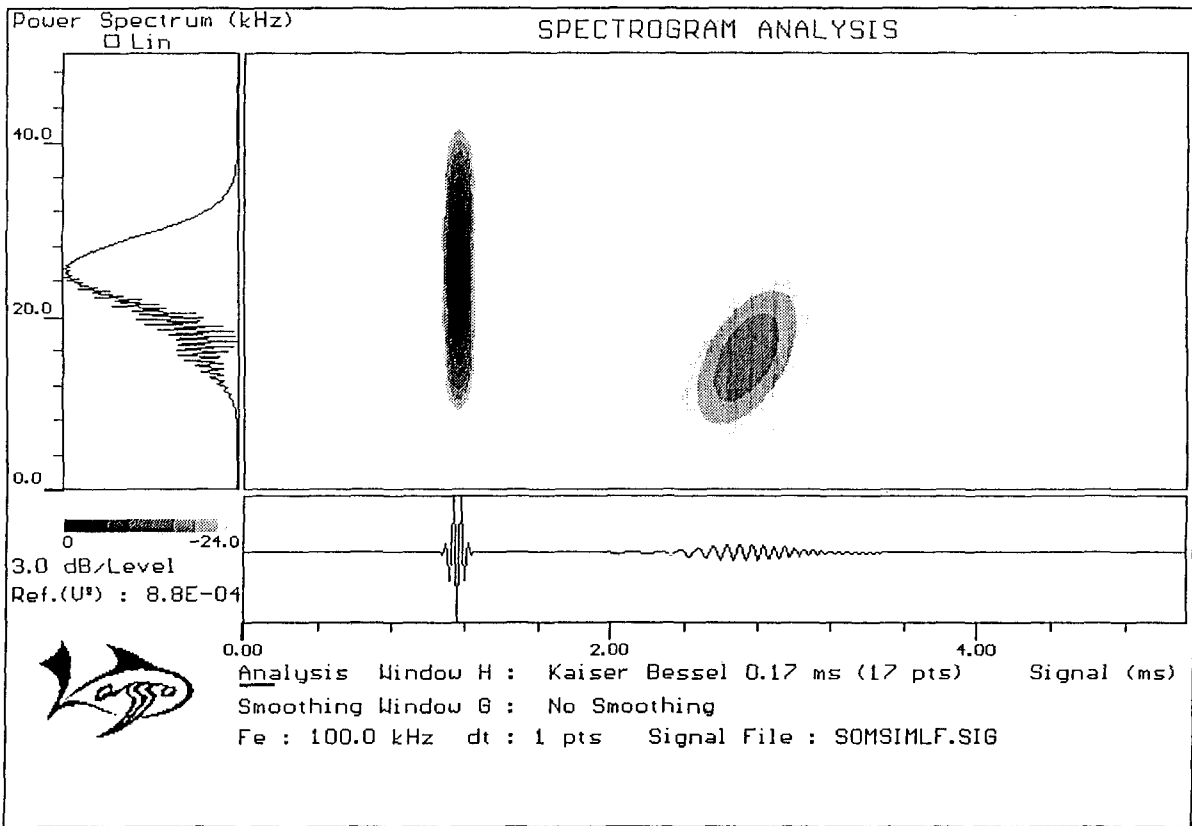
Figure 8: Spectrogram analysis of the test signal, short duration window (17 samples).

Power Spectrum (kHz)
0 Lin

SPECTROGRAM ANALYSIS

40.0

20.0

0.0

3.0 dB/Level
Ref.(U²) : 8.8E-04

0   -24.0

0.00   2.00   4.00

Analysis   Window H :   Kaiser Bessel 0.17 ms (17 pts)   Signal (ms)
Smoothing Window G :   No Smoothing
Fe : 100.0 kHz   dt : 1 pts   Signal File : SOMSIMLF.SIG
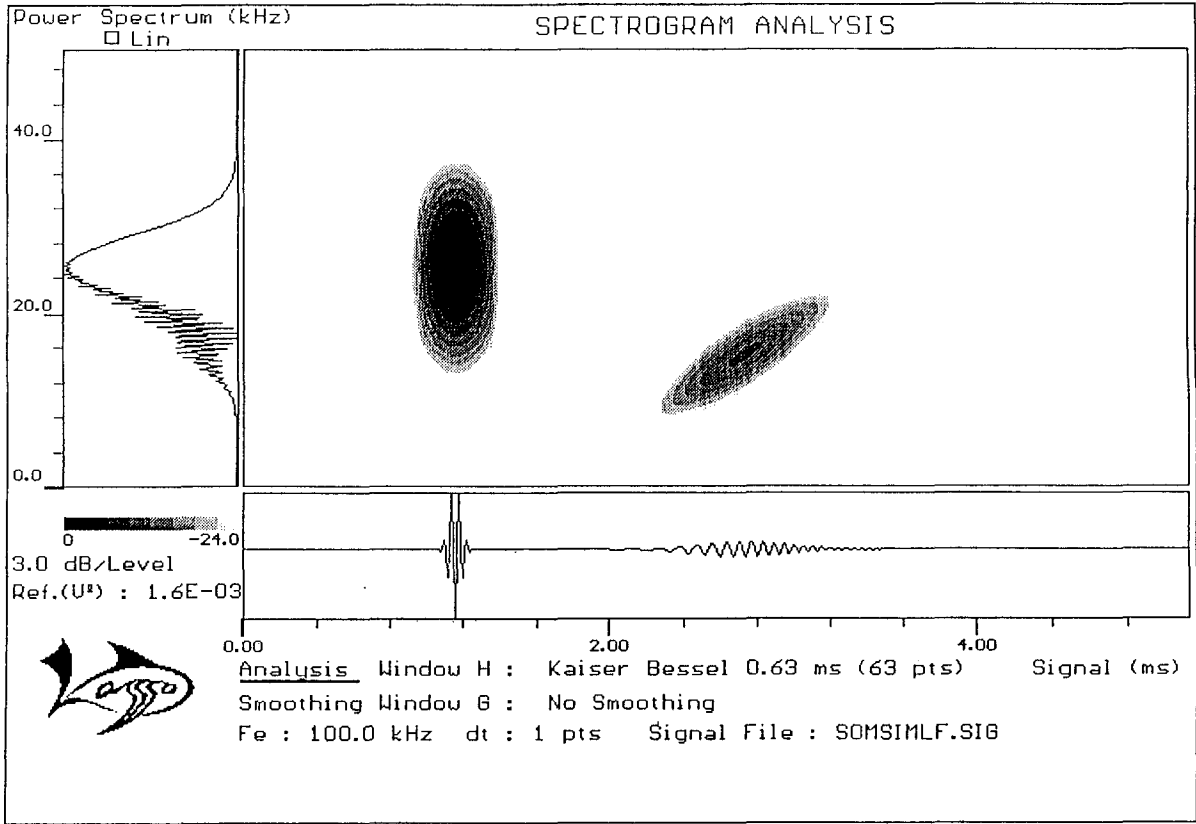
Figure 9: Spectrogram analysis of the test signal, medium duration window (63 samples).

Power Spectrum (kHz)
☐ Lin

SPECTROGRAM ANALYSIS

40.0

20.0

0.0

0   −24.0
3.0 dB/Level
Ref.(U²) : 1.6E-03

0.00   2.00   4.00

Analysis   Window H :   Kaiser Bessel 0.63 ms (63 pts)   Signal (ms)
Smoothing Window G :   No Smoothing
Fe : 100.0 kHz   dt : 1 pts   Signal File : SOMSIMLF.SIG
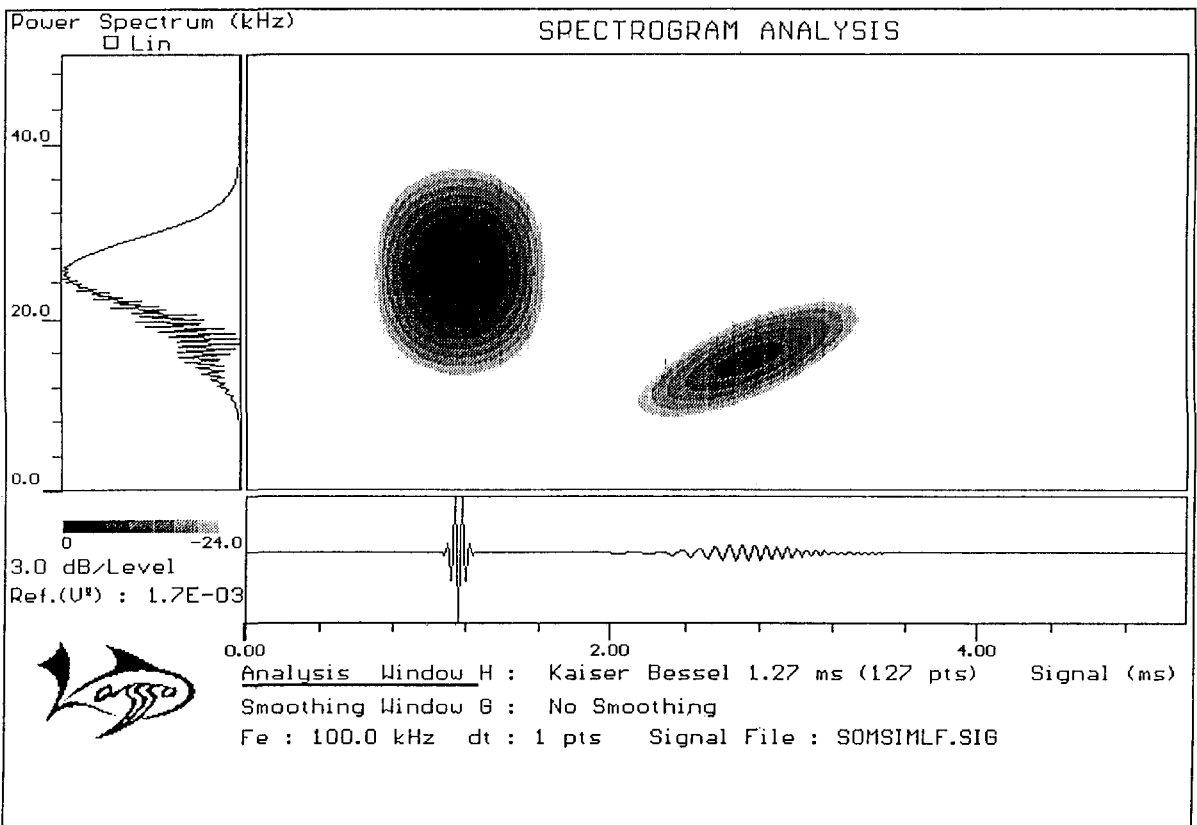
Figure 10: Spectrogram analysis of the test signal, long duration window (127 samples).
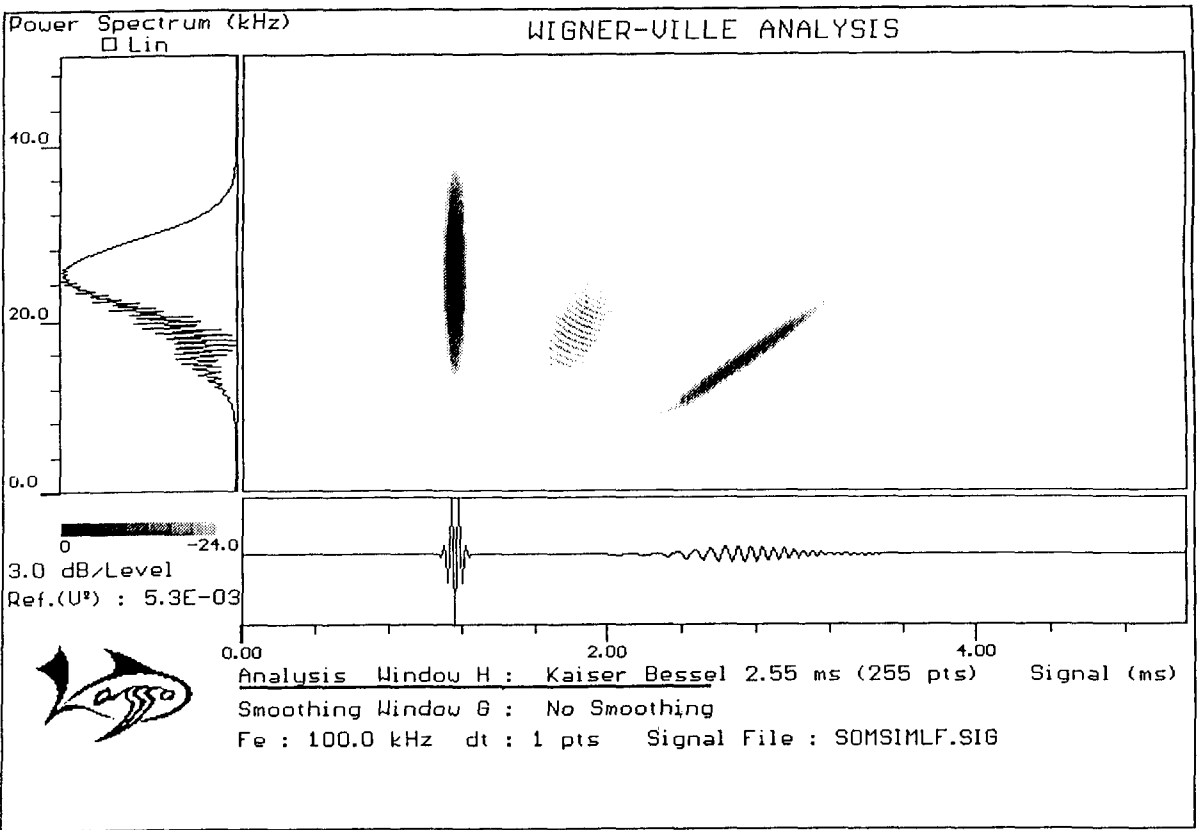
Figure 11: Wigner-Ville analysis of the test signal (windows: h: Kaiser-Bessel 255 samples, g: rectangular 1 sample).

WIGNER-VILLE ANALYSIS

Power Spectrum (kHz)
□ Lin

40.0

20.0

0.0

3.0 dB/Level
Ref.(V²) : 5.3E-03

0   −24.0

0.00   2.00   4.00

Analysis Window H :   Kaiser Bessel 2.55 ms (255 pts)   Signal (ms)
Smoothing Window G :   No Smoothing
Fe : 100.0 kHz   dt : 1 pts   Signal File : SOMSIMLF.SIG
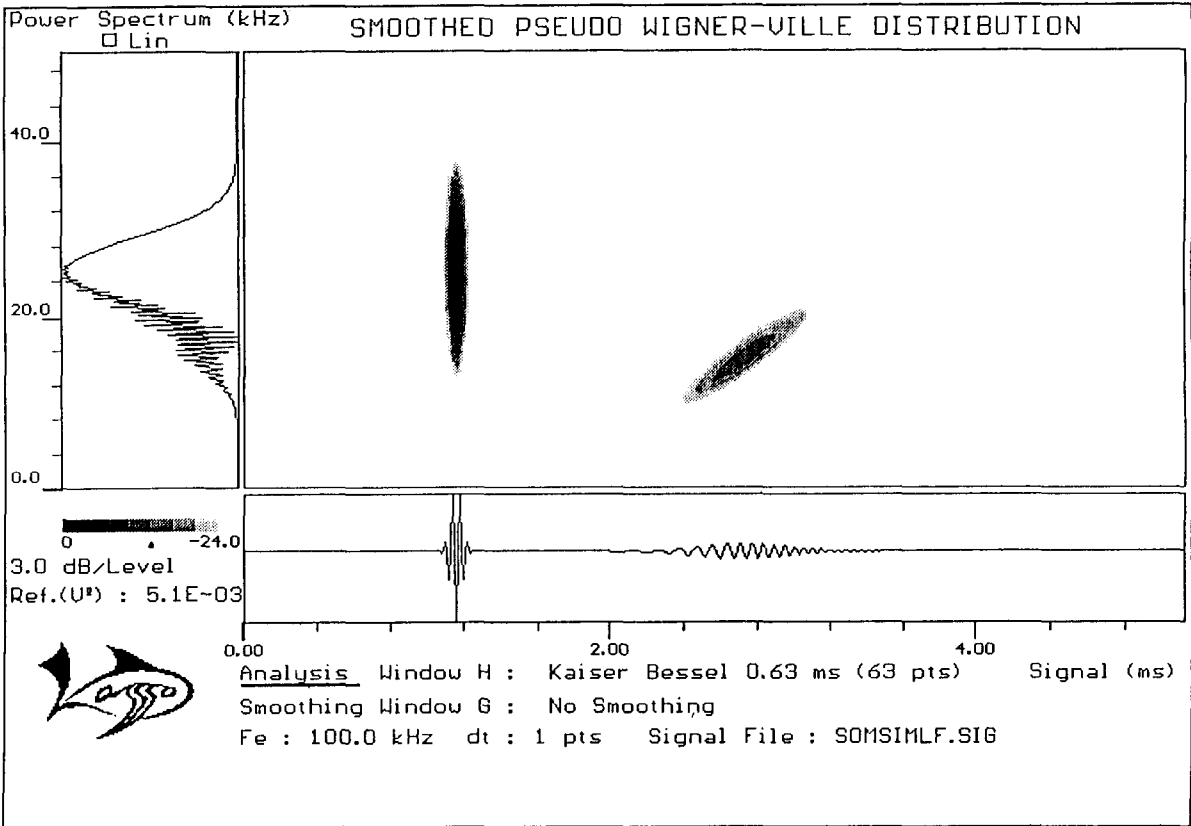
Figure 12: Pseudo Wigner-Ville smoothed distribution of the test signal vertical (windows: h: Kaiser-Bessel 63 samples. g: rectangular 1 sample).

4.4. Some limitations of pure tone burst analysis

Pure tone burst analysis has been widely used for hydrophones calibration [1], (and for electrical network analysis). Due to its convenient use, it has been also used for target echo processing.[18,20,22,25,26] Nevertheless, the highly resonant aspect of target form function and the large number of resonances can be misleading for the interpretation of the energy localization (envelope). This problem can be illustrated by the time-frequency analysis of such echoes. In the case of a pure tone burst (frequency f_0, duration T), the Wigner-Ville distribution can be expressed analytically as:

$$W_z(t,f) = \frac{\sin 2\pi(f - f_0)(T - 2\,|t|)}{\pi(f - f_0)} \text{ for } t \in \left[-\frac{T}{2}, +\frac{T}{2}\right] \tag{35}$$

and

$$W_z(t,f) \equiv 0 \text{ for } t \notin \left[-\frac{T}{2}, +\frac{T}{2}\right] \tag{36}$$

Figure 13 shows an example of such a distribution.

Both the analytic expression and the displayed example show clearly that a pure tone burst cannot be considered as a monochromatic signal especially in the transient areas (set up and set down).

Let us consider, for instance, the case of the spherical shell excited by a transmitted tone burst whose frequency f_0 is situated between two target resonances f_1 and f_2 :

$f_1 < f_0 < f_2$ ($f_0 = 253$ kHz, $f_1 = 247$ kHz and $f_2 = 259$ kHz).

This situation can often happen when a frequency scanning is used for echo characterization using tone burst, and no *a priori* information is available on the location of the target resonances.

The time-frequency representation of such an experimental echo is given in figure 14. It shows clearly that, in this case, the echo energy cannot be attributed to the central frequency of the transmitted signal. A close look at the signal after the burst end (ringing area, free mode excitation) shows that this area is the one where the monochromatic assumption is the less valid. In this example, we see clearly that the "ringing" energy is more concentrated around the resonance frequencies than around the transmitted burst frequency. Several other examples have led to similar observations.

This section is not meant, in any way, to claim that all measurements using pure tone burst are wrong ones, but only to point out that one should be very careful in associating the energy information contained in the echo of a pure tone burst to the central frequency of the burst when no *a priori* information is available on the target response.
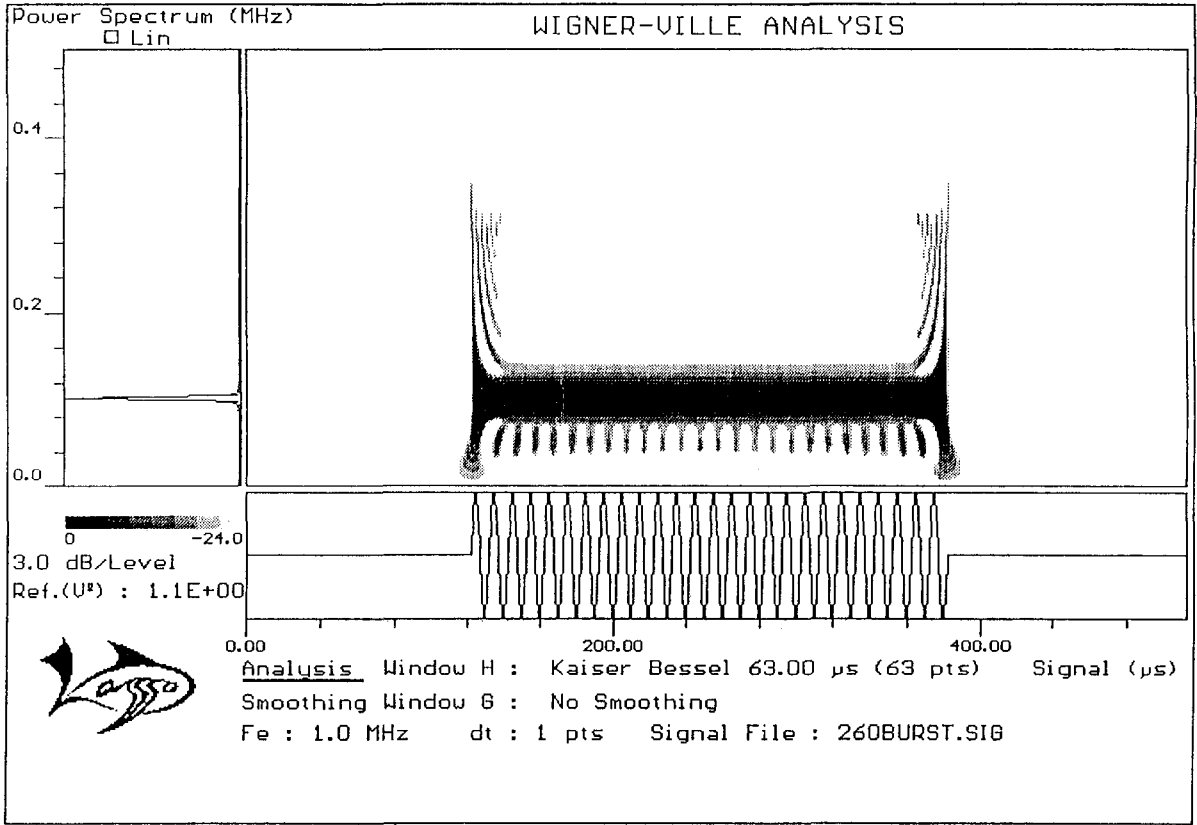
Figure 13: Wigner-Ville distribution of a pure tone burst: $f = 100$ kHz, $T = 260 \mu s$.
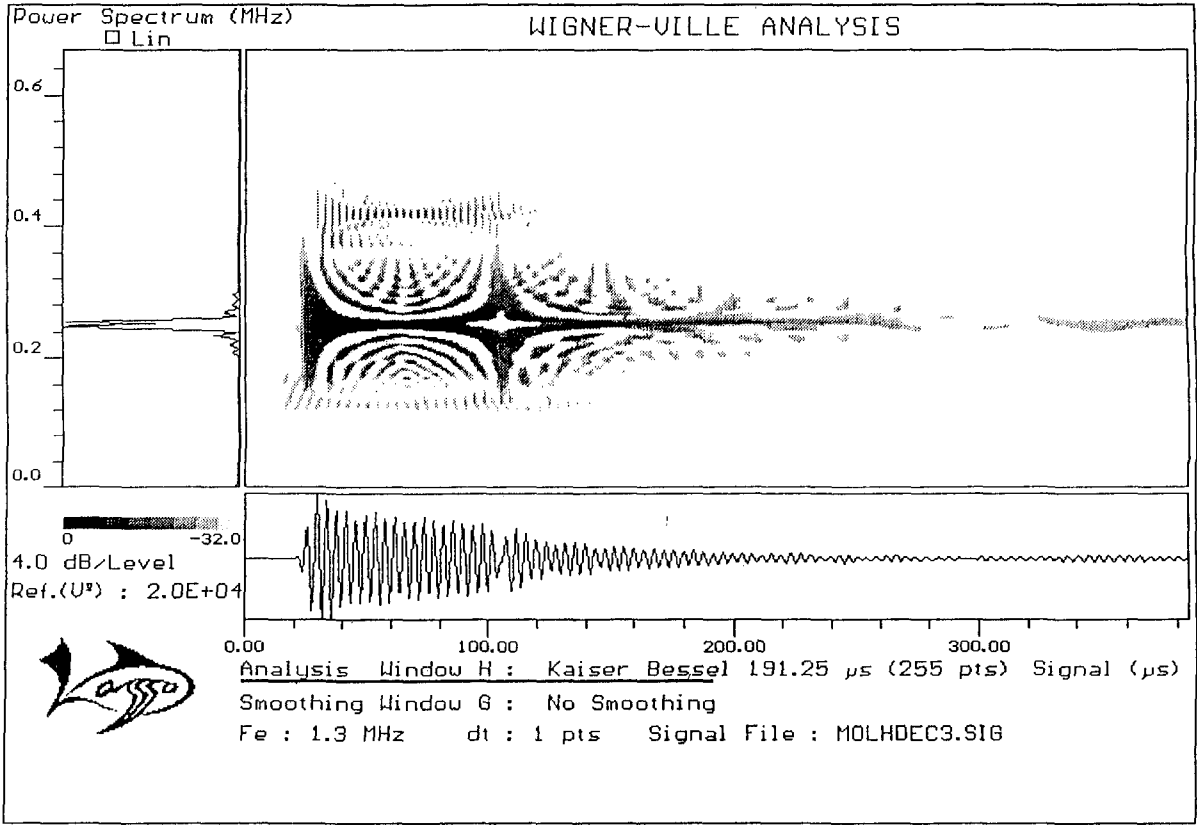
Figure 14: Illustration of problems encountered while using pure tone burst for resonance characterisation.

5. Experimental results

The concepts developed will now be applied to experimental data and measurements using the time-frequency analysis of impulse response will be compared to theoretical data.

5.1. Application to surface acoustic wave propagation on thin plates

The first experimental example shown is a very simple one dealing with surface acoustic waves.[30]

5.1.1. Experiment description

The experimental set-up is described in figure 15: surface acoustical waves are excited using a p-wave transducer associated to a wedge. The wedge angle is designed for generating Lamb waves.[30,35] The transducer is a wide band one and the transmitted signal is a short pulse. The signal is recorded, after propagation, by a similar transducer set-up. The central frequency of the transducers is 500 kHz and their bandwidth is 300 kHz (at -6 dB). Plate thickness is 10 mm. The plate is made of aluminium (longitudinal waves velocity 6380 $m.s^{-1}$; shear waves velocity 3100 $m.s^{-1}$).
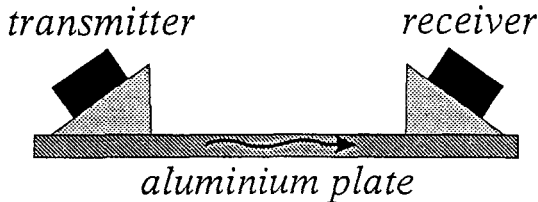
Figure 15: Lamb waves, experiment description.

5.1.2. Signal analysis

The received signals, as well as their spectrum and their time-frequency analysis are displayed in figures 16 and 17, for two propagation distances: $r = 60$ mm (figure 16) and $r = 120$ mm (figure 17) and for a single plate mode. These figures show that propagation leads to a "spreading" of the wide band signal energy, due to the velocity dispersion. In the case of a long propagation path (even in a slightly dispersive case), the signal energy becomes very hard to localize in the time domain.

Power Spectrum (MHz)
□ Lin

WIGNER-VILLE ANALYSIS

1.0

0.5

0.0

0 −32.0

4.0 dB/Level
Ref.(U²) : 3.3E+08

0.00   50.00   100.00   150.00   200.00

Analysis Window H : Kaiser Bessel 30.24 µs (63 pts)   Signal (µs)
Smoothing Window G : No Smoothing
Fe : 2.1 MHz   dt : 1 pts   Signal File : OL6DEC.SIG

Figure 16: Lamb waves; r = 60 mm.

Power Spectrum (MHz)
□ Lin

WIGNER-VILLE ANALYSIS

1.0

0.5

0.0

0   −32.0

4.0 dB/Level
Ref.(V²) : 1.5E+08

0.00   50.00   100.00   150.00   200.00

Analysis   Window H :   Kaiser Bessel 30.24 µs (63 pts)   Signal (µs)
Smoothing Window G :   No Smoothing
Fe : 2.1 MHz   dt : 1 pts   Signal File : OL12DEC.SIG
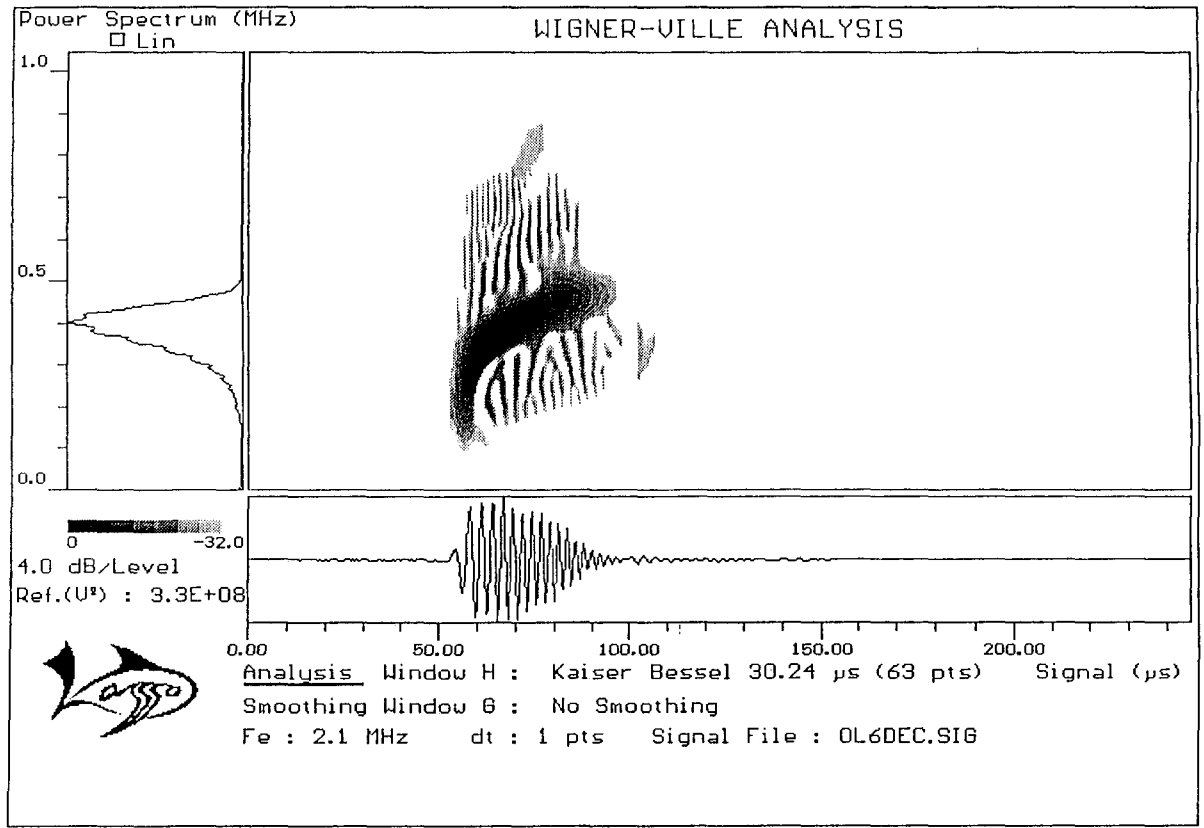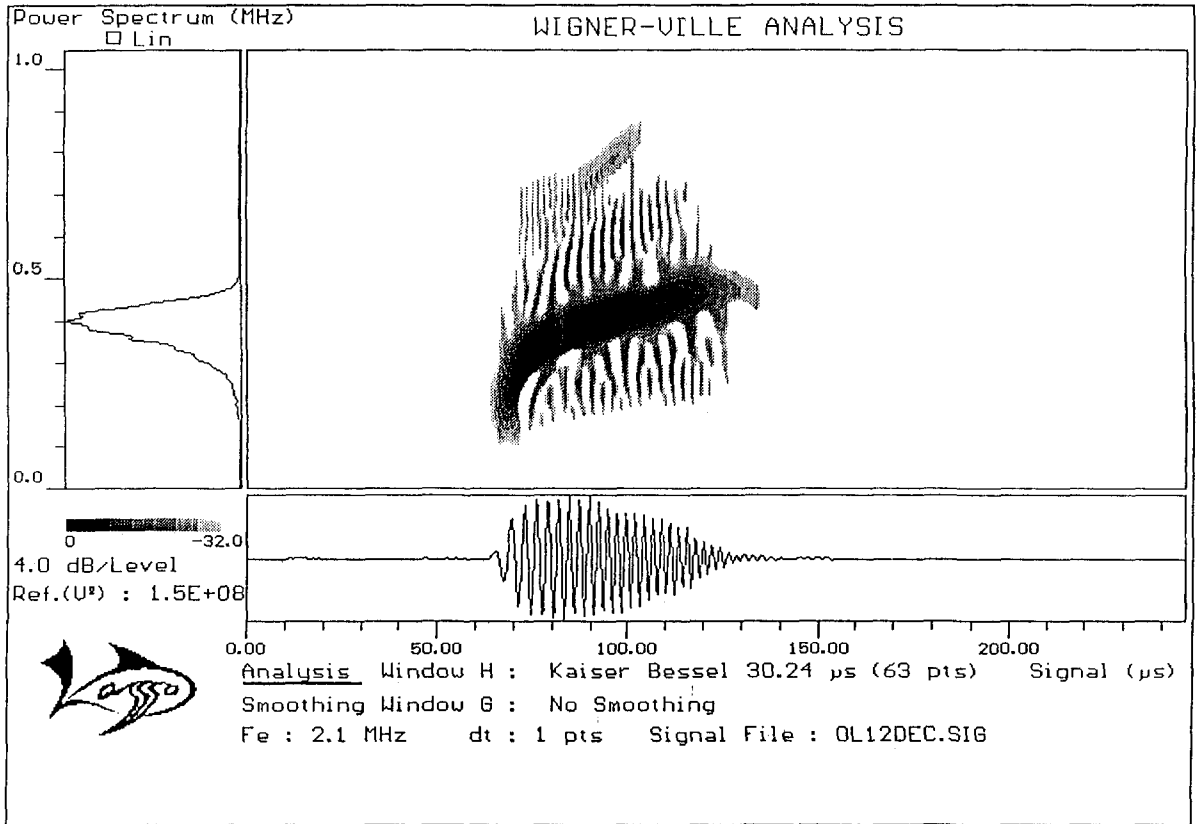
Figure 17: Lamb waves: r = 120 mm .

The Wigner-Ville distributions of those signals show clearly the velocity dispersion: the longer the path, the larger the difference between low frequency and high frequency propagation delays. Given both propagation paths, one can compute the time needed, for each frequency component, to travel the difference distance. The group velocity dispersion can then be estimated.

Figure 19 display experimental results when three plate modes are excited. The time and the frequency plots show that the modes cannot be separated neither in the time domain, nor in the frequency domain. Nevertheless they can be separated in the time-frequency domain. The computation of group velocity can then be achieved by isolating every signal component in the time-frequency domain.

5.1.3. Results

The experimental results extracted from the time-frequency plane are displayed in figure 18 together with the theoretical values (theoretical Lamb dispersion curves[35])when three modes are excited simultaneously (values extracted from figure 19). It is important to point out that, although several modes were investigated, the experimental results have been obtained on a wide frequency range by processing only two signals (at two ranges).

A quite good agreement between theoretical and experimental results is obtained (measurement error is of the order of magnitude of used symbols). It clearly shows the precision of such a measurement method (error of few percents) and validates the derivations developed in section 3.5.
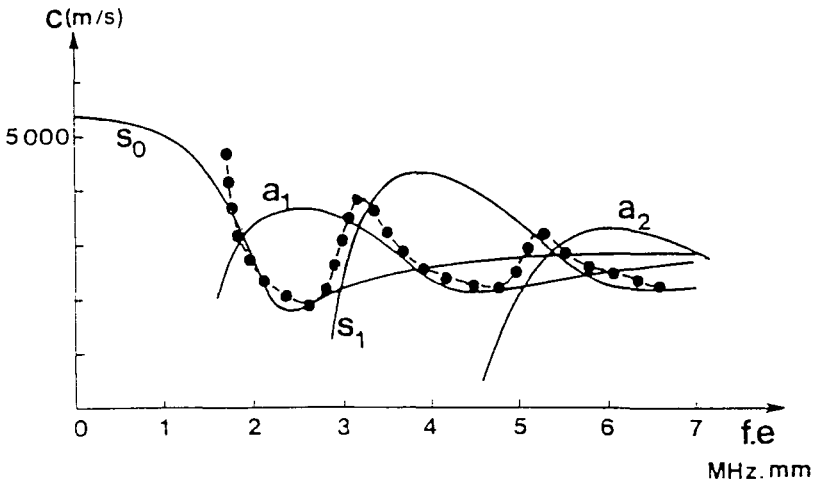
Figure 18: Group velocity dispersion of Lamb waves (3 modes).
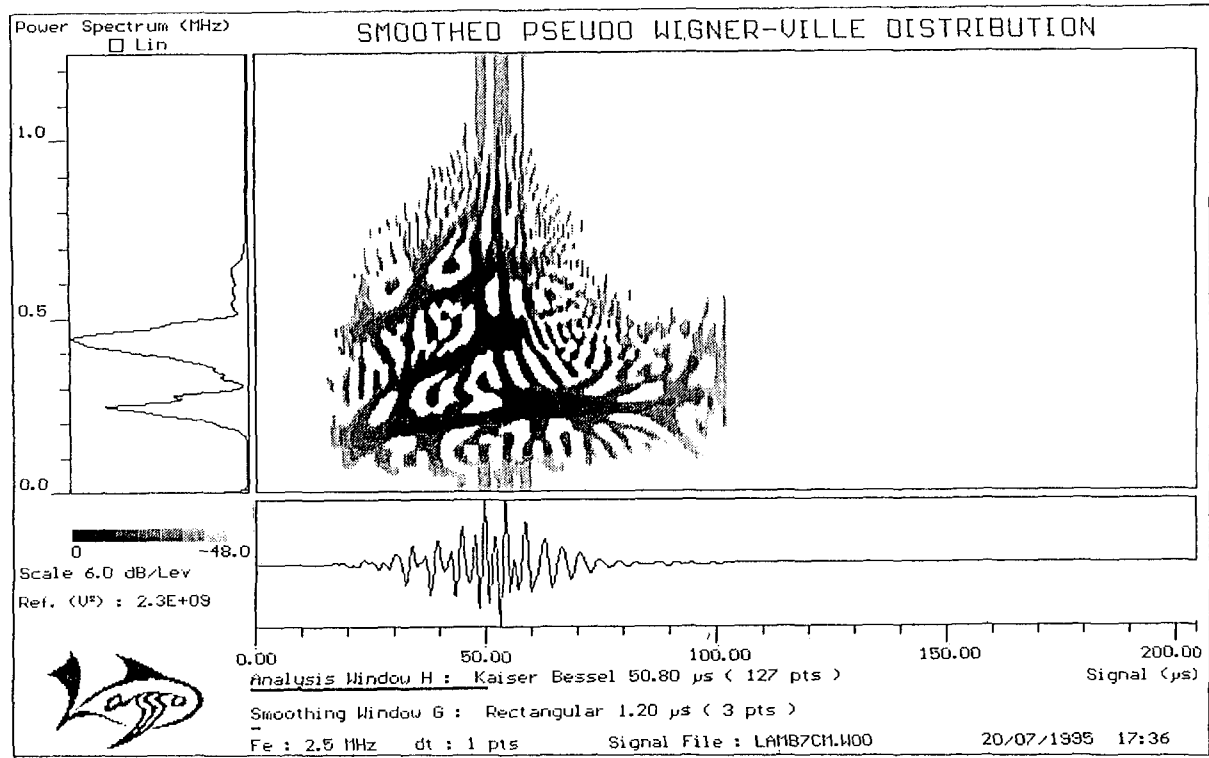
5.2. Application to a sonar target: spherical shell

Now that it has been proven, on simple cases, that Wigner-Ville analysis is a relevant method for studying dispersive waves, it will be used to address a more complex problem: the scattering of an acoustical wave by a thin spherical shell.

5.2.1. Experiment description

The experimental set up is described in figure 20. The same transducer is used for both transmission and reception (backscattering configuration), target range is about 50 cm (far field) and the whole target is insonified. The central frequency of the transducers is 250 kHz, its bandwidth is 250 kHz (at -6 dB). The transmitted signal is a very short pulse, only filtered by the transducer response. The received echo is amplified and filtered before being digitized and stored on a hard disk for further processing.

Figure 21 displays the echo reflected by the shell described in section 1 (Hastelloy alloy spherical shell, $a = 15 \pm 0.025$ mm, $b/a \cong 0.960$, thickness $= (b - a) = 0.6 \pm 0.025$ mm) together with its power spectrum and its time-frequency representation.

The specular echo, followed by some other echo components reradiated by surface waves that circumnavigate the shell are clearly displayed in the time plot of the impulse response. The power spectrum is very characteristic of thin shells echoes and very similar to the simulated spectra of figure 2 (a succession of maxima and minima due to the presence of acoustical resonance with variable damping) within the investigated frequency range (limited by the transducer bandwidth).
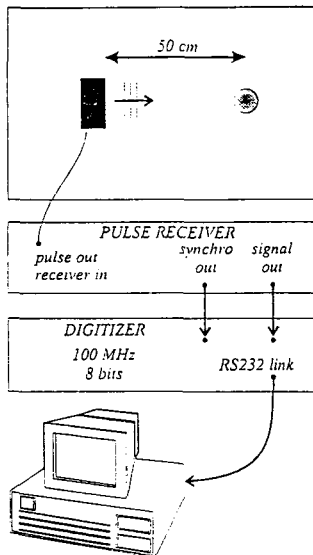
Figure 20: Spherical shell; experimental set up.
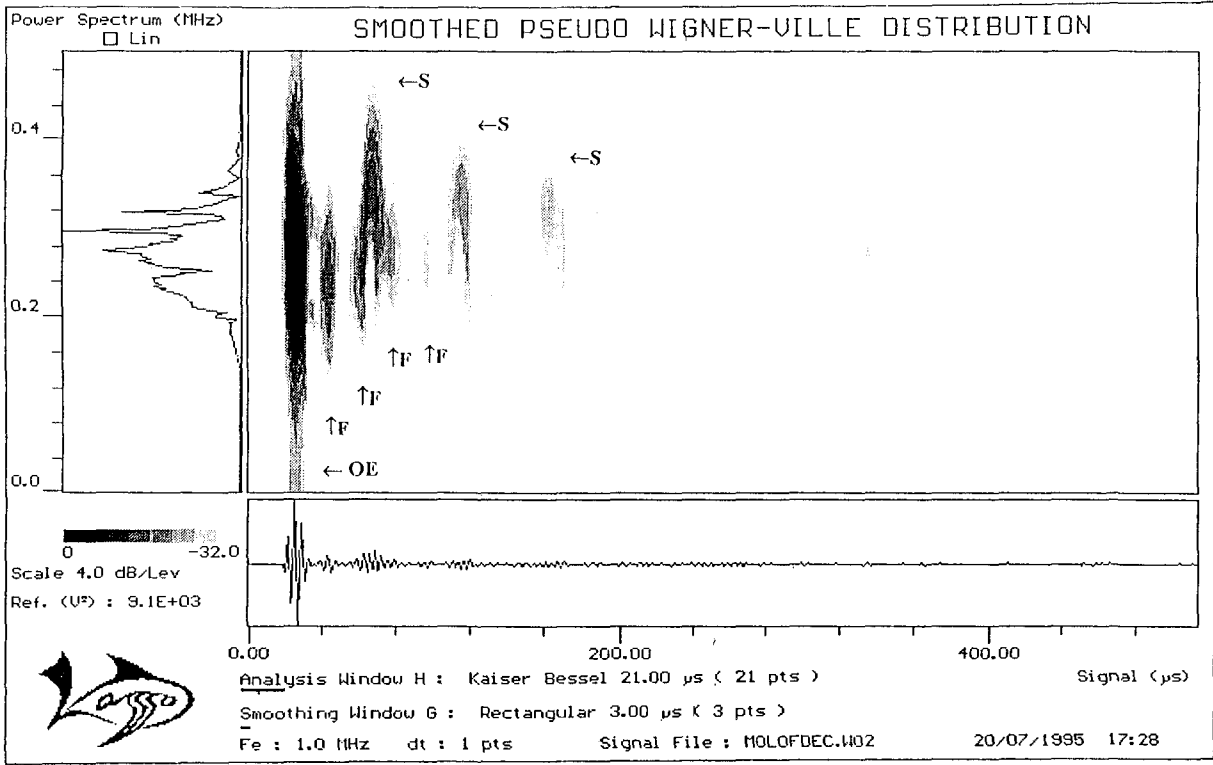
Figure 21: Time-frequency description of spherical shell echo.

5.2.2. Digital Smoothed Pseudo Wigner-Ville Distribution and target characterization

On the Smoothed Pseudo Wigner-Ville Distribution of the shell echo (figure 21), several wave packets can be distinguished. They have been labeled as follows: OE: Optical Echo, F: Fast wave (corresponds to $l = 2$), S: slow wave (corresponds to $l = 0$ or $l = 1$). F and S individual components correspond to the same wave which has travelled several times around the sphere; for each circumnavigation, the wave looses a fraction of its energy. Some velocity dispersion may be observed, as patterns bend slightly with the propagation.

Each component of figure 21 can be separated by a time-frequency filter. Knowing the propagation path, for each circumnavigation around the sphere $(2\pi a)$, the group velocity of both waves (Slow and Fast) can be computed.

The results are shown in figure 22. In addition to the measured values an error range of $\pm 10\%$ has been displayed. Some values of table 1 (corresponding to the frequency range of the transducer) have also been plotted. Figure 22 shows a good agreement between theoretical and experimental data. The estimation error on group velocity is about few percents (same order of magnitude than the error on the shell thickness.
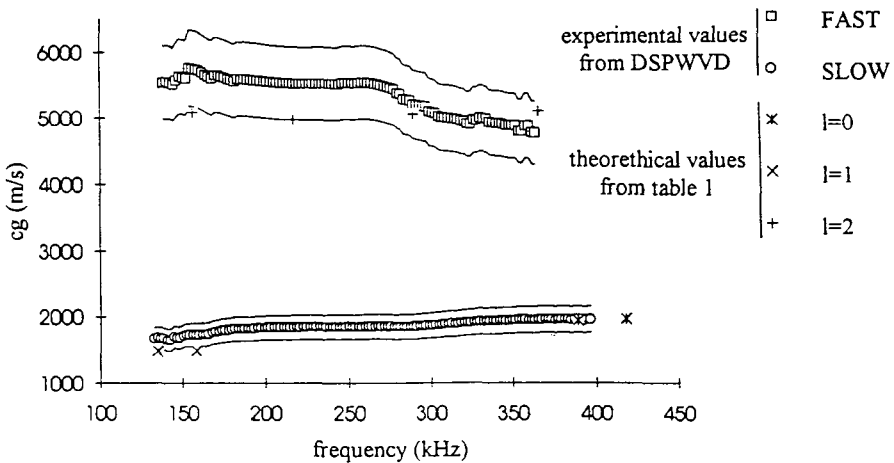
Figure 22: Velocity dispersion estimated from Wigner-Ville distribution (DSPWVD) of the impulse response of a spherical shell.

5.2.3. Target classification and method robustness

In typical sonar application, one can be interested in using time-frequency representation for target classification. Time-frequency analysis can be achieved either on raw data or, preferably, after pulse compression (higher signal to noise ratio). In the later case, the processing is similar to the time-frequency analysis of the target impulse response. For various applications, one may be interested in evaluating the

robustness of such a processing in comparison to classical methods such as resonance localization. A preliminary work has been conducted in the simple case of a spherical shell.[40] Only the influence of shell thickness has been investigated. The simulated echoes of shell with various thickness have been computed. The error induced by small variations of thickness on both resonance frequency and surface wave dispersion have been analyzed. The results show that velocity dispersion characteristics are less sensitive to shell thickness variations than the resonance position and that a gain factor of 4 to 8 in robustness can be obtained. These results are very encouraging and other studies using time-frequency approaches for target classification are conducted actually.

6. Conclusion

The results obtained for both simple and complex cases clearly show that the Wigner-Ville distribution is a relevant tool for processing wide band signals propagating in dispersive media.

The derivations developed as well as the results obtained on a thin plate and on a spherical shell show that such a processing is more than a qualitative one and that it can be used as a very accurate tool for group velocity estimation (error less than few percents).

The use of a wide band system, with impulsive excitation (or chirp, in sonar case), can provide with a very rich information on the sonar target, from a single sonar shot. Nevertheless this information becomes more and more complex and cannot be any more interpreted in terms of Target Strength as usually done in the narrow band case.

Time-frequency processing can then be used to display the wide band information in a more comprehensive way and to provide both a qualitative description of the acoustical phenomena involved in echo formation mechanisms and a quantitative and robust measurement of echo components characteristics. Moreover, patterns, in the time-frequency plane, can also be used for a robust target classification.

7. Acknowledgments

8. References

1. R.J. Bobber. *Underwater electroacoustic measurements.* Peninsula Publishing, 1988.
2. G. Bonnet. Au delà d'une vitesse de groupe: vitesse d'onde et vitesse de signal. Deuxième partie: déformation de l'amplitude et influence de l'affaiblissement. *Annales des Télécommunications.* 38(11-12):471–487, 1983.

3. G. Bonnet. Au delà d'une vitesse de groupe: vitesse d'onde et vitesse de signal. Première partie: l'opérateur vitesse de groupe en l'absence d'affaiblissement. *Annales des Télécommunications*, 38(9–10):345–366, 1983.

4. R.N. Bracewell. *The Fourier transform and its applications*. Mc Graw Hill, 1978.

5. D. Brill and G. Gaunaurd. Resonance theory of elastic waves ultrasonically scattered from an elastic sphere. *J. Acoust. Soc. Am.*, 81(1):1–21, 1978.

6. D.W. Brill, P. Ugincius, J. George, F.S. Chwieroth, and H. Überall. Sound scattering from thin shells in the kirchhoff approximation. *J. Acoust. Soc. Am.*, 62(6):1367–1372, 1977.

7. L. Brize Tramoni, J.-P. Sessarego, and J. Sageloli. Etude de la diffusion acoustique par des coques sphériques à parois minces. *J. Acoust.*, (1):177–184, 1988.

8. T.A.C.M. Claasen and W.F.G. Mecklenbräuker. The Wigner distribution - A tool for time-frequency signal analysis. Part I: continuous-time signals. *Philips Journal of Research*, 35(3):217–250, 1980.

9. T.A.C.M. Claasen and W.F.G. Mecklenbräuker. The Wigner distribution - A tool for time-frequency signal analysis. Part III: relations with other time-frequency signal transformation. *Philips Journal of Research*, 35(6):372–389, 1980.

10. L. Cohen. Time frequency distribution - a review. *Proceeding of the IEEE*, 77(7):941–981, 1989.

11. A. Derem. Relation entre la formation des ondes de surface et l'apparition de résonances dans la diffusion acoustique. *Revue du CETHEDEC*, 58:43–79, 1979.

12. P. Flandrin. *Représentation temps-fréquence des signaux non-stationnaires*. PhD thesis, Institut National Polytechnique de Grenoble, 1987.

13. P. Flandrin. *Temps-fréquence*. Hermès, Paris, 1993.

14. P. Flandrin and B. Escudié. Principe et mise en oeuvre de l'analyse temps-fréquence par transformation de wigner-ville. *Traitement du Signal*, 2(2):143–151, 1985.

15. P. Flandrin, W. Martin, and M. Zakharia. On hardware implementation of the Wigner-Ville transform. In V. Cappellini and A.G. Constantinides, editors, *Digital Signal Processing*, pages 262–266. Elsevier Science Publishers, North-Holland, 1984.

16. P. Flandrin, J. Sageloli, J.-P. Sessarego, and M.E. Zakharia. Application of time-frequency analysis to the characterization of surface waves on elastic targets. *Acoust. Lett.*, 10(2):13–28, 1986.

17. P. Flandrin, J.-P. Sageloli, J.-P. Sessarego, and M. Zakharia. Application de l'analyse temps-fréquence à la caractérisation de cibles. In *11ème Colloque GRETSI*, pages 329–332, Nice, France, 1987.

18. N. Gespa. *La diffusion acoustique*. CEDOCAR, 1987.

19. R.R. Goodman and R. Stern. Reflection and transmission of sound by elastic spherical shells. *J. Acoust. Soc. Am.*, 34(3):338–344, March 1962.

20. R. Hickling. Analysis of echoes from a solid elastic sphere in water. *J. Acoust. Soc. Am.*, 34(10):1582–1592, 1962.

21. G. Maze and J. Ripoche. Méthode d'isolement et d'identification des résonances (MIIR) de cylindres et de tubes soumis à une onde acoustique plane dans l'eau. *Revue de Physique Appliquée*, 18:319–326, 1983.

22. G. Maze, J. Ripoche, A. Derem, and J.L. Rousselot. Diffusion d'une onde ultrasonore par des tubes remplis d air immergés dans l'eau. *Acustica*, 55(2):69–

85, 1984.

23. Y. Meyer. *Ondelettes et algorithmes concurents.* Herman, Paris, 1992.
24. W.G. Neubauer. *Acoustic reflection from surfaces and shapes.* Naval Research Laboratory, Washington, 1986.
25. W.G. Neubauer, R.H. Vogt, and L.R. Dragonette. Acoustic reflection from elastic spheres. I. Steady-state signals. *J. Acoust. Soc. Am.*, 55(6):1123–1129, 1974.
26. W.G. Neubauer, R.H. Vogt, and L.R. Dragonette. Acoustic reflection from elastic spheres. II. Transient analysis. *J. Acoust. Soc. Am.*, 55(6):1130–1137, 1974.
27. A. Papoulis. *Signal analysis.* Mc Graw-Hill, 1977.
28. G. Quentin and A. Cand. Pulsed resonance identification method. *Electronics letters*, 25(5):353–354, 1989.
29. G. Quentin, A. Derem, and B. Poirée. Group velocity and acoustical resonance. *J. Phys.*, 50:1943–1952, 1989.
30. J.-P. Sessarego, J. Sageloli, P. Degoul, P. Flandrin, and M. Zakharia. Analyse temps-fréquence de signaux en milieu dispersif - application à l'étude des ondes de Lamb. *J. Acoust.*, 3:273–280, 1990.
31. D.J. Shirley and K.J. Diercks. Analysis of the frequency response of simple geometric targets. *J. Acoust. Soc. Am.*, 48:1275–1282, 1970.
32. H. Überall, editor. *Acoustic resonance scattering.* Gordon and Breach science publishers, 1992. 341 p.
33. H. Überall, L.R. Dragonette, and L. Flax. Relation between creeping waves and normal modes of a curved body. *J. Acoust. Soc. Am.*, 61:711–715, 1977.
34. N.D. Veksler. The analysis of peripheral waves in the problem of plane acoustic pressure wave scattering by a circular cylindrical shell. *Acustica*, 69:63–72, 1989.
35. I.A. Viktorov. *Rayleigh and Lamb waves.* Plenum Press, New-York, 1967.
36. J. Ville. Théorie et application de la notion de signal analytique. *Cables et Transmissions*, 2ème annnée(1):70–73, 1948.
37. E.P. Wigner. On the quantum correction for thermodynamic equilibrium. *Physics Review*, 40:749–759, 1932.
38. N.-C. Yen. Time and frequency representation of acoustic signals by means of the Wigner distribution function: implementation and interpretation. *J. Acoust. Soc. Am.*, 81(6):1841–1851, 1987.
39. N.-C. Yen, L.R. Dragonette, and S.K. Numrich. Time-frequency analysis of acoustic scattering from elastic objects. *J. Acoust. Soc. Am.*, 87(6):2359–2371, 1990.
40. M.E. Zakharia, F. Magand, J. Sageloli, and J.P. Sessarego. Time-frequency approaches for sonar target description: application to fisheries. In J.M.F. Moura and I.M.G. Lourtie, editors, *Acoustic Signal Processing for Ocean Exploration*, pages 541–546, Netherlands, 1993. NATO Advanced Study Institute on Acoustic Signal Processing for Ocean Exploration, Kluwer Academic Publisher.
41. M.E. Zakharia, J.-P. Sessarego, J. Sageloli, and P. Flandrin. Analyse temps-fréquence appliquée à la caractérisation acoustique de cibles. *J. Acoust.*, 1(1–2):185–188, 1988.

ACOUSTICAL RESONANCE SCATTERING THEORY FOR STRONGLY OVERLAPPING RESONANCES

H. PEINE and D. GUICKING

Drittes Physikalisches Institut
Universität Göttingen
Bürgerstraße 42–44
D-37073 Göttingen, Germany

ABSTRACT

The classification of submerged bodies with respect to internal properties (material etc.), and not only based on geometrical shape, should be possible by means of their scattering resonances. This approach is known as the resonance scattering theory (RST). In model experiments, many isolated resonances can be observed, thus experimentally confirming the RST. However, in real-world experiments isolated resonances can typically not be detected. An essential extension of the RST theory with respect to solving practical problems is possible by applying to the acoustical scattering problem the so-called R-matrix theory (RMT) which has been developed by Wigner and Eisenbud to describe nuclear reactions. Properly defined resonances provide the basis from which the whole formalism is constructed, while in the former theory the resonances are introduced after computing the scattering cross section. This allows an extension of the "acoustic spectroscopy" of isolated resonances as introduced by Brill et al. to the practically important case of strongly overlapping resonances. Isolated resonances are included in the RMT theory as special cases, too. A model function is proposed which can be matched—without knowledge of the scattering cross section—to measured differential cross sections in order to extract the resonance features.

1 Introduction

A problem of practical concern in underwater acoustics is the classification of targets from sonar echoes, e. g., the discrimination between metallic objects and stones; the targets may even be buried in the sediment. Classification cannot be based on the geometrical shape alone (as in high frequency acoustical imaging) but has to include material properties or the inner structure of the target.

Appropriate classification parameters are given by the scattering resonances. These are the frequencies where strong interaction between the impinging wave and the interior of the target occurs. They are strongly related to the vibration modes of the target.

The great importance of the eigenvibrations for acoustic radiation and scattering behavior has been documented by many articles (e. g., Hund[1], Boisch[2,3]).

A rapid variation of the backscattering cross section in a small frequency interval can be called a resonance. Several definitions are possible (some examples will be given below) which stem from nuclear theory and can desribe such variations, but give different resonance frequencies and widths. However, if a scatterer actually exhibits a rapid change of the backscattering amplitude in a small frequency interval, all the definitions lead to nearly the same resonance parameters.

It was hoped that the acoustical scattering resonances would characterize a target in a similar way ("acoustical fingerprint") as atoms, nuclei etc. can be identified from their resonance spectra. This is why much work has been devoted to the development of the resonance scattering theory (RST) by Überall, Gaunaurd and many others[4-8].

Roughly speaking, this theory is a transcription of the "S-Matrix Theory" from nuclear physics to acoustical scattering. First, the analytical form of the backscattering amplitude is computed, and afterwards the resonances are related to the poles of the scattering function. Much attention has been paid to isolated resonances: The scattering function is separated formally into one single isolated resonance and a background term. But one must keep in mind that the particular resonance picked out interferes coherently with the background term.

In general, acoustical resonances cannot be as sharp as nuclear ones because there are no "almost bound states" in acoustics ($k^2 < 0$ is impossible). Isolated acoustical resonances can, therefore, be observed with properly chosen objects only (see, e. g., Maze[9] and Neubauer[10] for such model experiments).

In typical real-world experiments a coherent superposition of many resonances is observed. Although the single resonances cannot be resolved in monostatic measurements, the overall resonance behavior of the object nevertheless provides features suitable for classification.

In the "R-Matrix theory" outlined below, the resonances are not introduced after computing the scattering cross section, but they are directly related to properly defined vibration modes from which the whole formalism is constructed. This theory includes the line widths and the coupling of the different resonant modes. So the "acoustic spectroscopy" of isolated resonances as conceived by Brill et al.[5] can be extended to the practically important case of strongly overlapping resonances.

Data reduction is another important aspect. The spectral parameters provide a data set of much lower dimension than the original time series of the backscattered sonar echo. This data set may serve as a proper input vector to a conventional or, e. g.. a neural network classifier.

2 Scattering resonances

The plane wave impinging on the object can be considered a superposition of spherical modes. If the scattering object is present, the outgoing modes are to be multiplied by a complex reflection coefficient S_l (modal scattering function) whereas the incoming modes are left unchanged. The target shall be understood here to be a sphere of homogeneous, lossless material admitting only compressional waves. This scatterer shows already all important features of the resonance concept. The scattered wave is obtained by subtracting the plane wave from this field:

$$
\begin{aligned}
\Phi_{sc} &= \Phi - e^{ikz} \\
&= -(2i)^{-1} \sum_{l=0}^{\infty} (2l+1)\, i^l \, (1 - S_l)\, h_l^{(+)}(kr)\, P_l(\cos\vartheta)
\end{aligned}
\tag{1}
$$

where P_l designates the Legendre-Polynomials, k is the angular wave number, and the spherical Hankel functions $h_l^{(+)}(kr)$ describe outgoing waves because a time dependence of the form $\exp(-i\omega t)$ is assumed. The incident plane wave $\exp(ikx)$ propagates in direction of the polar axis.

The measured differential cross section $d\sigma_{sc}/d\Omega$ is the power scattered into the solid angle $d\Omega$, divided by the intensity of the incident wave:

$$
\frac{d\sigma_{sc}}{d\Omega} = |g(\vartheta)|^2 = \left| \sum_l g_l(\vartheta) \right|^2 ,
\tag{2}
$$

$$
g_l(\vartheta) = (2k)^{-1} (2l+1) (1 - S_l)\, P_l .
\tag{3}
$$

Introducing the form function g, the total field in great distance from the object can be written as

$$
\Phi = e^{ikr\cos\vartheta} + g(\vartheta)\, \frac{e^{ikr}}{r} .
\tag{4}
$$

The field outside the scattering object is entirely determined by the S-Matrix elements S_l. If this field is written as

$$
\Phi_l^a = x_l\, h_l^{(+)} + y_l\, h_l^{(-)} ,
\tag{5}
$$

then one has

$$
S_l = -\frac{x_l}{y_l} .
\tag{6}
$$

The argument of all functions related to the interior of the object is $k_i r$, that of the functions describing the outer field is $k_a r$. At $r = R$, the boundary of the object, the two fields are connected by the requirement that the pressure,

$$
\rho_i\, \Phi_l^i = \rho_a\, (x_l\, h_l^{(+)} + y_l\, h_l^{(-)}) ,
\tag{7}
$$

and the radial component of the velocity,

$$
k_i\, \Phi_l^{\prime i} = k_a\, (x_l\, h_l^{\prime(+)} + y_l\, h_l^{\prime(-)}) ,
\tag{8}
$$

must be continuous (′ means derivative with respect to the arguments $k_i R$ and $k_a R$, respectively). These conditions yield the S_l which can be written for convenience as

$$
S_l = \frac{\frac{k_i}{\rho_i}\frac{\Phi_l^{\prime i}}{\Phi_l^i} - \frac{k_a}{\rho_a}\frac{h_l^{\prime(-)}}{h_l^{(-)}}}{\frac{k_i}{\rho_i}\frac{\Phi_l^{\prime i}}{\Phi_l^i} - \frac{k_a}{\rho_a}\frac{h_l^{\prime(+)}}{h_l^{(+)}}} \cdot \frac{h_l^{(-)}}{h_l^{(+)}} =: \frac{f_l - (\Delta_l - i\,s_l)}{f_l - (\Delta_l + i\,s_l)} \cdot \frac{h_l^{(-)}}{h_l^{(+)}} \; .
\tag{9}
$$

The expressions

$$
f_l := \frac{k_i R}{\rho_i}\left.\frac{\Phi_l^{\prime i}}{\Phi_l^i}\right|_{r=R}
\tag{10}
$$

and

$$
(\Delta_l + i\,s_l) := \frac{k_a R}{\rho_a}\left.\frac{\Phi_l^{\prime a}}{\Phi_l^a}\right|_{r=R}
\tag{11}
$$

introduced with the last equation are proportional to the acoustical surface admittances. The factor $h_l^{(-)}/h_l^{(+)}$ in Eq. (9) would be the whole scattering function if the object had a pressure release boundary (for the outer problem). Since its modulus equals unity, this factor represents the phase shift δ_l^w imposed to the outgoing waves by the geometry of the object:

$$
S_l^w = \exp(2i\delta_l^w) \, .
\tag{12}
$$

The first term in Eq. (9), containing the logarithmic derivatives f_l and $(\Delta_l \pm is_l)$, is related to the interaction of the incident wave with the interior of the object and, therefore, also to the resonances.

2.1   *Definitions*

A strong fluctuation of the differential cross section or at least of the modal form function in a small frequency interval can be called a resonance. Several definitions are used in the literature to describe resonance behavior, leading to different resonance frequencies and widths.

2.2   *Resonances as poles*

This way of introducing the resonances shall be called the "Natural resonance definition" here. Resonances are defined[11] as the complex poles k_n of the scattering function S_l:

$$
f_l(k_n) = \Delta_l(k_n) + i\,s_l(k_n) \, .
\tag{13}
$$

This means that there exists an outgoing wave without any incoming one. At a pole

$$
k_n \equiv k_n^\prime - i\,K_n \quad (K_n > 0)
\tag{14}
$$

one can write the outgoing wave at great distance from the scatterer,

$$x_l(k_n R) \cdot \frac{\exp[i\,(k_n r - 1/2\,l\pi)]}{k_n r} \cdot e^{-i\omega_n t} \,, \tag{15}$$

with $\omega_n = k_n \cdot c$ as

$$\Phi(k_n, r, t) = \frac{x_l}{k_n r} \cdot e^{i\,k'_n\,(r-ct)} \cdot e^{K_n\,(r-ct) - 1/2\,l\pi} \,. \tag{16}$$

For $K_n > 0$ the amplitude decays exponentially with time. This is the "ringing" of a resonance (e.g., Numrich[12]).

With increasing distance from the scatterer the wave amplitude grows without bound. This is, of course, physically impossible; the reason is that causality has not been considered so far[13]: The amplitude at location r and time t was radiated by the scatterer at the time $(t - r/c)$. The resonance state cannot have been decayed since an arbitrarily long time, but must have a definite beginning. If this time origin is called $t = 0$, then the spatially exponential growth of the wave ends at the distance $r = c\,t$.

The set of poles of S_l also contains those of the second factor in Eq. (9), which represents the scattering function of a sphere with pressure release boundary. These "geometrical" poles have a much larger imaginary part than the poles of the first factor in Eq. (9).

2.3 *"Actual" resonances*

This definition requires the f_l to be real for real frequencies (elastic scattering only) and is derived from the "natural definition"[14-16]: $f_l(k_n)$ is written in the vicinity of the real part of the pole k_n as a linear expansion:

$$f_l(k_n) \approx f_l(\Re k_n) + \left(\frac{\partial f_l}{\partial k}\right)_{\Re k_n} (k_n - \Re k_n) \,. \tag{17}$$

Then the "actual resonance wave number" $\Re \tilde{k}_n$ is defined by each of the two equivalent equations:

$$f_l(\Re \tilde{k}_n) = \Delta_l(\Re \tilde{k}_n) \tag{18}$$

$$i\,s_l(\Re \tilde{k}_n) = \left(\frac{\partial f_l}{\partial k}\right)_{\Re \tilde{k}_n} (\tilde{k}_n - \Re \tilde{k}_n) \,. \tag{19}$$

Therefore a complex resonance wave number

$$\tilde{k}_n := (\Re \tilde{k}_n) + \frac{i\,s_l}{\left(\frac{\partial f_l}{\partial k}\right)_{\Re \tilde{k}_n}} \equiv (\Re \tilde{k}_n) - i\,\frac{1}{2}\,\Gamma_l^s \tag{20}$$

can be introduced, where the width Γ_l^s is given by

$$\Gamma_l^s := \frac{2\,i\,s_l}{\left(-\frac{\partial f_l}{\partial k}\right)_{\Re \bar{k}_n}}\,. \tag{21}$$

At the resonance frequencies defined by Eq. (18) the relation

$$S_l = -S_l^w \tag{22}$$

holds. Eq. (18) was used by Überall et al.[17] to define the acoustical scattering resonances.

2.4 "Formal" resonances

This definition[15,18] also requires the f_l to be real. The real resonance frequencies k_n^f are defined in this case by

$$f_l(k_n^f) = 0\,. \tag{23}$$

They can, again, be assigned a complex value so that a resonance width is defined in the following way: the analytical continuation $F_l(k)$ of $f_n(k)$ for complex-valued k is defined by a linear Taylor approximation:

$$F_l(k) := 0 + \left(\frac{\partial f_l}{\partial k}\right)_{k_n^f} \cdot (k_n - k_n^f)\,. \tag{24}$$

The real value k_n^f can be assigned, by

$$F_l(\hat{k}_n) := \Delta_l(k_n^f) + i\,s_l(k_n^f)\,, \tag{25}$$

a complex wave number $\hat{k}_n$:

$$\hat{k}_n := \left(k_n^f + \frac{\Delta_l(k_n^f)}{\left(\frac{\partial f_l}{\partial k}\right)_{k_n^f}}\right) - i\,\frac{1}{2}\left(\frac{2\,s_l(k_n^f)}{-\left(\frac{\partial f_l}{\partial k}\right)_{k_n^f}}\right)\,. \tag{26}$$

The formal definition $f_l = 0$ is equivalent to prescribing a hard-walled boundary for all frequencies. This leads to discrete, real eigenfrequencies and real eigenfunctions in the interior of the scatterer. But in reality the surface impedance depends on frequency. Nevertheless, the scattering process can be described exactly on the basis of the formal eigenfrequencies, as will be explained below.

The three resonance definitions given above provide similar resonance frequencies if the widths are very small (poles near the real frequency axis):

$$k_n \approx \tilde{k}_n \approx \hat{k}_n\,. \tag{27}$$

3 Properties of the scattering function

The scattering function S_l has some generally valid properties which are independent of the special nature of the scatterer[19].

The wave packets in the actual scattering process are built up from the steady state solution by Fourier transformation. Because these wave packets are real-valued, the symmetry relation of the Fourier amplitudes must hold for the scattering function, too:

$$S(-k) = S^*(k). \tag{28}$$

Only elastic scattering shall be considered here so that energy conservation means

$$|S(k)|^2 = S(k)\,S^*(k) = 1, \tag{29}$$

or,

$$S(k)\,S(-k) = 1. \tag{30}$$

The analytical continuation from the real k-axis into the complex k-plane is governed by the requirement of causality, which leads to Titchmarsh's Theorem:
$S(k)$ is holomorphic in the upper k-plane and symmetrical with respect to the imaginary axis:

$$S^*(k) = S(-k^*). \tag{31}$$

The following symmetry properties hold: All poles of $S(k)$ lie in the lower half-plane, all zeros in the upper one. If k_n is a pole, $-k_n^*$ is a pole, too, while $-k_n$ and k_n^* are zeros. This pole distribution can be seen in the numerical calculations as reported in the literature[20-22].

Due to the above-mentioned properties the "canonical product expansion" is valid[13,19]:

$$S(k) = e^{-2ik\alpha} \prod_n \frac{k - k_n^*}{k - k_n}. \tag{32}$$

Each pole pair $(k_n, -k_n^*)$ gives the contribution

$$\frac{k - k_n^*}{k - k_n} \cdot \frac{k + k_n}{k + k_n^*}. \tag{33}$$

Therefore the scattering function $S_l(k)$ is determined uniquely by its poles k_{ln}. All information about the scatterer available in the backscattering amplitude is contained in the distribution of the "natural resonances." The factor $\exp(-2ik\alpha)$ reflects causality: at great distance r from the origin the scattered wave cannot be observed before $t = 2(r - \alpha)/c$, if the incoming wave has passed r at $t = 0$. If the scatterer is a sphere with radius R, $\alpha = R$ can be set for every l.

4   Resonances, cross sections and ringing

The differential cross sections are governed by

$$(1 - S_l) \,,$$

which is proportional to the amplitude of the scattered wave. In the scattered wave all contributions interfere coherently.

If there is a pole $k_n = K_n - i\Gamma_n \, (\Gamma_n > 0)$ with the width Γ_n being much smaller than the distances to the adjacent resonances, and if furthermore $\alpha K_n \ll 2\pi$, $\exp(-2ikR) \approx 1$, i.e., the wavelength at resonance is much greater than the radius of the scatterer, then the scattering function can be represented in the vicinity of such a resonance by only one factor of the product expansion:

$$\frac{k - K_n - i\Gamma_n}{k - K_n + i\Gamma_n} \cdot \frac{k + k_n}{k + k_n^*} \tag{34}$$

where the second factor, which stems from the pole $-k_n^*$, can be assumed unity because of $\Gamma_n \ll K_n$.

If the exponent $(2ikR)$ is not ≈ 0 or does not approximate a multiple of 2π, this "causality factor" interferes also with the resonances. If Γ_n is very small, the influence of all other poles can be neglected in the vicinity of the resonance frequency K_n. What remains is only the interference with the background $\exp(-2ikR)$. The expression $\exp(-2ikR)$ is called by Bethe and Placzek[23] the "Potential scattering in a narrower sense." It has neither poles nor zeros. The factor $h_l^{(-)}(kR)/h_l^{(+)}(kR)$ in S_l (see Eq. (9)) is often called potential scattering. It is related to the purely geometrical scattering of the incoming wave and has poles with large Γ_n corresponding to the free vibrations of the medium outside the sphere. In a ray approximation the "Franz surface waves" can be assigned to them. The product expansion, Eq. (32), of S_l contains all poles, the "outer" ones from $h_l^{(-)}(kR)/h_l^{(+)}(kR)$ and the resonances of the inner structure. Only in the special case $l = 0$ both definitions of potential scattering are equivalent:

$$\frac{h_0^{(-)}}{h_0^{(+)}} = e^{-2ikR} \,.$$

The concept of a "single resonance" suggests exceptional effects to be present and therefore small values for the widths Γ_n. There is some arbitrariness how to separate the scattering function in potential (or background) and resonance scattering parts. Poles with large values Γ_n will reasonably be assigned to the "background." In acoustics the Γ_n are typically so large that many resonances overlap. Then the background of a narrow resonance (leading to observable rapid variations in the scattering amplitude) comprises the adjacent broader resonances and the potential term $\exp(-2ikR)$.

S_l cannot only be written as a product expansion, but also as series expansion called "Mittag-Leffler series"[13,19]:

$$S(k) = e^{-2ikR} \left(c_0 + \sum_n \frac{c_n}{k_n - k} \right) . \tag{35}$$

The c_n are the residues of $S(k)$ at the poles k_n. The sum contains all pole pairs $(k_n, -k_n^*)$.

The expression

$$1 - S(k) = e^{-2ikR} \left(\sum_n \frac{c_n}{k - K_n + i\Gamma_n} + e^{2ikR} - c_0 \right) \tag{36}$$

formally resembles the "Breit-Wigner-formula" as introduced to acoustics by Überall[4,17] where, however, the resonances are defined differently ("actual resonances," see Section 2.3) and which is a symbolic sum with only one term being valid at a time.

The "Mittag-Leffler series" is not an approximation, i.e., the contributions of all resonance poles are summed up. (Approximation for a single resonance means omitting all but one term of the series. Then one has $c_n = 2i\Gamma_n$; the pole pair $(k_n, -k_n^*)$ has the sum of residues $k_n^* - k_n = 2i\Gamma_n$).

When transferring methods used in nuclear physics to acoustical scattering, one has to observe that acoustical resonances can, on principle, not be as sharp as nuclear ones because in the field equations the order with respect to time is different:

Acoustics is governed by the Helmholtz equation,

$$\nabla^2 \phi(\vec{r}) + k^2 \phi(\vec{r}) = 0 ; \quad \phi(r) = \text{velocity potential} , \tag{37}$$

and quantum mechanical phenomena by the Schrödinger equation,

$$\nabla^2 \Psi(\vec{r}) + (\epsilon - U(\vec{r})) \Psi(\vec{r}) = 0 \tag{38}$$

where $k^2 := \left| \vec{k} \right|^2$, $\epsilon := (2m/\hbar^2) E$ and $U(\vec{r}) := (2m/\hbar^2) V(\vec{r})$, E is the energy and $V(\vec{r})$ the potential. The time dependence has been assumed as $e^{-i\omega t}$ and $e^{-iEt/\hbar}$, respectively. The two equations become equivalent by setting

$$k^2 \equiv \frac{\omega^2}{c^2} = \epsilon - U(\vec{r}) . \tag{39}$$

In quantum mechanics k^2 can become negative ($\epsilon < U(\vec{r})$ so that basic solutions $A\,e^{\pm i\vec{k}\cdot\vec{r}}$ are possible which decay in all space directions. This leads to the well-known "almost bound states," i.e., scattering resonances with arbitrarily small width.

In acoustics k^2 is always a positive quantity. The field may decay in one or two dimensions of space (e.g., total reflection), but never in all three at the same time. In other words, no "almost bound states" are possible in acoustical scattering.

5   Detection of resonances

In the stationary state solutions considered so far the scattered wave interferes with the impinging plane wave. In order to observe the scattered wave alone, wave packets must be formed by Fourier transformation. Impulses with sharp boundaries are possible in three dimensions whereas in one and two dimensions an excitation is left after the impulse has passed.

Isolated resonances can be observed in model experiments in several ways:

1. Often[24-26] impulses with rectangular shape have been used:

$$p_{in}(x = 0, t) = \left\{ \begin{array}{ll} \sin(\omega_0 t); & 0 \leq t \leq T \\ 0 & ; \text{ else.} \end{array} \right.$$

   Here p_{in} is the incoming wave packet, T is the impulse duration, and $\omega_0/2\pi$ is the carrier frequency.

   After scattering, the resonances can be detected by their exponential ringing[12]. At resonance the impinging wave penetrates into the interior of the scatterer. The energy stored in the interior is re-radiated with some time delay. In other words, the time envelope of the impulse is substantially changed only if a resonance is excited. A wave packet suitable for exciting a single resonance must have a narrow bandpass spectrum which is smooth around the carrier frequency. Well suited will be a rectangular shaped power spectrum, i.e., an impulse with an envelope like $\sin(x)/x$.

   If $T \gg 2\pi/\omega_0$ resonances can also be observed in the steady state sector of the scattered impulse, i.e., after all transients have decayed, but before the impulse ends. In this time window a resonance is recognized by rapid variations of the amplitude if the carrier frequency is changed by a small amount (i.e., by the resonance width). In passing through the resonance, the quantity $(1 - S_l)$, which essentially is the modal backscattering amplitude, takes on all of its possible values between zero and two. Here the resonances are observed being influenced by the background, in contrast to measuring in the ringing sector.

2. An impulse of short duration is scattered as a train of many impulses due to the surface waves repeatedly circulating around the scatterer. This effect is especially pronounced with thin-walled, smoothly curved hollow scatterers, where dispersion of the (few excited) surface waves is small. The surface waves are strongly excited in resonance because of phase matching after every cycle. Describing the scattering process with surface waves is a ray approximation to the Rayleigh normal mode series, making use of the Sommerfeld-Watson Transform[16,22,26].

3. The echo is displayed as Wigner distribution (WD)[27-29]. The time-frequency distributions[30] give an impression of "which frequency arrives at which time."

Strifors[31] used the WD to investigate the structure of radar echoes. At convenient experimental conditions with this method acoustical surface waves and their dispersion behavior can be displayed[27].

The windowed WD is defined by[31]

$$W'_f(\omega, t) = 2 \int_{-\infty}^{+\infty} f(t + t') f^*(t - t') w_f(t') w_f^*(-t') e^{-i2\omega t'} dt' , \qquad (40)$$

and its discrete version reads

$$W_f(k, l) = 2 \sum_{n=0}^{N-1} f(l + n) f^*(l - n) w_f(n) w_f^*(-n) e^{-i(4\pi/N)kn} . \qquad (41)$$

Strifors[31] has chosen a window with Gaussian shape:

$$w_f(t) = \exp(-\alpha t^2) . \qquad (42)$$

For $w_f(t) \equiv 1$ the unwindowed Wigner distribution is obtained. As can be seen by the phase factor, the WD has period π. So there can be aliasing although the sampling condition is fulfilled. This spectral overlap can be avoided if the spectral width is halved by using the analytical signal instead of the original time series:

$$f_a = f(n) + i\hat{f}(n) . \qquad (43)$$

Here $\hat{f}(n)$ is the Hilbert transform of $f(n)$. The analytical signal is complex and contains only positive frequencies:

$$F_a(k) = \begin{cases} 2F(k): & 0 < k < N/2 \\ F(k): & k = 0, N/2 \\ 0: & N/2 < k < N \end{cases} \qquad (44)$$

where $F(k)$ is the discrete Fourier transform of $f(n)$.

4. Frequency and width of the resonances are estimated with the Prony method[32]. The scattered impulse is supposed to be a sum of exponentially decaying sine waves of the form $R_i \exp(x_i t)$ with x_i being the complex resonance poles and the amplitudes R_i being the residues of the impulses' Laplace transform. The partial sums over all mode numbers n for a particular radial index l in the resonances x_{nl} give the surface wave contributions, that is the impulse train mentioned above[32]. This method is well suited for the ringing section of the backscattered impulse.

6   Measurements with full-scale objects

Many isolated resonances can be observed in certain model experiments, whereby the RST has been confirmed experimentally.

In order to perform more realistic experiments, backscattering measurements have been made in a lake of about 40 m maximum depth.

In a first series of measurements, transmitter, receiver, and test object were suspended from a raft to about 10 m depth. The targets mainly used were:

1. A cylindrical steel shell of 40 cm length, 20 cm mean radius, and 1.7 cm thickness of wall, with aluminium endplates of 2 cm thickness ("big cylinder").

2. A cylindrical steel shell of 40 cm length, 11 cm mean radius, and 2.4 cm thickness of wall ("small cylinder"), with either flat endplates or hemispherical endcaps.

3. Stones of different size (approx. 30 cm ... 1 m diameter).

The shells were air-filled. The test signals used were wave trains of approx. 2 ms duration with carrier frequencies between 10 and 20 kHz and Gaussian shaped envelope. Object echoes were recorded for aspect angles at steps of ten degrees.

In a second series of measurements the targets were partially submerged in the sea floor. The measuring equipment was located on a stationary platform.

As targets were used stones and metallic cylinders filled with concrete. The stones had diameters between 0.5 m and 1.5 m and masses between 100 kg and 800 kg. The two cylinders had a length of 1.8 m and a diameter of 0.8 m, one of them was coated with absorbing material. The water depth was between 9 and 14 m.

The transmitter was a quadratic array of nine tranducers, the receiver was an array of 19 hydrophones arranged in two parallel lines.

The transmitted pulses were Gaussian shaped with a half-width of the envelope of 1 ms. The carrier frequency was varied in steps of 500 Hz between 5 kHz and 14 kHz[33].

The conclusion from these observations was that it would not be possible to measure an acoustic spectrogram of isolated resonances. Displaying the echoes with the Wigner distribution was not very informative, too. Instead, an evaluation of the echo signals with neural networks was applied. One motivation for this attempt was the fact that experienced sonar operators are able to classify targets by listening to the echoes. A successful application of the neural network technique to this type of problems has also been published earlier[34,35].

As experience shows so far, classification performance is not improved if the raw data are preprocessed by conventional methods such as taking the segmented power spectral density, Walsh transform, or the time envelope as input for the neural network. Trying such data reduction methods without reference to the physical content of the scattering process has not proven useful.

At the scattering resonances the incoming wave strongly interacts with the interior of the target. Therefore, the resonances provide the key information about the

scatterer. This statement is not invalidated by the fact that in real world experiments the resonances often cannot be observed isolated from each other but that only a coherent superposition of many overlapping resonances is measured.

As outlined in the next section, a model function can be derived with the help of the "R-Matrix" formalism explaining the general way how overlapping resonances influence the backscattering amplitude. Matching this model function to measured scattering data promises to provide a feature vector meeting the requirements of data reduction and high classification reliability as well.

7 R-Matrix Theory

The "R-Matrix Theory" (RMT) of nuclear physics has been developed by Wigner and Eisenbud[36] to describe nuclear reactions. Some aspects of this theory are useful in acoustics, too. In nuclear physics this theory is now well established (see, e. g., Barrett[37] for a presentation together with other methods in nuclear scattering). The basic ideas of the theory are contained in the earlier papers as well, of course. In particular we found the article of Lane and Thomas[38] very useful. In this theory, the concept of scattering resonances is included from the very beginning: The surface impedance of the object and, hence, the scattering amplitude is written as a superposition of discrete eigenvibrations.There is some freedom in choosing the frequency-independent boundary values defining the eigenvibrations. So they can be chosen appropriately to ensure computational ease. When applying the nuclear theory to acoustical scattering, some re-definitions are necessary because the continuity relations of the Helmholtz equation differ from those of the Schrödinger equation.

It is this way of introducing the resonances with reference to properly defined eigenvibrations—in contrast to assigning resonances to poles—that will be understood by "R-Matrix-Theory" here.

Another topic has been called "R-matrix theory of sound scattering" by Gaunaurd and Überall[39]: The surface impedance of a fluid sphere is recognized as belonging to the class of "mathematical R-functions"[13,38] which can be expanded in a Mittag-Leffler series with respect to its poles (the argument is ω, Wigner regarded his general R-functions as depending on $E \sim \omega^2$). More directly, the scattering function itself can be expanded in a Mittag-Leffler series yielding an exact series representation in terms of the pole contributions[13] as mentioned above.

The method of calculation used in the following will now be outlined briefly. Imagine a sphere just wide enough to enclose the object. Compute the eigenvibrations of the sphere subject to properly chosen frequency-independent boundary values. Then express the surface impedance in two ways: in terms of the inner eigenfunctions, and in terms of the waves outside the sphere. Because both expressions must be equal, the scattering amplitude is written as a function of the eigenfrequencies. The eigenfrequencies can be related to the resonance frequencies. Radiation damping and overlap of the resonances are included in a natural way.

In the general case of an inhomogeneous (non-separable) object with many over-

lapping resonances, all modes will be coupled and therefore the S and R matrices will no longer be diagonal as in the separable case. The computations will be very involved, if not unpracticable. So a model function is desirable which contains the resonance frequencies and widths as adjustable parameters.

The reference scatterer providing the model function is chosen to be a sphere consisting of homogeneous, lossless material admitting scalar waves only (a more complicated reference object can allow vector waves if the simple model does not apply). It was shown in nuclear theory that the coupling of the modes is equivalent to introducing a complex frequency if many single resonances statistically overlap. This model is analogous to the "Moderate Absorption Model" of nuclear physics which can be related to R-Matrix theory by the "complex smoothed R function"[38].

The scheme sketched above[38,40,41] will now be explained in some more detail for a scatterer being a homogeneous sphere with density ρ and sound velocity c.

The interior field,

$$\Phi(r,\vartheta) \;=\; \sum_{l=0}^{\infty} \Phi_l(r) \cdot Y_{l,0}(r,\vartheta)\,, \tag{45}$$

can be written as a superposition of discrete eigenfunctions: By prescribing rather arbitrarily chosen, frequency-independent boundary values, a set of real eigenvalues $k_{\lambda l}$ and corresponding eigenfunctions,

$$X_{\lambda l} \equiv: \Phi_{\lambda l} \cdot Y_l\,, \tag{46}$$

$$\nabla^2 X_{\lambda l} = -k_{\lambda l}^2 X_{\lambda l}\,, \tag{47}$$

is defined for every angular momentum l ($k_{\lambda l} = \omega_{\lambda l}/c_i$ is the angular wave number and c_i the velocity of sound inside the scatterer, $Y_{l,0}$ are the Spherical Harmonics).

At a particular frequency ω every partial field with angular momentum l has the expansion

$$\Phi_{\omega l}(r) = \sum_{\lambda} A_{\lambda}\, \Phi_{\lambda l}(r)\,. \tag{48}$$

Choosing as boundary values

$$\frac{d\Phi_{\lambda l}}{dr}\bigg|_{r=R} = 0\,, \tag{49}$$

the expansion coefficients

$$A_{\lambda} = \int_{0}^{R} \Phi_{\lambda l}\, \Phi_{\omega l}\, r^2\, dr \tag{50}$$

are obtained from Green's Relation as

$$A_{\lambda} \;=\; \frac{R^2\, \Phi_{\lambda l}(R)}{(k_{\lambda l}^2 - k^2)} \cdot \left(\frac{d\Phi_{\omega l}}{dr}\right)_R\,. \tag{51}$$

So one has

$$\Phi_{\omega l}(r) =: G(r,R) \cdot \left(R \cdot \frac{d\Phi_{\omega l}}{dr} \right)_R \tag{52}$$

where

$$G(r,R) := R \cdot \sum_\lambda \frac{\Phi_{\lambda l}(R) \cdot \Phi_{\lambda l}(r)}{(k_{\lambda l}^2 - k^2)} \tag{53}$$

is the Green's Function. Taking the values at the boundary, the "Acoustical R-Function" $\mathcal{R}_l$,

$$\rho \cdot G(R,R) \equiv \frac{\rho \cdot \Phi_{\omega l}(r)}{R \cdot \left(\frac{d\Phi_{\omega l}}{dr} \right)} \Bigg|_R \quad = \quad \rho R \sum_\lambda \frac{\Phi_{\lambda l}^2(R)}{(k_{\lambda l}^2 - k^2)} \tag{54}$$

$$=: \sum_\lambda \frac{\gamma_{\lambda l}^2}{(\omega_{\lambda l}^2 - \omega^2)} =: \mathcal{R}_l . \tag{55}$$

and the "reduced line widths,"

$$\gamma_{\lambda l}^2 = c^2 \cdot \rho \cdot R \cdot \Phi_{\lambda l}^2(R) , \tag{56}$$

shall be introduced. These terms were chosen like the corresponding quantities in the nuclear theory of Wigner and Eisenbud. $\gamma_{\lambda l}^2$ und $\mathcal{R}_l$ depend on the boundary condition by $\Phi_{\lambda l}^2(R)$. Therefore the above definitions hold for a hard-walled boundary condition. Only in this case $\mathcal{R}_l$ equals the inverse of f_l.

Now the field inside the scatterer has been written as a superposition of discrete modes, and outside the scatterer as a sum of traveling waves. Continuity at the boundary requires that the impedances are equal:

$$\mathcal{R}_l = \frac{\rho_a \left(h_l^{(-)} - S_l h_l^{(+)} \right)}{R k_a \left(h_l^{\prime(-)} - S_l h_l^{\prime(+)} \right)} , \tag{57}$$

and therefore

$$S_l = \frac{\mathcal{R}_l \frac{R k_a}{\rho_a} \frac{h_l^{\prime(-)}}{h_l^{(-)}} - 1}{\mathcal{R}_l \frac{R k_a}{\rho_a} \frac{h_l^{\prime(+)}}{h_l^{(+)}} - 1} \cdot \frac{h_l^{(-)}}{h_l^{(+)}} . \tag{58}$$

Introducing with

$$L_l = \frac{R k_a}{\rho_a} \cdot \frac{h_l^{\prime(+)}(R)}{h_l^{(+)}(R)} = \Delta_l + i \, s_l \tag{59}$$

the logarithmic derivatives of the outgoing wave, then that of the incoming ones is L_l^-, and S_l reads:

$$S_l = \frac{h_l^{(-)}}{h_l^{(+)}} \cdot \frac{1 - \mathcal{R}_l L_l^-}{1 - \mathcal{R}_l L_l} . \tag{60}$$

Since $\mathcal{R}_l$ is real, S_l has modulus unity and can be written as

$$S_l = e^{2i\delta_l} . \tag{61}$$

The term

$$\frac{h_l^{(-)}}{h_l^{(+)}} =: e^{2i\varphi_l} \tag{62}$$

again represents the scattering function of a sphere with pressure release boundary. The argument of the remaining term is

$$2 \cdot \arg(1 - L_l^* \, \mathcal{R}_l) = 2 \cdot \arg(1 - \mathcal{R}_l \, \Delta_l + i \, \mathcal{R}_l \, s_l) = 2 \cdot \arctan\left(\frac{\mathcal{R}_l \, s_l}{1 - \mathcal{R}_l \, \Delta_l}\right) \tag{63}$$

so that the total scattering phase shift is the sum of the "resonance" and "background" contributions:

$$\delta_l = \arctan\left(\frac{\mathcal{R}_l \, s_l}{1 - \mathcal{R}_l \, \Delta_l}\right) + \varphi_l . \tag{64}$$

7.1   *Resonance definition by the "One-Level" approximation*

If the frequency ω under consideration is very close to an eigenfrequency $\omega_{\lambda l}$, all other contributions in $G(R, R)$ can be neglected to a first approximation:

$$\mathcal{R}_l \approx \frac{\gamma_{\lambda l}^2}{(\omega_{\lambda l}^2 - \omega^2)} . \tag{65}$$

Then the scattering phase reads

$$\begin{aligned}
\delta_l &= \arctan\left(\frac{s_l}{\frac{1}{\mathcal{R}_l} - \Delta_l}\right) + \varphi_l \\
&\approx \arctan\left(\frac{\frac{1}{2}\Gamma_{\lambda l}}{\omega_{\lambda l}^2 + \nu_{\lambda l}^2 + \omega^2}\right) + \varphi_l ,
\end{aligned} \tag{66}$$

where

$$\Gamma_{\lambda l} := 2 \cdot \gamma_{\lambda l}^2 \cdot s_l \tag{67}$$

is the line width and

$$\nu_{\lambda l}^2 := -\Delta_l \cdot \gamma_{\lambda l}^2 \tag{68}$$

is the line shift.

The line width $\Gamma_{\lambda l}$ measures how fast the scattering phase changes in the neighborhood of the resonance frequencies, defined by

$$\omega_{rl}^2 := \omega_{\lambda l}^2 + \nu_{\lambda l}^2(\omega_{rl}) . \tag{69}$$

In this way, each eigenfrequency is assigned to a resonance frequency. Widths and shifts of the resonances are influenced by the logarithmic derivatives of the outgoing waves $h_l^{(+)}$, the widths by the imaginary part only, and the shifts by the real part only.

$\Gamma_{\lambda l}$ and $\nu_{\lambda l}^2$ depend on ω, but often they can be considered constant over a single resonance.

7.2 *Choice of boundary values*

To define the eigenfunctions, boundary values different from the "hard-walled boundary" can be prescribed. Then the values of $\gamma_{\lambda l}^2, \omega_{\lambda l}, \mathcal{R}_l$ become functions of the boundary conditions. The R-function valid for the new boundary value,

$$\left. \frac{R \cdot \frac{d\Phi_{\lambda l}}{dr}}{\rho \cdot \Phi_{\lambda l}} \right|_{R^-} = B \ , \tag{70}$$

is related to $\mathcal{R}_l(0)$, valid for the hard-walled case, by

$$\left(\frac{1}{\mathcal{R}_l(0)} - B \right) \cdot \mathcal{R}_l(B) = 1 \ . \tag{71}$$

With Eq. (71) and Eq. (60) the relation between the scattering function and the new boundary value B is obtained:

$$S_l = \frac{h_l^{(-)}}{h_l^{(+)}} \cdot \frac{1 - \mathcal{R}_l (L_l^* - B)}{1 - \mathcal{R}_l (L_l - B)} \ . \tag{72}$$

Since B is a real number, a change of B influences $\Delta_l(B) = \Re(L_l - B)$ and therefore the line shift, but not the width. So the scattering phase seems (by Δ_l) to depend on B. Because the scattering phase is determined by the target whereas the value B can be chosen rather arbitrarily for the same target, this dependency does not really exist. So the dependencies on B in $\mathcal{R}_l$ and Δ_l must cancel each other.

7.3 *Air bubble in water*

A rather good realization of the simple scatterer treated above may be an air bubble in water. In the acoustical literature several suggestions have been made how to choose an appropriate background whose subtraction from the total field gives the resonances as isolated peaks. In R-Matrix Theory no assumptions must be made with respect to the background: the background of a single resonance is obtained by computing the scattering function omitting the resonance term under consideration in the R-function.

A proper choice of the boundary values is, according to Peine[41],

$$B_l = -\frac{(l+1)}{\rho} \ . \tag{73}$$

Then the eigenfrequencies are determined by the equation

$$\frac{d(r\Phi_{\omega l})}{dr}\bigg|_{R} = -l\,\Phi_{\omega l} \,. \tag{74}$$

For $l = 0$ one has $\cos(k_{\lambda l}R) = 0$, and for $l > 0$ with $j'_l = j_{l-1} - \frac{(l+1)}{(kR)}j_l$ and $r \cdot \Phi_{\omega l} = r \cdot j_l(kr)$ the equation becomes

$$(k_{\lambda l}R) \cdot j_{l-1}(\omega_{\lambda l} \cdot R/c) = 0 \,. \tag{75}$$

The reduced line widths,

$$\gamma_{\lambda l}^2 = \frac{2\,\rho\,c^2}{R^2} \,, \tag{76}$$

do not depend on l or λ.

The "background R-function" $\mathcal{R}_l^\circ$ contains all the terms of the complete R-function except for the resonance term. The result is[38]:

$$\mathcal{R}_l^\circ(\omega_{\lambda l}) = \frac{2l+1}{2\,(k_{\lambda l}R)^2} \,. \tag{77}$$

For $l = 0$ the eigenfrequencies are known analytically $(\cos(k_{\lambda 0}R) = 0)$:

$$\mathcal{R}_0^\circ(\omega_{\lambda 0}) = \frac{2}{\pi^2(2\lambda - 1)^2} \,. \tag{78}$$

It can be seen that the contribution $\mathcal{R}_0^\circ(\omega_{\lambda 0})$ of the other resonances becomes smaller with increasing frequency $\omega_{\lambda 0}$. From Eq. (77) follows that the contribution of the other resonances becomes greater with increasing l.

8   Model function for statistically overlapping resonances

8.1   *Spherical reference target*

If one has a realistic target with many statistically distributed resonances, it seems to be a good approximation to describe the scatterer by the phenomenological model mentioned above[38,41]: the scatterer should not be understood to be the object itself, but the interior of a sphere containing the object. This scatterer can be treated as if it were a homogeneous sphere with density ρ and sound velocity c, if the energy leakage of the modes is taken into account by introducing a complex wave number in the interior:

$$(k\,c)^2 = \omega^2 + i\,d^2 \,. \tag{79}$$

Thereby the coupling of modes as well as energy dissipation can be described.

As mentioned above, this model is analogous to the "Moderate Absorption Model" of nuclear physics replacing the R matrix by "R functions"[38].

Defining the non-dimensional quantities

$$x_{\lambda l} := \frac{\omega_{\lambda l}}{c_i} \cdot R, \qquad x := \frac{\omega}{c_a} \cdot R, \tag{80}$$

$$y := \frac{d}{c_a} \cdot R, \tag{81}$$

$$u := \frac{\rho_i}{\rho_a}, \qquad v := \frac{c_i}{c_a} \tag{82}$$

one obtains with Eqs. (55) and (76)

$$S_l(x) = \frac{h_l^{(-)}(x)}{h_l^{(+)}(x)} \cdot \frac{1 - \mathcal{R}_l^b(x) \cdot \left(\frac{x\, h_l'^{(-)}(x)}{h_l^{(-)}(x)} + \frac{(l+1)}{u} \right)}{1 - \mathcal{R}_l^b(x) \cdot \left(\frac{x\, h_l'^{(+)}(x)}{h_l^{(+)}(x)} + \frac{(l+1)}{u} \right)} \tag{83}$$

where

$$\mathcal{R}_l^b(x) := \mathcal{R}_l^\infty(x) + i\,\pi\,p_l(x), \tag{84}$$

$$\pi\,p_l(x) := 2\,u\,v^2 \cdot \sum_\lambda \frac{y^2}{[v^2\,x_{\lambda l}^2 - x^2]^2 + y^4}, \tag{85}$$

$$\mathcal{R}_l^\infty(x) := 2\,u\,v^2 \cdot \sum_\lambda \frac{v^2\,x_{\lambda l}^2 - x^2}{[v^2\,x_{\lambda l}^2 - x^2]^2 + y^4}. \tag{86}$$

Especially for $l = 0$:

$$S_0(x) = e^{-2\,i\,x} \cdot \frac{1 - \mathcal{R}_0^b(x) \cdot \left(\frac{1}{u} - 1 - i\,x \right)}{1 - \mathcal{R}_0^b(x) \cdot \left(\frac{1}{u} - 1 + i\,x \right)}, \tag{87}$$

$$\mathcal{R}_0^b(x) := \frac{u \cdot v}{(x^2 + i\,y^2)^{1/2}} \cdot \tan\left(\frac{(x^2 + i\,y^2)^{1/2}}{v} \right). \tag{88}$$

If one of the functions p_l and $\mathcal{R}_l^\infty$ is known for all frequencies, the other one can be calculated because they are Hilbert transforms of each other. p_l will be called "pole strength" and $\mathcal{R}_l^\infty$ "background" further on.

The modal backscattering form function (and thereby the differential backscattering cross-section at $\vartheta = \pi$) is given by

$$g_l(\pi; x) = \frac{a}{2\,x} \cdot (2l + 1) \cdot (1 - S_l(x)) \cdot (-1)^l \tag{89}$$

where a is the radius of the separable reference scatterer.

Eqs. (83) through (88) are model functions that can be matched to measured backscattering amplitudes. The quantities u, v, $x_{\lambda l}$ and y are the adjustable parameters. More generally, y can be allowed to depend on the resonance frequency and the specific mode, for example.

So the number of free parameters can be reduced if the pole strength is approximately determined from the experimental data. This curve fit based on the above model can be justified beyond computational simplicity by physical arguments, too.

If the target has a separable geometry, each outer vibration mode excites only the eigenstates of one inner mode, and if outer and inner fields are weakly coupled $(\rho_i/\rho_a, c_i/c_a \ll 1$ or $\gg 1)$, only the value $\gamma_{\lambda' l}$ of that eigenstate $\Phi_{\lambda' l}$ will differ from zero considerably whose eigenfrequency is closest to the frequency ω of the impinging field. If the impedance discontinuity becomes smaller, coupling becomes stronger and more of the adjacent eigenstates will be excited as well. So the function $\gamma_{\lambda' l}(\omega)$ will no longer consist of single peaks, but will be smeared out over many eigenfrequencies. These considerations remain true in principle if the target is no longer separable, but then every outer mode is coupled with all inner eigenstates.

So the pole strength of a realistic target, which may be imagined as the envelope of the function $\gamma_{\lambda' l}(\omega)$, can be approximated by the pole strength of the phenomenological model.

Only the coherent superposition of all modes can be measured. This superposition is much more complicated in the general case than in the case of a separable target: replacing the R-matrix by the R functions does not mean a diagonalization of the R-matrix. It is a formulation which describes the behavior of one mode (diagonal element) or of two modes (off-diagonal elements) by "eliminating" formally all other modes[36].

However, if each outer mode is coupled with many inner modes, the $\gamma_{\lambda l}$ will have positive and negative signs with equal probability. So the diagonal elements will dominate, because the elements of $\mathcal{R}_{ll'}$ contain terms of the form $\gamma_{\lambda l}\gamma_{\lambda l'}$ all of which are positive within the diagonal elements only.

Therefore the application of the phenomenological model is justified if the inner eigenstates are "strongly mixed."

As few terms of the R-function as possible should be taken in the vicinity of the center frequency ω of the incident pulse. The set of parameters obtained in this way characterizes the scatterer and can be used as a feature vector for a classifier such as a neural network.

8.2   *Model calculations*

Some exemplary plots of the above functions follow. Computations are carried out for reference scatterers with $\rho_i < \rho_a$, $c_i < c_a$ (case 1) and $\rho_i > \rho_a$, $c_i > c_a$ (case 2) with different values for the parameter y. The surrounding medium is water. As an example for the first case, the data of air are taken for ρ_i and c_i. For the second case the density of the target is chosen to be that of steel, the sound speed c of the target material is set as the velocity of shear waves in steel rather arbitrarily, see Table 1.

Figure 1 shows typical forms of pole strength and background. Figure 2 shows an example of the scattering amplitude $(\equiv |1 - S_l(x)|,\ 0 \le |1 - S_l(x)| \le 2)$. In the plots "modal backscattering form function" is abbreviated by "form function." It is calculated with the radius a set to unity. If y is small, sharp isolated resonances are

Table 1: Data used for model computations.

	$\rho\ [kg/m^3]$	$c\ [m/s]$
case 1	1.2	344
water	1000	1480
case 2	7700	3240

obtained (Fig. 3). In the form function the resonances are less pronounced (Fig. 4). Not until y becomes very small (≈ 0.01), isolated resonances are visible in the form functions (Fig. 5) and even in the backscattering cross section (Fig. 6). Fig. 7 gives an example of the interference of two adjacent resonances.

It follows in turn that even when no isolated resonances are detectable in the cross section, resonance structures can be present in the pole strength and background functions.
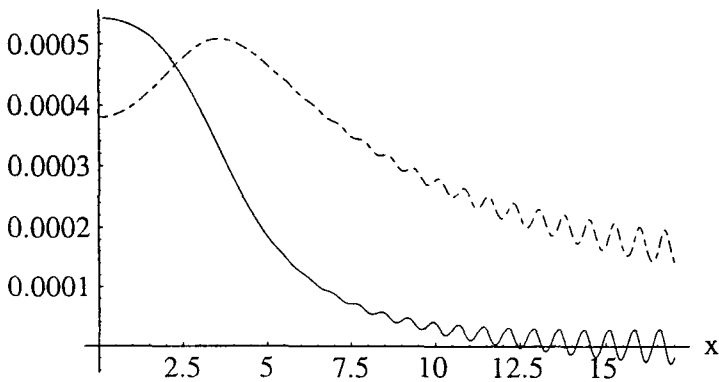
Figure 1: Pole strength (dotted line) and background (solid line) for case 1, $y = 3.1$ and $l = 7$.

Just to avoid possible confusion: The plots showing isolated resonances consist of a smooth curve, representing the geometrical shape, and the resonances. This smooth curve is often called "background" in the RST literature[4,17] and must not be confused with the "background R-function." Furthermore, in the plots the phases of $h_l^{(-)}(x)$ and $h_l^{(+)}(x)$ are chosen different from those used by Sage[17], leading to a shift of π in the scattering phase.

The *isolated* resonances shown here are those of the model function, of course. The Eqs. (83) through (88) with $y = 0$ are valid *exactly*, if the target *actually is* a sphere made of homogeneous material admitting only compressional waves propagating without any energy loss. Especially the sums in Eqs. (85) and (86) are not "symbolic" as in the Breit-Wigner formula[17], where only that term of the sum containing the resonance frequency nearest to the frequency of the impinging wave is valid (this corresponds to the one-level approximation described above). Here resonance behavior occurs at the eigenfrequencies, which depend on the choice of the boundary values used to define the eigenfunctions. Just to repeat it for clarity, boundary values different from those used here leading to different eigenfrequencies could be chosen in describing the same scatterer. To each of the eigenfrequencies can be assigned a "resonance line" via the one-level approximation: whereas the eigenfrequencies have no width (corresponding to poles *on* the real frequency axis), the resonance line has a width different from zero (corresponding to poles *off* the real axis), and there is a frequency shift between the eigenfrequency and the one-level resonance frequeny. The so-defined width of the one level resonance has nothing to do with the parameter y, of course.
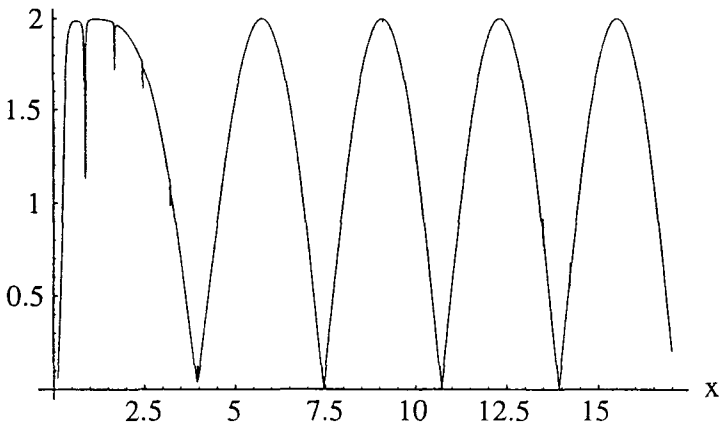

Figure 2: Case 1: Scattering amplitude for $l = 2$ and $y = 0.13$.

The boundary values taken here to define the eigenfrequencies allow reference to results known already in nuclear physics, they lead especially to simple values for the eigenfrequencies, Eq. (75), and reduced line widths, Eq. (76).

The model is supposed to reproduce the resonance behavior of a *general* target, if the target exhibits many statistically overlapping resonances. Then y will be rather large and *no isolated* resonances are visible in the form functions. The pole strength and background functions will then roughly look as in Figure 1 exhibiting no isolated

resonances. Then the eigenfrequencies of the reference scatterer can no longer be assigned to the many statistically overlapping resonances of the real target. As basis for the model function serves a sphere consisting of homogeneous, lossless material admitting scalar waves only. Analogous to the treatment in nuclear physics mode coupling and dissipation of any target can be taken into account by introducing a complex wave number.

A realistic target is likely to have a rather complicated structure (e.g., containing struts and electrical equipment), and shear- as well as compressional waves will propagate with dissipation in its components. Computing the exact scattering function with corresponding resonance poles for those targets may be very cumbersome, if not analytically unpracticable. However, matching the proposed model function to measured backscattering data provides a method to simulate the *general way* how resonances physically influence the scattering function.

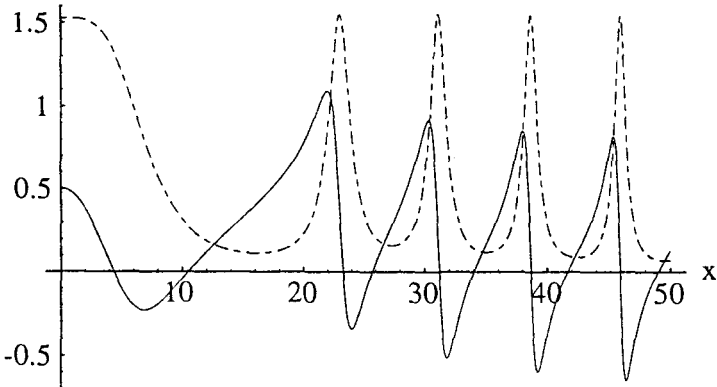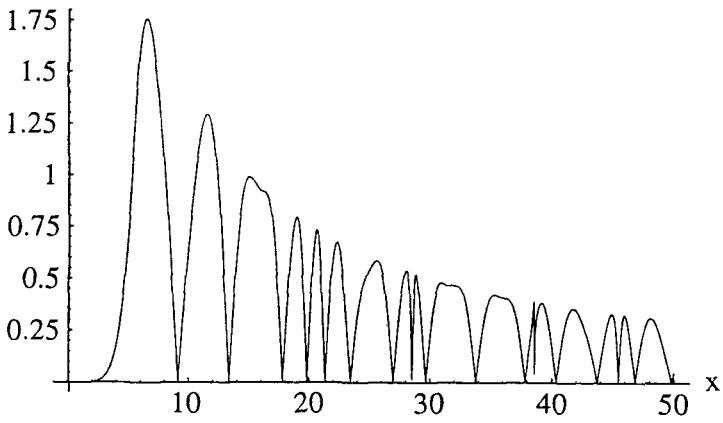Figure 3: Case 2: Pole strength (dotted) and background (solid) for $y = 7.0$ and $l = 7$.

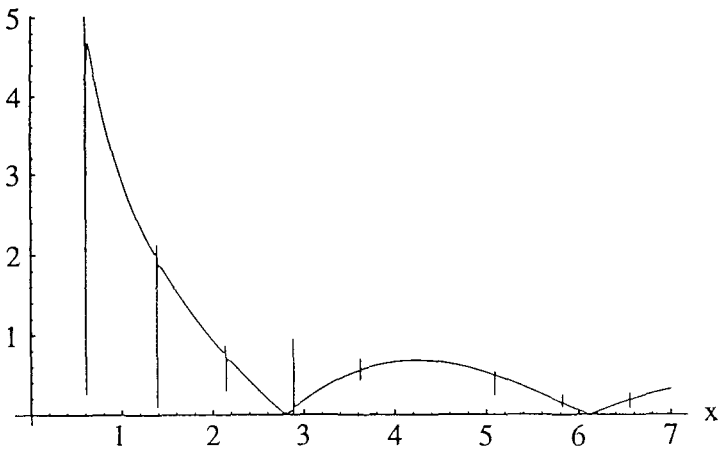Figure 4: Case 2: Modulus of form function for $l = 7$ and $y = 0.7$.

Figure 5: Case 1: Modulus of form function for $l = 1$ and $y = 0.01$.
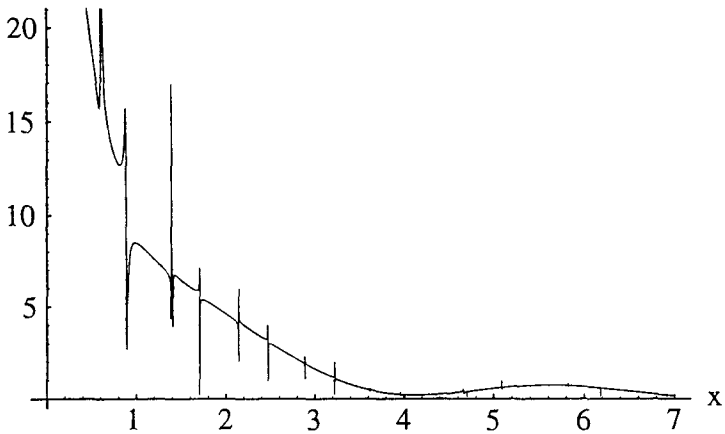
Figure 6: Case 1: Differential cross-section. The modes with $l = 0, 1, 2$ are summed up, $y = 0.01$.
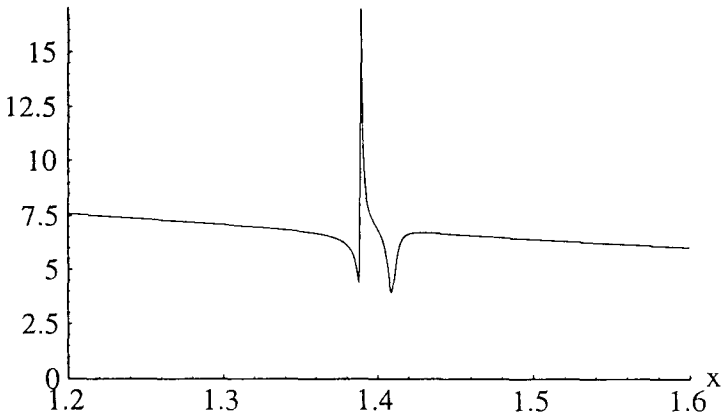
Figure 7: Detail of Figure 6 in the range $1.2 \leq x \leq 1.6$.

9   Conclusion

The resonances are important identification features because they represent the interaction of the impinging wave and the interior of the target. Therefore, the parameters obtained by matching the proposed model function to measured cross sections should yield better classification results than feature vectors obtained by other, rather heuristic data reduction methods. So the idea of acoustical spectroscopy is no longer restricted to isolated resonances.

The method outlined in this paper has not yet been tested experimentally. As a first step, model experiments with high signal-to-noise ratio should be made.

10   Acknowledgements

11 References

1. M. Hund, *Acustica* **15** (1965) 88–97.

2. R. Boisch, D. Guicking, *Acustica* **45** (1980) 322–339.

3. R. Boisch, D. Guicking, *Acustica* **51** (1982) 29–43.

4. L. Flax, G. C. Gaunaurd, H. Überall, in *Physical Acoustics*, ed. W. P. Mason, R. N. Thurston, Vol. **15** (1981) 191–294.

5. D. Brill, G. C. Gaunaurd, H. Überall, *Acustica* **53** (1983) 11–18.

6. M. F. Werby, *J. Acoust. Soc. Am.* **90** (1991) 3279–3287.

7. G. C. Gaunaurd, M. F. Werby, *J. Acoust. Soc. Am.* **77** (1985) 2081–2093.

8. H. Überall et al., *J. Acoust. Soc. Am.* **66** (1979) 1161–1172.

9. G. Maze, F. Lecroq, D. Décultot, J. Ripoche, S. K. Numrich, H. Überall, *J. Acoust. Soc. Am.* **90** (1991) 3271–3278.

10. W. G. Neubauer, R. H. Vogt, L. R. Dragonette, *J. Acoust. Soc. Am.* **55** (1974) 1123–1129.

11. J. Humblet, L. Rosenfeld, *Nuclear Physics* **26** (1961) 529–578.

12. S. K. Numrich, W. E. Howell et al., *J. Acoust. Soc. Am.* **80** (1986) 1161–1169.

13. N. G. Van Kampen, *Phys. Rev.* **89** (1953) 1072–1079.

14. E. B. Paul, *Nuclear and Particle Physics* (North Holland Publishing Company, 1969).

15. J. M. Blatt, V. F. Weisskopf, *Theoretical Nuclear Physics* (John Wiley & Sons, 1956).

16. K. B. Mather, P. Swan, *Nuclear Scattering* (Cambridge University Press, 1958).

17. K. A. Sage, J. George, H. Überall, *J. Acoust. Soc. Am.* **65** (1979) 1413–1422, here: p. 1415.

18. H. Feshbach, D. C. Peaslee, V. F. Weisskopf, *Phys. Rev.* **71(3)** (1947) 145–158.

19. H. M. Nussenzveig, *Causality and Dispersion Relations* (Academic Press, 1972).

20. G. C. Gaunaurd, D. Brill, *J. Acoust. Soc. Am.* **75** (1984) 1680–1693.

21. G. C. Gaunaurd, M. F. Werby, *J. Acoust. Soc. Am.* **82** (1987) 2021–2033, here: p. 2025.

22. M. L. Rumerman, *J. Acoust. Soc. Am.* **90** (1991) 2739–2750.

23. H. A. Bethe, G. Placzek, *Phys. Rev.* **51** (1937) 450–484.

24. C. Y. Tsui, G. N. Reid, G. C. Gaunaurd, *J. Acoust. Soc. Am.* **80** (1986) 382–390.

25. G. Maze, B. Taconet, J. Ripoche, *Physics Letters* **84A** (1981) 309–312.

26. H. Überall, in *Physical Acoustics*, ed. W. P. Mason, R. N. Thurston, Vol. **10** (1973) 1–60.

27. N.-C. Yen, L. R. Dragonette, S. K. Numrich, *J. Acoust. Soc. Am.* **87** (1990) 2359–2370.

28. E. C. Bekir, *J. Acoust. Soc. Am.* **93** (1993) 363–371.

29. D. H. Hughes, P. L. Marston, *J. Acoust. Soc. Am.* **94** (1993) 499–505.

30. L. Cohen, *Proc. IEEE* **77** (1989) 941–981.

31. S. Abrahamsson, B. Brunsmark, H. C. Strifors, G. C. Gaunaurd, SPIE Conference No. 1700 (Automatic Object Recognition II), Orlando, Florida, USA, April 22–24, 1992. Proceedings: pp. 102–113.

32. H. Überall, G. C. Gaunaurd, *Appl. Phys. Lett.* **39** (1981) 362–364.

33. D. Guicking, K. Görk, H. Peine, SPIE Conference 1700 (Automatic Object Recognition II), Orlando, FL, USA, April 22–24, 1992. Proceedings: pp. 2–15.

34. R. P. Gorman, T. J. Sejnowski, *IEEE Trans. Acoustics, Speech, and Signal Processing* **36** (1988) 1135–1140.

35. R. P. Gorman, T. J. Sejnowski, *Neural Networks* **1** (1988) 75–89.

36. E. P. Wigner, L. Eisenbud, *Phys. Rev.* **72** (1947) 29–40.

37. R. F. Barrett, B. A. Robson, W. Tobocman, *Rev. Modern Phys.* **55** (1983) 155–243.

38. A. M. Lane, R. G. Thomas, *Rev. Modern Phys.* **30** (1958) 257–352.

39. G. C. Gaunaurd, H. Überall, *J. Acoust. Soc. Am.* **68** (1980) 1850–1857.

40. H. Peine, D. Guicking, *"Acoustical resonance scattering theory for strongly overlapping resonances"*, to be published in ACTA ACUSTICA (Vol. 3, No. 3, July 1995).

41. H. Peine, *Theoretische und experimentelle Untersuchungen zur akustischen Resonanzstreuung und Resonanzklassifikation* (Doctoral Thesis, Universität Göttingen, 1993).

INVERSE SCATTERING BASED ON THE RESONANCES
OF THE TARGET

PIER PAOLO DELSANTO
Dipartimento di Fisica, Politecnico Torino, I-10129 Italy

ARDESHIR GURAN
Institute for Structronics, 275 Slater Street, Ottawa, Canada K1P 5H9

ANTON NAGL and HERBERT ÜBERALL
Physics Department, Catholic University of America, Washington, DC 20064, USA

ABSTRACT

The Resonance Scattering Theory (RST) has been developed for acoustic scattering in 1977 [L. Flax, L. R. Dragonette, and H. Überall, "Theory of elastic resonance excitation by sound scattering," *J. Acoust. Soc. Am.* **63** (1978) 723; first presented to the public at the Symposium on Modern Problems in Elastic Wave Propagation, Northwestern University, Evanston, IL, September 1977: H. Überall, "Modal and surface wave resonances in acoustic wave scattering from elastic objects and in elastic wave scattering from cavities," in *Proc. Internat. Union Theoretical and Applied Mechanics (IUTAM) Symposium: Modern Problems in Elastic Wave Propagation*, ed. J. Miklowitz and J. Achenbach (John Wiley, New York, 1978) pp. 239-263], and has very shortly thereafter been extended to the resonance scattering of elastic waves, and later on to the scattering of electromagnetic waves (radar). An overview of the acoustic development is given in the book *Acoustic Resonance Scattering*, ed. H. Überall (Gordon and Breach, New York, 1992) where also the experimental work in this domain is presented. It is seen that resonance amplitudes in acoustic scattering from submerged elastic objects, which the RST describes in a mathematical fashion, are a dominant feature in the acoustic echoes which can be used to effect an "acoustic resonance spectroscopy" (as pointed out by André Derem). Such a spectroscopy can be used for characterizing the target as to its size, shape, and composition, and can ultimately lead to a procedure or a mechanism for (automatic) target recognition.

1. Introduction and Historical Remarks

The echo returned in acoustic scattering from (submerged) elastic objects consists of two coherent parts: an amplitude which varies smoothly with frequency, and which would be present even if the object were impenetrable to sound (this will be referred to as the acoustic "background amplitude"); and a resonant amplitude which, plotted as a function of frequency, shows a spectrum of resonance peaks which coincide with the eigenfrequency spectrum of the vibrations of the scatterer. The Resonance Scattering

Theory[1,2] (RST), correspondingly, carries out two functions:

(1) It mathematically separates the background amplitude from the resonant amplitude (such a first step had already been accomplished by Junger[3], but in the RST this step is carried out using the formalism of the resonance scattering theory of nuclear physics, see below), and

(2) it mathematically expresses the resonant amplitude in a form where its resonance character is exhibited explicitly. This includes a determination of the target eigenfrequencies, as well as of the widths of the resonance peaks.

Steps (1) and especially (2) were accomplished in Ref. 1 by patterning the mathematical approach after the resonance scattering formalism previously developed in nuclear physics. Resonances in nuclear scattering were first discussed qualitatively by Niels Bohr[4], and are generally associated with the names of Breit and Wigner[5,6]. A simplified, lucid derivation of nuclear resonance scattering theory was provided by Feshbach, Peaslee, and Weisskopf[7], which has been utilized in our corresponding derivation of acoustic resonance scattering[1].

The derivation of the resonance formula, by linearization of the denominator of the amplitude via a Taylor expansion, is also given in the book by J. M. Blatt and V. F. Weisskopf[8], *Theoretical Nuclear Physics*. A corresponding procedure was applied to the acoustic scattering amplitude. For normal incidence on a solid elastic cylinder of radius a, this amplitude is[1] (k = acoustic wave number):

$$P_{sc} = \frac{1}{2} \sum (2 - \delta_{n0})\, i^n\, (S_n - 1) H_n^{(1)}\, (kr) \cos n\varphi, \tag{1}$$

the diagonal terms of Heisenberg's "S matrix", S_n, being given explicitly in quotient form N_n/D_n. Out of this quotient one may factor the rigid-cylinder scattering amplitude

$$S_n^r = -H_n^{(2)'}(x)/H_n^{(1)'}(x) \equiv e^{2i\xi_n}, \tag{2}$$

(x = ka), which here plays the role of the acoustic background mentioned above. This leads to S_n being of the form

$$S_n = S_n^r \frac{L_n^{-1} - z_2^{-1}}{L_n^{-1} - z_1^{-1}}, \tag{3}$$

with

$$z_i^{-1} = H_n^{(i)}(x)/x H_n^{(i)'}(x) \equiv \Delta_n \pm i s_n. \tag{4}$$

Expanding the known quantity

$$L_n^{-1}(x) \cong \Delta_n + \beta_n (x - x_n) + \ldots \tag{5}$$

about the resonance frequencies x_n, which are determined from the zeros of the denominator in Eq. (3), we get

$$S_n \equiv e^{2i\delta_n} = S_n^r \frac{x - x_n - (i/2)\Gamma_n}{x - x_n + (i/2)\Gamma_n} . \tag{6a}$$

This establishes the resonance form of S_n, and hence establishes the RST in acoustics, via its crucial step (2), see above.

The resonance width Γ_n is determined by the expression

$$\Gamma_n = -2s_n/\beta_n, \tag{6b}$$

so that all expressions in Eqs. (3) are known.

In the scattering amplitude of Eq. (1), there enters the quantity $S_n - 1 = 2i \exp(i\delta_n) \sin \delta_n$, which we may thus write

$$S_n - 1 = 2ie^{2i\xi_n} \left\{ \sum_l \frac{\frac{1}{2}\Gamma_n}{x_{nl} - x - (i/2)\Gamma_{nl}} + e^{-i\xi_n} \sin \xi_n \right\}. \tag{7}$$

This expression, first used in acoustics by Flax, Dragonette and Überall[1], shows that each modal amplitude has resonant terms, but also a nonresonant "background" term, i.e., step (1), see above (second term), corresponding here to rigid-body scattering (called "potential scattering" in nuclear physics). From Eq. (7), it is evident that if we subtract the rigid-body scattering amplitude $S_n^r - 1 = 2i \exp(i\xi_n) \sin\xi_n$ from $S_n - 1$, then we are left with the purely resonant amplitude

$$S_n^{\text{res}} = 2ie^{2i\xi_n} \sum_l \frac{\frac{1}{2}\Gamma_{nl}}{x_{nl} - x - (i/2)\Gamma_{nl}}. \tag{8}$$

This completes both step (1) and (2) of the RST, as mentioned above. A rigorous derivation of the background amplitude was given later on by Choi[9]; background amplitudes for elastic objects intermediate between rigid and soft ones were obtained by Werby[10].

In addition to this purely mathematical algorithm, the RST can also help us understand the physics underlying the resonances. Franz[11] has shown, using the Watson transformation, that the diffracted field about an obstacle can be mathematically resolved into a coherent sum of what he called "creeping waves" (also later known as

surface waves, circumferential or peripheral waves) which propagate along the surface of the target. He did this for impenetrable objects where the surface waves are excited at tangential incidence and propagate solely in the ambient medium. For elastic targets of acoustic waves, elastic body-type surface waves may be excited also at the angle of incidence $\alpha = \sin^{-1}(c/c_\ell)$, where c = sound velocity in the ambient medium, c_ℓ = phase speed of the ℓth elastic surface wave. These propagate below the surface of the target, and may be classified as a (leaky) Rayleigh-type wave, and a series of Whispering Gallery waves[12-14]; an additional Scholte-Stoneley wave also appears in the ambient medium.

The resonance representation of the scattered field can now be converted to a description in terms of surface waves[15,16], from which the origin of the resonances can be recognized as the condition that after each circumnavigation, the surface wave is in phase with itself. This "principle of phase matching" entails that a resonant reinforcement of surface waves will take place, generating the resonance at a specific resonance frequency (since the surface waves are dispersive). In this way, the physical origin of the resonances is understood. To sketch this derivation briefly, we represent the scattering amplitude of a cylinder in the form

$$f_n(\varphi) = \sum_{n=0}^{\infty} f_n(\varphi) \ , \tag{9}$$

f_n having the resonance form (see above)

$$f_n(\varphi, \omega) \cong A_n(\varphi) \frac{(\Gamma/2\pi)^{1/2}}{\omega - \omega(n) + \frac{1}{2} i \Gamma} \ , \tag{10}$$

now using the frequency variable ω and the resonance frequencies $\omega(n)$. This amplitude has a pole at the complex frequency $\omega = \omega(n) - (1/2)i\Gamma$, located below the real axis of the ω plane.

For a fixed frequency ω, $f_n(\varphi,\omega)$ may be considered a function of n; thus, one may expand

$$\omega(n) \cong \omega(n_\omega) + (n - n_\omega) \, \omega'(n_\omega), \tag{11}$$

where[1] $\omega'(n_\omega) > 0$, and one may choose n_ω so that $\omega(n_\omega) = \omega$, i.e., the fixed incident frequency lies at the resonance peak when $n = n_\omega$. Then, the amplitude

$$f_n(\varphi, \omega) \cong \frac{-A_n(\varphi)}{[\omega'(n_\omega)]^{1/2}} \frac{(\hat{\Gamma}/2\pi)^{1/2}}{n - n_\omega - \frac{1}{2} i \hat{\Gamma}} \tag{12}$$

appears with a pole in the complex n plane, located at $n = n_\omega + (1/2)i\hat{\Gamma}$ above the real n axis since

$$\hat{\Gamma} \equiv \Gamma/\omega'(n_\omega) > 0 \ . \tag{13}$$

In terms of the n variable, this is known as a Regge pole[17], and we see that one and the same pole of the scattering amplitude may appear as a resonance in the ω as well as in the n variable (although only integer values of n correspond to physical values of the amplitude). If n is considered a parameter and ω the variable, the n dependence of the resonance frequency $\omega(n)$ in Eq. (10) causes a "Regge recurrence" of the one Regge pole under consideration in all successive partial waves at successively higher resonance frequencies[1,15]. In the following, however, we shall discuss the aspects of the scattering amplitude given by Eq. (12), as it provides a physical picture of the scattering process in terms of surface waves, as well as a physical explanation of the mechanism of resonance excitation.

Applying the Watson transformation to the normal-mode series for sound scattering from an elastic cylinder, the surface waves generated in the scattering process were shown to be given by[18]

$$p_{sc} = -2\pi \sum_{l} \frac{\cos\nu_l\varphi}{\sin\pi\nu_l} e^{-i\nu_l\pi/2} \frac{b_{\nu_l}}{\dot{D}_{\nu_l}} H^{(1)}_{\nu_l}(kr) \quad , \tag{14}$$

where $D_\nu = \partial D_\nu/\partial\nu$, ν is the modal number of the Rayleigh series turned into a complex variable, b_ν is a 3x3 determinant, D_ν is the secular determinant of the problem[18] and $\nu = \nu_l(\omega)$ are the complex roots of the latter,

$$\nu_l(\omega) = \operatorname{Re}\nu_l(\omega) + i\operatorname{Im}\nu_l(\omega) \tag{15}$$

($l = 1,2,3,...$). As a function of frequency, the lth root $\nu_l(\omega)$ will, at some resonance frequency $\omega = \omega_{nl}$, move past the integer n, so that $\operatorname{Re}\nu(\omega_{nl}) = n$. In Ref. 15, the resonance frequencies ω_{nl} were shown to coincide with the eigenfrequencies of the elastic vibrations of the cylinder. In the vicinity of the resonance frequency where $\nu_l = n + \delta\nu_l$, and considering the case of $\operatorname{Im}\nu_l \ll 1$, one has

$$\frac{1}{\sin\pi\nu_l} \cong \frac{1}{(-1)^n\pi\delta\nu_l} = \frac{-(-1)^n}{\pi} \frac{1}{n-\nu_l} \tag{16}$$

If we now identify $\operatorname{Re}\nu_l = n_\omega$ and $\operatorname{Im}\nu_l = (1/2)\hat{\Gamma}$, then Eq. (16) and hence the scattering amplitude of Eq. (14) assumes precisely the Regge pole form of Eq.(10) where we can consider n to be a continuous variable. This shows that as the incident frequency ω passes past the nth resonance frequency of the lth surface wave, ω_{nl}, the corresponding surface wave goes through a resonance.

It is not hard to explain the physical origin of the frequency resonances with the help of the expansion

$$\frac{\cos\nu_l\varphi}{\sin\pi\nu_l} = -i\sum_{\lambda=\pm 1}\sum_{m=0}^{\infty} e^{i\nu_l(\lambda\varphi+\pi+2m\pi)} \quad . \tag{17}$$

If used in Eq. (14), and remembering the time factor exp(-iωt), it shows that for m = 0, two surface waves of mode ℓ propagate in the counterclockwise (λ = 1) and in the clockwise (λ = -1) direction around the cylinder, joined by other such waves with m > 0 that already have encircled the cylinder m times previously (of course with larger and larger attenuation since $\mathrm{Im}v_\ell \neq 0$), corresponding to the steady-state situation considered here. The wavelength λ_ℓ of the ℓth surface wave is given by

$$\lambda_\ell = 2\pi a / \mathrm{Re}\,\nu_\ell(\omega) \ , \tag{18}$$

and at the resonance frequency $\omega = \omega_{n\ell}$ where $\mathrm{Re}\,\nu_\ell = n$, one sees that exactly n wavelengths of the surface wave fit the circumference of the target (which may be referred to as the "phase matching condition"), and hence lead to a resonant reinforcement of the circumferential wave in the course of its repeated circumnavigations.

For historic reasons, and for demonstration of priorities, we document here the development of all the different aspects of the Resonance Scattering Theory as it was presented at successive semiannual meetings of the Acoustical Society of America (ASA), to wit:

(a) H. Überall, L. R. Dragonette and L. Flax, "Relation between creeping waves and normal modes of vibration of a curved body", 92nd ASA Meeting, San Diego, CA, 15-19 Nov. 1976 (abstract deadline: 17 August 1976), *J. Acoust. Soc. Am.* **60**, Suppl. 1, Fall 1976), talk Y6 [Mode resonances at the eigenfrequencies].

(b) J. W. Dickey and H. Überall, "Amplitudes of transmitted and circumferential waves in sound scattering from an elastic cylinder," ibid. talk Y7 [Separation of "geometrical" background and "diffracted" resonating surface (creeping) waves].

(c) L. R. Dragonette, L. Flax, and H. Überall, "Regge pole character of resonances in sound scattering from elastic bodies", 93nd ASA Meeting, Pennsylvania-State University, 6-10 June 1977 (abstract deadline: March 8, 1977), *J. Acoust. Soc. Am.* **61**, Suppl. 1, Spring 1977), talk T1 [Resonances in partial waves; relation to nuclear physics].

(d) K. A. Sage, J. George and H. Überall, "Multipole resonances in sound scattering from gas bubbles in a liquid", 95th ASA Meeting, Providence, R.I., 16-19 May 1978 (abstract deadline: 3 Feb. 1978), *J. Acoust. Soc. Am.* **63**, Suppl. 1, Spring 1978), talk D13 [Resonances of gas bubbles, described by nuclear physics techniques].

(e) A. J. Haug, S. G. Solomon and H. Überall, "Scattering of elastic waves by a resonating fluid-filled cylindrical cavity", ibid. talk 01 [Resonance scattering from cylindrical cavities].

(f) J. D. Murphy, E. D. Breitenbach, and H. Überall, "Resonance scattering of acoustic waves from cylindrical shells", ibid, talk 02.

(g) G. C. Gaunaurd and H. Überall, "Scattering of dilatational waves incident on a resonating fluid-filled spherical cavity inside a sound-absorbing material", ibid., talk 03 [Resonance scattering from spherical cavities].

The development presented above that leads from Eq. (9) to Eq. (18) shows how a physical explanation of the resonances can be obtained from the resonance expression
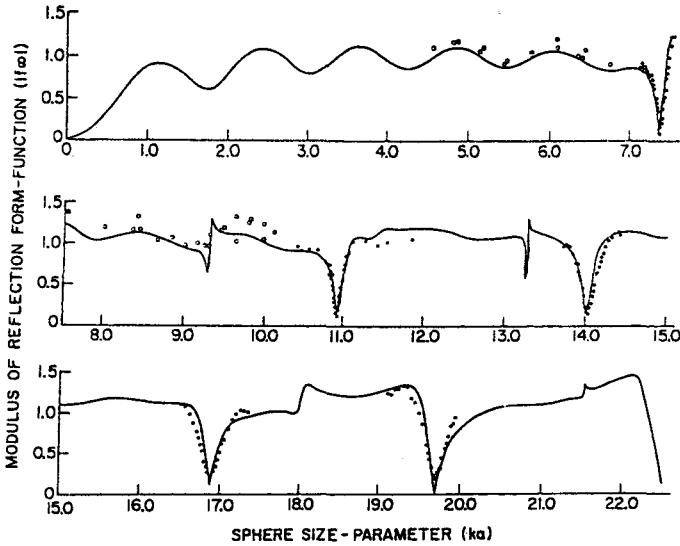
Fig 1.   Comparison between exact theoretical calculation of the form function versus ka (solid curve) for a tungsten carbide sphere and experimental measurements (points). From Ref. 20.

of Eq. (8). As to the background term in this equation, which was taken there as corresponding to a rigid object, experiments have shown that for solid metal cylinders submerged in water, such an assumption is indeed justified, even for the case of a cylinder with a borehole of moderate diameter. It is clear, however, that when dealing with a very thin air-filled shell, the rigid-background assumption must be given up since then, the background will in the limit of vanishing shell thickness approach that of a completely soft object (or, an air bubble) which is also known. However, for a certain intermediate shell thickness neither of these background expressions applies and the exact form of the appropriate background remained unknown for a long time. This problem has been solved by Werby[10,19] who published his first article on the subject in Ref. 2.

By considering the entrained mass of the ambient water, he obtained the spherical-shell scattering amplitude corresponding to the acoustic background contained in the amplitude coefficient b_n [the spherical equivalent of b_n in Eq. (14)]:

$$b_n = -\frac{\dfrac{3\rho}{\rho_s[1-(1-h)^3]}\,\mathrm{Im}\left(i\dfrac{h_n(ka)}{h_n'(ka)}\right)j_n(ka) - j_n'(ka)}{\dfrac{3\rho}{\rho_s[1-(1-h)^3]}\,\mathrm{Im}\left(i\dfrac{h_n(ka)}{h_n'(ka)}\right)h_n(ka) - h_n'(ka)} \tag{19}$$

where h is the ratio of the shell thickness to the shell radius, and ρ_s and ρ are the densities of shell material and water, respectively. The expression correctly tends towards the rigid-body expression in the limit $\rho/\rho_s \to 0$, and toward the soft-body expression for $\rho_s/\rho \to 0$. This remarkable results leads to our complete ability, now, to subtract the correct background from theoretical scattering amplitudes in order to obtain the pure resonance terms in the scattering amplitude. See, however, Ref. 9 where interaction terms were shown to arise also.

Resonant scattering experiments have been pioneered by Neubauer and his group in the mid 70's[20,21]. Figure 1 shows theoretical and experimental results for the far-field backscattering amplitude ("form function") vs. frequency. This plot shows a more or less smooth background which, at the resonance frequencies of the tungsten carbide sphere under consideration, is pierced by regularly-spaced, moderately wide, profound dips caused by the resonances of the Rayleigh-type surface wave, and by other narrower dips corresponding to Whispering Gallery waves.

Evidently, these measurements do not separate the resonant and background terms. Such a separation can be done experimentally, however, and this has been accomplished by the French acousticians at the University of Le Havre[22,23] by observing the ringing of the resonances when utilizing incident modulated pulses of long duration. This has been described in a recent review[24], where an alternative method for such a separation is also discussed, namely the use of short pulses[25,26], gating out the first echo corresponding to a reflection from the vertex of the target, and Fourier analysis of the remaining pulse time series to produce the pure resonance spectrum. Experimentally, thus, the acquisition of the resonance spectra of submerged elastic objects is now well under control, as demonstrated in Fig. 2 obtained by the Le Havre group[23] for a solid aluminum cylinder. The top curve is the counter part to Fig. 1, i.e. the total acoustic scattering amplitude, while the lower curve shows the spectrum of pure resonances, with the background removed. The striking sharpness and intensity of these resonances is well evident, and the idea comes to mind whether the experimental acquisition of the resonance spectrum of a target may not be used for characterizing this target as to its size, shape, and composition, i.e. for purposes of target recognition.

2. Target Recognition

In 1979, A. Derem wrote[27] "L'analyse de la diffusion des ondes acoustiques par un cylindre élastique immergé, fait surgir une véritable spectroscopie acoustique". This was said following an analysis of effects of the resonances of elastic objects, after their excitation by incident sound, as they appear in the scattered echoes, and it seems to be the first formulation of this concept of an acoustic specteroscopy in conjunction with elastic resonance frequency schemes. (The previous term "ultrasonic spectroscopy", and the related early experiments of Gericke[28,29], concern the general notion of the ultrasonic spectra reflected from scatterers in solids, and the information on these scatterers contained in the spectrum, not referring specifically to any resonances.) The new concept was brilliantly justified experimentally shortly afterwards by Maze, Ripoche et al.[22,23] in their pioneering experiments which exhibited in a direct fashion the
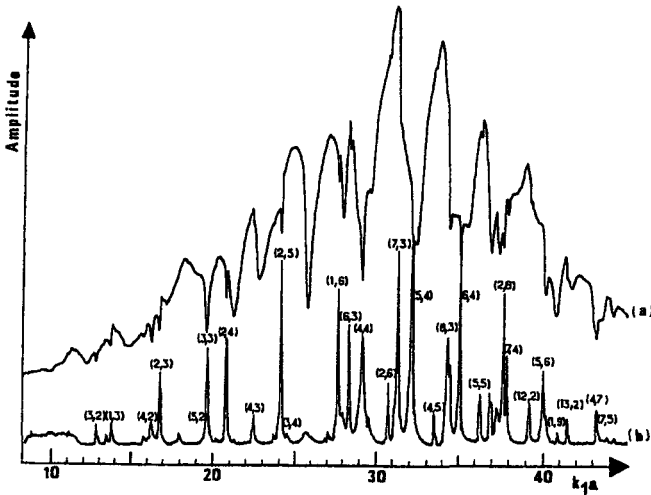
Fig. 2.   Experimental expectra (aluminum solid cylinder): (a) background signal spectrum (steady state); (b) resonance spectrum (ringing). From Ref. 23.

mechanical eigenvibrations of a submerged elastic cylinder, together with the "level scheme" of the corresponding resonances excited by incident sound, straightforwardly extracted from the reflected echo, Figure 2.

These facts then raise the question whether, as in the optical case, such a measured spectrum can provide information on the source of the spectrum (here, the scattering object). This led to a study of the sensitivity of the acoustic level scheme for internal[30,31] or external resonances[32,33] to changes in the shape of the target. As to the information which can be extracted from the spectrum regarding the consistency of the target, we have carried out illustrative calculations on fluid-filled spherical[34,35] or cylindrical[36] cavities in a solid, or on fluid cylinders in a fluid[37], which showed that in general, for a cavity of known shape, the sound velocity in the filler fluid can be obtained from the frequency values of the resonances (together with the size of the cavity), and the density of the filler fluid from the width of the resonances. Finally, the determination of the physical properties of ocean bottom layers has also been shown to be obtainable[38,39] from the effects of layer resonances contained in the acoustic echo.

2.1 Resonance Spectroscopy

A calculation of the eigenfrequencies for prolate fluid spheroids and finite-length fluid cylinders in vacuum, which will approximate the internal resonance frequencies when the objects are imbedded in another, much less dense fluid (except for the imaginary parts of the frequencies, which vanish for ambient vacuum) was carried out[30,31] in order to gauge the sensitivity of the level scheme under changes in shape.
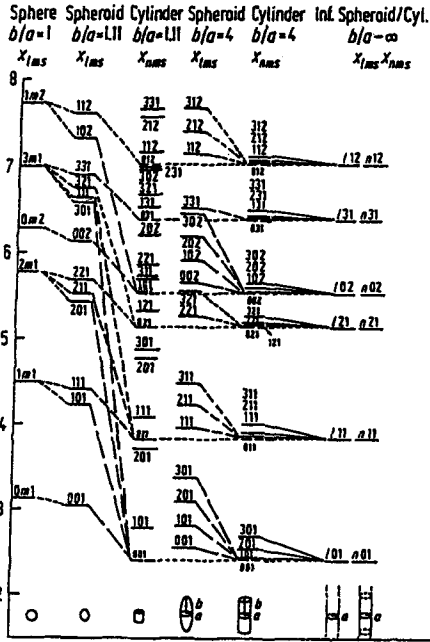
Fig. 3. Acoustic spectroscopy scheme. It displays the characteristic frequencies of various spheroids and cylinders which quantitatively identify their various shapes and sizes. From Ref. 31.

For the spheroids, the calculation was carried out by subjecting spheroidal wave functions to the appropriate (Dirichlet) boundary conditions on the inner surface; for finite-length cylinders, exact solutions are available. Figure 3 shows the eigenfrequency "level scheme" for spheres and infinite cylinders as limiting cases, as well as for finite-length cylinders and spheroids (axes ratios b/a = 1.11... and 4.0). The striking "splitting" (lifting of degeneracy) of the limiting-case levels for the smaller symmetry of finite non-spherical bodies, the azimuthal quantum number no longer being degenerate as for the sphere case, was explained later[33,40] in terms of the formation of helical surface waves with discrete pitch angles.

2.2 Determination of Cavity Contents

It has been shown analytically[34,35] for the example of a fluid-filled spherical cavity in a solid that obtaining the resonance frequencies can determine the sound velocity in the fluid, and obtaining the resonance widths can determine the density of the fluid. Numerical calculations for a fluid-filled cylindrical cavity in steel[41] bear this out. Figure 4 shows for the latter case the normal-incidence scattering of elastic p-waves of wavenumber k: (a) total backscattering amplitude; (b) moduli of the first six partial-wave amplitudes (modes); and (c) the same after subtraction of an empty-cavity background. Figure 5 presents similarly the scattering of elastic s-waves. In Figure 6,
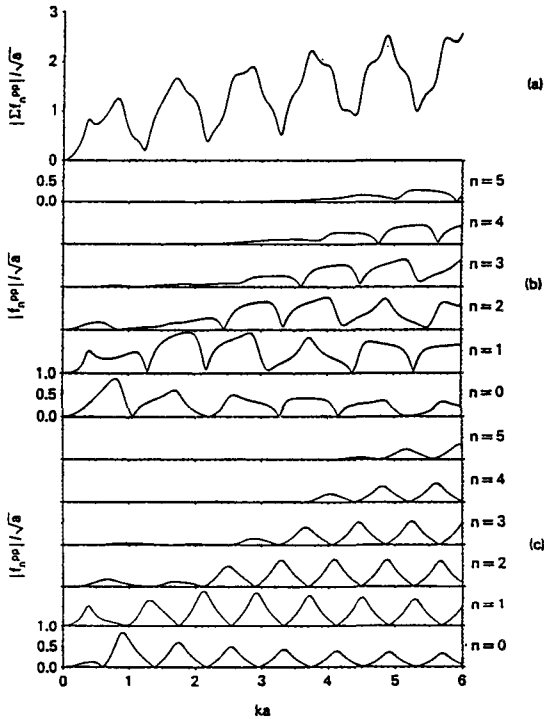
Fig. 4. Normal-incidence scattering of incident elastic p-waves of wave number k from a cylindrical water-filled cavity of radius a in steel: (a) total backscattering amplitude, (b) moduli of the first six partial-wave (mode) amplitudes; (c) as in (b), after subtraction of an empty-cavity background. From Ref. 41.

we show the dependence of the reduced resonance frequency spacing $\Delta x_{n\ell}$ ($x = ka$, k = wave number in the fluid, a = cavity radius) on the ratio c_1/c_2 of internal sound speed c_1 to external p-wave speed c_2, for different values of internal-to-external density ratio, n being the mode number and ℓ the order of the resonance frequency within the nth mode. The near-linear dependence on c_1/c_2, and the insensitivity to ρ_1/ρ_2 indicates the feasibility of determining c_1/c_2 from the resonance spacing.

In Fig. 7, we plot the resonance width $\Gamma_{0\ell}$ of the $n = 0$ resonances vs. $\rho_1 c_1^2/\rho_2 c_2^2$ for different values of c_1/c_2. This illustrates the feasibility of determining ρ_1/ρ_2 from the resonance widths.
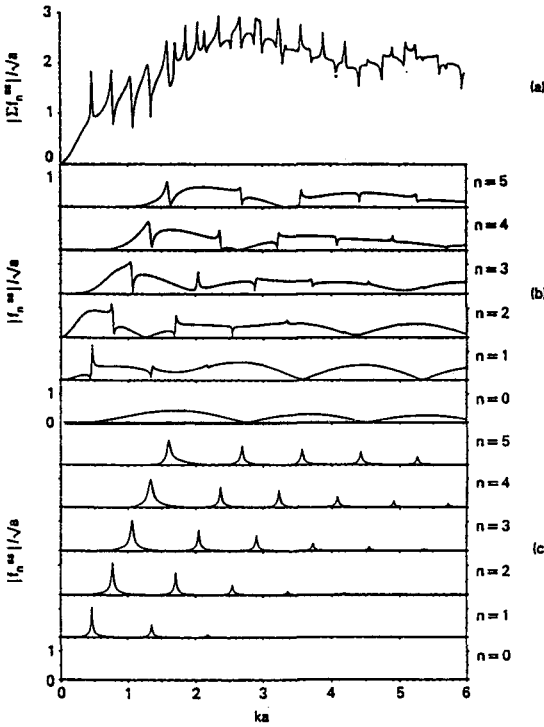
Fig. 5.   As in Fig. 4, for incident elastic s-waves. From Ref. 41.

2.3 Determination of Acoustic Absorptivity

It has been demonstrated[42,43] that the absorptivity of a viscous fluid layer can be determined by measuring the widths of acoustic resonances. The same method can be applied to viscoelastic solid plates if one restricts oneself to normal incidence of the sound wave, since in this case no shear waves are excited and fluid theory can be used in the analysis.   Figure 8 shows the fluid layer immersed in another fluid. Measurement of the critical angle of dilatational waves, $\theta = \theta_c = \sin^{-1} n_d$ where $n_d = c/c_d$ determines the sound speed c_d in the layer: θ_c can, e.g., be obtained by observing the reflection coefficient $R(\theta)$, since $| R | \equiv 1$ for $\theta > \theta_c$. With $x = (\pi/c)fd$, f = frequency, d = layer thickness, observation of the spacing in frequency of successive acoustic resonances which is given by[42]
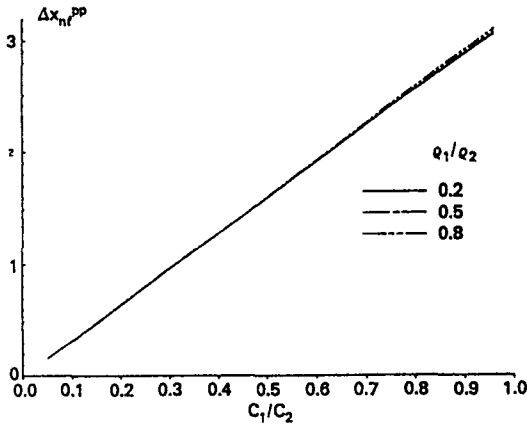
$$\Delta x = 2\pi(n_d^2 - \sin^2\theta)^{-1/2} \tag{20}$$

Fig. 6. Dependence of $\Delta x_{n,\ell} = x_{n,\ell+1} - x_{n,\ell}$, where $x = ka$, on the inside-outside sound speed ratio c_1/c_2 for different values of ρ_1/ρ_2 (curves with different n and/or ℓ overlap). From Ref. 41.

determines the layer thickness d. The determination of the layer density ρ_d, and of its absorption coefficient, can be achieved from measuring the widths Γ of the resonances, and of their frequency dependence.

For the absorption coefficient α_d, one may assume a power law with frequency f:

$$\alpha_d = Af^n, \tag{21}$$

and describe the absorptivity by a complex sound velocity c_d^*:

$$c_d^* = c_d/(1 + ir_d) \tag{22a}$$

where r_d is the loss factor,

$$r_d = Af^{n-1}(c_d/2\pi), \tag{22b}$$

which causes a widening of the resonances. This leads to an expression for the frequency-dependent resonance width Γ:

$$\Gamma = (4\rho/\rho_d \cos\theta) + (2d/n_d)Af^n, \tag{23}$$

which follows a power-law curve in f. The layer density ρ_d is determined from the intercept of this curve at $f = 0$. The coefficient A and the power n are determined from
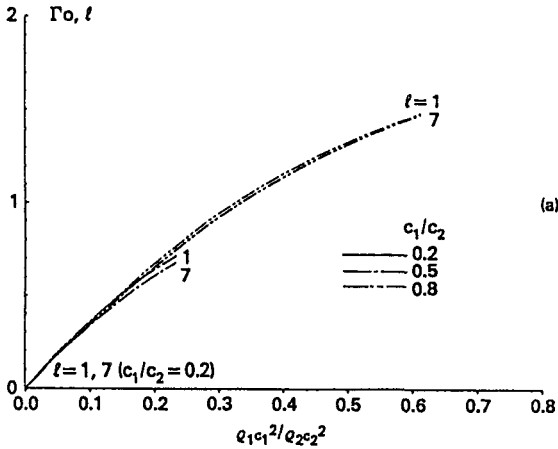
Fig. 7.   Dependence of resonance widths $\Gamma_{n,\ell}$ (with $n = 0$) on $\rho_1 c_1^2/\rho_2 c_2^2$ for different values of c_1/c_2 and of ℓ; curves for $\Gamma_{n,\ell}$ with $n \neq 0$ and the same ℓ overlap those for $n = 0$. From Ref. 41.

the frequency plot of Γ, best from a log-log plot in which Γ appears as a straight line.

Figures 9 and 10 show plots of Γ, and of the mentioned log-log plot, calculated for the example of a butyl rubber layer[42] as an illustration for how the mentioned determination of ρ_d, A and n can be achieved experimentally.

2.4 Exploration of a Layered Seafloor

The ocean floor is usually covered by at least one sediment layer, often by a multilayer structure. Resonances in the bottom reflection coefficient R can be striking, as illustrated in Fig. 11 which plots R vs. the grazing angle. The solid curve refers here to a solid sediment, the dashed curve to a fluid-type sediment. The first quantitative discussion of resonances in the reflection loss was given by Nagl et al.[38] for steady state signals, and later by Nagl et al.[39] for transient signals. It was shown there how bottom properties (density and sound speed in a fluid-type sediment and substrate) can be extracted from the resonances. Similar information can also be obtained from observing the resonances in the transmission loss[44,45]. The theoretical studies were extended later on to a consolidated sediment and substrate by Fokina and Fokin[46].

Hughes et al.[44] solve the inverse problem and determine the layer properties by a straightforward approach of adjusting parameters in their transmission loss code. Nagl et al.[38,39] solve the inverse problem analytically for the reflection loss. This is, of course, possible only if the analytical expressions are sufficiently simple, which is the case for a fluid-type layer on a fluid substrate.

The three-dimensional plots of Figs. 12a and b show $| R |^2$ plotted as a function of
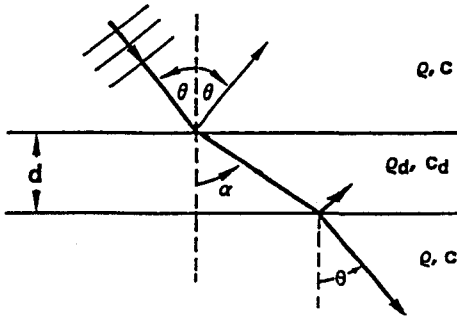
Fig. 8. Geometry of a fluid layer embedded in another fluid.

the frequency thickness product fd (d = layer thickness) between 5 and 10 kHz-m (a) or 20-25 kHz-m (b) and incident angle from the normal $0°\leq\theta_3\leq20°$, indicating that resonances will appear as a function of frequency for fixed angle of incidence θ_3, or also vice versa.

Nagl's resonance theory for the steady state case[38] proceeds from the familiar formula for the reflection coefficient of a fluid layer between two fluid half-spaces, written in the form

$$R = \frac{A \cos \delta - i(1 - \tau^2) \sin \delta}{S \cos \delta - i(1 + \tau^2) \sin \delta} \tag{24}$$

with

$$A = (z_1 - z_3)/z_2 \qquad S = (z_1 + z_3)/z_2 \tag{25a}$$

$$\tau^2 = z_1 z_3/z_2^2 \qquad \delta = (2\pi fd/c_2) \cos \theta_2 \tag{25b}$$

where

$$z_i = c_i \rho_i / \cos \theta_i \tag{26}$$

Angles are designated θ_3 (water), θ_2 (sediment), θ_1 (substrate), similarly for the sound speeds c_i. The minima of $|R|^2$ are located at $\cos \delta = 0$, i.e. at $\delta = \delta_n$,

$$\delta_n = (2n + 1)\pi/2, \qquad n = 0,1,2,\ldots \tag{27}$$

This resonance condition may be rewritten using Snell's law:

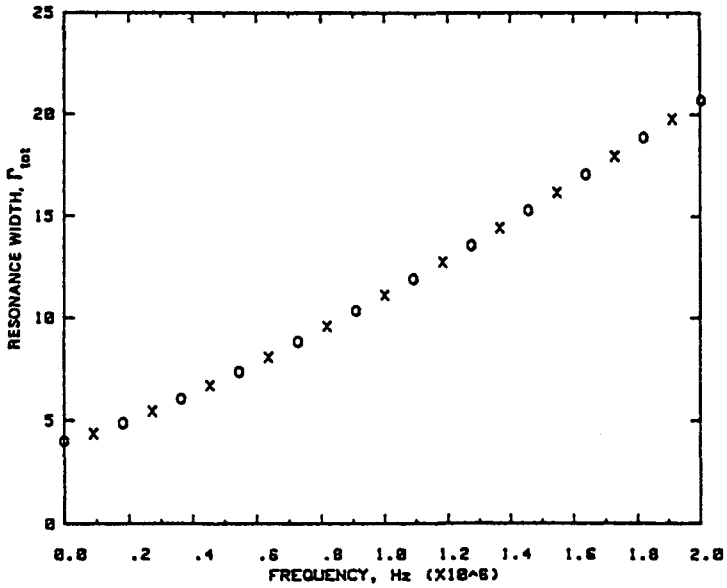$$fd \{n_d^2 - \sin^2 \theta_3\}^{1/2} = (2n + 1) c_3/4, \qquad n = 0, 1, 2, \cdots \tag{28}$$

Fig. 9.   Resonance widths vs. frequency in absorptive butyl rubber.   From Ref. 42.

$n_d = c_3/c_2$.   The reflection coefficient may be Taylor-expanded and linearized around $\delta = \delta_n$:

$$R = \sum_n \frac{F(\delta - \delta_n) + iG(1 + \tau^2)/S}{\delta - \delta_n + i(1 + \tau^2)/S} \tag{29a}$$

with

$$F = \frac{A}{S} = \frac{z_1 - z_3}{z_1 + z_3} \qquad G = \frac{1 - \tau^2}{1 + \tau^2} . \tag{29b}$$

Thus, $(1 + \tau^2)/S$ is the resonance half-width, and G^2 a continuous background level. To discuss the frequency resonances, we introduce the non-dimensional variable $x = 2\pi fd/c_3$,

$$x_n = \delta_n/(n_d^2 - \sin^2 \theta_3)^{1/2} \tag{30}$$

leading to the resonance width

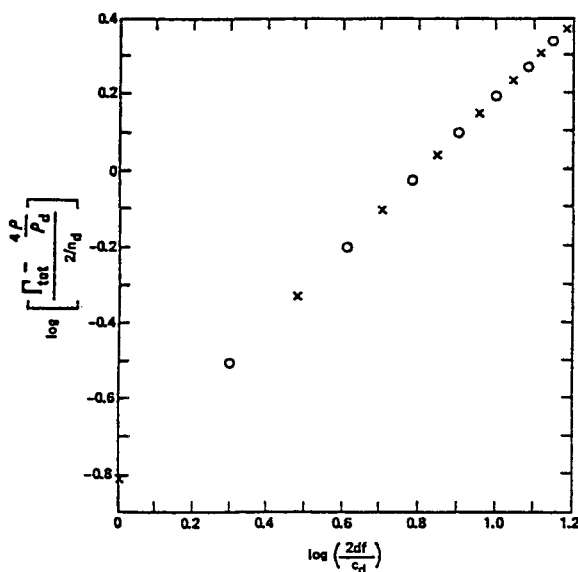$$\tfrac{1}{2} \Gamma_n = (1 + \tau^2)/\{S(n_d^2 - \sin^2 \theta_3)^{1/2}\} \tag{31}$$

Fig. 10. Straight-line log-log plot of Fig. 9. From Ref. 42.

and the resonance spacing

$$\Delta x = \pi/(n_d^2 - \sin^2\theta_3)^{1/2} \tag{32}$$

which increases with θ_3. The reflection coefficient becomes

$$R = \sum_n \frac{F(x - x_n) + \frac{1}{2}iG\Gamma_n}{x - x_n + \frac{1}{2}i\Gamma_n} \tag{33}$$

and its square is shown (exactly) in Fig. 12. The advantage of this linearized formulation is that it provides explicit analytical expressions for Γ_n and Δx_n, not just numerical values. A similar linearization can be done for the angular resonances[38].

The solution of the inverse problem for the fluid-type sediment layer can now proceed as follows. By measuring the critical angle θ_{cr}, the minimum value R_m of the reflection coefficient, and (at given θ_3) the spacing and the width of the frequency resonances (or, at given f, the position and width of the angular resonances) we can deduce the unknown parameters c_2, ρ_2, c_1, ρ_1 and d. Since many resonances are available to be measured, there is a redundancy and the problem is overdetermined, but
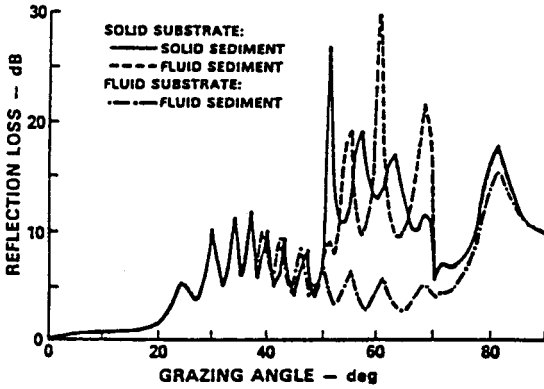
Fig. 11. Reflection loss vs. grazing angle for a 518-m thick turbidite layer at 20 Hz [from P. J. Vidmar and T. L. Foreman, J. Acoust. Soc. Am. **66**, (1979) 1830].

this may help to corroborate the correctness of individual measured values.

(i)   By measuring the resonance spacing Δx, Eq. (32), one obtains n_d.

(ii)   Measuring the position of angular resonances at given f, one obtains n_d and d.

(iii)   Measuring the critical angle θ_{cr} of the substrate, $c_1 = c_3/\sin\theta_{cr}$, determines c_1 in the substrate.

(iv)   Measuring Γ of the frequency resonances at a given θ_3 yields

$$(1 + \tau^2)/S = \tfrac{1}{2}\Gamma(n_d^2 - \sin^2 \theta_3)^{1/2}. \qquad (34)$$

The value of τ can be found from the minimum R_m of the reflection coefficient at θ_3,

$$\tau^2 = (1 - R_m)/(1 + R_m). \qquad (35)$$

Using this, we solve Eq. (34) for S which yields

$$S = (z_1 + z_3)/z_2 = (1 + \tau^2)/\{\tfrac{1}{2}\Gamma(n_d^2 - \sin^2 \theta_3)^{1/2}\}. \qquad (36)$$

Since S can be written as

$$S = \frac{z_1 + z_3}{(z_1 z_3)^{1/2}} \, \tau = \{(z_1/z_3)^{1/2} + (z_3/z_1)^{1/2}\} \, \tau \tag{37}$$

we may now obtain $(z_1/z_3)^{1/2}$ since S and τ are known. Since

$$(z_1/z_3)^{1/2} = \rho_1^{1/2} \left(\frac{1 - \sin^2 \theta_3}{n_r^2 - \sin^2 \theta_3} \right)^{1/4} \tag{38}$$

and $n_r \equiv \sin\theta_{cr}$ is already assumed to be known, Eq. (38) thus yields ρ_1. The density ρ_2 can then be found from the known value cf τ^2:

$$\tau^2 = \frac{\rho_1 \rho_3}{\rho_2} \, \frac{n_d^2 - \sin^2 \theta_3}{\cos \theta_3 (n_r^2 - \sin^2 \theta_3)^{1/2}} \, . \tag{39}$$

Fig.12 (a)
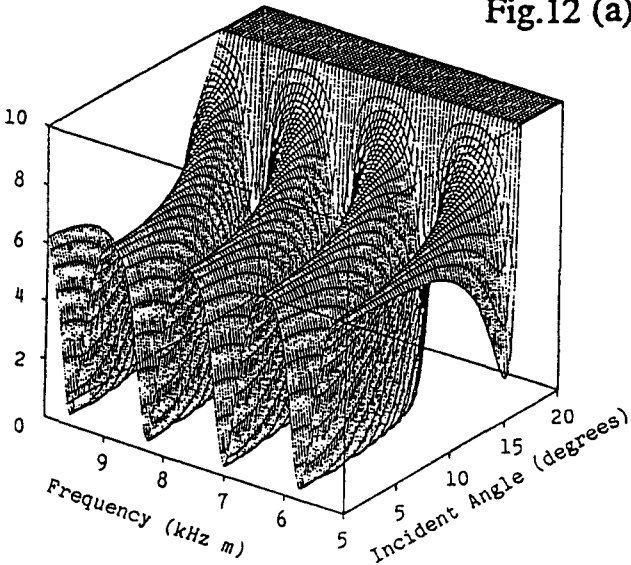
Fig. 12. Square of reflection coefficient for a fluid layer between two different fluids (c_3 = 1500m/s, c_2 = 2544m/s, c_1 = 5495m/s, ρ_3 = 1 g/cm³, ρ_2 = 2.2g/cm³, ρ_1 = 2.6g/cm³) plotted vs. $0° < \theta_3 < 20°$ and (a) 5 <fd<10kHz-m, (b) 20 <fd< 25 kHz-m. From Ref. 38.
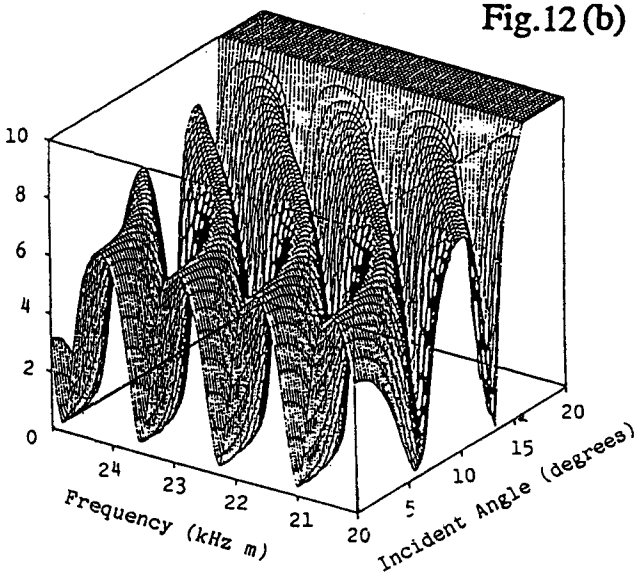
Thus all the parameters of the fluid-layer, fluid-substrate system have been determined.

For the transient case[39] applied to the same sediment-substrate system, one uses sinusoidal wavetrains and observes the ringing of the resonances, manifest as a tail to the returned echo wavetrain. Again, all parameters can be determined by measuring the amplitude of the specularly reflected signal, the delay time between successive internal reflections (as evident in the staircase-like, rather than exponential, behavior of the ringing tail), and the amplitudes of one or more internal reflections (step height in the ringing staircase).

Although for more complicated (multilayer) sediment systems this analytic approach may appear too involved, a recent study[47] has shown that one may isolate the acoustic resonances of individual layers, which leads us to expect that application of the analytic method may still be possible in this case.

3. Conclusion

The foregoing represents an historical account, and a description of the salient features, of the Resonance Scattering Theory (RST). It also presents an elaboration on the concept of Acoustic Resonance Spectroscopy, first pronounced by Derem[27], as a means of determining the properties of acoustic targets from the information on the target resonances which is contained in the observed echo returns. The feasibility of this concept, although yet to be generally demonstrated for cases of practical interest, appears evident for targets of large impedance contrast with the environment, in which case pronounced resonances result. It is also obvious, though, that an application of this approach has to proceed, at this time, with complete understanding of the physics of the scattering process. If this caution is disregarded, failure may possibly occur. After sufficient development of the approach, one may ultimately expect, however, that automated systems for experimental acoustic target recognition by resonance scattering can be devised.

4. Acknowledgements

5. References

1. L. Flax, L. R. Dragonette, and H. Überall, *J. Acoust. Soc. Am.* **63** (1978) 723.
2. *Acoustic Resonance Scattering,* H. Überall, ed. (Gordon and Breach, New York 1992).
3. M. C. Junger, *J. Acoust. Soc. Am.* **24** (1952) 366.
4. N. Bohr, *Nature* **137** (1936) 344.
5. G. Breit and E. P. Wigner, *Phys. Rev.* **49** (1936) 519.
6. E. P. Wigner, *Phys. Rev.* **70** (1946) 15.
7. H. Feshbach, D. C. Peaslee, and V. F. Weisskopf, *Phys. Rev.* **71** (1947) 145.
8. J. M. Blatt and V. F. Weisskopf, *Theoretical Nuclear Physics* (John Wiley, New York, 1952), Chap. VIII, Secs. 7-9.
9. M. S. Choi, *J. Acoust. Soc. Am.* **101** (1997) 2491.
10. M. F. Werby, *Acoustics Lett.* **15** (1991) 65; *J. Acoust. Soc. Am.* **90** (1991) 3279.
11. W. Franz, *Z. Naturforsch.* **A9** (1954) 705.
12. G. V. Frisk, J. W. Dickey, and H. Überall, *J. Acoust. Soc. Am.* **58** (1975) 996.
13. G. V. Frisk and H. Überall, *J. Acoust. Soc. Am.* **59** (1976) 46.
14. J. W. Dickey, G. V. Frisk, and H. Überall, *J. Acoust. Soc. Am.* **59** (1976) 1339.
15. H. Überall, L. R. Dragonette, and L. Flax, *J. Acoust. Soc. Am.* **61** (1977) 711.
16. J. W. Dickey and H. Überall, *J. Acoust. Soc. Am.* **63** (1978) 319.
17. See, e.g., R. G. Newton, *The Complex j-Plane* (Benjamin, New York, 1964).
18. R. D. Doolittle, H. Überall, and P. Ugincius, *J. Acoust. Soc. Am.* **43** (1968) 1.
19. M. F. Werby, "Recent Developments in Scattering from Submerged Elastic and

Rigid Targets", Chapter 12 of Ref. 2.

20. W. G. Neubauer, R. H. Vogt, and L. R. Dragonette, *J. Acoust. Soc. Am.* **55** (1974) 1123.

21. L. R. Dragonette, R. H. Vogt, L. Flax, and W. G. Neubauer, *J. Acoust. Soc. Am.* **55** (1974) 1130.

22. G. Maze and J. Ripoche, *Rev. Phys. Appl.* **18** (1983) 319.

23. J. Ripoche and G. Maze, "A New Acoustic Spectroscopy: the Resonance Scattering Spectroscopy by the Method of Isolation and Identification of Resonances (MIIR)", Chapter 5 of Ref. 2.

24. S. K. Numrich and H. Überall, in *Physical Acoustics* vol. **XXI** ed. A. D. Pierce and R. N. Thurston (Academic Press, New York, 1992).

25. S. K. Numrich, N. Dale, and L. R. Dragonette, in *Advances in Fluid-Structure Interaction* (American Society of Mechanical Engineers, 1984) PVP 78/AMD **64**, p. 59.

26. M. de Billy, *J. Acoust. Soc. Am.* **79** (1986) 219.

27. A. Derem, *Revue du CETHEDEC* **58** (1979) 43.

28. O. R. Gericke, *J. Acoust. Soc. Am.* **35** (1963) 364.

29. O. R. Gericke, "Ultrasonic Spectroscopy", U.S. patent No. 3,538753, 10 Nov. 1970.

30. D. Brill, G. C. Gaunaurd and H. Überall, *J. Acoust. Soc. Am.* **72** (1982) 1067.

31. D. Brill, G. C. Gaunaurd and H. Überall, *Acustica* **53** (1983) 11.

32. P. J. Moser and H. Überall, *Proceed. IEEE* **71** (1983) 171.

33. H. Überall, P. J. Moser, B. L. Merchant, A. Nagl, K. B. Yoo, S. H. Brown, J. W. Dickey and J. M. D'Archangelo, *J. Appl. Phys.* **58** (1985) 2109.

34. G. C. Gaunaurd and H. Überall, *Science* **206** (1979) 61.

35. G. C. Gaunaurd and H. Überall, *Ultrasonics* **18** (1980) 261.

36. P. P. Delsanto, J. D. Alemar, E. Rosario, A. Nagl and H. Überall, in *Transactions of the 2nd Army Conference on Mathematics and Computing* (Rensselaer Polytechnic Institute, Troy, NY, May 1984).

37. J. D. Alemar, P. P. Delsanto, E. Rosario, A. Nagl and H. Überall, *Acustica* **61** (1986) 14.

38. A. Nagl, H. Überall, and W. R. Hoover, *IEEE Trans. Geosc. Rem. Sensing* **GE-20** (1982) 332.

39. A. Nagl, H. Überall, and K. B. Yoo, *Inverse Problems* **1** (1985) 99.

40. A. Nagl, H. Überall, P. P. Delsanto, J. D. Alemar, and E. Rosario, *Wave Motion* **5** (1983) 235.

41. P. P. Delsanto, J. D. Alemar, E. Rosario, A. Nagl, and H. Überall, *Materials Evaluation* **46** (1988) 1000.

42. R. Fiorito, W. Madigosky and H. Überall, *J. Acoust. Soc. Am.* **69** (1981) 897.

43. R. Fiorito, W. Madigosky, and H. Überall, *J. Acoust. Soc. Am.* **77** (1985) 489.

44. S. J. Hughes, D. D. Ellis, D. M. F. Chapman, and P. R. Staal, *J. Acoust. Soc. Am.* **88** (1990) 283.

45. N. R. Chapman and D. M. F. Chapman, *J. Acoust. Soc. Am.* **94** (1993) 2731.

46. M. Fokina and V. Fokin, in *Proceed. 2nd EAA Internat'l Symp. on*

Hydroacoustics, ed. A. Stepnowski, R. Salamon and E. Kozaczka (Techn. Univ. of Gdansk, Poland, 1999), p. 101.
47.   H. Überall, A. Gérard, A. Guran, J. Duclos, M. El H. Khelil, X. L. Bao, and P. K. Raju, *Appl. Mech. Rev.* **49** (1996) S63.

MODERN DEVELOPMENTS IN THE THEORY AND APPLICATION OF CLASSICAL SCATTERING

MICHAEL F. WERBY

Naval Research Laboratory, Code 7181, Stennis Space Center, MS 39529, USA

and

NATALIA A.SIDOROVSKAIA

Physics Department, University of New Orleans, New Orleans, LA 70148, USA

ABSTRACT

The aim of this article is to study scattering from objects over a broad frequency range, in a free environment, near a smooth interface and in a wave guide. The objects have smooth surfaces either being spherical or axially symmetric and include impenetrable, fluid and elastic boundary conditions including the complicated case of elastic shells. An examination of the frequency domain is the main focus with some time-domain notions and examples discussed also. An attempt is made to present a broad perspective of the subject in terms of a formulation that will yield both mathematical expressions amenable to calculation and calculations that lead to solid physical insight. The mathematical formulation emphasized here is drawn heavily from a very powerful integral equation method - the extended boundary condition (EBC) or T-Matrix approach- and is outlined with some related computational strategies. The EBC-method in the simplest case requires the solution of two coupled integral equations while the elastic problems may require many coupled equations. Exact numerical calculations are presented that manifest interesting physical phenomena which are explained in some detail. This article is intended to be partly tutorial in nature and self contained with an attempt at a balance of the mathematical, the computational and the physical points of view.

1. Introduction

In the physical world, the propagation of waves and scattering of waves or particles from bounded entities is pervasive and is an important tool to gain knowledge of inaccessible objects. Remote objects in the sky, below the sea, and objects such as oil domes deep in the earth, are subject to probing by electromagnetic, acoustic or elastic waves to gain knowledge of what would otherwise elude one. Thus, an ability to simulate such events as well as an understanding of how to use or interpret scattering data is a very important area of study. Those concerned with understanding microscopic phenomena are out of necessity acquainted with scattering theory at some level of sophistication since both scattering and the more general area of rearrangement collision theory are the

principal ways one probes the microscopic world. Therefore, it should not be surprising that scattering as used in the quantum mechanical realm is more developed than the classical analog. Remarkably, much of the mathematical methodology and some of the physical events, such as resonances in quantum scattering, occur in classical scattering and the base of knowledge in one area has promoted "hybrid vigor" in the other. Indeed, many of the notions in this article and elsewhere were first used in quantum physics.

In this work we examine the classical scattering of waves from submerged bounded elastic objects of some canonical shapes. This is still a developing and growing area and in our view there is much progress to be made and the subject lacks unity in the sense that few researchers bring together all aspects of the problem; but rather focus on a specific aspect. Part of the reason is that reasonable physical problems are rather computational and only in the last decade have computers and numerical techniques even approached sufficiency to deal with the complexities associated with waves scattering from complicated elastic targets. Further, research groups that publish in the area of Acoustics come from diverse disciplines such as engineering, geophysics and mathematics and their perspectives and interests differ. In the United States Acoustics is often treated as an application of a more general discipline and the various groups have different objectives often with little common ground among them. Moreover, the terminology used by different groups varies, partly for historical reasons, and this has caused misunderstandings among communities. Most physicists with sufficient mathematical and theoretical backgrounds are engaged in modern quantum mechanical based areas, such as Particle, Nuclear or Solid State Physics. The remarkable exception to this trend is H. Überall of the Physics Department of the Catholic University of America. While still maintaining his interest in Nuclear Physics, H. Überall has been the most prolific pioneer and critical thinker in resonance scattering theory and related topics in general scattering in addition to other areas of Acoustics, Applied Mechanics, Ocean Engineering and Electromagnetism. Accordingly, he is a fellow of the main organizations associated with three disciplines, namely the APS, the ASA and the IEEE. There is little worth mentioning in the area of resonance scattering that has not been touched by his enormous insight and originality and it is tempting to comment that one can divide that part of Physical Acoustics into two eras, namely before Überall (BU) and after Überall (AU). With over 40 doctoral students to his credit, and his contributions to national laboratories and, indeed, for his devotion to his colleagues and his students, he forms the paradigm of what is best in University professors and what is worth emulating by all who wish to be servants to their science and a benefit to their fellow human beings.

Acousticians do come from Physics departments, but they are mostly found in Mechanical, Civil or Electrical Engineering Departments or in some Applied Mathematics, Applied Mechanics or Geophysics Programs, each with its own emphasis. With the application of scattering methods the problem is also complicated by the fact that scattering theory is one of the areas least appealing to one's physical intuition. In the sense that one learns concepts more easily in a contextual basis, the more physical events relate to ones common sensual notions the more adept one is at understanding the area and the

more populated it is with scientists. But in any kind of scattering theory one must create a new context for understanding related phenomena and that takes time for adaptation which many but the most devoted individuals have all too little. Concepts such as diffraction, refraction, resonances and partial wave studies are not in ones usual common experience and one must develop research instincts by a prolonged exposure to the subject. On the other hand, for those who have developed an intuition for the subject they find it rich in concept and phenomena and suitably challenging to consume a lifetime of research.

A major aim of this article is to describe some aspects of the classical scattering of waves from the viewpoint of one familiar with areas ranging from quantum scattering to the acoustical scattering from complicated elastic structures in which useful notions in one area are exploited in the other. The mathematical development used to describe scattering from targets is based mainly on an exact numerical technique by Peter Waterman who, in a series of elegant papers[1-5] outlined the course of treatment that constitutes a unified theory of the classical scattering of waves. The T-matrix or more properly, the extended boundary condition (EBC) method due to Waterman is in part a computational method which one may view to be as powerful in an algorithmic and general sense as Hamilton's principle or the Euler-Lagrange equations. This method (largely overlooked by some of the classical scattering communities) along with numerical or structural improvements has enabled researchers to perform enormously complicated calculations and understand physical phenomena previously not possible.

Along with the formal and numerical procedures outlined here, some physical phenomena in wave scattering are discussed that has similarities with quantum scattering. In the area of acoustical phenomena, such as resonance scattering, Herbert Überall[6-15] has been a towering contributor, both in introducing techniques and in describing phenomena in the context found in quantum physics. Of particular merit is his development of a resonance scattering theory[6-9] (RST) along lines parallel to that of Briet and Wigner[16] and Kapur and Peierls[17] as well as his clarification that resonances excited on elastic targets are mainly due to circumferential waves initiated at the fluid-elastic interface. Because of phase matching conditions, the surface waves form standing waves at distinct frequencies resulting in the resonance phenomena.[7] Analogies between quantum and classical scattering and propagation abound.[18] There are many older and approximate treatments such as the Born approximation and the related Kirchhoff approximations that have been used in a perturbation sense. Finite element methods and the method of moments and the weighted residual methods such as the Galerkin method have become popular among structural researchers but they presently seem to be limited in frequency range and appear tied to approximate thin shell theories. The separation of variables method useful for appropriate shapes (sometimes referred to as normal mode solutions) can be shown to be a special case of the more general EBC method and will not be discussed here except in relation to the acoustical background for spherical shells. Both a T-matrix and an S-matrix can be defined in wave scattering where the important concepts of symmetry, unitarity, and the generalized optical theory play a role.[19, 20] Überall has shown that even Reggie

poles[8] find their place in the classical scattering of waves and that one can divide scattering into a superposition of a form of direct scattering (called the background) and resonance scattering as was done earlier in quantum scattering. The background concept was introduced for elastic spheres by Flax, Dragonette and Überall in which they employed a rigid scatterer as the background for elastic solids[8] and was extended by Werby using the concept of entrained mass to elastic shells.[10,21,22] The analogy with quantum scattering has a correspondence at low energy where shape elastic scattering from nuclear particle adds coherently with resonance scattering due usually to collective or rotational motion of a nucleus. A comprehensive development of the interesting area of resonance scattering from elastic targets is presented in a recent book edited by H. Überall.[8]

The idea that many physical events of complicated systems often have simplified interpretations (in a sense the interpretations are metaphorical or paradigms) is exploited and the point made that one is obliged as a researcher to understand physical phenomena especially when striking effects appear even when they are only from computations. This "metaphorical" approach is intended to balance the older opinion that difficult exact computations and the use of large computers deprives one of physical insight; that is not true. One must always make sense of numerical results just as an experimentalist must make sense of complicated experimental results. It is the duty of a computational theorist to make physical sense of his or her results once one is sure that the method used is correct and working as desired.

The plan of this work is as follows. Section 2 a review of the Extended Boundary Condition (EBC) method for determining the field scattered from rigid and soft spheroidal objects. We next extend this development to include refinements to the formulation and outline results for elastic objects and impose useful constraints for the elastic case such as symmetry of the T-matrix and unitarity of the associated S-matrix. We next develop the problem of scattering from interfaces, scattering from two or more adjacent objects and finally, scattering from objects in a wave guide. We then present Section 3 that discusses some resonance concepts, the concept of acoustical backgrounds and partial wave analysis, and additional physical phenomena that can be interpreted in terms of the standing wave concept of resonances at fluid-elastic interfaces of bounded objects. We end that section with a discussion of time domain resonance scattering theory . The final section, 4 includes examples which make use of the formal and computational expressions along with notions discussed in Section 3 to make sense of the computational results.

2. A Mathematical Formulation of Classical Scattering

The Extended Boundary Condition (EBC) method proposed and largely developed by P. Waterman forms the basis of the equations used to develop the T-matrix and the eigen-expansion and transformation methods that follow. The emphasis in this section is on the mathematical basis of the methods which vary depending on the type of target. Focus, and our original contribution is on procedures that allow for restructuring the theory or by

suitable transformations that allow for more computationally viable expressions. What we mean by this is that the formal expressions we develop are not merely formal; they are in a form useful for implementing on computers without approximation. With the exception of scattering from impenetrable and fluid targets, details of the EBC derivations can be both intricate and subtle. Due to space limitations we, therefore, restrict detailed developments to the simple cases, and list the generalizations for more complicated scenarios.

2.1. The T-matrix for a Rigid Objects

The Helmholtz-Poincare' integral representation for a field $U(\mathbf{r})$ exterior to a bounded object is an integral representation of the Helmholtz differential equation. It is particularly useful for the scattering problem because it is an integral over the boundary of the object and thus appropriate for imposing surface boundary conditions. It is represented as:

$$U(\mathbf{r}) = U_i(\mathbf{r}) + U_s(\mathbf{r}) =$$

$$= U_i(\mathbf{r}) + \frac{1}{4\pi} \oint_{S'} [U_+(\mathbf{r'}) \frac{\partial G(\mathbf{r},\mathbf{r'})}{dn'} - G(\mathbf{r},\mathbf{r'}) \frac{\partial U_+(\mathbf{r'})}{\partial n'}] dS' , \quad \mathbf{r} \in D_{ext}, \quad \mathbf{r'} \in D_{int} \qquad (1)$$

where vector $\mathbf{r}$ is in D_{ext}, the set of points exterior to the object, $G(\mathbf{r},\mathbf{r'})$ is the outgoing wave Green's function for unbounded space, $\mathbf{r'}$ is in D_{int}, the set of points interior to the bounded object, S' represents the object surface, $\hat{n}$ is a unit outward normal to the surface, $U_i(\mathbf{r})$ is a known incident field, $U_s(\mathbf{r})$ is scattered field, and $U_+(\mathbf{r'})$ is the total field on the surface of the object. The surface is assumed to be piece-wise continuous. This expression reminds one of the integral form of Gauss's law for electric fields, because, when $\mathbf{r}$ is in the interior of the object, the total wavefield $U(\mathbf{r})$ is zero (extinguished or nulled), hence the terms "extinction theorem" or "null-field condition". Thus, we also have that:

$$0 = U_i(\mathbf{r}) + \frac{1}{4\pi} \oint_{S'} [U_+(\mathbf{r'}) \frac{\partial G(\mathbf{r},\mathbf{r'})}{\partial n'} - G(\mathbf{r},\mathbf{r'}) \frac{\partial U_+(\mathbf{r'})}{\partial n'}] dS' , \quad \mathbf{r}, \quad \mathbf{r'} \in D_{int} . \qquad (2)$$

where $\mathbf{r}$ is now an interior point. The above equations constitute the extended boundary condition equations. Note that Eq. (2) does not mean that the field is zero in the interior of the target. It merely means that the expression is evaluated to be zero in accordance with Eq. (2). Additional equations are required to determine the field in the interior region for objects that can support a field in that region.

Some researchers, particularly those in electromagnetism, refer to the combined use of Eqs. (1) and (2) as the null-field equations. The second equation was generally thought inconsequential, but Waterman[1] took advantage of Eq. (2) as a constraint to eliminate the surface terms involving $U_+(\mathbf{r'})$ and it's gradient which arise in the exterior solution.

Although Waterman[1] employed the condition algorithmically to eliminate the unknown terms, the procedure led to a method that also produced a unique solution for all positive frequencies of the exterior problem. This is of considerable importance, because exterior solutions have often suffered from "spurious resonances" at the so-called "irregular values" of incident frequencies. These irregular values correspond to the eigenfrequency of a problem related to the interior solution related to Eq. (2). This problem is well-known in the context of the Fredholm alternative theorem. It has been established that by coupling the interior points with the exterior solution the irregular values are eliminated. This is achieved by the EBC-equations. Thus, Waterman's equations actually serve two computational purposes, one algorithmic and the other mathematical. In their present form Eqs. (1) and (2) are not of immediate use. In what follows we describe how Waterman reduced the expressions to forms amenable to numerical computation. For the convenience of presentation we will simplify the problem to that of an impenetrable object (although solution of the fluid target case is quite similar). Elastic targets submerged in a fluid require far greater mathematical detail, and will not be elaborated here. Let us assume that we are dealing with a rigid scatter so that we obtain the expressions:

$$U(\mathbf{r}) = U_i(\mathbf{r}) + \frac{1}{4\pi}\oint_{S'} U_+(\mathbf{r}')\frac{\partial G(\mathbf{r},\mathbf{r}')}{\partial n'}dS' \ , \quad r \in D_{ext}, \ \ \mathbf{r}' \in D_{int} \tag{3}$$

and

$$0 = U_i(\mathbf{r}) + \frac{1}{4\pi}\oint_{S'} U_+(\mathbf{r}')\frac{\partial G(\mathbf{r},\mathbf{r}')}{\partial n'}dS' \ , \quad \mathbf{r}, \ \ \mathbf{r}' \in D_{int} \ . \tag{4}$$

To solve these expressions, it is necessary to represent U_i, U, and G in partial wave series, which upon truncation leads to matrix equations that are then solved using digital computers. The Green's function G is a normal operator, and can be represented by the biorthogonal expansion:

$$G(\mathbf{r},\mathbf{r}') = ik\sum_l \psi_l(\mathbf{r}_>)\,\mathrm{Re}\,\psi_l(\mathbf{r}_<) \tag{5}$$

where $\mathbf{r}_<$ and $\mathbf{r}_>$ are the lesser and greater of the magnitude of the two vectors $\mathbf{r}, \mathbf{r}'$ at the origin of the object, respectively, k is a wave number, i is an imaginary unit, and $\mathrm{Re}\,\psi_l$ is a notation for the regular function at the origin. The quantity U_i, the incident wavefield, is known. We express the incident and scattered fields as follows:

$$U_i(\mathbf{r}) = \sum_j a_j\,\mathrm{Re}\,\psi_j(\mathbf{r}), \tag{6a}$$

$$U_s(\mathbf{r}) = \sum_j f_j\psi_j(\mathbf{r}). \tag{6b}$$

The fact that expansions (6a) and (6b) can be obtained follows from the Hilbert-Schmidt theorem, where for incident plane waves, the a's are simple known numbers. The expression (6b) satisfies the outgoing radiation condition at infinity and is valid for any

region on and outside of a sphere with origin at the center of the object and that circumscribes the object. Thus, it can be used for calculating the near field within the limits determined by the largest dimension of the object. The main goal then is to find the unknown coefficients $\{f_j\}$. We now obtain from Eqs. (1) and (2) the relations after much manipulation:

$$a_j = -\frac{ik}{4\pi} \oint_{s'} dS' \ [U_+(\mathbf{r}') \frac{\partial \psi_j(\mathbf{r}')}{\partial n'}]$$

$$f_j = \frac{ik}{4\pi} \oint_{s'} dS' \ [U_+(\mathbf{r}') \frac{\partial \operatorname{Re} \psi_j(\mathbf{r}')}{\partial n'}]. \tag{7a}$$

The following expansion has been proven to be satisfied on the surface for the rigid problem:

$$U_+(\mathbf{r}) = \sum_j b_j \operatorname{Re} \psi_j(\mathbf{r}). \tag{8}$$

Expression (7) now becomes:

$$a_j = -\frac{ik}{4\pi} \sum_m b_m \oint_{s'} dS' \ [\psi_m(\mathbf{r}') \frac{\partial \operatorname{Re} \psi_j(\mathbf{r}')}{\partial n'}] = -ik \sum_m Q_{jm} b_m$$

$$f_j = \frac{ik}{4\pi} \sum_m b_m \oint_{s'} dS' \ [\operatorname{Re} \psi_m(\mathbf{r}') \frac{\partial \operatorname{Re} \psi_j(\mathbf{r}')}{\partial n'}] = ik \sum_m \operatorname{Re} Q_{jm} b_m \tag{7b}$$

which can be expressed in matrix form as follows:

$$\mathbf{a} = -ik\mathbf{Q}\mathbf{b} \tag{9}$$

$$\mathbf{f} = ik \operatorname{Re} \mathbf{Q}\mathbf{b} \tag{10}$$

There are a variety of numerical strategies to attack this computational problem. The most straightforward (but unfortunately the most problematic) method is direct numerical inversion, to eliminate $\mathbf{b}$ from Eq. (9) and replace it in Eq. (10), to arrive at a formally convenient expression for the scattered wavefield, represented by $\mathbf{f}$. This leads to Eq. (11), relating the scattered field coefficients $\mathbf{f}$ with the incident field coefficients $\mathbf{a}$:

$$\mathbf{f} = -\operatorname{Re} \mathbf{Q} \mathbf{Q}^{-1} \mathbf{a} = \mathbf{T} \mathbf{a} \tag{11}$$

We can view this as a mapping from the incident field to the scattered field via the quantity $\mathbf{T} = \mathrm{Re}\,\mathbf{Q}\mathbf{Q}^{-1}$. It is conventional in certain areas of physics to describe such a mapping as a transition; hence this computational mapping is often referred to as a transition or "T-matrix" operation. One of the salient features of this mapping formulation (henceforth referred to as $\mathbf{T}$) is that $\mathbf{T}$ is only a function of the boundary conditions and the shape of the object. Consequently, once $\mathbf{T}$ is known, the scattered field can be determined from any chosen incident field. Of course, the incident field must be represented in the same sort of coordinate representation as the target for which one usually uses the spherical representation. Use of a spherical representation does not imply only scattering from spheres any more than Cartesian coordinates imply scattering from a box. Use of spherical harmonics imply more complicated objects than a sphere, and if needed the more general Gegenbauer polynomials can be employed for example for ellipsoidal objects. We might add that it is not necessary to obtain matrix $\mathbf{T}$. One can obtain $\mathbf{f}$ directly from Eqs. (9) and (10) instead. The disadvantage of that is that one must use a solver for each incident field described by $\mathbf{a}$. It will become apparent that $\mathbf{T}$ can have a complicated structure as we discuss the elastic case. For the simplest cases elements of $\mathbf{T}$ are a function of three indexes, namely an ordered pair of integers (i,j) that couple each incident partial wave i with each outgoing partial wave j. Further each element is a function of the azimuthal index m associated with spherical harmonics .

2.2. *An Iterative Convergent T-Matrix*

When generating the T-matrix, one needs to insure that the appropriate number of basis functions have been used, otherwise, if too few were used, the T-matrix will not converge. When generating a T-matrix for well known shapes, there are usually rules of thumb pertaining to the number of basis functions to use. For example, for a sphere the number of terms 2ka (where k is the wave number in the fluid and a the radius of the sphere) is a suitable number of expansion terms. This can be determined from angular momentum barrier arguments. However, this is not the case for arbitrary shapes. In the past, if the T-matrix had not converged, then one would have to regenerate the T-matrix with more terms. It is possible to test for convergence by determining if the generalized optical theorem is satisfied, by testing for symmetry or by simply redoing the calculation with higher terms, until the same answer is reproduced. With this in mind, an iterative algorithm was created so that there would be no guessing as to how many basis functions one would need to insure convergence.

The procedure[23-25] is based on the method of bordering for the inversion of general matrices. In general we start with an (NxN) matrix $\mathbf{A}$. It is possible to construct another matrix of order (N+1 x N+1) based on the original matrix $\mathbf{A}$. It is thus possible to build any order matrix by this procedure, since the expanded matrix $\mathbf{A'}$ of order (N+1 x N+1) can be used as the next starting point to obtain the matrix $\mathbf{A''}$ of order (N+2 x N+2). Let us begin with an N-th order T-matrix expressed as,

$$T_{N,N} = -\operatorname{Re} Q_{N,N} Q_{N,N}^{-1}.$$

(12)

For more general acoustic boundary-value problem, in which fields penetrate the interior of the obstacle and propagation there is described by wave number k' and density ρ', the matrix Q has the following form,

$$Q_{jm} = \frac{1}{4\pi} \oint_S dS[\frac{\rho'}{\rho} \operatorname{Re} \psi_j(k'r) \frac{\partial \psi_m(kr)}{\partial n} - \psi_m(kr) \frac{\partial \operatorname{Re} \psi_j(k'r)}{\partial n}]$$

(13)

We can specify two extreme cases: either Neumann ($\frac{\rho'}{\rho} \to \infty$, $k' = k$ - rigid boundary) or

Dirichlet ($\frac{\rho'}{\rho} \to 0$, $k' = k$ - soft boundary) boundary conditions on the object and Eq. (13) will become either:

$$Q_{jm} = \frac{1}{4\pi} \oint_S dS \ [\operatorname{Re} \psi_j(kr) \frac{\partial \psi_m(kr)}{\partial n}]$$

$$\operatorname{Re} Q_{jm} = \frac{1}{4\pi} \oint_S dS \ [\operatorname{Re} \psi_j(kr) \frac{\partial \operatorname{Re} \psi_m(kr)}{\partial n}]$$

(14)

with a Neumann boundary condition or

$$Q_{jm} = -\frac{1}{4\pi} \oint_S dS \ [\psi_m(kr) \frac{\partial \operatorname{Re} \psi_j(kr)}{\partial n}]$$

$$\operatorname{Re} Q_{jm} = -\frac{1}{4\pi} \oint_S dS \ [\operatorname{Re} \psi_m(kr) \frac{\partial \operatorname{Re} \psi_j(kr)}{\partial n}]$$

(15)

with a Dirichlet boundary condition. In general, if we expand the T-matrix of order NxN to an order of (N+1)x(N+1), Eq. (12) becomes

$$T_{N+1,N+1} = -\operatorname{Re} Q_{N+1,N+1} Q_{N+1,N+1}^{-1},$$

(16)

where,

$$\mathbf{Q}_{N+1,N+1} = \begin{pmatrix} \mathbf{Q}_{N,N} & \mathbf{c}_{N+1} \\ \mathbf{r}_{N+1} & a_{N+1N+1} \end{pmatrix}, \tag{17}$$

and

$$\mathbf{r}_{N+1} = (a_{N+1\,1}, \ldots, a_{N+1\,N}), \qquad \mathbf{c}_{N+1} = \begin{pmatrix} a_{1N+1} \\ \vdots \\ a_{N\,N+1} \end{pmatrix} \tag{18}$$

and a_{N+1N+1} is a number. Now $\mathbf{Q}^{-1}$ is expressed as,

$$\mathbf{Q}^{-1}{}_{N+1,N+1} = \begin{pmatrix} \mathbf{D}_{N,N} & \mathbf{s}_{N+1} \\ \mathbf{q}_{N+1} & b^{-1}{}_{N+1N+1} \end{pmatrix}, \tag{19}$$

where,

$$\mathbf{D}_{N,N} = \mathbf{Q}^{-1}{}_{N,N} - \mathbf{Q}^{-1}{}_{N,N}\mathbf{c}_{N+1}\mathbf{q}_{N+1}$$

$$\mathbf{q}_{N+1} = -\frac{\mathbf{r}_{N+1}\mathbf{Q}^{-1}{}_{N,N}}{b_{N+1N+1}}$$

$$\mathbf{s}_{N+1} = -\frac{\mathbf{Q}^{-1}{}_{N,N}\mathbf{c}_{N+1}}{b_{N+1N+1}}$$

$$b_{N+1N+1} = a_{N+1N+1} - \mathbf{r}_{N+1}\mathbf{Q}^{-1}{}_{N,N}\mathbf{c}_{N+1}.$$

Finally we can rewrite Eq. (17) as,

$$\mathbf{T}_{N+1,N+1} = -\mathrm{Re}\begin{pmatrix} \mathbf{Q}_{N,N} & \mathbf{c}_{N+1} \\ \mathbf{r}_{N+1} & a_{N+1N+1} \end{pmatrix}\begin{pmatrix} \mathbf{D}_{N,N} & \mathbf{s}_{N+1} \\ \mathbf{q}_{N+1} & b^{-1}{}_{N+1N+1} \end{pmatrix} = \begin{pmatrix} \mathbf{M}_1 & \mathbf{M}_2 \\ \mathbf{M}_3 & \mathbf{M}_4 \end{pmatrix}, \tag{20}$$

where

$$\mathbf{M}_1 = \mathbf{T}_{N,N}(\mathbf{I} - \frac{\mathbf{c}_{N+1}\mathbf{r}_{N+1}\mathbf{Q}^{-1}{}_{N,N}}{b_{N+1N+1}}) + \operatorname{Re}\mathbf{c}_{N+1}\mathbf{r}_{N+1}\mathbf{Q}^{-1}{}_{N,N}$$

$$\mathbf{M}_2 = \frac{\operatorname{Re}\mathbf{Q}_{N,N}\mathbf{Q}^{-1}{}_{N,N}\mathbf{c}_{N+1}}{b_{N+1N+1}}) - \frac{\operatorname{Re}\mathbf{c}_{N+1}}{b_{N+1N+1}}$$

$$\mathbf{M}_3 = -\operatorname{Re}\mathbf{r}_{N+1}\mathbf{Q}^{-1}{}_{N,N}(\mathbf{I} - \frac{\mathbf{c}_{N+1}\mathbf{r}_{N+1}\mathbf{Q}^{-1}{}_{N,N}}{b_{N+1N+1}}) + \frac{\operatorname{Re}\mathbf{r}_{N+1}\mathbf{Q}^{-1}{}_{N,N}a_{N+1N+1}}{b_{N+1N+1}}$$

$$\mathbf{M}_4 = \frac{\operatorname{Re}\mathbf{r}_{N+1}\mathbf{Q}^{-1}{}_{N,N}\mathbf{c}_{N+1}}{b_{N+1N+1}} - \frac{\operatorname{Re}a_{N+1N+1}}{b_{N+1N+1}}$$

There are several advantages in using this algorithm. One that was already mentioned is that the algorithm takes the guess work out of choosing the number of basis functions. The T-matrix is conditioned as it is built-up. This relaxes some of the complications associated with ill-conditioning, which is sometimes encountered for various object shapes. Finally one can see by inspection that the addition of columns and rows is an operation involving either a matrix and a vector or two vectors, which when performed on vector machines and modern pipeline computers is very fast and economical.

2.3. The Coupled Higher Order T-matrix

As noted above, a straightforward evaluation of Eq. (11) is usually not the most efficient way to obtain for **f**. The reason for this is that in many cases, **Q** is very large and often ill-conditioned, and therefore finding the inverse of **Q** may not be possible. An alternative method[25,26] to obviate this difficulty is the coupled higher-order T-matrix method described below. The rationale behind this method is that Eq. (6a), describing the incident field, requires a limited number of partial waves (depending on frequency), while Eq. (8), used to obtain the surface field, etc., may require considerably more expansion terms, depending on the nature of the surface. However, for **Q** to be invertable, it must be a square matrix, requiring that Eqs. (6) and (8) have the same number of expansion terms. Since beyond some point the expansion coefficients of Eq. (6) become very small, this results in the ill-conditioned nature of **Q**. The coupled higher-order T-matrix method overcomes this problem by a formulation that "couples" only the relevant expansion terms in Eq. (6) with all order terms of Eq. (8). The most elementary formulation of this solution is to block **Q** into four sub matrices (**Q** (ij), where ij = (N,M) and demand that the **Q** (ii) matrices be square). This leads to a new **T** matrix of order (N,N) which is convergent and requires an inverse no larger than the largest pair of (ii):

$$\mathbf{T}_{N,N} = -\mathbf{P}\,\mathbf{G}^{-1} \tag{21}$$

$$\mathbf{P} = \operatorname{Re}\mathbf{Q}_{N,N} - \operatorname{Re}\mathbf{Q}_{N,M}\mathbf{Q}^{-1}{}_{M,M}\mathbf{Q}_{M,N} \tag{22}$$

$$\mathbf{G} = \mathbf{Q}_{N,N} - \mathbf{Q}_{N,M}\mathbf{Q}^{-1}{}_{M,M}\mathbf{Q}_{M,N} \tag{23}$$

A generalization of this method (for a nine-block representation of $\mathbf{Q}$) has been developed[26] and has been proven very effective in dealing with formerly difficult problems.

2.4. The Eigenexpansion Method

In this section another method based on eigenfunctions associated with specific surfaces is examined. The $\mathrm{Re}\,\psi_j$'s in Eq. (8) are not the most efficient functions to employ for general cases. Our intention is to determine more efficient expansion functions, i.e., those that would form as close as possible an orthonormal (ON) basis set on the surface of the bounded object. We then obtain a more effective expansion of U_+ on the object surface.[27,28] A way to do it is obtained by the premultiplication of Eq. (9) by the adjoint of $\mathbf{Q}$, namely $\mathbf{Q}^\dagger$, where the latter quantity is the conjugate transpose of $\mathbf{Q}$:

$$\mathbf{Q}^\dagger \mathbf{a} = -ik\mathbf{Q}^\dagger\mathbf{Q}\mathbf{b} = -ik\mathbf{H}\mathbf{b} \quad, \tag{24}$$

where the matrix $\mathbf{H}$ can easily be shown to be self-adjoint or Hermitian (where $\mathbf{H}^\dagger = \mathbf{H}$). The advantage of pursuing this course is that we can easily find the eigenvalues and eigenfunctions of $\mathbf{H}$ that have known and computationally desirable properties. In particular, the eigenvalues for self-adjoint operators are real, positive, and increase monotonically, and form an orthonormal set of functions on the surface. The eigenfunctions can be obtained as follows:

$$\mathbf{H}\mathbf{q}_m = \lambda_m \mathbf{q}_m. \tag{25}$$

Here, the adjoint of $\mathbf{q}_k$ is $\mathbf{q}_k{}^\dagger$, so that

$$\mathbf{q}_k{}^\dagger \mathbf{q}_m = \delta_{km}, \tag{26}$$

where δ_{km} is the Kronecker delta function. We also require the ordering $\lambda_1 < \lambda_2 < \lambda_3 \dots$, where the dimension of $\mathbf{H}$ is that required for convergence and relates to the number of surface quantities required in expanding U_+. One can show that the $\mathbf{q}_k$'s are related to an alternate representation of the functions of Eq. (9) with the desired property that they are an orthogonal representation (with another computationally desirable property to be discussed). Thus, we have

$$\mathbf{b} = \sum_m \alpha_m \mathbf{q}_m \quad, \tag{27}$$

so that Eq. (24) is:

$$\mathbf{Q}^\dagger \mathbf{a} = -ik\sum_m \alpha_m \mathbf{H}\mathbf{q}_m = -ik\sum_m \alpha_m \lambda_m \mathbf{q}_m \tag{28}$$

Thus, using the orthogonality property of the $\mathbf{q}_m$'s, we obtain:

$$\alpha_m = \frac{i}{k\lambda_m}\mathbf{q}_m^\dagger \mathbf{Q}^\dagger \mathbf{a}, \quad b = \frac{i}{k}\sum_m \frac{\mathbf{q}_m^\dagger \mathbf{Q}^\dagger \mathbf{a}\mathbf{q}_m}{\lambda_m} \tag{29}$$

We also expand the exterior problem as follows (see Eq.(7b)):

$$f_j = \frac{ik}{4\pi}\sum_m b_m \oint_{S'} dS' \ [\mathrm{Re}\,\psi_m(\mathbf{r}') \frac{\partial \mathrm{Re}\,\psi_j(\mathbf{r}')}{\partial n'}] = ik\sum_m \mathrm{Re}\,Q_{jm}b_m$$

The final expression for the scattered field in terms of the incident wave field is thus:

$$\mathbf{f} = -\sum_m \mathrm{Re}\,\mathbf{Q}\mathbf{q}_m \frac{1}{\lambda_m}\mathbf{q}_m^\dagger \mathbf{Q}^\dagger \mathbf{a} . \tag{30}$$

Although the above expression has proven computationally efficient, it is also possible and sometimes necessary to obtain an alternative T-matrix representation. This may be done by means of the following derived relation:

$$\mathbf{T} = -\mathrm{Re}\,\mathbf{Q}\mathbf{V}\mathbf{L}^{-1}\mathbf{V}^\dagger \mathbf{Q}^\dagger , \tag{31}$$

where the matrix $\mathbf{V}$ is constructed from the M column of eigenvectors $\mathbf{q}_1$ to $\mathbf{q}_M$ of the MxM square matrix $\mathbf{H}$ and an MxM diagonal matrix $\mathbf{L} = diag(\lambda_1, ..., \lambda_M)$ is constructed from the M eigenvalues of $\mathbf{H}$. The matrix $\mathbf{V}$ is obviously unitary because of the orthogonality of the eigenvectors. Since the set of eigenvectors forms a unitary matrix the above expression may be viewed as having been obtained by transforming $\mathbf{Q}$ via a unitary matrix obtained from $\mathbf{V}$ times its adjoint. This offers a generalization of this method to one more complicated. For the general problem a T-matrix may be written in the form:

$$\mathbf{T} = -\mathbf{P}\,\mathbf{G}^{-1}, \tag{32}$$

with solutions of the form:

$$\mathbf{T} = -\mathbf{P}\,\mathbf{V}\mathbf{L}^{-1}\mathbf{V}^\dagger \mathbf{Q}^\dagger. \tag{33}$$

2.5. The T-Matrix for Fluid Loaded Elastic Objects

We now consider the case of an elastic shell in a fluid. The procedure for the multilayered scatterer can be generalized from the following consideration. The starting point for this procedure makes use of the equation of motion in a fluid:

$$\nabla^2 \mathbf{u}^f + k^2 \mathbf{u}^f = 0, \tag{34}$$

where k is the acoustic wavenumber and $\mathbf{u}^f$ is the particle displacement in the fluid. Note here that for the elastic problem we are required to use a displacement (a vector quantity) rather than the scalar potential because in the elastic case the traction and other conserved quantities are the displacement vector functions. The equation of motion in an elastic body for the monochromatic wave of frequency ω is:

$$(\kappa_c^2)^{-1} \nabla\nabla \cdot \mathbf{u} - (\kappa_s^2)^{-1} \nabla \times \nabla \times \mathbf{u} + \mathbf{u} = 0$$
$$\kappa_c^2 = \frac{\rho\omega^2}{\lambda + 2\mu} \text{ and } \kappa_s^2 = \frac{\rho\omega^2}{\mu} , \tag{35}$$

where κ_c and κ_s are the longitudinal and transverse wave numbers corresponding to compressional and shear waves, respectively, μ is the shear modules of the medium and $\lambda + 2\mu/3$ is its compression modules (ratio of isotropic pressure to fractional rate of decrease of volume), ρ is a mass density of elastic material. Boundary conditions at the fluid-elastic interface are:

$$\hat{\mathbf{n}}\mathbf{u}_+ = \hat{\mathbf{n}}\mathbf{u}_-, \quad \hat{\mathbf{n}}\mathbf{t}_+ = \hat{\mathbf{n}}\mathbf{t}_-, \quad \nabla \times \mathbf{t}_- = 0, \tag{36}$$

where $\hat{\mathbf{n}}$ is a unit vector normal to the surface of the object. The traction $\mathbf{t}$ (that is a normal component of the stress tensor) for the outer (+) and inner (−) surfaces are:

$$\mathbf{t}_+ = \hat{\mathbf{n}} \cdot \{\lambda_+ \bar{\mathbf{I}} \nabla \cdot \mathbf{u}_+\}, \quad \mathbf{t}_- = \hat{\mathbf{n}} \cdot \{\lambda_- \bar{\mathbf{I}} \nabla \cdot \mathbf{u}_- + \mu(\nabla \mathbf{u}_- + \mathbf{u}_- \nabla)\} \tag{37}$$

Here $\bar{\mathbf{I}}$ is the unit dyadic. The boundary conditions for the elastic case are vectors, so the Green's function which serves to transform the boundary conditions and the source density into the solution must be a vector operator. Thus, we can define the elastic material Green's function $\overline{\mathbf{G}}(\mathbf{r},\mathbf{r}')$ which for the elastic problem is a dyadic and Green's stress tensor $\overline{\overline{\Xi}}(\mathbf{r},\mathbf{r}')$ of the third rank. The corresponding quantities in the fluid are denoted by $\overline{\mathbf{G}}_f(\mathbf{r},\mathbf{r}')$ and $\overline{\overline{\Xi}}_f(\mathbf{r},\mathbf{r}')$. The Green's dyadic for the elastic material is defined by:

$$(\kappa_c^2)^{-1} \nabla\nabla \cdot \overline{\mathbf{G}} - (\kappa_s^2)^{-1} \nabla \times \nabla \times \overline{\mathbf{G}} + \overline{\mathbf{G}} = \bar{\mathbf{I}}\delta(\mathbf{r} - \mathbf{r}'), \tag{38a}$$

and can be determined as a sum of the longitudinal and transverse dyadics:

$$\overline{\mathbf{G}} = \kappa_l{}^2 \overline{\mathbf{G}}_l + \kappa_t{}^2 \overline{\mathbf{G}}_t . \tag{38b}$$

We note that the two parts of the solution have different basic scalar Green's functions, corresponding to the different velocities of propagation of the two types of wave. When considering the inner shell, if one uses a fluid filled inclusion then the boundary conditions are similar to those of the outer shell and for the case of an evacuated inclusion then one merely requires that $\mathbf{t} = 0$ at the elastic-vacuum interface. For all EBC-formulations one employs a surface boundary integral representation which may be viewed as an expression of the Huygens' principle. The boundary integral equations that follow are such an expression for the elasticity equation and in the form used here was developed by Varadan and Pao.[29] The integral representation for the field in the fluid region is given by

$$\int_{S'} dS' \{ \mathbf{u}_+(\mathbf{r}') \cdot \hat{\mathbf{n}}' \cdot \overline{\Xi}_f(\mathbf{r},\mathbf{r}') - \mathbf{t}_+(\mathbf{r}') \cdot \overline{\mathbf{G}}_f(\mathbf{r},\mathbf{r}') \} + \mathbf{u}^f{}_i(\mathbf{r}) = \begin{cases} \mathbf{u}^f(\mathbf{r}), \ \mathbf{r} \text{ outside } S' \\ 0, \ \mathbf{r} \text{ inside } S' \end{cases}, \tag{39a}$$

where $\mathbf{u}^f{}_i(\mathbf{r})$ is an incident field from the fluid on the scatterer and $\mathbf{u}^f(\mathbf{r})$ is a total field in fluid. The integral representation for the displacement field $\mathbf{u}$ inside the elastic layer enclosed between S_1 and S_2 is given by

$$-\int_{S_1} dS' \{ \mathbf{u}_-(\mathbf{r}') \cdot \hat{\mathbf{n}}' \overline{\Xi} (\mathbf{r},\mathbf{r}') - \mathbf{t}_-(\mathbf{r}') \cdot \overline{\mathbf{G}}(\mathbf{r},\mathbf{r}') \} + \int_{S_2} dS' \{ \mathbf{u}_+(\mathbf{r}') \cdot \hat{\mathbf{n}}' \overline{\Xi} (\mathbf{r},\mathbf{r}') - \mathbf{t}_+(\mathbf{r}') \cdot \overline{\mathbf{G}}(\mathbf{r},\mathbf{r}') \}$$

$$= \begin{cases} \mathbf{u}(\mathbf{r}), \ \mathbf{r} \text{ between } S_1 \text{ and } S_2 \\ 0, \ \mathbf{r} \text{ outside } S_1 \text{ or inside } S_2 \end{cases}$$

$$\tag{39b}$$

In Eqs. (39a) and (39b), the + or - subscripts for $\mathbf{u}$ and $\mathbf{t}$ denote whether the surface is approached from the outside or inside. There are two expressions here. The first is the exterior problem and is used to determine the field external to the target. It yields the total field $\mathbf{u}^f(\mathbf{r})$ in the exterior of the target, and zero when in the interior of the target. The second expression is useful for determining the field in the shell and so one must integrate over both the outer surface and the inner surface, hence the two integral expressions. Here, the equation calculates the field $\mathbf{u}(\mathbf{r})$ in the interior region but leads to the value zero in the region outside the shell, which includes both the exterior region and the region inside the shell. There are alternative forms for surface integral representations but this form has been viewed as a major advancement required for the development of a T-matrix for elastic objects. We need to solve these equations subject to the boundary conditions at the interfaces and with the appropriate asymptotic boundary conditions. Once again one resorts to use of the partial wave expansions in three-dimensions but for this case in vector

form. In the spherical coordinate system the partial wave expansion functions in the fluid and the elastic body are:[30]

$$\bar{\psi}^f{}_{nm} = \xi_{nm} \nabla \{h_n(kr) Y_{nm}(\theta, \varphi)\},$$

$$\bar{\psi}^1{}_{nm} = \sqrt{\frac{\kappa_c}{\kappa_s}} \xi_{nm} \nabla \{h_n(\kappa_c r) Y_{nm}(\theta, \varphi)\},$$

$$\bar{\psi}^2{}_{nm} = \frac{\kappa_s \xi_{nm}}{\sqrt{n(n+1)}} \nabla \times \{r h_n(\kappa_s r) Y_{nm}(\theta, \varphi)\},$$

$$\bar{\psi}^3{}_{nm} = \frac{1}{\kappa_s} \nabla \times \bar{\psi}^2{}_{nm}, \quad \xi_{nm} = \sqrt{\frac{\varepsilon_n (2n+1)(n-m)!}{4\pi(n+m)!}}, \tag{40}$$

where ε_n is the Neumann constant, the Y's are spherical harmonics and the h's are outgoing spherical Hankel functions. The outgoing Hankel functions satisfy the radiation boundary condition. For the set of the basis functions regular at the origin one has to use the spherical Bessel functions in Eqs. (40) instead of the spherical Hankel functions. The essential step in the T-matrix method is the expansion of all fields and Green's functions in Eqs. (39) in terms of spherical basis functions which are the partial wave expansions natural to the 3-dimensional problem. We expand everything in these partial waves as follows:

$$\mathbf{u}^f{}_i(\mathbf{r}) = \sum_j a_j \operatorname{Re} \bar{\psi}^f{}_j(\mathbf{r}), \qquad \mathbf{u}^f{}_s(\mathbf{r}) = \sum_j f_j \bar{\psi}^f{}_j(\mathbf{r}),$$

$$\mathbf{u}(\mathbf{r}) = \sum_{i=1}^{3} \sum_j (\alpha^i{}_j \operatorname{Re} \bar{\psi}^i{}_j(\mathbf{r}) + \beta^i{}_j \bar{\psi}^i{}_j(\mathbf{r})). \tag{41}$$

Note that the interior displacement vector (in the elastic layer) includes components associated with the regular Bessel function and the expansion coefficients α's and an outgoing solution allowed for waves scattered from the inner shell, associated with the β expansion coefficients. The field in the innermost layer that includes the origin of coordinates is expanded in regular functions only. The Green's dyadics for the elastic and fluid cases are also represented using biorthogonal expansions for normal operators:

$$\overline{\mathbf{G}}(\mathbf{r}, \mathbf{r}') = \frac{i\kappa_s}{\rho\omega^2} \sum_{i=1}^{3} \sum_j \bar{\psi}^i{}_j(r_>) \operatorname{Re} \bar{\psi}^i{}_j(r_<),$$

$$\overline{\mathbf{G}}^f(\mathbf{r}, \mathbf{r}') = i \sum_j \bar{\psi}^f{}_j(r_>) \operatorname{Re} \bar{\psi}^f{}_j(r_<).$$ (42)

The details that lead to the following expressions are quite involved but in spirit similar to the rigid scatter case . The major difference is the use of additional constraints imposed by layering and the added boundary conditions for the fluid-elastic interface. The elasto-acoustic boundary interface introduces mode conversion which allows for the mechanism of the transition from a purely acoustical environment to one consisting of shear as well as compressional waves in the elastic medium. This results caused by such interface phenomena is responsible for a plethora of resonances that makes scattering from elastic targets a rich and exciting area to investigate. The T-matrix for the elastic case is:[30]

$$\mathbf{T} = -\{\mathbf{Q}[\operatorname{Re}, \operatorname{Re}] - \mathbf{Q}[\operatorname{Re}, O]\mathbf{T}^2\}\{\mathbf{R}[\operatorname{Re}, O]\mathbf{T}^2 + \mathbf{R}[\operatorname{Re}, \operatorname{Re}] + i\mathbf{T}^2\}^{-1}\mathbf{P}[\operatorname{Re}, \operatorname{Re}] \times$$

$$\times\{\{\mathbf{Q}[O, \operatorname{Re}] - \mathbf{Q}[O, O]\mathbf{T}^2\}\{\mathbf{R}[\operatorname{Re}, O]\mathbf{T}^2 + \mathbf{R}[\operatorname{Re}, \operatorname{Re}] + i\mathbf{T}^2\}^{-1}\mathbf{P}[\operatorname{Re}, \operatorname{Re}]\}^{-1}.$$ (43)

Notations Re and O indicate that matrix elements are functions of the regular or/and outgoing basis functions. Here $\mathbf{T}^2$ corresponds to a reflection from the inner face of a shell. For a solid $\mathbf{T}^2 = 0$ so that[32]

$$\mathbf{T} = -\mathbf{Q}[\operatorname{Re}, \operatorname{Re}]\{\mathbf{R}[\operatorname{Re}, \operatorname{Re}]\}^{-1}\mathbf{P}[\operatorname{Re}, \operatorname{Re}]\{\mathbf{Q}[O, \operatorname{Re}]\{\mathbf{R}[\operatorname{Re}, \operatorname{Re}]\}^{-1}\mathbf{P}[\operatorname{Re}, \operatorname{Re}]\}^{-1}.$$ (44)

The interior reflection $\mathbf{T}^2$ may be due to an elastic solid inclusion, a sound void, or a rigid inclusion which has the form:

$$\mathbf{T} = -\mathbf{Q}[\operatorname{Re}, \operatorname{Re}]\{\mathbf{Q}[\operatorname{Re}, O]\}^{-1}.$$ (45)

The matrix elements of $\mathbf{Q}, \mathbf{R}, \mathbf{P}$ for Eqs. (43) and (45) are as follows:

$$\mathbf{Q}_{in,i'n'}\begin{bmatrix} O & O \\ \operatorname{Re} & \operatorname{Re} \end{bmatrix} = \frac{\kappa_s}{\rho\omega^2} \int_{S_{inner}} dS\{\mathrm{t}\begin{bmatrix} O \\ \operatorname{Re} \end{bmatrix}\bar{\psi}^f{}_n\cdot\begin{bmatrix} O \\ \operatorname{Re} \end{bmatrix}\bar{\psi}^{i'}{}_{n'} - \begin{bmatrix} O \\ \operatorname{Re} \end{bmatrix}\bar{\psi}^f{}_n\cdot \mathrm{t}\begin{bmatrix} O \\ \operatorname{Re} \end{bmatrix}\bar{\psi}^{i'}{}_{n'}\}$$

$$\mathbf{R}_{in,i'n'}\begin{bmatrix} \operatorname{Re} & \operatorname{Re} \\ & O \end{bmatrix} = \frac{\kappa_s}{\rho\omega^2} \int_{S_{outer}} dS\{\mathrm{t}[\operatorname{Re}\bar{\psi}^i{}_n]\cdot\begin{bmatrix} \operatorname{Re} \\ O \end{bmatrix}\bar{\psi}^{i'}{}_{n'}\Big]_{\tan gent} - \hat{\mathbf{n}}\cdot\operatorname{Re}\bar{\psi}^{i'}{}_n\hat{\mathbf{n}}\cdot \mathrm{t}\begin{bmatrix} \operatorname{Re} \\ O \end{bmatrix}\bar{\psi}^{i'}{}_{n'}\}$$

$$\mathbf{P}_{in,n'}[\operatorname{Re}, \operatorname{Re}] = \frac{\kappa_s}{\rho\omega^2} \int_{S_{outer}} dS\{\hat{\mathbf{n}}\cdot \mathrm{t}[\operatorname{Re}\bar{\psi}^i{}_n]\hat{\mathbf{n}}\cdot\operatorname{Re}\bar{\psi}^f{}_{n'}\}.$$ (46)

The matrix elements of Eq. (45) are similar but less complicated than expressed by $\mathbf{Q}$ in Eq. (46). Peterson and the Varadans[30],who developed this formulation, have also shown

that one can have layers of interior shells which then involve recursive expressions that if terminated by a fluid inclusion lead to a series of expressions similar to that expressed by Eq. (43).

In this development we have avoided the issue of the so-called Rayleigh hypothesis which pertains to partial wave expansions of the elastic field in the shell. That issue is not entirely clear. A sufficient condition that one be able to expand the field in that region in a spherical representation is that it is possible to envelop a sphere in the annular region so that in that region the field is constant on that surface for any variation of angle. Clearly, if that is a necessary condition, then this formulation which is based on such a requirement is very limiting. Obviously, it would always be valid for spherical shapes and in fact, this formulation agrees with the results derived from separation of variables methods. However, for non-spherical shapes these expressions would not be useful for thin shells if arguments on the necessity of satisfying the Rayleigh hypothesis are true. To suggest that the demand for the Rayleigh hypothesis be satisfied may be too strong is determined by calculations in which these expressions have been used for thin spheroidal shells. The results appear to be valid and are consistent with expectations suggested from those of thin spherical shells. There is some suggestion that the spherical expansion is still useful, but requires more expansion terms with increasing aspect ratio along with higher precision. A test of this assumption[31,32] appears to substantiate this hypothesis, but the number of expansion terms and the requirement on precision increases rather dramatically with only small increases in aspect ratio. Hackman[33] and others have attempted to overcome this problem by making use of spheroidal basis states for which there are arguments that the Rayleigh hypothesis is less restrictive. Unfortunately, spheroidal functions do not separate in partial wave space for the elastodynamic equations and one can not take advantage of that feature with those functions. Nonetheless, Hackman has been able to obtain results for more elongated thin elastic shells than possible using the spherical basis formulation here. The Varadans have proposed making use of thin shell theory and developed a T-matrix that would be useful subject to the restrictions of thin shell theories. The Varadans[34] proposal seems promising and because of the variety of thin shell theories it is quite possible that some forms would be useful in understanding some features of scattering from elongated thin shells. The development proposed by the Varadans can avoid making use of finite element basis functions. Calculations making use of thin shell theories and the method of moments have shown promising results, though for water loaded shells we believe there are serious limitations for any known thin shell theory. There are massive engineering efforts to incorporate finite element techniques that include considerable structural properties of an object under investigation. Results in the air craft industry in which thin shell theories are more useful due to weak coupling of low impedance air with the elastic structure have proven useful. Unfortunately, thin shell theories are constructed from notions based on the free vibrations of surfaces that are difficult to couple with heavy fluid loading correctly. Many resonances observed for water loaded elastic shells are strongly coupled with or entirely dominated by the fluid loading which are missed by many thin shell theories. The form of the T-matrix above does deal

well with thick shells, which are physically uninteresting from a technological point of view. The return signals from thick water loaded shells manifest resonances of the symmetric and anti-symmetric (flexural) modal class as well as the enormous number of symmetric and anti-symmetric Lamb resonances which proliferate with increasing frequency. Thin shell theories which form the basis of finite-element techniques do not treat Lamb resonances, are not able to treat Pseudo-Stoneley resonances correctly, and are not likely to correctly treat flexing or resonances due to bending or flexing of the overall structure. One must conclude that much work is needed in this area to arrive at satisfactory predictive techniques for realistic objects imbedded in water. However, the T-matrix method described here offers a useful bench mark for any approximate theories that may be on the horizon. In the next section we examine an elegant technique to extend the range of the T-matrix. The initial idea was formulated by Waterman[19] to simple targets and was extended to more complicated targets by Werby and Green[20].

2.7. *The S-Matrix and the Imposition of Unitarity and Symmetry*

Eq. (43) is difficult to deal with because the matrices are often poorly conditioned. This leads to unmanageable matrix inversions as well as a disparity in convergence of the upper and lower matrix elements of the T-matrix. We obviate this problem by a method we refer to as the unitary method which we briefly outline. It is a generalization of one developed by Waterman for simpler cases and we have referred to it as the Generalized Waterman procedure. One of the salient features of this method is that symmetry is always maintained for the upper and lower elements of the T-matrix. Each element and its transpose converge at the same rate. Further, no elements of the T-matrix can ever be enormously large due to error because unitarity is always imposed. It is possible for the method to fail due to a problem in precision and the dynamic range of the exponential but that becomes obvious by examining certain output parameters. The T-matrix maps the incident field into the scattered field. We know from reciprocity that T is symmetric. Another quantity used in quantum physics is the S-matrix which relates the ingoing field with the outgoing field. An interesting feature of the scattering matrix S is that it relates the total flux amplitude before a scattering event to that after the event. Thus, if there is no energy lost in the scattering process, then S must be unitary, that is the mapping S must preserve the total energy flux. It is well known that the relation between S and T is $S=I+2T$. We assume that the target and fluid are not energy absorbing so that S must be unitary. We can write $T = -RP^{-1}$ which is the most general form of a T-matrix. It is trivial that due to the symmetry of T (a consequence of reciprocity of the wave equation), S is also symmetric. Then we represent S as follows:

$$S = I + 2T = I - 2RP^{-1} = UP^{-1} \ , \tag{47}$$

where $U = P - 2R$. S now becomes

$$S = S^{'} = P^{-1'}U' \ , \tag{48}$$

where $\mathbf{S}'$ is a transpose matrix.

We represent $\mathbf{U}$ (using Schmidts theorem) in the following decompositions $\mathbf{U} = \mathbf{U}_1 \mathbf{M}$ and $\mathbf{P} = \mathbf{P}_1 \mathbf{N}$ where $\mathbf{P}_1$ and $\mathbf{U}_1$ are unitary and $\mathbf{N}$ and $\mathbf{M}$ are upper triangular. Here "$\mathbf{I}$" will designate the unit matrix. Then $\mathbf{S} = \mathbf{P}_1^{-1'} \mathbf{L} \mathbf{U}_1'$, where $\mathbf{L} = \mathbf{N}^{-1'} \mathbf{M}'$. But $\mathbf{SS}^{\dagger} = \mathbf{I} = \mathbf{P}_1^* \mathbf{L} \mathbf{L}^{\dagger} \mathbf{P}_1^{*-1}$, where $\mathbf{P}_1^*$ is a complex conjugate matrix. It implies $\mathbf{LL}^{\dagger} = \mathbf{I}$. We see that $\mathbf{L}$ is unitary due to the uniqueness of the inverse of a matrix and the sufficiency that the relation $\mathbf{L}^{-1} = \mathbf{L}^{\dagger}$ guarantees unitarity. Since the product of two upper triangular matrices must be upper triangular, then $\mathbf{L}$ is upper triangular. But it has to be lower triangular too since the upper triangular elements are the complex conjugates of the lower triangular elements (due to unitarity) which are zero and therefore it must be diagonal. The diagonal elements have to be real since from the Graham-Schmidt construction they are composed simply of the norms of the rows of each matrix. This implies that $\mathbf{L}$ is the unit matrix. Thus, $\mathbf{S} = \mathbf{U}_1 \mathbf{P}_1^{\dagger}$ and this leads to the new expression:

$$\mathbf{T} = (\mathbf{U}_1 \mathbf{P}_1^{\dagger} - \mathbf{I}) / 2. \tag{49}$$

This expression is much easier to calculate than expressions dependent upon matrix inversion and it guarantees unitarity and symmetry of the T-matrix at any level of truncation.[20] An added feature of this new approach is that one can test for convergence by examining the diagonal elements of $\mathbf{L}$. They must be close to unity for convergence to be obtained. This is an interesting application of matrix abstractions that illustrates the power of formal mathematical manipulation to reduce a complicated problem to one not only simpler to solve, but with required constraints imposed on the final expression.

2.8. Scattering from Objects Near an Interface

To treat this problem correctly we must first add a few comments about Green's functions. For problems in free space single scatterers require an outgoing Green's function that satisfies the surface inhomogenious boundary conditions as well as the asymptotic condition (the Sommerfeld radiation condition). The function is defined at the origin of the object and has discontinuities in the normal gradient at the object surface in order to accommodate the inhomogenious surface boundary conditions at the object surfaces. In the event, if there are two or more objects, then an adjustment must be made because one can not use an outgoing Green's function in the region where a wave can reflect back and forth between the two surfaces. Thus, for that region rather than an outgoing Green's function, one must construct a standing wave Green's function just for that region. We will refer to Fig. (1).

We use the Huygens' principle, developed by P. Waterman[1-5] to construct the T-matrix for two objects:

$$U(\mathbf{r}) = U_i(\mathbf{r}) + U_s(\mathbf{r}) =$$

$$= U_i(\mathbf{r}) + \frac{1}{4\pi} \oint_{S_1 + S_2} [U_+(\mathbf{r}') \frac{\partial G(\mathbf{r}, \mathbf{r}')}{dn'} - G(\mathbf{r}, \mathbf{r}') \frac{\partial U_+(\mathbf{r}')}{\partial n'}] dS', \quad \mathbf{r} \in D_{ext}, \ \mathbf{r}' \in D_{int}, \quad (50)$$

where vector $\mathbf{r}$ is in D_{ext}, the set of points exterior to the object, $G(\mathbf{r}, \mathbf{r}')$ is the outgoing wave Green's function for unbounded space, $\mathbf{r}'$ is in D_{int}, the set of points interior to the bounded object, S' represents the two object surfaces, $\hat{n}$ is a unit outward normal to the surface, $U_i(\mathbf{r})$ is a known incident field, $U_s(\mathbf{r})$ is unknown scattered field, and $U_+(\mathbf{r}')$ is the total field on the surface of the object. The incident and scattered fields can be expanded by the complete set of eigenfunctions as it was done for a single scatterer:

$$U_i(\mathbf{r}) = \sum_j a_j \operatorname{Re} \psi_j(\mathbf{r}),$$

$$U_s(\mathbf{r}) = \sum_j f_j \psi_j(\mathbf{r}) \quad (51)$$
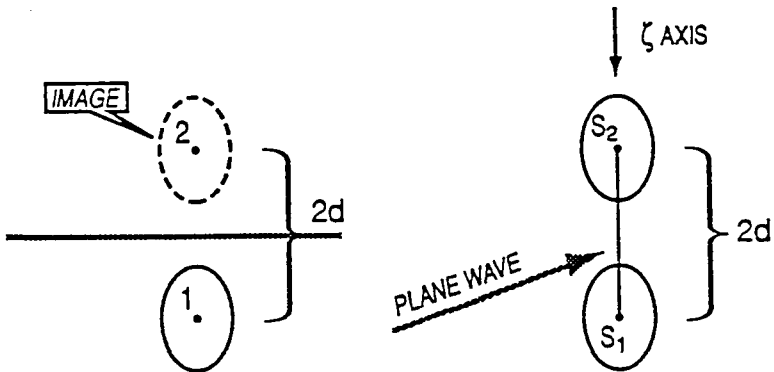
Fig. 1. Schematic of an object near an interface.

where ψ_j are outgoing functions, $\operatorname{Re}\psi_j$ are functions regular at the origin, a_j are known, and f_j are unknown.

   In a manner similar to the single scatterer a T-matrix was formulated by Strom[35,36], et. al. for the two-object case. The following formulation is also useful in consideration of the method of images for formulating the problem of scattering from objects near rigid and pressure release surfaces. Using the bi-orthogonal expansion for the Green's function, we have:

$$G(\mathbf{r}_1, \mathbf{r}_2, \mathbf{r}) = ik \sum_j \psi_j(\mathbf{r}_>) \operatorname{Re} \psi_j(\mathbf{r}_<), \quad (52)$$

for **r** outside of the sphere $r = r_0$. That is, the Green's function is strictly outgoing. However, if $\mathbf{r} \in S_1$, we have:

$$G(\mathbf{r}_1, \mathbf{r}_2, \mathbf{r}) = -ik \sum_j \psi_j(\mathbf{r}_>) \, \mathrm{Re}\, \psi_j(\mathbf{r}_<) \,, \tag{53}$$

when $\mathbf{r}_<$ is inside object 2 (1) and $\mathbf{r}_>$ is outside the surface 1 (2); and

$$G(\mathbf{r}_1, \mathbf{r}_2, \mathbf{r}) = -ik \sum_j \mathrm{Re}\, \psi_j(\mathbf{r}_>) \, \mathrm{Re}\, \psi_j(\mathbf{r}_<) \,, \tag{54}$$

when $\mathbf{r}_>$ is inside object 1(2) and $\mathbf{r}_<$ is on the surface of object 2(1).

It is important to note that the first two Green's functions are the standard outgoing Green's functions and satisfy the Sommerfeld radiation condition. Since, the third Green's function involves a strictly bounded region where the sound field reflects back and forth between the objects then the Sommerfeld radiation condition is not required since the sub-system is bounded and this calls for the standing wave Green's function. Thus, use of an outgoing Green's function would lead to an erroneous expression.

We are required to shift from the origin of object 1 to that of object 2: $\mathbf{r}_1 = 2\mathbf{d} - \mathbf{r}_2$ and $\mathbf{r}_2 = 2\mathbf{d} - \mathbf{r}_1$, when we integrate over the respective surfaces. Now we must deal with translation or rotation of the spherical Bessel functions which are regular (at the object origin) in the spherical coordinate system. That is, we must determine $j(kr + kd)$ in terms of the $j(kr)$'s. It is well-known that:

$$j_l(2\mathbf{d} - \mathbf{r}_1) = \sum_m R_{lm}(2d) j_m(\mathbf{r}_1) \,, \tag{55}$$

where R is an SO-3 transformation that translates or rotates spherical Bessel functions. The translation/rotation properties of the spherical Bessel functions $\{\, j_m(kr)\,\}$ are easy to derive by noting that $Exp\{ik(d+r)Cos(\alpha)\} = Exp\{ikrCos(\alpha)\}\, Exp\{ikdCos(\alpha)\}$ where α is the angle between k and $(d+r)$. Then by expanding each exponential in the Rayleigh series and using the addition theorem for spherical harmonics one need to multiply the left and right series by the complex conjugate of the spherical harmonics associated with the left hand side and integrate over all space using orthogonality of the spherical harmonics to obtain a series on the right equal to $\{\, j_m(k(r + d))\,\}$. The two integrals are well-known to be related to Clebsh-Gordan (C-G) coefficients so that the integrals may be replaced by the C(ll'l",m,0,m')'s. We use the more symmetric 3-j form of these overlap functions represented by double column brackets to obtain[35]:

$$R(\pm d)_{nn'}^{mm'} = \sum_{p=|n-n'|}^{n+n'} (-1)^{m+n+(n'+m'+p)/2} (2p+1)\sqrt{(2n+1)(2n'+1)} \left(\begin{matrix} nn'\,p \\ 000 \end{matrix} \right) \left(\begin{matrix} nn'\,p \\ mm'0 \end{matrix} \right) (\pm 1)^p \, j(kd)\delta_{mm'}$$

$$\tag{56}$$

where $\left(\dfrac{nn'\,p}{000}\right)$ are 3j-coefficients. This relation defines the R's . It is easy to see from the exponential nature of the Rayleigh series that $R(d)R(-d) = 1$ and $R(d)R(d) = R(2d)$. Indeed it is clear the R is a rotational matrix and forms a commutative set under multiplication with the unit matrix being $R(0)$. It can be shown easily that $R'(d) = R(-d)$. Unfortunately this sort of translation is most suitable for a sphere or an object in which the body z-axis (the axial symmetry of the target) is aligned with the z-direction of the waveguide. This is not frequently the case. In fact, it is more likely perpendicular with the z-axis. In that case the R's are not diagonal with respect to the m's (the azimuthal index). It is to be noted that for axi-symmetric objects the free space T-matrix and the Q-matrices are diagonal in m (they are block diagonal in m, i.e. of the Jacobi matrix form). Thus, we can invert the Q's for each m. Had that not been the case we would have to invert the Q's for matrix elements including mixed m's (this occurs for general targets) and this complicates calculation of the T-matrix. We have examined axially symmetric objects partly to retain this property and partly because such shapes are of sufficient interest to us. Because waveguides are not axisymmetric in depth we expect (in general) for the m components to be coupled and in fact the presence of the translation matrices in expressions of the form $(1 - R(-2d)TR(2d)T)^{-1}$ renders the evaluation numerically costly for high frequencies except for the special case mentioned above.(We omit the vector-matrix notation for R,T,Q and other matrices just to simplify reading in the next several expressions). To simplify matters, we can expand the terms as follows:

$$(1 - R(-2d)TR(2d)T)^{-1} = 1 + R(-2d)TR(2d)T + R(-2d)TR(2d)TR(2d)TR(2d)T +$$

Since elements of $R(-2d)$ that overlap with elements of T get smaller with increasing d, it is not difficult to suppose that this series terminates fairly quickly. Further, since each term corresponds to zero, one ,two...,etc., reflections from the surface then on physical grounds one expects convergence reasonably quickly on a physical basis. Indeed , if one has n multiple reflections it can be shown that the corresponding expansion term dies off at a rate greater than $1/(2dk)^{2n}$. By retaining only a few terms corresponding to only a few multiple interactions between the surface and the object it is then reasonable to include multiple reflections in the way just prescribed .

We easily arrive at the system of equations (we will omit vector-notation below):

$$f = -ik\{R(d)\operatorname{Re}Q_1\alpha_1 + R(-d)\operatorname{Re}Q_2\alpha_2\}$$
$$-R(2d)a_1 = -ik\{Q_1\alpha_1 + R(-2d)\operatorname{Re}Q_2\alpha_2\} \tag{57}$$
$$-R(-2d)a_2 = -ik\{Q_2\alpha_2 + R(2d)\operatorname{Re}Q_1\alpha_1\}$$

Let us set $\alpha_1 = Q_1^{-1}b_1$, $\alpha_2 = Q_2^{-1}b_2$ to make use of the definition of the single scatterer T-matrices. We are now able to solve the equations for b_1 and b_2 in terms of known quantities and arrive at:

$$f = -ik\{R(d)T_1b_1 + R(-d)T_2b_2\}$$
$$b_1 = \{1 - R(-2d)T_2R(2d)T_1\}^{-1}\{1 + R(-2d)T_2R(2d)\}a_1$$
$$b_2 = \{1 - R(2d)T_1R(-2d)T_2\}^{-1}\{1 + R(2d)T_1R(-2d)\}a_2 . \tag{58}$$

Thus, by eliminating the b's we obtain

$$f = -ik\{R(d)T_1\{1 - R(-2d)T_2R(2d)T_1\}^{-1}\{1 + R(-2d)T_2R(2d)\}a_1$$
$$+R(-d)T_2\{1 - R(2d)T_1R(-2d)T_2\}^{-1}\{1 + R(2d)T_1R(-2d)\}a_2\} .$$

$$\tag{59}$$

This expression is expressed relative to the center point of the two objects. By various transformations we can express the equation relative to some other position by making use of propertied of R. We would of course expand f in some outgoing basis set if we wished to obtain the far field form function and it would be relative to the central point or what ever axis coordinate we choose.

2.9. The Two-body Formulation - a New Approach

There is a more general method to implement the two target scattering problem which in turn leads to the more general n-body problem. There are no restrictions on the T-matrix here so it applies to bubbles as well as elastic shells. We outline it here and extend it in the next section to the n-target problem.[36] A signal coming from a_1 impinges on object 1 first (see Fig. 1). Then the scattering process can be shown schematically as follows where T_i is the transition matrix for object i and R_{ij} is the propagation matrix that carries the signal from object i to j:

From object 1 T_1a_1 $T_1R_{12}T_2R_{21}T_1a_1$

                 $\Downarrow$ / $\Downarrow$

From object 2 $T_2R_{21}T_1a_1$ $T_2R_{21}T_1R_{12}T_2R_{21}T_1a_1$

Let us define the following:

$\Gamma_{ij} = R_{ij}T_j$ - scatters from j and propagates to i,

$\Gamma'_{ij} = R_{ij}T_jR_{ji}T_i$ - scatters back and forth between i and j and back to i ,

Γ'^2_{ij} - rescatters back and forth two times.

We deal with the product of regular spherical Bessel functions and spherical harmonics in representing the propagation from 1 to 2 in a partial wave sum but we are required to shift from the origin of object 1 to that of object 2 or the converse depending on which target the signal reflects from: $r_1 = 2d - r_2$ or $r_2 = 2d - r_1$, since scattering relative to an object must originate at the origin of the object. Now we must deal with the most general problem of translations and/or rotations of the individual partial waves-product of the spherical Bessel functions regular at the origin and the spherical harmonics in the spherical system. In particular we must determine $j(kr + kd)$ in terms of the $j(kr)$'s. It was shown above that: $j_l(2d - r_1) = \sum_m R_{lm}(2d)j_m(r_1)$, where R is an operator that translates or rotates spherical Bessel functions. It can be shown that the matrix R forms a commutative, multiplicative field and that, $R(d)R(-d) = 1$, $R'(d) = R(-d)$, etc. Since we are concerned with a particular representation, manipulation of a scalar wave in three dimensions is isomorphic to any other representation and thus is a member of the SO-3 symmetry group. Thus, R is well studied and falls under Lie group theory. A signal coming from location 1 will have the following series and·we use those properties of R in what follows:

$$
\begin{aligned}
&(1)\, T_1 a_1 + T_1 \Gamma_{11}' a_1 + T_1 \Gamma_{11}'^2 a_1 + \dots \\
&(2)\, T_2 \Gamma_{21}' a_1 + T_2 \Gamma_{21}' \Gamma_{11}' a_1 + \dots
\end{aligned}
\tag{60}
$$

or we get at (1) due to the signal from a_1:

$$
T_1 [1 - \Gamma_{11}']^{-1} a_1 ..
$$

and at (2) due to the a_1 signal:

$$
T_2 \Gamma_{21}' [1 - \Gamma_{11}']^{-1} a_1 ...
$$

In a similar manner we get the signal from a_2, and so the total field is:

$$
U = T_1 [1 - \Gamma_{11}']^{-1} a_1 + T_1 \Gamma_{12}' [1 - \Gamma_{22}']^{-1} a_2 + T_2 [1 - \Gamma_{22}']^{-1} a_2 + T_1 \Gamma_{21}' [1 - \Gamma_{11}']^{-1} a_1 .
\tag{61}
$$

We can show that:

$$
\Gamma_{ij}' [1 - \Gamma_{jj}']^{-1} = [1 - \Gamma_{ii}']^{-1} \Gamma_{ij}' .
$$

Using the above identity we get:

$$
U = T_1 [1 - \Gamma_{11}']^{-1} [a_1 + \Gamma_{12}' a_2] + T_2 [1 - \Gamma_{22}']^{-1} [a_2 + \Gamma_{21}' a_1] .
\tag{62}
$$

We note that $a_1 = R_{12} a_2$, $a_2 = R_{21} a_1$, so:

$$
U = T_1 [1 - \Gamma_{11}']^{-1} [1 + \Gamma_{12}' R_{21}] a_1 + T_2 [1 - \Gamma_{22}']^{-1} [1 + \Gamma_{21}' R_{12}] a_2 .
\tag{63}
$$

The general expression for the total field in the presence of two scattering objects (use + sign) or near either hard (+) or soft (-) interfaces is:

$$U = T_1[1 - \Gamma'_{11}]^{-1}[1 \pm \Gamma_{12}R_{21}]a_1 \pm T_2[1 - \Gamma'_{22}]^{-1}[1 \pm \Gamma_{21}R_{12}]a_2. \qquad (64)$$

This expression agrees with earlier ones with the exception that R_{12} or R_{21} occurs in place of the translation-rotation for outgoing Hankel functions, reflecting the fact that earlier works assumed an outgoing Green's function even when waves were scattering (reflecting) back and forth between objects 1 and 2. Clearly a standing wave Green's function ought to have been used in all derivations.

2.10. The N-body Formulation

It is convenient to use the following notation for the consideration of N-body problem:[41]

Define $\quad \Gamma_{ij} = R_{ij} T_j$ with $\quad \Gamma_{ii} = 0$

Two – object scatter $\quad A_2^i = \displaystyle\sum_{i \ne j}^n \Gamma_{ij}\Gamma_{ji}$

Three – object scatters $\quad A_3^i = \displaystyle\sum_{j \ne i, k \ne i}^n \Gamma_{ij}\Gamma_{jk}\Gamma_{ki}$,

$\downarrow$

N – object scatter $\quad A_n^i = \displaystyle\sum_{j,k,\dots l}^n \Gamma_{ij}\Gamma_{jk}\dots\Gamma_{li}$

where i represents object I. Here we intend that the A's relate to expressions for 2 or more interactions. That means that the subscript n indicates that we intend for n-body interactions and the superscript i indicates that it involves object i. The significance of the A_n^i's is that it contains all n-body interactions with i , n at a time. We can, using the above terms derive expressions for m (m >2) objects in a manner similar to the 2-body case. Thus, we get from object i from signal a_i relative to the interaction with i the following:

$$\Omega_3^i = T_i + T_i A_2^i + T_i A_3^i + T_i A_2^i \left[\frac{1}{1 - A_2^i}\right]\left[\frac{1}{1 - A_3^i}\right]A_3^i + T_i A_3^i \left[\frac{1}{1 - A_3^i}\right]\left[\frac{1}{1 - A_2^i}\right]A_2^i$$

In general - for all possible orders of interactions - we derive an expansion for interactions relative to i to be:

$$\Omega^i_{n-1} = T_i + T_i \sum_{l=2}^{n-1} A^i_l + T_i A^i_2 \left[\frac{1}{1 - A^i_2} \right] \left[\frac{1}{1 - A^i_3} \right] \left[\frac{1}{1 - A^i_4} \right] \cdots \left[\frac{1}{1 - A^i_{n-1}} \right] A^i_{N-1}$$ (65)

+all permutations

We have only included closed paths since there are opened paths that are of higher order that connect object i with various orders of scattering with the signal exiting from object j. To include opened paths we need only take the expression above and count the interactions that it will have on all other objects in much the same way that we performed the previous two-body case. This would lead to a sum of terms arising from the remaining n-1 objects. The contribution to i from target j is clearly of the form:

$$\Omega^j_{n-1} \Gamma_{ji}$$

If we sum over all such terms and add the component above we obtain for the total signal at i to be:

$$U_i = \Omega^i_{n-1} + \sum_{i \neq j}^{n-1} \Omega^j_{n-1} \Gamma_{ji}$$

The total set of partial wave coefficients $\{ f_k \}$ expanded about some reference point at k is then the sum of all such terms and leads to:

$$f_k = \sum_{i=1}^{n} U_i R_{ik} a_k$$ (66)

Here the subscript k simply means that the origin is at some point $\mathbf{r}_k$ in space while *f* and *a* must be understood in terms of column vectors. The individual components of *f* are then used to expand in outgoing waves if one seeks the far field solution which must be expanded relative to the origin $\mathbf{r}_k$. It is to be noted that although the method leads to the inclusion of all permutations of the individual inverse operators, this ensures that the composite T-matrix is symmetric even if we truncate to 2 or 3 ... up to n-1 interactions. We then sum the above expressions for all n objects relative to what ever origin we choose. Typically we would choose the geometric center of a bubble plume as the origin for the aggregate bubble problem. Thus, we have outlined the derivation of a general method for writing the T-matrix in terms of 2,3,4 etc. interchanges where we include all n-body interactions. We may include as many interactions as we deem appropriate in our many body scheme. Typically we may terminate sums to adjacent objects and we need only employ A_n for small n's. For example, for two particle correlation's n=2, the expressions are fairly simple. For bubbles we can limit the calculations using monostatic terms and easily include two-particle correlation's for many problems of interest. Also we

can extend the sums to integrals to simplify calculations for high density plumes. We will not go beyond this stage in this article.

2.11. The Near Field Problem in a Waveguide

The T-matrix is developed in a spherical representation, it is a second rank tensor in irreducible form, and thus only has meaning when operating on a vector also in a spherical representation. Since it is in irreducible form it can be easily rotated once the simplest form of T is devised which is one of its salient properties. On the other hand, the fact that it requires the vector that it operates on to be in a spherical representation while having its value for plane waves (which are easily expanded in a spherical representation) imposes restrictions on the form of the guided wave. However, it is now possible to represent a waveguide solution in a spherical representation of a fairly general form so that what follows is quite easy to generalize. The plane wave solution may be written in a partial wave representation via the Rayleigh series as follows:

$$e^{\{irk\cos(\theta)\}} = \sum_n (2n+1)i^n j_n(kr)P_n(\cos(\theta)),\tag{67}$$

where θ is the angle between k and r. For the more general representation one can use the addition theorem for spherical harmonics to obtain the plane wave in coordinates relative to a fixed Cartesian system which we must ultimately use. That expression is:

$$P_n(\cos(\theta)) = \frac{4\pi}{2n+1}\sum_{m=0}^n \varepsilon_m Y_{mn}(\theta',\varphi')Y^*_{mn}(\theta'',\varphi''),\tag{68}$$

where θ is the angle between k and r, θ',φ' are the spherical angles relative to the Cartesian coordinates of k, θ'',φ'' are the spherical angles relative to the Cartesian coordinates of r, ε_m is the Neumann factor. Our interest at this point is in the guided wave impinging on a bounded object. Here the incident wave that insonifies the object for a stratified environment is of the form:

$$U_0 = \frac{1}{2d}e^{i\pi/4}\sum_{n=1}^N c_n\varphi_n(\gamma_n z_s)\varphi_n(\gamma_n z)\frac{e^{i\kappa_n r}}{\sqrt{\kappa_n r}},\tag{69}$$

where $\varphi_n(\gamma_n z)$ is the vertical eigenfunction with eigenvalue γ_n corresponding to the vertical wave number for mode n, while z_S and z are the values of vertical displacements at the source and at observation points respectively, r is the distance in the horizontal plane and κ_n is the horizontal wave number for mode n, d is the depth of the water column and the relation between the wave number and the eigenvalues is $k^2 = \kappa_n^2 + \gamma_n^2$. In this formulation we include only propagating modes and assume that the origin of the source is localized in space such that it may be approximated by a point source and that we are sufficiently far from the source that evanescent modes can be ignored. This

procedure is quite adequate for most environments. We will limit discussion to layered fluid bottoms so that U_0 symbolizes the velocity potential. For an elastic bottom we would have to formulate the problem using the displacement vector in order to satisfy the boundary conditions at the fluid-elastic interface. It would be instructive at this point to illustrate how to convert U_0 to a spherical representation for the case in which we represent the environment by n isovelocity layers. Let us pick a particular layer for which the submerged object resides. Then U_0 is of the form:

$$U_0 = \frac{1}{2d} e^{i\pi/4} \sum_{n=1}^{N} c_n \sin(\gamma_n z_s) \sin(\gamma_n z) \frac{e^{i\kappa_n r}}{\sqrt{\kappa_n r}} \tag{70}$$

where c_n is the expansion coefficient. We want to take advantage of the Rayleigh expansion of a plane wave so that we express the quantity:

$$\sin(\gamma_n z)e^{i\kappa_n r} = \left\{ e^{i(\kappa_n r + \gamma_n z)} - e^{i(\kappa_n r - \gamma_n z)} \right\} / 2i \tag{71}$$
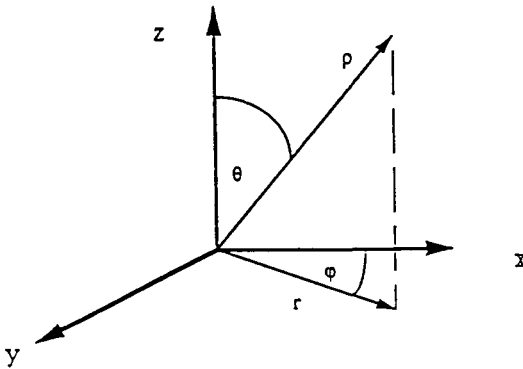
Fig. 2. Body coordinate system for object.
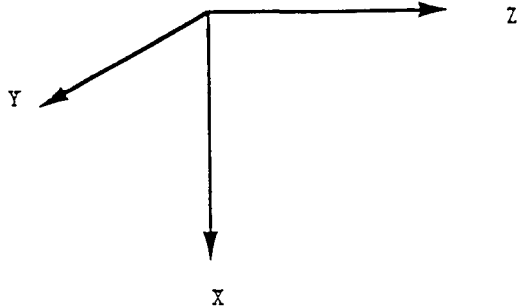
Fig. 3 Coordinate system of the object relative to the wave guide.

where the $(x,y,z),(r,z)$, are illustrated in Fig. (2). The coordinates (x,y,z) for the T-matrix must *perforce* be in the representation illustrated by Fig. (3), where z' is along the axis of symmetry of an axially symmetric object (our choice of target). We define $\alpha_{n\pm}$ such that $\cos(\alpha_{n+}) = (\gamma_n z + \kappa_n r)/kr$ and $\cos(\alpha_{n-}) = (-\gamma_n z + \kappa_n r)/kr$ and we have:

$$\sin(\gamma_n z)e^{i\kappa_n r} = \left\{ e^{ikr\cos\alpha_{n+}} - e^{ikr\cos\alpha_{n-}} \right\}/2i .\qquad(72)$$

Thus, after use of the Rayleigh series and the above expression we have U_0 in the following spherical representation:

$$U_0 = \frac{i}{4d}e^{i\pi/4}\sum_{n=1}^{N}c_n(i)^n(2n+1)\{P_n(\cos\alpha_{n-}) - P_n(\cos\alpha_{n+})\}\frac{j_n(kr)}{\sqrt{\kappa_n r}} ,\qquad(73)$$

where we must use the spherical harmonic addition theorem Eq. (68) to obtain the most general form of the expression. The above expression has been derived tacitly assuming that the interaction between the guided wave and the submerged object occurs at a point. In fact, the interaction is extended in space and we must allow for this in the final development. The final form depends on the way we interface the object with the guided wave. Let us assume we have derived the above expression to be valid at the origin of the submerged object. Further, we wish to find the field at some vertical line or over some surface with distance r_0 from the center of the object. This will be developed in the next section. We now make use of the T-matrix for scattering of objects near an interface. It takes the following form for only one impenetrable interface relative to the origin of the object:

$$T_{Half} = R(d)T\,[1 - \Gamma_{11}^{'}]^{-1}[R(-d) + \Gamma_{12}R(d)] + R(-d)T\,[1 - \Gamma_{22}^{'}]^{-1}[(R(d) + \Gamma_{21}]R(-d)\,.$$

(74)

Here we used a similarity transformation to shift from the origin to the target reference.

Now, when we have the near field solution in a waveguide, we proceed to the next step which involves coupling the near field solution into a waveguide. In the following section we use Huygens principle to carry this out. It is obvious that once one has the near field it is easy to use it as the starter field in any initial value problem by taking advantage of a one-way solution of the wave equation. The most prominent example of this is the parabolic equation (PE) approximation. One-way versions of the FFP and Full-wave finite element Galerkin methods exist and these models are therefore suitable for employing the near field approach in a straightforward manner. Further, it is possible to project the near field solution onto a normal mode basis set by making use of orthogonality as an approximate way to couple in the near field.

2.12. Huygens Principle and Coupling of the Near Field with a Waveguide

We outline the basis of a method useful to describe scattering from an object in a waveguide.[39-43] We begin by allowing a guided wave to impinge on an object as it traverses a given region. The object scatters the guided wave in some manner. We determine the scattered field near the object via either a free field transition matrix or more precise one derived for an object near a surface as described above. In order to use Huygens' principle we choose an imaginary surface circumscribing the submerged object. The surface is arbitrary to the extent that it is smooth and its dimensions do not exceed the boundaries of the wave guide and should be such that the largest dimension of the surface is such that the highest angle mode does not interact with the boundary of the circumscribed region. We next require the near field on the surface as well as its derivative normal to the surface of the imaginary object. To obtain this we must make a transformation from the coordinates of the wave guide to that of one relative to the axis appropriate to the submerged object. Recalling that the mode angles α_n were obtained above relative to the horizontal (and not the vertical as is usual in normal mode theory), we choose β_n to designate the angle that the mode makes with the axis of symmetry of the spheroid in the horizontal plane. It is to be noted that the reference axis of the spheroid and that of the wave guide differ. In particular, in order to exploit the axial symmetry of the object we must choose the z axis in the object body reference along the its axis of symmetry while we can choose x and y at our convenience (so long as we maintain orthogonality). In the wave guide z is in the downward direction while x and y are in the horizontal plane. The coordinate scheme chosen is indicated in Fig. (3) where θ_n and φ_n are the angles for the particular mode n and the appropriate angles to be implemented for the spherical harmonics. They are, in particular, the angles of the incident mode n relative

to the symmetry axis of the submerged object and the angle that the plane generated by the incident ray-mode n and the symmetry axis of the spheroid makes above (below) the horizon respectively. They are obtained from:

$$\tan(\varphi_n) = \tan(\alpha_n) / \sin(\beta_n) \tag{75a}$$

$$\cos(\theta_n) = \cos(\beta_n)\cos(\alpha_n), \tag{75b}$$

where the surface is chosen at a suitable region circumscribing the object (suitably near the object) with origin at the center of the object. The near field is then :

$$f(r,\theta,\varphi) = \sum_{nm}^{NM} c_{nn'm} T_{nn'm}(\alpha_{\pm}) Y_{nm}(\theta_{r_n}, \varphi_{r_n}) Y_{n'm}^{*}(\theta_{k_{n'}}, \varphi_{k_{n'}}) \frac{h_n(\kappa_n r)}{\sqrt{\kappa_n r}} \tag{76}$$

where the c's are projection coefficients of the normal-mode functions onto the spherical (partial wave) solutions and the plus (minus) signs mean that we must sum over both angles α. This is the most general form of the scattered near field. We now employ Huygens' principle which uses a surface integral representation of the near field $f(r,z)$ namely:

$$U_S(r,z) = \oint \{ f(r',z') \frac{\partial G(r,z,r',z')}{\partial n} - G(r,z,r',z') \frac{\partial f(r',z')}{\partial n} \} dS \tag{77}$$

Here we have expressed f in cylindrical coordinates. We showed how it is possible to represent simple isovelocity waveguides in terms of sin-functions. We have developed a general method of representing any waveguide solution in terms of a series of sin-functions based on a generalized perturbation theory. This involves a double sum which takes the form:

$$U_0 = \frac{1}{2d} e^{i\pi/4} \sum_{n,m=1}^{N} c_{n,m} \sin(\gamma_m z_s) \sin(\gamma_m z) \frac{e^{i\kappa_n r}}{\sqrt{\kappa_n r}} \tag{78}$$

We require the Green's function which takes the form:

$$G(r,r_0) = \frac{1}{2d} e^{i\pi/4} \sum_{n,m=1}^{N} c_{nm} \sin(\gamma_m z_s) \sin(\gamma_m z) \frac{e^{i\kappa_n r}}{\sqrt{\kappa_n r}} \tag{79}$$

where γ_m and κ_n are the vertical expansion eigenvaluses and the horizontal eigenvalues, respectively. If we insert Eq. (78) and Eq. (79) into Eq. (77), this leads to an expression far from the object of the form:

$$U_s(r,z) = \sum_{n=1}^{N} a_n \varphi_n(z) \frac{e^{i\kappa_n r}}{\sqrt{\kappa_n r}}, \tag{80}$$

where

$$a_n = \oint_s \{ f(r,\theta,\phi) \frac{\partial}{\partial n}(\varphi_n(z)\frac{e^{i\kappa_n r}}{\sqrt{\kappa_n r}}) - \varphi_n(z)\frac{e^{i\kappa_n r}}{\sqrt{\kappa_n r}}\frac{\partial}{\partial n} f(r,\theta,\phi)\}dS, \tag{81}$$

where $\varphi_n(z) = \sum_{m=1}^{N} c_{nm} \sin(\gamma_m z)$ is the vertical wave function in its expansion form.

Here the integral in Eq. (81) is over some prescribed surface S suitable for the problem.

Note that Eq. (80) is in the form of a normal-mode solution, and therefore the scattered wave forms a guided wave suitably far from the object, as one would expect. This solution is continuous throughout space and satisfies the boundary conditions of the confined environment that forms the guided wave. In the next sections we depart from the mathematical formulations of scattering and the numerical strategy for solution. We focus on some useful theoretical considerations that will help us to understand the actual physical phenomena related either to data or numerical results.

3. Notions Useful in the Interpretation of Scattering Events

In this section we develop three topics that are helpful in understanding numerical results in terms of physical considerations. One of the topics involves the concept of an acoustical background for elastic shells. At this point it is worth noting the origin of the background concept. In the early period of nuclear scattering theory, it became apparent that many low energy (below particle threshold) scattering processes could be separated into two events: one associated with few degrees of freedom and one associated with collective motion, or with many degrees of freedom. Each of the mechanisms could be treated separately and added coherently to describe a scattering event. Such notions found their way into the description of scattering from submerged elastic structures; namely, that one could divide the scattering process into two distinct phenomena, namely that associated with the non-resonances contributions (few degrees of freedom involved) and that associated with resonances[44] (many degrees of freedom). In particular, it was observed that scattering from elastic solids could be decomposed into rigid scattering and resonance scattering in the lower frequency region. This is similar to solving an inhomogenious second order differential equation in which the homogeneous solution corresponds to the resonance or eigenvalue solution while the particular solution relates to the background solution. In the higher frequency region one must include internal reflections of waves in the solid. There is a difference, however, between the nuclear and elastic solid models. For elastic solids the total response is determined; from that the rigid contribution is subtracted to obtain the elastic response. In the nuclear case,

however, the "direct" and "resonance" components are added to determine the total response. In contrast with the nuclear case in which resonances usually decrease with increasing energy, for the acoustic case the number of resonances proliferate with increasing frequency. This proliferation causes overlap between resonances to increase and renders the subtraction of a rigid background little more than useless in isolating resonances. However, in the lower frequency region where few resonances are present, this technique has proven quite useful for resonance isolation and classification. The bulk of the research in this topic has been done by H. Überall and his students.[10,43]

One of the most important developments in the study of elastic resonances pertains to an understanding of the physical mechanism responsible for their generation. In a series of studies at the Catholic University of America and the Naval Research Laboratory, it was determined that for solid elastic targets such as spheres and cylinders the resonances were circumferential in nature and (due to phase matching conditions on the object surface) corresponded to standing waves on the surface of the object. Thus, the combined determination that the resonances were circumferential in nature and could be treated as a separate component of the total scattering response in the seminal work of Überall, Flax and Dragonette[10] constitutes one of the major achievements in the understanding and interpretation of resonances on elastic targets.

3.1. Discussion of Resonances

Resonances are excited by incident acoustical signals as they impinge on elastic bodies of rotation as well as elastic bars. They are governed by the fact that they occur at discrete values of frequency and, when they occur, a characteristic event takes place. This event can be complicated and difficult to distinguish from other physical mechanisms unrelated to resonances but they are usually distinguishable and can be related to a particular process. The recent theoretical and numerical developments described here in additional to other works have enabled researchers to perform calculations and to understand the nature of resonances. Our interest at this point is to describe particularly pronounced and distinguishable resonances that manifest themselves in either the frequency or time domain. In the literature there have been three classes of resonances usually studied. Investigations of Lamb resonances due to symmetric and antisymmetric waves (labeled S_i and A_i for $i=0,1,2,...$) for shells have been vigorously investigated; for elastic solids, Rayleigh resonances (labeled as an ordered pair of integers $(n,1)$ with $n=2,3,4...$) and whispering gallery resonances (labeled as an ordered pair of integers (n,m) with $n=0,1,2...$ and $m=2,3,4...$) have also been extensively studied. Here n corresponds to the mode number of the resonance viewed as a surface standing wave with $n=0$ corresponding to a breathing mode. These resonances are not particularly pronounced in magnitude or signature (the characteristic shape of the resonance). In this work we wish to feature classes of resonances that are somewhat more pronounced in magnitude or pattern either in the time or frequency domains. We give a brief discussion of these phenomena including effects peculiar to spheroids such as orthogonal classes of resonances recently discussed in the literature.[46,47] However, emphasis will be placed on the following: 1) resonances at

coincident frequency (the frequency at which the speed of the flexural Lamb wave equals the speed of sound in the fluid) excited on submerged elastic shells; 2) "resonances" due to high frequency incident plane waves on a submerged elastic shell due to an internal reflection effects associated with the first symmetric Lamb mode, and 3) flexural or bending resonances excited by oblique incident waves on a spheroid. It will be seen that each of these classes of resonances are rather large, have characteristic signatures and have locations predictable using simplified expressions. In the time domain case a recently advanced methodology arising from a time-domain resonance scattering theory is used to discuss the existence of strong pseudo-Stoneley resonances[48-50] excited on elastic shells that give rise to a strong beat pattern in the time-domain resonance signature. The time domain methodology is outlined below. However, since we will have occasion to use the correct acoustical background for an elastic shell this recent development[51-53] will be outline in the next section.

The second topic involves interpretations of some types of resonances excited from the interaction of acoustical signals from elastic objects based on the standing wave picture of resonances due to H. Überall.

3.2 . The Acoustic Background for Submerged Elastic Shells

The background concept for elastic targets in which the total elastic response is viewed as a superposition of a resonance response and a non-resonant acoustical background (rigid for solid elastic targets, etc.) has proven quite successful as the "correct" background for some elastic targets submerged in water. The use of a rigid background for elastic solids is no more than an anzatz comparable to assuming that the object is massive compared to the ambient fluid while the soft background assumption for thin shells appears as a pressure release scatterer in the absence of a resonance.   In fact these assumptions do not follow from general physical principles but are under certain conditions physically reasonable and not as some authors imply *a' priori* true. In fact, any background concept ought to follow or be derivable from available physical principles. In addition, some authors imply that the rigid background is the correct one for shells at high frequency and that the soft one is correct at suitably low frequencies and that any background that works at intermediate frequencies is an intermediate background, or a hybrid background[56]. These assumptions are erroneous. Any background derivation from general physical principles can be the correct or adequate background over the entire frequency range and one only shows that in limiting cases they may reduce in approximation to the rigid or soft results thus showing why the rigid or soft backgrounds are adequate at certain frequencies and not for substantiation of the derived background. Recent papers focusing on the background concept for shells have met with success in isolating resonance phenomena. In this section a general principle is discussed to describe acoustical scattering from elastic targets in the absence of resonances.   Several of these methods follow from the same underlying principal and can be generalized to more complex targets such as fluid filled objects and spheroidal shells. We develop the acoustical background from a general concept in what follows.

3.3.   Green's Functions and Acoustical Backgrounds

The Greens function for a spherical radiator on the surface of the sphere was developed by Junger and Feit in partial wave form with radial dependence R and has the form: [54]

$$G(r,a_0) = \frac{1}{ka^2} \sum_{n}^{\infty} \sum_{m}^{n} \varepsilon_m \frac{(n-m)!}{n+m)!} (2n-1) \cos(\phi - \phi_0) P_n^m (\cos\theta) P_n^m (\cos\theta_0) \frac{h_n(kR)}{h_n'(ka)} \qquad (82)$$

where h_n is an outgoing spherical Hankel function of order n, k is the wave number in the ambient fluid and a is the diameter of the sphere. This expression can then be used to obtain the pressure field by integrating the Green's function over the surface which with known acceleration distribution leads to an expression which is once again proportional to the above expression. Thus, the pressure from a spherical radiator has the complex term given by expression (82). Since we know that the component of a pressure which is real is understood to be inertial and that which is imaginary is understood to be resistive it can be determined that Eq. (82) can be written in the form of a complex impedance Z_n, where we have:

$$z_n = i\frac{h_n(kR)}{h_n'(ka)} = r_n - i\omega m_n \qquad ,$$

$$\text{where} \quad r_n = \text{Re}\, z_n \quad \text{and} \quad m_n = \text{Im}\, z_n$$

where r_n is the resistivity and m_n is the inertial term. From dimensionallity, the term m_n is referred to as the entrained mass per unit volume. This is not merely terminology. In any conserving principles that incorporate inertial effects the entrained mass m_n must be included. Note that entrained mass is dependent on the modal number and becomes less significant with increasing mode number n. There is an analogy between entrained mass in acoustics and induced mass in electromagnetism which is known to play a part in special relativity. Further, the entrained mass for the monopole term is used in theories as the mass factor for bubbles. Thus in the development of an acoustical background by Werby the entrained mass was used as part of a conserving factor in the development of the acoustical background for submerged shells.[55-57] We outline that development below and apply a new entrained mass for scatterers that leads to an improved version of the acoustical background. The basis of the new idea of entrained mass for a spherical scatterer is obtained from a development of the Green's function for the spherical scattering problem with known velocity distribution in analogy with the radiator problem. Without going into detail the entrained mass following arguments similar to Junger and Feit[57] is:

$$m_n = ka\,\text{Re}(z_n) \qquad (83)$$

It is worth pointing out that the reason one would impose entrained mass results from approximate forms of a scatterer. In the event, that a real mass and material properties are used, such as the exact elastodynamic equations, then entrained mass is already included in

calculation, so are the resonances. That leads to the following ideas. If we could include all the inertial effects without including the part that caused the object to resonate, then it would also be possible to derive a good background by imposing those boundary conditions. That, in fact, has been done by at least two authors who approximated a fluid shell with a fluid density the same as the material and the compression velocity as the same as the elastic material. The problem with such a derivation is that it is possible to induce "other" kinds of resonances by including non-elastic parameters. In fact, fluid shells can be shown to produce large monopole resonances (breathing modes) at low frequency, as well as resonances similar to symmetric Lamb modes which take effect, when the wave length of the material is on the order of the shell thickness. Thus, there are two regions where this method breaks down, namely at very low wave numbers, where the breathing mode is important and for wave numbers above which the corresponding wavelength in the materiel is equal to or less than the shell thickness, which is a limitation of the high frequency end. Nonetheless, we examine this technique and we will use it for cases in which the new definition for entrained mass is difficult to impose such as for non-spherical and fluid filled targets. In general the partial wave expansion for any background takes the form:

$$b_l = \frac{\operatorname{Re} S_l}{S_l}$$

where $S_l = A_l h_l(ka) - h'_l(ka)$, $\operatorname{Re} h_l = j_l$, and A_l is to be determined from physical considerations. Here are several forms that have been derived for A_l:

$$A_l = 3kam_s / (1 + (ka)^2) m_w \tag{84}$$

from a pulsating monopole; [53]

$$A_l = 3m_s \operatorname{Im}(z_i) / m_w \tag{85}$$

from the entrained mass of a spherical radiator; [54,55]

$$A_l = 3m_s ka \operatorname{Re}(z_i) / m_w \} \tag{86}$$

from the entrained mass of a scatterer; [58] A_l is either 0 or infinite for rigid or soft backgrounds. To obtain the fluid background for very thin shells, the results can be shown to take the form:

$$A_l^{-1} = \frac{\rho_s \Delta a}{\rho_w a}, \tag{87}$$

where this expression includes the shell thickness ratio $\Delta a/a$ and the density of the shell to that of water in obvious notation. The ratios of masses are the ratios of the mass of water to the true mass of the shell in the above expressions.

3.4. Conservation Principles and Acoustic Backgrounds for Elastic Targets

We showed earlier[53-55] that the acoustical background for an elastic shell could be terminated by taking into account the inertial component of the radiation loading of a spherical shell . The inertial component is:

$$p_s = -i\omega \sum_{n=0}^{\infty} m_n \dot{w}_n (-1)^n,$$

where m_n is the entrained mass per unit area for mode n, ω is the angular frequency, and $\dot{w}_n$ is an expansion coefficient related to the displacement potential. If we excite the sphere by an incident monochromatic plane wave, then we have:

$$\dot{w}_n = -i\omega \{ a_n j_n(ka) + b_n h_n(ka) \},$$

where j_n is a regular Bessel function, h_n is the outgoing Hankel function, and b_n is an unknown coefficient which corresponds to the partial wave scattering amplitude which we seek and a_n is the plane wave expansion coefficient. The total pressure per unit area in the fluid due to the incident plane wave is:

$$p_t = \frac{\rho_s c\omega}{ka} \sum_{n=0}^{\infty} \{ a_n j_n(ka) + b_n h_n(ka) \} (-1)^n e^{-i\omega t}$$

The particle velocity at the surface of the object is:

$$v = -\frac{i}{\rho\,\omega} \frac{\partial p}{\partial r}$$

Here, c is the speed of sound in water. The particle acceleration α is the time derivative of v which leads to:

$$\alpha = -\frac{\omega^2}{ka} \sum_{n=0}^{\infty} \{ a_n j_n'(ka) + b_n h_n'(ka) \} (-1)^n e^{-i\omega t}.$$

The force at the surface of the object due to the incident plane wave is, then, simply the product of the particle acceleration and the mass of the spherical shell. The mass of the spherical shell is $4\pi\rho_s[a^3-(a-h)^3] / 3$. Here h/a is the ratio of the shell thickness to the shell radius. The force due to the total fluid loading at the object surface is equal to the total inertial fluid loading times the surface area $4\pi a^2$ of the sphere. Here, a is the radius of the spherical shell and ρ_s is the density of the shell material. We equate these two forces to obtain the unknown coefficient b_n which leads to the following expression:

$$b_l = \frac{A_l j_l(ka) - j_l'(ka)}{A_l h_l(ka) - h_l'(ka)} \qquad A_l = \frac{3\rho_s}{\rho_s[a^3 - (a-h)^3]} \mathrm{Im}(z_n). \qquad (88)$$

The scattered field for the new background is obtained by using the b_n's as the partial wave scattering amplitudes in a normal mode series. The b_n's define the new background and by subtracting this quaintly from the elastic response, we obtain the residual response that reflects mainly the pure resonance contribution. It is easy to show that the imaginary part of the enclosed brackets in Eq. (88) is approximately equal to $ka/(1+ka^2)$ so that for large ka, $b_n = -j'_n(ka) / h'_n(ka)$ which corresponds to a rigid scatterer and for both a very thin shell and at low frequency, $b_n = -j_n(ka) / h_n(ka)$ which corresponds to a soft scatterer. We mean here equal to in only an approximate sense. Thus, we see that the background represented by Eq.(88) has the appropriate limits for thin shells at low frequencies (soft) as well as the appropriate limits for high frequencies (rigid). That can also be shown to be that case for the new results from the entrained mass defined by Eq. (86).

3.5. The T-Matrix Background for an Elastic Shell

The T-matrix for an elastic thin shell can easily be derived from conservation of a thin fluid shell of uniform thickness with an overall mass consistent with the actual density of the shell using the above conservation principle for mass and then by taking the limit as the shell becomes very thin. This causes the internal wave numbers to cancel leaving only the density ratio and shell thickness. This is a desirable feature. Without going into the mathematical details we list the results below.[57] Indeed, the Q-matrix (the mode coupling analog for non-spherical objects) appears as a linear combination of a rigid scatterer and a soft scatterer with inertial terms being the coupling factor. This background has been tested and works well, and better than the previously used soft background:[60]

$$T = -\mathrm{Re}\, QQ^{-1} \qquad Q_{lm} = \oint \left\{ \mathrm{Re}\, \psi_l \psi_m - \frac{\rho_s ka\Delta a}{\rho_w a} \mathrm{Re}\, \psi_l \frac{\partial \psi_m}{\partial n} \right\} ds. \qquad (89)$$

This expression will not work well for very low and very high $kL/2$'s, two regions for which the T-matrix is of little interest and, thus, this background is quite adequate for elastic shell backgrounds.

3.6. Standing Wave Interpretation of Resonances Excited at the Fluid- elastic Interface

Many resonances can be explained in terms of surface waves traveling at a fluid-elastic interface that at discrete frequencies form standing waves. These standing waves then radiate into the ambient fluid and add coherently with the specular return creating resonance patterns.[61] The rationale behind the standing-wave argument for determining resonances is based on the fact that for special cases one can equate the measure P around the perimeter of the object (in the direction of the circumnavigating field) with either a half-integral or an integral number of wavelengths, depending on whether the background is close to an ideal rigid or an ideal pressure release background. For the case (here) for elastic solids we are close to a rigid background and one has:

$$p = \lambda_s (n + 1/2),$$ (90)

where n = 2, 3, 4, ... By conservation of frequency one can show that:

$$\lambda_s = \lambda_w \frac{v_s}{v_p}.$$ (91)

Since $kL/2 = 2\pi L/\lambda_w$, this leads to the standing wave condition for a resonance:

$$\left[\frac{kL}{2}\right]_{Res} = L\pi\{\frac{v_s}{v_w}\}\{n + 1/2\}.$$ 92)

For objects having an aspect ratio less than 2.0, the elliptical integral can be approximated by a closed expression for end-on incidence. This leads to the more convenient expression:

$$\left[\frac{kL}{2}\right]_{Res} = \sqrt{2}\frac{L}{D}\{\frac{v_s}{v_w}\}\{n + 1/2\} / \sqrt{(L/D)^2 + 1}.$$ (93)

We shall use these expressions to interpret the results that follow. The appropriate expression for the resonance locations of a sphere is:

$$\left[\frac{kL}{2}\right]_{Res} = \{\frac{v_s}{v_w}\}\{n + 1/2\}.$$ (94)

For spheroids the peripheral distance P around the spheroid is obtained from the elliptical integral:

$$p = 2L\oint\sqrt{(1 - \kappa^2 \sin^2 \phi}d\phi,$$ (95)

where $\kappa^2=1-(L/D)^2$, and ϕ ranges from 0 to 2π. By setting the radius of the sphere to be $L/2$, the resonance locations for the spheroid relative to the spherical case is obtained via ratios from expressions (92) and (93) with (94). It is:

$$\left[\frac{kL}{2}\right]_{Res} = \pi\{\frac{v_s}{v_s'}\}[ka]_{Res} / \oint\sqrt{(1-\kappa^2\sin^2\phi}d\phi, \tag{96}$$

where v_s' is the phase velocity of the resonance of the sphere. In general, v_s is a function of shape and material properties. For the cases presented here we can assume that $v_s'/v_s = 1$ and therefore the resonance locations are obtained for the spheroids directly from the spherical cases. We note that $kL/2$ must increase in value (if it is fairly constant) as L/D increases since the integrand in the denominator of Eq. (96) decreases for increasing aspect ratio. This explains why there is an upward shift in $kL/2$ with increasing aspect ratio. Überall, et al., have pointed out that the Rayleigh wave is dispersive and a function of the curvature of the target (larger curvature corresponds to a larger value of phase velocity), but that with increasing frequency, the phase velocity approaches that of a half space. Thus, since the phase velocity is a function of curvature one must employ a phase matching condition at least for higher aspect ratio targets. This requires the use of integral expressions and some assumptions regarding the variation of the phase velocity with curvature. The work of Überall[62] has proven to be quite a good tool for predicting the resonance locations. The following derivation is due in part to Überall[64,65,66].

The phase matching condition for a Rayleigh resonance about the largest meridian of a spheroid is

$$\int\frac{ds}{d\lambda} = n + 1/2 \tag{97}$$

where λ is the local Rayleigh wavelength. Here we have:

$$ds = 2L\sqrt{1-\kappa^2\cos^2(\phi)}d\phi, \tag{98}$$

where L is the semi-major axis and D is the semi-minor axis. We wish to find what λ_{Res} is. We know that the Rayleigh resonance is dispersive on a curved surface and thus that both λ_{Res} and c_{Res} vary with frequency (and thus with kL/2). We know that

$$\lambda_{Res}f = c_{Res} \tag{99}$$

and that

$$\lambda_w f = c_w, \tag{100}$$

where c_w is the speed of sound in water. We can thus obtain

$$f = \frac{c_w}{\lambda_w} = c_w \frac{ka}{2\pi a} \tag{101}$$

and finally;

$$\lambda_{Res} = (\frac{c_{Res}}{c_w})(\frac{ka}{2\pi a})^{-1} \tag{102}$$

We note that c_{Res} is mainly affected by the curvature of the scatterer's surface, but the relative size of scatterer to wavelength is also important at low frequencies. Since a sphere has fixed curvature, c_{Res} is constant for a given frequency, while for a spheroid both the curvature and c_{Res} will vary along the surface of the object.

A good guess for the value of c_{Res} on a spheroid is to evaluate the radius of curvature R along a meridian of the spheroid and use the corresponding value for a sphere with size parameter kR. For a spheroid the radius of curvature as a function of angle is

$$R(\phi) = \frac{\{a^2 \cos^2 \phi + b^2 \sin^2(\phi)\}^{3/2}}{ab} \tag{103}$$

Thus, we can extract the value of c_{Res} at each point on the surface of the spheroid from the corresponding value on a sphere. By interpolation we can obtain the values all along the spheroid except for very small values of the corresponding size parameter which can not be extracted from the spherical solid for low ka's. The final expression is then:

$$\left[\frac{kL}{2}\right]_{Res} = \int_0^{a/2} \frac{1}{c_{Res}} \sqrt{\left\{1 - \left(1 - \frac{a^2}{b^2}\right)\cos^2(\phi)\right\}} d\phi \tag{104}$$

or

$$\left[\frac{kL}{2}\right]_{Res} = \frac{\pi(n+1/2)}{2} \tag{105}$$

For a fixed n we can vary k on the left until it equals the fixed value on the right hand side at which point we obtain a resonance. Results obtained by this method agree well with extended boundary condition results. However, we will not include Überall's improvement to the present analysis. It was shown that broadside resonances for spheroids can be obtained from the simple expression

$$\left[\frac{kL}{2}\right]_{Res} = \left(\frac{L}{D}\right)\left(\frac{V_s}{V_w}\right)(n+1/2) \tag{106}$$

Here, we may use the phase velocity for the spherical case in place of V_s. Thus with simple expressions one can predict resonance locations for both end-on and broadside resonances. It was also shown[58,59] that only two degrees of freedom were apparent for resonances of solid spheroids, namely those due to standing waves traveling broadside and those along the axis of symmetry so that incident fields at oblique angles excite an a mixture of resonances from the two vibrational modes. This means that Eqs. (96) and (106) can predict the resonance locations for all incident angles with the exception of an oblique incident or broadside resonance at low $kL/2$ values.[60] It has been shown that those resonances are related to bending or flexural modes which are also predictable using Timoshenko theory for a finite circular cylinder[65,66] (which approximates a spheroid) as follows.

3.7. *The Bending Resonances Excited by Oblique Incident Sound Waves*

We can view the spheroid as a bar of variable radius. The condition for resonance is that the flexural wave that has made a complete circuit around the periphery of the spheroid is in phase with the wave being generated. This is the well known condition for standing waves in any kind of linear resonator. Let the phase shift at a fixed point during a peripheral travel time T be:

$$\Phi_0 = \omega T, \tag{107}$$

then resonance will occur, when

$$\Phi_0 = 2\pi n - (\Delta\vartheta_1 - \Delta\vartheta_2), \tag{108}$$

where $n>1$, ω is the angular frequency, and the last two terms on the right are the phase shifts for each of the ends. The round trip time T is

$$T = 2\int_0^a \frac{dz}{v_p}, \tag{109}$$

where v_p is the phase velocity of the wave along the scatterer. The phase shift is frequency dependent and at the free ends has the value:

$$\Delta\vartheta_1 + \Delta\vartheta_2 = -\tan^{-1}(\frac{1}{\delta}), \tag{110}$$

where

$$\delta = (1+\varepsilon)\frac{\omega}{2\Omega}\Gamma. \tag{111}$$

Here ε is the entrained mass and

$$\Gamma = \frac{5}{2}(1 + \frac{3}{4}\nu)$$ (112)

where ν is the Poisson,

$$\Omega = \frac{c_l}{\kappa}$$ (113)

where κ is the radius of gyration,

$$c_l = \sqrt{\frac{Y}{\rho}}$$ (114)

Y is the Young modules and ρ is the bar density. To obtain a phase velocity we use the Timoshenko equation for a uniform rod

$$\frac{\partial^2}{\partial t^2}\psi + c_l^2\kappa^2 \frac{\partial^4}{\partial z^4}\psi - (\Gamma + \alpha)\kappa^2 \frac{\partial^4}{\partial^2 z \partial^2 t}\psi + \frac{\alpha}{c_l}\frac{\Gamma\kappa^3}{c_l^2}\frac{\partial^4}{\partial t^4}\psi = 0,$$ (115)

where α is the coefficient of relative rotary inertia (=1 for a uniform bar), and ψ is the flexural displacement. Here we are ignoring the entrained mass ϵ. The generic solution is

$$\psi = Ae^{i(\alpha t - kz)}$$ (116)

which by substitution in Eq. (115) yields

$$\omega^2 + c_l^2\kappa^2 k^4 - (\Gamma + 1)\kappa^2 k^2 \omega^2 + \frac{\Gamma\kappa^3}{c_l^3}\omega^4 = 0$$ (117)

Since $k\omega = v_p$, we can use the above expression to find ω as a function of v_p. The phase matching condition is then determined by

$$4\left[\frac{kL}{2}\right]v_w \int_0^a \frac{dz}{v_p} = 2\pi n + \tan^{-1}\delta$$ (118)

The expression can be reduced to the following form for the lower frequency case:[61,62]:

$$\left[\frac{kL}{2}\right]_{Res} = \sqrt{2}\frac{\pi^2}{8}\frac{(2n-1)^2}{A_s^2 + \sqrt{A_s^2 + 3\Gamma\pi^2(n-1)^2/8}},$$ (119)

where A_s designates the aspect ratio and Γ is given by Eq. (112).

3.8.   Time Domain Resonance Scattering Theory (RST)

We present here a time-domain version of the frequency domain theory.[63-65]The partial wave series that emerges from normal mode theory for separable geometries can be represented in distinct partial waves or modes. It has been shown that a representation due to a distinct mode { n } can be written in the Breit-Wigner form.[6-10] This observation was made first by Überall who taking advantage of his experience as a Theoretical Nuclear Physics, recognized the similarity between Quantum Resonance phenomena and that due to resonances for acoustical scattering from submerged bounded objects. Elastic/Inelastic scattering at the quantum level is composed of the so called direct or shape elastic term and the resonance terms which add coherently. Note that terminology in Nuclear Physics uses the term elastic to mean that no energy is lost in the process which means that resonance effects are not excited. Inelastic contributions excite resonances which in the nuclear process result in energy loss. It is well known that shape elastic scattering or geometrical scattering varies slowly with frequency while the resonance terms vary rapidly with small changes in frequency. Often there is a relative phase change of 180-degrees or 360-degrees yielding a characteristic signature for certain resonances. This was recognized by Überall as also happening in much the some way in acoustic scattering and has been particularly nicely discussed in a thesis by Überall's student   L. Dragenette.[66]   The analogue of nuclear shape elastic scattering was recognized by Flax, Überall and Dragonette to correspond to rigid scattering for elastic solids.[6-10] Überall and his colleagues referred to this "geometric" scattering as "background"   scattering which is parlance often used in Nuclear Physics. Überall and his students also employed the rigid background effectively for thick elastic shells.[67] The general background for elastic shells is to be presented in this work but the essential features of the Überall approach is retained there too. It must be mentioned that both L. Flax and L. Dragonette   also played enormously important roles in the formulation of RST. The combined effort of the Naval Research Laboratory and the Catholic University were crucial in this development. A special session in the Spring 1994 American Acoustical Society meeting organized by Ralph Goodman and H. Überall is a testimony to the significance of the contributions of L. Flax for his contribution in this area.[73-75]   Überall has been generous in disseminating the theory for a variety of targets with several students and colleagues since its formation. [6-9] The partial wave term that we are interested in here is as follows:

$$f_n(\theta) = \frac{2}{ka} e^{2i\zeta_n^r} \left\{ \frac{\frac{1}{2}\Gamma_n^r}{\chi - \chi_n^r + \frac{i}{2}\Gamma} + e^{-i\zeta_n^r} \sin\zeta_n^r \right\},$$ (120)

where $\chi_n^r = ka$ determines the n-th resonance frequency, $\frac{1}{2}\Gamma_n^r$ is the resonance half-width, and

$$e^{2i\zeta'_n} = \frac{h'^{(2)}_n(\chi)}{h'^{(1)}_n(\chi)}$$

Here, we have absorbed the $2n + 1$ factor into the expression. The (1) or (2) superscript over the h's indicates Hankel functions of the first or second kind. This form is of interest, because it shows that one can represent a modal contribution in terms of an acoustical background as well as the resonance contribution. It is to be noted that this form of a resonance occurs in many branches of physics and engineering. The above representation presents the resonances in such a manner that the resonance component (the first term in the brackets) is clearly separate from the background part (the second term). Further, it shows explicitly the half-width as well as the frequency of the resonances. The form of Eq. (120) will also prove useful since we will use the residue theory to Fourier transform this equation to the time domain.

We consider two incident waveforms; the first one is a delta function in time which gives a continuous (cw) frequency spectrum, and the second one is a pulse which is sufficiently localized in time that we will be able to isolate individual events in the scattered signal. Specifically we use a Gaussian weighted cos-form with the carrier frequency ω_0

$$p(t) = \cos(\omega_0 t)e^{-\sigma^2 t^2} = \cos(kas)e^{-\sigma'^2 s^2}$$

where s is a reduced time variable, $s = ct/a$, k is the incident wavenumber and $\sigma' = \sigma a/c$. Here we refer to ω_0 as the carrier frequency. The spectral distributions of these incident waveforms are either 1 or :

$$g_i(ka) = \sqrt{\frac{\pi}{4a}}e^{-(ka-ka_R)^2/4\sigma'^2}$$

where it is assumed that ka is not small. The above form allows us to smooth out the edge effects that would produce undesirable effects due to sharp cut-off of the integral by adjusting σ'. The scattered signal in the time domain, when we fold the pulse form into the integral, is[76]

$$p(s) = \frac{1}{2\pi}\int_{-\infty}^{\infty}e^{-i(ka)s}f(ka)g_i(ka)d(ka),$$

in which the *f(ka)* is the Fourier transform of the expression in Eq. (120), namely the real part of the integral on the left is equal to the right side of Eq. (120):

$$\text{Re}\int_{-\infty}^{\infty}\frac{\frac{1}{2}\Gamma'_n}{\chi - \chi'_n + \frac{i}{2}\Gamma}e^{-i\chi s}d\chi \approx \Gamma'_n \sin(\chi'_n s)e^{-\frac{1}{2}s\Gamma'_n} \qquad (121)$$

It is a good assumption - due to phase averaging effect in the non-resonance region-to assume that the only contributions in Eq. (121) occur at resonances and thus one arrives at the expression,

$$p(s) \approx \sum_{n=M}^{n=N} \frac{\Gamma_n^r}{2} \sin(\chi_n^r s) e^{-s\Gamma_n^r/2} , \qquad (122)$$

where the sum is over a nest of resonances.

If we are in a frequency region, where the resonance widths and spacings are approximately uniform, then for several sets of n we have:

$$\Gamma_{n+1}^r = \Gamma_n^r \qquad \text{and} \qquad \chi_{n-1}^r - \chi_n^r = \Delta\chi_n^r .$$

These conditions are met in many cases including the lowest order symmetric resonance for thin shells and for pseudo-Stoneley resonances for submerged elastic shells. We will discuss both examples below.

Then, by summing 2M contributions from the nest of resonances, we obtain from Eq. (122) and the conditions of uniform resonance spacing and half-widths and through some trigonometric manipulation the important expression

$$p(s) = 2\pi 2^M \sin(\chi_n^r s)\big(\cos(\Delta\chi_n^r s / 2)\big)^M , \qquad (123)$$

which shows clearly the prominence of the "carrier frequency" and the existence of an "envelope frequency", $\Delta\chi_n^r$, as well as the exponential damping factor which is known to be related to the half-width. In this derivation we required that M be an integer but the expression still holds for half-integers. We can summarize the results suggested by Eq. (123) as follows.

(i) The half-width is associated with the decay of the response in the time domain solution: the response decreases exponentially with increasing value of the half-width. This is not altogether unexpected since narrow resonances are associated with long ringing times and is analogous to well defined energies being associated with long half-lives in quantum physics cases.

(ii) The larger the number of adjacent resonances (2M) sensed, the more sharply defined the return pulse or envelope function (the beats) and the more enhanced the return signal. Under appropriate conditions we can get the group velocity of a specific type of resonance.

(iii) The larger the carrier frequency the more oscillatory the signal is within the envelop.

(iv) If several adjacent resonances sensed by a signal are different in character in the region of the carrier frequency, then it becomes difficult to interpret results in terms of a group velocity associated with a particular resonance type. Attempts at such interpretations could lead to erroneous results. For example, if one senses two resonances, one a Rayleigh resonance and one a whispering gallery resonance, the extraction of a group velocity associated with a specific resonance type based on some perceived beat pattern would lead to error.

4. Application and Interpretation of Physical Results

We divide this section into the following parts. First, we treat impenetrable objects (rigid and soft objects) for spheroids and for cylinders with hemispherical end-caps. We then examine scattering from submerged elastic spheroids with a focus on the mechanism responsible for resonances, including bending or flexing resonances peculiar to elongated targets. We explore our knowledge of resonances as a tool to extract the material characterization of elastic solids. We then examine scattering from elastic shells which include some newly investigated resonance patterns due in one case to water borne waves and in the other to the importance of the first order symmetric Lamb mode S_1 which accounts for very large resonances from elastic shells. Some features of resonance scattering in the time domain are explored and finally we close this article with a section on scattering from objects in a wave guide.

4.1. Scattering from Rigid and Soft Targets

There are two classes of targets for impenetrable problems, i.e., soft and hard scatterers. Impenetrable acoustic targets do not support body resonances; therefore we examine acoustic characteristics appropriate for non-resonating objects. This kind of analysis is also useful for the high frequency limit for which resonances are not as distinct and geometrical features prove more useful as a remote sensing tool. The quantities are bistatic and monostatic angular distributions.   Bistatic angular distributions correspond to measurements of the scattered field at any point in space for some incident acoustic field fixed relative to some source-object orientation illustrated in Fig.(4).
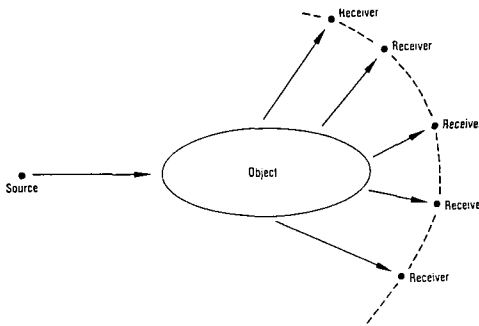
Fig. 4. Scheme of bistatic angular distributions.

Angular distributions thus depend on target geometry and can be useful in determining features such as target characteristics associated with symmetry and elongation. In particular, we can observed reflection, diffraction, and the generalized Snell's law behavior as curved-surface analogs for the plane-layered case. In Fig. (5) we examine a rigid spheroid of aspect ratio (ratio of length-to-width) of 15:1. The order of the plots

corresponds to: (a) - scattering from the object for the incident field along the axis of symmetry (end-on), (b) - scattering at 30^0, (c) - at 60^0 and (d) - at 90^0 relative to the symmetry axis (broadside). The values of the incident acoustic field frequency are expressed using the dimensionless quantity kL/2, where L is the object length and k the total wave number (k=2 π / λ). The value of kL/2 in Fig. (5) is 120, which implies that the object is about 40 wavelengths long and thus in the intermediate frequency region where neither low nor high frequency approximations apply. In all figures frequency is sufficiently high that wave diffraction effects are significant in the forward scattering direction. Perhaps the most interesting feature of the four plots, Fig.'s (5a)-(5d), corresponds to a reflection at the (fairly flat) side of the object for scattering angles of 30^0 and 60^0.
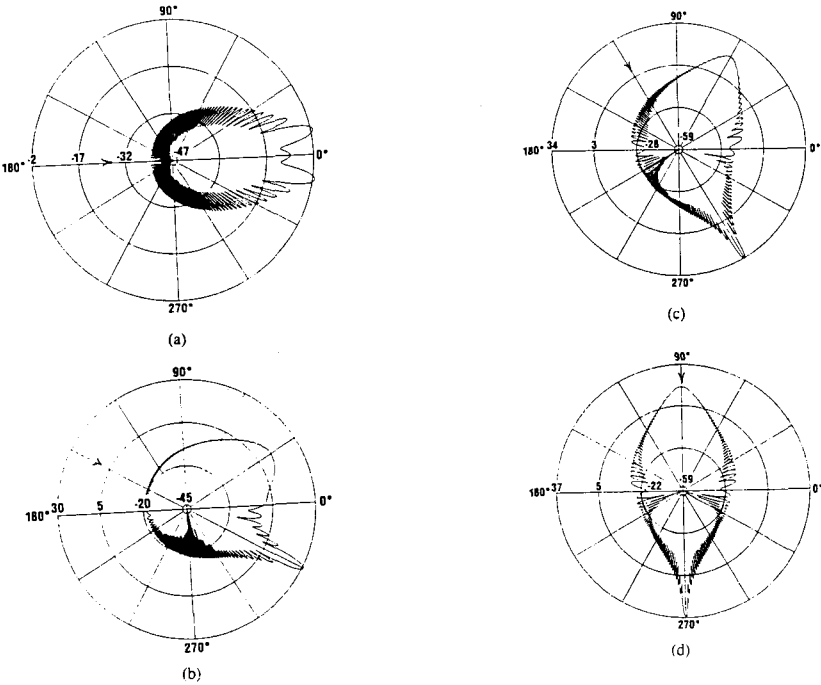
Fig. 5. Bistatic angular distributions from rigid spheroids.

This reflection can only occur for very elongated objects that approach flat surfaces, so that the reflected angle is almost the same as the incident angle (relative to a straight line through the axis of symmetry). We next consider the same scattering problem for sound-soft objects. Fig.'s (6a)-(6d) illustrate the response from a spheroid of 15:1 aspect ratio

and a kL/2 of 15. In terms of directionality and reflection, these angular response patterns are similar to those in the previous (rigid) case. The scattered field tends toward the forward direction and the reflected angles (relative to the axis of symmetry) coincide with the incident acoustic field. However, scattered fields are now more highly focused, even at the lower frequency value considered. This latter effect is due to the phase-change at the object surface (π radians). We see the same effect (as for the rigid case) in (b) and (c) for surface reflections at angles equal to the incident value relative to the axis of symmetry (the generalized Snell's law). Fig. (7) illustrates the scheme of monostatic angular distributions. Fig. (8) consists of plots of the monostatic angular distributions for rigid and soft spheroids and cylinders with hemispherical end-caps. The top three figures from left to right describe scattering from targets with aspect ratios of 24 for a kL/2 of 40 for rigid and soft spheroids and a cylinder with hemispherical end-caps. The three patterns differ according to target. Rigid targets present more pronounced diffraction patterns than soft scatterers while the rigid cylinders have stronger return signals end-on due to their larger relative cross sections. The minima may be viewed as the consequence of the destructive
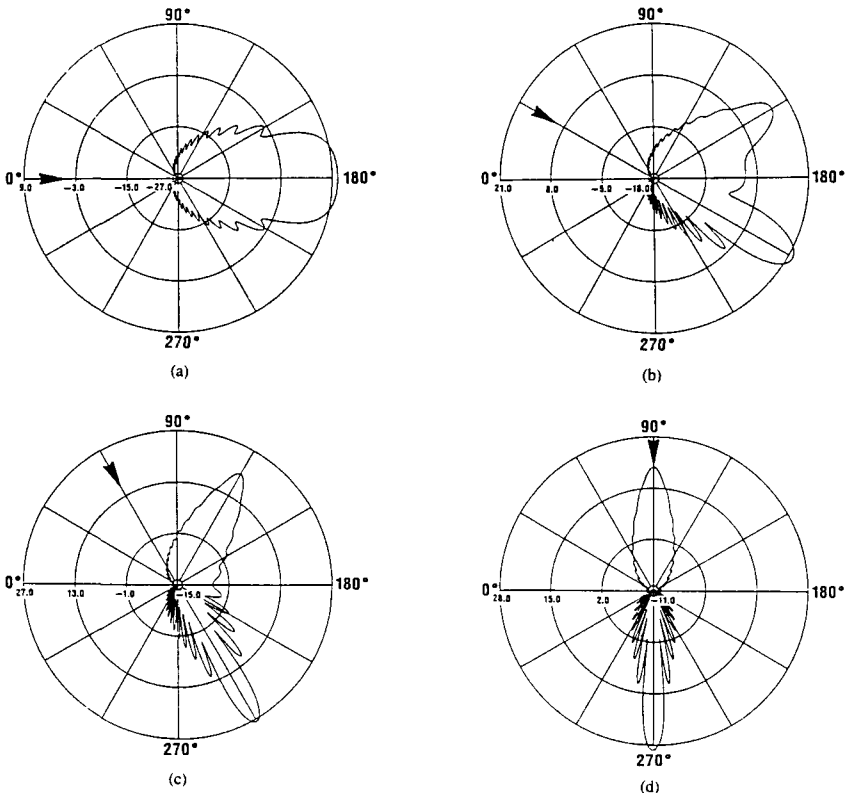
Fig. 6. Bistatic angular distributions from soft spheroids.
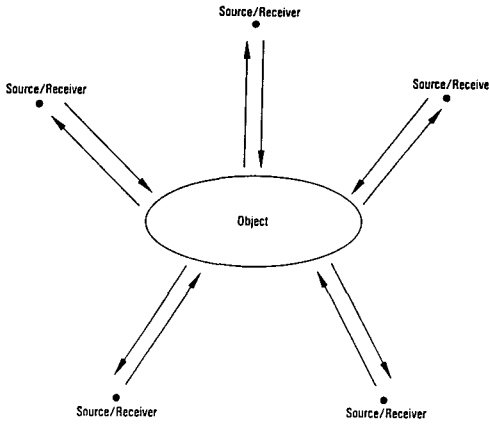
Fig. 7. Scheme of monostatic angular distributions.

interference between waves reflected from opposite ends of the elongated objects. The waves reflected from the regions away from the edges have a less than dramatic effect on interference and are ignored in this simple derivation. Because the objects are both long and narrow with respect to the incident wavelength, it can be effectively represented as a straight line to allow derivation of the interference locations θ_n and N the number of nulls by the expressions below:

$$\theta_n = \sin^{-1}\left[\frac{\pi(n+1/2)}{kL}\right] \tag{124}$$

$$N = \text{int}\left[\frac{kL}{\pi} - 1/2\right] \tag{125}$$

It is interesting to note that these equations predict quite accurately the location of nulls from EBC results. In Fig. (8) the upper middle plot illustrates the monostatic response for the acoustically soft target. Here the interference nulls are not a pronounced feature in contrast to the rigid case, due to the focusing effect of acoustically soft boundary conditions. The second and third rows of plots illustrate monostatic scattering from rigid spheroids for targets of aspect ratios of 15 (middle row) and 7.5 (bottom row) for kL/2 from left to right of 30, 60, and 120. Note that the geometric patterns are more pronounced as frequency is increased. We complete the study of scattering from impenetrable targets by examining back scattered and forward scattered signals which are shown in Figs. (9) and (10). There are two competing mechanisms in the back scatter case. One arises from specular scattering (geometrical) and the other arises from the creeping or Franz waves which are circumferentially diffracted by the surface of the

object. The consequence of this is a coherent effect in which the two waves add constructively at some point leading to a maximum value when they are in phase and destructively leading to a minimum value when they are out of phase. This can be seen in Fig. (9) for spheroids of aspect ratio: (a)1:1 (b)2:1 (c) 4:1 (d) 8:1 and (e) 16:1. The increased circumferential diffraction with increasing aspect ratio is due to the greater grazing angular region for higher aspect ratio targets which results in the stronger creeping waves. Fig. (10) illustrates the forward scattered signals for the same five targets. In those cases the forward signals grow with increasing frequency while the back scattered returns simply asymptote to the geometrical cross sections. The slope of the forward scattered signals can be shown to be proportional to the square of the aspect ratio's of the targets for end-on scattering as one approaches higher frequencies.

4.2. Applications to Elastic Targets

In this section we examine phenomena observed often when scattering from elastic objects with smooth boundary conditions surrounded by a fluid; namely, body resonances. It is also possible to have resonances from air inclusions in a fluid; but we will not examine those targets here. The resonances examined for the elastic solid case originate from the curved-surface equivalents of seismic interface waves of pseudo-Rayleigh or Scholte type, propagating circumferentially to form standing waves on a bounded object or from bending modes when scattering at oblique angles. These types of resonances occur at discrete values of $kL/2$ and manifest themselves in a characteristic manner. For elongated elastic solids, three distinct resonance types occur. The first kind (at lower frequencies) are due to leaky Rayleigh type waves and have been shown to be related to both target geometry and material parameters (notably shear modules and density). Resonances can, in this case, best be observed by examining the back scattered echo amplitude and phase response plotted as a function of $kL/2$, often referred to in acoustic scattering literature as a form function. Überall et. al.[6-9] determined that for spherical targets, resonances excited on elastic solids are connected to Rayleigh waves in a half-space -the phase velocities were close to one another- and he reasoned that the resonances corresponded to standing waves which at certain frequencies (half-integral wave lengths about the perimeter) arise from the waves traveling on the surface which at appropriate frequencies form standing waves that radiate energy into the water and add coherently with the specular waves. We illustrate these resonances for WC spheres. The elastic response is illustrated in Fig. (11) and in Fig. (12) we illustrate the residual obtained from subtracting the rigid from the elastic response. This later contribution mainly reflects the resonance component of the differential cross-section. We label the figures in obvious fashion according to the terminology of Rayleigh resonances (n,1), where n>1, and wispering gallery resonances (n,m) where n can be 0 or greater and m is greater than 1. The assumption was made by Überall that the higher harmonic resonances correspond to whispering gallery (WG) waves that travel along the inner surface of the sphere in the elastic material. That picture
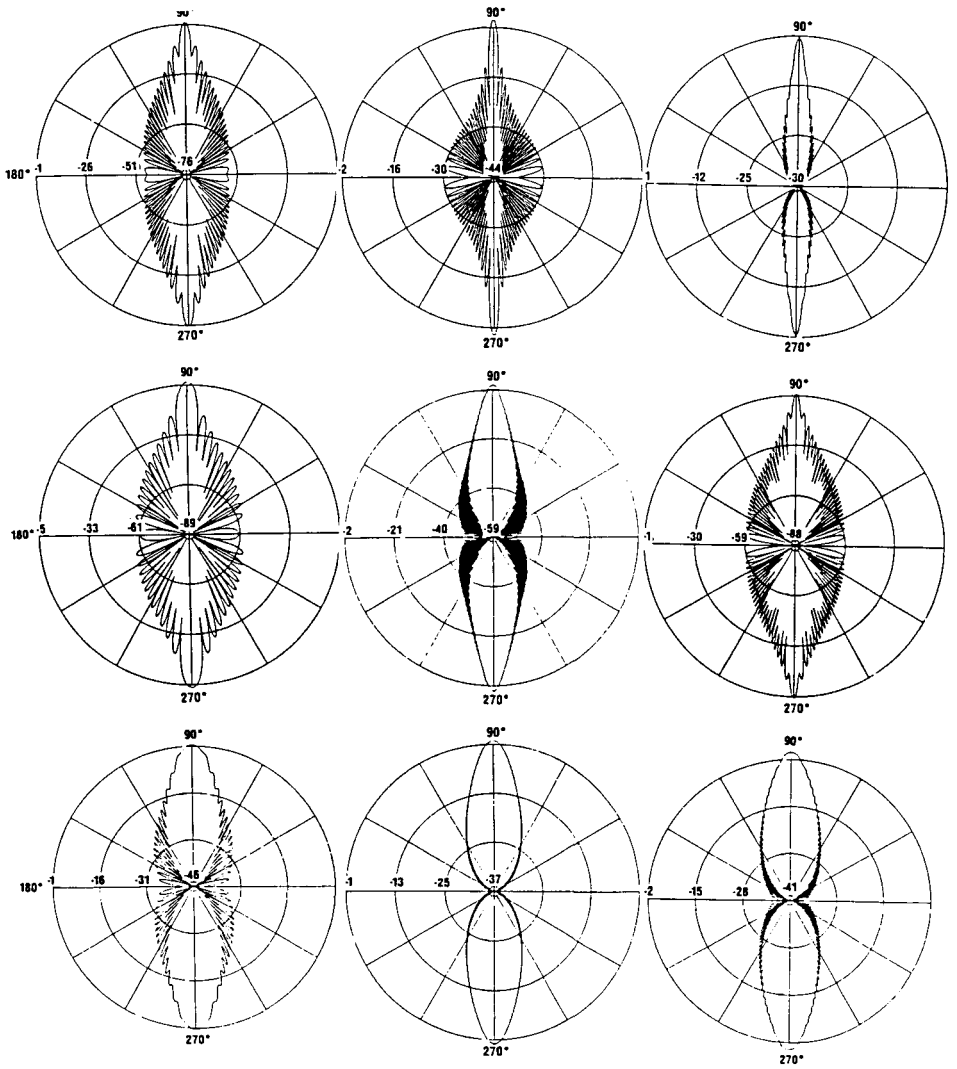
Fig. 8. Monostatic angular distributions.

is a a cleaver analogy to the Rayleigh wave arguement for the principle type of resonance. Although this terminology is still observed for this class of resonances and is likely a valid "metaphor" at the higher frequency, a more useful mechanism is suggested by R. Hickling's recent work[61] in which he plots intensity contours of the interior field at the frequencies corresponding to the value of frequencies at resonance. Based in Hickling's field plotts the WS resonances may be topological in origin and are similar to Lamb modes (see section below on shells) for the shell case. Lamb modes are either symmetric or antisymmetric and may be associated with either the shear or compression phase speeds. Lamb modes are topological in nature at critical frequency in the sense that they form standing wave pattterns in a plate. From Hickling's plots of the intensities of the field at resonance, topological features suggest standing waveguide type patterns internal to the object that terminate at the surface of the object. However, since there is only one surface and we are dealing with spheres, the standing waves rather than terminating at opposite surfaces for an elastic plate, must curve back and terminate on the same spherical surface. The contours that Hickling plots appear much like the TE_{lm} fields of an electromagnetic cylindrical waveguide in which the field lines terminate at the surface for $(0,0)$ values and form closed patterns for $(l,m>0)$. Just as the Lamb modes are actually guided waves in the elastic media bounded by the two surfaces of the plate; the WG resonances may be interpreted as from either symmetric or antisymmetric "wave guides" that fit in the spherical region. These curves rotate in time over at least 180° at resonance and account for a phase velocity effect. Hence, Hickling referred to them as rotational resonances. The terminology of rotational resonances, if they are related to waveguides, is appropriate since a guided wave in a sphere would only have rotational motion except for the breathing mode . It is possible that these sorts of waves would be restricted to the inner surface of the sphere at high frequencies and thus the terminology of whispering gallery resonances is appropriate.Hickling's observation that the field rotates in time in the sphere gives rise to the surface disturbance that leads to traveling waves on the surface and accounts for the phase velocity of the waves that form the resonances. Without the rotational effect, the description of resonances as standing waves at interfaces would not be valid. The lowest Rayleigh waves form closed ellipses in the contour plots of Hickling, two- followed by four, six, etc., which also rotate in time. As the ellipses open with increased frequency and resonances vanish, contours eventually form opened figures that terminate in a symmetric manner at the perimeter perhaps leading in some cases to the WG resonances. These effects must be seen on the Hickling video for full clarity of the mechanism, but to be sure, the resonances involve topological patterns that resulted in either opened or closed patterns and rotate in time at resonance. The interpretation of the Hickling work is speculative but it certainly should be considered in the final judgment of the WS resonance issue. Fig. (13) illustrates the standing wave pattern that results at resonance for the various types of resonances confirming Überall's notions of the standing wave picture, regardless of the physical mechanism of resonances. It is noted that only the residual response is useful in illustrating the standing wave picture and this notion in conjunction with the standing wave resonance methodology using phase integrals proves useful in the analysis of level crossing of resonances described below. We note that the
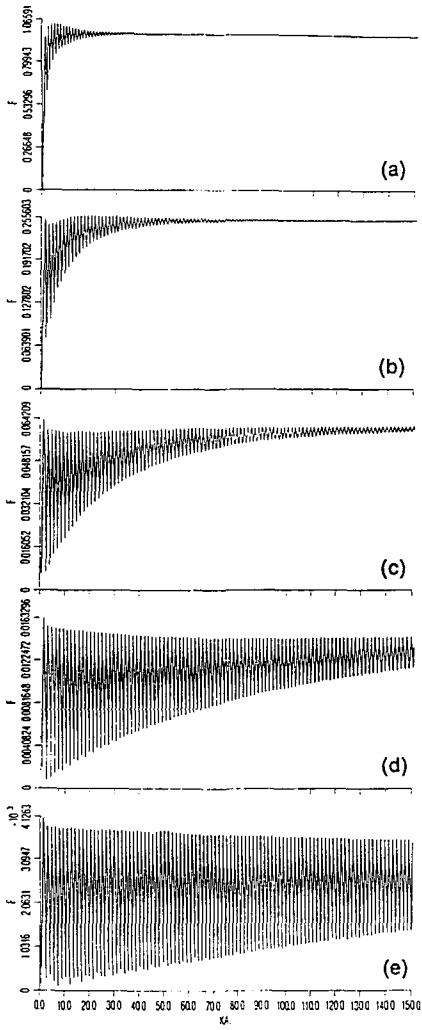
Fig. 9. Backscattering frequency plots
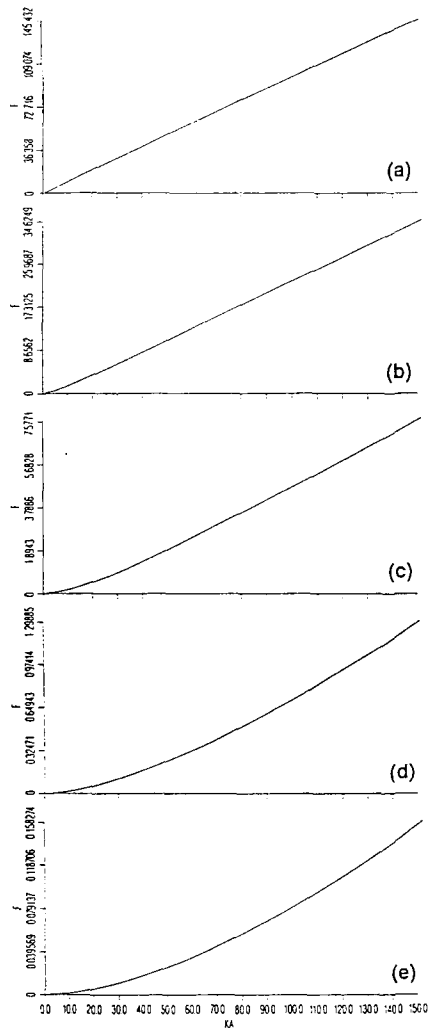
Fig. 10. Forward scattering frequency plots
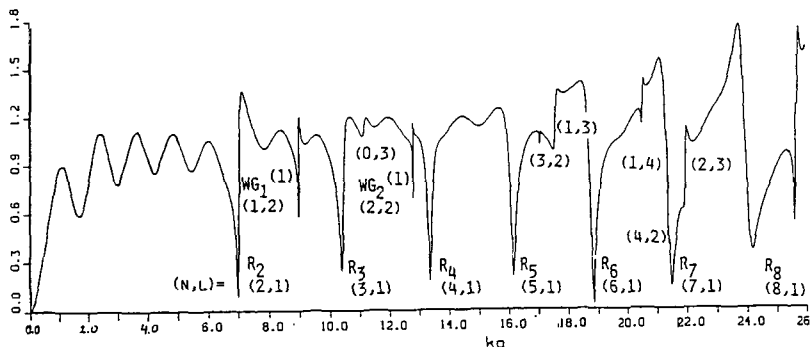
Fig. 11. Elastic response for scattering from solid elastic spheres.

terminology of Rayleigh resonances for spheroids and thus by extension for spheres was contested by R. Hackman, et. al [62]. Hackman argues that the resonances that are referred to as Rayleigh resonances for spheres and that were first referred to as Rayleigh resonances for spheroids by Flax, et. al.[63] and later in other works[64-66] is based on contour vector plots of the field. Hackman observes large interior contributions of the field which he argues are inconsistant with Rayleigh waves because they are referred to in the literature as surface waves and also argues that the vector plots appear to form patterns consistant with "bar" waves. Hackman had in mind very elongated spheroids and not the low aspect ratio spheroids that were treated by Flax and in a paper by Werby and Tango[64] which recieved much criticism in his work. There are only three types of bar wave theories. We have already treated the one on the transverse modes which cause the "bar" to flex. These resonances are now well accounted for and are not excited end-on. There is a theory for compressional modes due to Love and a related Poisson effect but they are useful only at a low frequency limit and do not predict resonances. There is a "bar" theory for torsional modes which can not be excited for end-on incidence and torsional modes are not likely what Hackman has in mind. Rayleigh waves were first studied by Lord Rayleigh[67] for free vibrations on an infinite elastic half-space. Rayleigh showed that in addition to the transverse and longitudinal bulk waves which traveled in the body of the material, there was also an interface wave that was non-dispersive and that traveled at speeds typically about 91% of the shear speed. Rayleigh was interested in earth quakes and reasoned that earth quakes had to be confined to the surface since they caused so much damage and traveled to long distances. The bulk waves lose most of their energy to the earth's interior. Since the waves attenuated at two wavelengths from the surface,
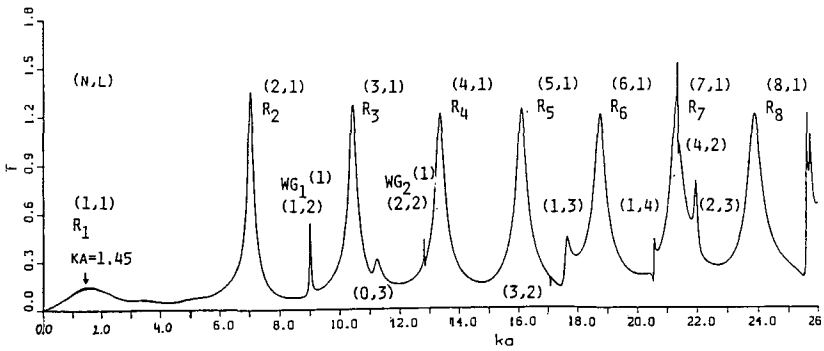
Fig. 12. Elastic residual response for scattering from spherical elastic solids.

Rayleigh waves are commonly referred to as surface waves. However, they are actually interface waves that arrise due to mode coupling of the transverse and longitudunal modes at a free surface. These modes are coupled at an interface but become uncoupled in a homogenous elastic medium as they progress away from the interface or an inhomogenuity. When a half-space is fluid loaded then the Rayleigh waves are dispersive and radiate energy into the fluid. They are then referred to as leaky Rayleigh waves. If the surface is curved then these interface waves are referred to as leaky pseudo-Rayleigh waves. It has been pointed out that arguements on the nature of surface restriction loses meaning at low frequeny for spheres, cylinders and spehroids since two wave lengths at the lowest resonances for these finite objects goe to the core of the object. We beleave that the terminology that these resonances are of the Rayleigh-type is valid at least in the sense that a phase velocity analysis is consistant with the Rayleigh phase velocity and that they are interface waves due to mode coupling. A "bar" resonance interpretation may be useful for very elongated spheroids and Hackman's work on the use of alternative basis functions for the T matrix is certainly one of the major contributions in the field. An interesting aside to all of this is that it turns out that all resonances on elastic shells asymptote to the Rayleigh phase velocity at heigh enough frequencies and this is true for plates and shells[67,68] and that includes the lowest symmetric mode (the same as the symmetric plate mode) and all of the Lamb modes. The flexural mode is expected to have such behavior and does asymptote rather quicky to the Rayleigh phase velocity and some thick plate theories constructed to describe the flexural mode even demand it. The bar theory presented in Sec. 3.7 for flexural modes is very similar in nature to the thick plate

theory used in Sec. 4.10.2 to derive Eq. (126) and also predicts a phase velocity that asymptotes to the Rayleigh phase velocity. It is evident that at very high frequencies a simple interpretation of resonances or vibrational modes is no longer possible because the phase velocites are no longer unique. Let us understand that any paradim that we feel comfortable with is useful if it has predictive value in understanding phenomena and is a useful descriptoin to communicate with others unambiguously. As a broader issue in discussing research issues many researchers from optics prefer to use a ray-type picture in describing events or even constructing theories based on this asymptotic description, while some engineers and physicists prefer a wave-like picture. These descriptions are not mutually exclusive and in some frequency regions they are equivalent. They are aids to thought.

Fig's.(14)-(16) illustrate the same type of results for scattering from steel spheroidal shells for aspect ratio of 4:1. The resonance types persist and the standing wave picture as well as the assignment of Rayleigh resonances also persist for the prolate spheroidal solid. Standing wave patterns in Fig.(16) are reasonably consistent with those of Fig. (13)
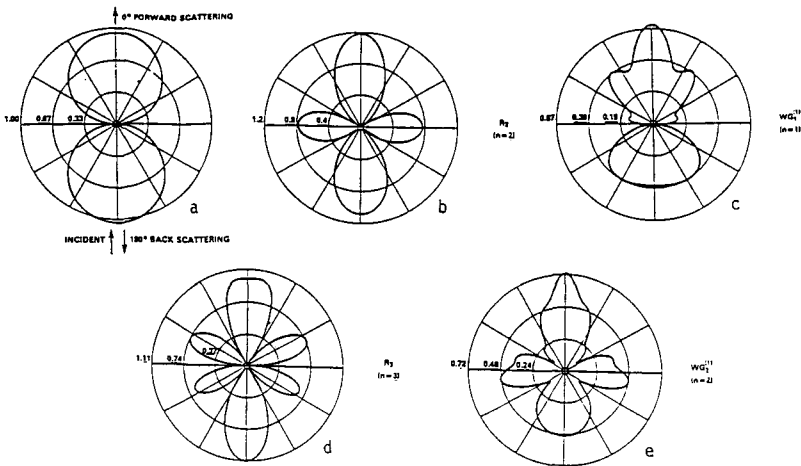
Fig. 13. Standing wave pattern for resonances on elastic objects.

and would best be represented when plotted on an imaginary spheroidal surface superimposed about the actual sphere. The patterns that we illustrate here are the far field patterns in which the surface is spherical. We should expect better standing wave patterns when we plot on a spheroidal surface.
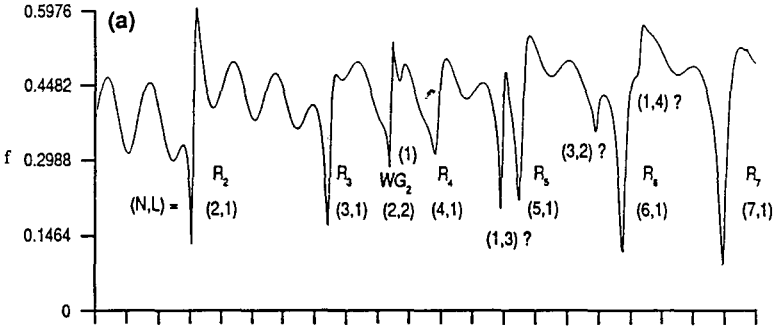
Fig. 14. Elastic response for scattering from spheroidal solids.
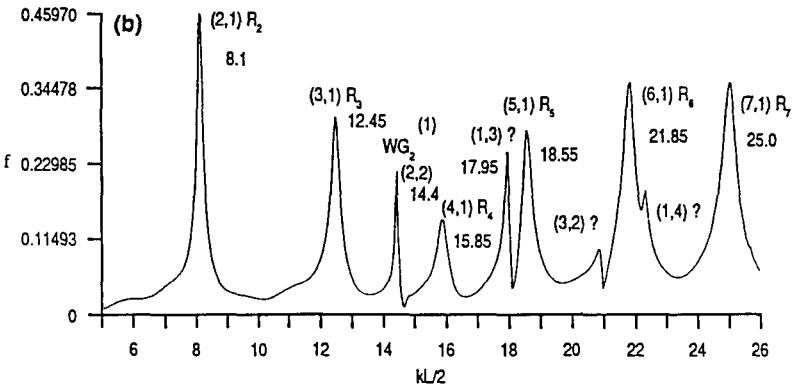
Fig. 15. Residual response for scattering from spheroidal elastic solids.
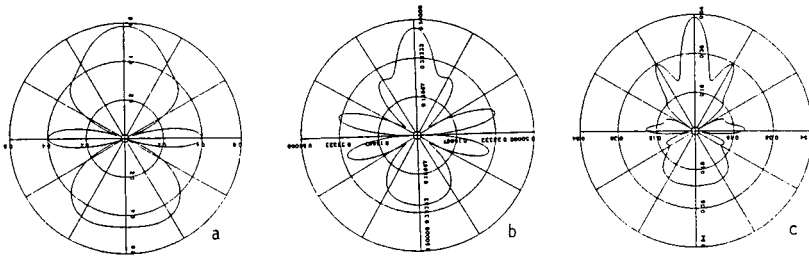
Fig. 16. Standing wave pattern for resonances on elastic spheroids.

Prior to Überall's analysis many researchers believed that resonances on elastic surfaces corresponded to fluctuations of the usually spherical shape from prolate to oblate. Presently, certain types of resonances excited by earthquakes in the earth are believed to be so-called foot ball resonances which correspond to the earlier picture of the elastic resonances.

4.4. Broad-side and Oblique Scattering from Elastic Solid Spheroids

In Fig. 17 we examine broadside resonances for 2, 3, 4, and 5 to 1 aspect ratio steel spheroids. Here we can excite three phenomena. At the lowest value we can see a spike representing a bending resonance[67-69] discussed below. The second lowest spike corresponds to the lower order Rayleigh resonance seen end-on, corresponding to a standing wave, circumnavigating the largest meridian of the spheroid. We also see weak Franz waves similar to those excited on a cylinder, and then we see the lowest order Rayleigh and whispering gallery resonances corresponding to circumferential waves around the smallest meridian. We discuss those issues in more detail below.

4.5. Flexural or Bending Resonances

The third kind of resonance we wish to illustrate has to do with bending modes or flexural resonances. The bending or flexural resonances (flexural in this context is not to be confused with antisymmetric plate modes) occur on elongated objects such as

both for solids and shells. For unsupported spheroids, a plane incident wave at 45^0 relative to the axis of symmetry can excite these modes. We illustrated these resonances in Fig.'s (18a)-(18d) for solid steel spheroids for aspect ratios that range from 2:1 through 5:1. The lowest mode corresponds to 2, and thereafter 3, 4, etc. The interesting thing about these resonances is that they can be predicted by exact bar theory described in Sec. 3.7 and coincide nicely with results here. Of particular interest is the effect that with increasing aspect ratio, the onset of resonances occur at lower kL/2 values; the opposite effect observed for Rayleigh resonances. The modal pattern is illustrated in Fig. (19) for the first four modes. These resonances can be excited on spheroidal elastic solids at any incident angle other then along the axis of symmetry where clearly the flexing effect can not be initiated. However, the strongest excitations are close to 45^0 relative to the axis of symmetry. We illustrate the comparison between the resonances predicted by the simpler picture outlined in sec. 3.7 and the EBC calculations. This comparison between the resonance locations and those predicted from the beam theory is illustrated in Fig. (20). The results are remarkablly close even for targets of aspect ratio's of 2:1. It is to be noted that the simple beam theory can only predict these bending modes and is based on a limited physical description, while the EBC-equations which first gave evidence of the flexural modes are so complicated that there is nothing in the expressions derived from exact theory that would suggest such modes. Here is a case where it is possible to use a simpler more limited picture to account for events predicted from very complicated expressions. This is what we mean by a "metaphorical" approach, namely in making use of a simple picture that is only able to account for a pronounced physical process that is not obvious from a more comprehensive theory we gain insight in the mechanism responsible for the event. To complete this analysis we illustrate 3-dimensional plots of the flexural modes in Fig. (21). The calculations illustrated in these plots vary over the kL/2 range in which the object behaves as a rigid target to that of the flexing target and then back to the rigid target. The resonance responce is large and very pronounced for values of the angular region off the principle axis. There is some contribution to the scattered signal even at angles perpendicular to the axis of symmetry; but the most pronounced contribution [67,68] occurs at about 42^0.

4.5. Level Crossing Effects for Elastic Solids

Here, we discuss a "level diagram" illustrated in Fig. (22) for WC spheroids for aspect ratio's ranging from 1 to 4 in steps of 0.25. The diagram represents plots of the relative levels and associated ordered pairs (n,m) for the various resonances. Remember that Rayleigh resonances correspond to the ordered pair (n,1) where n is 2 or greater and WG resonances correspond to (n,m) where n is any of the natural numbers and m is 2 or greater symbolizing higher harmonics. We see that the Rayleigh resonances gradually shift upward with increasing aspect ratio while the whispering gallery resonances shift up more rapidly for fixed index n. Eventually, the whispering gallery resonances shift upward to the extent that they cross over the Rayleigh resonances.
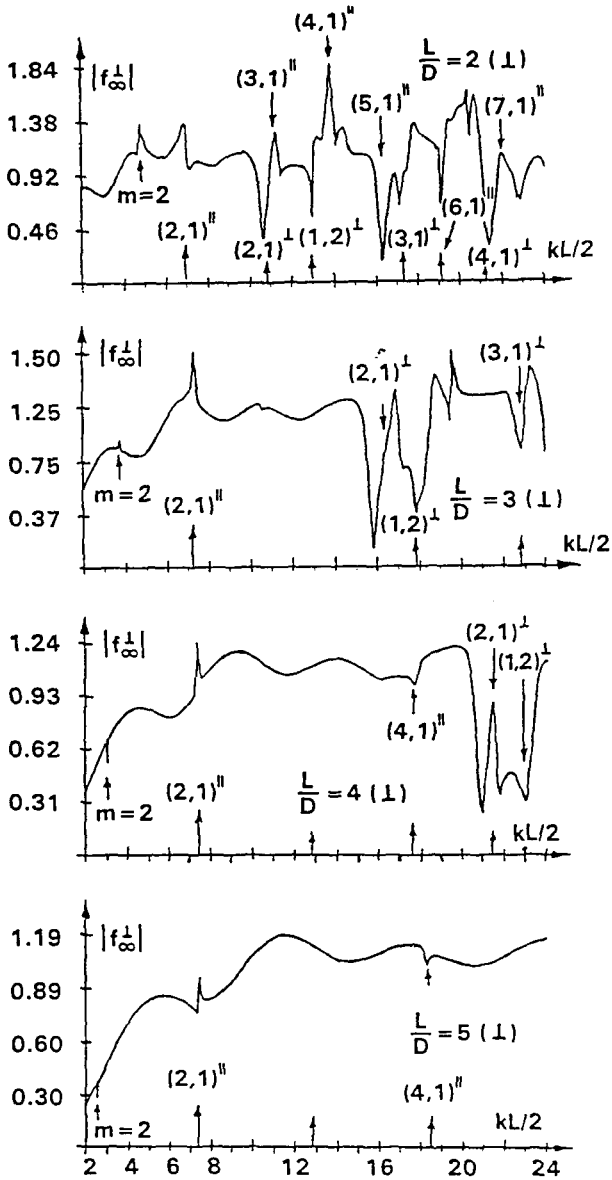
Fig. 17. Broad -side resonance from a solid steel spheroids.
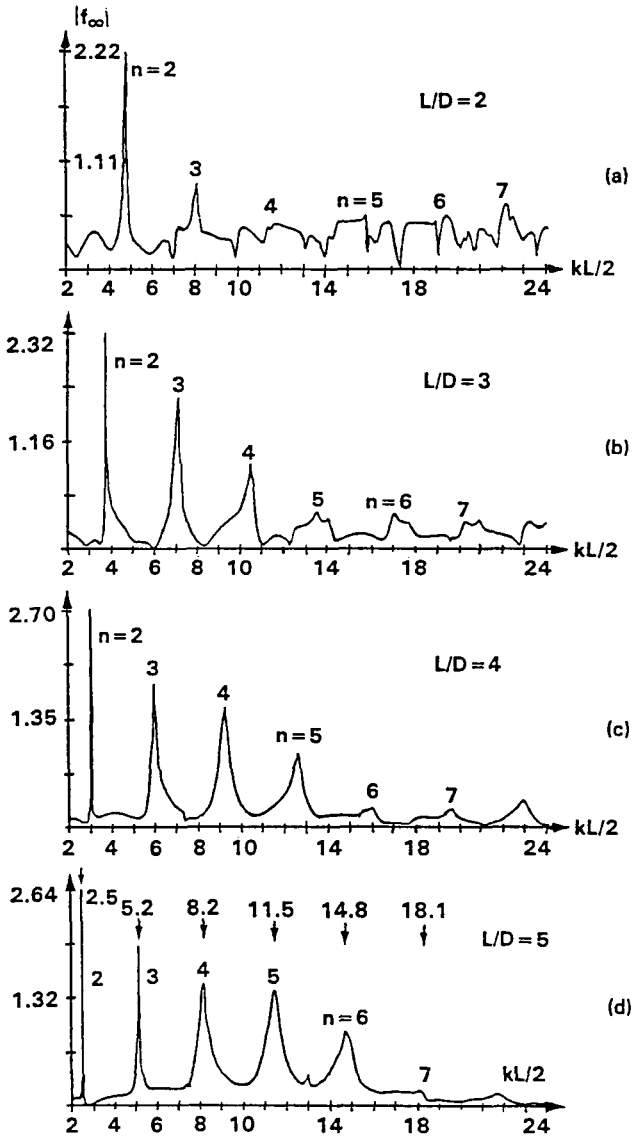
Fig. 18. Flexural resonances from elastic solid spheroids.
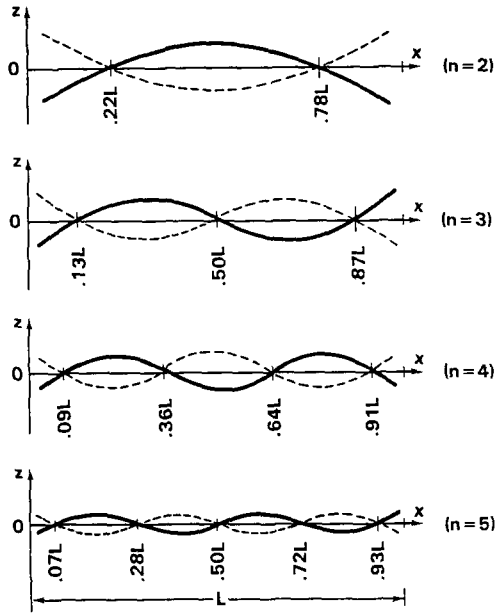
Fig. 19. Modal patterns of flexural resonances.
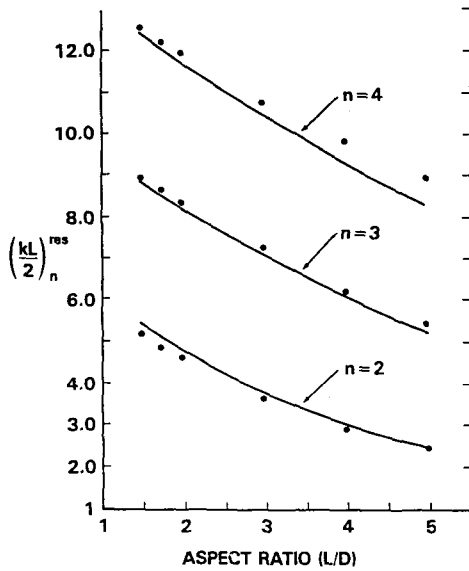
Fig. 20. Comparison of elastic resonances with beam theory predictions.
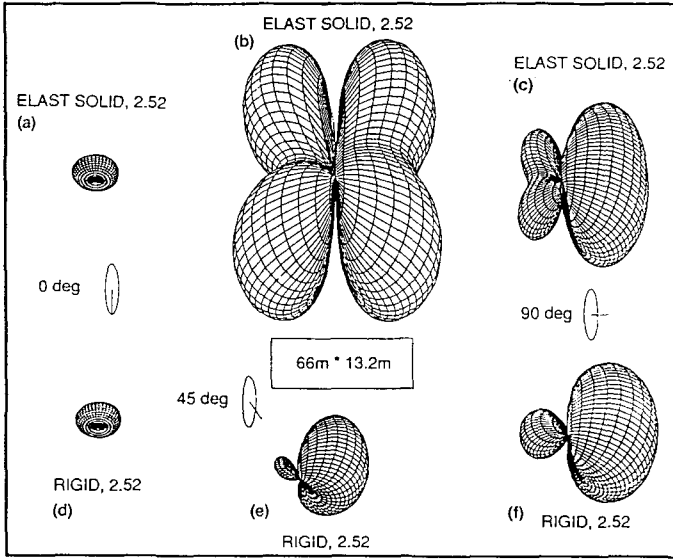
Fig. 21. 3-D plots of monostatic angular distributions at and near the lowest flexural resonance.
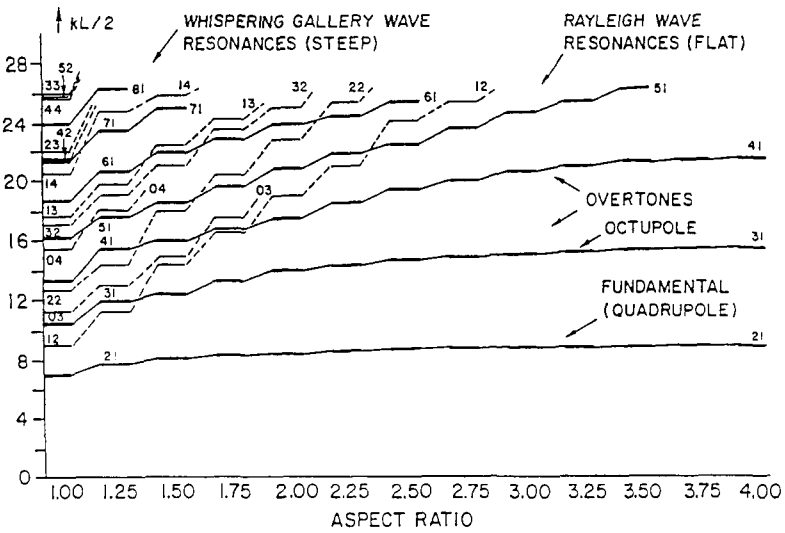
Fig. 22. Spectroscopic diagram vs aspect ratio of WC spheroidal shells for Rayleigh and WG Resonances

We have referred to this as "level crossing" in analogy with a similar event for prolate nuclei.[71,72] It is amusing to compare the two phenomena. The analysis followed much collaboration between Überall et. al. of Catholic University and Werby of the Naval Research Laboratory[72]. The effect was, however, first noticed in a collaborative effort between Hackman and Werby[73]. In the theory of scattering from nuclei, it is simple to treat those examples in which one has a nucleon (a proton or neutron) outside of a core (the nuclear core) in which the core can be treated as inert and spherical. One views the nucleon as being in the outer energy shell and it becomes possible to build on this model by adding more nucleons in a picture in which the addition of each nucleon is treated by some perturbation method. This is called the shell model of the nucleus and it accounts for many of the energy levels of large nuclei. However, as one adds more nucleons to the picture, the additional nucleons influence the nuclear core and cause it to be distorted so that it begins to appear prolate. The consequence of this distortion is that the energy levels predicted for the ideal nuclei begin to exchange places with previously lower energy states so that as the nucleus becomes more distorted, the energy level assignments begin to switch places; their energy levels cross. Thus, when a similar effect showed up for the resonance levels for the elastic problem as one varied from a sphere to that of a spheroid, it was tempting to form the analogy between the two and examine similar mechanisms to account for this effect in elastic targets. Although the explanations for each effect are different, the level spectrums are very much alike. The explanation of the nuclear case is rather Quantum Mechanical while that for the elastic solid has been tentatively resolved as follows[73]. There were two possible explanations at first. Both concerned knowledge of the phase velocity of the different types of resonances and the standing wave picture of the resonances. One explanation is that the lowest order WS resonances observed for shells may be excluded for the spheroidal cases as one examines targets of higher aspect ratios. This effect was determined as possible by Nagle[74] since there appeared to be a cut-off effect of the WG modes based on preliminary calculations. It was deemed, however, that the phase matching method was not useful for the WG resonances at low KL/2's because of the lack of reliable ways for extracting the phase velocity for the lower frequency limit. The other explanation is based on the analysis that the phase velocity of the Rayleigh waves vary more slowly with curvature than the WS waves and thus at some aspect ratio the levels cross due to the greater increase in phase velocity of the WS waves over the Rayleigh waves. The second explanation is judged in the analysis to be the more likely one because the small variation in aspect ratio and the correspondingly smaller but continuous change in the level structure does not suggest cut-off effects.

4.6. Extraction of Material Properties from Resonances Excited on Elastic Solids

In this section we present results from calculations for acoustical scattering from submerged prolate spheroidal scatterers for end-on incidence.[75] The shells are composed of the six materials namely (a) brass (Br), (b) nickel(Ni), (c) aluminum(Al), (d) steel, (e)

molybdenum (Mo), and (f) tungsten carbide (WC). The speed of sound in water is 1.4825 km/s with a density of 1.0. By subtracting the rigid scattered field from the elastic field we arrive at the residual response which isolates the resonance. Note that resonance scattering theory maintains that the backscattered echo is a superposition of the acoustic background and the resonance response. Fig.'s (23) and (24) show the residual response for 3:1 and 6:1 aspect ratio scatterers, respectively. They are arranged in order of the increasing shear velocity of the materials. We note that corresponding peaks move to higher resonance frequencies with increasing shear velocities. Tables (1) and (2) demonstrate that the position of frequency resonance peaks is related to the Raleigh velocity of the material. They show that the ratio's of the Rayleigh velocities of pairs of similar materials (that is, similar in shear velocity) is very close to the ratio of the first and second resonance frequencies of the material for both 3:1 and 6:1 aspect ratio scatterers. This is in agreement with the interpretation that these are indeed Rayleigh type resonances as discussed in Sec. 4.2. Further, the higher aspect ratio examples have resonances shifted upward in $kL/2$ space in accordance with the expressions in Sec. 3.6 and in accordance with the notions of Rayleigh resonances.

Table 1. Ratios of first resonance peaks compared with Rayleigh velocities.

Material Pairs	Ratio of Rayleigh Velocities	2nd Peak Ratio for 3:1 Aspect Ratio	2nd Peak Ratio for 6:1 Aspect Ratio
Al/brass	1.56	1.53	1.54
steel/brass	1.64	1.62	1.63
steel/Ni	1.07	1.06	1.07
Mo/Ni	1.20	1.17	1.19
WC/Mo	1.08	1.09	1.08

Table 2. Ratios of second resonance peaks compared with ratios of the Rayleigh velocities.

Material Pairs	Ratio of Rayleigh Velocities	2nd Peak Ratio for 3:1 Aspect Ratio	2nd Peak Ratio for 6:1 Aspect Ratio
steel/brass	1.64	1.66	1.62
steel/Ni	1.07	1.07	1.07
Mo/Ni	1.20	1.20	1.19
WC/Mo	1.08	1.09	1.08

Fig.'s (25) and (26) show the residual response for a 4:1 spheroid for various incidence angles. Fig.(25a) gives the response for end-on incidence while Fig. (25b) shows the broadside response. Fig. (26) shows the response for two intermediate incidence angles. In Fig. (26a) the first resonance frequency is lower than in the broadside case of Fig. (25b). This is because at broadside incidence, surface waves are excited that follow a *minimal* path around the spheroid; that is, parallel to the equator. For end-on incidence, the surface waves that are excited follow a *maximal* path; that is, from pole to pole. It is also possible to take adjacent end-on and broadside resonance locations (for equal mode numbers n) and by use of Eq.is. (93) and (96) we can extract the aspect ratios. For the case of 4 :1 Ni, if we use the crude Eq.(93) we extract a value for the aspect ratios of 3.6.
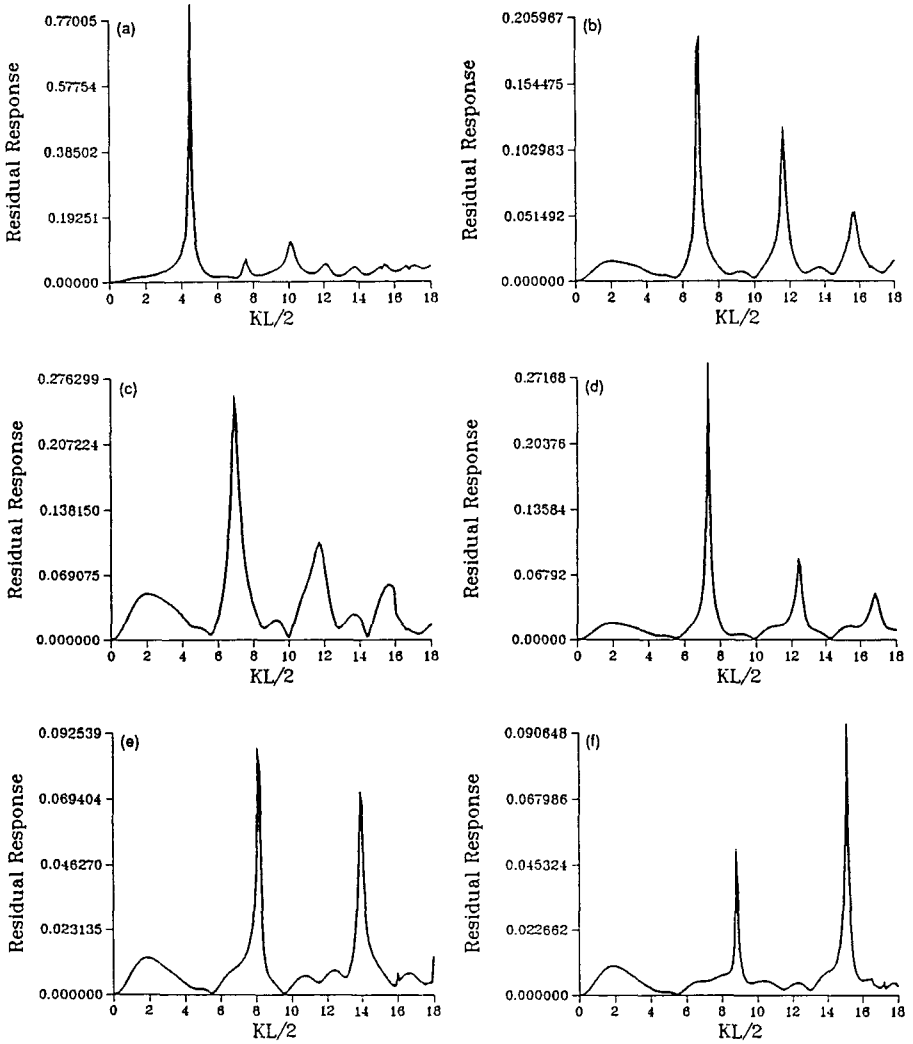
Fig. 23. Residual for 3 to 1 spheroid for: (a) Br, (b) nickel, (c) Al, (d) steel, (e) Mo, and (f) WC targets.
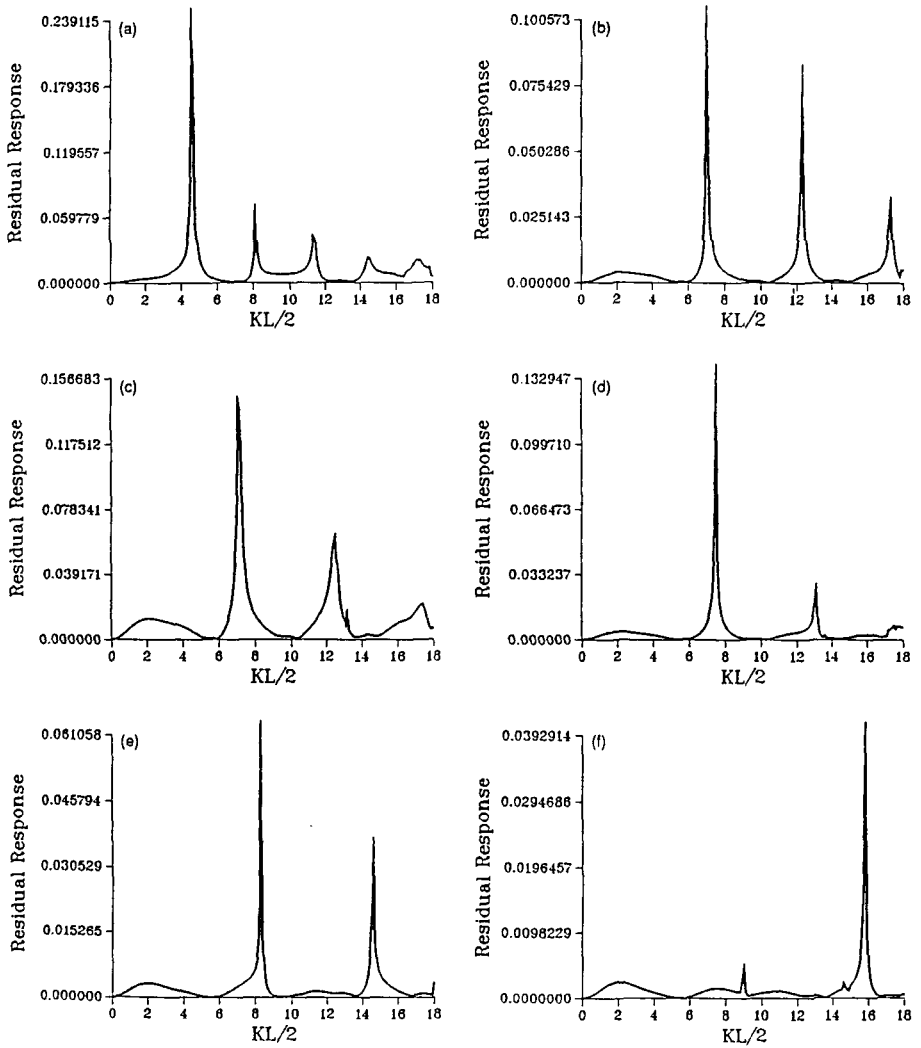
Fig. 24. Residual for 6 to 1 spheroid for: (a) Br, (b) nickel, (c) Al, (d) steel, (e) Mo, and (f) WC targets.
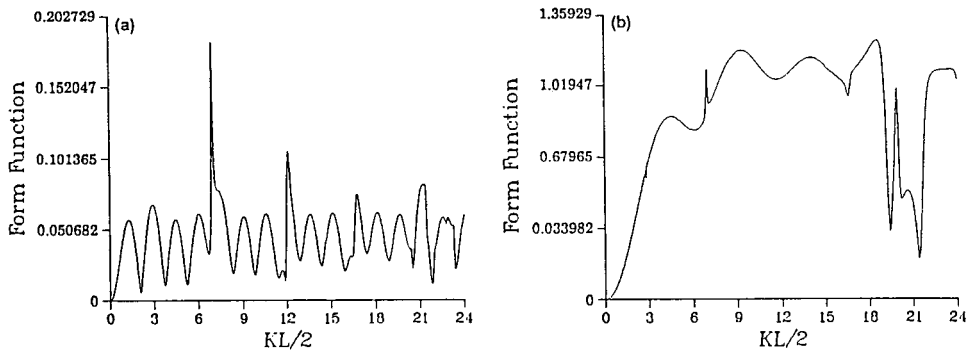
Fig. 25. Residual for a 4 to 1 aspect ratio Ni spheroid: (a) end-on incidence, (b) broadside incidence.
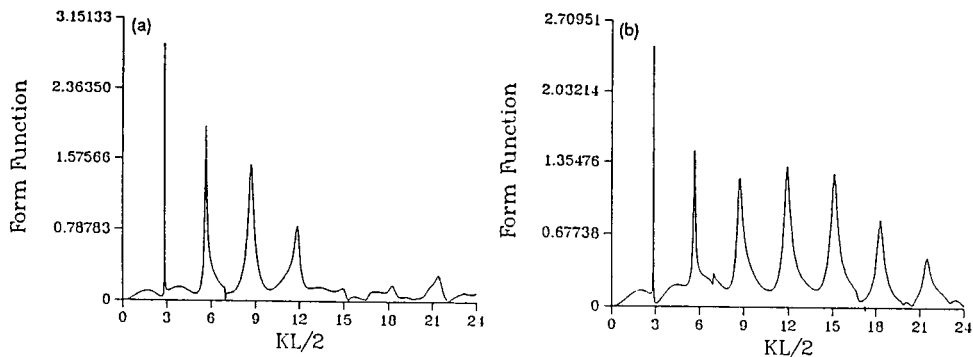
Fig. 26. Residual for a 4 to 1 aspect ratio Ni spheroid : (a) at 40° , (b) at 50° relative to symmetry axis.
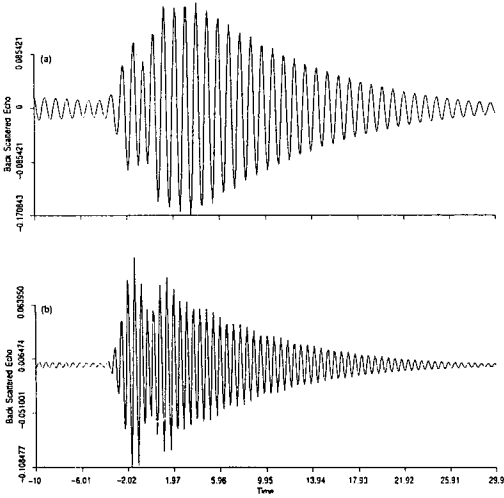
Fig. 27. Time response to a Gaussian pulse for a 3 to 1 aspect ratio: (a) brass and (b) nickel targets
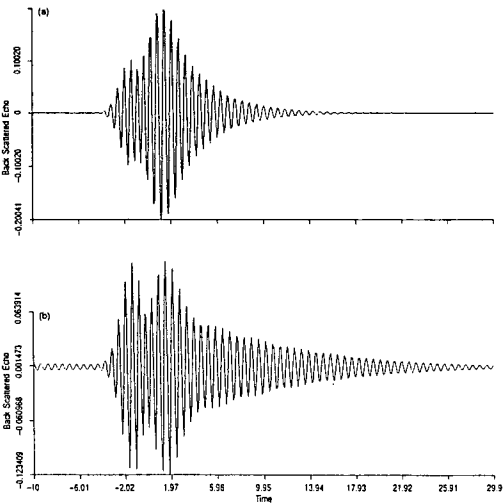
Fig. 28. Time response to a Gaussian pulse for a 3 to 1 aspect ratio: (a) Al and (b) steel targets.
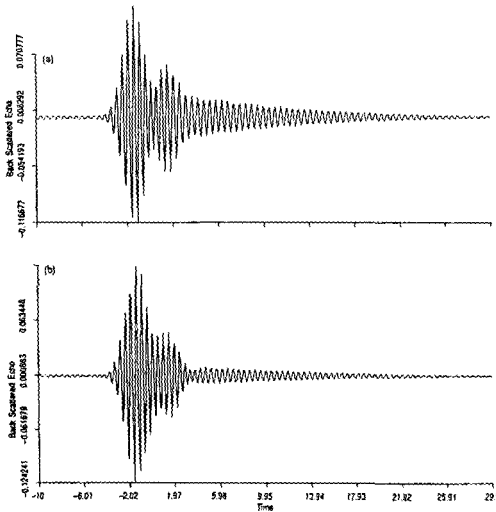
Fig. 29. Time response to a Gaussian pulse for a 3 to 1 aspect ratio: (a) Mo and (b) WC targets.

More precise expressions for the resonance location end-on yield closer agreement with the actual results. Finally, in Fig.'s (27), (28), and (29) we illustrate the time response of 3:1 aspect ratio scatterers from a Gaussian burst, arranged in order of the increasing shear velocity of the six materials. The response is a dampened sinusoid, as expected. We note that the damping is proportional to the half-width of the corresponding resonant frequencies of the respective materials. Thus the more narrowly defined frequency response (such as that for WC) gives rise to a long decay envelope; that is, such scatterers "ring" longer, while broader half-width materials such as Al yield a more rapid decay rate. Al does not make as good a bell. We see from this analysis that when one is able to isolate a pulse signal in terms of a damped sinusoid there is some correlation with the material providing the object is a solid.

4.7. Classes of Elastic Shell Resonances

There are several classes of resonances that can be excited on bounded submerged elastic shells. Here we will restrict discussion to evacuated or air filled shells. It is useful to compare the excitation of waves on plates with those on shells. Indeed, many notions that arise from shells are suggested from an understanding of the simpler plate theory. In the study of plates the easiest picture to understand is that of an infinite plate of thickness h that experiences no loading on either side. There are many types of vibrations that are associated with elastic plates. They are characterized by their phase velocities and the type of symmetry that they experience either vibrarions can be symmetric or antisymmetric. Fluid loading on only one side has an effect on damping and shifting some of the modes of vibration and in the initiation of water borne waves at the fluid-plate interface. Two types of water borne waves are apparent, both subsonic. The most important is the antisymmetric (the Stoneley) wave and occurs over a limited frequency range and is dependent on the nature of the flexural mode and the ambient fluid. There is also a weaker symmetric water borne wave that is subsonic and begins below coincidence frequency and remains significant to high frequency. It is almost non-dispersive and is more prominent with lower density plates. For the spherical shell, the shell thickness also has an effect on the water borne waves but we can not make that comment for in infinite plate because it is not meaningful to refer to an infinite plate as thin or thick. Fluid loading on both sides of a plate has an even greater effect and produces a strong water borne wave (the Sholte wave) that occurs over all frequencies. The two lowest body modes are true interface waves in the sense that the transverse and longitudinal modes are coupled at the interface while the internal waves can be resolved into the shear and longitudinal waves. We will refer to the two interface waves as the shell modes to distinguish them from the internal (waveguide) modes which we refer to as Lamb modes. The first observable shell mode is symmetrical and has a phase velocity close to the speed of the longitudinal phase velocity and can be excited at any frequency. We refer to these waves , S_0, as the lowest symmetrical modal wave (the dilatational mode). This wave has no frequency cut-off (no lowest value). It starts with a very large phase velocity, and out to intermediate frequencies it reaches the plate velocity which is lower than the compressional velocity, but eventually at very high frequencies it reaches the Rayleigh phase velocity. The next wave is the lowest order antisymmetric or flexural wave. It has a phase velocity that is strongly dispersive and rises from zero to the Rayleigh velocity at moderate frequencies. It has its kinship with the Rayleigh wave on an infinite half space. It will not influence on ambient fluid (no radiation into the fluid) until the phase velocity is equal to the speed of sound of the contiguous fluid. At the point for which the phase velocity reaches the same speed as the ambient fluid -referred to as coincidence frequency- two things happen. It begins to radiate into the fluid and also subsonic fluid borne waves are excited at the fluid-plate interface. These waves are antisymmetric and are only observable at frequencies close to coincidence frequency. Some authors refer to those water borne wave as A waves but we refer to them as Stoneley waves. The flexural modal wave is designated by A_0 and is usually referred to as the flexural mode and sometimes as a transverse plate mode. The next class of waves

really begin as waveguides in the plate and are associated with either the compression or the shear waves of the material. These waves are referred to as Lamb modes and are designated by A_i or S_i where i is equal to or greater than 1. The rules for the onset of the Lamb modes -referred to as the critical frequencies- are simple and relate to standing waves in the material.[77] Based on a study of these waves, we know that $h/2 = n\lambda_s$, n is odd for antysymmetric modes, $h/2 = n\lambda_s$, n is even for symmetric, $h/2 = n\lambda_l$, n is odd for symmetric, $h/2 = n\lambda_l$, n is even for antisymmetric modes. Here s designates the shear and l designates the compressional wave respectively. One can see that there is no clear association between the ordering of these modes with either shear or compressional waves and the spectral ordering of the actual waves since the ordering can shift according to variation in the material property. We will make this point clearer when we present an example. The question then arise how close an analogy are results from plates with those of shells? Our study of elastic spherical shells shows that the critical frequencies for Lamb resonances (the lowest frequencies for which resonances occur) may be obtained from the equation for flat plates.[77,78] Thus, we may derive the following expressions that predict the critical frequencies for the Lamb modes on shells so long as the shells have uniform thickness:

$$[ka]_{\mathrm{Res}} = \pi \frac{v_s}{v_w} \frac{a}{h} i, \tag{124}$$

where we have the A_i-wave when i is odd and the S_i-wave when i is even, and

$$[ka]_{\mathrm{Res}} = \pi \frac{v_l}{v_w} \frac{a}{h} i, \tag{125}$$

where we have the S_i-wave when i is odd and the A_i-wave when i is even. Here h is the thickness of the shell and a is the radius of the shell. The interesting thing about this scheme is that the ordering of the A_i's and S_i's is a function of material so that, for example, the important S_1 resonance for a 5% thick shell is determined from Eq. (124) for aluminum, occurs at a ka of 538 and is thus associated with the shear velocity while the S_1 resonance for steel is determined from Eq. (125), occurs at a ka of 504 and is associated with the compressional wave of steel. This is rather remarkable because the behavior of the S_1 resonance has a very special significance as we describe below. It is useful to plot the residual partial waves obtained from the exact elastodynamic equations that describe scattering from submerged elastic spherical shells to determine the critical frequencies. Since critical frequencies occur at their lowest possible partial waves a plot of the residual partial wave contribution should result in sharp spikes corresponding to the critical frequency at the lowest possible mode. Only symmetric modes are allowed for the lowest
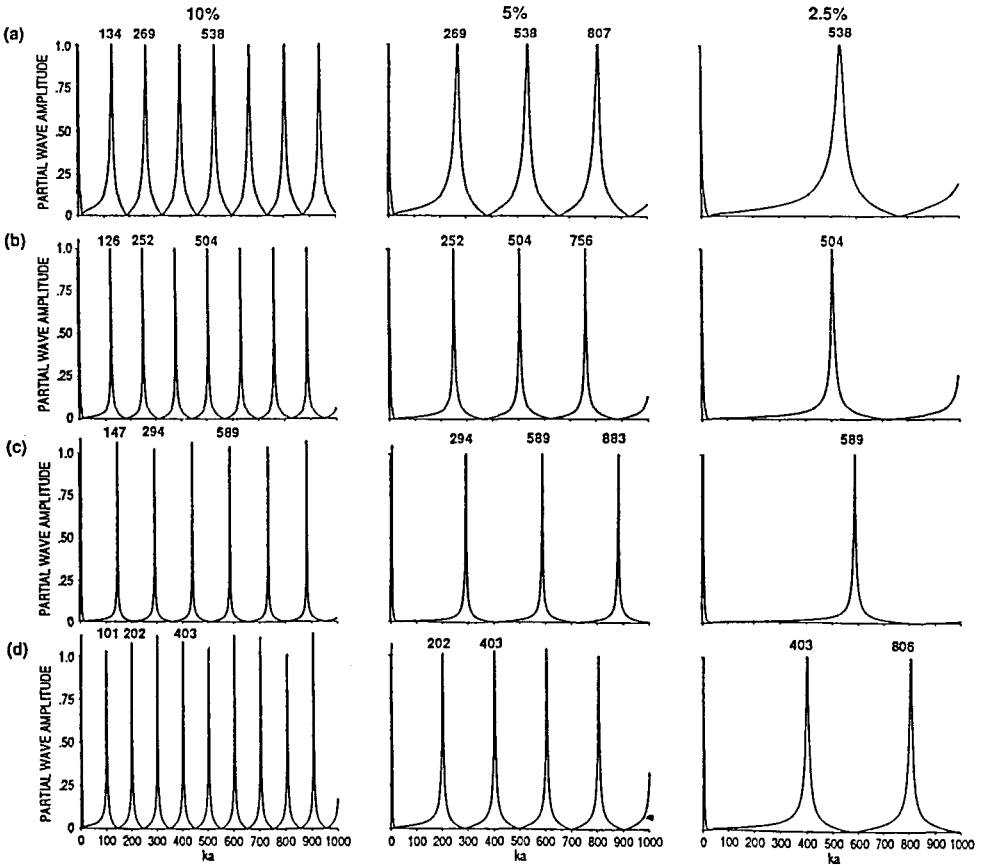
Fig. 30. The lowest partial waves for 10%, 5% and 2.5% thick shells: (a)-Al, (b)-steel, (c)-WC and (d)Br.
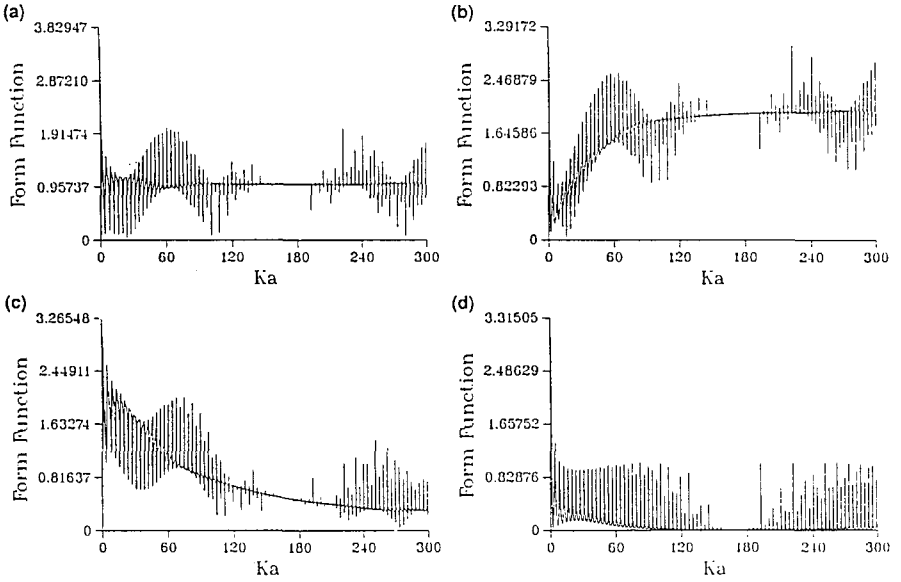
Fig. 31. Back scatter 0.3% steel: (a) Elastic (b) minus soft (c) minus rigid (d) minus new back ground.
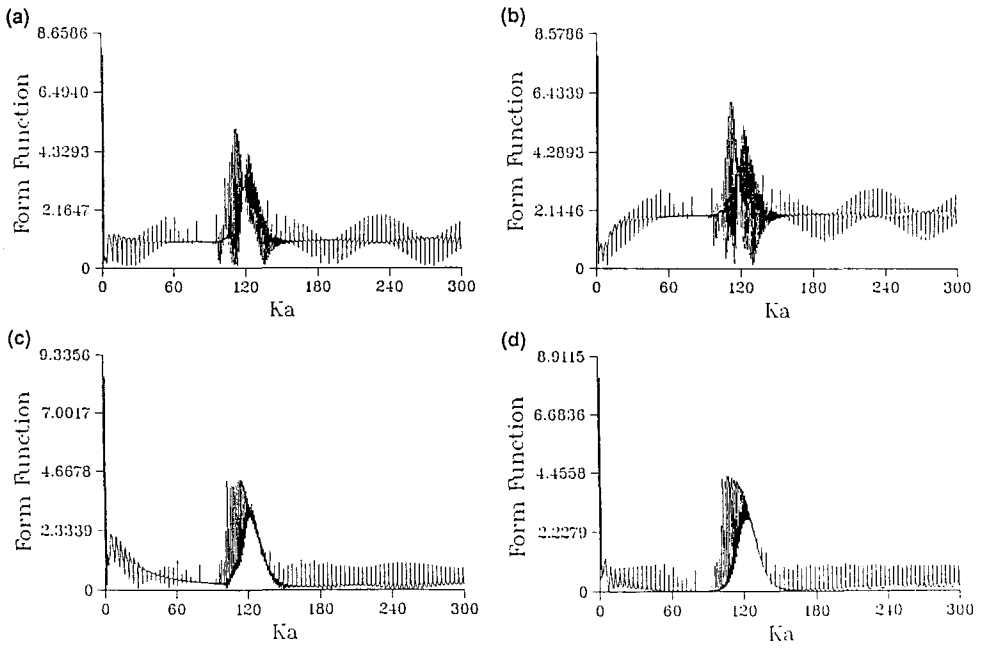
Fig. 32. Back scatter 1% steel: (a) Elastic (b) minus soft (c) minus rigid (d) minus new back ground.

partial wave while the antisymmetric mode must begin with the second lowest partial wave. Fig. (30) is an illustration of the lowest partial waves for shells of 10%, 5% and 2.5% thick for (a)-Al, (b)-steel, (c)-WC and (d)-Br materials. A comparison of the critical frequencies determined from these plots agrees extremely well with Eq.'s. (124) and (125).

4.8. The Acoustic Background for Shells

In an earlier work, the form function due to an incident plane wave on a steel spherical shell with thickness 0.3% of the radius was examined.[22] Fig. (31a) is the form function for the shell for a ka range between 0 and 300. At the lower frequency, a soft background appears adequate, but at quite high frequencies a rigid background appears adequate; intermediate regions are poorly represented by both backgrounds. In Figures (31b), (31c) soft and rigid backgrounds are subtracted (in partial wave space) to illustrate that only at the extreme ends does either background appear adequate. Fig. (31d) illustrates the case for which the new background is subtracted from the form function and it is evident that it is superior for the entire region of ka. Figs. (32a-d) illustrate the same example for a shell of 1% thickness (the form function, the residual obtained by subtracting soft, the residual obtained by subtracting rigid and the residual obtained by subtracting the new background). Again, it is evident from Fig. (32) that the new background is indeed adequate even in the region at coincidence frequency around $ka = 120$.

Figs. (33a-d) illustrate plane wave scattering from a 1% thick WC shell for the elastic response (33a), the elastic response minus the soft background (33b), the elastic response minus the rigid background (33c), and the elastic response minus the new background (33d). For the WC case the new background is also quite superior to the others. In contrast to aluminum, the rigid background is adequate over a larger range due to the high density of WC. Further, the isolation of resonances at the higher ka region is superior to either steel or aluminum; the explanation has to do with the presence of the symmetric water borne wave which is weaker for WC than aluminum and steel.

4.9.1. The Importance of the Symmetric S_1 Resonance

Figs. (34a)-(34c) are the form functions due to an incident plane wave on spherical shells of 10%, 5%, and 2.5% thickness for steel shells respectively. It is evident that in the region between about ka=126,252 and 504, respectively, there are rather pronounced returns which are significantly larger in amplitude than usually observed for symmetric and antisymmetric resonances. The explanation for this event was first thought to arise from the condition that when a wave goes into a layered material, and when the wave length of the layer is equal to half the wavelength of the penetrating wave, the reflection coefficient is just equal to that due to the next interior layer. In this case, it corresponds to a soft scatterer (the inclusion was evacuated) and thus the reflected signal when added to the usual surface reflected signal is at a maximum. To determine where this happens we use Eq. (125). Here $c_1 = 5.95$ and $c_w = 1.4825$ are the compressional speed of sound for steel
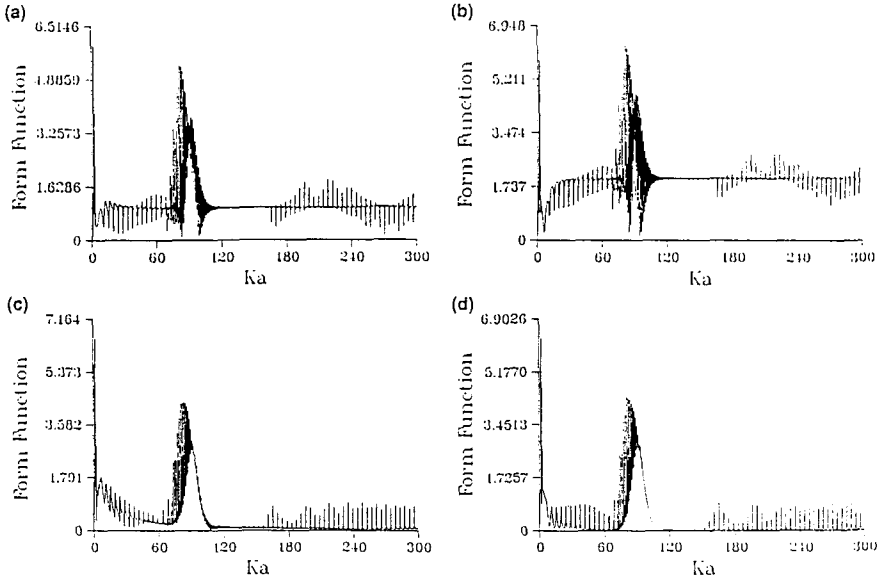
Fig. 33. Back scatter 1% WC: (a) Elastic (b) minus soft (c) minus rigid (d) minus new back ground.

and water respectively and h/a is 0.1, 0.05% and 0.025. Thus, ka =126, 252 and 504, are associated with the large returns. An argument based on reflection coefficients is not sufficient to explain this effect; it only occurs at the S_1 resonance. In Fig. (35) we illustrate the contributing partial waves for the 5% shell for ka=226-256. For n=0 (critical frequency) ka=252 and we see the lowest S_1 component. The modal partial wave is then associated with a declining ka as mode number increases until zero group velocity at ka=236 at which point the component begins to increase. The multiple contribution from the S_1 Lamb mode causes the enhanced signal. Perhaps the proximity of the S_1 and A_1 (A_2) vibrations is too small and some spacing condition in ka is responsible for this effect.
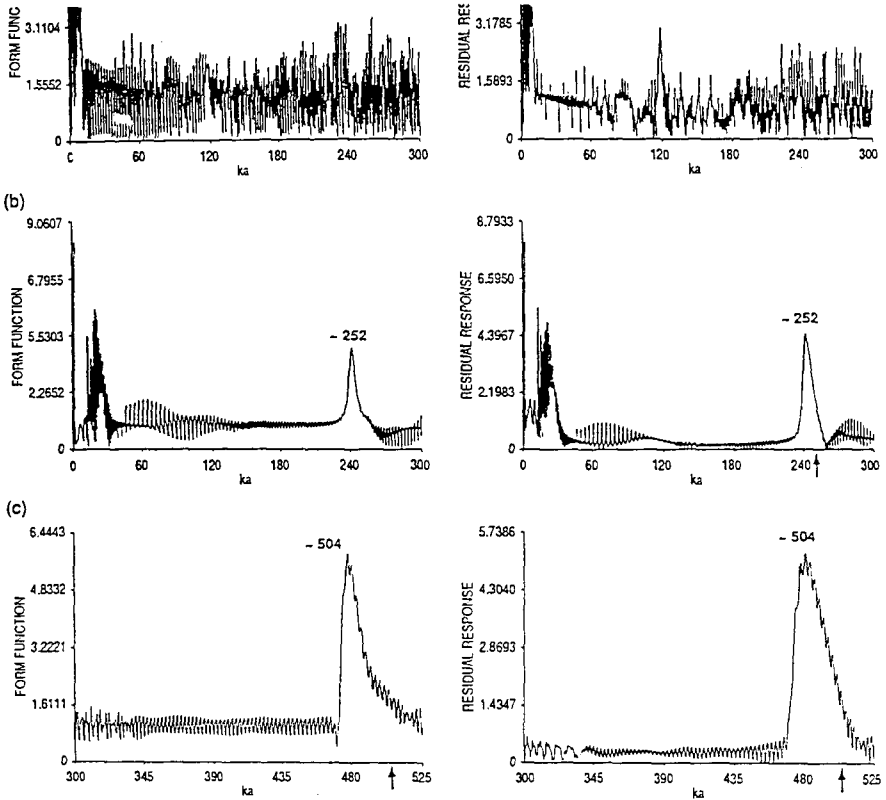
Fig. 34. Form functions for steel shell for: (a) - 10%, (b) - 5%   and (c) 2.5% thickness.
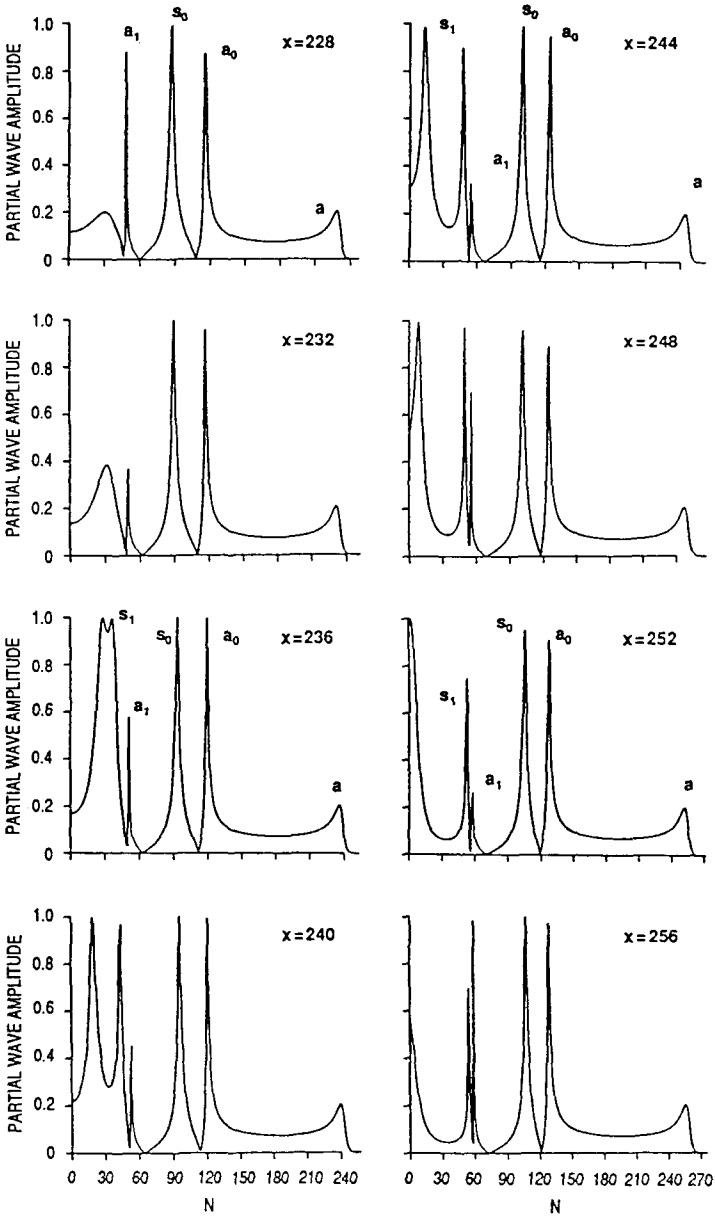
Fig. 35. Partial wave amplitudes vs ka and mode number N for 5% steel shell.
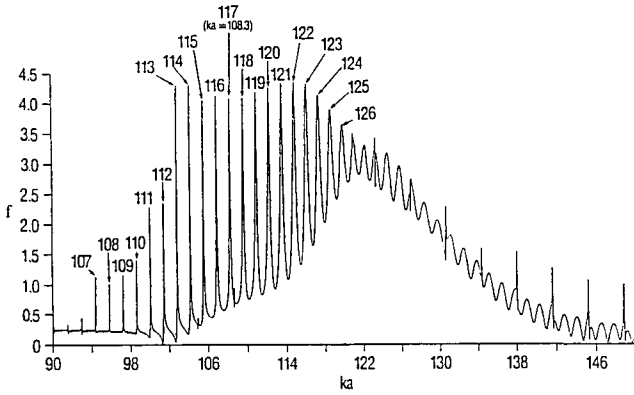
Fig. 36a. Modal assignment of resonances at coincidence frequency.

(a)

(b)
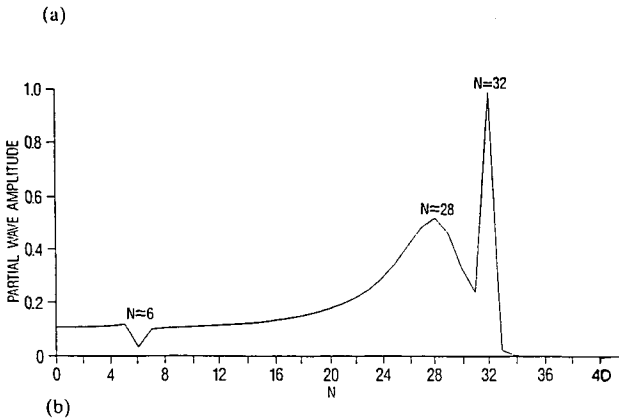
Fig. 36b. Partial wave resolution of flexural and pseudo-Stoneley waves.

4.9.2. Pseudo-Stonely Resonances

We mentioned earlier that flexural waves do not yield resonances from fluid-loaded shells until the phase velocity is about equal to the speed of sound in the ambient fluid. The value in frequency for which this happens is referred to as the coincidence frequency; however, some subsonic fluid-borne waves produce sharp resonances below coincidence frequency.[78,79] These waves are referred to as pseudo-Stoneley waves and the related resonances as pseudo-Stoneley resonances.[78,80] The pseudo-Stoneley resonances are well defined in partial wave space; they correspond a unique partial wave mode number with a narrow half-width with a weakly dispersive phase velocity, which approaches the speed of sound in the fluid. Theese resonances diminish in significance at the point at for which the flexural resonances begin to dominate. It can be determined that a phase change occurs in the pressure field in the transition region from subsonic to supersonic. This change accounts for the envelope of the resonance curve at coincidence frequency where the waves are in phase until coincidence, and are sharply out of phase afterwards. Large resonance returns characterized as an envelop signature superimposed with sharp spikes have been noted earlier in this article on scattering from elastic shells. In Figure (36a) the analysis used to resolve the matter of the origin of these resonances is illustrated. It is determined that the sharp spikes correspond to waterborne waves, referred to as pseudo-Stoneley resonances, superimposed on broad overlapping flexure resonances. Figure (36b) illustrates this effect by examining the contributing partial waves for a fixed frequency. N = 32 corresponds to the sharp waterborne wave and N =28 corresponds to the broad flexural resonance. N = 6 relates to a fast symmetric mode. It is useful to analyse this effect in the time-domain presented in the following section.

4.9.3. Orthogonal Resonances and Bending Modes on Elastic Spheroidal Shells

We focus our attention here on spheroidal shells. We have carried out numerous studies of elongated elastic shells and one of the most interesting features pertains to the generation of duel classes of resonances in the lower frequency region. They relate to the S_0 vibrational modes. These modes are observed to form traveling waves on the surface. It is clear that a plane incident wave along the axis of symmetry will initiate model vibrations that form standing waves at discrete frequencies. All types of resonances subject to the standing wave interpretation have resonance locations approximately in inverse proportion to the path length about the object. In this case the maximal path length about the object goes from pole to pole. That resonances is illustrated in Fig. (37a) where we observe the n=1 and n=2 S_0 resonances. When the plane wave is incident normal to the objects axis of symmetry we see what we expect: the lowest S_0 n=1 and n=2 resonances (the second and third nulls) which are shifted up in location in proportion to the inverse of the (now shorter) distance about the equatorial path. We may refer to the two classes of resonances as polar and equitorial resonances. However, there is something unexpected here. The lowest null is not accounted for by the S_0 family of resonances nor can it be from the flexural or Lamb modes. The shell is too thin to be excited by those modes at this kL/2 range. We can take a hint from our work on elastic solids and examine the possibility that

these modes correspond to a flexing or bending mode (of the entire object and not just the surface). We have carried out an extensive study of these modes for various thicknesses, materials and aspect ratios and our conclusion is that the interpretation of this mode is consistent with "bending" resonances first encountered for elastic solids.

The next interesting effect is observed when a plane wave is incident at oblique angles to the axis of symmetry. It is not clear without calculation what to expect. The results illustrated in Fig. (37b) are both interesting and important. We continue to observe the lowest "flexing" mode but we also observe five additional modes. It is clear by comparing comparing all the null locations that most of the nulls are at the same location as either the equitorial or the polor resonances. We infer from this that an oblique incident plane wave excites orthogonal modes that vibrate either equitorially or along a polar path. Thus, we only observe orthogonal resonances of the S_0 class. The extra null that we observe at about kL/2=8 is the n=3 "bending" resonance which is excited weakly at 45^0 incidence and isn't observed at normal incidence. We note from our work on "bending" resonances for elastic solids that these class of resonances are more strongly excited at oblique incidence, and not at all at axial incidence. We are presently carrying out a study of this mode of resonance for elongated shells in which we vary aspect rario, shell thickness and material parameters and the results so far are consistant with the analysis presented here.

4.10. *Analysis of Results in Time Domain*

In this section we analyze time domain scattering from three types of targets. The first target is a very thin aluminum spherical shell chosen because only the S_0 waves are present with a fairly constant phase velocity over most of the frequency ranges examined. We also analyze WC and steel shells at coincident frequency partly to confirm the existence of water borne resonances discussed earlier. These representative examples prove useful in exploiting expressions derived in section 3.8 which give us guidance on what to expect for time-domain scattering from objects that resonate. For thin elastic shells the phase velocity of the S_0 wave asymptotes rather quickly to the plate velocity given by the expression $C_p = C_s \sqrt{\dfrac{2}{1-\nu}}$ where ν is the Poisson ratio of the material and C_s is the shear velocity of the shell material. We caution that at very high frequencies the S_0 phase speed begins to decline in value and finally is equal to the Rayleigh phase velocity; but there is a large plateau in ka for which this expression is useful. We can take advantage of thick plate theory given below to determine when the phase velocity of the flexural wave is equal to that of the surrounding fluid so that in what follows- thin shells or thick shells- we can determine the region for which our time-domain resonance scattering theory will make sense. We presented time-domain results earlier for solid spheroids at low frequency but we chose to place that analysis there because it has a bearing on the material composition of the targets in terms of the half-widths of the resonances. There are other interesting features that may be examined such as the bending

modes which "ring" in frequency for long times as well as a class of resonances at low frequency excited on elongated objects.
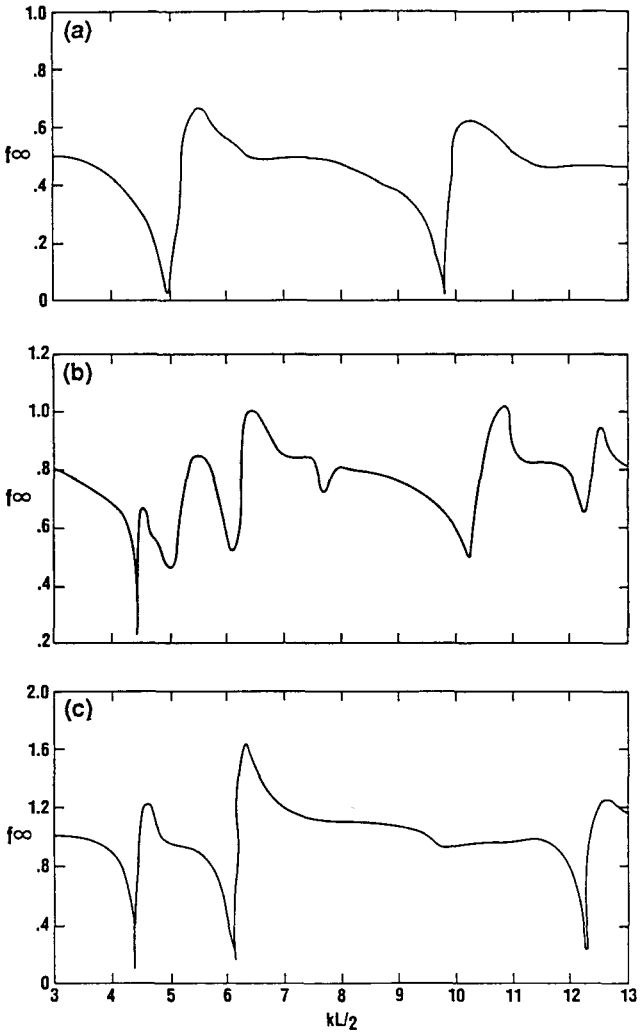
Fig. 37 Scattering from spheroidal shell at (a) 0^0, (b) 45^0 0 and 90^0 incidence.
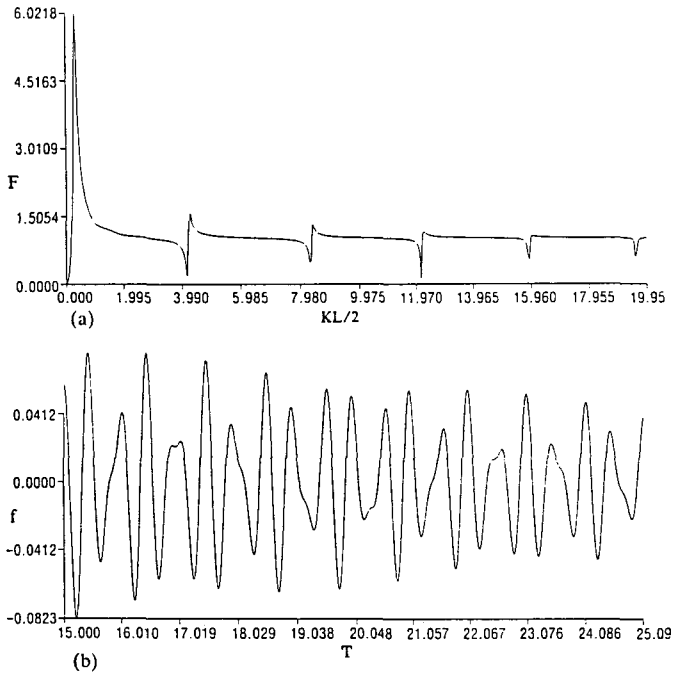
Fig. 38. Frequency (b) and pulse (a) solution for back scatter from an Al shell for ka=0-20.

4.10.1. Scattering from Very Thin Spherical Shells

For very thin submerged spherical shells, only symmetric Lamb waves are present out to fairly high frequencies. For shells in which the ratio of the outer to inner radii is 0.999, flexural resonances are not present for values below a ka of about 500. The phase velocity for the symmetric wave is quite dispersive at low frequency but rapidly approaches a fairly constant value corresponding closely to the plate velocity at the moderate frequencies of concern here. The resonance pattern over a broad frequency range is characterized by resonances of narrow half widths and fairly uniform spacing. Thus, conditions expressed in Sec 3.8. are satisfied. We perform time-domain solutions with carrier frequencies at the mid-point of ka in each of Fig.'s (38) and (39) with a value of σ chosen so that only adjacent resonances are included in the process, i.e., only a narrow frequency region about the carrier frequency are sensed. The calculation described in Fig. (38b) is associated with a strongly dispersive phase velocity and so the resonance spacing and the half-widths are not yet constant and consequently we do not expect to observe a well defined envelope function, i.e., a meaningful group velocity. This is indeed reflected in Fig. (39a). At the higher frequency (ka>80), we observe a very well-defined envelope function illustrated in Fig. (39a) with an even more pronounced oscillatory pattern, consistent with Eq. (123) of Sec 3.8. We observe back scatter in frequency in Fig. (39b) which illustrates the even spacing.. We can obtain the group velocity for these examples. The time t between peaks of the envelope function corresponds to the time required for an energy packet to circumnavigate the sphere.   The time it takes is approximately 1.16 milliseconds. This, divided into 2π for a unit sphere, leads to a value of 5.4 km/seconds, which is very close in value to the phase velocity of the lowest symmetric resonance for aluminum at this frequency. Since the phase velocity is essentially constant at ka>80 and the group velocity is equal to the phase velocity for constant phase velocity, then our result for extraction of the phase velocity is justified. Finally, the slow decrease in the value of the envelope function with increasing time is consistent with the small half-widths of these resonances.

4.10.2. Time Domain Backscattering From Spherical Shells at Coincidence Frequency

In contrast to symmetric Lamb waves which yield resonances at low frequencies in a submerged fluid, the lowest antisymmetric or flexural wave does not yield resonances until the phase velocity of the flexural wave is about equal to the speed of sound in the ambient fluid. There are, however, subsonic fluid borne waves which produce sharp (fluid borne) resonances below coincidence frequency. These "pseudo-Stoneley" resonances are well-defined in partial wave space, usually corresponding to only one partial wave mode number and a very narrow half-width with a dispersive phase velocity which approaches the speed of sound in the fluid with increasing values of ka. Our interest at this point is in examining the time domain response   since we expect the conditions of Sec. 3.8 to be partially met over a broad frequency range and thus to yield a strong coherent response with a carrier frequency in the neighborhood of the frequency at coincidence. We

examine two cases in Fig.'s (40b) and (41b) at the ka values 113 and 87, respectively, for steel and WC that exhibit these characteristic returns.

a) TIME SERIES

b) FORM FUNCTION
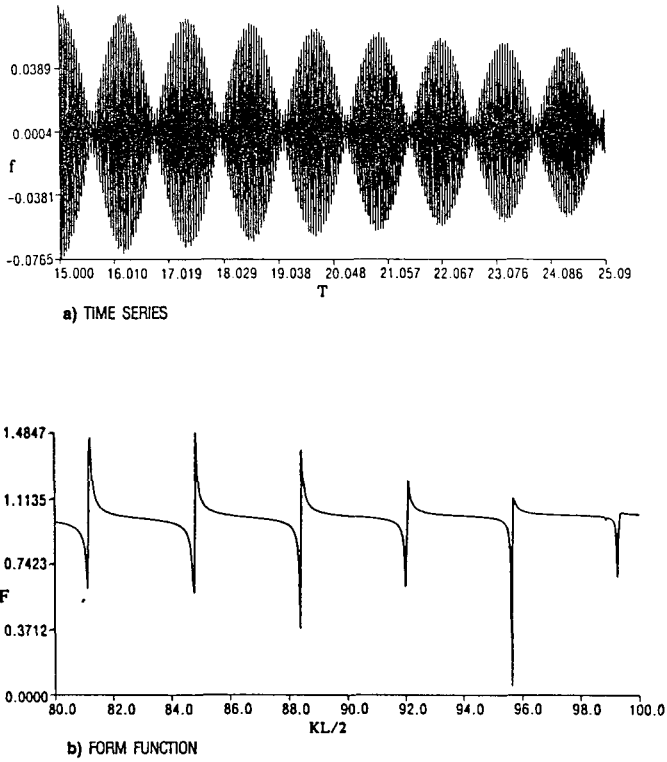
Fig. 39. Frequency (b) and domain (a) solution for back scatter from a Al shell for ka=80-100.
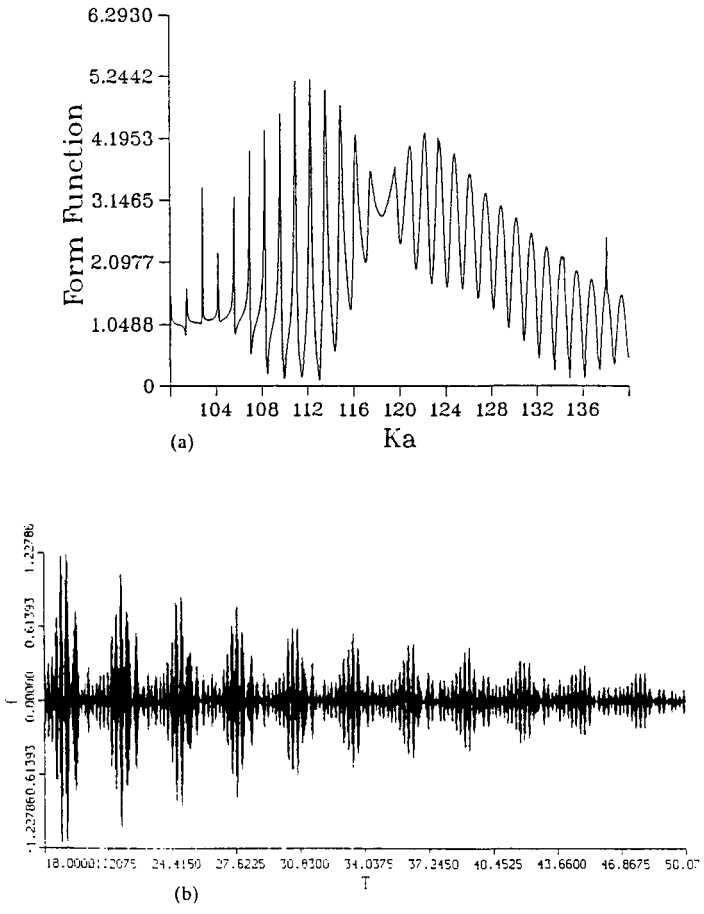
Fig.40. Frequency (b)and pulse (a) solutions of 1% thick steel spherical shell at coincidence frequency.
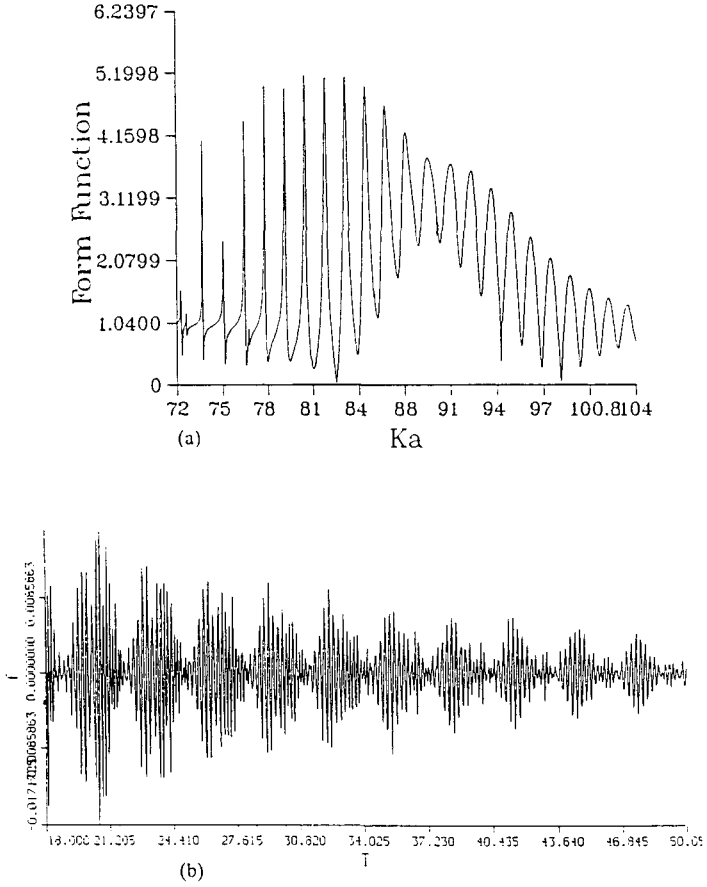
Fig. 41. Frequency (b) and pulse (a) solution of 1% thick WC spherical shell at coincidence frequency.

We use Mindlin-Timoshenko[78] thick plate theory to determine the value for which the flexural phase velocity will equal to the speed of sound in water. The expressions we use are from thick plate theory but they prove to be quite reliable in predicting the phase velocity for the curved surfaces of the spheres at the frequency limits in the vicinity of coincidence frequency. We have determined that the expression for the phase velocity is:

$$
v_f = \frac{v_p \left\{ \left[(\Gamma - 1)^2 \left(\frac{\omega}{\Omega} \right)^4 + 4 \left(\frac{\omega}{\Omega} \right)^2 \right]^{1/2} - (\Gamma + 1) \left(\frac{\omega}{\Omega} \right)^2 \right\}}{\left[2 \left(1 - \Gamma \left(\frac{\omega}{\Omega} \right)^2 \right) \right]^{1/2}}.
\tag{126}
$$

where $\Omega = \dfrac{C_p \sqrt{12}}{h}$, $\Gamma = 2.65(1 + 1.5\upsilon + 0.75\upsilon^2)$ and $\dfrac{\omega}{\Omega} = \dfrac{(ka)V_w \dfrac{h}{a}}{C_p \sqrt{12}}$.

$C_p = C_s \sqrt{\dfrac{2}{1 - \upsilon}}$ is referred to as the plate velocity.

Here C_s is the shear speed and υ is the Poisson ratio of the material. The ratio $(h \, a)$ is a thickness parameter and V_w is the speed of sound in water. For the cases presented here *(h/a)* is 0.01, where *a* is the radius of the sphere. The group velocity is determined by us to be:

$$
\frac{d\omega}{dk} = \frac{\left\{ 2C_p^2 - (\Gamma + 1)v_f^2 \right\} \left(\frac{\omega}{\Omega} \right)^2}{12 v_f^3 C_p^2 + \left[(\Gamma + 1)C_p^2 v_f - 2\Gamma v_f^3 \right] \left(\frac{\omega}{\Omega} \right)^2}
\tag{127}
$$

In both Figs. (42) and (43) the phase and group velocities are plotted for ka values out to 200 for 1% thick steel and WC shells.

We now examine the time domain calculations. For the first example we examine the steel shell of 1% thickness, illustrated in Fig. (40a). In this case we observe a well defined envelope with pronounced oscillations within the envelope consistent with expressions in Sec. 3.8. The enhancement due to the factor 2^M is obvious both here and in Fig. (41a). We can obtain the group velocity from the peak to peak distance. The result leads to a value of 2.23 km/sec. The expression for flexural waves predicts a value of 2.53 km/sec at coincidence and a range of 2.44-2.68 km/sec. over the ka range of 100-140, where the strong flexural resonances are significant. In that range the phase velocity varies from 1.37-1.58 km/sec.
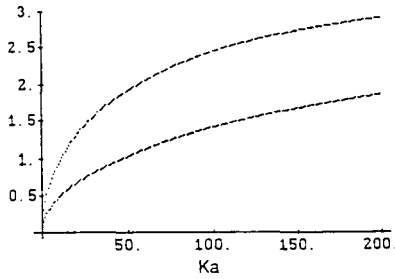
Fig. 42 Phase and group velocity for a steel shell.
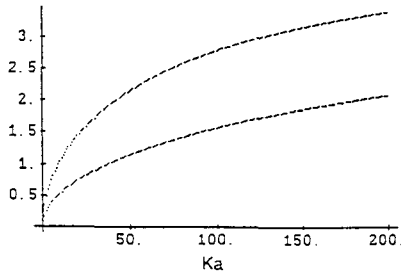
Fig. 43 Phase and group velocity for a steel shell.

The values of the predicted and extracted group velocities are not in extremely good agreement; the disagreement is about 12%. This could be due in part to the fact that flat plate theory may be in error or inadequate for spherical fluid-loaded targets, the conditions in Sec. 3.8 are not well met and there is a mixture of pseudo-Stoneley waves leaking into the fluid. We have determined the group velocity of the pseudo-Stoneley wave for this case to be 2.16 km/sec based on plate theory. In addition, the phase velocity is in the range from 88% to 98% of the speed of sound in the fluid. This value of group velocity is within 3% of the extracted value from the time domain solution. Moreover the pseudo-Stoneley resonances have very narrow widths while the flexural resonances are quite large. The conditions in Sec. 3.8 demonstrate that the flexural resonances rapidly dampen while the pseudo-Stoneley resonances attenuate slowly. Thus, based on the similarity of the extracted group velocity for the pseudo-Stoneley waves and the conditions in Sec. 3.8, we conclude that the time domain calculations in Fig. (40a) represent pseudo-Stoneley resonances.

The final example is for the WC shell of 1% thickness. The results here are consistent with that of the steel case and are illustrated in Fig. (41b). Here the group velocity is extracted to be 2.33 km/sec. compared with the plate theory value of 2.65 km/sec for flexural waves. The range of values for the group velocity predicted from the flat plate theory is between 2.49-2.78 km/sec over the ka range of 74-102. Here again the difference is 12% between plate theory and the extracted value. On the other hand, the group velocity for pseudo-Stoneley waves is 2.26 which is within 3% of the extracted value. As in the previous example the pseudo-Stoneley resonances are quite narrow while the flexural resonances are broad and we conclude that the results of Fig. (41a) represent predominantly pseudo-Stoneley resonances.

4.10.3. Conclusions on Pulse Scattering

We believe that the results shown here demonstrate that if proper conditions are met in time domain studies, quite reliable and interesting interpretations can be made, while it is easy to come to erroneous conclusions when the proper conditions are not met. The trick obviously is to control the pulse widths as well as the carrier frequency if one wishes to extract group velocities correctly. Further, there can obviously be conditions for which it is not possible to make sense of a group velocity within the context of a particular type of phenomena (i.e., Lamb waves, Rayleigh waves, etc.) particularly for narrow frequency bands in which different types of resonances are sensed with equal weights. Accordingly, one should use caution when interpreting an envelope function as associated with a particular group velocity. Finally, it is difficult to see how the presence of a single resonance or for that matter for very low frequency resonance scattering where phase velocities are highly dispersive and resonance widths are usually quite variable this typye of analysis can lead to unambiguous results. It is also clear that we can take advantage of the different resonance half-widths and employ gating methods to examine pulse arrivals for different times which allows for distinctions to be made between different types of resonances.
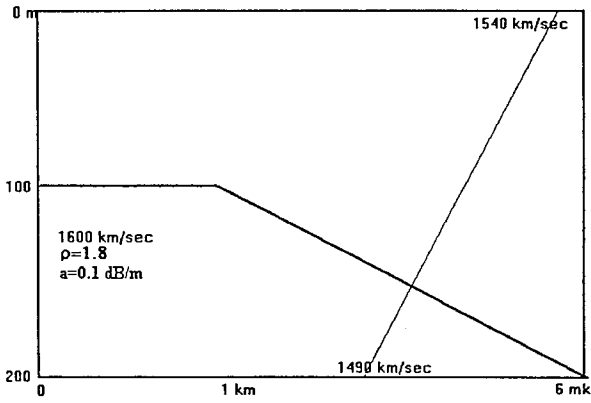
Fig. 44. Range-dependent waveguide properties.
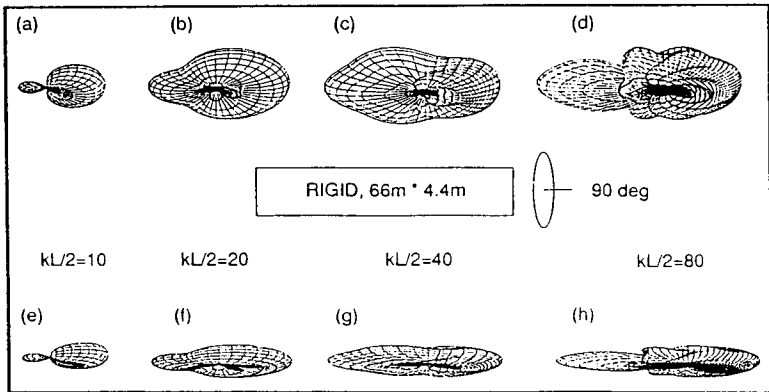
Fig. 45. Free-field scattering of rigid target looking (a) down, (b) in the plane.
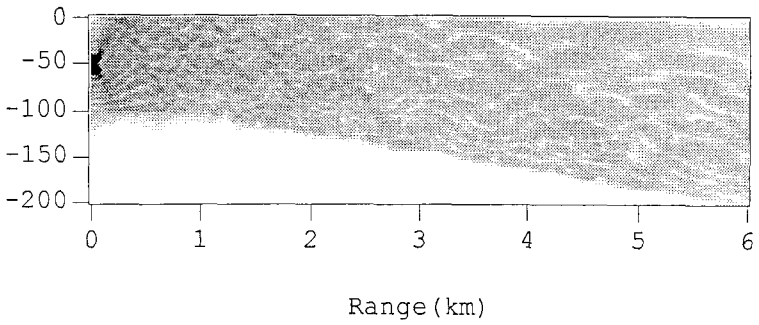
Fig. 46. Contour plot of Transmission Loss for target free waveguide.
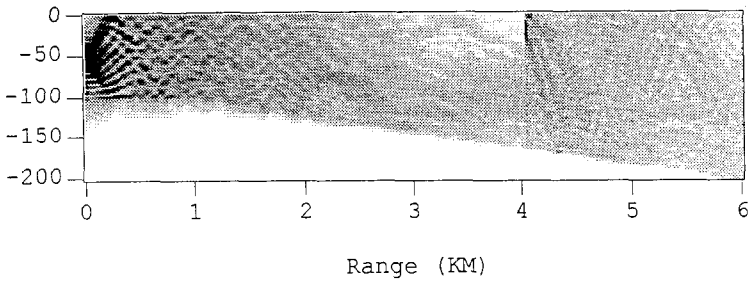
Fig. 47. Contour plot of Transmission Loss for target in waveguide.
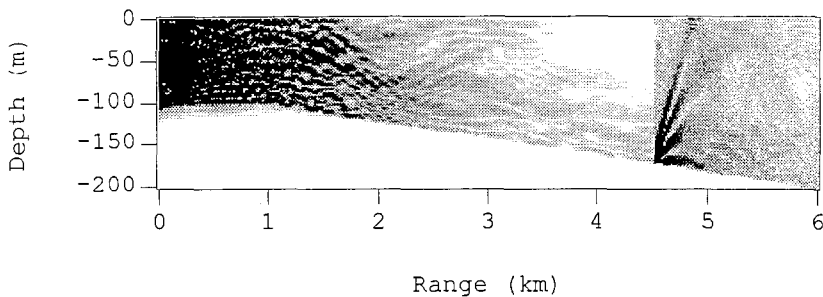
Fig. 48. Contour plot of Transmission Loss for target in waveguide.

4.11. A Touch of Scattering from Objects in a Waveguide.

Our aim has been to create the capability to describe scattering from objects in the most realistic environment. That includes placing objects in a range dependent waveguide. We outlined the formulation to deal with this problem in Sec. 3. By using a new coupled mode development we are able to place an object in a range dependent waveguide. A detailed analysis which takes into consideration many features that may be important in such a study is still under development and would in any case require a great deal of space. We therefore limit discussion to the following picture. We examine a range dependent waveguide described in Fig. (44). Note that the velocity profile is bottom limited. We examine a rigid spheroidal target of large aspect ratio. The near field of the target is illustrated in Fig.(45) for several values of kL/2. Note that the near field becomes limited to the planer region as values of kL/2 are increased which means that it departs from a point source approximation as frequency increases and becomes mode selective. We use the term mode here in the sense of the normal modes of the guided wave and not the material modes. Fig. (46) illustrates the contour plot of the transmission loss in a target free environment at a frequency of 400 Hz. In Fig.'s (47) and (48) we illustrate two examples of a target at two different receiver locations at 4.0 km down range and 20 m below the surface for 400 Hz illustrated in Fig.(47) and 4.5 km down range and 160 m from the top at 800 Hz illustrated in Fig.(48). We have exaggerated the contribution of the

target by enhancing the target strength since the results in terms of transmission loss relative to the incident signal would not be evident with out cleaver signal processing methods. The main point we observe here is that the object behaves as a secondary source, but with out going into detail it is strongly coupled to the environment and can not be represented as a free source contribution. More interesting features are present particularly for pulse scattering but that is beyond the scope of this article.

5. Concluding Remarks

In this article we represent our contribution to the collection of articles in honor of H. Überall in marking his retirement from the Physics department of the Catholic University of America. It is our hope that he continues to make advancements in the study of classical scattering and that this does not signal the end of a golden era in our discipline. Überall's contributions have been steady for the past three decades and continue to be significant and illuminating. His contributions are unique in that he presents a perspective of this area of physics that departs from the usual engineering approach and is more in line with the perspective of a modern physicist. This perspective in conjunction with an extremely keen mind, a love for science and a most generous nature has in our view marked his contributions both to physics and in support of his many colleagues and students as extraordinary. His perspective has been comprehensive and he has united many facets of this discipline. In our view he has set the standard for how a physicist may now understand acoustic scattering from submerged elastic objects, most specifically in the area of resonances. He has also made significant and invaluable mathematical contributions in all areas of scattering. In our work on acoustical scattering it has been difficult to find useful notions that did not have their origin in an Überall paper. Our intention here has been simply to present some of our own contributions that were influenced by the work of Überall and to elaborate on some work that we did in collaboration with Überall. To be sure, the T-matrix work was heavily influenced by P. Waterman, V.V and V. K. Varadan whom we failed to present due credit because of the limited scope of this work. We also acknowledge valuable interactions with L. H. Green who played a most important role in the development of some of the T-matrix methods and the computer codes used here as well as our understanding of the physics, to Roger Hackman whose critical discussions and unique contributions to the body of scattering theory are of supreme importance, and to our (MFW) dearly departed mentor L. Flax whom many of us own so much. We close this work by commenting that a significant body of research in this area was funded by the Office of Naval Research (ONR) and was carried out at Naval Laboratories. Without the interest and support of the Naval community and without the creative contributions of dedicated men like Überall whom we can attest works far into the night and has added far more than was required of him to the community of scattering, much of what we now understand would still be a mystery. There are still many mysteries in scattering from submerged objects that await understanding and some topics that await refinement. The computational aspects alone are still severely problematic and we wonder upon Überall's retirement if there will long be dedicated people such as the Varadan's, H. Green, L.

Dragonette, R. Hickman and R. Hackman who have moved on to other areas as well as the many others that have the focus, the intelligence and the dedication to advance the area with such vigor as they have in the current climate of shrinking funds and shrinking interest in these topics. With the declining generation of dedicated people and the absence of men like Überall, there is an urgent need to advance this great body of knowledge for future communities.

6. REFERENCES

1. P. C. Waterman, "New foundation of acoustic scattering," *J. Acoust. Soc. Am.* **45**, 1417-1429 (1969).

2. P.C. Waterman, "Matrix formulation of electromagnetic scattering", Proc. IEEE, 53(3), 802 (1965).

3. P. C. Waterman, Scattering by Perodic Surfaces", *J. Acoust. Soc. Am 57,791-802(1975)*

4. P. C. Waterman, "Matrix theory of elastic wave scattering," *J. Acoust. Soc. Am.* **60**, 567-580 (1976).

5. P.C. Waterman, "Matrix theory of elastic wave scattering II: a new conservation law", J. Acoust. Soc. Am.,63(6), 1320 (1977).

6. H. Überall, in *Proceedings of the IUTAM Symposium: Modern Problems in Elastic Wave Propagation*, edited by J. Miklowitz and J. D. Auchenbach, (Wiley Interscience, New York, 1978), pp. 239–263.

7. H .Überall,L. R. Dragonette, and L. Flax, J. Acoust. Soc. Am. **61**, pp. 711–715 (1977).

8. L.Flax, L.R. Dragonette, and H. Uberall, " Theory of elastic resonance excitation by sound scattering ", J. Acoust. Soc. Amer. 63, 723-731, (1978)

9. L. Flax, G.C. Gaunaurd and H. Uberall, " The theory of resonance scattering", in Physical Acoustics , Vol. 15, Ch. 3 pp. 191-294, W.P.Mason and R.N. Thurston, Editors, Academic, (1981)

10. H. Überall, Editor, *Acoustical Resonance Scattering*, edited by Herbert Uberall, Gordon and Bresch Science Publishers, 1992

11. H. Überall, et al., Appl. Mech. Rev. 43(10) (1990).

12. Murphy J.D., George,J, Nagl, A, and Uberall,H.," Isolation of resonance component in acoustic scattering from fluid loaded elastic spherical shells", J. Acoust. Soc. Am. 65(1979),368

13. Y. J. Stoyanov, A. Nagle, H. Überall, M. F. Werby, S. H. Brown, S. K. Numrich, and J. M. D'Archangelo, "Surface Waves on Elastic Spheroids and Related Objects: Acoustic Resonances," 12th International Congress on Acoustics, Toronto, July, 1986, in *Proceedings of The 12th ICA* Paris, 1986.

14. A. J. Haung, S.G. Soloman and H. Uberall, " Resonance Theory of Elastic Wave Scattering from a Cylindrical Cavity, J. Sound Vib. 57(1978) 51

15. J. W. Dickey and H. Uberall, "Surface Wave Resonances in sound Scattering from Elastic Cylinders", J. Acoust. Soc. Am. 63(1978)319

16. G. B. Briet and E. P. Wigner, Phys. Rev. **49**, 519 (1936).

17. P. L. Kapur and Peierls, Proc. Roy. Soc., London, A166, 277 (1938).

18. M. F. Werby, " The classical scattering of waves: Some analogies with quantum scattering", in Computatonal Quantum Physics, Editors: Umar, Oberacker, Strayer and Bottcher, Americal Institute of Physics, New York Vol. 260,1992, PP 180-206 and J. B. Keller, "Progress and Prospects in the Theory of Linear Wave Propagation", SIAM SEREV **21**(2), 229–245 (1979).

19. P. C. Waterman, Phys. Rev. D **3**, 825–839 (1971).

20. M.F. Werby, and L.R. Green, An extended unitary approach for acoustical scattering from elastic shells immersed in fluids, J. Acoust. Soc. Am., Vol 74(2),(1983) 625-632.

21. M. F. Werby, Acoustic Lett. **15**, (4), 65–69 (1991).

22. M. F. Werby, J. Acoust. Soc. Am., Dec. (1991).

23. M.F. Werby, & S. Chin-Bing, Numerical techniques and their use in extension of T-matrix and null-field approaches to scattering, Int. J. Comp. Math. Appls., 11(7/8), 717 (1985).

24. M.F. Werby and G.V. Norton, " An Iterative T-Matrix", Math Modelling and Sci. Computing. Vol 2 pp 792-797, 1993

25. M. F. Werby and G. J. Tango, Eng. Analysis, 5(1), 12–20 (1988).

26. M. F. Werby, "A coupled higher order T-matrix ," submitted to *J. Acoust. Soc. Am.*

27. M. F. Werby, M. K. Broadhead, M. R. Strayer and C. Bottcher, " Solution of the Helmholtz-Poincare' wave Equation using the coupled boundary integral equations and optimum surface eigenfunctions", in Boundary Element Technology VII, Edited by Brebbia and Ingber, Computational Mechanical Mechanics Publications Elsevier Applied Science, 1992, PP. 245-258

28. M.F.Werby, G.Tango and L.H. Green, Eigenvalue and Similarity transformation methods in the solution of Acoustical scattering problems", in Computational Acoustics: Algorithms and Applications, D. Lee, R.L. Sternberg, M.H. Schultz (Editors) Elsevior Science Publishers B. V. (North Holland), 1988, Vol. 2 257-278.

29. Y.-H. Pao, and V. Varatharajulu, Huygen's principle, radiation condition, and integral formula for the scattering of elastic waves, J. Acoust. Soc. Am., 60(7), 1361 (1976).

30. P. M. Morse and H. Feshback,*Methods of Theoretical Physics* (McGraw-Hill,NewYork,1993),Vol. I and II

31. B.A. Peterson, V.V. Varadan, and V.K. Varadan, T-matrix approach o study of vibrational frequencies of elastic bodies in fluids, J. Acoust. Soc. Am., 74(5), 1051(1983).

32. A. Bostrom, Scattering of stationary acoustic waves by an elastic obstacle immersed in a fluid, J. Acoust. Soc. Am., 67(2), 390 (1980).

33. M.F.Werby and H.L.Green, " Correspondence of scattering from spherical and end-on Incident Spheroidal Shells", J.Acoust. Soc. Am. 81,783 (1987).

34. R. H Hackman, et al. "A reanalysis of the acoustic scattering from a prolate spheroid",J.Acous. Soc. Am83,1255-1266(1988)

35. R. Hackman and M. F. Werby, "A comparison of spheroidal ans spherical bases T-matrices",

36.S. Baskar, V. V. Varadan, V. K. Varadan," Thin Shell theories and acoustic wave scattering by long cylindrical shells of arbitrary cross section", J. Acoust. Soc. Am. 75,1673-1679(1984)

37. R. D. Miller.E.T. Toyer,H. Haung,and H. Uberall, "A comparison between the boundary element method and the wave superposition approach for the analysis of elastic fieldsfrom rigid bodied and elastic shells",J. Acoust. Soc. Am. 89(1991)2185-2196

38. M.F. Werby, R. Miller, H. Uberall,etc, "Sound scattering from submerged elastic shells and shells of general shape", Proceedings from the 3rd international conference Computational Acoustics, Cambridge, MA, Vol. 1,pp 285-291

39. C. E. Dean and M. F. Werby, " Shell Theories with Fluid Loading to Approximate Scattering From Submerged Bounded Objects", Journal De Physique IV, avril 1992, 1099-11102;C. E. Dean and M. F. Werby, " Construction of realistic shell theories with fluid loading", in Automatic Object Reconition II, Vol 1700, April, 1992, pp. 314-326

40. C.E. Dean and M. F. Werby,"The construction of shell theories with fluid loading from submerged bounded objects via techniques of differential geometry", Proceedings from the 3rd international conference Computational Acoustics, Cambridge, MA, Vol. 1,pp 247-262;C. E. Dean and M. F. Werby, "Variational methods and the derivation of shell theories to approximate vibrations of bounded shells,Math Modelling and Sci. Computing. Vol 2 pp882-886, 1993

41. Peterson and Strom, " Scattering from two objects near interfaces", J. Acoust. Soc. Am. 1976

42. M. F. Werby and N.A. Sidorovskaia, " A New Theory for Scattering from n-objects", Mathematical Modeling and Scientific Computing Vol 6 (1996)

43. M.F. Werby, "Strategies for the solution of scattering from an object in a waveguige: Some Numerical Examples", 2nd IMAC Conference at Princeton March, 1989, Proceedings of the 2nd IMACS Symposium on Computational Acoustics, Princeton, NJ, USA, Vol. 2, PP. 93-112 ;G.V. Norton and M.F. Werby,' The influence wave guides on backscattered signals in the far field", SPIE Vol. 1960 (199), 384-393

44. G.V. Norton and M.F.Werby," A Numerical Technique to describe Acoustical Scattering and Propagation from an Object in a Waveguide", in Journal of Applied Physics 70(8),4101-12(1991); M.F. Werby and G.V. Norton, "Near Field Scattering from an Object in a Waveguide with Applications", Proceedings from the 3rd international conference Computational Acoustics, Cambridge, MA, Vol. 1, 1992, pp 163-186
M.F.Werby, " Transient Solutions From Scattered Fields in a Waveguide",in Oceans'90, Engineering in the Ocean Environment, IEEE, pp. 600-605, Oct. 1990
45. M. F. Werby and R. D. Evans, "Scattering from unbounded and bounded objects," *IEEE J. Ocean Engineering* special edition on scattering, OE-12, 380-384, July, 1987.
46. M.D. Collins and M.F. Werby," A Parabolic Equation Model to Predict Scattering and Propagation from an Object in a Waveguide", J. Acoust. Soc. Amer. 85,(1989),1895-1902
M.D.Collins and M.F.Werby," A Parabolic Equation Based Model for Scattering from an Object in a Waveguide", Proceedings of the IMAC Conference on Numerical Modeling , Paris 1988
47. M.F. Werby and G.C. Gaunaurd, " Broadside Resonances Scattering from Elastic Spheroids", IEEE Journal of Oceanic Engineering, vol 14, Oct. 1989, pp. 400-406
48. M.F. Werby and G. C. Gaunaurd, " Resonance Scattering from Submerged Elastic Spheroids of High Aspect Ratio and it's 3-Dimensional Interpretation", J. Acoustic Soc. Am. 88, pp 951-961 (1990)
49. Talmant,Maryline,Uberall, H., Miller, R.D., Werby, M.F.,Dickey,J.W.," Lamb Waves and Fluid Borne waves on water-loaded, air-filled thin spherical shells", J. Acoust. Soc. Amer. 86,(1989)278-289
50. Quentin, Gerard, and Talmant,Maryline, " The plane plate model applied to scattering of ultrasonic waves from cylindrical shells", in the proceedings of the Int. Conf. on Elastic Wave Propagation, M.F. McCarthy, and M.A. Hayses,editors, Elsevier Publications B.V., North Holland,1989
51. M. Talmant, H. Überall, R. D. Miller, M. F. Werby, and J. W. Dickey, J. Acoust. Soc. Am. 86, 278–289 (1989); M. F. Werby, Acoustic Lett. 15(3) 39–42 (1991).; M. F. Werby and H. Uberall, "The exication of water-borne waves at the interface of evacuated elastic spherical shells and pseudo-Stoneley Resonances", Journal De Physique IV, avril 1992, 1087-1090
52. H. Uberall, M. F. Werby, et. al, Ratiation and scattering at oblique incidence from oblong elastic bodies",Second International congress on recent developments in air- and Structure-borne sound and vibrations, March, 1992 Edit. Crocker and Raju, 1195-1202:
M. F. Werby and H. Uberall, "An inferential treatment of resonance scattering from elastic shells", Second International congress on recent developments in air- and Structure-borne sound and vibrations, March, 1992 Edit. Crocker and Raju, 1653-1660:
53. M.F. Werby, etc. "Resonance Acoustic Scattering From Elastic Spheroids", Journel d' Acoustique 3 (1990),201-212
54. M.F.Werby and H.Uberall, " Bistatic Cross Sections and the Resonance Order; the Rayleigh Wave Dipole Resonance", in J. Acoust. Am. 82,265,270 (July 1987).
H.Uberall,M.F.Werby, Etc., "Resonance Spectra of Elongated Elastic Objects", J. Acoust. Soc. 81,312-317 (Feb. 1987)
55. M.F.Werby, and H. Uberall, " Phase Matching Methods for Predicting Resonances of Submerged 3-D Elastic Bodies", in Mathematical Modeling and Scientific Computing Vol 4 (1994)446-451
56. M.F.Werby, H.Uberall, etc. " Residual Bistatic Scattering and the Identification of Resonances of Elastic Spheroids" J. Acous. Soc. Amer. 84(4) 75-80 (1988)
57. M. F. Werby and G. Gaunaurd, "Transition From Soft to Hard Behavior in Scattering From Submerged Thin Elastic Shells," *Acoustics Letters* 9, No. 7, (1986).
58. M.C. Junger and D. Feit, Sound Structures and theior Interaction MIT Press Cambridge, MA (1972)
59. M. F. Werby and N. A. Sidorovskaia, " Green's functions and the Acoustical Backgrounfd for General Objects",

60. M. F. Werby and L. H. Green, "A comparison of acoustical scattering from fluid-loaded elastic shells and sound soft objects," *J. Acoust. Soc. Am.* 76, 1227-1230 (1984).

61. M.F. Werby, H. Uberall, A. Nagle, S.H. Brown and J. Dickey," Bistatic scattering and identification of the resonances of elastic spheroids", 84(1988)681-688

62. H. Uberall, Y.J. Stoyanov, A. Nagl, M.F. Werby, S. H. Brown J. W. Dickey and S. Numerich, and J. M. D'Archangelo,"Resonance spectra of elongated objects",J. Am. Soc. Am. 81 (1987)312-316

63. M.F.Werby and G.Gaunaurd, "The Effect of Aspect Ratio on Resonances in the Echos of Solid Elastic Spheroids in Water", Acoustics Letters 12 No. 6 97-101 Dec. 1988

64. M.F. Werby and G. C. Gaunaurd, " Resonance Scattering from Submerged Elastic Spheroids of High Aspect Ratio and it's 3-Dimensional Interpretation", J. Acoustic Soc. Am. 88, pp 951-961 (1990)

65. M.F.Werby and C.G. Gaunaurd, "Flexural Resonances in Obliquely Insonified Solid Elastic Spheroids", J. Acoust. Soc Am. Vol 85 (1989) 2365-2371

66. J.George and M.F.Werby, "Three dimensional angular distributions of acoustic scattering from flexural and Rayleigh resonances of elastic spheroidal targets",J. Acoust. Soc. Amer. 90(5)2847-50(1991)

67. M. F. Werby and H. B. Ali, in *Computational Acoustics* edited by D. Lee, Cakmak, R. Vichnevetsky (Elsevier Science Publishers B. V., North Holland, 1990),vol. 2, pp. 133–158.

68. M. F. Werby and J. W. Dickey, "Transient Resonance Scattering from bounded objects", in " Acoustics Resonance Scattering, edited by Herbert Uberall, Gordon and Bresch Science Publishers, 1992, pp. 257-276 (chapter in book)

69. L. R. Dragonette, "Evaluation of the relative importance of circumferential or creeping waves in acoustic scattering from rigid and elastic solid cylinders and cylindrical shells," *NRL Rep. 8216* (1978).

70. Michael F. Werby, Hasson B. Ali and Michael K. Broadhead, " Critical Frequencies in Scattering from Submerged Elastic Shells", IEEE, Oceans 92,Mastering the Oceans through technology, pp 471-476

71. A. J. Rogers, " Acoustic Pulse Scattering by a Rigid Sphere Immersed in a Fluid", J. Acoust. Soc. Amer. 45,900-910 (1969)

72. Robert Hickling, et. al, " Rotational waves in the elastic response of spherical and cylindrical targets in water", J. Acoust. Soc. Am. 89(1991)971-979

73. Hackman, ibis

74. L. Flax and V.V. Varadan and V.K. Varadan," Scattering from elastic spheroids using the T-matrix", J. Acoust. Soc. Am. 1982

75. M. F. Werby and G. J. Tango, "Numerical study of material properties of submerged elastic objects using resonance response," *J. Acoust. Soc. Am.* 79, 1260-1268 (1988).

76. M.F. Werby, H. Uberall. et. al." Resonance Spectroscopy of Elastic Spheroids and the Level Crossing Phenomenon", J. Acoustic Soc. Am. 88, pp 2822-2829 (1990)

77. H.Uberall,M.F.Werby, Etc., "Resonance Spectra of Elongated Elastic Objects", J. Acoust. Soc. 81,312-317 (1987)

78. Lord Rayleigh, *The Theory of Sound* (Dover,New York,1945)

79. L.M. Brekhovskih, *Introduction to the mechanics of continuous media,*(Nauka, Moscow,1982)

80. M. F. Werby and M. K. Broadhead," Study of higher order Lamb resonances on elastic shells: their prediction and interpretation", in Automatic Object Reconition II, Vol 1700, April, 1992, pp. 341-349

81. M.F. Werby and S.A. Chin-Bing, "Large Resonance Signatures in Scattering From Submerged Elastic Targets in the Time and Frequency Domain", Oceans 94 (1994)

82. S. G. Nilsson, K. Dan. Vidensk. Selsk. Mat. Fys. Medd. 29, No. 16 (1955).

83. M.F. Werby, H. Uberall,et. al. " Resonance Spectroscopy of Elastic Spheroids and the Level Crossing Phenomenon", J. Acoustic Soc. Am. 88, pp 2822-2829 (1990)

84. M.F. Werby, R. Hackman, "The level crossing phenomena in scattering from prolate spheroids", NCNC, Rep. 1984

85. H. Uberall, private communication

86. E. White, M. F. Werby and C. E. Dean, " Numerical prediction for scattering from elastic solid cylinders with hemispherical caps with data", in Automatic Object Reconition II, Vol 1700, April, 1992, pp. 327-340; M. F. Werby and C. E. Dean, " Theoretical prediction for scattering from elastic cylinders with hemispherical caps and comparison to data", Journal De Physique IV, avril 1992, 1019-1022

87. M.F. Werby and G.C. Gaunaurd, "Transition from soft to rigid behavior in scattering from submerged thin elastic shells", Acoustics Letters, Vol. 9, No. 7, pp. 89-93 (1986)

88. M. F. Werby and M. K. Broadhead," Study of higher order Lamb resonances on elastic shells: their prediction and interpretation", in Automatic Object Reconition II, Vol 1700, April, 1992, pp. 341-349;H. B. Ali and M. F. Werby, " The importance of the symmetric Lamb wave and high-frequency scattering from spherical shells",in Automatic Object Reconition II, Vol 1700, April, 1992, pp. 350-359

89. M.F. Werby and N.A. Sidorovskaia, " Evidence of flexing modes on elastic spheroidal shells from oblique incidence plane waves",to be submitted to J. Acos. Soc. Am.

90. G. C. Gaunaurd and M.F.Werby, " Acoustic Resonance Scattering by Elastic Shells", Applied Mechanics Reviews Vol 43, no 8, August 1990, pp 171-208 (Invited review article)

91. M.F. Werby and N.A. Sidorovskaia, "Material characteristics, shell thicknesses and their connection with the exitation of resonances on elastic stuctures",to be submitted to J. Acos. Soc. Am.

92. D. Ross, *Mechanics of Underwater Noise*. New York: Pergamon Press (1976);
S. P. Timoshenko, Philos. Mag. 43:125–131 (1922).

MODELING AND ULTRASONIC
MEASUREMENTS OF DAMAGE

A. GÉRARD
Laboratoire de Mécanique Physique, University Bordeaux I
351 cours de la Libération, 33405 Talence cedex, France

ABSTRACT

The main objective of this chapter is to study and to assess the anisotropic damage coupled with anisotropic elasticity in ceramic-ceramic composite materials. We show that the conventional mechanics metrologies are not well adapted to this kind of study by a single sample. However an ultrasonic interferometer method allows to assess the anisotropic damage and to follow its evolution. The constitutive and evolution laws adapted to the damage phenomenon in uniaxial tensile test are fully verified.

1. Introduction

In the great family of fibrous composite, the composite materials with brittle matrix constitute a recent class of materials. They are developed to make up for fragility, the main drawback of monolithic ceramics.

The high hardness of the brittle matrix composite is tied to the capacity of the interface fibrous-matrix to stop or to deviate the matrix microcracks. This phenomenon confers to the composite a typical non-linear behavior, and allows to reach a significant rupture strain for ceramics[1]. These properties open a large field of application in particular to high temperature. As we have need of thermostructural composites, the composites with brittle matrix are in the working industrialization phase in spite of their complexity and ignorance of their accurate behavior in use. The studies of damage processes, microscopic phenomena, and their role in the constitutive law, represent an important theme that is the subject of an effort of consistent research following from the importance of industrials applications.

The micromechanical approaches emphasize and underline the fundamental character of matrix microcracking for the non-linear behavior of the brittle matrix composites. However the scale of the microstructure is poorly adapted to the modeling of the global behavior of a real material that only interests the engineer. The continuum damage theory finds an application as a favored field in composite materials. This theory consists in

quantifying the microstructural evolution by the effect of its strain behavior on the material[2]. The microcracking (micromechanical phenomenon) is quantified at the macromechanical level by an inner variable (damage) in the sense of the thermodynamic irreversible process (TIP). The modeling of the behavior of the brittle matrix composites under load requires the introduction of a coupling between an anisotropic elastic law and a volumic damage[3].

On the other hand the classical mechanical metrologies (gauge of strain, tong test extensometer) allow to get a monodimensional modeling in terms of Young's modulus variations along the direction of the loading[4]. We emphazie that these metrologies permit the assessment of the phenomenon solely in the load axis and do not allow a direct measure of Young's modulus perpendicular to the loading direction and of the shear modulus requisites for identification of an anisotropic damage by only one sample. In the case of anisotropic materials, this imposes carrying out measurements on a large number of samples (cut following differents composite axes) to obtain a maximum of components of the damage tensor associated with the behavior of the material. Obviously, the large number of handling necessary, on samples sometimes hardly comparable, cause mediocre accuracy often connected to strong dispersion of the results. Moreover, for the more sophisticated models of tridimensional anisotropic damage these conventional mechanical metrologies do not give a direct check on the modeling validity.

The experimental coherence of anisotropic damage thus consitutes a major challenge for improvement before one is able to approach on a reliable basis the three dimensional damage. By the same principle, the ultrasonic methods allow a complete characterization of elastic properties of an anisotropic solid[5] and their essential variations for the evaluation volumic damage[6].

The ultrasonic measurements of damage induced by loading rest on the identification of the variations of the elasticity constants from the velocity development of ultrasonic wave propagation within the material[7]. The dependence of the velocities with the stress is significant for ceramic matrix composites[8].

The determination of elastic constants of a material is an inverse problem[5]. It consists in calculating the coefficients of the characteristic equation of the propagation tensor from an adequately selected collection of its roots obtained by measurements of wave propagation velocity in known directions. The method adopted allows the complete determination of nine independent elastic constants of a material presenting an orthotropic symmetry[9]. This evaluation is carried out from a single sample.

2. Description of Damage

The mechanical properties and the ultimate performance of engineering materials depend on all the microdefects in their structure that represents the state of damage. The various modes of the microstructural kinetics, such as dislocation glides, grain boundary sliding, vacancy diffusion, microvoid and microcrack evolution, etc., are observed externally as an inelastic deformation. To predict the behavior of engineering materials under a variety of circumstances, a rational theory must reflect the influence of the microstructural kinetics on the reponse of structural modes of this material in use.

The initial effort in surmounting the mysteries of the non-linear behavior of solids was developed almost exclusively within the framework of the theory of plasticity. This theory was constantly modified in order to satisfy the demanding nature of many authors trying to use the old theory to describe the mechanical macroscopic response of materials such as rocks, concrete, ceramics, granular materials and others under a variety of conditions of use. Phase transitions, corrosion and microcracking are entirely different both by virtue of their physical nature and the effect they have on material macroscopic response in use. This is often forgotten in the attempt to use algorithms of the theory of plasticity to describe the behavior of materials, such as ceramics-ceramics composites, often leading to erroneous results.

A reasonable approach in these problems is to accept the distinction existing between various classes of microdefects and to introduce separate field variables for each class of microdefects. This opinion is confirmed by the recent advances in electron scanning microscopy, acoustic emission techniques, and other newly developing methods of non destructive testing (ultrasonic method for instance). A strong conviction is emerging that the material response of solids to a large extent depends not only on the basic structure of the matrix but also on a thin interfacial zone, an interphase, which has its own stiffness properties and the type and distribution of defects in the matrix, the nature of the reinforcing fibers. The objective of our study is to emphasize this point and to discuss a relatively new branch of continuum mechanics known as continuum damage mechanics (CDM). A particular damage theory may be either phenomenological or micromechanical in nature. We choose the first point of view. CDM consists of a phenomenological approach to the progressive material strength deterioration due to microcavities, nucleation and growth of microcracks. Such defects or deterioration can weaken the material leading to its failure[10]. The theory is illustrated for a bi-directional ceramic-ceramic composite material. It consists of SIC fibers that are reinforced with a SIC matrix. It is well known that this composite is fabricated from parts built from multiple layers of SIC cloth[11]. The SIC matrix is added by a chemical vapor infiltration

process which results in samples with a porosity of about 20 percent[12]. Under load, the ceramic-ceramic composite is of the type brittle-brittle and exhibits a non-linear behavior (Figure 1). This is associated with intense matrix microcracking since the strain failure of the matrix is smaller than the strain to failure of the fibers[1]. It is the inverse situation of this to a polymer matrix composite whose rupture is generally governed by fibers.
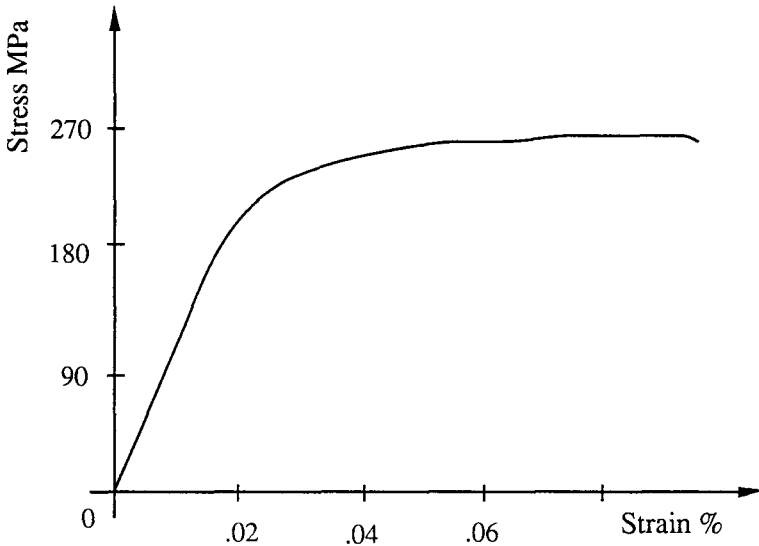
Figure 1. Non-linear behavior of brittle-brittle composite under monotonic loading.

Under monotonic loading micrographic observations were carried out at various stress-strain levels. Intense microcracking of the matrix was detected which related to the presence of fibers. The fibers provide toughness and resistance to the rapid propagation of microcracks in the composites. Experimental studies have shown extensive damage and associated non-linear stress-strain reponse prior to multi-failure. The macroscopic response of ceramic matrix composites has four different configurations of distributed damage at the microscopic level[13]. Figure 2a shows the first of these configurations consisting of matrix microcracks. The matrix microcracks have their planes normal to the fiber axis and lie between fibers. The fiber-matrix interfaces are undamaged in this configuration and we have no interphase. Figure 2b shows the second of these configurations, including fiber-matrix interfacial slipping in conjunction with the matrix microcracks as in the first damage configuration. This configuration will result if the fibers are

maintained in the matrix by frictional forces at the interfaces. The third damage configuration shown in Figure 2c consists of fiber-matrix debonds distributed along the interfacial surfaces within the volume of the composite. This configuration is likely to result from a non-uniform distribution of interface bond strength when the composite is loaded. The fourth damage configuration shown in Figure 2d represents distributed debonds along with matrix microcracks (as in the first configuration).
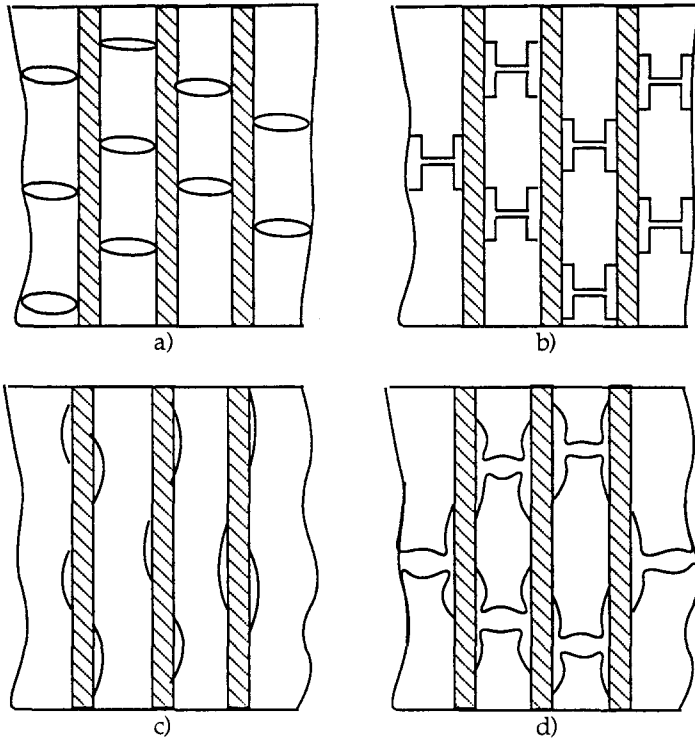
Figure 2. Schematic distribution of defects in the matrix. a) Matrix planes microcracks, b) interfacial slip in connection with matrix microcracks, c) debonding, d) debonding in connection with matrix microcracks.

These descriptions give a first approach to the typical non-linear behavior associated to the slope modification or/and the inelastic strain that appears in the monotonic stress-strain diagram. Nevertheless, this does not schematize the slope rupture observed in the case of brittle-brittle materials, such as CMC, during the successive loading-unloading cycles. The stress-strain

diagram in isothermal state, Figure 3, shows the damaged behavior (microcrack evolution) of a CMC during load-unload cycles[14].
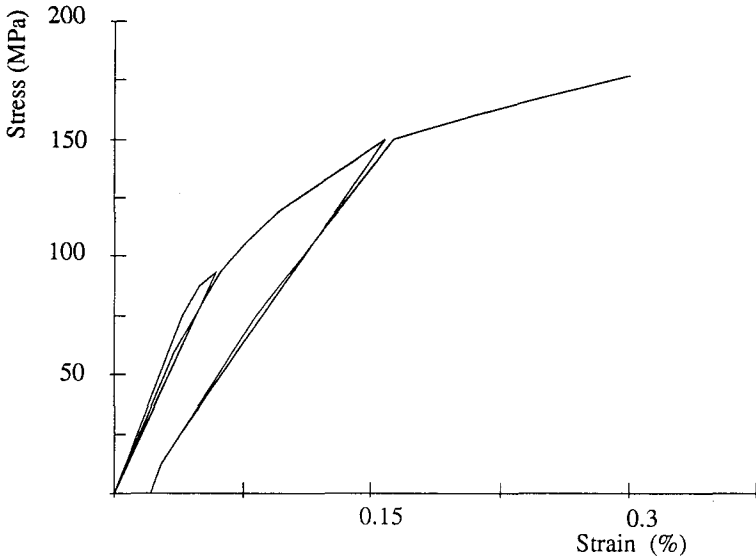
Figure 3. Experimental curve during loading-unloading cycles of CMC.
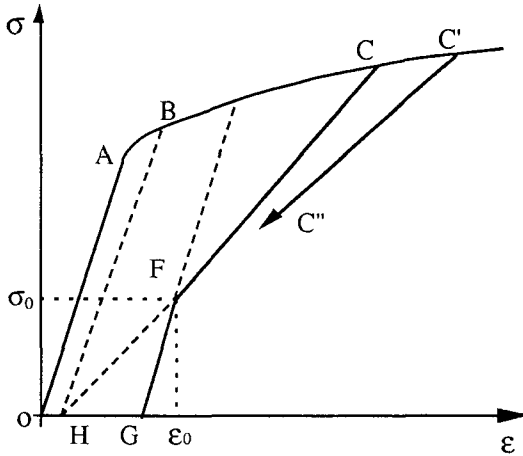
Figure 4. Schematic curve during loading-unloading cycle of CMC.

Neglecting the very flat hysteretic micro-loops in the schematic representation of this one-dimensional behavior, Figure 4, deserves some comments[15]. From point A until C, the damage increases and a pseudo-plastic threshold induced by the damage also increases. The preexistent microcracks or those created by loading are opened if their plane is perpendicular to the load. A hardening of material appears at point F when unloading the sample (path CFG, Figure 4). At point G when the load is applied again, three distinct regions can be observed. The first one, path GF, has a slope corresponding to Young's modulus E of the uncracked material as the first loading (OA). The microcracked material has the behavior of a virgin material and has forgotten the presence of microcracks. These have no influence on the rigidity of the material and are therefore inactive. The second region, path FC, is executed with a smaller slope than the previous one (GF). Also, for a stress level higher than σ_0 (point F), the behavior of the material is influenced by the effect of the microcracks that are active. As soon as the stress level passes through that of the previous loading (path C C') the propagation of microcracks continues (third region) and damage increases as is shown by a new unloading (path C' C"). This phenomenological analysis reveals that at the point F (stress σ_0, strain ε_0) there is an unexpected change of slope in the elastic constitutive law which corresponds, in advance, to a closing-opening threshold. This phenomenon may be taken into account in the damage modeling.

3. Constitutive Equations

Numerous methods lead to the formulation of the constitutive equations of damaged materials. The micromechanical approach consists in analyzing the microscopic phenomena to predict the macroscopic behavior. The microdefects are defined by their geometrical parameters (microcrack lengths, discontinuity spacing,...) for the calculation of the properties of the continuous equivalent damaged medium. But the microscopic level is unsuitable for modeling the global behavior because the microdefects usually present a disordered geometry. The description of damage by a macroscopic representation approach leads to a more convenient analysis and identification of the behavior, for structural optimization and computations.

The purpose of this section is the macroscopic representation of the inelastic behavior of a ceramic matrix composite. In the general framework of the thermodynamic continuum mechanics this microscopic phenomenon is represented by an internal variable that describes the effect of these microdefects on the macroscopic scale[16]. The more simple approach is that of three-dimensional isotropic damage where we suppose that the microdefects are statistically distributed in all space directions. The damage is then

quantified by one scalar variable d. This variable[2] allows to define the effective stress tensor $\underline{\sigma}_{eff}$ connected to the stress tensor $\underline{\sigma}$ by $\underline{\sigma}_{eff} = \underline{\sigma} (1 - d)^{-1}$. The insertion of $\underline{\sigma}_{eff}$ in the orthotropic elastic constitutive law of the virgin equivalent material (without any damage) shows that Poisson's ratio is not affected by damage. Generally, this description is not verified experimentally because the damage is anisotropic, especially concerning composite materials. Also tensorial variables must be introduced[2]. Several kinds of variables can be considered, eighth, fourth or second order tensor, field vectors, etc. A fourth rank diagonal tensor (6 components) privileges the symmetry axis of the material and this tensor is well adapted to describe the damage of composites whereas a two rank tensor privileges the principal direction of the load, i.e., the anisotropy induced by the load[4]. Ladevèze[17] assumes a strain equivalence between the virgin and damaged material and schematizes a purely uniaxial anisotropic damage in neglecting Poisson's ratio variations. They introduce then six scalar variables :

$$E_i = E_i^0 (1 - d_i) , i = 1, 2, 3 ; G_{ij} = G_{ij}^0 (1 - d_{ij}) , ij = 12, 13, 23. \qquad (1)$$

This is equivalent to considering a fourth rank diagonal tensor. Finally, we analyze below the results deduced from a fourth rank diagonal tensor. For instance, Kamimura[18] considers a fourth rank diagonal tensor and observes that this approach allows the symmetry of compliances ($S_{ij} = S_{ji}$) but the Poisson's ratios of damaged material are: $v_{ij} = v_{ij}^0(1 - d_{ij})$ and $v_{ji} = v_{ji}^0(1 - d_{ji})$ where the superscript 0 corresponds to the characteristic of virgin material. These relations prove that the Poisson's ratio evolution is generated solely by stiffness variation in the load axis that is contrary to the anisotropic damage notion. This model describes a particular anisotropic damage of plane parallel microcracks and orthogonal to the load direction, Figure 2a. The restrictive assumption of this damage model is that does not suppose an interaction between the different directions of damage[19]. In fact the symmetry condition directly imposed in the constitutive equation when we made a strain equivalence is too restrictive. As Sidoroff has established[3], postulating an energy equivalence between virgin and damaged material automatically impose symmetry of the elasticity tensor. We need to specify the tensorial nature of the damage and the transformation law for the stress tensor.

In the case of orthotropic materials, the shear moduli are independent of the other all elastic properties. We can admit the uncoupling between traction-compression and shear and so introduce the fourth diagonal damage tensor (d_1 to d_6) which privileges the composite symmetry axis[19]. Experimentally, this energy equivalence obviously improves the damage description in the transverse directions. The relations giving the elastic properties of damaged material are[18] :

$$E_i = E_i^0 (1 - d_i)^2, \, v_{ij} = v_{ij}^0 (1 - d_i)(1 - d_j)^{-1}, \, i, j = 1, 2, 3 \, ; \tag{2a}$$

$$G_{12} = G_{12}^0 (1 - d_6)^2, \, G_{13} = G_{13}^0 (1 - d_5)^2, \, G_{23} = G_{23}^0 (1 - d_4)^2 \, . \tag{2b}$$

These expressions are poorly adapted for ultrasonic methods; so we prefer a dual formulation. An extension of the preceding step is made through the enthalpy. Introducing the effective elastic strain tensor $\underline{\varepsilon}_{eff}^e$, connected with the strain tensor $\underline{\varepsilon}^e$, in the energy equivalence[8] gives the relation between the stiffness tensor $\underline{C}$ and $\underline{C}^0$ of damaged and virgin material. Thus, we obtain the constitutive law for the damaged material in the form $\underline{\sigma} = \underline{C}(\underline{D})\underline{\varepsilon}^e$. For $\underline{D}$, we choose a fourth rank tensor that privileges the composite symmetry axis. The non-zero C_{ij} are[19]:

$$C_{ii} = C_{ii}^0 (1 - d_i)^2, \, i = 1 \text{ to } 6 \, ; \, C_{ij} = C_{ji} = C_{ij}^0 (1 - d_i)(1 - d_j), \, ij = 12, 13, 23. \tag{3a}$$

For any loading, these relations allow the whole determination of the damage tensor components d_i by:

$$d_i = 1 - (C_{ii} / C_{ii}^0)^{1/2} \, , \, i = 1 \text{ to } 6. \tag{3b}$$

This choice induces a coupling between off-diagonal stiffness and the diagonal one which is not experimentally verified as we shall seen in the following section. This explains the aberrations discovered in the strain measurement[19] and imposes to choose another damage variable to describe the change in non-linear elastic behavior of microcracking composites.

A theory of tridimensional damage must be general enough to fully describe anisotropic elastic degradation. The most general choice possible is to consider the elastic tensor as the damage inner variable[20]. Thus the damage state is entirely determined by measuring the elastic tensor of the damaged material. The comparison of the damaged elastic tensor C_{ij} with the initial one assumed undamaged C_{ij}^0 leads to a non-diagonal fourth order damage tensor :

$$\omega_{ij} = C_{ij}^0 - C_{ij} \, . \tag{4}$$

This definition is analogous, in this beginning, to the one proposed by Ortiz[21] in which the values of the elastic constants themselves are taken as a characterization of the state of damage of the material. Traditionally, in the phenomenological models based on the thermodynamics of inner variables, the damage parameter varies from zero, for the initial state, to the critical value equal to 1 at the failure of the volume element[2]. To this end, one can

define the damage variable, no longer as the absolute variation ω_{ij} but instead as the relative tensorial stiffness change[22]

$$D_{ij} = 1 - C_{ij} / C_{ij}^0 . \tag{5}$$

Nevertheless, this definition involves some difficulties about the off-diagonal components of the elastic tensor. No direct thermodynamic restriction exists on their variations[20]. The initial values of a large number of them are identically zero. To obtain a change within the interval [0, 1] of all components of the damage tensor it is necessary to normalize them by their thermodynamically admissible maximum values such that the elasticity tensor still is a positive definite operator. Thus the normalized variations of the elastic tensor describe in a complete and simple manner the evolution of damage in a principal plane. We have access to the normalized damage variable components as follows[23] :

$$D_{ii} = 1 - C_{ii} / C_{ii}^0 , \, i = 1 \text{to} 6;$$
$$D_{ij} = (C_{ij}^0 - C_{ij})[C_{ij}^0 + \text{sign}(C_{ij}^0 - C_{ij})(C_{ii}C_{jj})^{1/2}]^{-1}; \, i,j = 1 \text{ to } 6; \, i \neq j. \tag{6}$$

This representation has many advantages; no hypothesis on the geometry or the distribution of microcracks is made, as is the case in micromechanical and numerical approaches; no equivalence postulate is required and all anisotropic damage can be described.

However, this model has a restriction. It is only valid for material which in its initial state is undamaged, i.e., without microcracks and for monotonic loading. In our experiments presented in the following section, the sample was subject to pre-stress (around 80 MPa) and was in fact damaged and microcracks were then created. Without applied stress these microcracks are closed. At the time of loading an opening-closing threshold σ_0 appears (around 20 MPa) and a second inner variable β should be introduced to specify the state, opened or closed, of microcracks. This new state variable quantifies the proportion of opened microcracks and should satisfy the relation $0 \leq \beta \leq 1$ (as for shape memory alloys[24]) whereas the damage parameter D becomes the product βD (= D^*)[25]. Thus, before the opening-closing threshold all damage components are quasi-null and the microcracks are closed ($\beta = 0$). After this threshold these are quasi-constant till about the level of initial loading σ_m (= 80 MPa) and the microcracks are opened ($\beta = 1$). Beyond the pre-loading, the damage components increase. Thus, the damage is in fact dependent only on microcrack distribution whether the microcracks are closed or opened[26]. The inner variable D^* is called apparent damage

variable and D the accumulated damage variable. According to this, for all damage components the complementary law of evolution is of the form :

$$D^* = D(\sigma_m) + [D(\sigma) - D(\sigma_m)] \, H(\sigma - \sigma_m), \text{ or}$$
$$D^* = D(\sigma_m) \, H(\sigma - \sigma_0) + [D(\sigma) - D(\sigma_m)] \, H(\sigma - \sigma_m) , \tag{7}$$

where H is the Heaviside function, $D(\sigma)$ the damage for the stress level σ ($\sigma > \sigma_m$) and $D(\sigma_m)$ the damage reached at the stress level σ_m.

4. Ultrasonic Characterization

Composite life prediction using continuum damage mechanics requires identification of the entire complex damage process. In order to describe the fracture process all the damage modes need to be measured and taken into account. It has been shown that the conventional mechanics metrologies (gauge of strain, tongs test extensometer) are not well adapted to measure the anisotropic damage[19]. This result is not surprising because the variation of off-diagonal components (Poisson's ratio) and of a diagonal component (Young's modulus) of the elastic tensor cannot allow an indirect access to another diagonal component of this elastic tensor (Young's modulus perpendicular to the loading axis). Moreover, with a single sample, the classical mechanic metrologies only permit the strain measurements along and perpendicular to the loading axis.

Measurements of the nine elastic constants constituting the stiffness matrix by the classical static technique -loading extensometry- requires a large number of samples with suitable orientations. However, such sample cuts are often unavailable from the manufacturing process and a full evaluation cannot be achieved in this way. A means to circumvent this difficulty is to conceive of metrologies permitting a complete determination of the stiffness components of the elasticity matrix[5]. Precisely it is the case of ultrasonic methods that allow an investigation of the broad angular slight of one given plane[7, 8]. The ultrasonic evaluation technique makes it possible to measure the nine stiffness coefficients describing completely the elasticity of an orthotropic material. In anisotropic materials exhibiting an elastic behavior, even in monotonic loading, the constitutive equation can be written in terms of the small displacement field of an elastic plane wave[5]. It leads to the wave equation written in its Christoffel form. The wave velocities depending on the stiffness and direction of propagation are the solutions of the secular equation[7].

For example, in the principal plane (1,3), the relations between velocities, stiffness and direction of propagation are[27] :

$$2\rho V_{L,S}^2 = A \pm (A^2 - 4B)^{1/2}, \; A = C_{33}\cos^2\theta + C_{11}\sin^2\theta + C_{55},$$

$$B = (C_{33}\cos^2\theta + C_{55}\sin^2\theta)(C_{55}\cos^2\theta + C_{11}\sin^2\theta)$$

$$- (C_{13} + C_{55})^2\cos^2\theta \; \sin^2\theta, \tag{8}$$

where θ is the transmission angle and L (resp. S) designate the longitudinal (resp. shear) mode. The coordinate axes associated with the sample are given in Figure 5.

Test piece under load σ.
Ultrasonic beam is
limited to the grey area.
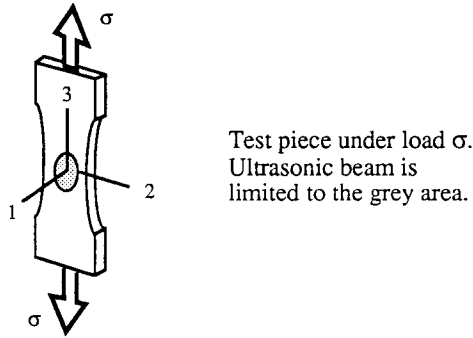
Figure 5. Sample under load.

At each stress level, damage characterization is founded on the measurement of the phase velocities of longitudinal and shear waves transiting a plate sample immersed in water for various propagation directions[8]. Ultrasonic experiments are performed in pulse trough transmission. Velocities are obtained from the measurements of the transit time of the waves by a filtering correlation technique and normal mode tracking[28]. This correlation technique gives good results when the material can be assumed not to be dispersive. The measurement technique for transit time is founded on the concept of Hilbert transformation[29]. It leads to the correct measurement of the phase velocities of the pulses through the sample. Data handling of pulsed waves, angular scanning and transit time measurements are completely computer assisted. The study of the acoustical properties of the material has shown a transition frequency around 2.5 MHz for ultrasonic response of a homogeneous medium[30]. This justifies the use of 2.25 MHz central frequency transducers. The composite is homogeneous and continuous at this frequency used. The expressions of the velocities of the two propagated modes are obtained by solving the inverse problem given by the relation (8). The material is assumed orthotropic (9 independent

stiffnesses) and is supposed to stay orthotropic during the uniaxial loading test.

The exploitation of experimental data needs the knowledge of the inverses relations between velocities and stiffness in each direction of measurement. Let N be the number of these directions of measurements. We solve an overdetermined system of N non-linear equations (with N > 9) whose unknowns are the nine stiffness coefficients. This recovering of the stiffness coefficients from the experimental data is solved by an optimization inversion method[31]. It minimizes, in the least square sense, the shift between the experimental values, and the one calculated from (8) for the optimum values of the stiffness.

The optimization scheme is broken up into three parts. The first two parts consist of the measurements in the two accessible principal planes and lead to the identification of seven coefficients of the stiffness tensor, namely C_{11}, C_{22}, C_{12}, C_{66} for a propagation in the plane (1,2) and C_{11}, C_{33} C_{13}, C_{55} in the plane (1,3). The two remaining coefficients C_{23} and C_{44} (3rd part) are identified by propagation in the non-principal plane (1, 45°) of orthotropic materials. The variations of the stiffness C_{ij}, in the coordinate axis of the sample, calculated from equation (8) at each level of stress give the evolution of the damage tensor components D_{ij} in this coordinate system. An identification process using the Newton-Raphson method allows to calculate the whole stiffness at every level of stress from the set of experimental velocity data[32].

A complex device was designed to have access under load to the velocities of propagation as a function of the transmission angle (or the incidence angle) and stress[8]. The association of this spectro-interferometer with a tensile machine leads to the identification of the elastic tensor changes during tensile test and then to an assessment of the damage phenomenon[33]. We give some experimental results below.

5. Experimental Results

The ultrasonic evaluation of damage requires that the sample is submitted to a tensile stress increasing by steps. During each step the stress is controlled to remain constant and the angular investigation in the plane is performed. We have built a specific immersed interferometer which is incorporated into a tensile machine[34]. The tank lying on the lower traversing saddle is crossed by the tensile axis and supports the positioning system of the transducers. This latter device generates two degrees of rotation, the Euler angle, and it positions the transducers on a sphere surrounding the material under test (Figure 6). The specific shape of the plate sample locates the damage in the part investigated by the ultrasonic beam. It also ensures that the stress state is homogeneous in that zone[35].
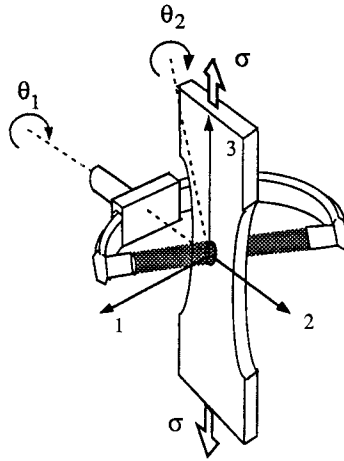
Figure 6. Ultrasonic characterization. The transducers are moved (rotations θ_1 and θ_2) while the sample is loaded along direction 3.

For example, by ultrasonic evaluation and using relations (8), and (3b) in the plane (1,3) we obtain three components d_1, d_3, d_5 of the fourth-rank damage tensor. Figure 7 represents the evolution of these damage components versus applied stress.
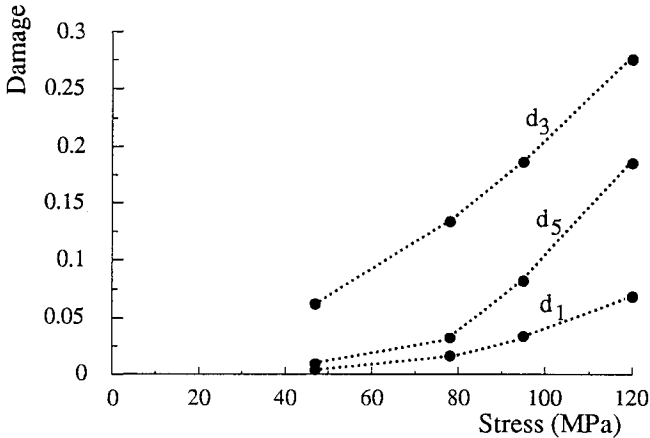
Figure 7. Damage tensor component evolution in (1,3) plane.

These three inner variables increase with the stress and their different variations reveal clearly the anisotropy of the damage phenomenon[8]. We note that d_3, damage in the loading direction 3, is the largest while d_1, the damage in the direction 1, is smallest. Moreover, the component d_5 has a faster increase. This lets us predict a more ruining damage in the (1,3) interlaminar shear plane.

However, the model's validity must not be forgotten. In the investigated plane (1,3), after relations (3a), the validity is ensured if the off-diagonal constant C_{13} variation is proportional to those of material stiffness along the 1 and 3 axis, i.e., if the minor M_{13} evolution is:

$$\delta M_{13} = \frac{C_{13}^2}{C_{11}C_{33}} = \frac{(C_{13}^0)^2 (1-d_1)^2(1-d_3)^2}{C_{11}^0 C_{33}^0 (1-d_1)^2(1-d_3)^2} = \frac{(C_{13}^0)^2}{C_{11}^0 C_{33}^0} = \text{Const.} \qquad (9)$$

The minor M_{13} is positive, but C_{13} is not proportional to the product $C_{11}C_{33}$. Figure 8 shows the gap between the experimental values δM_{13} extracted from ultrasonic measurements at different stress levels and this initial value of which the model does not anticipate any variation.
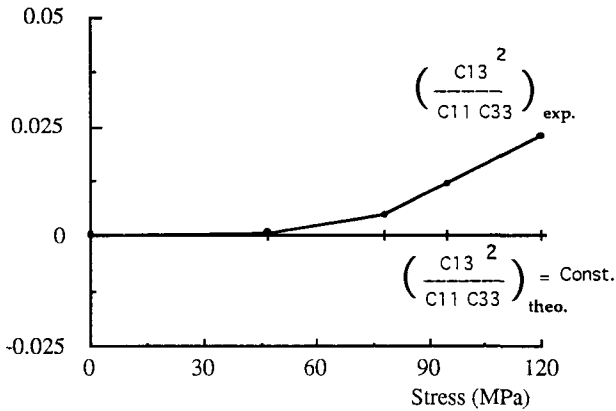
Figure 8. Deviation between experiment and model.

However, we observe that this gap, in absolute value, stays weak (about 2 percent). In return, carried back to the off-diagonal constant evolution C_{13}, the gap is important between this experimental value C_{13} and the "theoretical" value $C_{13}^0 = (1-d_1)(1-d_3)$. Thus, this choice induces a coupling

between off-diagonal stiffness and the diagonal ones that is not experimentally verified. This explains the aberrations discovered in the strain measurement[19] and imposes to choose an another damage variable, as we have indicated in the previous section, to describe the change in non-linear elastic behavior of microcracking composites (6).

However, before using a different three-dimensional anisotropic damage approach, it is interesting to compare ultrasonic damage measurements with those obtained by strain measurements. We have observed in Ref. 19 that only the damage evaluation by classical mechanical mesurements in the load axis (here d_3) is reliable. These measurements, compared with ultrasonic ones, are shown in Figure 9. We note a good agreement between these two types of metrologies although the measurements come from different samples of the same material.
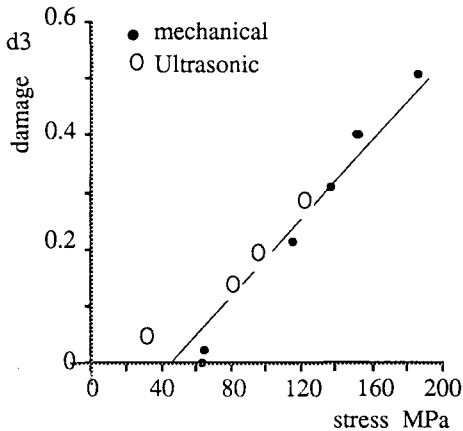
Figure 9 Comparison between strain and ultrasonic damage measurements.

Now let us use the variations of the elastic tensor to measure the evolution of damage in a principal plane. We have access to the normalized damage variable components by Eq. (6). For instance, in the (1,3) plane D_{33} is the damage along the 3 axis (load direction), D_{11} is the damage along the 1 axis, D_{55} is the interlaminar shear damage in the (1,3) plane and D_{13} describes the variation of the coupling between the 1 and 3 axis.

The measurements made in the two accessible principal planes lead to the identification of seven coefficients of the stiffness tensor, namely $C_{11}, C_{22}, C_{12}, C_{66}$ for a propagation in the plane (1,2) and $C_{11}, C_{33}, C_{13}, C_{55}$ in the plane (1,3). The two remaining coefficients C_{23} and C_{44} are identified by propagation in the non-principal plane (1, 45°) of orthotropic materials[9]. The variations of

the stiffness C_{ij}, in the coordinate axes of the sample, calculated from equation (6) at each level of stress give the evolution of the damage tensor components D_{ij} in this coordinate system.

For example, in the (1,3) plane the evolution of the four damage tensor components D_{11}, D_{33}, D_{55}, and D_{13}, using relations (6) (loading by step 5 MPa) is shown in Figure 10.
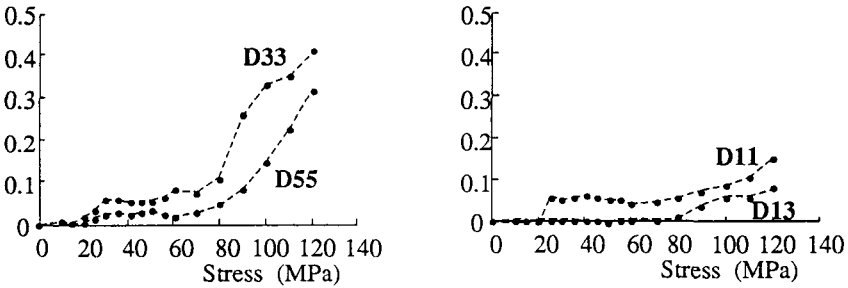
Figure 10. In the plane (1,3) damage tensor components evolution.

These four damages inner variable components increase with applied stress. These variations are different for different components and show clearly the anisotropy of the damage phenomenon[34]. The greatest increase occurs along the 3 axis, that is the tensile axis, and reaches values of about 0,5. But because of the texture of the composite the microcracks propagate also along the fibers and D_{11} and D_{22} increase more or less. The less important one is along the 1 axis, perpendicular to the plane of the layers that never exceeds 0,15. The variation of the coupling between the 1 and 3 direction remains weak. On the contrary the interlaminar shear damage in the (1,3) plane induced by the tensile loading is important reaching 0,3. This last result confirms a more ruining damage in the interlaminar shear plane[35].
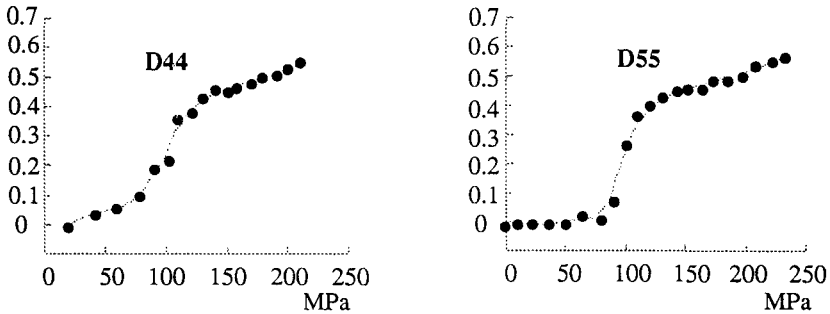
Figure 11. Evolution of shear damage in a plane containing the load direction.

It is important to note that the favored orientation of the micocracks has also an important effect on the shear moduli and especially on those in the planes containing the load direction (i.e. C_{44} and C_{55}). The damage level (D_{44}, D_{55}) reached into these shear planes is similar to those estimated for the damage component in the load direction 3. An example of results obtained is presented on Figure 11 for a sample that has been subject to pre-stress of about 100 MPa[35]. Finally the inner deterioration process of material is expressed at the macroscopic level by a damage that modifies all the components of the elastic tensor. The anisotropic character of damage is obvious because it affects differently each stiffness.

This model has a restriction as it appears on Figure 10 for instance. It is only valid for material which in its initial state is undamaged, i.e., without microcracks and for monotonous loading as in the previous experiments associated with Figure 8. In our case the sample was subject to pre-stress of about 80 MPa and was in fact damaged and microcracks were then created. Without applied stress these microcracks are closed. At the time of loading an opening-closing threshold σ_0 appears at about 20 MPa (Figure 10) and it is necessary to consider the complementary law evolution of damage (7) with the new inner variable β . Before the opening-closing threshold all damage components are quasi-null and the microcracks are closed ($\beta = 0$). After this threshold they are quasi-constant till about the level of initial loading $\sigma_m = 80$ MPa (Figure 10) and the microcracks are opened ($\beta = 1$). Beyond the pre-loading, the damage components increase, as is shown by the curves in Figure 10, after 80 MPa. Thus, the damage is in fact dependent only on microcrack distribution whether the microcracks are closed or opened[15].

The different variations of damage parameters characterize the anisotropy of the damage phenomenon and justify the requirement of the independent identification of each stiffness coefficient. These measurements show that the damage associated to the shear modulus (C_{55}) is as critical as the one associated to the stiffness in the tensile direction (C_{33} Eq. (6)). In the loading-unloading cycles, the tridimensional effect of pre-stress higher than the damage threshold has been measured. Thus this global description shall be divided using two internal variables. The first one relates to the accumulated and growth damage corresponding to the initiation and propagation of microcracks. The second inner variable is related to the opening-closing of existing microcracks without propagation. Thus, the present theory is in good agreement with the experiment. However, the slipping of microcracks is not taken into account.

In other respects, by the same ultrasonic measurements it is possible to obtain access to others properties of composites. For example the elastic stiffness of carbon-carbon composites was measured in four steps during the fabrication process[30]. Velocity, elastic stiffness and anisotropy factor ($2C_{66}/C_{22}$-

C_{12}) are affected by the processing. The ultrasonic measurements show that the carbonization-induced porosity drastically affects the anisotropy factor. These and others results suggest that the use of ultrasonic waves could provide a meaningful technique for monitoring the fabrication process and thereby allow optimization of the control parameters and ultimately the quality and processing speed of the final product. The ultrasonic immersion technique let us identify also the viscoelastic constants in principal and non-principal planes of an orthotropic medium. From velocities and attenuation in any direction of propagation can be computed, and obtained information on, the inner damage[36].

6. Conclusion

The classical mechanic metrologie employs only strain measurements along and perpendicular to the loading axis. This limtation is at the origin of the low number of stiffness and damage parameters evaluated on only one sample. To try to describe the three-dimensional damage phenomenon of material at best, increasingly sophisticated models are elaborated. As these appear, the model involves coupling of anisotropic damage with isotropic or anisotropic elasticity, or coupling of anisotropic damage, anisotropic elasticity and plasticity induced by damage. But in the panoply of measurements executed, any one gives the required information.

For anisotropic material, only bi-axial tests, in particular off axis tests[14] shall permit substantial progress in the identification of three-dimensional damage. Finally, if the essentials of the one-dimensional behavior are obtained by strain measurement, any information of the transverse damage induced by testing of strain hardening (i.e. perpendicular to the load axis) does not actually appear possible. A method to avoid this difficulty is to devise the metrologies permitting a complete determination of the stiffness components of the elasticity matrix.

Precisely, it is the case of the ultrasonic method which allows an investigation in the broad angular slight of one given anisotropic plane appear[6, 32]. The immersion spectro-interferometric method used in this work has allowed a qualitative study of the phenomenon in following the evolution of the ultrasonic gauge (velocity wave propagation) of damage. These indicators show strong variations with the applied stress. The method allows a complete determination of the four elastic constants in a principal plane at various levels of stress. In effect, in spite of the somewhat dispersive character of the material and the small thickness of the studied samples, the testing in the plane (1,3) has permitted determination of the stiffnesses C_{11}, C_{33}, C_{55} and C_{13} at every load level.

These four constants are precisely those that completely characterize the principal plane (1,3): their variations are large, particularly that of the stiffness in direction 3 (load axis). These losses of rigidity are macroscopic (phenomenological) measures of microcrack of the matrix (microstructural phenomenon), a fundamental mechanism of the behavior of this fragile-fragile composite. As a consequence, now possessing all information relative to this plane, it is easy to describe the development of elastic behavior in this plane. An investigation in the symmetry plane (1,2) and in the 45° -plane containing the load axis permits a complete identification of the damage tensor which, a priori, appears difficult when using the conventional mechanical methods employing a single test direction. In addition, the sensitivity of the method will certainly allow the determination of the "initial" state of the material (virgin or not) on a qualitative level, in terms of the velocities or even the attenuation. The complete non-destructive evaluation of a test should thus permit the solution of some problems of intrinsic dispersion in composite materials.

7. References

1. J. Aveston, G.A. Cooper, A. Kelly, *Single and multiple fracture. Properties of fiber composites* , IPC science and technology press, Guildford, Surrey, (1971), 15-24.
2. J. Lemaitre, J.L. Chaboche, *Mechanics of materials*, Cambridge University Press, Cambridge (1990).
3. F. Sidoroff, *Damage mechanics and its application to composite materials. Mechanical characterization of load bearing fiber composites*, Ed. A. H. Cardan, G. Verchery, (1985), 21-35.
4. S. Baste, A. Gérard, C. R. Acad. Sci. Paris, t. **305**, Serie II, (1987), 1511-1516.
5. A. Gérard, *Étude des possibilités d'évaluation de l'endommagement par des mesures ultrasonores*. Thèse d'État, 1980, Université Paris 6. See also, A. Gérard, Lett. in Appl. Engng. Sc., **19**, (1981), 1169-1174.
6. A. Gérard, Rev. Franç. Méca., **82**, (1982), 49-56.
7. A. Gérard, Non Dest.Testing Int. octobre, (1982), 257-261.
8. S. Baste, R. El Guerjouma, A. Gérard, Rev. Phys. Appl., **24**, (1989), 721-731.
9. S. Baste, A. Gérard, J. Roux, Comp. Mat. Avan., **3**, (1993), 129-144.
10. D. Krajcinovic, G. U. Fonseka, J. Appl. Mech., **48**, (1981), 809-824.
11. R. Naslain, J. Phys., France, **47**, (1986), C1-703, C1-715.
12. E. Inghels, J. Lamon, Revue Phys. Appl., **23**, (1988), 193-200.
13. R. Talreja, Mech. of Mat., **12**, (1991), 165-180.
14. A. Gérard, S. Baste, C.R.Acad.Sc. Paris t. **313**, série II, (1991), 1361 - 1366.
15. A. Gérard, S. Baste, Int. J. Engng. Sc., **23**, (1994), 557-567.
16. G. Hermann, J., Kestin, *Cracking and damage*, Ed. Mazars J., Bazant Z.P., Elsevier, (1989), 228-232.
17. P. Ladevèze, JNC 5, Paris (1986), 685-697, Ed. Pluralis.
18. K. Kamimura, J. Méca. Appli., **4**, (1985), 537-553.
19. S. Baste, A. Gérard, 13th conf. Energy Sources Technology; New-Orleans 14-18 Jan. 1990, Proc. ASME *Composite Material Technology*, Ed. D. Hui, (1989), 71-76.

20. R. El Guerjouma, *Évaluation ultrasonore des matériaux sous charge: acoustoélasticité-endommagement anisotrope*, Ph. D. Thesis, **341**, University Bordeaux I, (1989).

21. M. Ortiz, Mech. Mater., **4**, (1985), 97-93.

22. S. S. Wang, E. S. M. Chim, H. Suemasu, J. Appl. Mech., **53**, (1986), 347-353.

23. S. Baste, B. Audouin, Eur. J. Mech. A/Solids, **10**, (1991), 587-606.

24. M. Fremond, C.R.Acad.Sc. t. **304**, série II, (1987), 239-244.

25. A. Gérard, S. Baste, 14th Energy sources technology conference and exhibition, Houston, Jan. 26-30, 1992, Proc. ASME PD, **45**, *Composite material technology*, (1992), Ed. D. Hui, T. J. Kozik, O. O. Ochoa.

26. S. Baste, A. Gérard, 14th Int. Cong. on air -and structure- borne sound and vibration, Montreal, Jun 13-15, (1994), Proc., **3**, 2025-2032.

27. B. Auld, *Acoustic fields in solids*, **1**, (1973), John Wiley and Sons, New York.

28. B. Castagnède, J. Roux, B. Hosten, Ultrasonic, **27**, (1989), 280-287.

29. B. Audouin, J. Roux, Rev. Phys. Appl., **25**, (1990), 1011-1017.

30. S. Baste, A. Gérard, NATO ASI, **126**, Martinus Nijhoff, (1987), 381-391. See also, S. Baste, A. Gérard, *Harmonic wave in three directional carbone-carbone composites*, (Tutoral paper). Summer School, Erice (Sicily), (Trapani), (1985), October 15-25.

31. B. Castagnède, J. T. Jenkins, W. Sachse, S. Baste, J. Appl. Phys., **67**, (1990), 2753-2761.

32. J. Roux, B. Hosten, B. Catsgnède, M. Deschamps, Rev. Phys. Appl., **20**, (1985), 351-358.

33. J. Roux, S. Baste, A. Gérard, J.N.C.7, Proc., 433-442, Invited conference, Lyon nov. 6-8, (1990), Ed. G. Fantozzi and P. Fleischmann.

34. B. Audouin, *Évaluation ultrasonore de l'endommagement anisotrope d'un composite à matrice fragile*, Ph. D. Thesis, **620**, Université Bordeaux I, (1991).

35. S. Baste, Habilitation à Diriger des Recherches, University Bordeaux I, (1991).

36. B. Hosten, M. Deschamps, B. R. Tittmann, J. Acous. Soc. Am., **82**, (1987), 1763-1770.

SOME ASPECTS OF NONLINEAR WAVE PROPAGATION

Alan Jeffrey
Department of Mathematics
City University of Hong Kong ·
and
Department of Engineering Mathematics
University of Newcastle upon Tyne, UK

ABSTRACT

The effects of dispersion and dissipation in linear wave propagation are interpreted in terms of nonlinear wave propagation and used to describe the qualitative properties of several fundamental nonlinear evolution equations. The effects of nonlinearity are reviewed, hyperbolicity is defined and conservation laws are introduced. A review of Riemann invariants, simple waves and generalized simple waves is presented and a conservation law is then used to remove the restriction of differentiability and continuity placed on solutions of hyperbolic equations in order that they can admit discontinuous solutions (shocks). The Riemann problem is examined and, finally, a number of topics related to fundamental nonlinear evolution equations are reviewed, amongst which are included solitons, the reductive perturbation method and Backlund transformations.

1. Waves, Linearity and the Interpretation of Derivatives

Nonlinear wave propagation is defined as wave propagation governed by partial differential equations that are not linear. . Thus any introduction to nonlinear wave propagation such as this must, of necessity, be prefaced by a definition of a wave and some remarks about the significance of linearity in wave propagation.

The physical concept of a wave is a very general one, including as it does cases in which a clearly identifiable disturbance, possibly localized, propagates through space as time increases; a time dependent disturbance throughout a region of space that may or may not be repetitive in nature and does not necessarily have persistent features that can be seen to propagate; or even a periodic spatial disturbance that is completely independent of time, like the waves in desert sand.

The essential feature that characterizes the waves in what follows, and which distinguishes them from the mere dependence of a solution on time, is that some attribute of the wave can be shown to propagate through space at a finite speed. In such situations the partial differential equations most closely associated with wave propagation are those of hyperbolic type, though we shall see that parabolic equations with certain types of nonlinearity may also describe waves in the above sense. For obvious reasons, partial differential equations that describe the development of a solution with time are called evolution equations.

In order to appreciate the significance of nonlinearity in wave propagation we must first recall the notion of a linear operator. Let $u(x,t)$ be a suitably differentiable

scalar function of position vector x and time t. Then the partial differential operator L in the expression $L[u]$ is said to be a linear operator if it is a linear combination of partial derivative operators of various orders with respect to x and t, with the multipliers of these operators functions of only x and t. It is then a direct consequence of the definition of L that if u and v are any two suitably differentiable functions

$$L[u + v] = L[u] + L[v]. \tag{1.1}$$

If we now consider the homogeneous partial differential equation

$$L[u] = 0, \tag{1.2}$$

and let u and v be any two different solutions of Eq.(1.2), it follows from the linearity property in Eq.(1.1) that

$$L[u + v] = L[u] + L[v] = 0, \tag{1.3}$$

which illustrates the linear superposition property of solutions that plays an essential role when solving linear partial differential equations by separation of variables.

The simplest linear first order evolution equation describing wave propagation is the advection equation, sometimes called the dissipationless Burgers' equation,

$$u_t + cu_x = 0, \tag{1.4}$$

in which c is a constant, while the most familiar second order evolution equation describing wave propagation is the wave equation

$$(1/c^2)\, u_{tt} = \Delta u, \tag{1.5}$$

in which Δ is the Laplacian and $c = c(x,t)$ is the phase speed of the wave.

In order to give a physical interpretation to the derivative terms appearing in evolution equations we shall consider the one-dimensional form of Eq.(1.5) and the following linear scalar equation which is first order in time but third order in its spatial derivative with respect to x, and in which c, v and μ are constants

$$u_t + cu_x - \eta u_{xx} + \mu u_{xxx} = 0. \tag{1.6}$$

This is a linearized form of the Korteweg-deVries, Burgers (KdVB) equation whose full nonlinear form will be discussed later, and it contains Eq.(1.4) as a special case when the parameters $\eta = \mu = 0$.

Let us consider one-dimensional plane waves for which elementary solutions have the form

$$U = a \exp[i(kx - \omega t)],\qquad(1.7)$$

in which a is the amplitude, k is the wave number and ω is the angular frequency, with k being defined in terms of the wavelength λ by $k = 2\pi/\lambda$. For elementary solution (1.7) to satisfy either Eq.(1.5) or Eq.(1.6) it is necessary that k and ω satisfy a compatibility condition obtained by substituting Eq.(1.7) into the appropriate partial differential equation and finding a relationship of the form

$$\omega = \omega(k)\qquad(1.8)$$

between ω and k. Eq.(1.8) is called the dispersion relation for the partial differential equation and the reason for this name will become apparent later.   The general solution of the equation may then be expressed as the Fourier integral

$$u = \int_{-\infty}^{\infty} A(k) \exp[i(kx - \omega t)]dk,\qquad(1.9)$$

in which the spectrum function $A(k)$ is determined by the initial and boundary conditions of the problem.   The phase velocity V_P with which the wave profile is propagated, and the group velocity V_G with which the wave energy is propagated are defined as [1,2]

$$V_P = \omega/k \quad\text{and}\quad V_G = \partial\omega/\partial k,\qquad(1.10)$$

and in general these two velocities are different.   When the phase velocity V_P depends on the wave number k the wave is said to be dispersive, because different components of the initial spectrum will propagate with different speeds causing the wave profile to change shape and spread out, or disperse.

Partial differentiation of the elementary solution in Eq.(1.7) with respect to t and x gives

$$U_t = -i\omega U,\ U_{tt} = -\omega^2 U,\ U_x = ikU,\ U_{xx} = -k^2 U,\ U_{xxx} = -ik^3 U.\qquad(1.11)$$

Thus if the elementary solution U is to satisfy the one-dimensional form of the wave equation it follows after substitution of U_{tt} and U_{xx} from Eqns.(1.11) into the equation that the dispersion equation for Eq.(1.5) is

$$\omega^2 = c^2 k^2,\ \text{or}\ \omega/k = \pm c,\qquad(1.12)$$

showing that the phase velocity $V_P = \pm c$, which is independent of k so waves governed by the wave equation propagate without dispersion.

A similar argument applied to Eq.(1.6) shows its dispersion relation to be

$$\omega - ck + i\eta k^2 + \mu k^3 = 0, \tag{1.13}$$

from which the phase velocity is seen to be given by

$$V_p = \omega/k = (c - \mu k^2) - i\eta k. \tag{1.14}$$

Substituting for ω/k in the elementary solution in Eq.(1.7) then shows that

$$U = a\, e^{-\eta kt} \exp\{ik[x - (c - \mu k^2)t]\}, \tag{1.15}$$

from which we see that provided $\eta > 0$ the wave will dissipate (attenuate) as it propagates, though as the real part of the phase velocity depends on k the wave will also experience dispersion.

In the special case in which $\eta = \mu = 0$, Eq.(1.6) reduces to the advection equation given in Eq.(1.4) whose solution in Eq.(1.15) is then seen to correspond to a wave that translates with constant speed c without change of shape or attenuation. This result can, of course, be derived independently of the above argument. All that is necessary is to observe that inspection shows the general solution of Eq.(1.4) to be

$$u = f(x - ct), \tag{1.16}$$

where f is an arbitrarily once differentiable function of its argument. Thus u is constant along the lines (characteristics) $x - ct = \text{const.}$, with the result that the initial waveform determined by the initial condition at $t = 0$, say $u(x,0) = \Phi(x)$, is translated to the right with speed c without change of shape. Such waves of constant form are called traveling waves.

The considerations leading to Eq.(1.15) show that in a general linear partial differential equation that is first order in time and similar to Eq.(1.6), but possibly possessing even higher order partial derivatives with respect to x, the partial derivatives with respect to x of even order greater than or equal to two correspond to dissipative terms provided the signs of their coefficients are chosen appropriately, while partial derivatives with respect to x of odd order greater than one correspond to dispersive terms, irrespective of the signs of their coefficients.

This interpretation of the significance of spatial partial derivatives in linear evolution equations like Eq.(1.6) is also used to provide a *qualitative* description of the nature of nonlinear evolution equations of similar type. Thus Burgers equation

$$u_t + uu_x = \eta u_{xx} \tag{1.17}$$

with $\eta > 0$, which is nonlinear because of the product term uu_x, is classified as purely dissipative, whereas the Korteweg-deVries (KdV) equation

$$u_t + uu_x + \mu u_{xxx} = 0 , \qquad (1.18)$$

which is also nonlinear for the same reason, is classified as purely dispersive. In the same way the full nonlinear KdVB equation

$$u_t + uu_x - \eta u_{xx} + \mu u_{xxx} = 0, \qquad (1.19)$$

of which Eq.(1.6) is the linearized form, is classified as both dissipative when $\eta > 0$ and dispersive when $\mu \neq 0$. A different and purely physical justification for classifying Burgers' equation as dissipative, based on Burgers' own use of the equation as a model for the decay of free turbulence in a fluid, was given in the early paper by Cole [3] in which, independently of the work by Hopf [4], he also developed the transformation enabling the solution of Eq.(1.17) to be determined in terms of the solution of the linear heat equation

$$\kappa u_t = u_{xx} , \qquad (1.20)$$

in which $\kappa = $ const., but more will be said about this later.

2. The Effect of Nonlinearity

The effect of nonlinearity is most easily demonstrated by considering the following initial value problem for the quasilinear equation (an equation is quasilinear if it is linear in its highest order derivative)

$$u_t + f(u)u_x = 0, \qquad (2.1)$$

where $f(u)$ is an arbitrary continuous function of the scalar function $u(x,t)$ which is subject to the initial condition

$$u(x,0) = g(x), \qquad (2.2)$$

with $g(x)$ an arbitrary continuous function of x.

Taking the total derivative of a differentiable function $u(x,t)$, later to be identified with the solution of Eq.(2.1) subject to the initial condition in Eq.(2.2), leads to the result

$$du/dt = u_t + u_x \, dx/dt . \qquad (2.3)$$

A comparison of Eq.(2.1) and Eq.(2.2) shows that Eq.(2.1) may be replaced by the pair of ordinary differential equations

$$du/dt = 0 \quad \text{along the curves defined by} \quad dx/dt = f(u). \qquad (2.4)$$

The first of these equations asserts that u = const., while the second shows that the curve in the (x,t)-plane corresponding to this constant value of u must be a straight line. The curves in the (x,t)-plane defined by the second equation in Eqns.(2.4) are, of course, the characteristic curves of Eq.(2.1) which in this case comprise a family of straight lines, while the pair of ordinary differential equations in Eqns.(2.4) are called the characteristic form of the original partial differential equation. The constant value of u transported along a characteristic curve (straight line) is simply the initial value assigned to u at the point on the initial line from which the characteristic curve originates, and the constant gradient of the characteristic curve $dx/dt = g(u)$ will depend on u.

Consequently, the characteristic curves through the distinct points $(x_1,0)$ and $(x_2,0)$ on the initial line, where in general $u(x_1,0) \neq u(x_2,0)$, will transport these different constant values of u into the half-plane $t > 0$ along straight lines with different gradients. This observation has two important consequences for wave propagation governed by Eq.(2.1). The first is that, unlike the advection equation given in Eq.(1.4), the quasilinear equation in Eq.(2.1) cannot describe traveling waves, because the waveform must, of necessity, change its shape as it propagates. The second observation, which is a consequence of the first, is that if all the characteristics in the (x,t)-plane diverge for $t > 0$, the solution of Eq.(2.1) subject to the initial condition Eq.(2.2) is determined by this system of characteristics for all time (Fig.1(a)).

However, if the characteristics converge, which depends only on the function f and the pointwise values of $u(x,0) = g(x)$ and is in no way dependent on the differentiability of $g(x)$, the characteristics will intersect. As different values of u will be transported along different characteristics, the intersection of characteristics corresponds to a non-uniqueness of u. In general the intersection of characteristics will usually take place, and the earliest elapsed time $t_c > 0$ at which it occurs corresponds to a breakdown in the differentiability of u and to the subsequent development of non-uniqueness (Fig.1(b)). We will see later when considering a typical case that the family of intersecting characteristics can form an envelope in the (x,t)-plane, and that the point at which this envelope first forms determines the time and place at which differentiability of the solution first breaks down. Thus the governing differential equation ceases to be valid after time t_c .

(a)   (b)
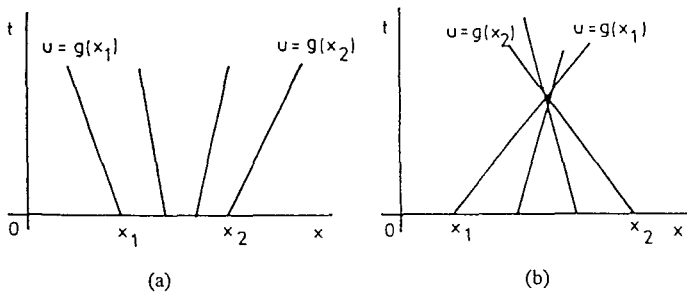
Fig.1 (a) Diverging characteristics, and (b) Converging characteristics

It follows by using the fact that u = const along a characteristic, and then integrating the second of Eqns.(2.4), that the equation of the characteristic through the point $(\xi,0)$ on the initial line will have the equation

$$x = \xi + tf(g(\xi)) \text{ while along it } u = g(\xi).\tag{2.5}$$

Eliminating ξ between Eqns.(2.5) leads to the implicit solution

$$u = g(x - tf(u)).\tag{2.6}$$

Notice that, independently of the reasoning leading to Figs.1, the implicit nature of the solution automatically implies the possibility that u may evolve to the point at which it becomes non-unique after some finite elapsed time.   The condition for the breakdown in differentiability can be derived from Eq.(2.6) by differentiating it partially with respect to x to obtain the result

$$u_x = g'(x - tf(u))/[1 + tg'(x - t(f(u))f'(u)],\tag{2.7}$$

in which a prime indicates differentiation with respect to the argument of the function involved.   This result shows that u_x becomes infinite if some time t_c exists for which the denominator of Eq.(2.7) vanishes.

A typical case involving the loss of differentiability of u is illustrated in Fig.2, corresponding to Eq.(2.1) with $f(u) = u$ and Eq.(2.2) with $g(x) = a \sin x$.   Specifically, Fig.2 shows the formation of an envelope of characteristics E, the cusp of which at $x = \pi$ corresponds to the first time $t_c = 1/a$ at which the characteristics intersect leading to the breakdown in differentiability of u.   In this case, from Eq.(2.6), the implicit solution is seen to be

$$u = \sin(x - ut).\tag{2.8}$$

Here, because of the periodicity of the initial condition, the solution becomes multivalued (non-unique) at time $t = t_c$ for $x = (2n + 1)\pi$, for $n = 0,\pm 1,\pm 2,\dots$. The graph in Fig.2 also shows the formation of similar cusps for t < 0, though these are not relevant because they occur before the initial time $t = 0$.
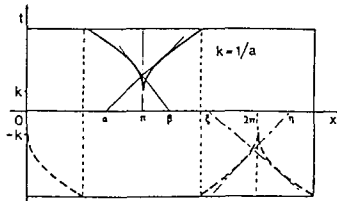
Fig.2   The envelope of characteristics E and the cusp at the point $(0,1/a)$

The loss of differentiability illustrated in the case of the scalar first order quasilinear equation in Eq.(2.1) is typical of the loss of differentiability in systems of such equations that describe nonlinear wave propagation, and the time and place at which this occurs can be determined [5]. Naturally, when u ceases to be differentiable, the partial differential equation or system describing the evolution process up to that point in time ceases to be valid. Thus, if an attempt is to be made to extend the solution beyond this critical time, some way must be found by which to replace the governing evolution equation involving partial derivatives of u by an equivalent equation in which u appears in an undifferentiated form, for this will then lift the differentiability requirement and even allow u to be discontinuous. The generalization of a solution used to achieve this objective forms the subject of Section 5.

3. Hyperbolicity and Conservation Laws

Hyperbolic equations describe wave propagation, and it is a familiar elementary result that the linear second order partial differential equation for $u(x,t)$

$$A(x,t)u_{xx} + 2B(x,t)u_{xt} + C(x,t)u_{tt} = f(x,t,u,u_x,u_t) \tag{3.1}$$

is hyperbolic in a domain D of the $(x.t)$-plane when $B^2 - AC > 0$ in D. Thus the one-dimensional form of the wave equation given in Eq.(1.5) is seen to be unconditionally hyperbolic throughout the (x,t)-plane. As the general solution of the one-dimensional wave equation can be expressed as

$$u = \Phi(x - ct) + \Psi(x + ct), \tag{3.2}$$

with Φ, Ψ arbitrary twice differentiable functions of their arguments, it follows that the solution comprises a linear combination of two traveling waves, one moving to the right with speed c along the family of characteristic lines $x - ct = $ const., and the other moving to the left with the same speed along the other family of characteristic lines $x + ct = $ const. In each case, the profile of the traveling waves will be determined by the initial conditions at $t = 0$ which will define the functions Φ and Ψ.

The relationship between the solution of the wave equation given in Eq.(3.2) and the solution of the advection equation Eq.(1.4) given in Eq.(1.16) can be seen by writing the one dimensional wave equation in either of the two equivalent forms

$$(\partial_t - c\partial_x)(u_t + c\,u_x) = 0, \tag{3.3}$$

or

$$(\partial_t + c\partial_x)(u_t - cu_x) = 0. \tag{3.4}$$

For if u is such that

$$u_t + cu_x = 0, \tag{3.5}$$

then it is a special traveling wave solution of Eq.(3.1) moving to the right with speed c corresponding to $\Phi(x - ct)$, in Eq.(3.2), while if it is such that

$$u_t - cu_x = 0, \tag{3.6}$$

then it is a special traveling wave solution of Eq.(3.1) moving to the left with speed c, but this time corresponding to $\Psi(x + ct)$ in Eq.(3.2). These special solutions are degenerate solutions of the wave equation because they are solutions of first order equations, whereas the solution in Eq.(3.2) must satisfy the wave equation which is second order.

More general than the linear second order partial differential equation in Eq.(3.1) is the quasilinear system

$$U_t + A(U)U_x + B(U) = 0, \tag{3.7}$$

in which $U = U(u_1, u_2,...,u_n)$, $A = A(u_1, u_2,...,u_n)$ and $B = B(u_1, u_2,...,u_n)$ are $n \times 1$ vectors, and suffixes indicate partial differentiation. This system is said to be totally hyperbolic[5] in any domain D of the (x,t)-plane in which A has n distinct real eigenvalues $\lambda_1, \lambda_2,...,\lambda_n$ and a complete set of corresponding left eigenvectors $l_1, l_2,...,l_n$ satisfying the equation

$$l_i A = \lambda_i l_i, \qquad i = 1,2,...,n. \tag{3.8}$$

We mention here that a partial differential equation of any order greater than or equal to two for a scalar function $u(x,t)$ may always be reduced to an equivalent first order system of this type by introducing higher order derivatives as new dependent variables [5,6].

When the independent variables involved are a spatial coordinate x and the time t the requirement that the eigenvalues are real ensures that they represent real speeds of propagation, because they have the dimensions of a length divided by a time. The existence of a complete set of linearly independent eigenvectors allows Eq.(3.7) to be reduced to a characteristic normal form [5,6,7] in which n functions related to the n elements of U are differentiated along n separate families of characteristic curves $C^{(i)}$, $i = 1,2,...,n$ defined by

$$C^{(i)}: \quad dx/dt = \lambda_i, \qquad i = 1,2,...,n. \tag{3.9}$$

We now consider the important class of systems called hyperbolic conservation laws. These are systems of hyperbolic equations, each member of which can be written in the divergence form

$$u_t + \operatorname{div} F(u) = 0, \tag{3.10}$$

in which $u = u(x,t)$ and $F(u)$ is a verctor function of u.

To appreciate why these are called conservation laws we consider the typical example provided by the dissipationless Burgers' equation given in Eq.(2.1). By setting $F(u) = \int f(u)du$, Eq.(2.1) may be written in the one-dimensional form of Eq.(3.10) as

$$u_t + F_x(u) = 0. \tag{3.11}$$

Let us now integrate Eq.(3.11) over an arbitrary interval $-a \le x \le a$ to obtain

$$\int_{-a}^{a} u_t\, dx + F(u)|_a - F(u)|_b = 0. \tag{3.12}$$

Then for the class of solutions u that vanish sufficiently rapidly as $|x| \to \infty$ so that the function $F(u)|_{x = \pm a} \to 0$ as $a \to \infty$, it follows that

$$\frac{d}{dt} \int_{-\infty}^{\infty} u\, dx = 0,$$

showing that the integral

$$\int_{-\infty}^{\infty} u\, dx$$

is a conserved quantity as it is independent of t.

A typical example of a system of hyperbolic conservation laws is provided by the one-dimensional equations of gas dynamics [5,8,9,10,11,12] that in matrix form may be written

$$U_t + F_x = 0, \tag{3.13}$$

with

$$U = \begin{bmatrix} \rho \\ \rho u \\ \rho u^2/2 + \rho e \end{bmatrix} \quad \text{and} \quad F = \begin{bmatrix} \rho u \\ \rho u^2 + p \\ u(\rho u^2/2 + \rho e + p) \end{bmatrix}, \tag{3.14}$$

where u is the one-dimensional gas speed, ρ is the gas density, $p = p(\rho)$ is the gas pressure and e is the specific internal energy of the gas. The first equation in the system describes conservation of mass, the second conservation of momentum and the third conservation of energy.

The significance of the requirement that the hyperbolic systems be expressible in divergence form will become apparent later when we come to consider discontinuous solutions, because only for such systems is there a means by which to relate the solution on one side of the discontinuity to the solution on the other by using the Gauss divergence theorem.

4. Riemann Invariants, Simple Waves and Generalized Simple Waves

Because of its importance we now review the classical theory of Riemann invariants   The method is applicable to any totally hyperbolic system of two first order equations in the two dependent variables x, t, and the two independent variables u,v of the form

$$u_t + a_{11}u_x + a_{12}v_x = 0,$$

$$v_t + a_{21}u_x + a_{22}v_x = 0, \tag{4.1}$$

subject to the initial conditions

$$u(x,0) = u_1(x) \quad \text{and} \quad v(x,0) = v_1(x), \tag{4.2}$$

where the $a_{ij} = a_{ij}(u,v)$ depend explicitly on u and v and only implicitly on x and t through u and v, while $u_1(x)$ and $v_1(x)$ are the prescribed initial conditions. For our purposes t is the time, though it may also be a spatial variable like x, in which case it is usually denoted by y.

Systems of this form are said to be reducible, which is a name derived from the the application of the hodograph transformation[7,8] to the system, that involves interchanging the roles of the dependent and independent variables.   This reduces the system of equations to one that is linear in x and t, and so is much easier to solve. However, the price paid for this simplification is that boundaries in the (x,t)-plane are transformed into far more complicated ones in the (u,v)-plane, thereby usually introducing considerable mathematical difficulties when seeking the solution of even the simplest problem.

Defining the matrices A and U as

$$A = \begin{bmatrix} a_{11} & a_{12} \\ a_{21} & a_{22} \end{bmatrix} \quad , \quad U = \begin{bmatrix} u \\ v \end{bmatrix}$$

enables Eqns.(4.1) to be written as the system

$$U_t + AU_x = 0. \tag{4.3}$$

This system will be be totally hyperbolic provided the eigenvalues λ_i , $i = 1,2$ of matrix A are real and distinct.   Using the corresponding left eigenvectors l_i introduced in Eq.(3.8), and pre-multiplying Eq.(4.3) by l_i , leads to the result

$$l_i\{ U_t + \lambda_i U_x \} = 0, \quad \text{for } i = 1,2. \tag{4.4}$$

The bracketed expression in Eq.(4.4)is simply a directional derivative of U with respect to t along the family of characteristic curves $C^{(i)}$ defined in Eq.(3.9). Denoting such differentiation along $C^{(1)}$ characteristics by $d/d\alpha$ and along the $C^{(2)}$ ones by $d/d\beta$ allows Eqns.(4.4) to be replaced by the pair of ordinary differential equations

$$l_1 dU/d\alpha = 0 \quad \text{along the } C^{(1)} \text{ characteristics} \tag{4.5}$$

and

$$l_2 dU/d\beta = 0 \quad \text{along the } C^{(2)} \text{ characteristics.} \tag{4.6}$$

Thus β = const. along $C^{(1)}$ characteristics, and α = const. along $C^{(2)}$ characteristics as indicated in Fig.3.
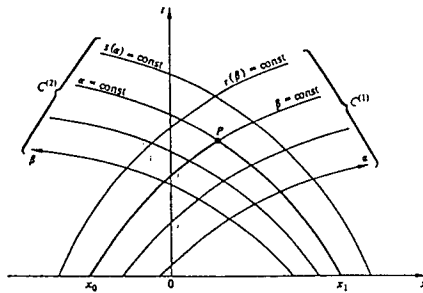
Fig.3   Families of characteristics with associated Riemann invariants

Writing the left eigenvector $l_i = \{l_1(i), l_2(i)\}$, for $i = 1,2$ allows Eqns.(4.5),(4.6) to be expressed in the form

$$l_1(1) \, du/d\alpha + l_2(1) \, dv/d\alpha = 0 \tag{4.7}$$

along the $C^{(1)}$ characteristics, and

$$l_1(2) \, du/d\beta + l_2(2) \, dv/d\beta = 0 \tag{4.8}$$

along the $C^{(2)}$ characteristics.

As A depends only on u and v, so also will the elements of l_i, showing that the above equations will always be integrable along their respective characteristics, though multiplication by an integrating factor μ may be necessary.

Integrating Eq.(4.7) with respect to α along the $C^{(1)}$ characteristics and Eq.(4.8) with respect to β along the $C^{(2)}$ characteristics gives

$$\int \mu \, l_1{}^{(l)} \, du \, + \, \int \mu \, l_2{}^{(l)} \, dv \, = \, r(\beta) \tag{4.9}$$

along the $C^{(1)}$ characteristics, and

$$\int \mu \, l_1{}^{(2)} \, du \, + \, \int \mu \, l_2{}^{(2)} \, dv \, = \, s(\alpha) \tag{4.10}$$

along the $C^{(2)}$ characteristics, where r and s are functions of their respective arguments α and β, while the two families of characteristics are determined by integration of the equations

$$C^{(i)}: \quad dx/dt \, = \, \lambda_i \,, \text{ for } i = 1,2. \tag{4.11}$$

The functions $r(\beta)$ and $s(\alpha)$ are called Riemann invariants because they are invariant quantities along their respective characteristics. Thus $r(\beta)$ is constant along any $C^{(1)}$ characteristic, though as it is a function of β it will, in general, be different for different characteristics, and a corresponding statement is true for $s(\alpha)$ along $C^{(2)}$ characteristics. Eqns.(4.9),(4.10) enable u and v to be expressed in terms of r and s, the values of which are determined at points of the initial line $t = 0$ by the initial data in Eq.(4.2).

Suppose $r(\beta)$ in Eq.(4.9) is denoted by $R(u,v)$ and $s(\alpha)$ in Eq.(4.10) is denoted by $S(u,v)$. Then along the characteristic $C^{(1)}$ issuing out from an arbitrary point $(x_0,0)$ of the initial line as t increases we have

$$R(u,v) \, = \, R(\, u_1(x_0),v_1(x_0)), \tag{4.12}$$

while along the characteristic $C^{(2)}$ issuing out from a different arbitrary point $(x_1,0)$ on the initial line we have

$$S(u,v) \, = \, S(\, u_1(x_1),v_1(x_1)). \tag{4.13}$$

Solving these two implicit equations for u and v determines the solution at the point of intersection P of the $C^{(1)}$ and $C^{(2)}$ characteristics in Fig.3 along which their respective constant values of r and s are transported. In principle the initial value problem is now solved, because the points $(x_0,0)$ and $(x_1,0)$ on the initial line were arbitrary, so the point of intersection P of the associated characteristics may be any point in the half-plane $t > 0$. However, in particular cases the task of solving the two implicit relationships and of finding the characteristic curves in order to determine their point of intersection P is not always possible analytically. Furthermore, the implicit relationships imply the possibility of the non-uniqueness of the solution at some point in the (x,t)-plane.

Simple wave solutions arise when one of the Riemann invariants is an absolute constant. Suppose, for example, that $s(\alpha) = s_0$, so that Eqns.(4.9) ,(4.10) may be written

$$f_{11}(u) + f_{12}(v) = r(\beta) \text{ and } f_{21}(u) + f_{22}(v) = s_0. \tag{4.15}$$

Then, in general, for any value of β determining a specific $C^{(1)}$ characteristic, these equations will have a unique constant solution $u = u_1(\xi)$, $v = v_1(\xi)$ determined by the point $(\xi,0)$ on the initial line from which the $C^{(1)}$ characteristic originates.

Setting $\lambda_1 = \lambda_1(u_1(\xi),v_1(\xi)) = \Lambda_1(\xi)$, say, we see that for any given ξ the associated characteristic is the straight line given by

$$x = \xi + t\Lambda_1(\xi). \tag{4.16}$$

Thus the associated simple wave solution corresponds to the transport of the initial values of u and v at the point $(\xi,0)$ as constants along straight line characteristics where, in general, different straight line characteristics will have different gradients. In the event that characteristics form an envelope we arrive at a situation analogous to the one illustrated in Fig.2 for a single equation.

The notion of a simple wave can be generalized to systems of the form

$$U_t + AU_x = 0, \tag{4.17}$$

in which U is an $n \times 1$ column vector with elements $u_1, u_2, \ldots, u_n$ and $A = A(U)$ is an $n \times n$ matrix with elements depending explicitly only on the elements of U. The generalization is based on the fact that in an ordinary simple wave v may be regarded as a function of u so, by analogy, a generalized simple wave solution of the system in Eq.(4.17) will be taken to be one in which $u_i = u_i(u_1)$, for $i = 2, 3, \ldots, n$.

Setting $U = U(u_1)$ and substituting in Eq.(4.3) gives

$$(\partial u_1/\partial t\, I + \partial u_1/\partial x\, A)\, dU/du_1 = 0, \tag{4.18}$$

where I is the unit matrix. This homogeneous system will have a non-trivial solution only if

$$|A - \mu I| = 0, \tag{4.19}$$

where $\mu = -(\partial u_1/\partial t)/(\partial u_1/\partial x)$. Thus the n solutions μ_i for $i = 1, 2, \ldots, n$ are seen to be the eigenvalues λ_i of A, while the corresponding n vectors dU/du_1 are seen to be proportional to the associated right eigenvectors of A.

Here, as with ordinary simple waves, the characteristics $C^{(i)}$ are again families of straight lines determined by integrating

$$C^{(i)}: \quad dx/dt = \lambda_i, \tag{4.20}$$

while the variation of u_1, which then determines the variation of the u_i for $i = 2, 3, \ldots, n$ is itself determined by the scalar generalized Burgers' equation

$$(\partial u_1/\partial t) + \lambda_i(u_1)(\partial u_1/\partial x) = 0. \tag{4.21}$$

A more detailed discussion of these generalized simple waves and their associated generalized λ_k-Riemann invariants is to be found elsewhere [5].

5. Discontinuous Solutions, Shocks and Generalized Simple Waves

The discussion of first order quasilinear hyperbolic equations given in Section 2 showed that even when the initial data is arbitrarily smooth the solution may still develop an infinite spatial derivative after a finite elapsed time t_c, beyond which time a classical solution ceases to exist. Furthermore, the particular solution in Eq.(2.8) demonstrated the fact that an attempt to continue a classical solution beyond the critical time t_c can lead to it becoming non-unique. This same pattern of behaviour can also be shown to be exhibited by quasilinear hyperbolic systems in general [5].

In order to extend the equations governing wave propagation so they allow the possibility of discontinuous solutions it is necessary to reformulate them in such a way that the loss of differentiability caused when a solution becomes discontinuous no longer invalidates them. When conservation equations are involved this may be accomplished by re-expressing them in integral form using the following well known vector transport theorem and then using the result to relate the solution on either side of a discontinuity to its speed of propagation.

Let a scalar function $f(x,t)$ be defined in an arbitrary volume $V(t)$ in space, throughout which there exists a velocity field $s(x, t)$ that also determines the motion of the surface $S(t)$ bounding $V(t)$. Then, in terms of the derivative $D/Dt \equiv \partial/\partial t + s.\nabla$, called the material derivative,

$$\frac{D}{Dt} \int_{V(t)} f dV = \int_{V(t)} \left[\frac{Df}{Dt} + \text{div} \ (fs) \right] dV \tag{5.1}$$

If, now, f is a conserved quantity in volume $V(t)$, it follows from this last result that

$$\int_{V(t)} \left[\frac{Df}{Dt} + \text{div} \ (fs) \right] dV = 0 \tag{5.2}$$

To develop the argument further, and for the sake of simplicity, we now apply the result of Eq.(5.2) to the familiar one-dimensional scalar generalized Burgers' equation

$$u_t + f(u) u_x = 0. \tag{5.3}$$

However, vector notation will be retained throughout the following argument to indicate how the same method may be applied to a system of vector conservation laws. As in Section 3, by setting $F(u) = \int f(u)\, du$, Eq.(5.3) may be written in the conservation form given in Eq.(3.1), namely as

$$u_t + \operatorname{div}(F(u)) = 0, \tag{5.4}$$

where in one space dimension $F(u) = F(u)$ and $\operatorname{div}(.) = \partial(.)/\partial x$.

Setting $f = u$ in Eq.(5.2) and substituting for u_t from Eq.(5.4) then gives

$$\int_{V(t)} \operatorname{div}\left(us - F(u) \right) dV = 0 \tag{5.5}$$

Applying the Gauss divergence theorem to Eq.(5.5) allows it to be re-written in the form of the surface integral

$$\int_{S(t)} \left(us - F(u) \right) \cdot n\, dS = 0, \tag{5.6}$$

where n is the outward drawn unit normal to the surface $S(t)$ bounding volume $V(t)$ and dS is the element of area on $S(t)$. In this one-dimensional case $s.n = s$ is the speed of the velocity field along the x-axis, and $F(u).n = F(u)$.

Suppose now that u is discontinuous across some surface Σ_t that divides $V(t)$ in two, and identify the adjacent sides of the surface by the suffixes - and +. Next we shrink $V(t)$ to an arbitrarily small volume containing Σ_t in such a way that $S(t)$ is parallel to each side of Σ_t while the distance between the two sides of $S(t)$ bounding the discontinuity surface is negligible. Because of the arbitrary nature of $V(t)$ the integral in Eq.(5.6) can only vanish if the integrand vanishes, so we conclude that

$$(su - F(u))_- = (su - F(u))_+, \tag{5.7}$$

where the suffixes $\pm$ now signify that the associated results are to be evaluated on the adjacent sides - and + of the discontinuity surface. By virtue of its manner of derivation, in this result s is constrained to lie on the discontinuity surface, and so as it moves with the surface it must be continuous across it, while u and $F(u)$ are discontinuous across it. Using the notation $[[.]]$ to denote the jump $(.)_1 - (.)_2$ in a quantity $(.)$ across the discontinuity surface, the result of Eq.(5.7) becomes

$$s[[u]] = [[F(u)]]. \tag{5.8}$$

This nonlinear result is known as the generalized Rankine-Hugoniot jump condition and it is named after Rankine and Hugoniot who, independently, were the first

to introduce a relationship of this type into the study of gas dynamics. In the one-dimensional case considered here in relation to the generalized Burgers equation, this jump condition relates the solution on either side of the discontinuity surface to the speed s of propagation of the discontinuity surface in the x-direction. Discontinuous solutions of this type are given the generic name shocks, or shock waves, because of the analogous situation in gas dynamics in which gas flows through a shock, across which the field variables comprising the pressure, density and velocity experience discontinuous jumps.

A similar result holds for a system of vector conservation laws, in which case s is the speed of propagation normal to the discontinuity surface. It is important to recognise that the condition in Eq.(5.8) is a nonlinear one, so that specifying u on one side of a shock together with the shock speed v will not necessarily determine u on the other side in a unique manner. In this case, for uniqueness, it is necessary that $f(u)$ is convex (or concave) and satisfies certain additional conditions. However, the arguments involved will not be developed any further because the details can be found in a number of references [9,10,11,12].

Suffice it to say here that in this case, for a physically realizable shock, the characteristics in the (x,t)-plane on either side of the shock must converge onto the line followed by the shock. That is, the characteristics behind the shock must have speeds faster than that of the shock speed s, while the characteristics in front of the shock must have speeds slower than that of the shock speed. If the characteristic speed $\lambda(u)$ behind the shock is denoted by a suffix - and its value ahead of the shock is denoted by a suffix +, then the condition for a shock to form becomes

$$\lambda(u_-) > s > \lambda(u_+). \tag{5.9}$$

Conditions of this type are called entropy conditions, because of the situation in the gas dynamic case for which the first entropy condition was introduced. In gas dynamics two discontinuous mathematical solutions are possible, one an expansion shock and the other a compression shock, though the expansion shock is rejected as being non-physical because it violates the change of entropy required by the second law of thermodynamics. Thus the first selection principle (entropy condition) for a physically realizable stable shock in gas dynamics came from outside the system of gas dynamic equations used to derive the Rankine-Hugoniot jump condition. In more general systems, where the thermodynamical concept of entropy is not available, alternative mathematical conditions are necessary to determine shocks with acceptable mathematical properties (stability), though the name entropy condition is still applied to them.

When in Section 4 we considered a system of the type

$$U_t + A(U) U_x = 0, \tag{5.10}$$

with U an $n \times 1$ vector with elements $u_1, \ldots, u_n$ and $A = A(U)$, the system was seen to be hyperbolic if the matrix $A(U)$ has n distinct and real eigenvalues $\lambda_1, \ldots, \lambda_n$ for each U.

Furthermore, in Section 4, this system was shown to have generalized simple wave solutions with certain properties similar to those of ordinary simple waves, the behaviour of which is governed by the scalar generalized Burgers Eq.(4.19). The main property of generalized simple waves is that in them the the characteristic lines comprise a family of non-parallel straight lines, while along each characteristic $u_i = u_i(u_1)$ for $i = 2,3,...,n$.

Now let Eq.(5.10) be a system of hyperbolic conservation laws, which will be the case if it can be written in the form

$$U_t + F_x = 0, \tag{5.11}$$

with A obtained by taking the gradient of an $n \times 1$ vector $F = F(U)$ with respect to the elements of U, so that $A = \nabla_U F(U)$. It then follows immediately that when a family of characteristic lines converges this system can also admit solutions in the form of shock waves.

As with the simple scalar case already outlined, the discontinuous shock solutions associated with the system shown in Eq.(5.10) will not be unique, so an entropy condition is again needed in order to select the stable solution. Using the idea of characteristics converging onto the shock line from both sides to create a shock, this entropy condition can be shown to be capable of formulation in the following form [5,9,10,11,12].

For a stable shock with speed s there must be some index k, with $1 \le k \le n$, such that

$$\lambda_k(u_-) > s > \lambda_k(u_+), \tag{5.11}$$

while

$$\lambda_{k-1}(u_-) > s > \lambda_{k+1}(u_+). \tag{5.12}$$

These inequalities ensure that k characteristics converge onto the shock line from the rear and $n - k + 1$ converge onto it from the front. Taken together with the generalized Rankine - Hugoniot condition

$$s[[U]] = [[F(U)]], \tag{5.13}$$

that may be derived for the system in Eq.(5.11) in the same way as for the scalar generalized Burgers' equation, after eliminating s these results are sufficient to determine the $2n$ values assumed by the elements of U on either side of the shock.

6. The Riemann Problem and the Random Choice Method

The introduction of shock solutions now makes it possible to discuss the Riemann problem that is of fundamental importance in the study of nonlinear hyperbolic conservation systems.   In the case of the system in Eq.(5.10), the Riemann problem may

be formulated as follows.   Find the solution of the reducible hyperbolic conservation system

$$U_t + A(U)\, U_x = 0, \tag{6.1}$$

subject to the piecewise initial data

$$U(x,0) = \begin{cases} U_0 \text{ for } x < 0 \\[2mm] U_1 \text{ for } x > 0, \end{cases} \tag{6.2}$$

where U_0 and U_1 are constant n element column vectors.

Thus the Riemann problem involves resolving the discontinuity in the piecewise constant initial data at the origin on the initial line.   In what follows, the problem is simplified by reducing it to finding the solution of a typical scalar Riemann problem, because this problem contains all the features to be found in the more general case. Specifically, we solve

$$u_t + u^2\, u_x = 0, \tag{6.3}$$

subject to the initial condition

$$u(x, 0) = \begin{cases} u_0 \quad \text{for } x < 0 \\[2mm] u_1 \quad \text{for } x > 0, \end{cases} \tag{6.4}$$

where u_0 and u_1 are arbitrary constants.

When Eq.(6.3) is written in conservation form by setting $F(u) = u^3/3$ it becomes

$$u_t + F_x(u) = 0, \tag{6.5}$$

from which, by using the Rankine-Hugoniot jump condition of Eq.(5.8), it follows that the shock speed s can be determined from

$$s(u_1 - u_0) = (u_1^3 - u_0^3)/3, \tag{6.6}$$

and so

$$s = (u_0^2 + u_0 u_1 + u_1^2). \tag{6.7}$$

Thus, when a shock can exist for $t > 0$ and emanate from the origin, it follows from Eq.(6.7) that the gradient of the line in the (x,t)-plane followed by the shock must have the constant value s, and so the shock will propagate along a straight line through the origin.

The characteristic curves C (straight lines) for Eq.(6.3) are determined by using the fact that $u = $ const. and integrating

$$\text{C:} \quad dx/dt = u^2. \tag{6.8}$$

Thus for $x < 0$ the characteristics of are seen to be parallel straight lines with slope u_0^2, whereas for $x > 0$ they are parallel straight lines with slope u_1^2.
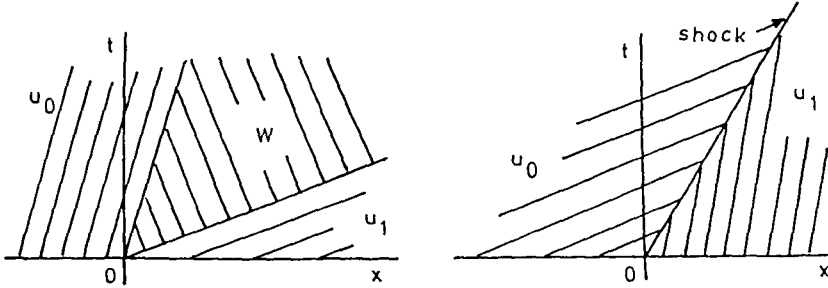
Fig.4   (a) Centered simple wave region   (b) Shock connecting two constant states
                    connecting two constant states

If $u_0^2 < u_1^2$ these two families of characteristics diverge as shown in Fig.4(a), and the wedge shaped region W in the (x,t)-plane is not traversed by any member of these two families of characteristics. As the characteristics must be straight lines, and they are constrained to pass through the origin, they must have the equation $x/t =$ const. Thus in region W we must seek a solution of the form $u = u(x/t)$. This leads to an ordinary differential equation for $u(z)$, where $z = x/t$, and in region W this differential equation has the solution $u(x,t) = (x/t)^{1/2}$ for $u_0^2 \leq u_1^2$. Finally, combining this result with the constant solutions on either side of W shows the required complete solution for $u(x,t)$ to be given by

$$u(x,t) = \begin{cases} u_0 & \text{for } x/t < u_0^2 \\ (x/t)^{1/2} & \text{for } u_0^2 \leq u_1^2 \\ u_1 & \text{for } x/t > u_1^2. \end{cases}$$

This is a simple wave centered on the origin and it provides the unique solution of the Riemann problem in region W. The uniqueness follows because although the line traversed by the shock in the (x,t)-plane also lies in W, no characteristics converge onto it as required by the entropy condition for the shock to be genuine, so in this case the shock solution must be rejected. However, if $u_0^2 > u_1^2$ the two families of characteristics converge and lead to the immediate formation of a shock that is then propagated with the speed s given in Eq.(6.7).

Fig.5 shows how the centered simple wave resolves the initial discontinuity in the initial data at the origin for the case in which $u_0 = 0$ and $u_1 = 1$, while Fig. 6 shows how when $u_0 = 1$ and $u_1 = 0$ the initial discontinuity is propagated immediately as a shock.
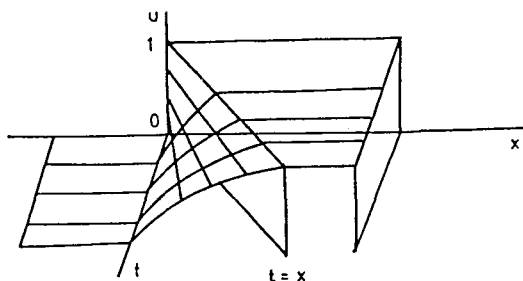
Fig.5   Resolution of the initial discontinuity by a centered simple wave
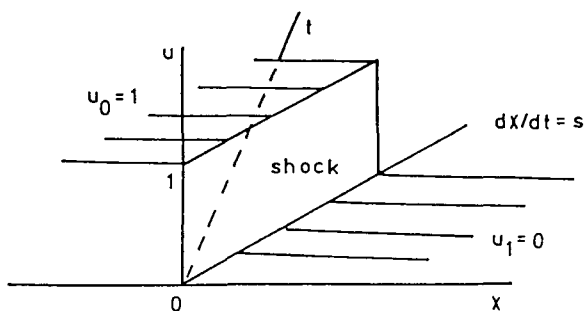
Fig.6   Propagation of initial discontinuity as a shock wave

An important application of the Riemann problem to the numerical solution of conservation systems was made by Glimm[13] who introduced the random choice method. This is a method of first order in accuracy, and the fundamental idea involved is to replace arbitrary initial data by a piecewise constant approximation in spatial intervals of length h.   Then, until such time as the centered simple waves and shocks that result interact, an analytical solution of the piecewise constant approximation to the initial data is provided by the set of solutions to the appropriate set of Riemann problems.   If, for a suitably small time step k, this composite solution is used as an approximation   to the actual solution, a new set of Riemann problems may be derived from the analytical solution at time $t = k$, and thereafter the process may be repeated to advance the solution step by step in time.

The special feature of Glimm's method lies in the way each new set of Riemann problems is derived from the corresponding set of analytical solutions.   In the random choice scheme the constant value to be associated with each interval of length h is found by random sampling of the analytical solution derived for that interval.   For a detailed discussion of the application and accuracy of this method   we refer to the papers by Glimm[13]Lucier[14] and Chorin[15]. Alternative methods of solution for nonlinear hyperbolic equations are to be found in the book by LeVeque [12].

An important extension of the Riemann problem was made to the two dimensional case by Wagner [16]. In this problem a two-dimensional hyperbolic equation is considered subject to different constant initial data assigned to each quadrant, leading to extremely complicated behaviour of the solution. The most detailed discussion of this problem to date is given in the monograph by Zhang and Hsiao [17], with an important conjecture concerning gas dynamics being reported in the paper by Zhang and Zheng [18].

7. Burgers Equation

The parabolic quasilinear partial differential equation given in Eq.(1.17), namely

$$u_t + uu_x = \eta u_{xx}, \tag{7.1}$$

was introduced in fluid mechanics by Burgers in his 1948 paper [19] as a model illustrating turbulence. Because of its importance in fluid mechanics and its significance as a prototype nonlinear purely dissipative equation it is now known as Burgers equation, though the differential equation itself first appeared in the 1906 treatise by Forsyth[20]. In the context of fluid mechanics the parameter $\eta > 0$ measures the strength of the dissipative effect that is present in the fluid motion, and for obvious reasons when $\eta = 0$ Eq.(3.11) (also Eq.(2.1)) is often called a generalized dissipationless Burgers equation.

It was demonstrated in Section 2 that quasilinear hyperbolic equations like Eq.(2.1) cannot describe traveling waves of the type possessed by the advection equation. That is, waves of constant form that translate steadily without change of amplitude, as in the solution of Eq.(1.4) given in Eq.(1.16).

The presence of the term ηu_{xx} in Burgers equation changes the properties of the dissipationless form of the equation completely, because whereas the nonlinear term uu_x causes wave steepening that if unchecked leads to the loss of differentiability as discussed in Section 2, the dissipative term ηu_{xx} exerts a smoothing effect that counteracts the wave steepening process leading to the formation of a traveling wave. The traveling wave can be found by seeking a solution of the form $u(x,t) = U(z)$, where $z = x - st$ and s is a constant (the wave speed) to be determined. To find such a solution it is also necessary for the solution to satisfy appropriate boundary conditions at infinity that will, in general, determine the permissible range of values of the wave propagation speed s.

When these conditions are taken to be that all derivatives tend to zero as $|x| \to \infty$, the following solution is obtained [11]

$$U(z) = (u^- + u^+)/2 - (1/2)(u^- - u^+)\tanh[(u^- - u^+)z/(4\eta)], \tag{7.2}$$

subject to the boundary conditions

$$\lim U(z) = u^{\pm} \text{ as } |z| \to \infty, \text{ with } u^- > u^+, \tag{7.3}$$

and

$$s = (u^- + u^+)/2 . \tag{7.4}$$

This traveling wave solution, usually knows as the Burgers shock wave, exhibits a monotonic transition between the values u^- and u^+ at minus and plus infinity, respectively. A typical example of a Burgers shock wave profile is shown in Fig.7.
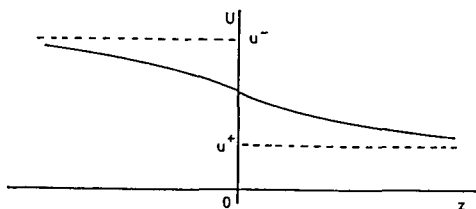
Fig.7   The Burgers shock wave

Examination of Eq.(7.2) shows that the smaller η becomes, the sharper is the transition of the Burgers' shock wave between the states at minus and plus infinity.

An important and useful property of Burgers equation is its invariance under a Galilean transformation. That simply means that the translation of the origin of the x and t coordinates along the x-axis at a uniform speed leaves the form of the equation unchanged. To see this it is only necessary to change the dependent variable $u(x,t)$ to the new translated dependent variable $k + u(x - kt, t)$ in which k is a constant, and then to set $v(z,t) = u(x - kt, t)$, with $z = x - kt$, for the equation then becomes

$$v_t + vv_x = \eta v_{xx} ,$$

which has the same form as Eq.(7.1).

We now outline how the solution of a general initial value problem for Burgers equation may be obtained. It was shown independently by Hopf [3] and Cole [4] that by writing Burgers equation in the form

$$u_t + (u^2/2)_x = \eta u_{xx}, \tag{7.5}$$

the transformation

$$u = -2\eta \varphi_x/\varphi , \tag{7.6}$$

now called the Hopf-Cole transformation, reduces Eq.(7.5) to the linear heat equation

$$\varphi_t = \varphi_{xx} , \tag{7.7}$$

whose solution is well understood.

Using Fourier transforms, the solution of Eq.(7.7), subject to the general initial condition $\varphi(x,0) = \Phi(x)$, can be shown to be [21,22]

$$\varphi(x, t) = \frac{1}{2\sqrt{\pi \eta t}} \int_{-\infty}^{\infty} \Phi(\zeta) \exp\{-(x-\zeta)^2 / (4\eta t)\} d\zeta \tag{7.8}$$

from which it follows that

$$u(x, t) = \frac{\int_{-\infty}^{\infty} \{(x-\zeta)/t\} \Phi(\zeta) \exp\{-(x-\zeta)^2 / (4\eta t)\} d\zeta}{\int \Phi(\zeta) \exp\{-(x-\zeta)^2 / (4\zeta t)\} d\zeta} \tag{7.9}$$

The initial condition $\Phi(x)$ for φ is related to the initial condition $u(x,0) = u_0(x)$ for Burgers equation by the result

$$\Phi(x) = \exp\{-\int_0^x u_0(\zeta)/(2\eta) d\zeta\} \tag{7.10}$$

Thus the solution of Eq.(7.1) subject to the arbitrary initial condition $u(x,0) = u_0(x)$ is given by Eqns.(7.9) and (7.10).

The relationship between the dissipationless Burgers equation in which $\eta = 0$, and the limit of Eq.(7.1) as $\eta \rightarrow 0$ was first examined by Hopf [3] (see also Smoller [11] and Whitham[23]), while a comprehensive study of Burgers' equation and related problems has been given by Smoller [11].

8. The KdV Equation and Solitons

The equation

$$u_t + uu_x + \mu u_{xxx} = 0, \tag{8.1}$$

called the Korteweg-de Vries (KdV) equation, was first derived in a paper published in 1895 by Korteweg and de Vries [24] devoted to the examination of a special form of long wave in shallow water. When the coefficient μ of the dispersive term vanishes the equation reduces to the dissipationless Burgers equation that has no travelling wave solution. However, the dispersive term μu_{xxx} has a smoothing effect on the wave steepening process produced by the nonlinear term uu_x making it possible for the KdV equation to have a traveling wave solution.

The reason for the current interest in this particular scalar nonlinear evolution equation will become clear in Section 9 where it will be shown how it governs the asymptotic nature of a complicated system to which belong many different types of physical problem.   Accounts of the connection between long waves in shallow water and the KdV equation are to be found elsewhere [25,26].

As with Burgers equation, the travelling wave solution for the KdV equation is found by seeking a solution of the form $u(x,t) = U(z)$, where $z = x - st$ and s is a constant (the wave propagation speed) to be determined.   Here also u is required to satisfy a similar smoothness conditions at infinity to those satisfied by Burgers shock wave solution.   The details of the derivation of the traveling wave solution can be found elsewhere [25] so we give only the result of the integration, namely,

$$U(z) = u_\infty + a \operatorname{sech}^2 \{z[a/(12\mu)]^{1/2}\}, \tag{8.2}$$

subject to the boundary conditions

$$\lim U(z) = u_\infty \text{ as } |z| \to \infty, \text{ with } u_\infty \geq 0, \tag{8.3}$$

and

$$s = u_\infty + a/3. \tag{8.4}$$

The pulse-like shape of the KdV traveling wave in Eq.(8.2), illustrated graphically in Fig.8, has caused it to be called a solitary wave.   Examination of the Eqns.(8.2)-(8.4)
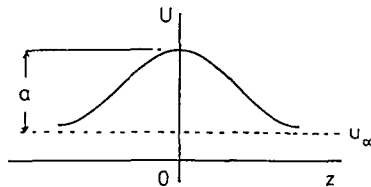
Fig.8   A KdV solitary wave with amplitude a relative to the condition u_∞ at infinity

shows the speed of propagation s is proportional to the amplitude a of the solitary wave relative to the value u_∞ at infinity, while a measure of the width of the solitary wave is seen to be provided by $a^{1/2}$.   Unlike the Burgers shock wave, the KdV solitary wave speed is not determined by the boundary conditions at infinity, but solely by the amplitude $a > 0$.

The KdV equation and Burgers equation are both invariant with respect to the same Galilean transformation, which are results that are used in a number of ways, one of which is in the solution of the KdV equation by means of the a technique known as the inverse scattering method, to which reference will be made later.   As the KdV equation is first order in time it can only describe uni-directional wave propagation and this, coupled

with the fact that the wave speed is proportional to the amplitude, has a very important consequence. If two well separated solitary waves exist with the larger one to the left of the smaller one, while propagation is to the right, then the larger solitary wave will overtake the smaller one, though as the KdV equation is nonlinear the wave interaction during overtaking will not exhibit the linear superposition properties of linear equations.

In a pioneering paper Zabusky and Kruskal [27], and later Zabusky [28], examined numerically the development of a sinusoidal initial condition for the KdV equation in a finite interval with fixed boundaries and discovered that the initial condition evolved into a train of solitary waves. Furthermore, they discovered that KdV solitary waves preserved their identity after repeated interactions, and because of this particle-like behaviour they called the solitary waves solitons. The only lasting effect after such an interaction was found to be the displacement of a soliton to the left or right relative to the position in which it would have been had no interaction taken place. Subsequently various analytical methods were developed for the exact solution of certain types of initial value problem for the KdV and other nonlinear evolution equations. Detailed accounts of the inverse scattering method and other methods for solving initial value problems for the KdV equation are to be found in a variety of sources [29-33] so no discussion of these topics will be offered here. A typical example of interacting solitons is shown in Fig.9.
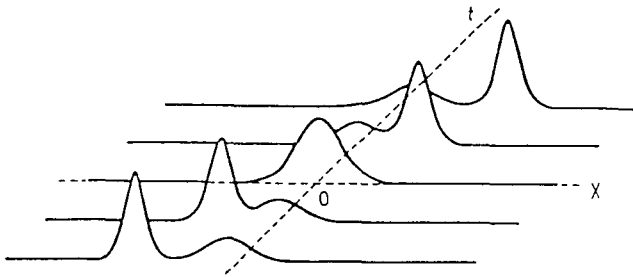
Fig.9 A typical example of two interacting solitions during overtaking

Although the KdV equation is only one of a family of nonlinear evolution equations that possess soliton solutions, we will see that its importance arises from the fact that it governs the asymptotic nature of a wide class of nonlinear dispersive systems of equations. Other nonlinear evolution equations also possess traveling wave solutions though they are not necessarily solitons. The KdVB equation given in Eq.(1.19) that arises in dispersive problems in which dissipation cannot be ignored belongs to this category. We refer to the papers by Halford and Vlieg-Hulstman [34,35] for an interesting study of the integrability problem for such equations.

9. The Reductive Perturbation Method

The reductive perturbation method developed by Taniuti and Wei [36], and also described in detail elsewhere [25,33], is a method by which the asymptotic nature of solutions of very general systems of the form

$$U_t + A(U) + B + \left\{ \sum_{\beta=1}^{s} \prod_{\alpha=1}^{P} \left(H_{\alpha\beta}\partial_t + K_{\alpha\beta}\,\partial_x \right) \right\} U = 0 \qquad (9.1)$$

may be determined.   In the system in Eq.(9.1) U is the n element vector encountered previously, while A, $H_{\alpha\beta}$ and $K_{\alpha\beta}$ are $n \times n$ matrices depending on U, and B is an $n \times 1$ element vector also depending on U.

We shall only consider the case when this system is weakly dispersive, which happens when $B = 0$ and A has at least one real eigenvalue λ, so a wave will propagate governed by the first order system associated with Eq.(9.1) (the first two terms).

The approach is to replace the space coordinate x by a coordinate ξ moving to the right with an appropriate speed c , and to scale the time t in such a way that the solution can be studied for large time.   To accomplish this we first change our time scale from t to $\tau = \varepsilon t$, so that for fixed τ, when ε is small the time t is large.   The coordinate ξ will be taken to be $\xi = \varepsilon^\beta (x - ct)$ where β and c will be determined later.   Thus the coordinate scaling to be adopted is

$$\xi = \varepsilon^\beta (x - ct), \qquad \tau = \varepsilon t. \qquad (9.2)$$

Our objective will be to obtain a perturbation solution in terms of ξ, τ of the form

$$U = U_0 + \varepsilon U_1(\xi, \tau) + \varepsilon^2 U_2(\xi, \tau) + \dots , \qquad (9.3)$$

with U_0 the constant solution of the homogeneous form of Eq.(9.1) ($B = 0$).

Let us first consider the case of a linear equation with pure dispersion of the form

$$u_t + \lambda u_x + k u_{xxx} = 0 . \qquad (9.4)$$

A change of variable $(x, t) \rightarrow (\xi, \tau)$ in Eq.(9.4) leads to the result

$$\varepsilon^\beta (\lambda - c) u_\xi + \varepsilon u_\tau + k\varepsilon^{3\beta} u_{\xi\xi\xi} = 0. \qquad (9.5)$$

The orders of these terms will be balanced with respect to ε if we set $c = \lambda$ causing the first term to vanish identically, and then set $\beta = 1/3$ so the remaining terms are of equal order. Thus to take account of pure dispersion the scaling of ξ, τ must be

$$\xi = \varepsilon^{1/3} \quad \text{and} \quad \tau = \varepsilon t. \tag{9.6}$$

A similar argument determines the ratio of the powers of ε to be used in the case of pure dissipation and, in general, the scaling required to take account either of dissipation or dispersion can be shown to be

$$\xi = \varepsilon^a(x - \lambda t), \quad \tau = \varepsilon^{a+1}t, \quad a = 1/(p\text{-}1) \quad \text{for } p \geq 2, \tag{9.7}$$

where $p = 2$ for dissipation and $p = 3$ for dispersion. The important feature of this scaling is the ratio of a to $a + 1$ rather than their absolute values, and for dissipation

$$a : a+1 = 1 : 2,$$

while for dispersion

$$a : a+1 = 1 : 3,$$

as was found in Eq.(9.6).

The approach we now follow is to develop a perturbation solution for the full nonlinear system in Eq.(9.1) based on the linear scaling just discussed, because for large time this will determine the deviation of the nonlinear system from a related linear one.

Rewriting the system in Eq.(9.1) in terms of derivatives with respect to ξ and τ, and equating corresponding powers of ε gives

$$O(\varepsilon^{a+1}): \qquad (-\lambda I + A_0)\, U_{1\xi} = 0, \tag{9.8}$$

$$O(\varepsilon^{a+2}): \qquad (-\lambda I + A_0)\, U_{2\xi} + U_{1\tau} + \{U_1 \cdot (\nabla_u A)_0\} U_{1\xi}$$
$$+ \sum_{\beta=1}^{s} \prod_{\alpha=1}^{p} \left(-\lambda H_{\alpha\beta\,0} + K_{\alpha\beta 0} \right) \partial^p U / \partial \xi^p = 0. \tag{9.9}$$

In these results the suffix zero indicates that the associated terms are to be evaluated in the constant state solution U_0 while $(\nabla_u A)_0$ is the gradient operator with respect to the elements of U acting on A.

If l and r are the left and right eigenvectors of A_0 corresponding to the eigenvalue λ, so that

$$l(A_0 - \lambda I) = 0 \quad \text{and} \quad (A_0 - \lambda I)r = 0. \tag{9.10}$$

Eq.(9.8) may be solved in the form

$$U_1 = r\,\phi_1(\xi, \tau) + V_1(\tau), \tag{9.11}$$

with ϕ_1 any element of U_1 and V_1 an arbitrary column vector that is a function of τ.

Pre-multiplying Eq.(9.9) by l shows that when solving for $U_{2\xi}$ the compatibility condition is

$$l_1 U_{1\tau} + l_1[V_1 \cdot (\nabla_u A)_0] U_{1\xi} + l \cdot \sum_{\beta=1}^{s} \prod_{\alpha=1}^{p} (-\lambda H_{\alpha\beta\,0} + K_{\alpha\beta 0})\, \partial^p U / \partial \xi^p = 0. \tag{9.12}$$

Assuming the boundary condition $U \to U_0$ as $x \to \infty$ allows us to set $V_1 = 0$, and we find that ϕ_1 satisfies the nonlinear evolution equation

$$\phi_1 + c_1 \phi_1\, \phi_{1\xi} + c_2\, \partial^p \phi_1 / \partial \xi^p = 0 , \tag{9.13}$$

where

$$c_1 = l \cdot \{r \cdot (\nabla_u A)_0\} / (l \cdot r) \tag{9.14}$$

and

$$c_2 = l \cdot \sum_{\beta=1}^{s} \prod_{\alpha=1}^{p} (-\lambda H_{\dot{\alpha}\beta\,0} + K_{\alpha\beta 0}) \cdot r / (l \cdot r). \tag{9.15}$$

When $p = 2$ Eq.(9.13) becomes Burgers equation, and when $p = 3$ it becomes the KdV equation. Thus we see that the scalar evolution equation in Eq.(9.13) governs the asymptotic nature of the entire system in Eq.(9.1) that is associated with the eigenvalue λ. This follows because combining Eq.(9.3) and Eq.(9.11) (in which $V_1 = 0$) we have to order ε that

$$U = U_0 + \varepsilon\, r\, \phi_1(\xi, \tau). \tag{9.16}$$

The method described here is called the reductive perturbation method because it is a singular perturbation method in which the rank of the associated system is reduced.

It is a simple matter to show that the coefficient c_1 is proportional to the expression $(\nabla_u \lambda) \cdot r$, the non-vanishing of which is called the genuine nonlinearity condition that was introduced by Lax[9,37] and developed in a related context elsewhwere[5,38]. This condition is associated with the breakdown of differentiability in a quasilinear hyperbolic system, and when this expression vanishes the characteristic field associated with λ is said to be exceptional. Thus when the hyperbolic mode associated with λ in the first order system derived from Eq.(9.1) is genuinely nonlinear the

coefficient $c_1 \neq 0$, thereby ensuring that Eq.(9.13) governing ϕ_1 is nonlinear (either Burgers equation or the KdV equation). However, if the characteristic field associated with λ is exceptional, Eq.(9.13) becomes linear and a different scaling becomes necessary to determine the nonlinear evolution equation that governs the asymptotic nature of the nonlinear system in Eq.(9.1).

10. Backlund Transformations

The interaction of solitons may be regarded as a form of nonlinear superposition of traveling wave solutions of the KdV equation. More general nonlinear superposition laws can be found for other nonlinear evolution equations with soliton solutions and a constructive method by which to seek them is provided by the use of a Backlund transformation.

A Backlund transformation is a special form of contact transformation that transforms two surfaces with a common point of tangency in one space into two corresponding surfaces with a common point of tangency in another space. The transformation is difficult to define in general, but the essential idea involved can be described as follows. Consider two independent partial differential equations involving the independent variables x and t with one involving the dependent variable u, and the other the dependent variable v, and denote them by

$$F(u) = 0 \qquad \text{and} \qquad G(v) = 0, \tag{10.1}$$

where, in general, these equations are nonlinear. Now suppose that two relationships can be found between u and v of the form

$$H_i(u, v, u_x, v_x, u_t, v_t, \ldots; x,t) = 0, \qquad i = 1,2. \tag{10.2}$$

Then this pair of relationships is said to constitute a Backlund transformation if one of them is integrable with respect to u when $G(v) = 0$, and the function u so obtained is a solution of $F(u) = 0$, and conversely.

A special case arises if it happens that $F = G$, for then u and v satisfy the same Backlund transformation. When this occurs the transformation is called an auto-Backlund transformation. An introduction to Backlund transformations is to be found in the text by Drazin and Johnson[30], while an advanced account with many applications is given in the monograph by Rogers and Shadwick[39]. We now illustrate Backlund transformations by means of two simple classical examples, the first of which involves the Liouville equation

$$\partial^2 u / \partial x \partial y = e^u, \tag{10.3}$$

in which the nonlinearity arises through the term e^u.

Consider the two relationships (the H_i for $i = 1,2$),

$$\partial v/\partial x = \partial u/\partial x + \alpha \exp\{(u + v)/2)\} \, , \partial v/\partial y = -\partial u/\partial y - (2/\alpha)\exp\{(u - v)/2)\}, \qquad (10.4)$$

where $\alpha \neq 0$ is called the Backlund parameter.

The requirement of equality of the mixed derivatives (an integrability condition) in the form

$$\partial^2 v/\partial x \partial y = \partial^2 v/\partial y \partial x \qquad (10.5)$$

leads immediately to the Liouville equation in the form given in Eq.(10.3). Alternatively, the requirement of equality of the mixed derivatives in the form

$$\partial^2 u/\partial x \partial y = \partial^2 u/\partial y \partial x \qquad (10.6)$$

leads to the linear wave equation in the canonical form

$$\partial^2 v/\partial x \partial y = 0. \qquad (10.7)$$

Thus the general solution of the Liouville equation, which is nonlinear, can be found by transforming the general solution of the linear wave equation.

As a final example, if we consider the Backlund transformation

$$\partial v/\partial t = u^2 v/(4\eta) - (v/2)\partial u/\partial x \, , \; \partial v/\partial x = -1/(2\eta)uv, \qquad (10.8)$$

the imposition of the equality of mixed derivatives in the form

$$\partial^2 u/\partial t \partial x = \partial^2 u/\partial x \partial t \qquad (10.9)$$

leads to the linear heat equation
$$\partial v/\partial t = \eta \, \partial^2 v/\partial x^2, \qquad (10.10)$$

while the imposition of the equality of mixed derivatives in the form

$$\partial^2 v/\partial t \partial x = \partial^2 v/\partial x \partial t \qquad (10.11)$$

leads to Burgers equation
$$u_t + uu_x = \eta u_{xx}. \qquad (10.12)$$

This result is, of course, simply the one obtained by the Hopf-Cole transformation given in Section 7.

We conclude by remarking that using a Backlund transformation for the KdV equation, together with the invariance of the equation under a Galilean transformation, it is possible to generate a hierarchy of soliton solutions, starting only from one known solution but using two different Backlund parameter values[30,39]. These may all be regarded as nonlinear superposition principles, and when a Backlund transformation can be found the same approach extends to other evolution equations possessing soliton solutions.

11. Traveling Wave Solutions for the mKdV Equation

The fact that a nonlinear evolution equation possesses a solitary wave solution does not necessarily mean that such a solution is a soliton. Unless a soliton solution can be found explicitly, the existence of such solutions to an arbitrary nonlinear evolution equation is related to the possibility that the equation can be solved by the inverse scattering transform. This, in turn, leads to the conjecture that soliton solutions exist if the equation possesses what is called the Painleve property. The ideas involved in this integrability question have been developed at some length in a number of papers, though the conjecture itself has still to be either proved or disproved. For a detailed account of the approach involved we refer to the fundamental paper by Weiss, Tabor and Carnevale[40]. Rather than pursue this topic here we choose instead to present a simple method by which a traveling wave solution can be found to a modification of the KdV equation introduced earlier.

In the study of applications of the KdV equation[25], which for the purposes of this Section we choose to write in the form

$$u_t + 6auu_x + cu_{xxx} = 0, \tag{11.1}$$

there also arises the modified KdV (mKdV) equation

$$u_t + 6bu^2u_x + cu_{xxx} = 0. \tag{11.2}$$

We now describe the simplest of several different approaches for the determination of a traveling wave solution to the combined KdV and mKdV equations

$$u_t + 6auu_x + 6bu^2u_x + cu_{xxx} = 0. \tag{11.3}$$

Details of alternative approaches and of the use of the Painleve property to conclude that a certain higher order KdV equation is non-integrable (cannot be solved by the inverse scattering transform) can be found elsewhere[41,42].

We use a direct approach to the determination of a traveling wave by seeking a solution of the form $u = u(\zeta)$, where

$$\zeta = kx - \omega t, \tag{11.4}$$

with k and ω constants to be determined. Substitution of Eq.(11.4) into Eq.(11.3) followed by integration yields

$$-\omega u + 3kau^2 + 2kbu^3 + ck^3 u'' = K, \tag{11.5}$$

where K is a constant of integration.

Based on the known form of traveling wave solutions of the KdV equation and the mKdV equation we now conjecture that a traveling wave solution of Eq.(11.3) is of the form

$$u(\zeta) = A + B \operatorname{sech}^n \zeta, \tag{11.6}$$

where constants A and B have yet to be determined.   Thus, for any choice of the integer n, the four constants k, ω, A and B must now be determined if the solution is to be of the given form.

Setting the integration constant equal to zero and substituting Eq.(11.6) into Eq.(11.5) shows that only when $n = 1$ can a system of four independent simultaneous equations be obtained for the four unknown constants.   When $n \geq 2$ five independent equations are obtained connecting the four unknown constants, and only trivial solutions are then possible.   For the case $n = 1$ we have

$$-\omega + 3kaA + 2kbA^2 = 0,$$

$$-\omega + 6kaA - 6kbA^2 + k^3 c = 0,$$

$$a + 2bA = 0,$$

$$bB^2 - k^2 c = 0. \tag{11.7}$$

These equations have the solution

$$k = \pm a\sqrt{[1/(2bc)]}, \ B = \pm k\sqrt{(c/b)}, \ A = -a/(2b), \ \omega = -ka^2/b. \tag{11.8}$$

Substituting these results in the traveling wave solution gives

$$u(x,t) = a\{ \pm\sqrt{(1/(2b^2))} \operatorname{sech}(\pm a\sqrt{[1/(2bc)]}(x + (a^2/b)t)) - 1/(2b)\}. \tag{11.9}$$

It follows from Eq.(11.8) that when $bc > 0$ Eq.(11.9) is a solitary wave solution of the combined KdV and mKdV equations.   This result is similar to one given by Coffey [43].

In conclusion, we observe that neither the sech^2 - type solution of the KdV traveling wave nor the sech - type solution of the mKdV equation traveling wave can be derived from Eq.(11.9) by letting either $a \rightarrow 0$ or $b \rightarrow 0$.

12. References

1. M.J.Lighthill, *J.Inst.Math.Appl.* **1**(1965),1 - 28.
2. W.D.Hayes, *Proc.Roy.Soc.Lond.* **332**A(1973),199-221.
3. J.D.Cole, *Q.J.Math.* **9**(1951),225-236.
4. E.Hopf, *Comm Pure Appl.Math.* **3**(1950),201-230.
5. A.Jeffrey,*Quasilinear Hyperbolic Equations and Waves*, Research Note in Mathematics **5** (Pitman, London, 1976).
6. R.Courant and D.Hilbert, *Methods of Mathematical Physics*, Vol.II (Interscience, New York, 1962).
7. P.R.Garabedian, *Partial Differential Equations*, (Wiley, New York, 1964).
8. R.Courant and K.O.Friedrichs, *Supersonic Flow and Shock Waves* (Interscience, New York, 1948).
9. P.D.Lax, *Hyperbolic Systems of Conservation Laws and the Mathematical Theory of Shock Waves*, Regional Conference Series in Applied Mathematics **11** (SIAM Publications, Philadelphia, 1973).
10. J.G.Glimm and P.D.Lax, *Decay of Solutions of Systems of Nonlinear Hyperbolic Conservation Laws*, Memoirs of Am.Math.Soc. **101** (Rhode Island, 1970).
11. J.Smoller, *Shock Waves and Reaction Diffusion Equations*, (Springer Verlag, Berlin, 1983).
12. R.J.LeVeque, *Numerical Methods for Conservation Laws* (Birkhauser Verlag, Boston,1990).
13. J.Glimm, *Comm Pure Appl.Math.*, **18**(1965),697-715.
14. B.J.Lucier, *SIAM J.Num.Anal.*, **22**(1985),1074-1081.
15. A.J.Chorin, *J.Comput.Phys.*,**22**(1976),517-533.
16. D.H.Wagner, *SIAM J.Math.Anal.*, **14**(1983),534-559.
17. T.Zhang and L.Hsiao, *The Riemann Problem and Interaction of Waves in Gasdynamics*, Monographs in Pure and Applied Mathematics **41**(Pitman-Longman,London, 1989).
18. T.Zhang and Y.X.Zheng, *SIAM J.Math.Anal.*, **21**(1990),593-630.
19. J.Burgers, *Adv.Appl.Mech.***1**(1948),171-199.
20. A.R.Forsyth, *Theory of Differential Equations* Part IV, (Camb.Univ.Press, London,1906, also a Dover Reprint, 1959).
21. H.S.Carslaw and J.C.Jaeger, *Conduction of Heat in Solids* 2nd. Ed. (Clarendon Press, Oxford, 1965).
22. J.Crank, *The Mathematical Theory of Diffusion,*(Oxford University Press, London, 1955).

23. G.B.Whitham, *Linear and Nonlinear Waves,* (Wiley,New York,1974).
24. D.J.Korteweg and G.deVries, *Phil.Mag.London* (5), **39**(1895),422-443.
25. A.Jeffrey and T.Kakutani, *SIAM Appl.Math.Rev.,***14**(1972),582-643.
26. M.Rahman, *Water Waves,*(Oxford University Press,London,1995).
27. N.J.Zabusky and M.D.Kruskal, *Phys.Rev.Lett.,* **15**(1965),240-243.
28. N.J.Zabusky, *A Synergetic Approach to Problems of Nonlinear Dispersive Wave Propagation and Interaction, in Nonlinear Partial Differential Equations* ed.W.F.Ames (Academic Press, 1965),223-258.
29. M.J.Ablowitz and H.Segur, *Solitons and the Inverse Scattering Transform,* SIAM Studies in Appl.Math.,4(Philadelphia,1981).
30. P.G.Drazin and R.S.Johnson, *Solitons: an Introduction* (Cambridge Univesity Press, 1989).
31. A.C.Newall, *Solitons in Mathematics and Physics,* SIAM Studies in Appl.Math. (Philadelphia,1985).
32. G.L.Lamb Jr., *Elements of Soliton Theory* (Wiley, New York,1980).
33. A.Jeffrey and T.Kawahara, *Asymptotic Methods in Nonlinear Wave Theory* (Pitman-Longman, London, 1982).
34. W.D.Halford and M.Vlieg-Hulstman, *J.Phys.A:Math.Gen.,***25**(1992),2375.
35. M.Vlieg-Hulstman and W.D.Halford, *Wave Motion* **14**(1991),267.
36. T.Taniuti and C.C.Wei, *J.Phys.Soc.Japan* **24**(1968),941-946.
37. P.D.Lax, *Comm. Pure Appl. Math.***10**(1957),537-566.
38. A.Jeffrey, *Arch.Rat.Mech.Anal.***14**(1963),27-37.
39. C.Rogers and W.F.Shadwick, *Backlund Transformations and their Applications,* Maths. in Sci. and Eng. Vol **161**(Academic Press, New York,1982).
40. J.Weiss, M.Tabor and G.Carnevale, *J.Math.Phys.,***24**(1983),522-526.
41. A.Jeffrey and S.Xu, *Int.J.Nonlinear Mech.,***24**(1989),425-429.
42. A.Jeffrey, in *Partial Differential Equations with Real Analysis,* Research Note in Mathematics **262** ed. A.Jeffrey and H.Begehr (Pitman, London,1992),1-12.
43. M.W.Coffey, *SIAM J.Appl.Math.,***50**(1990),1108-1111.

Subject Index

Author Index

Acoustic Interactions with Submerged Elastic Structures

With a foreword by Hans A. Bethe

Part III: Acoustic Propagation and Scattering, Wavelets and Time Frequency Analysis

Editors

Ardéshir Guran, Adrianus De Hoop, Dieter Guicking & Francesco Mainardi

The interaction of acoustic fields with submerged elastic structures is being investigated at various institutions and laboratories worldwide with ever-increasing sophistication of modeling, experiment and analysis. This book offers the reader a sampling of contributions from these research centers that *represent the present state-of-the-art in the study of acoustic-elastic interactions, being on the cutting* edge of these investigations. The topics covered in this volume include the description of acoustic scattering from submerged elastic objects and shells by the resonance scattering theory (RST), and the interpretation of these phenomena in terms of interface waves. It also includes the use of this theory for the purpose of inverse scattering, i.e. determination of the scattering objects' properties from the received signals. The problem of acoustically excited waves in inhomogeneous and anisotropic materials, and of inhomogeneous propagating waves, is considered. Vibrations and resonances of elastics shells, including shells with various kind of internal attachments, are analysed. Acoustic scattering experiments are described in the time domain, and on the basis of the Wigner-Ville distribution. Acoustic propagation in the water columns over elastic boundaries is studied experimentally both in the laboratory and in the ocean, and is analysed theoretically. A variety of models for oceanic sound propagation is discussed, including matched field processing. Applications of the theory of wavelets and solitons are presented. A comprehensive picture of these complex phenomena and other aspects is presented in this book by researchers who are experts in each of these domains, giving up-to-date accounts of the present state of the field in all these aspects. Because of the large number of contributions to the present volume, it had to be subdivided into several parts of which this is Part III.

This book shows how underwater acoustics and wave propagation is currently utilized and investigated. It will be of interest to engineers, physicists and applied mathematicians.